Afar, Ethiopia: a local seismic survey

William G. Rigden

AFAR, ETHIOPIA: A LOCAL SEISMIC SURVEY

by

William G. Rigden

A thesis submitted for the degree of
Doctor of Philosophy at the
University of Durham

Department of Geological Sciences March 1981

DECLARATION

I declare that this thesis is my own work, with the exception of Appendix 3 which was researched in equal partnership with J.E.G. Savage.

No part of the material of this thesis, other than Appendix 3, has previously been submitted for a degree in this or any other university.

W.G. Rigden
University of Durham
March, 1981

ABSTRACT

A network of four independently-recording seismic stations was operated by the University of Durham in South-Central Afar during 1973 and 1974. Each station consisted of a three-component set of seismometers, whose signals were recorded on to magnetic tape. This study concerns local earthquakes recorded from February to September, 1974.

250 earthquakes were located from relative arrival times of P and S phases using an optimized, laterally homogeneous, 4-layer structural model. Upper crustal P-wave velocities are found to be 4.4 ± 0.2 km s^{-1} (0 to 4.5 km depth) and 6.2 ± 0.1 km s^{-1} (4.5 to 11 km). Deeper structure is poorly constrained. Anomalous upper mantle exists, with low seismic velocity (V_p about 7.4 km s^{-1}) and raised Poisson's ratio (0.31). S_n is transmitted. 8.0 km s^{-1} upper mantle cannot exist above about 43 km depth.

Earthquake focal depths within Afar do not exceed 5 km. Epicentres correlate well with Recent axial volcanism. Spatial epicentral patterns reflect intense regional NW-SE extensional faulting. One line of epicentres shows the NNE-SSW trend of the Main Ethiopian rift. Focal mechanisms are very poorly constrained, but are consistent with NW-SE strike-slip or normal faulting, or with NE-SW dextral transcurrent faulting.

Signal duration magnitude and Richter local magnitude

scales are defined for Afar. Frequency-magnitude b-coefficient values are Ø.87 ± Ø.Ø5.

The three-component records are polarization filtered, a technique previously applied only to teleseisms. The performance of the filters is discussed. Azimuths and apparent angles of incidence of events are determined from their first arrivals at a single recording station. Hypocentres are then obtained by ray tracing.

Earthquake frequency spectra are computed through the fast Fourier transform. The spectra are dominated by the effects of the superficial crust below the receivers. Crustal transfer ratios are discussed. Increased attenuation is demonstrated below the Tendaho graben. Seismic source parameters are calculated using BRUNE's (1970) method.

All results are consistent with diffuse NE-SW crustal extension. It is concluded that well-defined spreading axes do not yet exist.

ACKNOWLEDGEMENTS

When I began this work I was employed as a student research assistant in the Department of Geological Studies, Durham. I thank Prof. Martin Bott and Dr. Roger Long (my supervisor) for the opportunity to work in the department.

I am grateful to all who helped me during difficult times in Ethiopia. Amongst these were Ato Biretti of the Awash Valley Authority, Mr. David Blackburn of Hunting Engineering Ltd., Mr. Jim Cleland and Mr. and Mrs. Malcolm Valentine of Tendaho Plantation Shares Company, Father Pierre Gouin and the staff of the Addis Abeba Geophysical Observatory, and Dr. Melake Mengesha and his staff at Alemaya College of Agriculture. I was given free access to unpublished material by Father Gouin and by Ato Seife Berhe of the Ethiopian Ministry of Mines.

I have had helpful discussions with former student colleagues in Durham, particularly Dr. Richard Backhouse, Mr. Hugh Ebbutt and Dr. John Savage. I am extremely grateful to John, to Dr. Long, to Dr. Ron Girdler of Newcastle University, and to Mr. Peter Marshall and Dr. Hal Thirlaway of UKAEA, Blacknest, who have willingly read all or part of this typescript. They have greatly encouraged me, and their constructive criticism has led to many improvements.

This thesis has been largely drafted in the Durham University Science Library, where the staff have attended

cheerfully and efficiently to my requests for work-space and obscure publications. I am also very grateful for the courtesy of Mr. Brian Lander and the staff of the Computer Unit, who allowed me terminal facilities to type and prepare my own text.

I thank my employer, Mr. Derek Handforth, manager of Lindley Lodge Hollowford Centre, for giving me leave of absence to write up this work. Most of all I thank my parents, on whose continuous support I have always been able to rely.

CONTENTS

CHAPTER 3 PRELIMINARY PROCESSING AND EXAMINATION OF FIELD TAPES

CHAPTER 4 HYPOCENTRAL LOCATIONS FROM SEISMIC ARRIVAL TIMES

CHAPTER 5 MAGNITUDES

CHAPTER 6 THREE-COMPONENT ANALYSIS

CHAPTER 7 SPECTRAL ANALYSIS

CHAPTER 8 SPATIO-TEMPORAL CHARACTERISTICS OF ESP EVENTS, AND THEIR RELATION TO REGIONAL TECTONIC PROCESSES

CHAPTER 9 DISCUSSION

APPENDICES

LIST OF FIGURES

LIST OF TABLES

The heavens are telling the glory of God;
  and the firmament proclaims his handiwork.
Day to day pours forth speech,
  and night to night declares knowledge.
There is no speech, nor are there words;
  their voice is not heard;
yet their voice goes out through all the earth,
  and their words to the end of the world.

(Psalm 19:1, RSV)

By faith we understand that the world was created by the word of God, so that what is seen was made out of things which do not appear.

(Hebrews 11:3, RSV)

As for the earth, out of it comes bread;
  but underneath it is turned up as by fire.

(Job 28:5, RSV)

COLOUR COMPOSITE LANDSAT IMAGES

(reproduced from SHORT et al,1976)

(A) Ethiopian Rift system. Note the dark areas of Recent axial volcanics in N Afar; the curvilinear faulting of SE Afar; and the regional fault trends.

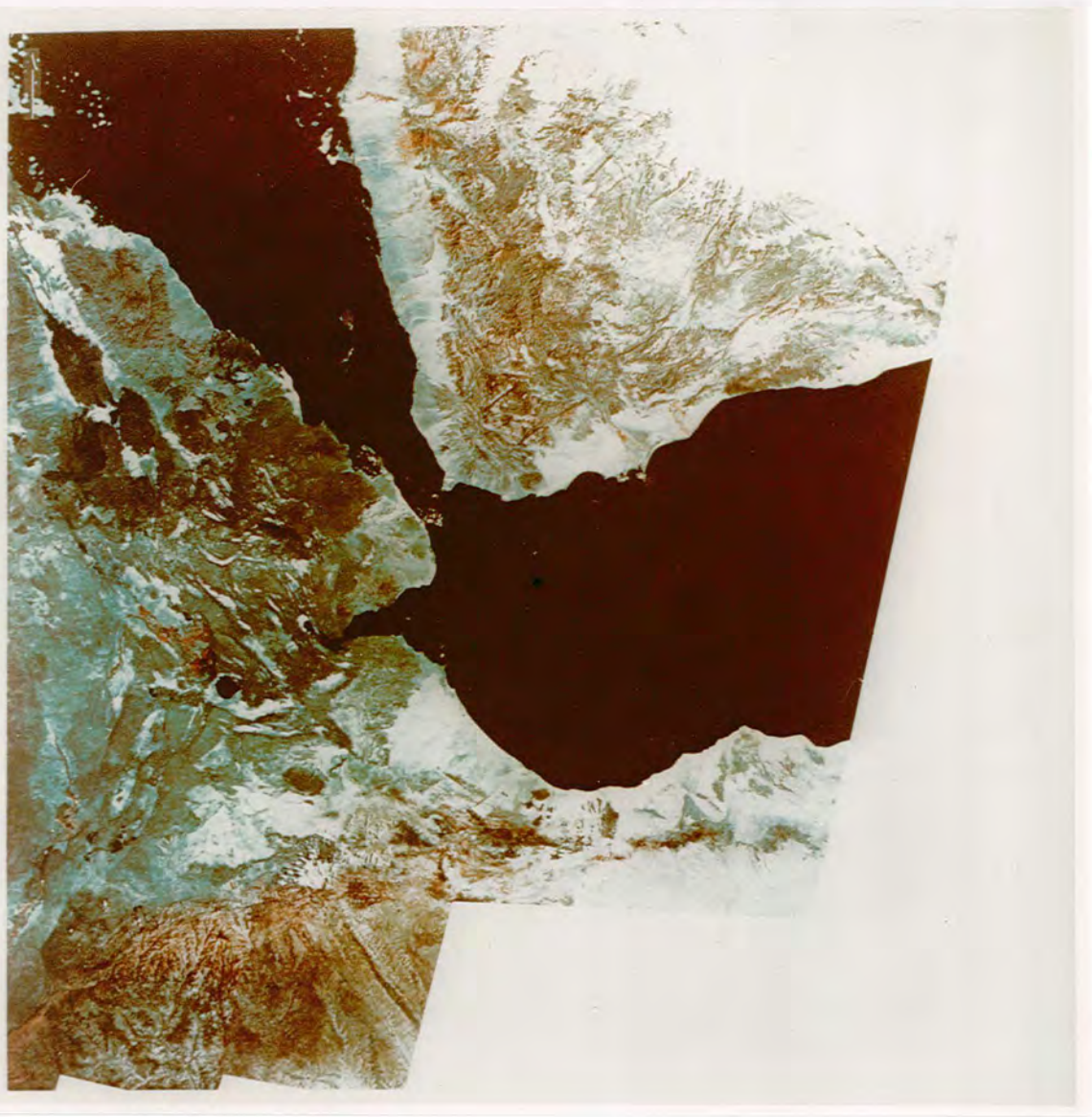

COLOUR COMPOSITE LANDSAT IMAGES

(reproduced from SHORT et al,1976)

(B) Afar. The Gulf of Tadjoura (V7), Lake Abhe (K15), Lake Gamari (I1Ø) and the Gawa graben (G2) are well shown. The ESP network was centred at A9. The Tendaho graben (A8-G1Ø) is demarcated by the (red) areas of cotton, corn and sesame irrigated by the Awash river.

EXPLANATORY NOTE ON TERMINOLOGY

The word 'Afar', meaning 'the free', is correctly applied only to an ethnic group (DAKIN et al,1971; GERSTER,1976). The region termed 'Afar' by earth scientists is generally known as 'the Danakil desert' or 'Dancalia'. 'Afar' is used here in the now accepted scientific sense, as defined in Section 1.1. 'Danakil Depression' refers only to that northern part of Afar situated between the North Danakil block (or Arrata microhorst) and the Western Ethiopian plateau escarpment.

The term 'Ethiopian rift system' has been coined to denote Afar and the adjoining rift structures: the Red Sea, the Gulf of Aden and the Main Ethiopian rift.

The spelling of Ethiopian place names is not standardised. At the request of the Ethiopian Awash Valley Authority, the spellings adopted here follow the guidelines laid down by the Imperial Government of Ethiopia in 1973, except where these are in conflict with recognised scientific usage.

CHAPTER 1

AFAR: A REVIEW

1.1 Introduction

Afar is the low-lying, triangular region of north-east Ethiopia and west Djibouti (formerly T.F.A.I., formerly French Somaliland) extending from 10° to 15°N and from 40° to 43°E (Figure 1.1.1). It forms the apex of the Ethiopian rift system, which is linked through the Red Sea and Gulf of Aqaba to the Levantine rift system and through the Gulf of Aden to the Carlsberg Ridge of the Indian Ocean. South West Afar funnels into the Main Ethiopian rift, the most northerly section of the East African rift system.

The particular geophysical significance of Afar is that it is at least partially composed of new oceanic crust. This has been shown by petrological and radiochemical analysis of its lavas (BARBERI et al,1975a; BARBERI and VARET,1977), and by other data reviewed below. Afar is unique among land areas as an accessible testing ground for hypotheses of ocean formation and the initiation of sea-floor spreading. This study examines the problematical structure and tectonics of Afar through a local seismicity investigation.

Afar is surrounded by high plateaux of continental basement. To the west and south east, the Western Ethiopian and South Eastern (Somalian) plateaux have elevations

FIGURE 1.1.1

LOCATION OF THE ETHIOPIAN RIFT SYSTEM

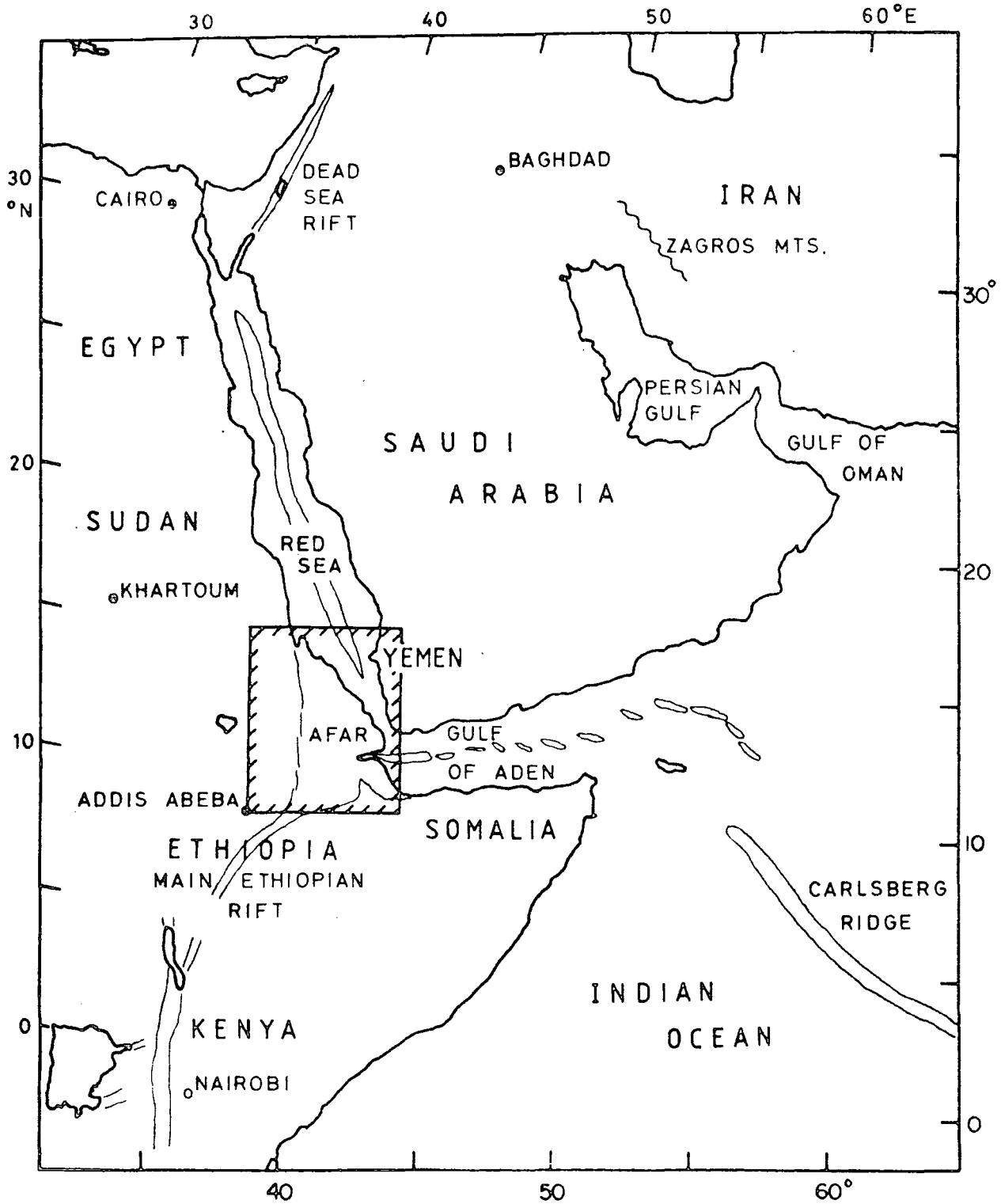

exceeding 4000 m and 3000 m respectively. Their margins are down-faulted towards Afar. East of the Red Sea, the Yemen plateau rises to 4000m and is geologically similar. A further continental basement feature, the North Danakil block, separates Northern Afar from the Red Sea and forms part of its north-east margin (Figure 1.1.2). The elevation of Afar ranges from -125m in the Danakil Depression to +600m in the south west. The depth of the Danakil Depression is the more impressive as it has an infill of at least 2.2 km of evaporites (BEHLE et al,1975).

Afar is largely floored by stratoid basalts, extruded within the last 4 Myr, which conceal the nature of the underlying crust. In places, especially in southern Afar, the basalts are themselves overlain by Quaternary sediments. They are intensely structurally deformed, chiefly by Lower-Middle Pleistocene faulting distributed throughout the width of Afar (e.g. MOHR,1967a,1972a; TAZIEFF,1971,1972; SCHAEFER,1975). The predominance of normal faults and the presence of open fissures, resembling Icelandic 'gja', indicate extension, which is consistent with the separation of Arabia from Africa. Current extension is concentrated along axial basaltic volcanic ranges, disposed 'en échelon' as spreading ridge segments (see Figure 1.4.2).

Many faults are currently active. New tensional features and lava extrusions, accompanied by earthquakes, have appeared during the last 15 years (DAKIN et al,1971; ALLARD et al,1979). The dominant fault trends are controlled by the margins of the bounding Arabia, Somalia,

FIGURE 1.1.2

AFAR AND ITS MARGINS

(for details of volcanic ranges, see Figure 1.4.2)

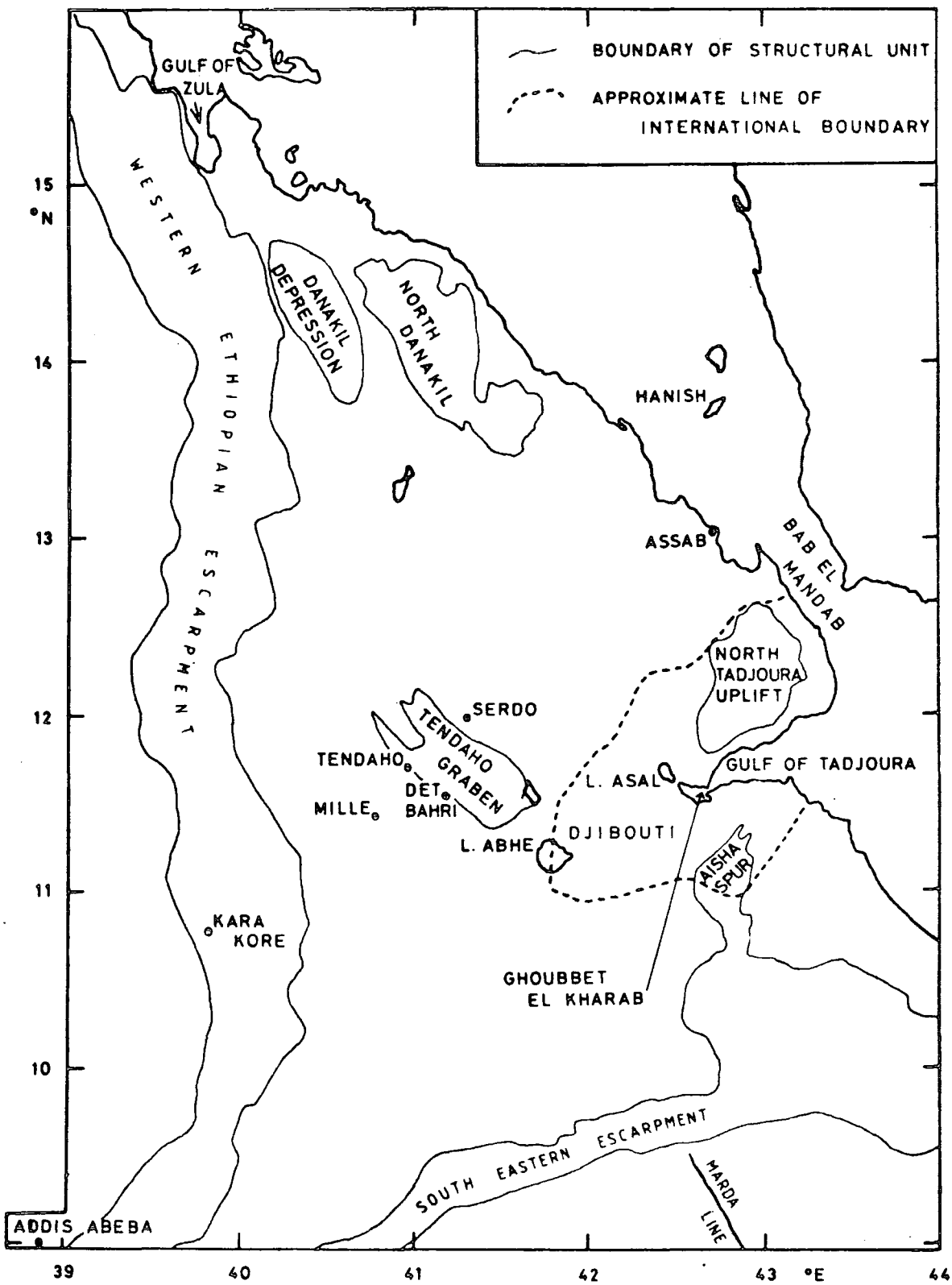

Nubia and North Danakil blocks (Figure 1.1.3). Throughout Northern and Central Afar their direction is NW-SE (Nubia-Danakil, Arabia-Somalia plate pairs), and the NE-SW and NNE-SSW faults that occur show shear movements (e.g. CHRISTIANSEN et al,1975). They are associated with Gulf of Aden transforms and not, as widely suggested following MOHR (1967b,1968a, but see 1972b), with the NNE-SSW trend of the East African rift system. NNE-SSW tensional features are confined to South West Afar (Nubia-Somalia). There is no evidence for shear in the Main Ethiopian and Kenya rifts, where geological mapping, fault plane solutions and volcanism suggest crustal tension (MOHR,1967a; BAKER and WOHLENBERG,1971).

Complex mosaics of intersecting and arcuate faults within Afar have been mapped in detail (e.g. MOHR,1968b,1971b; BARBERI and VARET,1977, fig.9). They are now usually interpreted as the surface expression of transform faults, as first proposed by TAPPONNIER and VARET (1974) and COURTILLOT et al (1974).

1.2 Plate Tectonic Setting

1.2.1 Regional Setting

Arabia has been separating from Africa by continental drift during the Cainozoic. The existence of oceanic crust beneath the Red Sea and Gulf of Aden has been shown by geological (e.g. WHITEMAN,1968; BEYDOUN,1970) and palaeomagnetic (TARLING,1970) data from the continental

FIGURE 1.1.3

CONTINENTAL BLOCKS (HATCHED) INFLUENCING THE TECTONICS OF AFAR

(Dominant fault trends are indicated schematically)

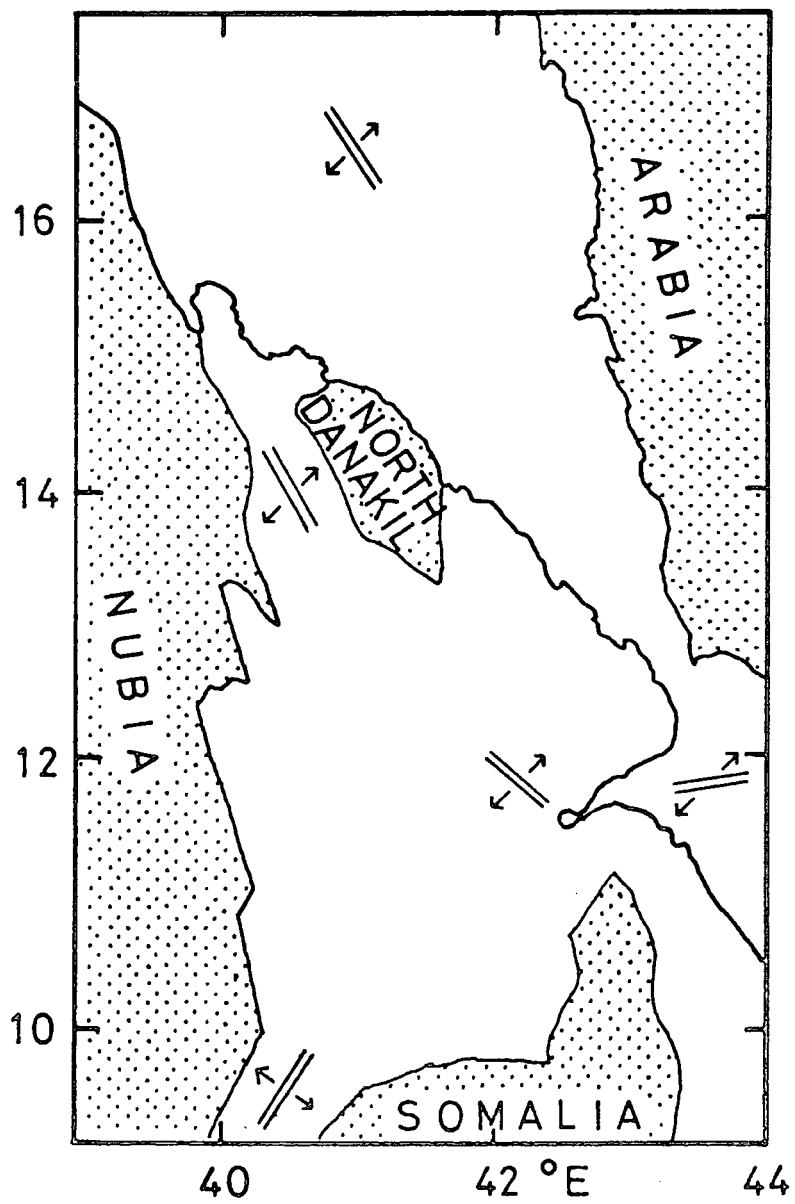

plateaux; and by marine studies of gravity, bathymetry, seismic velocities and the geomagnetic field (DRAKE and GIRDLER,1964; LAUGHTON,1966a,b,1970; VINE,1966; PHILLIPS et al,1969; ROBERTS and WHITMARSH,1969; LAUGHTON et al,1970; PHILLIPS,1970; BACKER et al,1975; PLAUMANN,1975; ROESER,1975; SEARLE and ROSS,1975; COURTILLOT et al,1980; GIRDLER et al,1980; and others). The geological histories of the Dead Sea rift (FREUND et al,1970; BEYTH,1978), the Gulf of Aqaba (ALLAN and PISANI,1966) and Iran (GIRDLER,1966; FORSTER,1976; JUNG et al,1975) also impose constraints on regional spreading hypotheses. There is agreement on two major points: the direction of relative motion between Arabia and Africa is NE-SW; and the axial troughs of the Red Sea and Gulf of Aden are oceanic and have been formed during a spreading phase initiated 5 to 3 Myr ago and still active.

The Gulf of Aden is oceanic to within a few kilometres of the Arabian and Somali coastlines. Large-amplitude, short-wavelength magnetic anomalies, typically oceanic, exist but their interpretation is ambiguous. Sea-floor spreading may have been occurring continuously over the past 10 Myr at an approximate (half-) spreading rate of 0.9 cm yr^{-1} (LAUGHTON et al,1970; COURTILLOT et al,1980); or may have occurred discontinuously in two (GIRDLER and STYLES,1978) or more (GIRDLER et al,1980) episodes commencing in the Oligocene or Upper Eocene, or even in the uppermost Cretaceous.

The nature of the main trough of the Red Sea, where the

structures are obscured by several kilometres of evaporites (HUTCHINSON and ENGELS,1972), is less certain. It has been variously interpreted as largely oceanic (e.g. DAVIES and TRAMONTINI,1970; McKENZIE et al,1970; ROESER,1976), largely continental (DRAKE and GIRDLER,1964; HUTCHINSON and ENGELS,1972), or attenuated continental with basaltic intrusions. The last possibility is supported by considerable evidence for dyke injection or even fossil spreading along rifts parallel to the axial trough, particularly near the present coastline (KNOTT et al,1966; TAZIEFF,1968; PHILLIPS et al,1969; FRAZIER,1970; LOWELL and GENIK,1972; GARSON and KRS,1976; GASS,1977).

Alternatively, Red Sea main trough magnetic anomalies are consistent with an oceanic crust largely formed by sea-floor spreading during the Oligocene (GIRDLER and STYLES,1974) or Miocene (GIRDLER and STYLES,1976); or with several episodes of spreading since the early Miocene (GASS,1977). Which of these models is to be preferred depends on the interpretation of independent geological data, summarised by Gass and by GIRDLER et al (1980).

Attempts have been made to determine the poles of rotation between plate pairs from sea-floor spreading rates, bathymetric fits, transform fault trends and earthquake slip vectors. Calculations for the Gulf of Aden (i.e. Arabia - Somalia) have resulted in the same pole, within 95% confidence limits, whether obtained from a coastline fit (LE PICHON,1968), magnetic anomaly data (LAUGHTON et al,1970), continental shelf bathymetry (LAUGHTON,1966b, 500-fathom

isobars; BEYDOUN,1970) or from the Plio-Pleistocene opening of the axial trough (CHASE,1978). The 'Le Pichon' pole, at 26.5°N, 21.5°E, has been most widely quoted. Thus although the rate of spreading across the Gulf of Aden may have varied, its direction has remained constant and is probably strongly stabilised by the whole Aqaba - Levant shear system.

For Arabia-Nubia, fits of the Red Sea coastlines (McKENZIE et al,1970) and of lines of constant offshore distance (FREUND,1970; GIRDLER and DARRACOTT,1972) consistently indicate a pole at approximately 36.5°N, 18.0°E. This pole is consistent with the trend of transform faults mapped in detail by BACKER et al (1975). (Models proposing widely varying poles (e.g. ALLAN,1970; BAKER,1970) are quite inconsistent with more recent data). The direction of opening of the Northern and Central Red Sea has therefore remained constant. Spreading in the Southern Red Sea has been affected by the Afar microplates and cannot be explained at a regional level.

The East African rift system has commonly been regarded as the third arm of a three-plate system (Arabia - Nubia - Somalia) (Figure 1.1.3). This plate geometry permits movement of the Horn of Africa relative to Nubia in response to extension across the Ethiopian and Kenya rifts. Rotation poles for Nubia - Somalia can be inferred from the Nubia - Arabia and Somalia - Arabia poles. The results are inconsistent and sometimes nonsensical (ROBERTS,1969; MUNSTER and JORDAN,1978) and are subject to

gross error (see discussions by AL-CHALABI,1971; GIRDLER and DARRACOTT,1972; CHASE,1978).

Nubia - Somalia separations of 50 km or more (McKENZIE et al,1970; MOHR,1971a; and by implication LE PICHON and FRANCHETEAU,1978) are inconsistent with geological evidence, which shows that crustal extension across the Ethiopian rift cannot exceed 10 km (BAKER and WOHLENBERG,1971; MOHR,1972a). There is no field evidence for major shear along the East African rift, as proposed by GASS and GIBSON (1969), BAKER (1970) and MOHR (1971a). The dominant tectonic stress is tensional, and is oriented approximately WNW-ESE, as is evident from surface faulting (e.g. GIBSON and TAZIEFF,1970; MEYER et al,1975) and suggested by earthquake fault plane solutions (McKENZIE et al,1970). Within the Ethiopian rift there is no evidence for oceanic crust, except in the development of the Herta Ale and Issa graben of southernmost Afar during the past 1 Myr (CHRISTIANSEN et al,1975; SCHAEFER,1975).

Since the separation of Somalia from Nubia is seen to be minimal, two-plate (Africa, Arabia) tectonic models (LE PICHON and HEIRTZLER,1968; GASS and GIBSON,1969; MUNSTER and JORDAN,1978) are sufficient. They imply a common evolutionary history for the Red Sea and Gulf of Aden that has not yet been convincingly demonstrated, although GIRDLER and STYLES (1978) have hypothesised the formation of both main troughs during a spreading phase 29 to 16 Myr ago. The discrepancy between the rotation poles for Arabia - Somalia (26.5°N, 21.5°E) and Arabia - Nubia (36.5°N, 18.0°E) exceeds

reasonable estimates of their errors (e.g. CHASE,1978). This is not unexpected if a significant part of the separation across the Red Sea is due to continental crustal attenuation and dyke injection along more than one NW-SE or NNW-SSE axis. BARBERI et al (1972a) are correct in asserting that "The Red Sea and the Gulf of Aden constitute one and the same oceanic megastructure. The main Ethiopian rift, on the contrary, is a continental structure and merely runs into an oceanic one."

1.2.2 Local Setting

Pre-drift reconstructions which close the Gulf of Aden and the Red Sea require a substantial overlap of the Yemen basement rocks on to Afar. This is a fundamental problem which has long been recognised, and has seemed to imply that much of Afar must be floored by new oceanic crust.

The Danakil block on the eastern margin of Afar, and the Aisha block south of the Gulf of Tadjoura, are continental (MOHR,1967a). Further, field observations around the Afar margins indicate that the younger post-rift volcanics and sediments normally rest on the older sialic rocks with subhorizontal or gently dipping unconformity (MORTON and BLACK,1975). This suggests that the total extent of continental basement (of which small splinters are observed up to 60 km from the Western Ethiopian escarpment (MOHR,1967a; TAZIEFF et al,1972)) beneath Afar is considerably greater than its surface outcrop. It is likely that much of the extension that took place across Afar

before 5 to 3 Myr ago was accommodated by attenuation of continental crust, in which case the theory of rigid plate tectonics has limited application.

The remainder of this section refers to the subsequent spreading. South of 16°N the Red Sea axial trough becomes less distinct and volcanism is more alkaline (LAUGHTON et al,1970; BACKER et al,1975). Southern Red Sea spreading decreases about a pole of rotation located to the south (ROESER,1975; RICHARDSON and HARRISON,1976; GIRDLER and STYLES,1974,1976; LE PICHON and FRANCHETEAU,1978), and is progressively taken up west of the Danakil block through the 'en échelon' Recent axial volcanic ranges of Northern and Central Afar (e.g. TAZIEFF et al,1972; BARBERI and VARET,1977). The North Danakil (or Arrata) platelet rotates anticlockwise as a hinge between the Gulf of Zula and the Hanish islands, as attested by palaeomagnetic data (BUREK,1970,1974,1978; SCHULT,1975) and by the comparative geology of the North Danakil block and the Western Ethiopian plateau margin (e.g. MOHR,1967a).

The North Danakil platelet does not extend southward to the Gulf of Tadjoura, as drawn on most maps prior to 1975, but terminates at or near the Bidu - Hanish line (Figure 1.4.2), with North Tadjoura now generally considered as an oceanic accretion on to the Arabian plate. The geological evidence for this is compelling, and has been summarised by MARINELLI and VARET (1973) (and briefly, in English, by BARBERI and VARET,1975). The geophysical evidence is presented in Section 1.5. Further, the Strait of Bab el

Mandeb is aseismic. The axial channel of deeper water shown on bathymetric maps (LAUGHTON et al,1970; ROESER,1975) is largely infilled by sediments, suggesting that any current spreading is very slow.

GIRDLER and STYLES (1978) have interpreted aeromagnetic anomalies over the Western Gulf of Aden in terms of a subsidiary spreading axis branching towards the Strait of Bab el Mandeb. This conclusion has been specifically repudiated by COURTILLOT et al (1980), interpreting a more detailed aeromagnetic survey. It is generally agreed that the major tectonic link between the Red Sea and the Gulf of Aden lies through Afar and the Gulf of Tadjoura.

In order to explain the Yemen overlap the continental Aisha block was assumed on earlier spreading models (BAKER,1970; ROBERTS,1970; MOHR,1970a,1972a) to have migrated from the mouth of the Ethiopian rift to its present position adjacent to the South-Eastern plateau. Geological fieldwork by BLACK et al (1972b) led to the conclusion that the block "is an integral part of the [attenuated continental] Afar floor, albeit a part with greater than normal elevation because of recent uplift". Further field mapping and fracture system analysis based on ERTS images (CHRISTIANSEN et al,1975) have shown it to be autochthonous and connected to the South-Eastern escarpment. It follows geometrically that there cannot have been in Southern Afar any NE-SW crustal extension in response to the movement of Arabian plate.

The plate boundary defined by the Gulf of Aden axial

trough passes by means of a series of 'en échelon' ridge segments, offset by NE-trending dextral transform faults, through the Gulf of Tadjoura and the Ghoubbet el Kharab to Lake Asal within Afar (DEMANGE and STIELTJES,1975; DELIBRIAS et al,1975). Lake Asal is now filling with water from the Ghoubbet el Kharab (LANGGUTH and POUCHAN,1975; VALETTE,1975) and the Asal (or Ardoukôba) rift, which has a typical oceanic profile (HARRISON et al,1975; NEEDHAM et al,1976), will shortly be submerged.

Volcanism (ALLARD et al,1979), field tectonic observations, seismicity (ABDALLAH et al,1979) and horizontal and vertical ground displacements (TARANTOLA et al,1979,1980) studied following major seismo-volcanic activity in the Asal rift during November, 1978, are all typical of an active accreting plate boundary. COURTILLOT's (1980) suggestion that this area marks the present tip of a lithospheric crack propagating westward into Afar is considered in Chapter 9.

The manner in which spreading is taking place in Central Afar, between the Manda Hararo volcanic range and Lake Asal, is disputed. The significance of Recent spreading in SW Afar, along the East African rift (NNE-SSW) trend, is not clear. Detailed plate geometric models (SCHAEFER,1975; BARBERI and VARET,1977), based on volcanic and tectonic features formed within the past 1 Myr, are discussed later in the light of the present study.

1.3 Origin and Development of Afar and its Margins

The Precambrian geology of the Ethiopian region has been summarised by KAZMIN et al (1978) and by ROGERS et al (1978). Closure of the "Proto Red Sea basin" at about 1000 Myr was followed by a period of collision and folding in the area which now borders the Red Sea. Contemporaneously, collision and crustal thickening were occurring along the Mozambique Belt, the site of the present East African rift system. Both regions suffered further ...etamorphic and plutonic activity during the Pan-African orogeny.

Detailed mapping of the Western Ethiopian escarpment (KAZMIN and GARLAND,1973) has indicated that the opening of Afar was to some extent controlled by Precambrian block-faulted structures. Ancient fractures with the trends of current Red Sea and Gulf of Aden opening have been observed all around Afar. NW- and NNW-trending Precambrian faults are prominent in Saudi Arabia and Somalia (BEYDOUN,1970) and are clearly seen in satellite photographs (MOHR,1974). The Marda line (Figure 1.1.2), the major NW-SE lineament cutting across the South Eastern plateau in the vicinity of 9°N, 43°E, is also evident on the Bouguer anomaly map (MAKRIS et al,1975) and has been discussed in detail by PURCELL (1976). It can be projected north-westwards into the Erta Ale volcanic range or on to the Eritrean highlands, and south-eastwards as far as the Somali coast. It has been suggested (BLACK et al,1974) that Lower-Middle Tertiary transcurrent movement along the entire

Suez - Red Sea - Marda line determined the locus of the later Nubia - Arabia plate separation.

NW-SE and NE-SW to ENE-WSW trends dominate Precambrian dyke swarms in the Gulf of Suez (EL-ETR et al,1976). KRONBERG et al (1975) have recognised the Precambrian ENE-trending structures which cut across the Afro-Arabian dome as reflecting "fundamental fractures in the deeper crust" indicative of "an old regional to global pattern of crustal weakness or shearing". Surprisingly, their paper does not consider any possible correlation of these structures with the opening of the Gulf of Aden along the same trend, or with Afar transverse tectonics (MOHR,1968b,1974; CHRISTIANSEN et al,1975).

Although the above evidence suggests that Cainozoic fracturing has preferentially followed old lines of crustal weakness (see also KING,197Ø), it does not prove that the present rift geometry has existed since the Precambrian, as postulated by DIXEY (1956). Since the origin of the rifting is generally agreed to be sub-lithospheric, this would imply that relative horizontal motions between lithosphere and asthenosphere have been absent since this time.

'Dynamic' formation mechanisms such as membrane tectonics (TURCOTTE and OXBURGH,1973) and MORGAN'S (1972) model which requires the African plate to be riding currently over a mantle plume, are also geologically unsupported. There is no evidence for progressive and continuous N-S age variations along the Ethiopian and East African rift systems, although it may be argued that the

southern section of the East African rift is at an earlier stage of development. In particular OXBURGH and TURCOTTE's (1974) diagram, purporting to show migration of the onset time of volcanic activity southward along the rift at about 0.25°Myr-1, is invalid north of 4°N.

BRIDEN and GASS (1974) have invoked the spasmodic polar wander pattern of the African plate to explain the episodic phases of intra-plate thermal activity. They demonstrate that such thermal activity has occurred only during those periods when the plate has been stationary relative to the underlying asthenosphere. Domal uplifts, of which the Afro-Arabian is the most prominent, are thought to be widely distributed throughout Africa at present (Le BAS,1971; GASS,1972a).

GASS (1975) relates Ethiopian and East African magmatism since the late Tertiary to the lack of movement of the African plate since 40 Myr ago, and argues that it is only when asthenospheric heat sources are focussed on the same lithospheric target for many millions of years that large scale upper mantle and crustal melting will occur. Gass' model has sub-lithospheric heat input triggering upward movement of geisotherms within the upper mantle, with mantle equilibration closer to the surface. This leads to mantle fusion, domal uplift (perhaps by 'penetrative convection' (ELDER,1966; GASS,1970,1972b)) and intra-plate tectonics. The evidence for large areas of anomalous upper mantle beneath the rift zones is presented in Section 1.5. Gass' model can explain many of the volcanic and tectonic

phenomena observed in the Ethiopian rift system.

Alternatively, it can be argued that mantle fusion and domal uplift are consequences of rifting. BROWN and GIERDLER (1980) take this view on the ground that rift faulting is seen to exist where there is no long-wavelength Bouguer anomaly. "Underlying convection in the deeper mantle" is invoked as the cause of tensional stress across the African plate.

Unless the Ethiopian and Kenyan domes are linked an additional mechanism is required to explain the temporal coincidence of magmatic and tectonic episodes in the East African rift (BAKER et al,1972) and in Ethiopia. No connection is indicated by surface elevations, or by long-wavelength Bouguer anomalies (FAIRHEAD,1979)(Section 1.5.4).* Satellite photographs (MOHR,1974) and detailed ground mapping in the Omo river area of southern Ethiopia (MOORE and DAVIDSON,1978) show no surface expression of any link between the Main Ethiopian rift and the Stephanie and Lake Rudolf rifts of Kenya. Several detailed studies of teleseismic arrivals at the University of Durham Kaptagat array (FORTH,1975; LONG,1976) and west of Lake Turkana (MICENKO,1977) have all tended to indicate that the upper surface of the Kenya dome upper mantle anomaly deepens to the north; and the Kenya axial gravity high begins to die

---

*However, GIRDLER and BROWN's (1980) gravity model shows massive replacement both of light crustal and dense normal upper mantle material by anomalous asthenosphere of intermediate density. The replacement of crustal material causes a large positive Bouguer anomaly which partially offsets the long-wavelength negative anomaly.

out north of 10N (KHAN and MANSFIELD,1971).

Erosion occurred in Ethiopia during much of the Palaeozoic. The Mesozoic (largely Jurassic) succession has been described by MOHR (1967a), HOLWERDA and HUTCHINSON (1968), HUTCHINSON and ENGELS (1970), and others, and summarised by MOHR (1970a) and by CHESSEX et al (1975). The Jurassic marine transgression, which has also been described for the Red Sea and Gulf of Aden (e.g. SWARTZ and ARDEN,1960; BEYDOUN,1970), provides the first definite evidence of subsidence in Afar: the associated sediments thicken and downwarp towards the present rift system (JUCH,1975).

Cainozoic volcanism and rifting in the Afar region are related to uplifts of the Afro-Arabian dome. GASS (1975) believes that the dome was formed by initial uplift in the Upper Eocene. The western limit of marine sedimentation retreated sharply from 43°E to 49°E at this time (MOHR,1975). The pre-Miocene Cainozoic history is uncertain, since it rests on disputed K-Ar age determinations. Early Tertiary ages for basaltic dykes on the Western Ethiopian plateau (MEGRUE et al,1972) are inconsistent with the regional geology (MOHR,1975) and are likely to be in error. ZANETTIN and JUSTIN-VISENTIN (1974) have also published early dates for the Western Ethiopian plateau volcanics, on which they have based two cycles of volcanics, the Ashangi (older than 34 Myr) and Aiba (35 to 32 Myr) basalts (ZANETTIN and JUSTIN-VISENTIN,1975). Subsequently, rocks from the same sequence have been dated

as Miocene (McDOUGALL et al,1975; JONES,1976).

Several recent interpretations of the tectono-volcanic evolution of the Afar region (e.g. PILGER and RÖSLER,1976), based on the pre-Miocene age data, have concluded that Ethiopian plateau volcanism preceded Afar rifting. All published ages for volcanic rocks in and around Afar are collated in Appendix 1. Although volcanism may have been occurring earlier, widespread eruption of flood basalts over the plateau probably began in the Miocene and continued until approximately 13 Myr ago. This is consistent with GIRDLER and STYLES' (1978) revised date of 29 to 16 Myr for the formation of the Red Sea and Gulf of Aden main troughs by sea-floor spreading (Section 1.2).

The total volume of the flood basalt sequence* has been estimated as 400,000 km^3 (GASS,1970). It occurs thickly and very widely over Ethiopia, Djibouti, part of Somalia and the Yemen and was erupted from meridional fissures (GASS,1972b). It now seems probable that the sequence, which thickens towards Afar, was being erupted on the plateaux during the formation and initial rifting of Afar.

The tectonic development of the outer Afar margins by large-scale faulting and warping occurred in the Lower Miocene (MOHR,1975), possibly commencing about 25 Myr ago (BARBERI et al,1972b,1975a). It continued by normal

---

*Formerly known as the Lower Trap Series. Following the Bad Bergzabern symposium on the Afar region and related rift problems, in 1974, it was agreed to drop the volcanic classification, introduced by MOHR (1968c), based on the terms 'Trap Series', 'Afar Series' and 'Aden Series'.

faulting, and by localised dyke injection (MOHR,1975; ZANETTIN and JUSTIN-VISENTIN,1975). Lower Miocene peralkaline granitic bodies on the Afar margin (Asa Ale and Limmo, Figure 1.4.2 (BLACK et al,1972)) and in Central Afar (Affara Dara), together with Lower Miocene marginal basalts (TAZIEFF et al,1972), are internal evidence of the first stage of Afar rifting.

No other rocks exposed within Afar predate the voluminous Afar Stratoid Series extruded from approximately 4 to 1 Myr ago. The development of Afar from its Miocene inception until this time must be inferred from mapping of the bounding plateaux and their escarpments, including the Danakil and Aisha blocks. Since no comparison of the geology of these areas has yet appeared, Table 1.3.1 has been compiled on the basis of petrographic details given in the papers cited. There is no evidence that the Balchi Rhyolite and Pliocene Silicic sequences have counterparts in Djibouti, where the tectonic situation is complicated by apparent rapid changes in the local stress system related to the formation of the Gulf of Tadjoura at approximately 3.5 Myr (ARTHAUD and CHOUKRONNE,1976).

It is generally considered that only minor rifting took place between the Miocene and the Plio-Pleistocene. The area within the Afar inner margin dates from the early Pleistocene, and its subsequent development is more conveniently related in terms of its volcanicity.

TABLE 1.3.1 REGIONAL CORRELATION OF VOLCANIC ROCK SEQUENCES

WEST ETHIOPIAN PLATEAU MARGIN* (Zanettin and Justin-Visentin 1974,1975)	SOUTH EAST PLATEAU ESCARPMENT (Juch,1975)	ALI SABIEH (SOUTH DJIBOUTI) (Chessex et al, 1975)	NORTH DJIBOUTI (Barberi et al 1975)	FOOTHILLS OF SOUTH EASTERN ESCARPMENT (DJIBOUTI) (Christiansen et al,1975,Black et al,1975)
Alaji Ignimbrites (25-16My)	Main Silicic Formation (13-11My)	Damerkadda Formation (14.1-9.6My)	Mabla Rhyolites (14.2-9.7My)	Lowermost Afar Series (11-9My)**
Termaber Basalts (15-13My) Fursa Basalts (12-10My)	Upper Trap Basalt (possibly 10.5-9My)	Galemi Formation (7.9-4.6My)	Dahla Basalts (8-6.5My)	Lowest Afar Series (B3, B2) (8-5My) Afar Series (B1) (5-2My)
Balchi Rhyolites (8-2My)	Pliocene Silicics			

*New K-Ar determinations on rocks from this area, by McDOUGALL et al (1975) and JONES (1976), suggest younger ages for this sequence (see Appendix 1).

**Fissure basalts were erupted initially, but 100 m of rhyolites, ignimbrites and pumice beds occur at the top of the sequence.

1.4 Macroseismicity and Volcanism of Afar

1.4.1 Macroseismicity

The seismicity of Afar must be regarded in the context of the Ethiopian rift system as a whole. Appendix 2 tabulates all earthquakes instrumentally recorded at teleseismic distances for the area 05° to 20°N, 36° to 48°E.

Accurately located earthquakes which have occurred in the vicinity of Afar since 1955 are shown in Figure 1.4.1. Epicentres of events that have occurred since the installation of the World Wide Seismic Survey Network (WWSSN) in 1963 have an estimated accuracy of 10 to 25 km. The same accuracy is claimed by SYKES and LANDISMAN (1964) for epicentres obtained during the period 1955 to 1963. Earlier events are not shown, since their locations may be in error by 200 km or more (FAIRHEAD and GIRDLER,1970). Locations of teleseismically recorded African earthquakes are liable to a network bias caused by the disproportionately large number of recording stations to the north west (see SYKES and LANDISMAN,1964). Only one WWSSN station (AAE) is within 1000 km of Afar. Epicentral groupings have been improved using DOUGLAS's (1967) joint epicentral determination (JED) technique (e.g. FAIRHEAD and GIRDLER,1970,1971).

The Ethiopian rift, and the axial zones of the Gulf of Aden and the Red Sea, are seismically well delineated. There are concentrations of events in the Gulf of Tadjoura and near the Gulf of Zula, where the regional spreading axes

FIGURE 1.4.1

TELESEISMS INSTRUMENTALLY RECORDED FROM AFAR AND SURROUNDING AREAS, 1955-1980

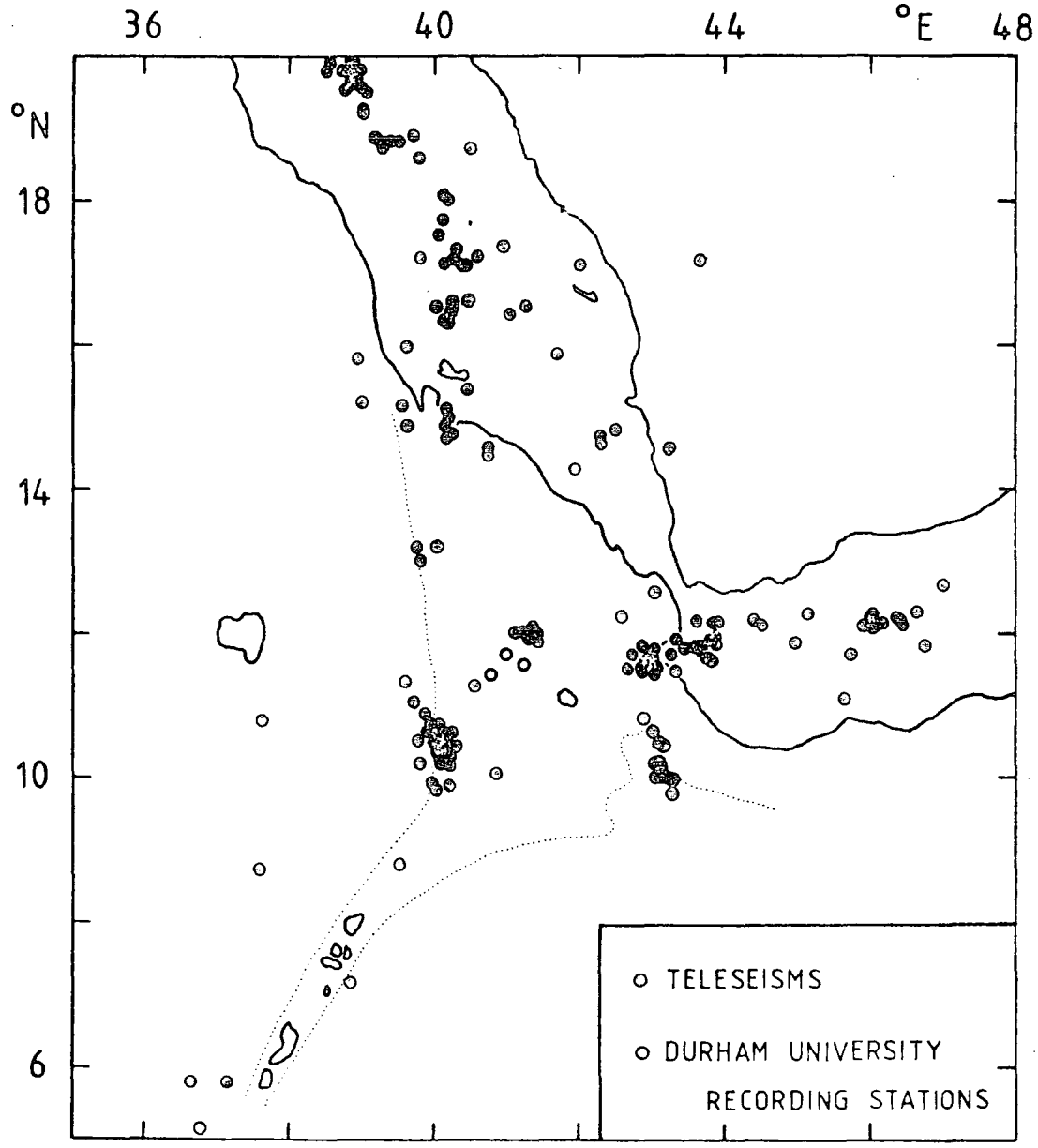

penetrate into Afar (Figure 1.4.1). In the Red Sea south of 16°N, where the crustal spreading rate is currently very slow (ROESER,1975), seismicity is sparse. The four events in the southern Red Sea show a NE - SW linearity, but do not coincide with any known transform fault.

The 26 year data period of Figure 1.4.1 is too short to demarcate the long-term pattern of major seismicity. GOUIN's (1979) comprehensive Earthquake History of Ethiopia and the Horn of Africa covers all documented seismic phenomena from 1400 A.D. The early earthquakes cannot be accurately located, but they are of major importance as they probably represent the events of highest felt intensity during the past six centuries. The principal additional fact shown by data covering a longer time period (e.g. GOUIN,1976, fig.4) is that seismic activity has occurred along the whole length of the Western Ethiopian escarpment.

There is minimal evidence for spatial or temporal macroseismicity patterns within Afar. FAIRHEAD and GIRDLER (1970) postulated a 255° seismic line from the Gulf of Tadjoura to the Western Ethiopian escarpment and GOUIN (1970) a SSW to NNE line from the Ethiopian rift to the western Red Sea coast at 14°N, 42°E. Both lines are poorly defined, and are geologically and tectonically untenable. LONG,R. (1974a) has suggested a possible 7.5 km yr^{-1} migration of seismic activity along a SE-NW axis, with an activity wavelength of approximately 150 km. The statistical basis for this is poor: 8 events, of which 6 have probable location errors exceeding 100 km.

Almost all the epicentres plotted on the Western Ethiopian escarpment at 10° to 11°N belong to the Kara Kore swarm of 1961. 34 events, the largest having magnitude M_S = 6.5 (USCGS), were located by international agencies. Over 4000 were recorded at AAE (DAKIN,1975, see Chapter 8). The major events have been relocated by SYKES and LANDISMAN (1964), FAIRHEAD and GIRDLER (1970, (by JED)) and GOUIN (1975). On the basis of local observations, Gouin imposes on the JED locations a lateral shift of 0.05°S and 0.30°W, followed by a 10° clockwise rotation. His relocated epicentres coincide with features of the Borkenna-Robi marginal graben (MOHR,1967a). The Kara Kore shocks, and other earthquakes along the Western Ethiopian escarpment, probably reflect the continuing development of the Afar western marginal graben (ROGERS,1966; MOHR,1970a).

The group of earthquakes located near 10°N, 43°E occurred during 1980 in an area of complex basement on the South Eastern escarpment (RUEGG et al,1981). No earthquakes of any magnitude had previously been recorded in this area. The 1980 events indicate that the south-eastern margin of Afar also remains active.

All the epicentres plotted NE of Tendaho belong to the 1969 Serdo swarm. These events are discussed in Chapter 8, along with recent teleseismically-recorded activity in the Gulf of Tadjoura. This study shows that Serdo is a region of continuing seismic activity.

1.4.2 Volcanism

The Afar floor consists almost entirely of volcanic rocks. Following BARBERI and VARET (1977), three units are distinguished:

(1) The Afar 'stratoid' series, predominantly stratified flood basalts, emplaced 4 to 1 Myr ago.

(2) Basaltic axial ranges accreted along fissures of the dominant regional trend.

(3) Marginal units related to transverse tectonics. Both the latter units are currently active.

The basaltic axial ranges are important indices of recent geodynamic processes. They show a tectonically-controlled evolution from fissural basalt eruptions along central graben (Asal, Manda Hararo, Manda Inakir, East Alayta, South Erta Ale, Issa, Herta Ale)(Figure 1.4.2), through shield volcanoes elongated along the regional structural trend of the feeding system (West Alayta, Dama Ale range, Erta Ale volcano), to more complex, central volcanoes (Boina, Tat Ali, NW Erta Ale, Dama Ale volcano) which have erupted highly differentiated lavas.

The geochemistry of the axial ranges is related to their structural position and relation to spreading axes. Both major and trace elements show that basalts with the same composition as typical mid-ocean ridge basalts (low-K olivine tholeiites) are found in the fissural basaltic Asal and Manda Hararo axial ranges, with series variation towards more alkalic compositions in other axial ranges (BARBERI and VARET,1977).

FIGURE 1.4.2

LOCATION MAP FOR AFAR VOLCANIC RANGES

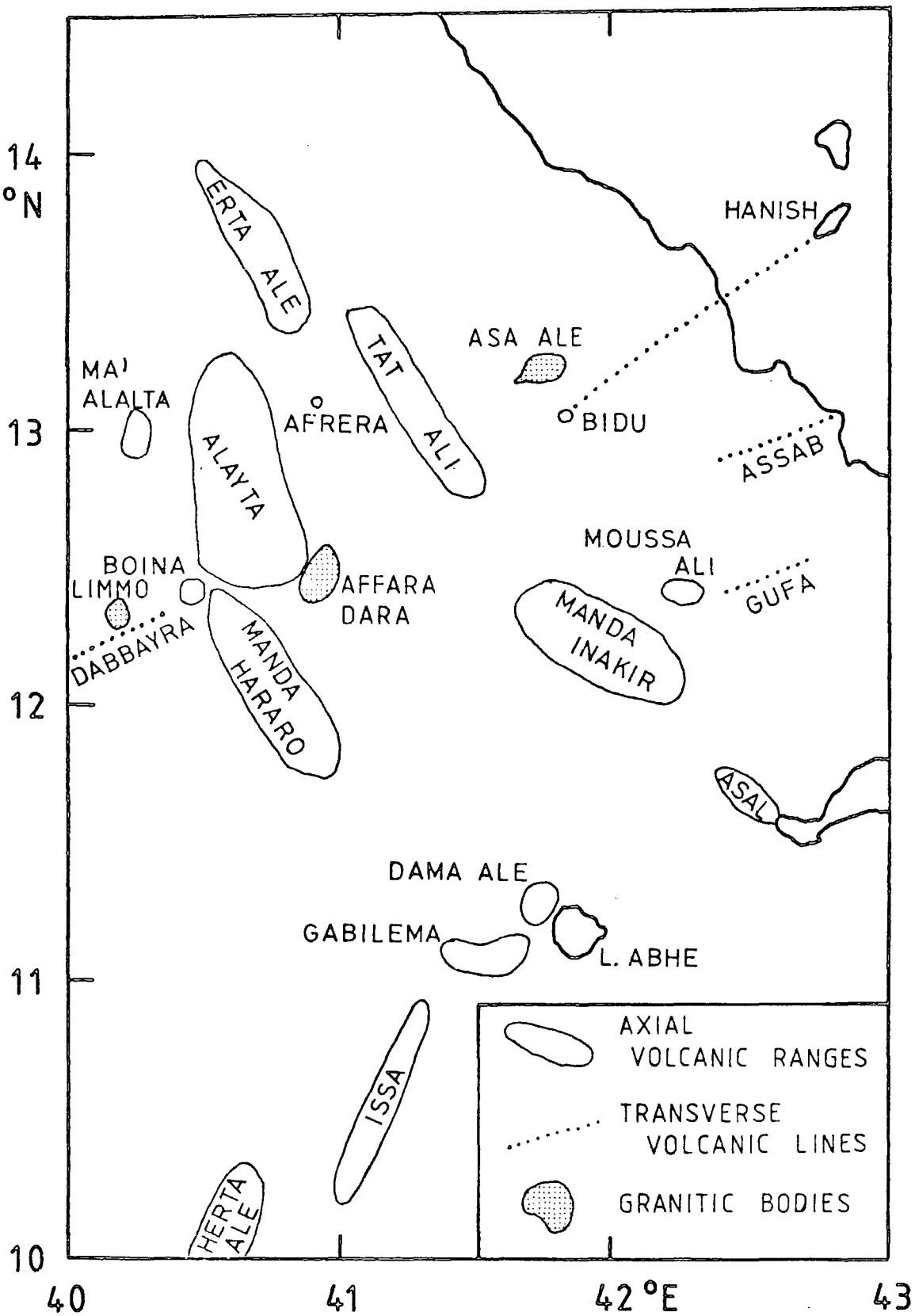

Flows erupted from the more evolved volcanoes show complete series from basalts to pantellerites or comendites. They derive from the differentiation of upper mantle transitional basalt parental magmas by fractional crystallisation at shallow depth (e.g. BARBERI and VARET,1970; de FINO et al,1973a). Similar rock suites in the southern Red Sea (GASS et al,1973), Iceland (SIGURDSSON,1967), Pantellaria (VILLARI,1974), the Azores (SELF and GUNN,1976) and the Ethiopian rift (WEAVER,1976) have also been explained by fractional crystallisation. Alternative genetic hypotheses, such as crustal contamination (e.g. BAILEY and MacDONALD,1970), gaseous transfer (GIBSON,1972), or mixing (SCHILLING,1973), have been shown to be untenable. For example, the scarcity of pyroclastic products (BARBERI et al,1974) argues against an origin by gaseous transfer, and Schilling's mantle plume mixing model is incompatible with many structural and geochemical features (see BARBERI and VARET,1975). Samples from Afar axial volcanic ranges give uniformly low $^{87}Sr/^{86}Sr$ ratios (0.70328 to 0.70410) (BARBERI et al,1970,1975b,1980; GASS,1970; MOHR,1971c; FERRARA and TREUIL,1974). The ratios are constant throughout basalt-comendite sequences. These observartions indicate a mantle origin without crustal contamination.

Conclusive evidence in favour of fractional crystallisation comes from the linear correlation between pairs of hygromagmatophile (alternatively called 'incompatible', or 'residual') elements, whatever the

crystallising phase (TREUIL and JORON,1975,1976). It has been shown (FERRARA and TREUIL,1974) that only a fractional crystallisation process can maintain unchanged the concentration ratio of hygromagmatophile elements. Moreover, commenting on detailed studies of the fractionation process in the Boina Centre sequence (BARBERI et al,1975b), TREUIL and JORON (1975) have given an explanation of the "Daly gap" between basic and hyperalkaline compositions, often invoked as an argument against their generation from a single initial melt by a simple fractional crystallisation process (e.g. for Afar, RASCHKA and MÜLLER,1975). Strong oxygen fugacity (fO_2) variations, as deduced from europium behaviour, occur in the domain $0.35 > f > 0.25$, where f is the fraction of the initial composition formed by the residual liquid. This fO_2 variation "seems to be a general property of hyperalkaline series. It underlines the absence, at this stage of evolution, of an fO_2 'buffer' (French: 'tampon') which can explain how the crystallisation of a relatively small amount of solid can lead to important modifications in the properties of the liquid" (TREUIL and JORON,1975, present author's translation). Lava types corresponding to this transition are therefore scanty. The sudden rise in fO_2 may initiate rapid crystallisation of Fe-Ti oxide minerals (WEAVER,1976).

Compositional variations between magmas exist throughout their differentiation series and are due to different initial melts rather than to varying fractionation

conditions. This has been well demonstrated from major and minor element analyses of Erta Ale and Boina series lavas (BIZOUARD et al,1976). Any parameter of the magma which is not modified during the course of fractional crystallisation is characteristic of the parental liquid composition and thus reflects the nature of the underlying upper mantle. Afar rock suite analyses have utilised several such parameters (TREUIL and JORON,1975). Figure 1.4.3 is an example of the variation of a Ch^+/Ch^- ratio, where Ch^+, Ch^- are respectively concentrations of strongly and weakly hygromagmatophile elements. Tholeiites are characterised by low Ch^+/Ch^- ratios, and strongly alkaline suites by raised ratios. The figure thus shows clearly the linkage through Afar of the Red Sea and Gulf of Aden spreading zones. Ch^+/Ch^- increases with distance from the active spreading zones, and is inversely proportional to the spreading rate. Note that Figure 1.4.3 has no radial character, as required by SCHILLING's (1973) mantle plume model. On the contrary, the most tholeiitic samples within Afar are found at the proposed hotspot centre (Manda Hararo). Major element geochemistry leads to the same results (e.g. $K_2O/(K_2O + Na_2O)$) molecular ratios, BARBERI and VARET,1977, fig.7).

It is well known that mid-ocean ridge tholeiites are characterised by light rare earth element (REE) depletion. TREUIL and JORON (1976) have plotted on a Masuda-Coryell-Winchester diagram the relative abundance of REEs in mantle-derived material from Afar, Iceland and a

FIGURE 1.4.3

VARIATION OF THE TANTALUM/TERBIUM RATIO FOR VOLCANIC ROCKS OF AFAR (after TREUIL and JORON,1975)

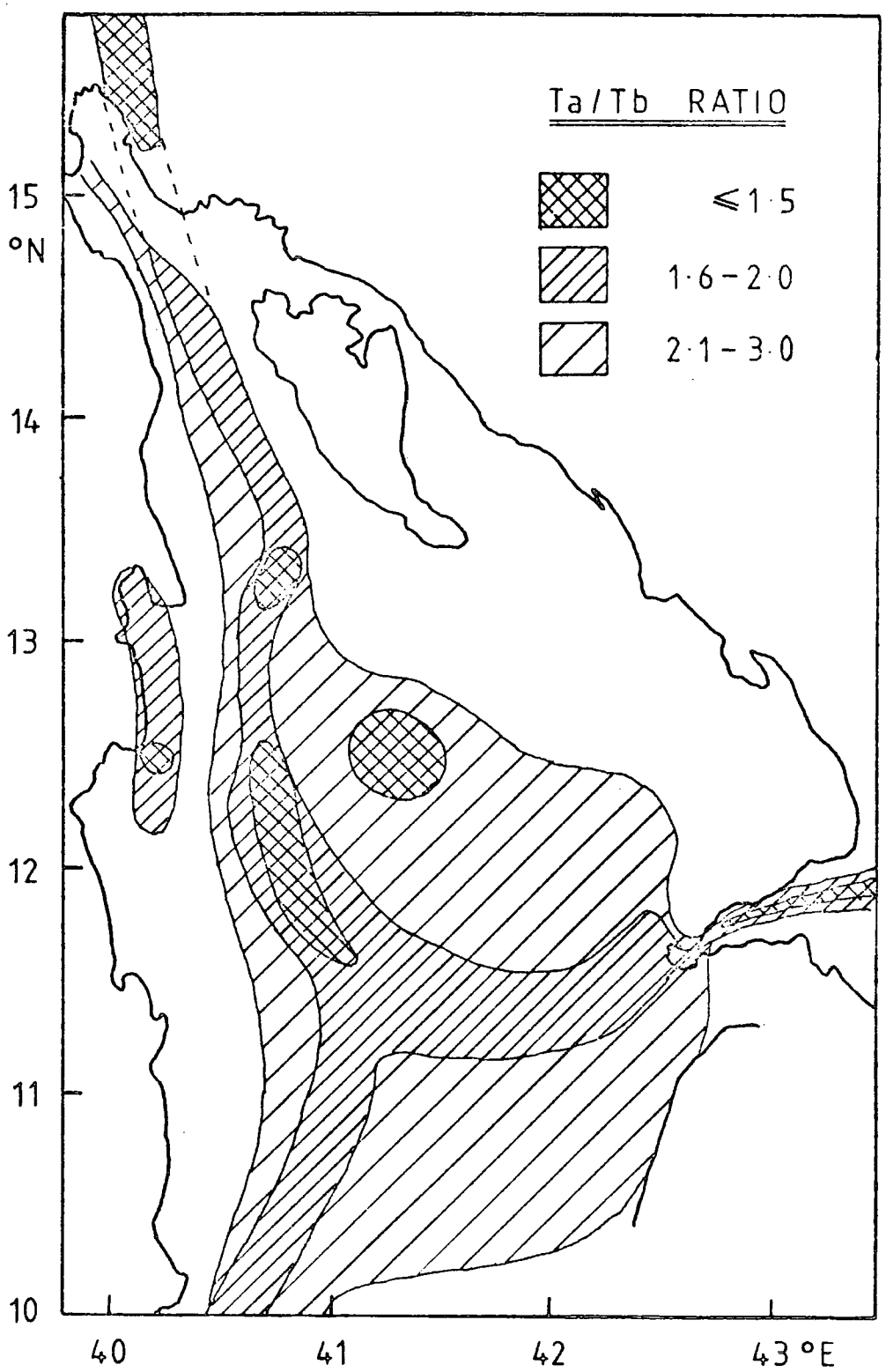

typical oceanic region (Famous, Azores). Their results show that the tholeiites derive from melting of a mantle zone already very depleted in light REEs.

The faster spreading axial ranges in Afar (Asal (DELIBRIAS et al,1975); South Erta Ale (BARBERI and VARET,1970; BARBERI et al,1970); Manda Hararo) show basalts compositionally more similar to mid-ocean ridge tholeiites, although they never reach such low TiO_2 content as ocean basalts (RASCHKA and MULLER,1975). Other axial ranges (e.g. Boina; Manda Inakir (de FINO et al,1973a)) are relatively enriched in light REEs. The Asal rift is topographically very similar to mid-ocean ridges (HARRISON et al,1975; NEEDHAM et al,1976), but important geochemical variations occur within it (e.g. of Th/Ta ratios, TREUIL and JORON,1976) corresponding to the decrease in age of the basalts towards the rift axis.

These variations are explained by the very early stage of oceanic rift evolution, during which melting occurs of mantle zones of slightly different composition. Detailed analyses indicate either an increased rate of melting or melting at shallower depths (STIELTJES et al,1976). BARBERI et al (1980) favour the latter interpretation because $^{87}Sr/^{86}Sr$ ratios, although low (see above), are slightly more radiogenic than those from the Red Sea, Gulf of Aden and most mid-ocean ridges (0.7022 to 0.7035, HOFFMAN and HART,1978). A vertically zoned upper mantle is implied, more radiogenic in its upper parts, although the normal distribution of Afar isotope ratios suggests that their

source regions are fairly homogeneous on a regional scale.

Transverse (NE-SW) structures are generally considered to occur only on the Afar margins, and have been shown to be analogous to oceanic fracture zones (BARBERI et al,1974a).* They are petrologically quite distinct from the axial ranges, and are characterised by alkali basalt volcanism and the common occurrence of ultramafic xenoliths of mantle material. Their alkaline affinity is shown by abundant potassium, titanium and phosphorus and by large, highly charged cations (BARBERI and VARET,1977). They are often related to offsets of the NNW - NW axial ranges and of the Ethiopian Plateau escarpment, and are demonstrably analogous to Atlantic fracture zones (BARBERI et al,1974). However, they are also observed on the eastern margin where no active NNW - NW tectonics occur.

The most studied marginal volcanics are the Ma'alalta (or Pruvost) range to the west (BARBERI et al,1970) and the Assab (de FINO et al,1973b; CIVETTA et al,1975a; OTTONELLO et al,1975,1978) and Gufa (MARINELLI and VARET,1973) structures to the east. Other marginal structures are listed by BARBERI et al (1974). Predominantly alkali basalts from the Zukur-Hanish islands (GASS et al,1973), whose dominant structural lineament is NE - SW, strongly suggest a continuation of Afar transform faulting into the Red Sea.

The marginal volcanoes are of a complex, central type,

---

* However, CHRISTIANSEN et al, (1975, fig.8) show currently active "zones of fissural basaltic activity" in five NE - SW parallel zones of Central Afar, with minor extension.

frequently having summit calderas and associated with acid lava domes and flows, ignimbrite sheets, pumice beds and basalt lava fields. Their petrology and varying strontium ratios have suggested formation by a crustal contamination process. Direct crustal melting has also been proposed (BARBERI et al,1972a), but recent geochemical studies are interpreted in terms of fractional crystallisation of alkaline upper mantle magma which is at some distance from the active spreading zone and thus deeper and less depleted than that giving rise to the tholeiites (OTTONELLO et al,1978). This explanation of their genesis is also more acceptable for xenolith - alkali basalt associations found elsewhere in the Red Sea (El Shazly and Sheely, 1972, in OTTONELLO et al,1978; HUTCHINSON and GASS,1971).

The Afar stratoid series was emplaced through fissures parallel to the general tectonic trend. The series is deeply affected by intense extensional faulting, commonly with block tilting. Normal faults show throws of upwards of 150m. Faulting and tilting were contemporaneous with emplacement of the series (BARBERI and VARET,1977), and the fault pattern reflects continuous tectonism during the past 4 Myr. This corresponds to the most recent (axial trough) stage of oceanic spreading in the Red Sea and Gulf of Aden. The major rock types are transitional and alkali basalts. Alkalic rhyolites are found mainly in the upper part of the series, both related to fissural activity and as products of central volcanoes which characteristically occur at the intersection of different fracture trends.

The nature of the underlying material cannot be determined. Rhyolites are more abundant than on ocean floors, but this need not indicate a continental crust. It can be satisfactorily explained by a slow extension rate permitting mantle-derived magmas to rest and differentiate in magma chambers. It is likely that the stratoid series basalts were emplaced in a similar manner to the Recent axial basalts, through feeding fissures. TREUIL and VARET's (1973) trace-element geochemical studies have led them to relate lateral compositional variations in the stratoid series to different degrees of partial melting, but again the nature of the underlying crust is not indicated.

In South West Afar the predominant direction of faulting is NNE, the trend of the East African rift. Plio-Pleistocene faulting occurred over the full width of South West Afar, although faults are obscured in places by thick sediments from the Pleistocene lacustrine basin which existed between 9° 40'N and 11° 40'N, preceding the formation of the Issa and Tendaho graben (CHRISTIANSEN et al,1975). Farther south, the volcano-tectonic evolution of the Main Ethiopian rift has been reviewed by MEYER et al (1975). A major faulting phase dated at 1.8 to 1.6 Myr is held to mark the onset of a transition from continental to incipient oceanic rifting. This is consistent with SCHAEFER's (1975) observations of the Issa and Herta Ale graben in southernmost Afar, where spreading has begun only in the Pleistocene.

MOHR and WOOD (1976) have examined volcano spacings

along the Main Ethiopian rift and elsewhere in Afar in the light of VOGT's (1974) proposal that volcano spacing is approximately equal to lithospheric thickness. They infer crustal thicknesses of 20 to 35 km all along the Main Ethiopian rift, 18 to 25 km below Dubbi and 16 km below Erta Ale. These figures are comparable to those from other evidence (Section 1.5). The volcano spacings also show a direct relationship to the age of the volcanoes, the youngest being associated with the closest spacings and thinnest crust. This is consistent with the concept of progressive lithospheric attenuation.

In summary, the volcanism of Afar spotlights the processes of tectonic evolution active during the past 4 Myr. The Afar stratoid series, underlying most of central and southern Afar, reflects repeated episodes of extensional faulting and tilting throughout this period.

The axial basaltic ranges are analogous to oceanic ridges. Their products can be completely explained by a process of fractional crystallisation within the crust of basalic magmas originating in the upper mantle. Analysis of suitable chemical parameters indicates directly the composition of the underlying upper mantle and, through comparison with results from oceanic ridges, the position, evolution and current activity of the spreading axes. Shield volcanoes, erupting differentiated lavas, indicate a decrease in spreading rate or cessation of spreading.

Transverse volcanic structures of the Afar margins show alkali basaltic volcanism, indicating a deeper mantle source

and a lower degree of partial melting than the axial basalts. They are analogous to oceanic fracture zones. Their orientation is typically NE-SW or ENE-WSW, and some continue into the Southern Red Sea.

The volcanological data are more complete than those so far obtained from geophysical investigations.

1.5 Evidence for Crustal and Upper Mantle Structure

1.5.1 Regional Seismic Studies

Seismic structural studies are based on observations of seismic wave propagation. Earthquakes are the most widely-occurring high-energy sources for such studies.

Away from the rift zones, Africa has a lithospheric structure similar to that of other continental shield areas: that is, a crust of thickness 35 to 45 km overlying an upper mantle characterised by high (8.0 to 8.1 km sec^{-1} for P-waves) seismic velocities. This is inferred from surface wave dispersion studies (e.g. BLOCH et al,1969; GUMPER and POMEROY,1970); and, in Southern Africa, from refraction studies (WILLMORE et al,1952; HALES and SACKS,1959).

Large positive P-wave travel time residuals are observed near the rifts (e.g. LONG and BACKHOUSE,1976), indicating lowered seismic velocities. AAE has the largest delay associated with any WWSSN station (LILWALL and DOUGLAS,1970), approximately $+2.7 \pm 0.3$ sec (95% confidence limits) relative to Bulawayo (SUNDARALINGAM,1971).

Surface wave dispersion techniques have also been used

to study the lithosphere of the rift zones. At short periods, reflecting crustal structure, the Rayleigh wave dispersion curves for paths which have sampled the East African rift (SUNDARALINGAM,1971; LONG et al,1972,1973) are similar to those found for the rest of Africa (GUMPER and POMEROY,1970). For waves of longer periods, which penetrate the upper mantle, significantly lower velocities have been found. Rayleigh and Love wave phase velocity dispersion curves can be inverted to give shear-velocity structural models. For the path AAE-NAI, KNOPOFF and SCHLUE (1972) have found S_n velocities between 4.25 and 4.45 km sec^{-1} extending to a depth of 120 to 200 km. These velocities are about 10% lower than the 'normal' African values given by Gumper and Pomeroy.

Seismic waves that have traversed the major rift zones show abnormal propagation features. Specifically, S_n and L_g are severely attenuated across the African rift zones north of the equator (GUMPER and POMEROY,1970), indicating a 'gap' in the lithosphere. This important result is strongly supported by gravity observations (Section 1.5.4).

The accumulated evidence establishes beyond reasonable doubt the existence beneath the Ethiopian and East African rifts of mantle material of anomalously low Q and low seismic velocity. A raising of the lithosphere-asthenosphere boundary is implied. This may be either a cause or an effect of domal uplift (Le BAS,1971; GASS,1972a,1975). Its relevance here is its influence on current magmatic processes in Ethiopia.

1.5.2 Local Seismic Studies

The structure beneath AAE has been studied from spectral response ratios of long-period body waves from two Hindu Kush earthquakes (BONJER et al,1970). Assuming a two-layered crust with P-wave velocities of 6.0, 6.7 km sec^{-1}, a Moho depth of 38 km was inferred with normal upper mantle beneath (Figures 1.5.1,1.5.2). In a later paper (MUELLER and BONJER,1973) a better fit to the experimental data was achieved by adopting the Moho depth given by SEARLE and GOUIN (1971a). Searle and Gouin examined local earthquake phases recorded at AAE. Constructing a P_n travel-time curve, they deduced an upper limit for the crustal thickness of 48 ± 5 km, assuming a homogeneous crust of velocity 6.3 km sec^{-1} above an isotropic upper mantle velocity of 7.95 km sec^{-1}. MAKRIS et al (1975) have asserted that Searle and Gouin "added to the crustal thickness that part of the upper mantle with P_n less than 7.95 km sec^{-1}".

Surface-wave group velocity dispersion curves for Gulf of Tadjoura earthquakes recorded across Afar at AAE are best fitted to structural models intermediate between typical oceanic and typical continental. A P-velocity of 7.2 to 7.6 km sec^{-1} below about 17 to 21 km depth is suggested (SEARLE,1975). In all Searle's models Poisson's ratio increases with depth from 0.25 at the surface to 0.27 or 0.29 at about 20 km. An earlier surface wave dispersion study (JONES,1968) had deduced a predominantly continental Afar crust, but did not fit numerical models to the data or

KEY TO FIGURE 1.5.1

MODELS OF THE CRUSTAL STRUCTURE OF AFAR AND ITS MARGINS

Bracketed velocities shown on the profiles are for S-waves. All other velocities are for P-waves. Units: km sec^{-1}

(a)-(d) after BERCKHEMER et al (1975)

(a) profiles II and III (Mille to Awash Station) (SW Afar)

(b) profile IV (Assab to Asayita) (E Cent Afar)

(c) profile V (Asayita to Afrera) (N Cent Afar)

(d) profile VI (Afrera to Dallol) (N Afar)

(e)-(g) after RUEGG (1975a,b)

(e) profiles 2 and 5 (Djibouti to Lake Abhe) (SE Afar, S of Gulf of Tadjoura)

(f) profile 4 (Obock to Lake Abhe) (SE Afar, N of Gulf of Tadjoura)

(g) profile 7 (Moulhoule to Matgoul) (E Afar margin)

(h)-(i) after SEARLE (1975)

(h) model 130N

(i) model 125G

(j) after BONJER et al (1970)

(k) after MUELLER and BONJER (1973)

(l) after SEARLE and GOUIN (1971a)

Note the different scale of models (j) to (l)

FIGURE 1.5.1

MODELS OF THE CRUSTAL STRUCTURE OF AFAR AND ITS MARGINS

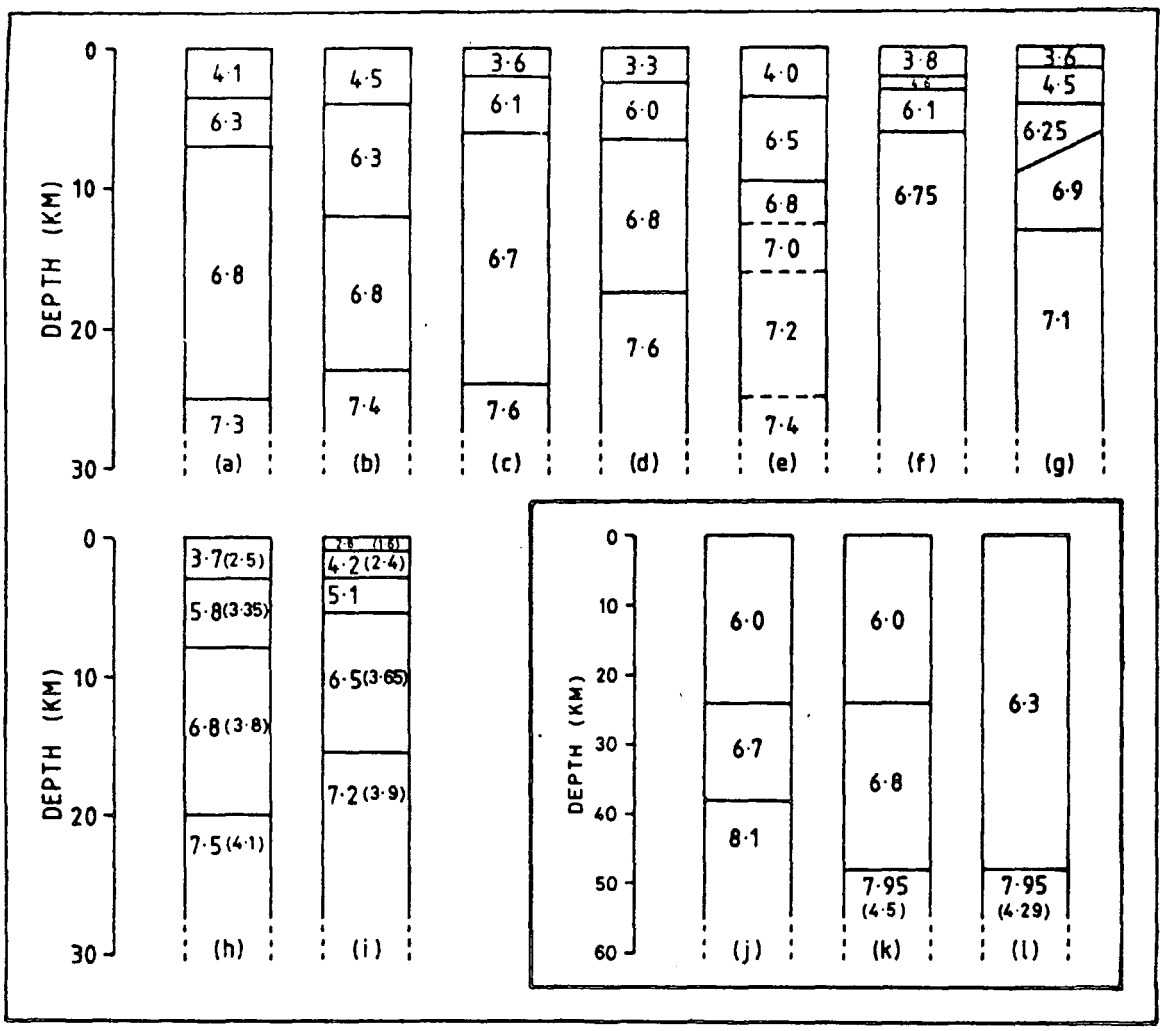

FIGURE 1.5.2

LOCATION MAP FOR PROFILES (A)-(G) OF FIGURE 1.5.1

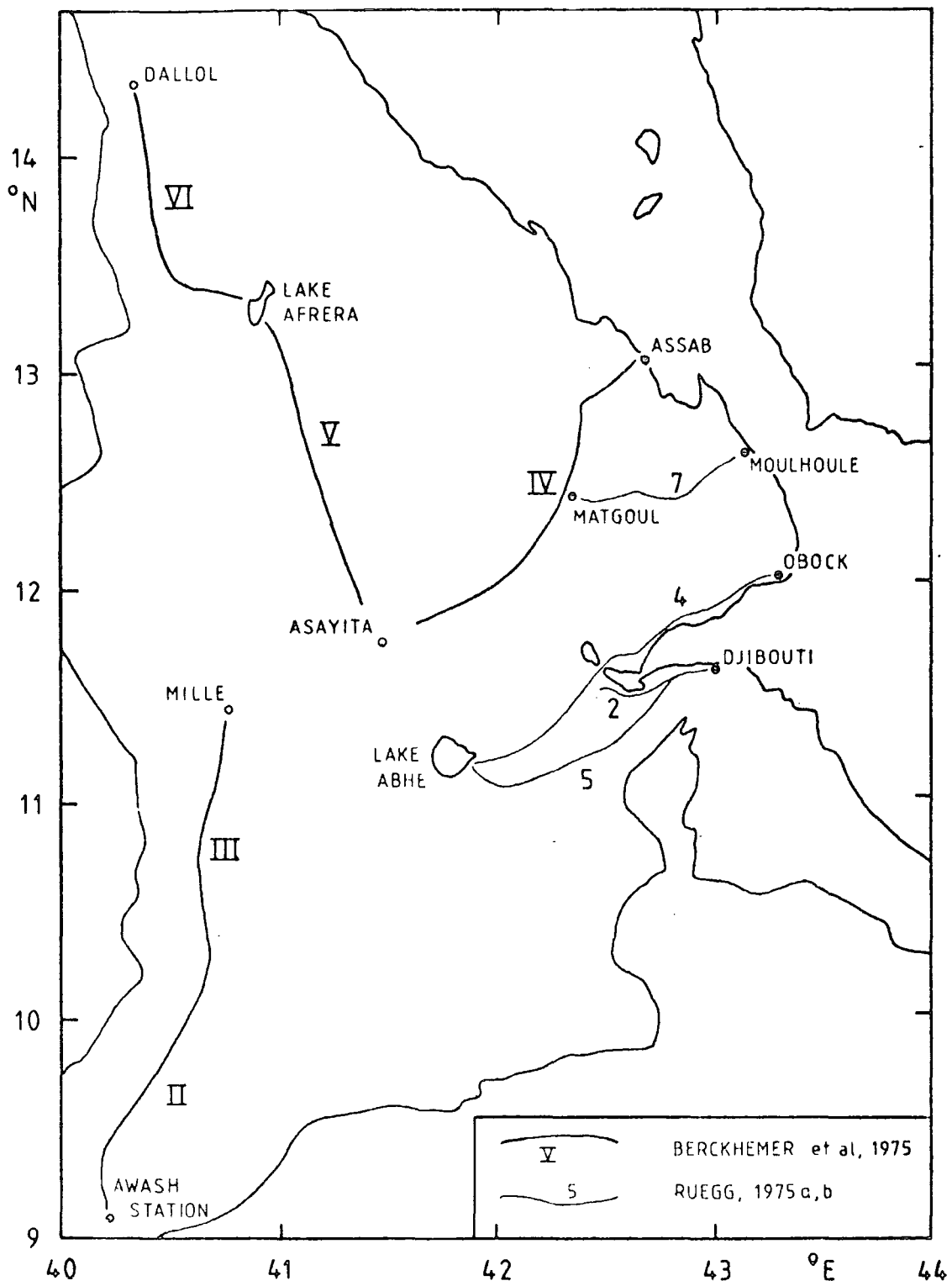

allow for the significant part of the wave path that lies across the Western Ethiopian plateau. Searle's study corrects for this by assuming for the plateau a normal continental structure, but inevitably a further degree of uncertainty is introduced into the Afar crustal models.

SEARLE and GOUIN (1971a,1972) found no evidence for S-wave attenuation across Central and Southern Afar; nor for the path Gulf of Tadjoura - AAE; nor across the southern Danakil Depression along a path crossing 200 km of Afar (Figure 1.5.3). S_n is not propagated across the northern Danakil Depression, the Red Sea or the Gulf of Aden. Their tentative S_n velocity, 4.29 ± 0.04 km sec^{-1}, corresponds to an anomalously high Poisson's ratio of 0.294 ± 0.006, indicating abnormally hot and plastic upper mantle. L_g was well propagated across Afar and well seen at AAE even from the Red Sea axial trough, implying that there is little oceanic crust in the Western Red Sea. L_g was not seen from the Gulf of Aden east of 45°E.

From the 1969 Serdo earthquakes DAKIN et al (1971) report that both L_g and R_g were unusually well recorded at AAE. Unfortunately, the authors do not describe how the phases were identified. R_g is a vertically polarized crustal channel wave. Its successful propagation across Southern Afar implies a crustal thickness of at least one wavelength, in this case 20 to 25 km, which is inconsistent with an oceanic crust.

FIGURE 1.5.3

EFFICIENCY OF S_n TRANSMISSION ACROSS AFAR

(after SEARLE and GOUIN,1971a)

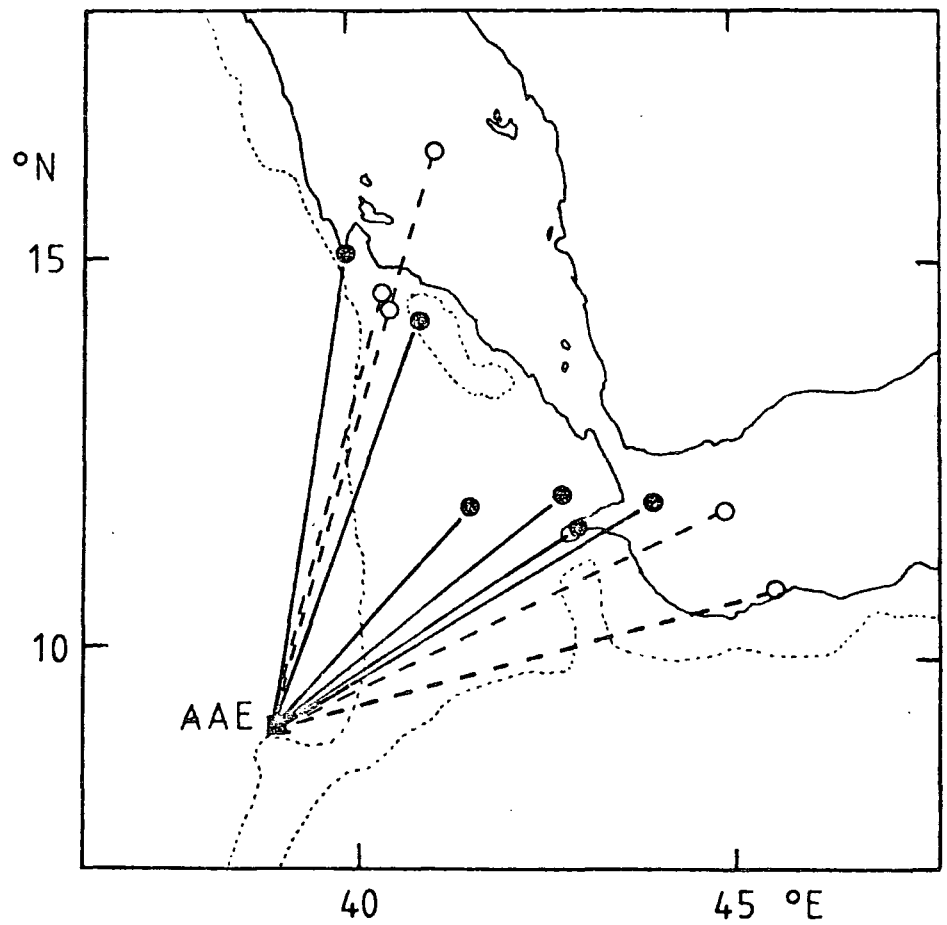

Closed circles and full lines: events from which S_n was clearly received at AAE.

Open circles and dashed lines: events from which S_n was not observed.

1.5.3 Seismic Refraction Studies in Ethiopia and Djibouti

Seismic refraction profiles in Ethiopia (BERCKHEMER et al,1975) have yielded more detailed crustal information. Beneath the Ethiopian plateau west of Addis Abeba a typical continental shield structure was observed: 38 km of crust overlying an upper mantle with a clearly identified P-velocity of 8.0 km sec^{-1}. The crust was found to thicken towards the Afar marginal escarpment, in accordance with MAKRIS et al's (1975) interpretation of gravity observations.

Beneath Afar an intermediate crust was found. The data were best fitted by a three-layered crustal velocity-depth structure above a fourth layer of P-velocity 7.3 to 7.7 km sec^{-1} which was interpreted as anomalous upper mantle. The depth to layer 4 was 22 to 26 km in Southern Afar, thinning to 16 km beneath the Danakil Depression. A more sophisticated analysis, including examination of wide angle reflections, suggested that the transition to layer 4 is not a simple first order discontinuity, and indicated in Southern Afar a possible slight crustal velocity inversion at a depth of 15 to 20 km.

The velocity-depth distributions for Berckhemer's profiles are shown in Figure 1.5.1. The ubiquity of the 6.0 to 6.3 km sec^{-1} P-velocity layer was interpreted as indicating a highly attenuated continental crust even below Northern Afar, composed of basement gneisses and granites with intruded basaltic dykes. However, no xenoliths of such continental material have been found in Afar volcanics. The

rock type of the bulk of the crust cannot be determined from its P-velocity of 6.6 to 6.8 km sec^{-1}, which could be attributed to metamorphic or to igneous rocks. Even in the light of other geophysical data it has only been concluded that "it must be a rather continuous series of rocks which are feldspar-rich at the top and gradually become richer in dark minerals (pyroxenes, amphiboles) in the lower parts" (GEHLEN et al,1975).

Seismic refraction studies carried out in South East Afar and around the Gulf of Tadjoura (LÉPINE et al,1972; RUEGG,1975a,b) have given generally lower velocities than Berckhemer's (Figure 1.5.1). Ruegg's layers 1 and 2 are equivalent to Berckhemer's layer 1 (Berckhemer's stations were more widely spaced), and Ruegg's layer 3 to Berckhemer's layer 2. However, below 6 to 10 km layer 4, with a P-velocity increasing gradually from between 6.7 and 6.9 km sec^{-1} to 7.4 km sec^{-1} at approximately 20 km, is interpreted by Ruegg as anomalous upper mantle, consistent with LAUGHTON and TRAMONTINI's (1969) interpretation for the Gulf of Aden and DRAKE and GIRDLER's (1964) for the Red Sea axial trough.* Mantle P-velocities of 8.0 km sec^{-1} were not observed even on profiles 250 km long, and cannot therefore occur above 35 km depth.

Ruegg's layer 3 and layer 4 P-velocities are

---

*Drake and Girdler found seismic P-velocities of 5.5 to 6.4 km sec^{-1} away from the axial trough, which they attributed to continental basement. TRAMONTINI and DAVIES (1969) observed 6.6 km sec^{-1} outside the axial trough at 22°N. This is too high to be continental basement and was referred to a body of coarse-grained, basic igneous material, typical of oceanic layer 3.

systematically 6 to 15% slower than those for normal oceanic crust, and become progressively lower towards the Gulf of Tadjoura spreading axis (RUEGG,1975a, fig.29c). Exceptionally high values for Poisson's ratio (Table 1.5.1) support an interpretation in terms of upper mantle partial melting, although it could be argued that such melting should hinder S_n being observed at all. P and S arrivals from earthquakes in the Gulf of Tadjoura are strongly attenuated when they have travelled for 50 km or more along the rift axis, but S_n is well seen on most explosion profiles. BERCKHEMER et al (1975) do not mention S-arrivals from their shots, but state that "no suspicious Poisson's ratio is found" in the 6.8 to 7.0 km sec^{-1} layer. A local earthquake fortuitously recorded in north Central Afar gave an average value of $\sigma = 0.27 \pm 0.015$ for 6 to 15 km depth.

Ruegg considers his layer 3 (6.0 to 6.5 km sec^{-1}) too thin to be due to attenuated continental crust. Berckhemer's corresponding layer, interpreted as continental, is sometimes no thicker. However, the difference between Berckhemer's and Ruegg's results is apparently more than one of interpretation. Ruegg finds no discontinuity within his layer 4 that could correspond to Berckhemer's postulated crust-mantle boundary. Ruegg observes extremely high values for Poisson's ratio, whereas Berckhemer's are normal.

Ruegg's data strongly support the assertion that North Tadjoura is an oceanic accretion on to the Arabian plate (MARINELLI and VARET,1973; BARBERI and VARET,1975) rather

TABLE 1.5.1 VALUES FOR POISSON'S RATIO WITHIN AFAR

SOURCE	POISSON'S RATIO	DEPTH (KM)
SEARLE and GOUIN (1971a)	0.294 ± 0.006	below 48
MUELLER and BONJER (1973)	0.264	below 48
SEARLE (1975, model 130N)	0.245 0.250 0.273 0.287	0-3 3-8 8-20 below 20
SEARLE (1975, model 125G)	0.258 0.258 0.273 0.270 0.292	0-1 1-3 3-5.4 5.4-15.5 below 15.5
BERCKHEMER et al (1975)	0.27 ± 0.015	6-15
RUEGG (1975a,b)*	0.267-0.284 0.267-0.315 0.267-0.339	layers 1,2 (0-4) layer 3 (3-9.5) layer 4 (6.5 and below)

*Values for Poisson's ratio are taken from RUEGG's histograms (1975b,fig.2c). Refer to profiles of Figure 1.5.1 for details of layer depths.

than a southerly prolongation of the Danakil block. However, if South East Afar and the Gulf of Tadjoura are floored by oceanic crust it is hard to accept that elsewhere in Afar, even below the axial volcanic ranges, there exists a strongly attenuated crust with only limited basaltic intrusions.

1.5.4 Other Geophysical Data

The seismic evidence discussed above indicates that Afar is underlain by low-velocity, anomalous upper mantle, probably at an abnormally high temperature. This view is further supported by magnetotelluric measurements (BERKTOLD et al,1975). Typical continental crust and upper mantle has a high resistivity, of the order of thousands of ohm metres, at depths down to about 70 km. Below Afar, apparent electrical resistivities of 10 to 50 Ωm are found at 15 km depth. Similar conductivity anomalies have been discovered in other tectonically active areas, notably Iceland (HERMANCE,1973) and the Gregory rift (ROONEY and HUTTON,1977). On the basis of resistivity-temperature relations deduced from laboratory experiments on a variety of rock types, the low resistivities are referred to abnormally high temperatures (800° to 1200°C, depending on the petrology), consistent with upper mantle partial melting.

A degree of partial melting beneath Afar is consistent with the hypothesis of shallow magma chambers containing differentiating upper mantle material (BARBERI and

VARET,1975,1977), but this would be a local effect. Widespread partial melting would result in raised Poisson's ratios and S-wave attenuation, contrary to BERCKHEMER's (1975) seismic observations.

Beneath the Western Ethiopian escarpment the inferred temperature is even higher, unless the melting point is lowered by volatiles. Apparent resistivity decreases with increasing period, contrary to normal behaviour for continental-type crust, indicating that the high-conductivity region observed below Afar continues at greater depth below the escarpment. This is further evidence for a highly anomalous upper mantle. The western boundary of the resistivity anomaly is unknown, since no magnetotelluric measurements exist from the Western Ethiopian plateau. Beneath the South Eastern plateau the long-period resistivity values are as high as for typical continental crust.

The dominant feature of the Bouguer gravity anomaly map of Africa (FAIRHEAD,1979; BROWN and GIRDLER,1980) is a broad negative anomaly associated with the East African rift system. Beneath Ethiopia it reaches -240 mGal (-2400 gu) and has a width of about 1000 km. Such an anomaly must be caused by a large region of low-density material at depth. It could be due either to crustal thinning (e.g. SOWERBUTTS,1969, model 1), or to the presence of a large 'cushion' of very low density material beneath the rift (SOWERBUTTS,1969, model 2), or to thinning of the lithosphere (SEARLE,1970). BROWN and GIRDLER (1980) follow

the last interpretation. They assume a 'standard African lithosphere' 100 km thick, with a Moho depth of 36.2 km. The broad, negative Bouguer anomaly is interpreted as being due to variations in lithospheric thickness rather than to compensation at the base of the crust.

To satisfy the gravity, the whole of the upper mantle part of the lithosphere has to be thinned away beneath much of the Ethiopian and Kenyan rifts, and some of the crust beneath the rift floor. The required degree of thinning increases from south to north. Perpendicular to the Ethiopian rift at about 8°N the upper mantle part of the lithosphere is absent for a width of 350 km. Even allowing for uncertainties in the lithospheric model, the results show impressive agreement with the conclusions derived above from regional seismic and magnetotelluric studies.

Gravity data for Afar and surrounding areas have been presented in a series of papers by MAKRIS et al (1970, 1972, 1973, 1975) (Figure 1.5.4), incorporating earlier results summarised by GOUIN (1970). Negative Bouguer anomalies occur beneath the Western Ethiopian and South Eastern plateaux, where a continental crust is expected. The Western Ethiopian plateau is the more negative, the maximum negative anomaly lying below the western margin of the Western Ethiopian escarpment. MAKRIS et al (1975) interpret this to indicate crustal thickening towards the rift, but in view of the seismic and magnetotelluric results BROWN and GIRDLER's (1980) interpretation in terms of differing upper mantle densities is to be preferred.

FIGURE 1.5.4

SIMPLIFIED BOUGUER GRAVITY ANOMALY MAP OF AFAR

(after MAKRIS et al, 1975)

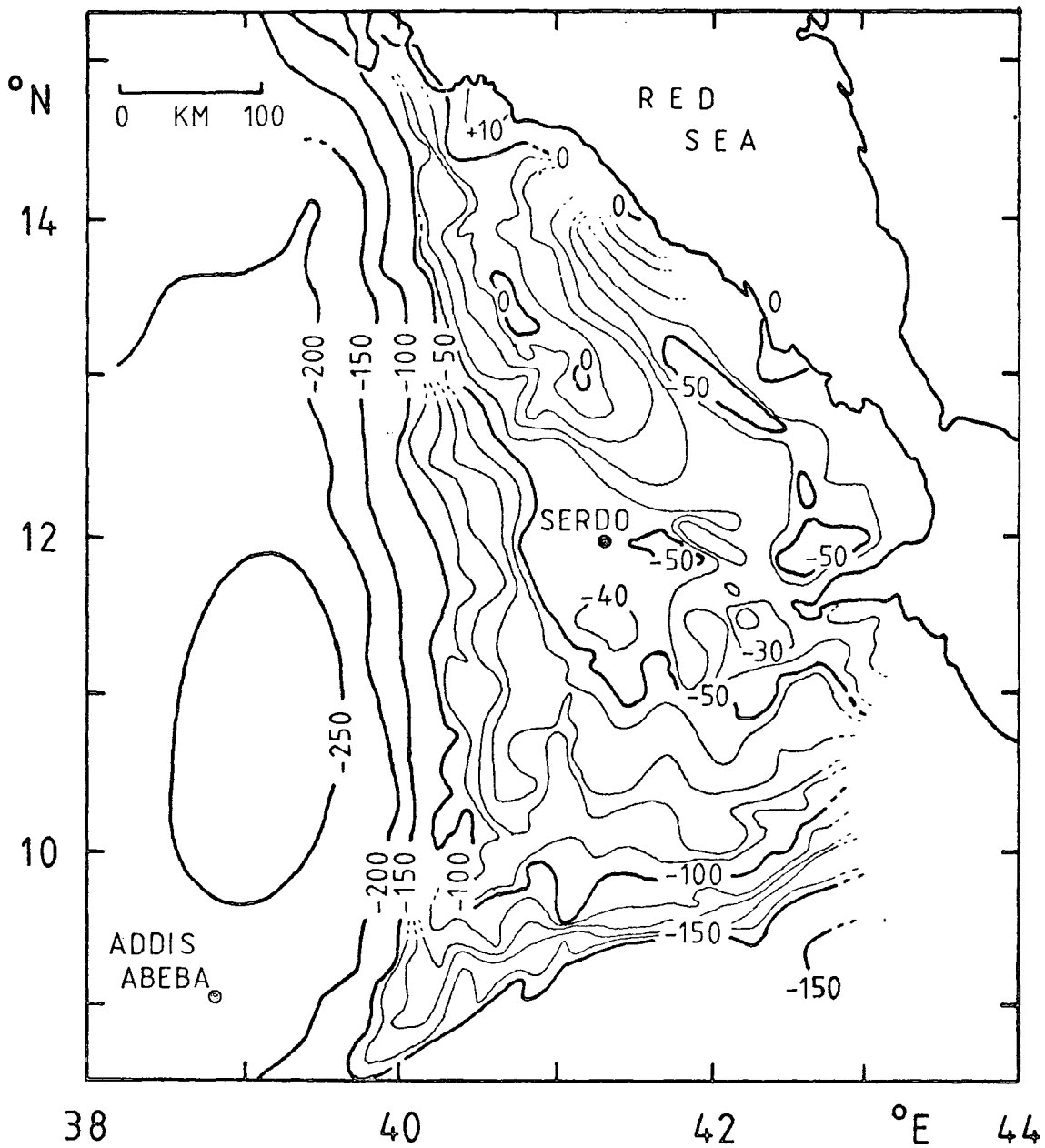

Within Afar the gravity field is largely flat and featureless, particularly in and around the Tendaho graben (SEARLE and GOUIN,1971b), the area of the present study. Small gravity maxima delineate the Erta Ale volcanic range in the Danakil Depression, and the Herta Ale and Issa graben in South West Afar. Like the axial positive anomalies over the East African rifts (e.g. KHAN and MANSFIELD,1971, for the Gregory rift) they are attributed to basaltic intrusions into the lower-density crust. The gravity maximum coincident with the Asal rift is less marked, although the evidence already presented has shown clearly that this area is undergoing currently active crustal spreading. A small maximum exists east of Serdo, perhaps related to a localised magnetic anomaly in the same area (COURTILLOT et al,1980). It has no surface topographic expression. It is difficult to assess the effect of light volcanics in this region.

The gravity data of themselves do not permit detailed conclusions as to the nature of the Afar crust. They have been shown to be consistent with very attenuated and partially oceanised crust, as thin as 5 km in Northern Afar (MAKRIS et al,1972); and with an attenuated continental crust throughout, of thickness 14 to 22 km or greater (MAKRIS et al,1975), in harmony with BERCKHEMER's (1975) seismic refraction profiles. Such ambiguity is inherent in gravity interpretations.

HALL (1970) has prepared a total intensity magnetic anomaly map from 76 aeromagnetic profiles flown over Afar in 1968 at altitude 6000 ft with 10 km spacing. The original

interpretation was in terms of "most impressive" anomalies trending WSW from the Gulf of Aden across Southern Afar to the Western Ethiopian escarpment (GIRDLER,1970; GIRDLER and HALL,1972). Girdler may have been influenced by the hypothetical seismic line of the same trend, postulated by FAIRHEAD and GIRDLER (1970) but not supported by more recent geophysical evidence, except for the observed preference direction of an induced electric field (BERKTOLD et al,1975).

BARBERI and VARET (1975,1977) have reinterpreted Hall's map to show short NW- and NNW-trending magnetic lineations, which have been dated back to anomaly 2 positive*. The dates are consistent with radiometric age determinations. If real, these lineations strongly suggest that widespread oceanic spreading has been occurring in North and Central Afar since 4.5 Myr, as in the Southern Red Sea.

The evidence is by no means conclusive. Recent results from other areas have shown that the magnetic structure of the oceanic crust is much more complex than had previously been realised (e.g. BULL. GÉOL. SOC. FR.,1976; JOHNSON and MERRILL,1978). A new aeromagnetic survey over land in SE Afar (altitude 2000 m, 54 N-S lines with 5 km spacing) has yielded "low amplitude (< 200 nT), longer-wavelength (40 to 50 km) anomalies ... more randomly organized and somewhat

---

*Anomaly 4 (age 7 My), shown in North Tadjoura by BARBERI and VARET (1975, fig.1), has been deleted from the otherwise identical maps of VARET and BARBERI (1976, fig.2a) and BARBERI and VARET (1977, fig.13). These figures also show WNW-trending magnetic lineations in Southern Afar which have no other geophysical or geological justification.

typical of continental anomalies" (COURTILLOT et al,1980).

1.6 Summary

Many data have been presented which show the existence of an anomalous, low-velocity, high-temperature upper mantle beneath most or all of Afar. What they do not show is the depth of the crust-mantle transition.

There is abundant evidence that the basaltic axial ranges of Afar are spreading segments of new oceanic crust. Only KÜRSTEN (1975) has recently contested this view. In Southern Afar the autochthonous position of the Aisha block geometrically proscribes the formation of any significant amount of oceanic crust by NNW-SSE or NW-SE sea-floor spreading. Detailed geophysical investigations in this area have been few. The magnetic anomaly maps of BARBERI and VARET (1975,1977) suggest crustal spreading in a NNE-SSW direction, but the weight of other evidence has been shown to favour attenuated continental crust.

It is generally accepted that the Danakil block has undergone 10° to 30° of anti-clockwise rotation with respect to the Western Ethiopian plateau. This is attested by palaeomagnetic (BUREK,1970,1974,1978; SCHULT,1975) and other evidence. It follows that major crustal extension must have taken place across Northern and Central Afar. It is a major unresolved problem to what degree this extension has been accommodated by attenuation of continental crust, and to what degree by emplacement of new oceanic crust.

A second major problem is that of recognising the major

plate boundaries within Afar. It is widely agreed that the Asal rift in South East Afar is the western extension of the Gulf of Aden spreading axis; and that the Erta Ale range in the Danakil Depression marks an 'en échelon' continuation into Afar of the Red Sea trend. In the crucial intermediate area of Central Afar, which is macroseismically very quiet, the prospective line of major rupture is contested.

The present study of local earthquakes throws some light on both problems. Arrival time data have enabled the construction of a crustal and uppermost mantle model for South-Central Afar, and the degree of seismic wave attenuation has been investigated. The spatial and temporal distribution of the earthquakes, and their source parameters, have provided information on the local stress fields and current activity.

CHAPTER 2

THE ETHIOPIAN SEISMIC PROJECT: DATA ACQUISITION

2.1 Synopsis of the Project

The data derive from a feasibility study undertaken by the Ethiopian Awash Valley Authority, in connection with a proposed dam across the Awash river at Tendaho in South-Central Afar. A seismicity study was sub-contracted to Durham University as part of the site investigation. Political unrest in Ethiopia caused the contract to be terminated prematurely.

The objectives of the study, referred to as the Ethiopian Seismic Project (ESP), were:

(1) to predict the likely distribution and magnitudes of earthquakes in the vicinity of Tendaho during the expected lifetime of the dam, and in particular to detect local events which might indicate active faults close to the dam site. The 1969 swarm of destructive earthquakes, teleseismically located near Serdo, had demonstrated the likelihood of potentially damaging activity.

(2) to estimate the ground response of the site to earthquake motions. For this purpose a station was placed at the dam site. The specific information required was an estimate of expected ground acceleration at site.

No seismic stations had previously been operated within Afar. The seismicity was poorly known from the few events recorded at teleseismic distances (Section 1.4), and from

local historical non-instrumental records (GOUIN,1979).

The first stage of the experiment employed 4 widely spaced stations (separations approximately 50 km, see Figure 2.2.1) to obtain the overall pattern of local seismicity. The stations were not originally conceived as a network, but were intended to detect microearthquakes and to locate them using three-component analysis. For a later, second stage it was intended to install additional, closely spaced stations to study areas of particular interest. It was considered especially important to identify the focal depth of local events, information which is difficult to obtain from teleseismic measurements.

The traditional problem in feasibility studies is to obtain, in a realistically short time, sufficient data for reliable long term probability estimates. Usually this is done by extrapolating the magnitude-frequency relationship obtained for small earthquakes. The mechanisms and distribution of small events are not necessarily the same as those of large destructive earthquakes. Estimates can be obtained, however, and gross errors should be apparent after checking the results against teleseismic observations of the local seismicity.

Only the first stage of the ESP was realised before the project was abandoned. The stations were operated from 1973 July 21 until 1974 September 27. The present study covers the seven month period from 1974 February 20 (following the recording adjustments described in Section 2.4.2) to 1974 September 27.

2.2 Siting of the Recording Stations

The recording network, centred on the proposed dam site at Tendaho, consisted of 4 stations distributed widely across the Tendaho graben. Individual stations were sited on solid foundations wherever possible. Details are given in Section 2.3.

Considerations of security and accessibility placed very severe restrictions on the station sites. For ease of access the stations at Mille, Tendaho and Serdo were built adjacent to the Combolcia - Assab highway, the only all-weather road in the area. In retrospect, station Serdo was too close to the highway, as passing oil tankers caused ground vibrations which frequently saturated the recorder. Station Det Bahri was located about 2 km from the Det Bahri cotton plantation, and could normally be reached by Landrover. All stations were placed close to villages so that local tribesmen could be employed to guard them.

The resulting network had an overall length of 88.6 km from Mille to Serdo, but measured only 28.8 km perpendicular to the Mille-Serdo axis (Figure 2.2.1). The deficiencies of this configuration for locating earthquake hypocentres are discussed in Chapter 4. The network's detection capability could have been greatly enhanced by placing an additional station on the stratoid basaltic lavas north of Tendaho, at approximately 12°04'N, 40°57'E, but such a station would have been impractical to guard.

FIGURE 2.2.1

GEOMETRY OF THE ESP STATION NETWORK

(All distances are in km)

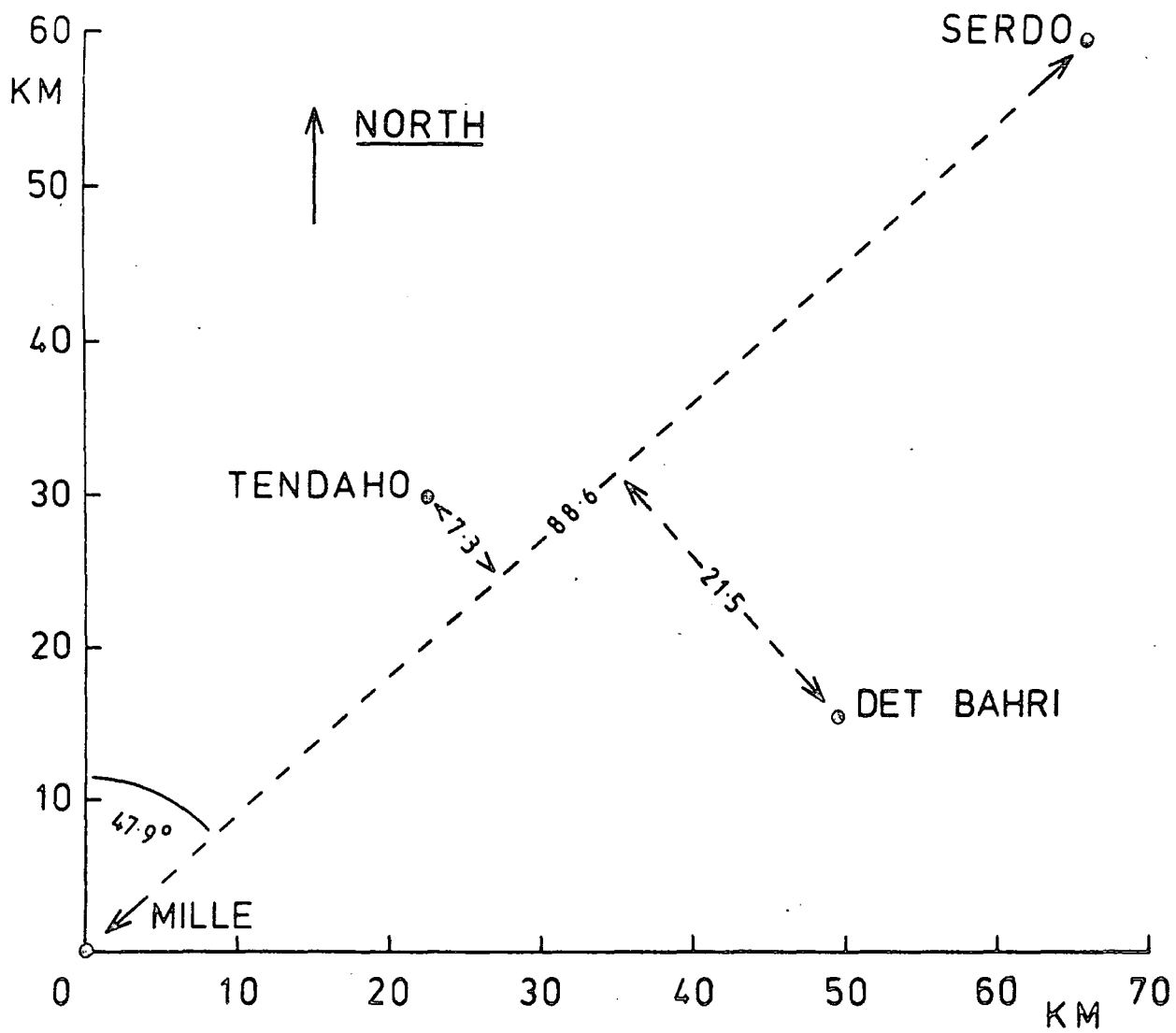

2.3 The Geology of The Tendaho Graben

It is clear from its position within Afar (Figure 1.1.2) that the Tendaho graben is crucial for the solution of the problems posed in Section 1.6. The new structural information obtained from ESP records throws light on the structure of Afar in general, and in particular on SCHAEFER's (1975) hypothesis that the Tendaho graben is currently a major spreading zone. This section describes the geology of the Graben, with specific reference to the ESP station sites.

The Tendaho graben (Figures 2.3.1, 2.3.2) is a conspicuous, sediment-filled NW-SE trough 50 km wide and 100 km long. Intense NW-SE and NNW-SSE faulting occurs at its margins (see also Figures 8.3.1, 8.3.3, 8.3.4 for greater detail). The same trends are seen cutting Recent volcanics on its floor, and are also inferred from hydrothermal activity at Airobera and at Dubti Plantation (UNDP,1973). Afar stratoid basalts on the western (Magenti Ale) and eastern (Gamari) flanks have K-Ar ages of 3.9 to 3.0 Myr (BARBERI et al,1975a). The graben began to form during the Pleistocene, by tensional faulting accompanied by both basic and silicic volcanism.

Magenti Ale is a major structural boundary within Afar, marking the most northerly expression of faults having the NNE-SSW trend of the Main Ethiopian rift. The rift terminates in the Tafeta and Allallobeda graben (Section 8.7). These graben are sinistrally offset 'en échelon' from the Issa graben, in contrast to the dextral offsets found

FIGURE 2.3.1

LOCATION MAP FOR THE TENDAHO GRABEN

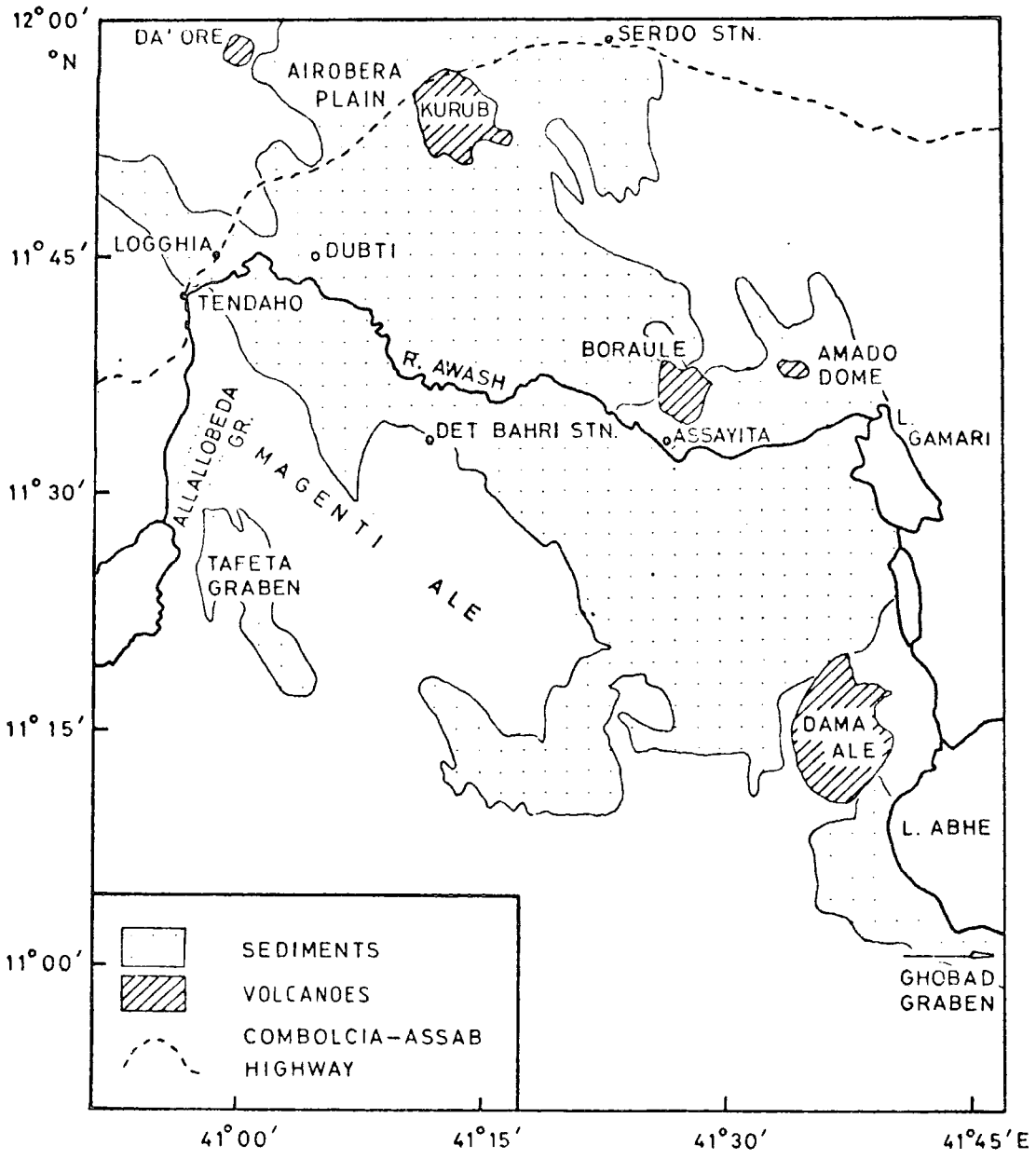

FIGURE 2.3.2

TECTONICS OF THE TENDAHO GRABEN AND SW AFAR

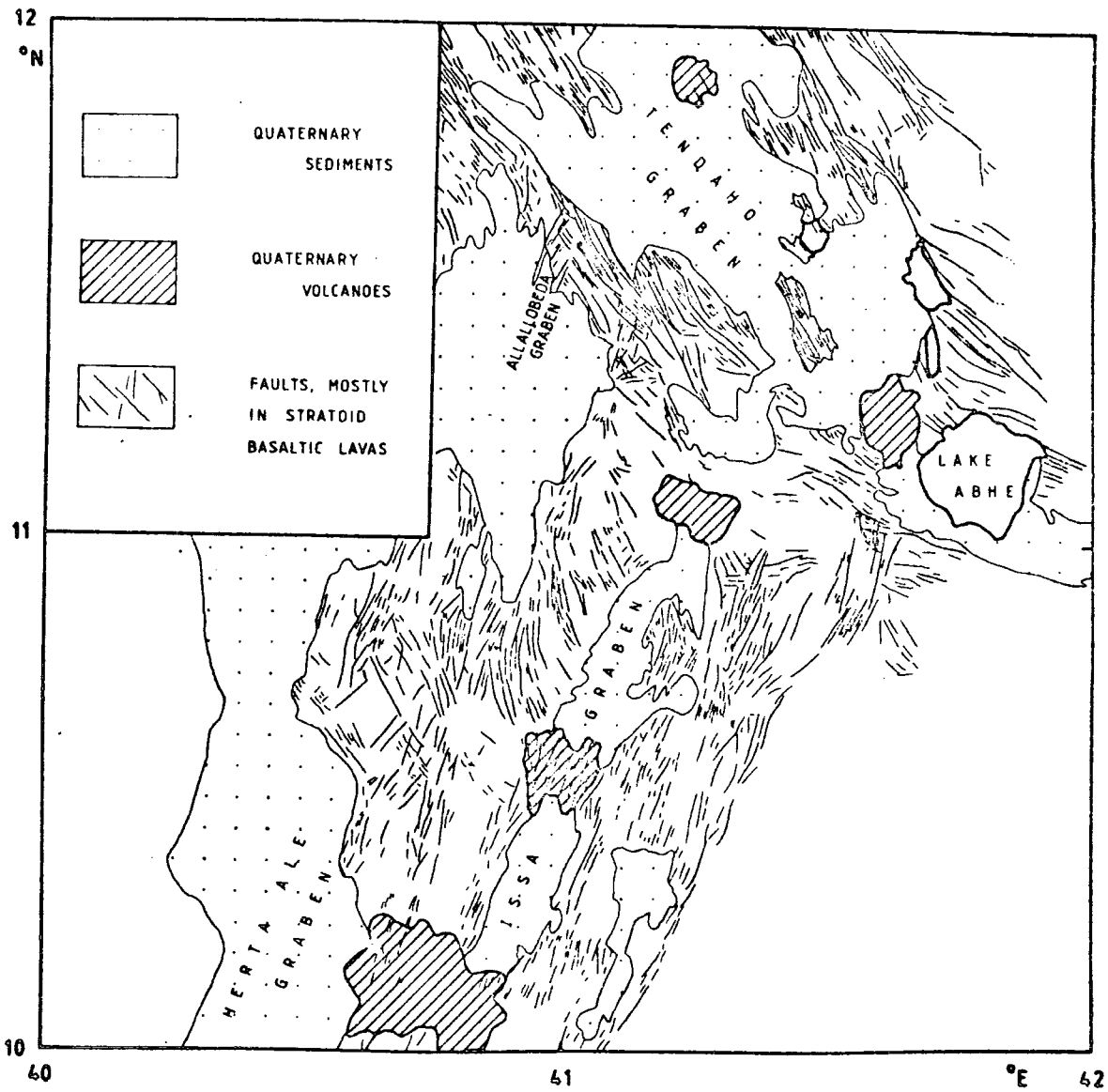

along the rest of the Ethiopian rift (Figure 2.3.2). In the terminal Allallobeda graben both NW-SE and NNE-SSW fault systems have been recently active, with structural evidence that the NNE-SSW faults are in some places the younger (UNDP,1973). Hot springs at Allallobeda have received attention due to their geothermal potential (MARRIOTT,1969; UNDP,1973; UN/ETHIOPIAN GOVT., no date). Their water is chemically similar to that from a well just west of Serdo, supporting the contention (TAZIEFF,1970) that the Tendaho graben is underlain by a large aquifer.

The total thickness of sediments in the graben is unknown, but probably exceeds 1000 m. TAIEB (1971) has shown that Quaternary marine transgressions affecting North and East Afar (ROUBET et al,1969; LALOU et al,1970; BONATTI et al, 1971) did not reach the Lower Awash valley.

Subsequent lacustrine sediments abound. Pure diatomite was deposited in deep lakes in all the basins of Central Afar from 35,000 to 20,000 years ago; and the Tendaho and Ghobad graben were covered by a single, smaller lake from 11,000 to 6,000 years ago (GASSE,1975). Study of these and of more minor lacustrine episodes (TAIEB,1971; GASSE and ROGNON,1973; ROGNON and GASSE,1973; GASSE,1974) has shown that neotectonic movements have been small, although down-tilting of the Tendaho graben towards the east has been inferred (GASSE,1974), and north of Lake Abhe deposits less than 2,000 years old are disturbed by groups of open faults (ROGNON,1975, orientation not stated). Major lake level variations are contemporaneous with those in East Africa and

in the South Sahara belt (GROVE and GOUDIE,1971), and are governed by regional climatic changes rather than local tectonism.

The majority of the igneous rocks exposed in the Tendaho graben are flood basalts. The oldest sequence has not been dated locally, but near Serdo and west of Det Bahri it overlies rhyolites correlated with Gad'elu rhyolite dated at 0.34 Myr (UNDP,1973). Many volcanic centres within the graben post-date the Lower Holocene lake, and all are cut by NW-SE or NNW-SSE faults. Examples include the shield volcano Kurub, Da'Ore and the centres to its south east, and the basalts north west of Asayita. The largest rhyolitic massif, Boraule volcano, is elongated along a NW-SE axis. Its lavas were probably extruded from a major NW-SE fault whose surface expression is concealed by young sediments.

Several recently active volcanic centres have erupted both basalts and rhyolites on different occasions. South east of Da'Ore the rhyolite pre-dates the basalt, but the rhyolitic volcano Amado Dome, the youngest in the graben, has arisen over Recent basalt extrusions. Amado Dome may have been the source of the destructive seismic activity, associated with a volcanic eruption, recorded in Aussa in 1627, although Dama Ale has also been suggested (GOUIN,1979; DAKIN et al,1971).

The geology of the station sites is significant in the interpretation of reverberations caused by very shallow structures (Chapter 7). The following notes are based on the author's field observations, augmented by the local map

reproduced in UNDP (1973, fig.53) (see Figures 8.3.1, 8.3.3, 8.3.4).

Station MILLE was situated on stratoid basaltic lavas approximately 1 km south west of Mille village. Less than 1 km to the east the basalts are overlain by Pleistocene conglomerates and then by Quaternary alluvium, sand and silt deposited by the Weranso and Awash rivers. One NNE-SSW and three NNW-SSE minor faults are mapped in the vicinity.

Station TENDAHO (Figure 2.3.3a) was sited on stratoid basalts above the true left bank of the Awash river at the proposed dam site. Quaternary deposits of the Awash flood plain occur nearby to the north east. A line of fumaroles and hot springs south east of the station trends NNW and is associated with the major Logghia fault. A few fumaroles on the Awash flood plain suggest that the fault continues 2 km to the east of the station, where it is obscured by sediments. Many other NNW-SSE faults occur locally, downthrown to the east to form the graben margin. The closest NNE-SSW faults of the Allallobeda graben system are 8 km to the south south east.

Station SERDO was located in an area of intense NW-SE faulting approximately 4 km east of Serdo village and north east of the plain of Kurub, which consists of water-lain sediments of tuffaceous sand, gravel and clay. It was sited on one of a series of ridges of highly contorted pink rhyolite. "These ridges are long, parallel fault blocks, trending N40°W and tilted toward the south west. They present a steep, almost vertical fault scarp toward the

FIGURE 2.3.3

(a) Station Tendaho, overlooking the Awash river at the proposed dam site

(b) Durham seismic recorder, GRUNDIG receiver and LECLANCHÉ dry cells (Section 2.4) in operation at Dubti during the aborted second phase of ESP, November 1974 (Section 2.7)

(a)

(b)

north east and a gentle slope on the dip side" (DAKIN et al,1971). 500 m north east of the station a band of loose basalt boulders overlies the rhyolite. 3 km to the east occurred the faulting, cracks and rockslides associated with the 1969 Serdo earthquakes.

Station DET BAHRI lies on a small extrusion of Quaternary rhyolite, bordered to south and west by stratoid basalts exhibiting intense NW-SE faulting. Hot ground occurs 1 km to the east. 50 m to the north and east are the Quaternary graben floor sediments.

2.4 Seismic Recording Equipment

2.4.1 Choice of Recording Equipment

The ideal recording system for the ESP would have been a telemetrically-linked network, consisting of a number of outstations linked to a single recorder and clock. A telemetric network has several obvious advantages over separately recording instruments. Such a system has been used successfully by the IPG (Institut de Physique du Globe, Paris) seismic project in Djibouti (LEPINE and RUEGG,1973,1976 and pers. comms.), but was impractical for the ESP for security reasons. The auxiliary stations, particularly their aerials, would have been too vulnerable, and the employment of local tribesmen to guard them would have afforded insufficient protection.

Again for obvious reasons, in this application event-triggered recording would have been preferable to

continuous recording. However, it would not have been possible to set up an automatic event detector so as to avoid an excessive number of triggers by noise bursts. Furthermore, weakly recorded events which might not trigger an event recorder are useful in this study in cases where they have been more strongly received at other stations.

It was consequently decided to use independent, continuously recording stations. The equipment at each recording site consisted of a three-component set of Willmore Mk II seismometers, a Durham-built seismic recorder incorporating amplifier and time code generator units, a Grundig radio receiver and a power source (Figure 2.3.3b). To ensure security, the sets of equipment were placed in permanently guarded huts built of breeze blocks and having steel doors. The huts were windowless, except for small steel grilles placed as air vents just below roof level. They were floored with concrete and roofed with corrugated iron. The roofs were weighted with sandbags to reduce wind-induced seismic noise, which was initially excessive.

Equipment repairs were made at Dubti in the site engineer's caravan, where a supply of tools and spare parts was available. The caravan also contained limited test facilities, including a storage oscilloscope and a single-channel pen oscillograph.

2.4.2 The Seismic Recorders

The Durham seismic recorder has been described by LONG,R. (1974b). It is a F.M. recorder designed for use in remote areas where portability and low power consumption are desirable, coupled with the possibility of continuous unattended operation over periods of several days. It comprises three separate modules (normally housed together): tape unit; three-channel amplifier and frequency modulator; and digital clock and time code generator. It incorporates exhaustive checking facilities, which were routinely monitored during station visits.

The tape transport is that of a Tandberg model 11 recorder, modified to run continuously at speeds of 0.05 or 0.1 in s^{-1} and to record through an eight-track head on to quarter-inch magnetic tape. In this application the three seismic channels were separated by blank tracks in order to reduce possible "cross-talk". The three remaining tracks were used to record a 100 Hz reference frequency, a radio signal and a time code.

Initially, the tape transports used Scotch Instrumentation Quality recording tape. The extremely high temperatures (greater than 120°F) inside the recording huts caused a loosening of the oxide coating on the tape. This not only impaired the quality of the records, but made the tape guides so sticky that the tape would ultimately twist over or stop. The problem was resolved in February, 1974, by using a different brand of tape, Agfa-Gevaert triple play. The tape speed initially used was 0.05 in s^{-1}.

Shortly after the introduction of the Agfa tape the speed was increased to Ø.1 in s⁻¹, further improving the recording quality. With tape reels 36ØØ ft long this should give a running time of exactly 5 days, but in practice each tape was found to last for approximately 4.8 days only.

The most frequent cause of poor quality recording was worn or misaligned tape heads. Once the supply of spare heads in Ethiopia was exhausted it was necessary to re-use the least worn of the previously discarded heads. Alignment of the record head is critical, and site engineers did not always take sufficient care. On two recorders the positions of the tape guides were moved, so that the tape ran unevenly over the heads. Faulty record head alignment was shown by loss of recorded signal strength on one or other of the outside channels (E-W seismometer and time code), apparent from routine field checks (Section 2.5); and by time differences between the recorded tracks which had to be compensated on playback. The problem has been reduced on the current version of the seismic recorder by fitting non-adjustable tape heads.

Minor difficulties involving the tape units included the slackening of springs controlling the tension of the teflon brake pads, causing excessive wear on the latter; and wear on one set of rubber tape driving belts due to initial misalignment.

Radio and time code are also recorded in F.M. mode. The frequency modulated forms are obtained by allowing the code pulses to switch the carrier frequency between 5Ø Hz

and 100 Hz. Both recorded channels thus have a binary character. On playback in Durham the 50 Hz and 100 Hz frequencies correspond to binary 0 and 1 respectively, so that sharp-edged time code and G.M.T. pips are produced. Both frequencies are derived from the clock, as is the 100 Hz reference frequency. The reference frequency is used for flutter compensation on playback (see Section 3.2 and Appendix 3). In part of this work it is also used in a servo loop to maintain the replay speed at a constant multiple of the recording speed.

The source for the clock frequencies and time code is a thermally compensated 5 MHz crystal oscillator with a nominal stability of one part in 10^6. Clock drift may arise from inexact adjustment of the crystals' frequencies in the laboratory prior to setting up the experiment, or from alteration of their fundamental frequencies due to ageing. There is no necessity for highly accurate clocks, provided their drift is linear and they can be calibrated against an absolute time reference. The clocks at Serdo and Tendaho lost approximately 0.5 s day^{-1}, while the Det Bahri and Mille clocks drifted at about 1.0 s $week^{-1}$. The features of the time code are explained in Section 3.9.

The amplifier unit contains three amplifiers set electronically to the same nominal gain, adjustable over the range 100 to 51200 in ten stages of approximately x2, so that a gain setting 'n' corresponds to a gain of 100×2^n ($0 \leqslant n \leqslant 9$). This system allows the amplifier gain setting (which is logged within the time code) to be altered in the

field to accommodate variations in the level of ambient seismic noise and/or expected seismic signal.

In the initial search for microseisms the amplifier gains were set to gain 9. In February, 1974, the gain was decreased by a factor of 4 to gain 7. This not only reduced noise interference but also increased the high frequency cut-off (Figure A3.1, Appendix 3). After amplification the seismic signals are used to frequency modulate a carrier having a nominal centre frequency of 84 Hz.

2.4.3 The Seismometers

Three-component sets of Willmore Mk II seismometers (HILGER and WATTS,1964) were used, adjusted to operate with a natural period of 1.Ø s. The periods could be checked by direct observation of the undamped motion of the mass.

The seismometers were connected to the seismic recorder through screened coaxial cables, and through the input circuitry shown in Appendix 7, Figure A7.3. The resistances were chosen to give about 1Ø% of overshoot following displacement of the mass, equivalent to a seismometer damping factor of approximately Ø.7. The cables were colour-coded to lessen the possibility of their being wrongly connected into the amplifier.

The seismometers are calibrated by applying a sequence of current steps through a Wheatstone bridge, of which the seismometer coil and sampling resistor comprise one arm. The current steps effect small displacements of the seismometer mass, which then executes damped oscillations

which are recorded on to tape in the usual way, giving on playback the impulse response of the complete recorder-playback system. The bridge is so balanced that the current itself produces no voltage input to the recorder.

Positive and negative calibration current steps are applied automatically by depressing a switch on the recorder. During every station visit each seismometer was calibrated both at the operating gain and at the lowest gain setting. The latter calibration gives the system's impulse response with minimum contamination from any external seismic signal or noise source. The amplitude of the current steps is varied automatically with the gain of the recorder, so that the recorded amplitude of the impulse response does not depend on the gain setting.

Considering the extremely hot and dusty operating environment, the seismometers were notably reliable. One jammed and another went open circuit, in both cases due to loose sealing plugs permitting the entry of dust and water. The cases of the seismometers became encrusted in up to half an inch of dust and sand. They were thoroughly cleaned and covered by polythene sheeting. Very little dust had penetrated the cases.

2.4.4 The Radio Receivers

The sole purpose of the radio receiver at each site was to enable the recording of G.M.T. pips for absolute time reference. Portable domestic GRUNDIG receivers were used, and were usually left tuned to the East Mediterranean (15.42 MHz) transmitter of the British Broadcasting Corporation overseas service. This service transmits time pips, on the hour, at every hour between 04.00 and 21.00 hrs G.M.T., excepting 08.00 and 10.00 hrs.

The GRUNDIG receivers were modified to use the tone switch to cut out the external loudspeaker, thus saving power during normal use. The loudspeaker could be switched into circuit by the site engineer in order to monitor the time pips or retune the receiver. The radio signal was fed to the frequency modulator via an amplitude discriminator, causing a binary high to be recorded when the input was above a threshold value. Adjustment of the threshold control was critical. Too high a setting caused triggering by noise, while too low a setting resulted in poor detection of G.M.T. pips.

2.4.5 The Power Source

When used in Europe the Durham seismic recorders are usually powered by eight PP9 (1.5 V) dry cells, housed internally, with a life-time of approximately five days. For ease of operation in Ethiopia the power source was a bank of nine 1000 Ampere-hour LECLANCHÉ dry cells, connected in series to give approximately 12 V. The cells, freighted

dry from England, were activated in the field by being filled with distilled water. They provided power for the first nine months of continuous operation of the seismic stations, after which their voltage output had fallen to a level (9.5 to 10.0 V) no longer sufficient to power the clocks.

Replacement sets of LECLANCHÉ cells were sent from Durham, but were held up in customs in Addis Abeba. During the period June to September, 1974, the four seismic stations were therefore powered by five 12 V accumulators, which were recharged periodically in rotation. Thus the accumulators each provided power for five days of continuous recording, and were replaced whenever a tape was changed.

2.5 Routine Field Recording

To obtain continuous recordings it was necessary to visit each station a minimum of once every 4.8 days to change the tape. While the author was in the field each station was routinely visited every two or three days, and Tendaho station (which lay on the route from Dubti to Mille) almost every day. Frequent station visits were desirable so that the radio receivers could be retuned and any recording difficulties corrected as soon as possible.

The thoroughness of routine tape-changing visits varied from site engineer to site engineer. The author's routine will be described. On arrival, each seismometer was calibrated at the operating gain on the old tape, provided it still appeared to be running satisfactorily. The tape

was then wound off and the tape heads and guides cleaned with ethyl alcohol to remove dust and tape residue.

The new tape was set in motion at the lowest amplifier gain setting and run in this way for two or three minutes, during which time the seismometer was calibrated. It was easier on playback to minimise the residual flutter on the seismic channels in the absence of large amplitude signals. When the amplifiers had been switched back to the operating gain the seismometers were calibrated again.

During the calibration the induced oscillations of the seismometers were checked visually and audially, both before and after recording, using the meter and loudspeaker in the amplifier unit. The amplitude and shape of the recorded calibration pulses indicate the gain and linearity of the seismometers, while the degree of overshoot signifies their damping. Short-circuited or open circuit seismometers are immediately detectable, as are any seismometer masses which are not moving freely over their range of displacement.

The correct operation of the recording system was verified using the checking facilities built into the Durham recorder. The meter on the amplifier unit was switched to monitor in turn the amplifier outputs, recording head currents, radio, clock and reference signals; and the voltages of the stabilised power lines. The F.M. signals at the recording head were also checked audially as a final guarantee of correct system operation. The results were noted on log sheets, of which an example is shown in Figure 2.5.1. The time and status of the clock, and the amplifier

FIGURE 2.5.1

SPECIMEN FIELD LOG SHEET

SEISMIC INVESTIGATION PROJECT — TENDAHO DAM SCHEME-ETHIOPIA

STATION IDENTITY TEN DAM HO — LOG SHEET NOS. 192 — DATE 13/9/74

ARRIVAL TIME	12.40	DEPARTURE TIME	13.10
TIME GAIN SWITCHED TO ZERO	13.04	TIME GAIN SWITCHED BACK TO NORMAL SETTING OF	13.05 7

VERT GAIN 0	E – W	GAIN 0	N – S	GAIN 0			D. L. V. T.
SEIS 13.04	SEIS	13.04	SEIS	13.05			VOLT CHECK
CHECK GAIN 7	CHECK	GAIN 7	CHECK	GAIN 7			SUPPLY TO INST.
AT 13.06	AT	13.06	AT	13.06			ACC.
TIME	TIME		TIME				

TIME TAPE SWITCHED TO 0.1 INCH PER SEC	TIME TAPE SWITCHED BACK TO 0.05 INCH PER SEC.

AMP SELECT SWITCH	DIRECT PLAYBACK	TAPE PLAYBACK	TAPE NOS.
CH. 3 VERT	OK	OK	54 removed
CH. 1 E-W	"	VERY LOW	
CH. 2 N-S	"	OK	55 started
CH. 4 REF.	"	"	
RADIO	"	"	
TIME CODE	"	LOW	

F.M.-SW. UP	METER INDICATION.	F.M. - SW. DOWN.	METER INDICATION
ZERO (0V)	OK		
CLOCK POWER (0V)	"	(POS) CLOCK POWER	OK
TIME CODE	"	TIME CODE REC. HEAD VOLT.	"
DETECTED RADIO	"	F.M. RADIO REC. HEAD VOLT.	"
TIME CODE AND RADIO	"	REF. FREQ. REC. HEAD VOLT.	"
GLOBAL POWER (NEG).	"	GLOBAL POWER (P.S.)	"
AMP. POWER (NEG)	"	AMP. POWER (POS.	"
OUTPUT OF VERT. SEIS. I.	"	OUTPUT O. VERT. SEIS. I.	"
OUTPUT OF E-W SEIS. II.	"	OUTPUT OF E-W SEIS. II.	"
OUTPUT OF N-S SEIS. III	"	OUTPUT OF N-S SEIS. III	"
RECORD HEAD ALIGNMENT AT TIME		PLAYBACK HEAD ALIGNMENT AT TIME	
VISUAL CLOCK CHECK	"	CLOCK ERROR	25.44 SECS. SLOW AT 13.00 HRS.
RADIO OFF	/	TAPE STOP	OK
RADIO ON	/	TAPE START	12.49

OBSERVATIONS — Cleaned heads etc. with ethanol
installed plastic knob from Sit Bahri

CHECK MADE BY ....W. G. Rigden..... ALL TIME IN G. M. T.

gain setting, were checked by switching on the incandescent display panels of the recorder and reading the successive blocks of time code information being recorded on to the tape.

At each station visit particular attention was given to the quality of recording of G.M.T. pips. Reception conditions were extremely variable. Station visits were made in the early morning whenever possible, not only to avoid the heat of the day but because radio reception was usually best at this time. The GRUNDIG receivers are inductor-capacitor tuned, and tended to drift off-frequency. The scarcity of well-recorded time pips in the evenings, when the stations were seldom visited, might also be due to a systematic diurnal tuning fluctuation caused by the large variations in the ambient temperature.

The author usually arranged to arrive at the recording stations at about ten minutes before an hour, to give time for retuning before the G.M.T. pips. He then listened to the pips through the radio's external speaker (to verify their adequate reception) and observed on the recorder's monitoring meter the pulses corresponding to binary highs recorded on to the tape (to check the setting of the trigger threshold).

It was possible to use the single-channel pen recorder to obtain in the field a reading of the clock error. For a few seconds before and after the hour the encoded clock time was recorded, but for the duration of the G.M.T. pips the radio channel was displayed. The clock error could then be

measured with a ruler, essentially as described in Section 3.10, to an accuracy of ±0.03 s.

Occasionally, no signal could be received on 15.42 MHz. The receiver could then not be tuned and the site would be revisited a few hours later. Time pips transmitted by other broadcasting stations are not necessarily synchronised to G.M.T., and no other frequency proved to be a viable alternative to 15.42 MHz.

2.6 Station Maintenance Difficulties

2.6.1 The Environment

All four stations were inaccessible during most of August 1974 due to unusually severe seasonal flooding. The track to Det Bahri regularly became impassable for periods of several days after storms.

Two stations were disabled by thieves' attempts to break in through the protective steel grilles of their air vents: Mille, where battery leads were disconnected but no serious damage done to the equipment; and Serdo, from which the radio was removed through the grille, presumably by its aerial.

On one occasion the wooden lid of the recording unit at Serdo was left unlocked. By the time of the next visit six tape head leads had been severed, apparently chewed by a rodent whose droppings were found on the tape deck.

2.6.2 Field Staff

The job of providing site engineers to operate and maintain the ESP recording equipment was contracted to Hunting Engineering Ltd. Due largely to the impending political upheaval in Ethiopia it was a major problem to find suitably trained personnel to staff the Project. Four site engineers, some of whom lacked both experience and commitment, were employed during the seven months covered by this study. The author acted as site engineer during the final five weeks of recording. One site engineer visited each station only once during a period of over two months, during which he entrusted the job of station maintenance to his untrained Ethiopian interpreter. The major recording discontinuity in May and early June results from his negligence.

The running time of each magnetic tape was approximately 4.8 days. Periodic short breaks in recording at individual stations were caused by some engineers changing tapes every fifth rather than every fourth day. Longer recording discontinuities resulted from their incompetence to detect and remedy equipment faults. The clock circuits in particular were beyond their skill to repair. Maintenance difficulties were aggravated towards the end of the Project by lack of spare parts.

Periodic visits to Addis Abeba were necessary in order to despatch tapes and receive equipment to and from Durham. The seismic stations could not be visited during these periods. Figure 2.6.1 shows the state of operation of each

station during the time period covered by this study, and Table 2.6.1 summarises the causes of the major recording discontinuities.

Any future long-term experiment along the lines of the ESP should recruit one experienced engineer, who should train two or more local employees to assist with tape changing and routine station maintenance. The modular design of the Durham seismic recorders makes them suitable for medium-term maintenance by unskilled personnel, provided that complete spare modules are available at site. If a fault cannot be immediately repaired it is simple to substitute a replacement module. The engineer need not therefore remain permanently on site, but must return at intervals of not longer than three months to carry out complete checks of all instruments and to make necessary repairs.

2.7 Use of ESP Data for Research

At the start of the research project the ESP records were intended for use with two main objectives: (1) a study of local earthquakes; and (2) an investigation of the deep structure beneath the network using teleseismic events. As the work evolved, it was decided to restrict this project to the first study, the second being continued by Mr Hugh Ebbutt.

Following the cancellation of the commercial project in October, 1974, it became possible to use the equipment for pure research. Since it was no longer possible to safeguard

FIGURE 2.6.1

RECORDING STATUS OF THE ESP STATIONS

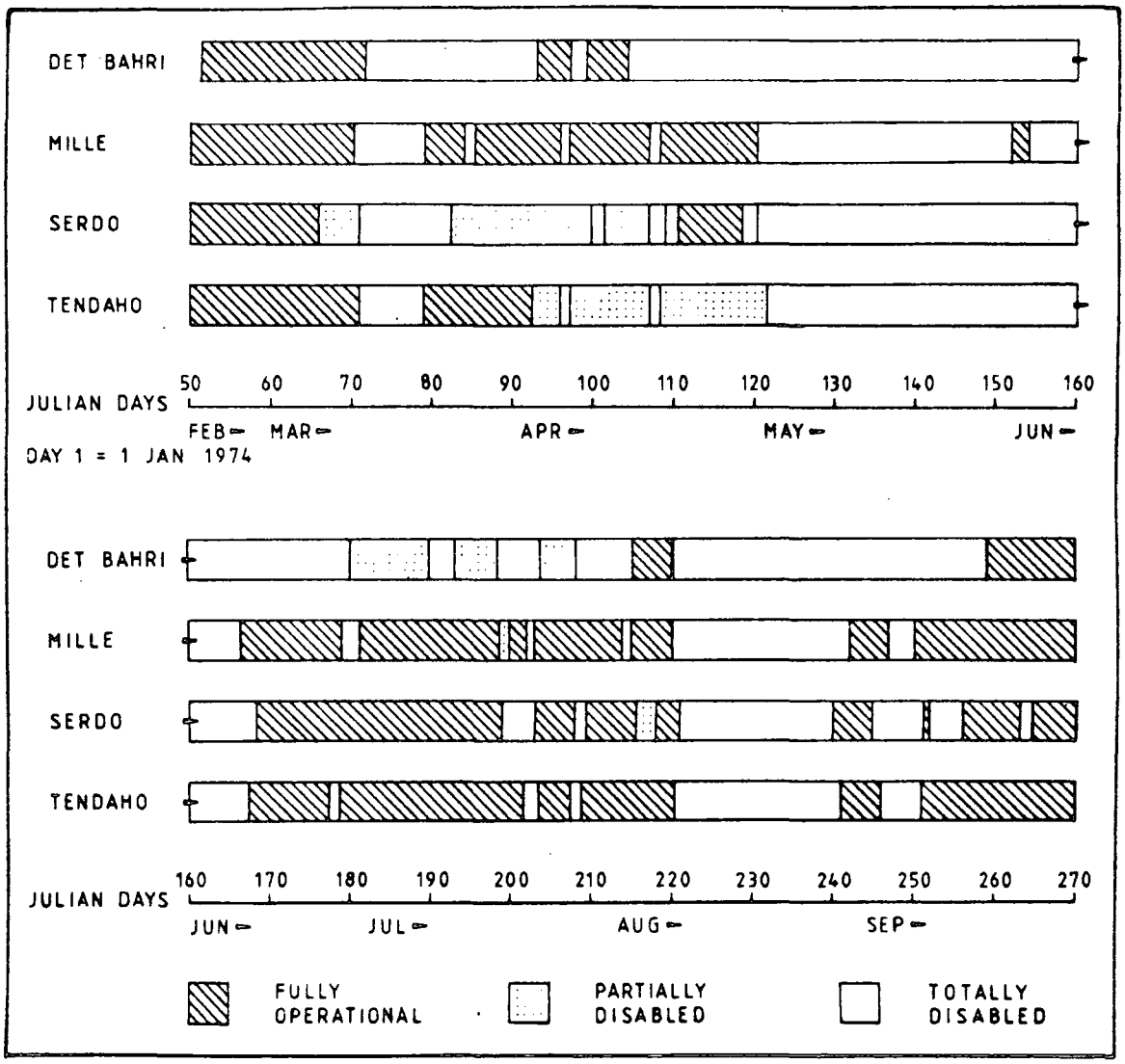

TABLE 2.6.1 RECORDING DISCONTINUITIES AT ESP STATIONS

DATES	STATIONS	CAUSE OF DISCONTINUITY
7 Mar to 19 Apr	Serdo	Clock fault
11 Mar to 19 Mar	All (illegible records)	Scotch tapes used
16 Mar to 2 Apr	Det Bahri	Flooding
20 Mar to 23 Mar	All	Site engineer absent
4 Apr to 9 Apr	All	Site engineer absent
13 Apr to 14 Apr	Serdo	Tape drive fault
14 Apr to 3 May	Det Bahri	Station not visited
20 Apr to 23 Apr	All	Site engineer absent
21 Apr to 26 Apr	Serdo	Tape stuck
1 May to 6 Jun	All	Inadequate power supply
? Jun to 15 Jul	Det Bahri	Intermittent radio fault
18 Jun to 28 Jun	Det Bahri (no spares available)	No record head
1 May to 6 Jun	All	Inadequate power supply
28 Jun to 30 Jun	Mille (power supply interrupted)	Vandals
8 Jul to 26 Jul	Det Bahri	Jammed seismometer
15 Jul to 17 Jul	Mille	Clock fault
15 Jul to 23 Jul	Det Bahri	No record head
18 Jul to 22 Jul	All	Site engineer absent
23 Jul to 2 Aug	Det Bahri	Jammed vertical seismometer and flooding
24 Jul to 25 Jul	Serdo, Tendaho	Landrover out of service
2 Aug	Mille	Dust storm
3 Aug to 5 Aug	Serdo	Radio stolen
7 Aug to 28 Aug	All	Flooding
2 Sep to 7 Sep	All	Site engineer absent
2 Sep to 7 Sep	Det Bahri (lack of parts for repairs)	Station closed
9 Sep to 13 Sep	Serdo	Tape twisted and stuck
21 Sep to 22 Sep	Serdo	Tape head leads damaged

desert sites within Afar, it was decided to extend the range of the project by operating a regional network for a further twelve months. The purpose was to locate and analyse larger earthquakes occurring throughout Afar and its margins. Three of the recording stations were relocated at Dubti, Alemaya and Addis Abeba, and the fourth was intended for Asmara. Continuing deterioration of the political situation in Ethiopia necessitated the rapid evacuation of these stations before they had yielded any useful information.

The following chapters describe the results of analyses of the local earthquakes recorded by the 4 ESP stations.

CHAPTER 3

PRELIMINARY PROCESSING AND EXAMINATION OF FIELD TAPES

3.1 Introduction

The ESP field recorded analogue magnetic tapes were played back and analysed in the University of Durham seismic processing laboratory. Selected records were digitized for further processing using the CTL MODULAR 1 computer. The processing facilities available at Durham are summarised in Figure 3.1.1.

This chapter presents the techniques used for demodulation and frequency filtering, and the means of obtaining hard copies of seismic events. The problem of event recognition is described, and the digitization procedure outlined. Finally, the accurate timing of the seismograms is discussed, and an assessment made of the causes of timing errors.

3.2 Playback

Three different playback systems have been in use at Durham since the start of the Ethiopian Seismic Project. Until late 1974 a standard set of E.M.I. F.M. demodulators was used, in conjunction with a modified deck manufactured by Tape Recorder Developments Ltd. and operated at 23.81 mm s^{-1} (15/16 inches per second). All records originally processed with the E.M.I. demodulators were reprocessed using one of the subsequent systems.

FIGURE 3.1.1

DURHAM UNIVERSITY STANDARD SEISMIC PROCESSING FACILITIES

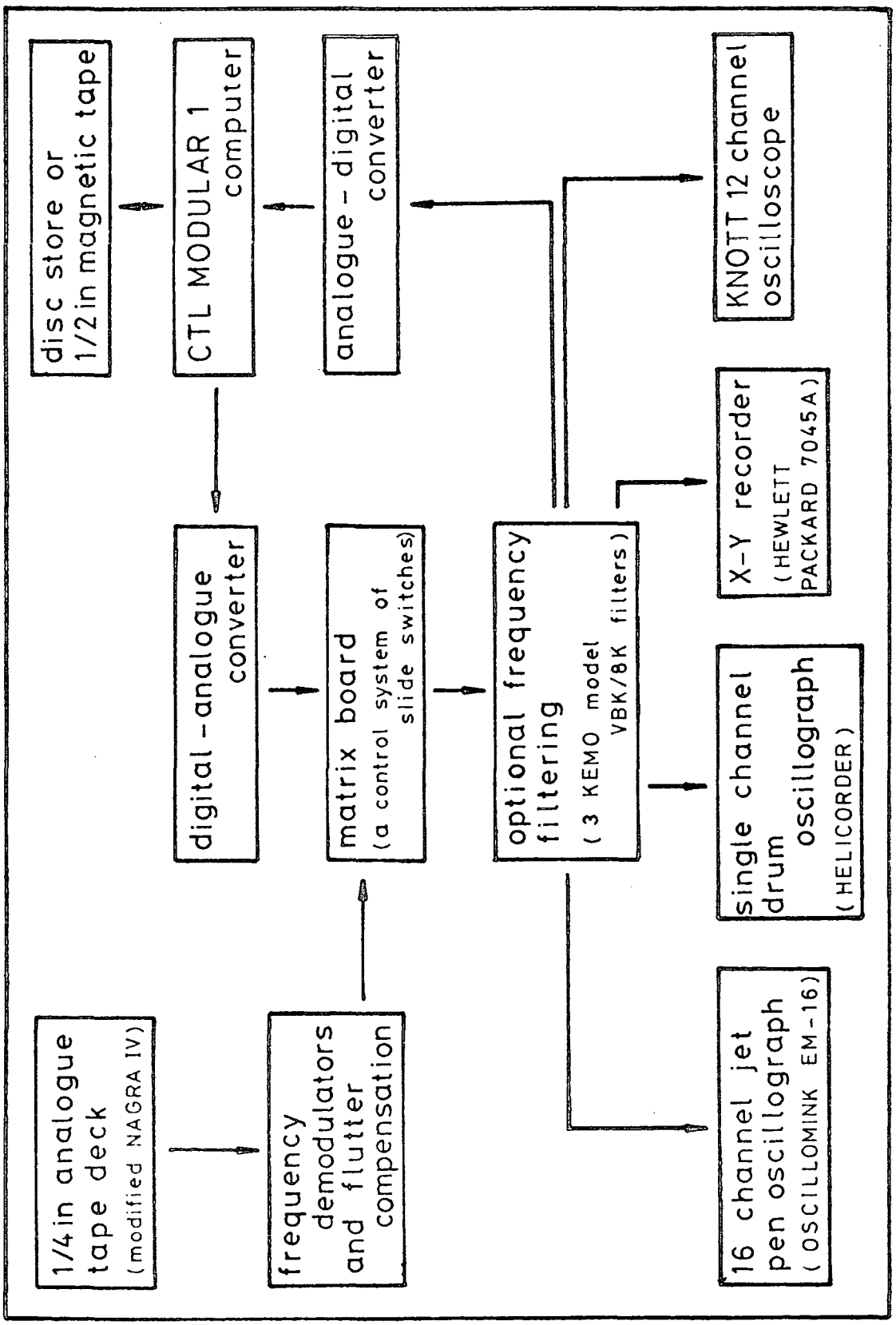

The second playback system utilised demodulators designed and built at Durham. The tape transport was a commercial NAGRA IV deck, modified to run at a constant speed of approximately 25.4 mm s^{-1} (1 inch per second). The deck was fitted with a head of the same type as used on the field recorders, which was adjustable to reproduce the setting of the field recording head. Tape skew was therefore minimised.

The demodulators converted the modulated carrier frequency on all channels to a voltage proportional to that frequency. The conversion was carried out using phase locked loop circuits. After demodulation, flutter compensation was carried out by electronic subtraction of the demodulated reference signal from the other recorded signals. This operation is only effective if the tape head is correctly aligned, so that there is no time difference between the recorded signals.

Demodulator gains were adjusted for optimum flutter compensation while the tape was running and the reference signal and uncompensated output of the seismic channels displayed on the 12-channel oscilloscope. The position of the tape head was adjusted through its mounting screws until the flutter signals on all output channels were in phase. Then, with subtraction of the reference channel in effect, the amplitude of each seismic channel in turn was matched to that of the reference signal by minimising the residual flutter seen on the oscilloscope. Finally, it was usually necessary to alter the d.c. levels of the voltage outputs to

compensate for variations of the seismic modulator centre frequencies. These adjustments were carried out each time a tape from a different field recorder was to be processed and whenever the setting of a field tape head was altered, and at the start of each laboratory session if the playback system had been adjusted by other users. Where the tape had not run evenly over the field recording head it was sometimes necessary to readjust for individual seismic events.

The frequency range of the phase locked loop used in the second playback system was insufficient. As explained in a different context in Appendix 3, the effect of a seismic signal of amplitude S is to modulate the carrier centre frequency by an amount $\Delta f = kS$, where k is a constant. If S is large, Δf may exceed the range of the phase locked loop, causing it to 'lose lock'. This problem was manifested on seismic playouts as replacement of high amplitude seismic signals by a spurious high frequency (carrier breakthrough) superimposed on a slowly decaying d.c. voltage pedestal (the demodulation circuitry required several seconds to recover from the out of lock condition). The problem was exacerbated by any drift of the carrier centre frequency from the centre of the demodulator locking range.

Another problem with the second playback system was that there was no means of compensating for variations of field recording speed, which were reproduced on playback as spurious frequency variations. Accordingly, the system was

superceded during 1976.

The third playback system, also designed and built in Durham, has a greater frequency range in the phase locked loop and successfully overcomes the problem of signal loss at high amplitudes. The quality of the binary output from the time and radio tracks has also been improved, by modifying the demodulators for these tracks. The demodulators now act as frequency comparators, outputting a binary high or binary low according to whether the recorded frequency is above or below a threshold value. The leading edges of the pulses are sharpened and any residual carrier is eliminated.

Both improvements are illustrated in Figure 3.2.1, which is a tracing of playouts on the 16 channel jet pen oscillograph. The same nominal paper speed was used for the two sets of traces, which show the same saturating seismic arrival and associated time code. (The paper speed was faster for the lower set of traces because the oscillograph had been recently overhauled). Note that all traces are inverted on the third playback system, with respect to the second system.

The major modification in the third playback system concerns the playback speed. The average playback speed is now held at exactly ten times the recording speed by feedback from the demodulated reference signal, which controls the speed of the deck drive motor. However, the NAGRA deck is being operated far below its lowest design speed of 95.25 mm s^{-1} (3.75 inches per second), resulting in

FIGURE 3.2.1

ILLUSTRATION OF DIFFERENCES BETWEEN THE TWO DURHAM-BUILT PLAYBACK SYSTEMS

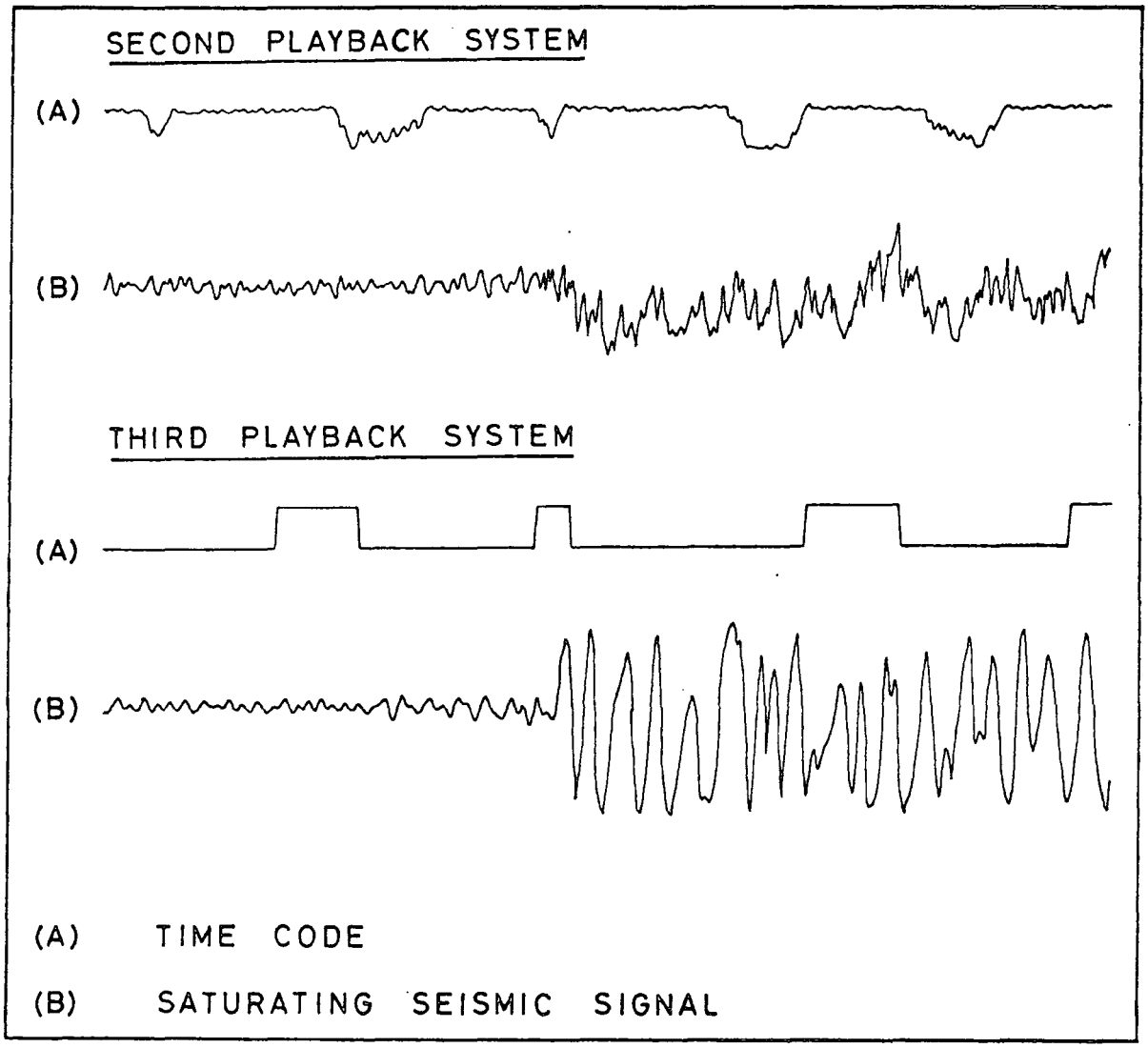

an instability that causes the instantaneous speed of the deck to oscillate about the controlled average speed. Additional flutter is thus produced. It is shown in Appendix 3 that complete flutter compensation by subtraction is theoretically impossible, and that the flutter generated is so great that at signal amplitudes near to saturation the dynamic range of the system is reduced to 23 dB.

Full flutter compensation may theoretically be achieved by dividing a linear function of the signal by a linear function of the reference track. However, accurate electronic division is far less easy than subtraction, and the only practical alternative is to use computer processing of digitized channels. Although the method has been shown to work in principle on the MODULAR 1 it has proved to be less effective than subtraction compensation at low signal amplitudes, where efficient compensation is most important. This is due to cross-talk between channels in the analogue-digital converter.

The third playback system has the further disadvantage that tapes with a poorly recorded reference track cannot be played back.

3.3 Performance of the Recorder-Playback System

No record existed of the frequency response and dynamic range of the Durham-built seismic recording equipment and associated playback electronics. Tests to determine these characteristics are described in Appendix 3. The major results may be summarised as follows:

(1) The frequency response was constant to ~3 dB over the frequency range of interest in this study (Table A3.1), during which the amplifiers were operated at gain setting 7.

(2) The dynamic range at gain 7 and 1 Hz was 36 ± 3 dB (Table A3.2), falling to 30 ± 3 dB at 8 Hz. It was not possible to approach the dynamic range in excess of 50 dB reported by LONG,R. (1974b) using the E.M.I. demodulation electronics. At maximum signal amplitude the dynamic range did not exceed 23 dB.

These tests were made using the third playback system. The performance of the second playback system was never measured, but was unlikely to have been better. The input impedance of the recorder used in the tests was matched to that for field operation.

The specification of the Willmore Mk II seismometers has been published (HILGER and WATTS,1964). When operated at a natural period of 1.0 s, as in this study, their frequency response is essentially flat throughout the range of interest (1.0 Hz to 15 Hz).

3.4 Determination of Seismometer Polarities

Three component analyses (Chapter 6) and focal mechanism studies (Chapter 8) can be carried out only if the polarity of the recording seismometers is known. This information was not available from ESP station logs. However, for an explosive source the initial P motion should be compressional in all directions. The sense of the first motions of seismometers recording explosions is therefore

predictable, and their polarities can be checked.

A nuclear explosion of magnitude M_b = 6.4 occurred at Novaya Zemlya (73.4°N, 54.9°E) on 1974 Aug 29 at 10.00 hr. From Novaya Zemlya the ESP network has approximate azimuth 195° and distance 63°. The first motions observed on ESP seismometers should be:

Vertical	Up (+)		
North-South	Down (South)	(-)	
East-West	Down (West)	(-)	(with lower amplitude)

The explosion was well recorded at Tendaho (Figure 3.4.1) and at Serdo, and shows clearly the correct polarity of all the seismic traces at these stations, as played out using the second playback system (Section 3.2). The third playback system (to which the senses of all motions will subsequently be referred) inverts all channels relative to the second playback system. Thus all three seismic channels at Tendaho and Serdo have reversed polarities with respect to the newer system.

No explosions were detected at Mille or at Det Bahri. However, after correcting for reversed polarities at Tendaho and at Serdo the most distant events recorded throughout the study showed the same direction of first motion at all ESP stations. This was to be expected if all the seismometers now had the same polarity, since these events have very similar azimuths from each station. It was therefore likely that Mille and Det Bahri seismometers had correct polarity.

As further evidence of correct polarity it was found that the first motions of teleseisms on the vertical seismometers agreed with those observed at AAE and ART

FIGURE 3.4.1

SEISMIC TRACES OF A NUCLEAR EXPLOSION AT NOVAYA ZEMLYA, PLAYED OUT USING SECOND PLAYBACK SYSTEM

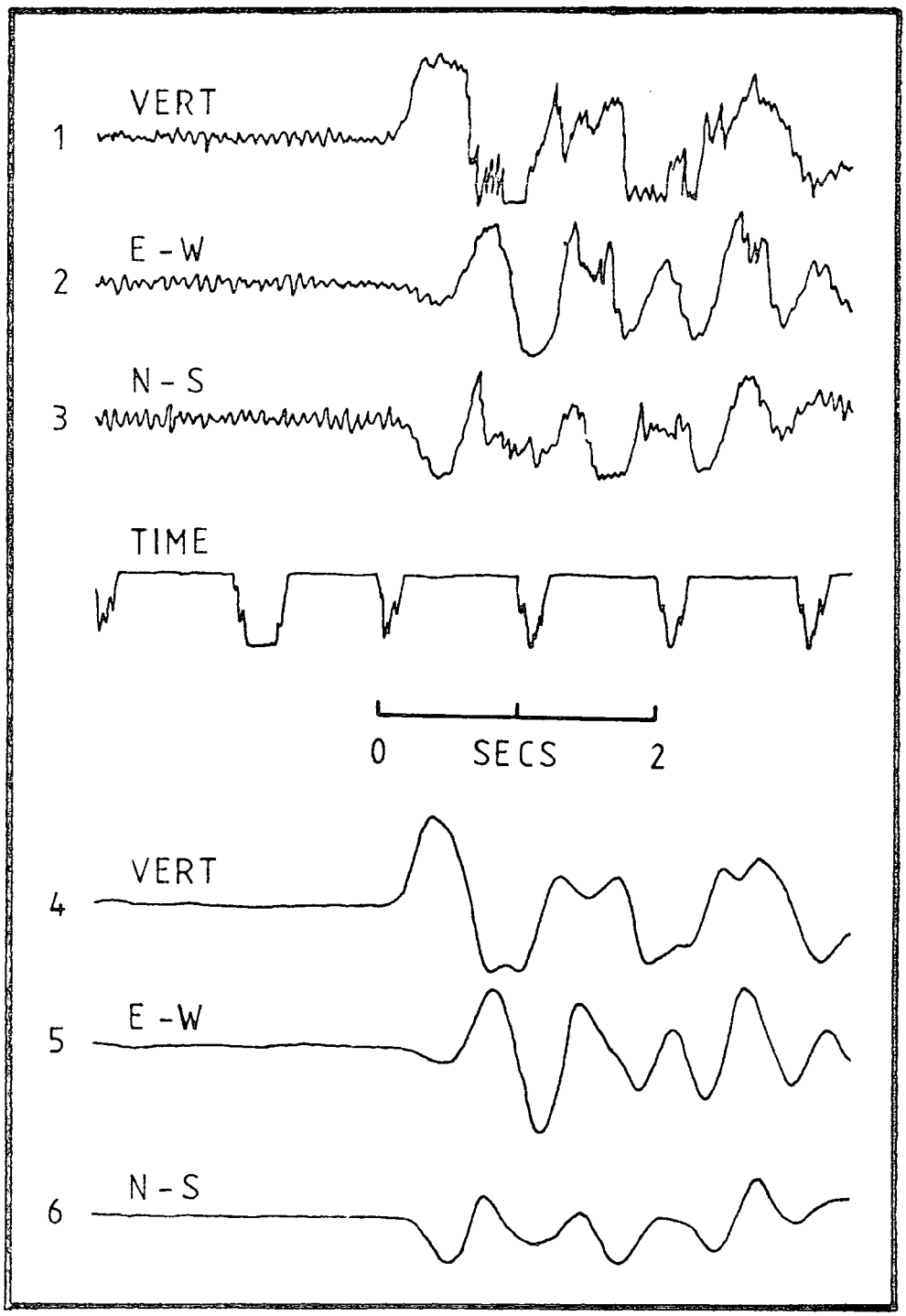

(Gouin, Ruegg, pers. comms.). For the horizontal seismometers, confirmation came from the concordance between event azimuths determined by three-component analysis (Table 6.6.1) and by phase arrivals at several stations (Chapter 4).

3.5 Filtering

The purpose of filtering is to enhance the required seismic signal relative to noise. For routine processing of ESP data the only filtering used was electronic band-pass filtering. Unfiltered and filtered seismic tracks were played out side by side on the jet pen oscillograph. More sophisticated processing techniques, discussed in Chapter 6, were used on selected records to enhance particular phase arrivals.

Band-pass filtering can only be used to reduce those components of noise which have frequencies outside the frequency range of the required signal. The pass band must be carefully selected to prevent the signal waveform being severely distorted by differential attenuation and phase shifting of its various frequency components. Events with epicentral distances up to approximately 150 km were filtered with a band pass of 2 to 12 Hz. For more distant events the band pass was 1 to 10 Hz.

During most of the processing period three KROHN HITE model 335 variable frequency filters were in use. These produced unacceptable phase distortion. They were superceded by three KEMO model VBK/8K filter units with

greatly superior performance. Both types of filters had variable corner frequencies and 24 dB Oct-1 roll-off.

Unfiltered and frequency filtered records were Fourier transformed, and when compared the filtered records showed a spurious peak at 5 Hz. This corresponds to a 50 Hz peak on playback, and was traced to mains pick-up within the filter and associated wiring.

3.6 Initial Recognition of Seismic Events

Initially, tapes recorded at all four sites throughout one full month were played out on to the Oscillomink 16 channel jet pen oscillograph and searched for near-contemporaneous disturbances on the seismic channels at two or more stations. This enabled the character of records of local earthquakes to be established. The majority of recorded events were large enough to be identified at more than one station.

In order to find all useful events, tapes from at least one station must be played out continuously throughout the period of the study. Mille station, which was generally the quietest, was selected for this purpose. Tendaho and Det Bahri, the central stations of the network, were better positioned, but the recordings from both were unsuitable. Det Bahri was out of service for long periods (Figure 2.6.1), while Tendaho was subject to frequent periods of saturation by noise bursts resulting from other contractual operations at the prospective dam site.

The routine event identification procedure at Durham is

for tapes to be played out on to the HELICORDER single channel drum oscillograph. The vertical seismometer channel is normally displayed. The HELICORDER consists of a hot wire scriber, attached to a galvanometer movement, which reproduces the seismic trace on heat sensitive paper rolled around a revolving cylindrical drum. The galvanometer base moves slowly parallel to the drum axis, giving rise to a helical trace. Three and a half days of continuous recording can be displayed on a single sheet of paper, at a recording density of 9 mm per recorded minute. The playout time required for this (at 10 times recording speed) is approximately 8.5 hr, and the oscillograph can conveniently be left running overnight.

Numerous attempts, at various gains and with and without KROHN HITE frequency filtering, were made to obtain satisfactory HELICORDER traces of the Mille tapes. It was found that many noise bursts had sharp onsets and decay envelopes so similar to those of the seismic events sought that noise and earthquakes could not be distinguished on a single, condensed trace. All the Mille tapes were therefore played out at a nominal speed of 1 mm per recorded second on to the Oscillomink 16 channel jet pen oscillograph. Ideally, all Serdo tapes should also have been played out in this way to ensure that no events from the east were missed, but lack of system time precluded this. Disregarding playback problems and system adjustments, initial playout of 200 days of tape from one station at ten times the recording speed required 480 hr of processing time and 17.3 km of

paper.

An advantage of 16 channel initial playout was that the radio and time traces could be played out alongside the seismic channels. Thus the hours could be noted at which G.M.T. pips had been well recorded, and the approximate time of the seismic events read. (No correction was made at this stage for clock errors, which seldom amounted to more than a few seconds).

Events found at Mille were then sought at the other stations. When an earthquake was found to have occurred close to another station two or more days of tape from that station, both before and after the earthquake, were played out continuously to see if the earthquake was part of a swarm with smaller events not identifiable at Mille.

During periods when Mille station was not functioning, seismic events were sought by continuous playout of the Serdo records.

3.7 Reading and Identification of Seismic Onsets

All onset times were picked from paper records produced by the Oscillomink 16 channel jet pen oscillograph. This instrument passes constant streams of ink through its sixteen jets on to moving sheets of paper. Each jet is mounted on a galvanometer movement, which is deflected in a plane perpendicular to the motion of the paper according to the electrical signal applied to it. The galvanometers are mechanically damped.

Before use for seismic playouts the alignment of the

pens was checked by generating a calibration pulse simultaneously on all channels, and was corrected if necessary. Misalignment along the plane of paper motion, which would correspond to systematic skewing of the playouts, could be reduced to less than Ø.1 mm (the error detectable with a ruler) using the galvanometer movement adjusting screws.

The demodulated traces were displayed in the following order: time, 3 seismic unfiltered, time, 1ØØ Hz reference, 3 seismic filtered, time, radio. The amplitudes of the unfiltered seismic channels were equalised by adjusting the jet pen gains and checked by playing out the seismometer calibration pulses at the start of each tape. For matched seismometers, these pulses should have the same amplitude and shape when recorded on to tape. To ensure consistency, they were always compared with a standard trace, which had a peak-to-peak amplitude of 3Ø.Ø mm. This method of checking was preferred to displaying the same signal on all three channels, since it compensates for any gain variations between the amplifiers of the recorder/playback electronics.

All events were first played out at a nominal paper speed of 5 mm per recorded second. This playback density gave the clearest indication of each event's overall character, and provided the amplitude and signal duration measurements required for magnitude estimates. The majority of events were then replayed at a nominal playout speed of 5Ø mm per recorded second. At this speed, time is easily measured to better than Ø.Ø1 s (Ø.Ø5 mm). Onset times were

measured against the second pulses of the flanking time code, as depicted in Figure 3.7.1. It was necessary to measure the paper distance, b, between each second marker since the tape and paper speeds were not constant from record to record. For the second playback system, for which the leading edges of the time pulses were less sharp and rapid fluctuations in playback speed were not a problem, b was measured as the mean over 5 s of playout.

P-wave onsets were measured from the first break on the unfiltered vertical seismic traces. Most events closer than 100 km had predominant frequencies of 5 to 10 Hz. Their onsets were sharp and could be picked unambiguously as abrupt amplitude discontinuities (e.g. Figure 4.3.3).

First arrivals from events beyond 150 km (Figure 3.7.2) were often emergent and of lower predominant frequency (2 to 4 Hz). The unfiltered waveforms at different stations were sufficiently similar for a waveform matching technique (EVERNDEN,1953) to be used. The waveform from the station at which the event was most clearly recorded was traced on to transparent paper, together with the estimated first break. The records at other stations, where the first break might not be visible, were matched with the tracing (it was sometimes first necessary to reverse their polarity, see Section 3.4). Relative picking errors were thus reduced. The superiority of waveform matching over the alternatives of measuring either first peaks or first cross-over points (which require the accurate recognition of these characteristics) has been demonstrated by CORBISHLEY

FIGURE 3.7.1

MEASUREMENT OF ONSET TIMES

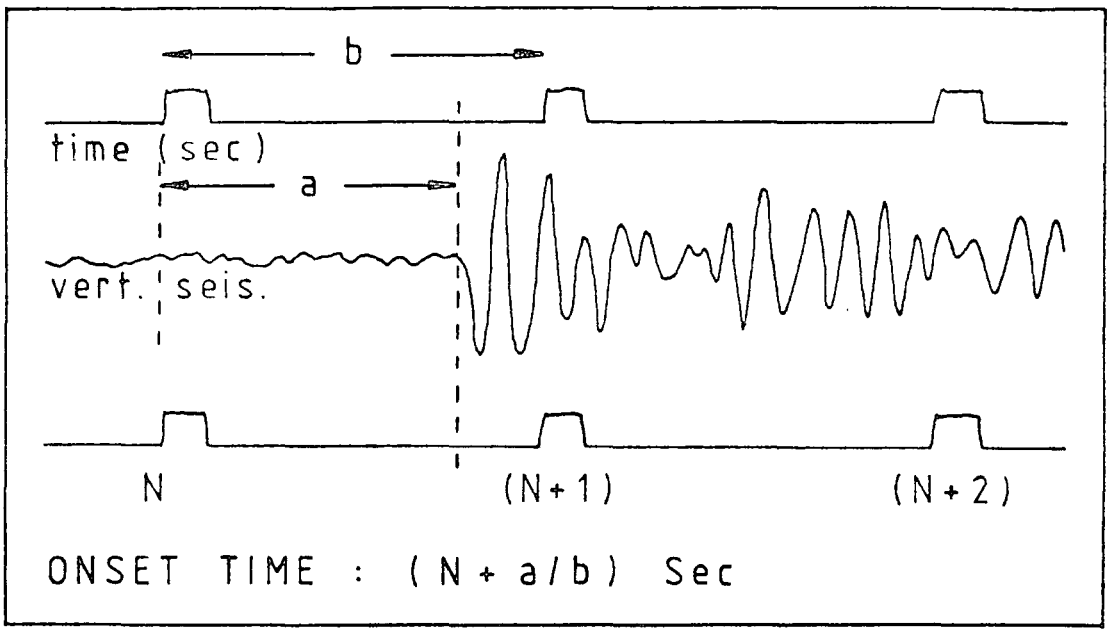

FIGURE 3.7.2

ORIGINAL ANALOGUE PLAYOUTS OF TWO MORE DISTANT ESP EVENTS

(a) M274. Distance 210 km, azimuth 231°
(b) T340. Distance 351 km, azimuth 27°

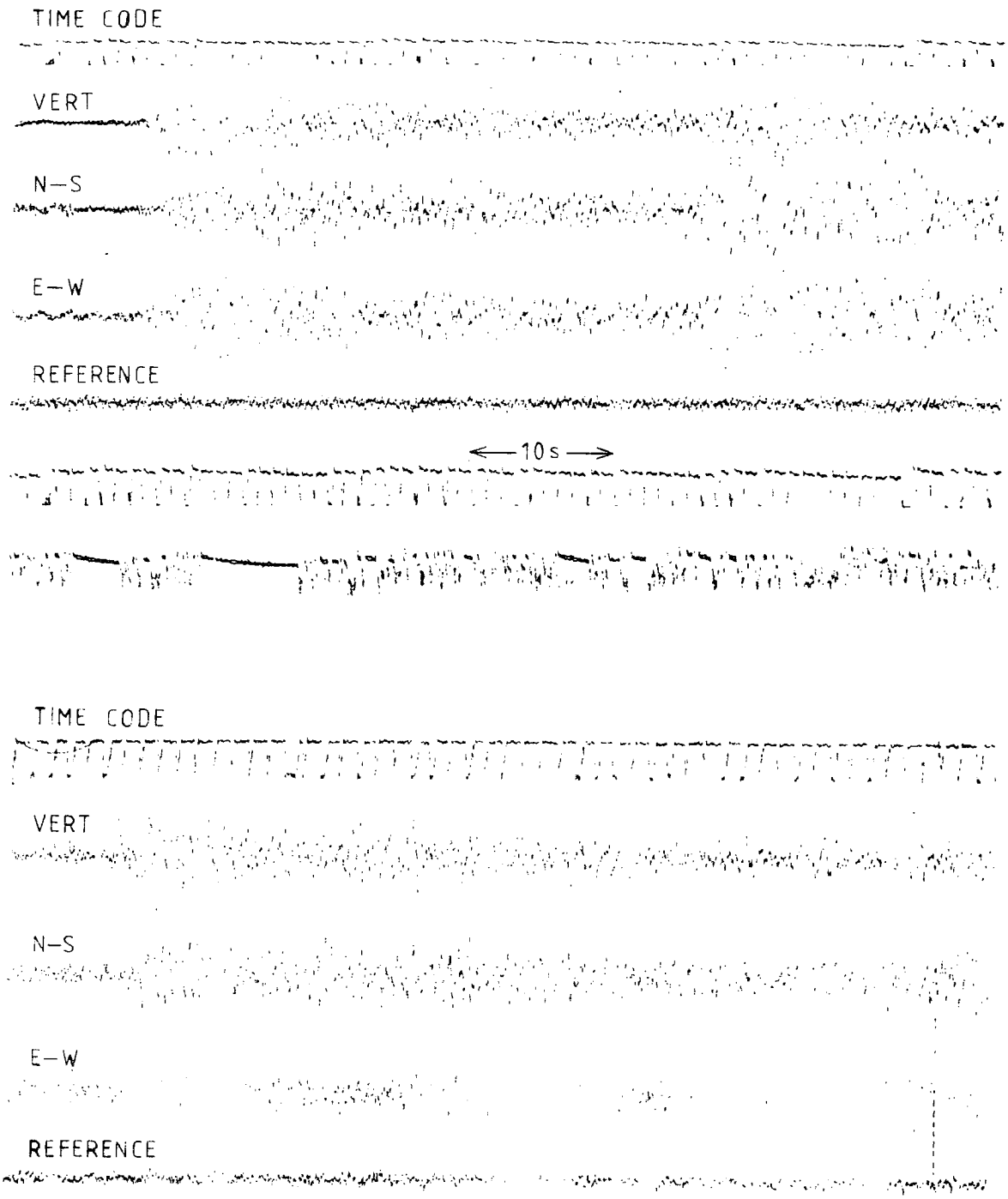

(1969,p.18) for teleseismically recorded explosions which could be treated as repetitions of the same event.

S-wave onsets were read from the unfiltered horizontal seismometer traces. They were harder to pick, being perturbed by earlier arrivals and sometimes of low amplitude. They characteristically showed slightly higher frequencies than the preceding cycles of the P-wave coda, because of coda multipathing.

S-waves can be distinguished from P and surface waves by their polarization. For digitized records, identification was checked by three-component analyses: polarization filtering and display of the particle motion (Chapter 6). It was particularly important to ensure that S arrivals were not confused with surface waves, since systematically late picking of S would have indicated spuriously high values of Poisson's ratio. This study does not attempt the analysis of surface waves.

All seismic onsets were picked twice, at an interval of approximately eighteen months. The two sets of readings were essentially independent, since the records were left unmarked on the first occasion. Before the second readings, preliminary hypocentres had been determined where possible, and events with similar hypocentres grouped together. In this way intra-group inconsistencies in picking the onsets were reduced.

The two independent readings showed a time difference of 0.03 s or less for over 90% of fair or well-recorded arrivals from 75 km or closer. In a few cases the earlier

readings were discounted on grounds of reader inexperience: otherwise mean values were taken.

Other possible arrivals occurred between the first P and first S. To reduce the likelihood of spurious readings of superpositions of earlier phases, these arrivals were only picked when clearly visible as similar phase or amplitude discontinuities on records of two or more similar events. They were observed from well recorded events that caused ground velocities of moderate amplitude at the recording stations: not so large that later onsets were swamped by the first arrival, nor so small that they were hidden in noise. They are discussed more fully in Section 4.3.

3.8 Digitization and the CTL MODULAR 1

Records were digitized using the Durham CTL MODULAR 1 computer. The MODULAR 1 incorporates a disc store and a half-inch tape drive. It is programmed with Durham-written software designed to facilitate the handling of the pseudo-infinite time series encountered in seismic records.

The records were digitized to allow the use of more sophisticated processing techniques. It was originally intended to use the MODULAR 1 for all digital processing, and a number of computer programmes were written for this purpose. However, breakdowns were frequent and the small storage capacity of the MODULAR 1 was a handicap when attempting processing in the frequency domain.

Although the MODULAR 1 computer has been used in this

study for some three-component analyses, the NUMAC (Northumbrian Universities Multiple Access Computer) IBM 360/370 has been preferred for Fourier transforms. A programme written by the author in conjunction with FEATHERSTONE (1976, appx.2.2) enables half-inch digital tapes recorded using the MODULAR 1 to be read by FORTRAN programmes written for NUMAC. An improved version is incorporated in programme TRANSF (Appendix 9, this study). The peculiar format of MODULAR 1 magnetic tape files has been fully described by ARMOUR (1977).

Transfer of ESP data from quarter-inch analogue tapes to half-inch digital tapes was not the routine procedure that had been expected. ESP seismic records contain no significant frequencies above 20 Hz, as subsequently confirmed by spectral analysis (Chapter 7). This is approximately the high frequency limit of the recorder/third playback system instrumental band pass. Thus a digitization rate of 50 samples s^{-1} should have been sufficient to avoid aliasing. However, spurious frequencies of 35 to 40 Hz were present on records processed with the second playback system and could not be satisfactorily removed by the KROHN HITE filters then in use. Records were therefore digitized at 100 samples s^{-1}. At this sampling rate it was beyond the capacity of the half-inch tape drive to accept the newly digitized records directly without loss of information. The records were therefore digitized on to disc files, which were then transferred to tape.

170 records were digitized in this way. Eight tracks

were available on the digital tape. Each seismic channel was digitized unfiltered and band-pass filtered with a 2 to 12 Hz band pass. The two remaining tracks were the demodulated 100 Hz reference channel and the time code.

Several digitization programmes were written for the MODULAR 1. The programme eventually adopted employed an amplitude detector on the vertical seismic channel, with a threshold adjusted for each event so that digitization would be initiated by the first arrival. The system memory was set so that the preceding 2 s of signal would also be captured on to each channel. This allowed for the first half-cycle of the first arrival, which was sometimes of low amplitude. It also enabled the signal/noise ratio to be evaluated and used as a trigger criterion in subsequent processing.

Digital records were also made of noise samples and of the system response to seismometer calibration pulses at each station. The maximum length of each digital record was limited to 71 s by the capacity of the disc store.

Digitized tapes were subject to varying sample rates from file to file, and sometimes within a file. The author's programme DCHECK, written for the MODULAR 1, samples the digitized time channel and recognises the onsets of second markers. It prints out the mean and standard deviation of the sampling rate along the file. DCHECK also calculates and subtracts from the seismic channels the d.c. voltage bias caused by drift of the carrier centre frequency; and associates each sample with its position in

time within the digital file, for use in later analyses.

Tapes digitized by the MODULAR 1 sometimes contained parity errors. These errors were eliminated by taking the tapes to Newcastle for copying on NUMAC, which overrode them. The copied tapes were entirely satisfactory when subsequently played out on the MODULAR 1. They faithfully reproduced the analogue traces, demonstrating that the parity errors had not arisen as the consequence of inaccurate recording.

3.9 The Time Code

Encoded time, generated internally in the seismic recorder, was recorded on to tape along with other system information as described in Chapter 2. Before the seismograms can be timed the time channel trace must be decoded.

The demodulated time code comprises a series of binary high pulses whose leading edges should occur at intervals of exactly one second. The pulse lengths are Ø.1, Ø.3 or Ø.7 s. Pulses of length Ø.1 and Ø.3 s represent binary zeros and ones respectively. Every sixtieth pulse has length Ø.7 s and serves as a minute marker.

Each minute of time code is divided into six ten-second blocks by a binary one pulse every tenth second. Within each block, the first eight pulses indicate a binary coded two digit decimal number. The ninth pulse of each block is always binary zero. The first three blocks following the minute marker indicate the current clock time in minutes,

hours and Julian days (up to 99), while the less significant digit of the fourth block shows hundreds of Julian days. The more significant digit of block four is the station code. The fifth block displays the current amplifier gain, and the sixth is empty. The contents of each block are automatically upgraded each minute.

A tracing of a well-recorded one minute length of time code is shown in Figure 3.9.1. On many tapes the recording quality is poor, and several minutes of code may be needed in order to infer the values of digits where pulses are missing or are obliterated by spurious binary highs.

3.10 Absolute Timing of Seismograms

All the tapes were searched for G.M.T. pips by playing out the radio trace for a few minutes on either side of each recorded hour (as determined from the time code). The second playback system was in use at this stage of the processing, and the tapes were played out on to the jet pen oscillograph at a speed of 2.5 mm per recorded second. The third playback system gave time and radio traces which were easier to read (Figure 3.2.1). For the few residual pip searches made after the introduction of this system it was possible to use the 12 channel oscilloscope instead of the jet pen oscillograph.

As explained in Section 2.4, G.M.T. pips were not often adequately recorded on the tapes, due to indifferent reception, drifting of the tuning between station visits or incorrect setting of the binary trigger threshold. Pips

FIGURE 3.9.1

A SAMPLE OF TIME CODE

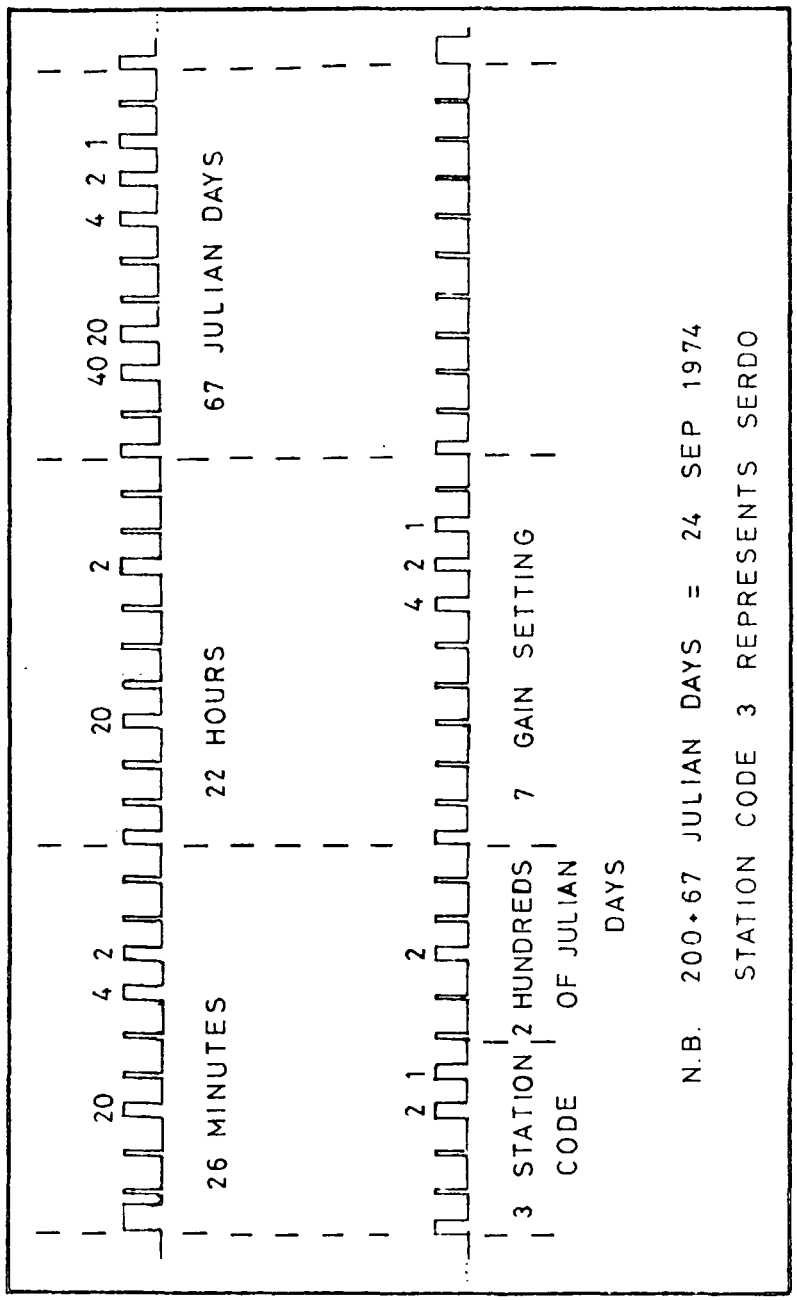

were usually best recorded in the early mornings, the time of day when the stations were most frequently visited. Although the network aperture was small, there was no significant correlation between stations for the times of well-recorded pips. This indicates either very local variations in propagation conditions, or differential drift of the tuning of individual sets. Tuning drift is considered to be the major cause of inadequate reception.

An average of two sets of well-recorded pips per day is quite sufficient to define the drift curves of well-behaved clocks. However, the quality of the radio traces was poor and it was usually necessary to search every hour when G.M.T. pips were transmitted in order to find enough. This was a time-consuming process, and constitutes a major disadvantage of independently recording stations.

G.M.T. pips consist of a sequence of six pulses of a 1 KHz tone, whose leading edges are separated by precisely one second. The final pulse is longer than the others, and commences at the exact instant of the hour. Once a set of pips was found, it was played out again at the faster nominal oscillograph speed of 50 mm per recorded second. The time trace was played out closely on either side of the radio trace. The number of integral seconds of clock error was determined by inspection of the position of the final G.M.T. pip relative to the time code. A line was then ruled between the leading edges of equivalent second pulses on the two time traces. The distance between this line and the leading edge of the next G.M.T. pip, expressed as a

fraction of the mean paper distance between adjacent second markers, gave the remaining fractional clock error.

The fractional component of the clock error was measured with reference to each well-recorded pip, to the nearest Ø.Ø1 s. On re-examination, inconsistent values could normally be attributed to distorted pips. They were then discarded. The mean of the remaining measurements was used in plotting the drift curves, and their standard deviation indicated their accuracy.

Standard deviations were typically Ø.Ø25 and Ø.Ø3 s for the second and third playback systems respectively. Sets of measurements with significantly higher standard deviations were discarded. At first sight it may be surprising that the third playback system gives rise to slightly higher standard deviations. These reflect its poor instantaneous speed stability. Sharper pulse onsets are not necessarily more accurate onsets (Section 3.11).

For each station, measured clock errors were plotted against time in Julian days as encoded on the tapes. 1974 January 1 was day 1. For a constant clock rate, the curves would be linear. This was not quite the case. Quartz crystal oscillators tend to 'age', their frequency varying linearly with time, resulting in a quadratic drift curve. Occasional clock jumps also occurred.

The clock rate should have been independent of battery voltage, since the internal power rails were stabilised. However, when the voltage fell below about 1Ø.7 V the clocks would begin to run increasingly slowly. This

complicated the curve-fitting procedure.

To plot the 1095 measured time errors required 64 drift curve segments. The curves were frequently replotted as more sets of pips were found and as individual points were reassigned to different curve segments to improve the fit. A computer programme, TIMFIT, was written in FORTRAN for NUMAC, to fit polynomials to the station clock errors.

TIMFIT is described and listed in Appendix 4. It performs the following operations:

(1) Read clock error data for all drift curve segments, in any order.

(2) Sort data according to station and time (NUMAC library subroutine SORT).

(3) Fit polynomials of required order to data (NAG Mk IV library subroutine E04ABF), and calculate time error residuals for each polynomial.

(4) Print out details of each polynomial fitted, and/or

(5) Plot input data points and fitted polynomials on I.B.M. 11 in plotter.

(6) Read event times at all stations, and correct for clock errors.

(7) Print out corrected times, with estimate of accuracy.

A warning message is printed whenever any time error calculated from the polynomial fit differs from the measured error by more than 0.04 s.

Clock error data were fitted to straight lines and to

quadratics. Higher order polynomials were unnecessary and were avoided, since they might 'follow' inaccurate data points and become unreliable when used for interpolation. For most segments of the curves the difference between the linear and quadratic fits was everywhere less than Ø.Ø2 s. Quadratics were used unless data points were sparse or the correction of any event time involved substantial extrapolation. 6Ø of the 64 drift curve segments gave R.M.S. residuals of less than Ø.Ø2 s.

3.11 Timing Errors

It is assumed in this section that there is no problem in identifying the point on the waveform that is to be timed. Picking errors are discussed in Chapter 4.

3.11.1 Radio Wave Propagation Time

The propagation time from London to Ethiopia for the radio waves of the B.B.C. overseas service is approximately Ø.Ø25 s. The propagation time across the network is, of course, negligible.

3.11.2 Electronically-Induced Errors

Systematic delays within the recorder-playback electronics are negligible. The possibility of significant relative delays was excluded by two simple tests:

(1) Seismometer calibration pulses recorded at site showed that frequency response differences among the seismometers were negligible.

(2) Sudden power failures occurred at all stations at some time during the field recording, causing effectively simultaneous pulses on all recorder channels. Except for some filtered traces, discussed in Section 3.11.3, 16 channel oscillograph playouts of the corresponding sections of tape showed no measurable relative time delays.

The position of the leading edges of demodulated time code pulses and G.M.T. pips is subject to error due to the limited resolution of the demodulators. Approximately two cycles of the waveform are required to determine frequency. For carrier frequencies of 50 to 100 Hz this implies a timing error of ±0.01 to ±0.02 s.

Instantaneous tape speed variations will give rise to random timing errors. SAVAGE (1979) has derived an expression for the time error from this cause, and has shown that for the third playback system the maximum error is approximately 0.008 s. Tape speed stability was not a problem with the second playback system.

3.11.3 Filter Delays

The KROHN HITE filters were known severely to distort the seismic waveforms. KROHN HITE filtered traces were never used in the picking of seismograms. KEMO filtered traces were used for a small number of events where phase onsets were weak. For these events, the filtered traces were used for picking the onsets at all stations. Any filter-induced timing errors were consequently systematic.

The time error delay introduced by the KEMO filter

settings described in Section 3.5 was not greater than 0.01 s, as measured on large amplitude, well-recorded P-wave onsets. S-wave onsets could not be picked with sufficient accuracy for similar measurements, but it was noted that the filters caused very little waveform distortion.

3.11.4 Measurement Errors

Seismogram measurements were normally made on jet pen oscillograph traces with a nominal density of 50 mm per recorded second. Assuming that measurements with a ruler are accurate to ±0.1 mm, the measurement error does not exceed 0.004 s.

A few measurements were made at densities of 25 or 10 mm per recorded second, giving errors of approximately 0.008 and 0.02 s respectively. The slower oscillograph speeds were used only for event onsets too poor to be picked at lower densities. They were not used for G.M.T. pips.

3.11.5 Clock Calibration Errors

For a quadratic fitted to 'n' points, with an R.M.S. residual of 0.02 s, the standard error is $0.02(n-2)^{-1/2}$. The number of points on the curves varied between 67 and 5, giving an error range of 0.0025 to 0.012 s.

There were a few occasions when either a clock was not working or G.M.T. pips were not recorded during an extended period. Events which may have been affected are labelled 'uncertain' in the listing of Appendix 6 and are considered specifically, where necessary, in Chapter 8.

3.11.6 Discussion

Relative timing errors between ESP stations are crucial, since they directly affect the accuracy of hypocentral locations. Summing the random errors from the sources discussed in Sections 3.11.2 to 3.11.5, assuming no correlation, gives typical timing errors of approximately Ø.Ø2 s, with worst error Ø.Ø33 s.

Systematic timing errors are important only when data from other sources are used in the locations. Events were timed systematically late by about Ø.Ø25 s due to the radio wave propagation time of G.M.T. pips. Exactly the same is true of events recorded at AAE, so no error was introduced even when AAE arrivals were used. AAE arrivals are in any case only timed to Ø.1 s. IPG network arrivals are timed with respect to signals from Radio Djibouti, whose relationship to G.M.T. is not known. AAE and ART (the IPG station at Arta, Djibouti) arrivals were used in this study only to help provide approximate epicentres for a few distant events whose onsets at the ESP stations were emergent and subject to picking errors of Ø.25 s or more. A very substantial error is introduced in these cases by assuming a homogeneous crust extending beneath Djibouti, Addis Abeba and Afar. The systematic timing errors described in this section are unimportant.

CHAPTER 4

HYPOCENTRAL LOCATIONS FROM SEISMIC ARRIVAL TIMES

4.1 Introduction to Location Routines

This chapter describes the hypocentral location of ESP events from their observed arrival times at the several recording stations. The general problem of earthquake location is considered, and particular difficulties associated with the ESP network are discussed. The choice of location routines is influenced by the station distribution.

Traditionally, location procedures compute time residuals of the form

$$\Delta t_i = \tau_i - t_i \qquad (4.1.1)$$

where τ_i is the observed arrival time of an event at station i. t_i is the computed arrival time of the trial solution with origin time t and hypocentre (x, y, z). This formulation was introduced by Geiger in 1910 (Geiger did not treat focal depth as a variable), was used in early computer programmes for earthquake location (BOLT,1960; FLINN,1960; HERRIN et al,1962; NORDQUIST,1962; ENGDAHL and GUNST,1966) and still forms the basis of most routines. The equations of condition used are

$$\Delta t_i = \Delta t + (\partial t_i/\partial x)\Delta x + (\partial t_i/\partial y)\Delta y + (\partial t_i/\partial z)\Delta z + e_i \qquad (4.1.2)$$

where e_i is the residual error.

The standard procedure is to solve for Δt, Δx, Δy, Δz by minimizing $\sum_{i=1}^{p} (e_i)^2$, where the summation refers to

p stations. Note that this least squares method assumes that the travel-time residuals are random variables, normally distributed with zero mean and with the same variance for all stations.

The solution yields the improved hypocentral parameters $(t+\Delta t)$, $(x+\Delta x)$, $(y+\Delta y)$, $(z+\Delta z)$, which are used as the next trial solution. Iterations are continued until convergence criteria are met which indicate that the current set of hypocentral parameters is sufficiently close to the optimum estimate.

To obtain e_i from Equation 4.1.2 requires the travel time function and its derivatives, which are obtained by assuming a model for crustal structure i.e. V(z). The model must be such that the partial derivatives always exist and, since Equation 4.1.2 contains no azimuthal dependence, it must be laterally homogeneous. Systematic residuals will be obtained if the V(z) model is seriously in error, and may contain information enabling the model to be improved.

Advances in computer technology have permitted the simultaneous least squares optimization of hypocentre and V(z) model. t_j in Equation 4.1.1 is replaced by t_{ji}, where

$$t_{ji} = t_{ji}(x_{1j}, x_{2j}, x_{3j}, x_{4j}, c_1, c_2, \ldots, c_g) \quad (4.1.3)$$

$$j = 1,\ldots,q \qquad i = 1,\ldots,p$$

t_{ji} is now the computed arrival time for the j^{th} of q events to be simultaneously located from observations at p stations, and is a function of the four hypocentral parameters $x_{1j},\ldots,x_{4j}$ and also of g parameters $c_1,\ldots,c_g$ which define the trial V(z) model. Equation 4.1.2 becomes

$$\Delta t_{ji} = \sum_{k=1}^{4} (\partial t_{ji}/\partial x_{kj}) \Delta x_{kj} + \sum_{k=1}^{q} (\partial t_{ji}/\partial c_k) \Delta c_k \quad (4.1.4)$$
$$+ \text{error terms.}$$

Equation 4.1.2 is the special case of Equation 4.1.4 for which all the c_k are fixed.

Equation 4.1.4 gives rise to a set of p x q = n normal equations in 4q + g = m unknowns, which as before are the corrections to the initial trial solution to produce the next solution. In matrix notation Equation 4.1.4 can be written

$$\underline{\Delta T} = \underline{A}\,\underline{\Delta x} \quad (4.1.5)$$

where $\underline{A}$ is the n x m coefficient matrix whose elements are the partial derivatives, $\underline{\Delta x}$ is the m x 1 solution vector containing the parameter corrections and $\underline{\Delta T}$ is the vector of travel-time residuals Δt_{ji}.

Provided n > m the system of Equations 4.1.5 is overdetermined. Solving by least squares we calculate the normal equations

$$\underline{A}^T \underline{A}\,\underline{\Delta x} = \underline{A}^T \underline{\Delta T} \quad (4.1.6)$$

which have as their solution the estimated correction vector

$$\underline{\Delta x}' = (\underline{A}^T \underline{A})^{-1} \underline{A}^T \underline{\Delta T} = \underline{H}\,\underline{\Delta T} \quad (4.1.7)$$

$\underline{H}$ is the generalised inverse operator for the least squares procedure, provided $\underline{A}^T\underline{A}$ is nonsingular. Iterative solution of Equations 4.1.6 is carried out until the convergence criteria are satisfied.

Some observations should be made regarding the use of the above method, particularly as here applied to earthquake locations in a multi-layered medium.

Care must be taken over the initial trial solution.

When the travel time function for the V(z) model is calculated the general solution of Equation 4.1.4 is nonlinear. A quasi-linear set of equations is obtained by considering only the first order expansion. Approximate linearity obtains close to the correct solution, i.e. linearity may be assumed in estimating the errors (FLINN,1965a; EVERNDEN,1969; BULAND,1976). If the initial trial solution is too poor, the travel-time residuals are large and the iterative routine may not converge, or may converge to a subsidiary minimum.

The observed arrival times may contain insufficient data to constrain some of the model parameters. $\underline{A}^T\underline{A}$ may then be singular or near-singular. For instance, in the V(z) model the number of layers may be somewhat arbitrary, resulting in large and unstable, or oscillating, changes in the solution vector. This can be seen if $\underline{A}$ is decomposed into the product

$$\underline{A} = \underline{U}\,\underline{\Lambda}\,\underline{V}^T \qquad (4.1.8)$$

where $\underline{U}$ is a n x p matrix (data space),

$\underline{\Lambda}$ is the p x p diagonal matrix of non-zero eigenvalues of the operator $\underline{A}$,

$\underline{V}$ is a m x p matrix (solution space),

and p is the rank of $\underline{A}^T\underline{A}$ (JACKSON,1972, after Lanczos,1961).

Taking advantage of the semiorthogonal properties of $\underline{U}$ and $\underline{V}$ (see CROSSON,1976a), Equation 4.1.5 is soluble in the form

$$\underline{\Delta x}' = \underline{V}\,\underline{\Lambda}^{-1}\,\underline{U}^T\,\underline{\Delta T} \qquad (4.1.9)$$

Λ^{-1} is a diagonal matrix with elements $1/\lambda_i$ $(i = 1,\ldots,p)$,

where the λ_i are the eigenvalues of $\underline{A}$. For near singularity, one or more of the λ_i may be very small, causing one or more of the components of the correction vector, $\underline{\Delta x}'$, to become large and unstable. Furthermore, identically zero λ_i, which are theoretically ignored in the decomposition of $\underline{A}$, take small non-zero values because of rounding errors.

The near-singularity problem is a fundamental difficulty in the traditional least squares approach, whether or not the parameter set includes V(z) model variables. A particular difficulty occurs when layered V(z) models are used, unless at least one recording station is sufficiently close that the first arrival is the direct wave. Where all the first arrivals are head-wave refractions, the partial derivatives $(\partial t_{ji}/\partial x_{kj})$ are constant. A small change in depth can be traded off linearly for a change in origin time, i.e. the arrival times provide no focal depth information.

Various methods have been used to circumvent the near-singularity problem. The widely applied location programme HYPO71, and its modifications (LEE and LAHR,1975) (only the hypocentral parameters are optimized), use a step-wise multiple regression. A statistical analysis determines which independent variables should be included in the regression. Only parameters that will be significantly altered are varied at each step, so that the matrix to be solved is never ill-conditioned. An unfortunate consequence (noted by Wesson et al,1971, in BULAND,1976) is that one or

more parameters may never be altered from their starting values. Convergence problems are still encountered when the distribution of recording stations is poor. The subroutine HYPCTR, developed here for simultaneous hypocentre and V(z) model optimization, also uses a step-wise multiple regression (Section 4.2.3).

BULAND (1976) has examined the convergence of the traditional least squares method and has shown that the convergence domain is much enlarged by damped Gauss-Newton iteration (performed numerically); while the numerical stability, and hence the convergence rate, is improved by use of the 'QR' algorithm (after Wilkinson and Reinsch, 1971, and so called because $\underline{A}$ in Equations 4.1.6 is decomposed into a m x n unitary matrix $\underline{Q}$ times a n x m right triangular matrix $\underline{R}$).

CROSSON (1976a) has improved the classical least squares approach by applying a procedure which he terms the Levenberg-Marquardt algorithm (it was first suggested by Levenberg in 1944 and by Marquardt in 1963). Its effect is to modify Equation 4.1.9 to give

$$\underline{\Delta x}' = \underline{V} \, [(\lambda^2 + \theta^2 \underline{I})^{-1} \underline{\Lambda}] \, \underline{U}^T \, \underline{\Delta T} \qquad (4.1.10)$$

The quantity within square brackets is a diagonal matrix whose typical element is $\lambda_i/(\lambda_i^2 + \theta^2)$, where θ is a weighting coefficient (or matrix, if the residuals have not already been weighted by the reciprocal of the variances of the observations) which is adjusted to the requirements of the problem. Then as any λ_i decreases, the corresponding component of x' does not blow up according to $1/\lambda_i$ as

before but is smoothly tapered towards zero.

Crosson's programme has the additional advantage of removing the customary restriction that the velocity increase monotonically with depth. It has been applied with impressive results to model the crustal structure below the Puget Sound region, Washington (CROSSON,1976b) and below Hawaii (CROSSON and KOYANAGI,1979), indicating in both cases a low velocity layer at the base of the crust.

LOMNITZ (1977,1978) has noticed that if the space domain is used rather than the time domain, the condition equation is

$$\sum (\partial t/\partial \Delta) [\Delta_i - \Delta_{(t_i)}]^2 = \text{minimum} \qquad (4.1.11)$$

summed over the recording stations. t_i is the TRAVEL time to the i^{th} station, Δ_i the epicentral distance, and $t(\Delta_i)$ the travel time function, including focal depth dependence (but independent of azimuth). The advantage is that when the trial epicentre is close to the real epicentre the normal equations are truly linear. Convergence is extremely rapid, and much computing time is saved. Note that only the epicentral variables x, y are included in the normal equations. Focal depth and origin time are both estimated subsequently (and independently) from the distance residuals.

For teleseismic locations, an interactive programme has been described by GARZA et al (1977,1979) which requires neither least squares nor travel-time tables. In other words, no *a priori* structural model is needed. The principle is that triads of stations are selected which lie

at approximately the same hypocentral distance (but which preferably have widely varying azimuths). With the usual limitation of laterally homogeneous earth structure, it may be assumed that the seismic velocities are the same along each of the three travel paths. Small groups of data are selected, so that the effect of any given observation on the solution may be appreciated. Garza's criticism is that, where many observations of a single earthquake are available, "utilization of highly redundant least-squares methods represents a wasteful use of valuable seismic information." Although Garza's method is not applicable to the present study, the principle of uniform station distribution is fundamental, and the method also emphasises that most current location routines fail to extract structural information that exists in interactive programmes.

4.2 Methodology of Routines used in This Study

4.2.1 General Considerations

The fundamental problem in obtaining good determinations of ESP earthquake parameters concerns the paucity and poor distribution of recording stations. Over 90% of ESP events are recorded by 3 stations or fewer. In order to locate events from small numbers of arrival observations a programme is used (LEADL, Section 4.2.2) which (1) assumes a V(z) model and (2) restrains the event focal depths. This reduces the number of unknown parameters

for each event to 3 (2 epicentral co-ordinates and origin time). As the data set is small, it is computationally practical to locate each individual epicentre for a range of assumed focal depths. This enables the trade-off between origin time and focal depth to be examined explicitly.

For 11 events, recorded at all four ESP stations, independent hypocentral estimates were obtained using a routine (Subroutine HYPCTR, Section 4.2.3) which optimizes the V(z) model jointly with the earthquake parameters of a group of events. Subroutine HYPCTR operates with a much larger set of variables than programme LEADL, and its solutions may not be so well constrained. It has been used because it provides a check on the assumed V(z) model input to LEADL, and on the hypocentral locations obtained; it uses P arrivals only, and thus requires no assumptions (nor allows any estimation!) of Poisson's ratio; and it has been adapted by the author to output graphical confidence regions for the computed hypocentres.

The number of available travel times may be increased by utilising, where possible, more than one seismic phase at each recording station. In practice, the first S phase is the only phase other than initial P that can regularly be identified. S arrivals are normally less accurately measured than P (see Sections 3.7, 4.6), because of the noise from the P coda. They are difficult to pick automatically for the same reason. Current automatic local earthquake detection/location routines (e.g. STEWART,1977) are therefore tending to utilise P data only from large

numbers of closely spaced instruments.

Here we are forced to use S data with programme LEADL, and this has positive merits. P and S arrivals from the same station enable origin time to be determined independently of the spatial hypocentral co-ordinates (JAMES et al,1969). Model studies by BULAND (1976) have shown that the condition number* of A in Equation 4.1.5 is greatly reduced when both P and S arrivals are used, i.e. the addition of S information enhances stability and convergence, and always improves the quality of the locations.

4.2.2 Programme LEADL

Hypocentral locations have been obtained using a modified version of the FORTRAN IV programme LEADL written by Dr Roy Lilwall of UKAEA, Blacknest. LEADL is specifically designed for small station networks. It requires a fixed input V(z) model of any number of constant-velocity horizontal layers. P and S V(z) structures are input separately, so that Poisson's ratio may be varied with depth. Velocities must increase monotonically with depth. Subject to this constraint any laterally homogeneous structure is approximated, although in practice the number of layers is limited by availability of

---

*For a definition and bibliography of this quantity see VARGA (1962) pp. 66 and 95.

It should be remembered that Buland's P and S arrival times were not picked from seismic records. They were computed at each station, and perturbed by normally distributed pseudo-random numbers with standard deviations of 0.1 and 0.3 s respectively.

computer time. Input for each event consists of the P and/or S arrival times at each recording station. The arrivals may be individually weighted by the user.

LEADL uses the traditional least squares approach. Adequate stability is assured by the focal depth constraint, provided that both P and S phases are available from at least one station. (The treatment of instances of numerical instability is discussed in Section 4.4). A flat Earth is assumed, and station elevation corrections are made. P and S station time residuals may also be included.

The origin time, T_O, for the trial solution is found from the first station (I) which has recorded both P and S phases, using

$$T_O = (T_P)_I - [(T_S)_I - (T_P)_I]/(V_P/V_S - 1),$$

where $(T_P)_I$ and $(T_S)_I$ are the P and S arrival times at station I, and V_P and V_S the P and S wave velocities. For this purpose the value $V_P/V_S = 1.73$ is assumed, irrespective of the input V(z) model. The programme then computes the travel-time residuals at 36 points distributed at 10° azimuth intervals around the S-P circle for station I (i.e. the circle with centre I and radius $V_P[(T_S)_I - (T_P)_I]$). The point with the minimum sum of residuals is taken as the trial epicentre. If no station observes both P and S, the earliest recorded arrival time is used as trial origin time and the co-ordinates of the station that records it as trial epicentre.

The iterative procedure is as follows:

(1) Using the current trial solution, calculate the

travel-time residuals for the k observations of the event (either P or S phases).

(2) Zero the sum of the residuals. (This partially corrects for non-linearity.)

(3) Set up the normal equations (4.1.6), adjusting the coefficients of $\underline{A}$ according to the weight of each observation. ($\underline{A}$ is here a k x 3 matrix, since there are only 3 unknowns.)

(4) Solve for $\underline{\Delta x}'$ (Equations 4.1.7) and form the new trial solution.

(5) Check the new solution against the convergence criteria. If they are not satisfied, return to (1).

In normal use, convergence was evaluated from the calculated weighted standard error,

$$E = \left(\sum_{i=1}^{k} \Delta t_i^2 w_i^2 / \sum_{i=1}^{k} w_i\right)^{1/2}$$

If, after the r^{th} iteration, $E_{r-1} - E_r < 0.001$ s, the solution was assumed to have converged. The routine was terminated if convergence had not been obtained after 10 iterations, or if $E_r > 10E_{r-1}$ (i.e. gross divergence).

4.2.3 Subroutine HYPCTR

Subroutine HYPCTR is a modification of a subroutine written by Dr Graham Westbrook of the Department of Geological Sciences, Durham University, for use in conjunction with the non-linear optimization package MINUIT (JAMES and ROOS,1974) described in Appendix 5. When called by MINUIT, HYPCTR performs joint hypocentral determinations for a group of earthquakes specified by their P arrival

times, and concurrently will optimize a V(z) model comprising a constant velocity refractor overlain by a layer in which the velocity increases linearly with depth. Focal depths are constrained.

Four parameters are required to specify the V(z) model: the velocity at datum, the velocity gradient and thickness of the upper layer, and the refractor velocity. Additionally, there are three hypocentral variables (x, y, t) for each event. For a group of q events, all of whose P arrivals are observed at all four ESP stations, 4q normal equations are available in (3q + 4) unknowns (Equations 4.1.5). The solution is overdetermined if $4q > (3q + 4)$.

Like LEADL, HYPCTR assumes a flat Earth, calculates station elevation corrections and will correct for station time residuals. Each arrival time observation can be weighted exponentially. The objective function, F, provided by HYPCTR and minimized by MINUIT, is the weighted sum of squared travel-time residuals

$$F = \frac{\sum_{j=1}^{N}\sum_{i=1}^{M_j}(t_{ij} - u_{ij} - T_j)^2 \exp(W_{ij})}{(n-1)\sum_{j=1}^{N} M_j} \qquad (4.2.1)$$

where

N = number of events jointly located,

M_j = number of stations receiving the j^{th} event,

t_{ij}, u_{ij}, W_{ij} are respectively the observed arrival time, calculated travel time and weighting factor for the j^{th} event at the i^{th} station,

T_j = computed origin time for the j^{th} event

$$= (1/M_j)\sum_{i=1}^{M_j}(t_{ij} - u_{ij})$$

The u_{ij} are altered at each iteration in response to the parameters of each new trial solution.

4.3 Constraints on the Structural Model

4.3.1 Introduction

We have seen that V(z) model and hypocentres cannot be optimized independently. This section considers structural constraints that can be applied independently of the optimization procedure.

Later arrivals were observed within the P codas of over 80% of intermediate-magnitude earthquakes recorded in the epicentral distance range 25 to 100 km. 47 such later phase observations are discussed in Section 4.3.2. They are most useful for constraining the shallower structural parameters. Deeper structure is examined in Section 4.3.3 by treating the ESP network as an array. Section 4.3.4 describes an attempt to use two teleseismically-located earthquakes to place limits on the upper mantle velocity. All results are summarised in Section 4.3.5.

Afar V(z) models of previous workers have been presented in Section 1.5. The starting point for this study was BERCKHEMER et al's (1975) 4-layer crustal refraction profile IV (Figure 1.5.1b), the nearest profile to the ESP network. However, it is shown in Section 4.5 that the P velocity of layer 2 is well constrained to 6.2 km s^{-1}, so this value is used throughout this section (c.f. Berckhemer et al's 6.3 km s^{-1}).

Focal depths of earthquakes within Afar, obtaned from LEADL, range from Ø to 5 km (Section 4.4) with a weighted mean depth of 3.Ø km. These shallow foci are confirmed by S-P times as short as 1 s for very close earthquakes, and 2 to 3 s for earthquakes large enough to be recorded at all stations and to yield accurate epicentres.

4.3.2 Later Arrivals within the P Coda

In this section travel time differences (Δt) between the first P onset and later arrivals are plotted against epicentral distance (d) calculated using programme LEADL. The travel time differences were calculated using a FORTRAN programme written by the author.

Other studies have plotted Δt against S-P time (e.g. RYKOUNOV et al,1972, using S_g-P_g). The advantage of S-P time is that it is a directly measurable parameter related to structure and focal depth. It is not used here because for some events S cannot be reliably read. Epicentral distance varies only slightly with V(z) or focal depth. When d is calculated from any of the models considered in this section the range of variation is less than 2 km, which is insignificant.

Later arrivals are valuable for placing constraints on upper crustal model parameters. Their identification has been discussed in Section 3.7. They were rejected unless they could be matched across a group of records of events with similar epicentral distances. Because of contamination by earlier arrivals they may still be mispicked by up to one

cycle, equivalent to timing errors of 0.1 to 0.2 s for frequencies in the range 10 to 5 Hz. No attempt was made to pick onsets appearing to occur within one second of the first arrival.

Within the epicentral distance range 25 to 100 km the observed first arrivals are likely to be either the direct P phase (P_g), or P head waves from intermediate interfaces, or simply reflected P arrivals. The notation used for these is 'Rn' for the head wave in layer n, and 'rn' for the simple reflection from layer n (Figure 4.3.1a). It is unlikely that multiple reflections capable of causing the observed time delays relative to the first arrival would have observable amplitudes. P to S mode conversions were not identified by particle motion analysis (Chapter 6), which showed the later arrivals to be P phases. Finally, diffracted waves would not be seen consistently from such widely separated sources.

Within the epicentral distance range 25 to 70 km the first arrival is likely to be R2, as demonstrated by a set of curves (Figure 4.3.2) for structures similar to those obtained by BERCKHEMER et al (1975). At very short distances P_g arrives first, whilst at some distance between 70 and 100 km R3 becomes the first arrival. For R3 to arrive before R2 at $d < 70$ km requires either very large V_3/V_2 or very shallow h_2 (see Figure 4.3.1b for notation).

Other phases which may be observed following R2 are r2 and r3. The travel time of rn of course becomes equal to that of Rn at the latter's critical distance. The time

FIGURE 4.3.1

A) NOTATION FOR SIMPLE REFLECTIONS AND HEAD WAVE REFRACTIONS

B) NOTATION FOR EQUATIONS IN THIS SUB-SECTION

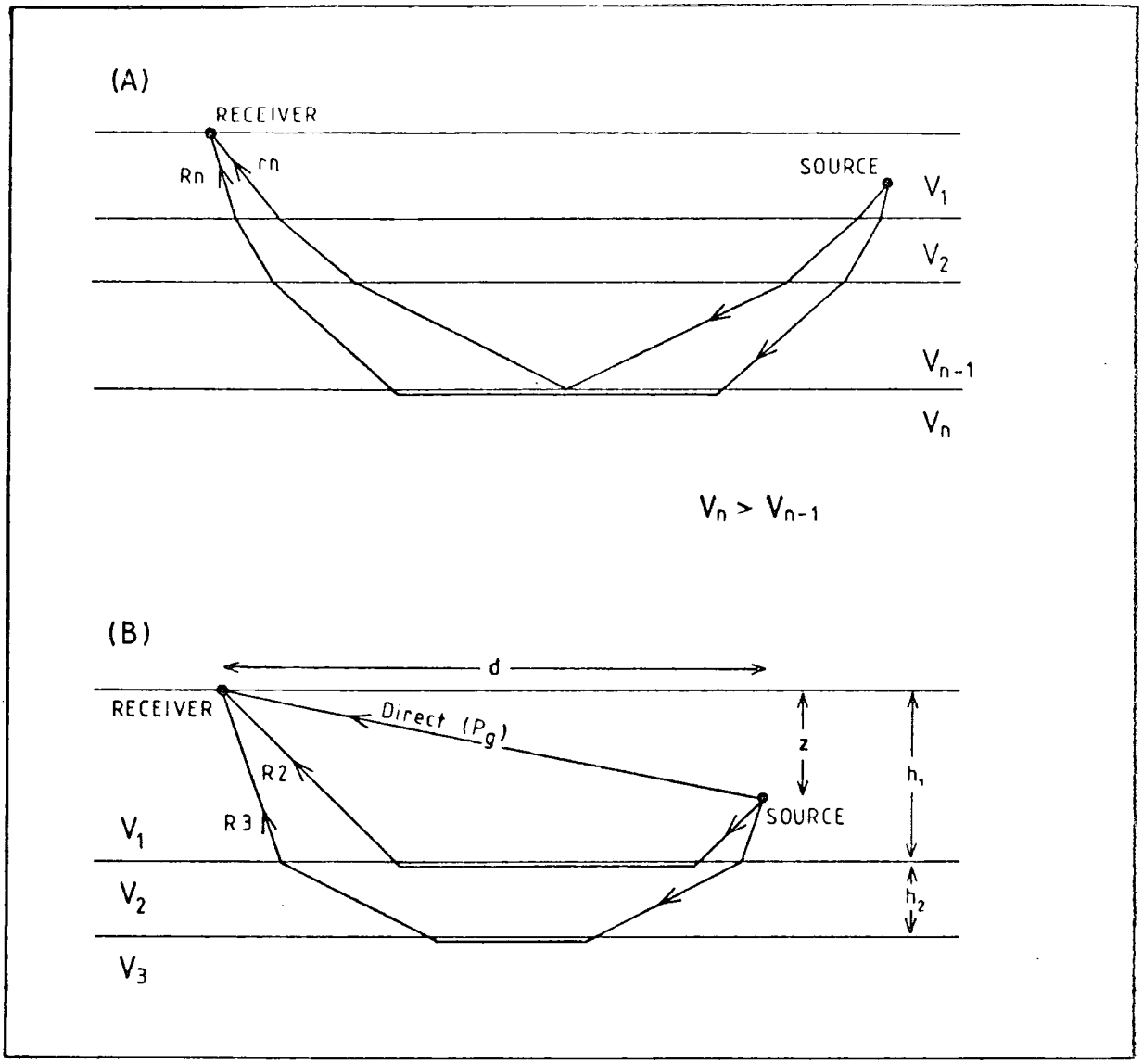

Rn is head wave in layer n

rn is reflection from layer n

V_n is velocity of layer n

h_n is depth of layer n

z is event focal depth

FIGURE 4.3.2

EFFECT ON CURVES OF TRAVEL TIME DIFFERENCES (Δt) AGAINST EPICENTRAL DISTANCE (d), FOR THE DEPICTED V(z) MODEL, OF VARYING UPPER CRUSTAL LAYER THICKNESSES (h_1, h_2)

(Structural diagrams are inserted to clarify the notation)

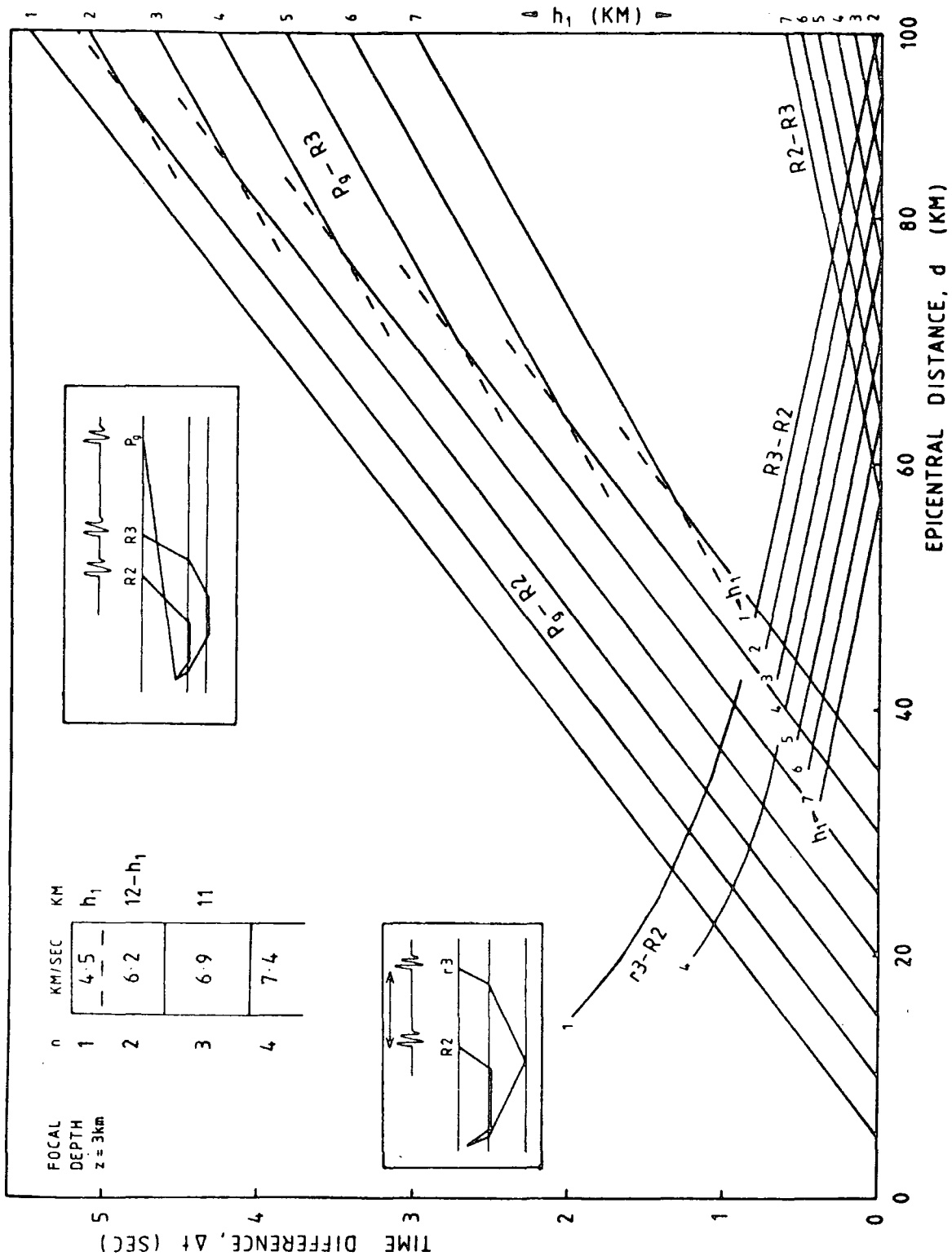

differences $t(P_g) - t(R2)$ and $t(r2) - t(R2)$* increase with increasing d, while $t(r3) - t(R2)$ decreases with increasing d. The critical distance for R4 is approximately 70 km when $(h_1+h_2+h_3)$ lies between 20 and 25 km and $V_4 = 7.4$ km s^{-1}; values which are typical of Berckhemer's profiles for central and southern Afar.

The later arrival data are given in Table 4.3.1. A few groups of records exhibit more than one later phase. We consider first the arrivals which show Δt increasing with d in a manner similar to the $(P_g - R2)$ curves of Figure 4.3.2. With the notation of Figure 4.3.1b,

$$t(R2) = \frac{d}{V_2} + \frac{(2h_1 - z)(V_2^2 - V_1^2)^{1/2}}{V_2V_1} \qquad (4.3.1)$$

$$\text{and } t(P_g) = (d^2 + z^2)^{1/2}/V_1 \qquad (4.3.2)$$

Assuming $\Delta t = t(P_g) - t(R2)$,

$$\Delta t = \frac{V_2(d^2 + z^2)^{1/2} - V_1 d}{V_2V_1} - \frac{(2h_1 - z)(V_2 - V_1)^{1/2}}{V_2V_1} \qquad (4.3.3)$$

Since $d>>z$,

$$\Delta t \approx \frac{d(V_2 - V_1)}{V_2V_1} - \frac{(2h_1 - z)(V_2^2 - V_1^2)^{1/2}}{V_2V_1} \qquad (4.3.4)$$

These equations are only applicable to events with foci in layer 1 of the V(z) model, and the observations of this

---

*When $d>>h_1$, as for most events in this study, r2 closely follows P_g and has not been distinguished from it on the seismic records. The following analysis is unaffected if some observed later phases interpreted as P_g are in fact r2, as is increasingly possible as d increases. For the structural parameters $V_1 = 4.4$ km s^{-1}, $V_2 = 6.2$ km s^{-1}, $h_1 = 4.5$ km, with $z = 3$ km, $t(r2) - t(P_g) = 0.12$, 0.07 and 0.03 s for $d = 25$, 50 and 100 km respectively.

TABLE 4.3.1

GROUPS OF EARTHQUAKES EXHIBITING LATER P CODA ARRIVALS

Recording Station	Number of Records	Swarm Origin	Azimuth Range* (degrees)	Distance Range* (d) (km)	Time between First and Later Arrivals** (Δt) (sec)	Group
Tendaho	8	NW Tendaho Graben	194-200	23.5-27.3	1.48 ± 0.04	2
Serdo	3	NW Tendaho Graben	66- 80	34.4-38.1	1.51,1.51,1.59	1
Det Bahri	3	Kurub	179-181	39.9-40.8	1.73,1.75,1.76	1
Det Bahri	7	SE of Serdo	223-226	46.5-47.9	2.09 ± 0.04	1
Mille	11	NW Tendaho Graben	208-223	57.5-62.3	1.78 ± 0.05	3
Mille	4	NW Tendaho Graben	201-215	57.5-65.0	3.10 ± 0.07	1
Tendaho	2	SE of Serdo	251,253	63.2,63.4	3.90,3.93	2
Mille	2	N of Mille	182,182	63.5,63.9	3.25,3.32	1
Det Bahri	2	N of Mille	135,135	67.1,67.9	1.58,1.64	3
Det Bahri	2	N of Mille	135,135	67.1,67.9	3.61,3.74	1
Mille	3	SE of Serdo	239-239	95.4-95.9	1.14,1.16,1.25	3

*As determined from model C, Figure 4.3.6.
**Mean time difference and standard deviation are given for groups of more than 3 records.

Group 1: records from Mille, Serdo, Det Bahri (Δt increasing with d).
Group 2: records from Tendaho.
Group 3: other records (from Mille and Det Bahri).

study cannot be explained otherwise. The restriction d>>z is therefore justified. Equation 4.3.4 gives $\partial\Delta t/\partial d = (V_2 - V_1)/V_2V_1$, which is a constant. If this equation is satisfied a plot of Δt against d will be linear, provided all the events occur at the same depth (z). Assuming a value for V_2, V_1 can be found from the gradient of the line and $(2h_1 - z)$ from its intercept.

A linear fit of the records in Table 4.3.1, group 1, gave

$$\Delta t = (0.067 \pm 0.003)d - (0.961 \pm 0.171) \qquad (4.3.5)$$

Arrivals from all the events at Mille, Serdo and Det Bahri with epicentral distances less than 70 km plot on the same line, with observed minus calculated time differences of the same order as the observational time errors (see Figure 4.3.5). Typical records are shown on the gathered seismograms of Figure 4.3.3 (d < 70 km).

A similar linear fit to the group 2 (Tendaho) records gave

$$\Delta t = (0.068 \pm 0.002)d - (0.230 \pm 0.085) \qquad (4.3.6)$$

Sample records are shown in Figure 4.3.4. Values of V_1 and $(2h_1 - z)$ calculated from Equations 4.3.5 and 4.3.6 for a range of velocities V_2 are presented in Table 4.3.2. Both equations have the same gradient, and therefore the same ratio V_2/V_1. The likely explanation of this is that the velocities are the same below Tendaho as below the other stations.

Using the values $V_2 = 6.2$ km s^{-1}, z = 3 km yields $h_1 = 4.5$ km below Mille, Serdo and Det Bahri. For Tendaho,

FIGURE 4.3.3

GATHERED SEISMOGRAMS OF EVENTS TAKEN FROM TABLE 4.3.1

(recorded at Mille, Serdo and Det Bahri stations)

First arrival is R3 on M467, R2 on all other records

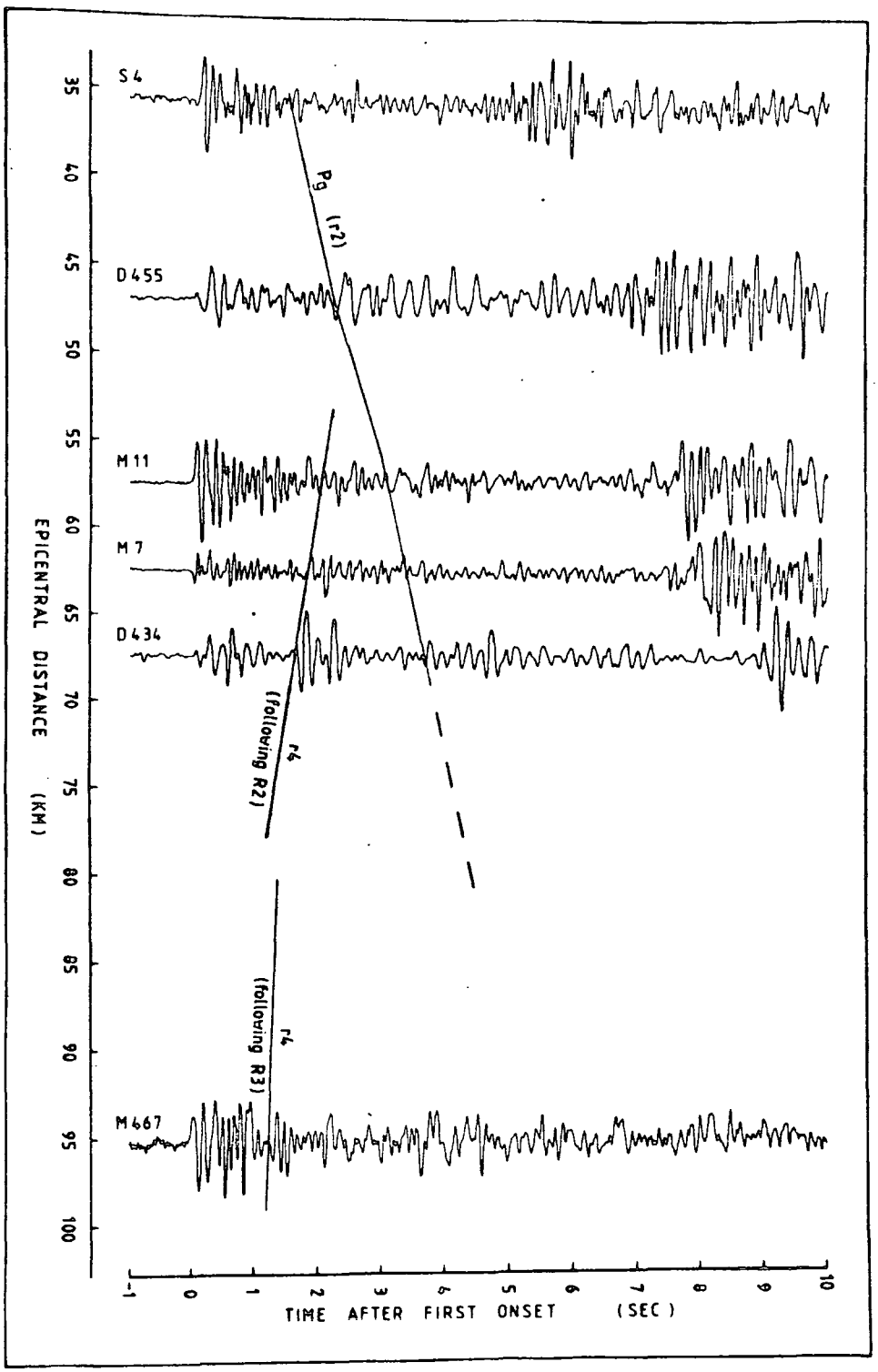

FIGURE 4.3.4

EXAMPLES OF TENDAHO RECORDS

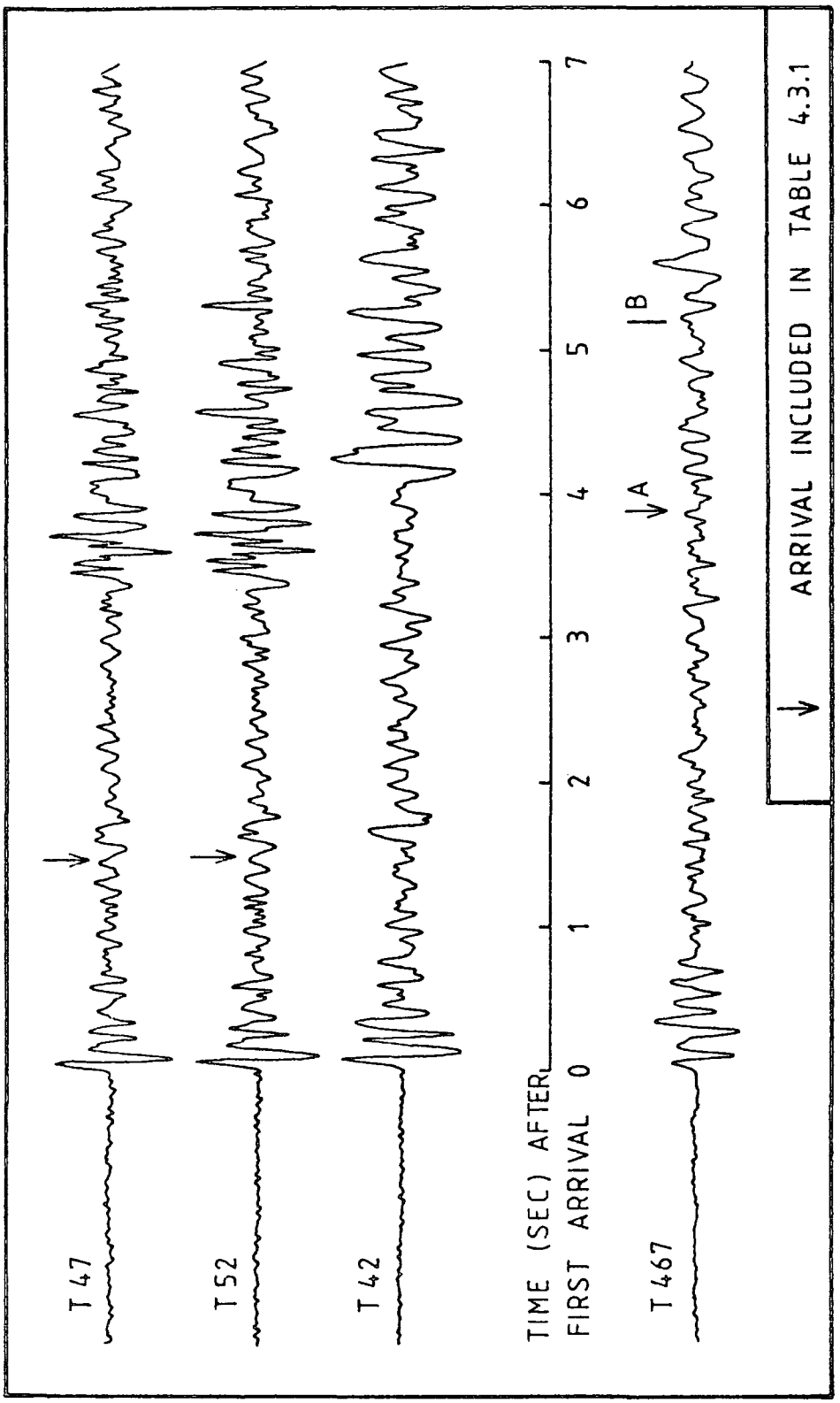

TABLE 4.3.2

UPPER CRUSTAL STRUCTURAL MODEL PARAMETERS CALCULATED FOR VARIOUS VALUES OF V_2

V_2	V_1	$(2h_1 - z)$ (Tendaho)	$(2h_1 - z)$ (other stations)	V_3	h_2
6.00	4.28	1.41	5.87	6.65	18.55
6.10	4.33	1.42	5.91	6.77	18.71
6.20	4.38	1.43	5.95	6.90	18.88
6.30	4.43	1.44	5.99	7.02	19.04
6.40	4.48	1.45	6.03	7.15	19.20
6.50	4.53	1.45	6.07	7.27	19.37

Velocities are in km s^{-1}, depths in km.

the later arrival data are less clear, but the figures for Tendaho imply $z < 1.4$ km. This is possible, since z is not well constrained, but it is also possible that the Tendaho data have been misinterpreted. The two arrivals at $\Delta t \approx 3.9$ s from d = 63 km (marked A on Figures 4.3.4, 4.3.5) are weak and possibly spurious. The arrival at $\Delta t = 5.25$ s on T467 (marked B on Figure 4.3.4) is unique to this record, and is unexplained. P_g is almost certainly the largest later arrival at 25 to 30 km (as observed by BERCKHEMER et al,1975), but may have been systematically mispicked due to the complexity of the records from such a close source. However, some upper crustal thinning or other inhomogeneity is implied below Tendaho, since the arrivals are 0.5 s later than for the other stations.

Events of group 3, Table 4.3.1, show Δt decreasing with increasing epicentral distance over the range 60 to 95 km. There are five possible interpretations:

(1) $\Delta t = t(R3) - t(R2)$

(2) $\Delta t = t(R4) - t(R3)$

(3) $\Delta t = t(r4) - t(R2)$

(4) $\Delta t = t(r4) - t(R3)$

(5) The later arrival seen from events at about 95 km is not the same phase as is seen from 60 to 65 km.

(1) The necessary conditions are easily calculated. Using the notation of Figure 4.3.1b, t(R3) is obtained analogously to t(R2) (Equation 4.3.1). Then

$$\Delta t = t(R3) - t(R2)$$

$$= \frac{d(V_2 - V_3)}{V_3V_2} + \frac{2h_2(V_3^2 - V_2^2)^{1/2}}{V_3V_2}$$

$$+ \frac{(2h_1 - z)(V_3^2 - V_1^2)^{1/2}}{V_3V_1} - \frac{(V_2^2 - V_1^2)^{1/2}}{V_2V_1} \qquad (4.3.7)$$

Under the same conditions as before, the plot of Δt against d is linear. A linear fit to the relevant data gave

$$\Delta t = -(0.016 \pm 0.001)d + (2.756 \pm 0.098) \qquad (4.3.8)$$

Values for V_3 and h_2 were determined from the gradient and intercept, respectively, using the upper crustal structural parameters deduced above (V_1 = 4.5 km s^{-1}, h_1 = 4.5 km, V_2 = 6.2 km s^{-1} and z = 3 km). The results are given in Table 4.3.2.

Assuming V_2 = 6.2 km s^{-1}, the corresponding layer 3 velocity is 6.9 km s^{-1}. Computed travel time differences for the resultant 'ideal' 3-layer structure are shown in Figure 4.3.5, together with the observed values of Δt. h_2 is in fact so thick that R3 does not occur at d < 80 km, although the arrivals from sub-critical distances are explicable as Δt = r3 - R2. More seriously, a seismic P velocity as low as 6.2 km s^{-1}, extending to below 20 km depth, would be extremely unusual. It is concluded that the observed time differences cannot be fully explained as Δt = t(R3) - t(R2). All the remaining possible interpretations for Δt require a 4-layer structural model.

(2) This possibility can be discarded. If the layer 3/4 interface is sufficiently shallow that the critical distance for R4 is 60 km or less, R4 arrives too soon after R3 to explain the observations.

(3,4) These possibilities were examined numerically.

FIGURE 4.3.5

RELATIVE TRAVEL TIMES FOR THE 3-LAYER MODEL DERIVED TO FIT THE OBSERVATIONS

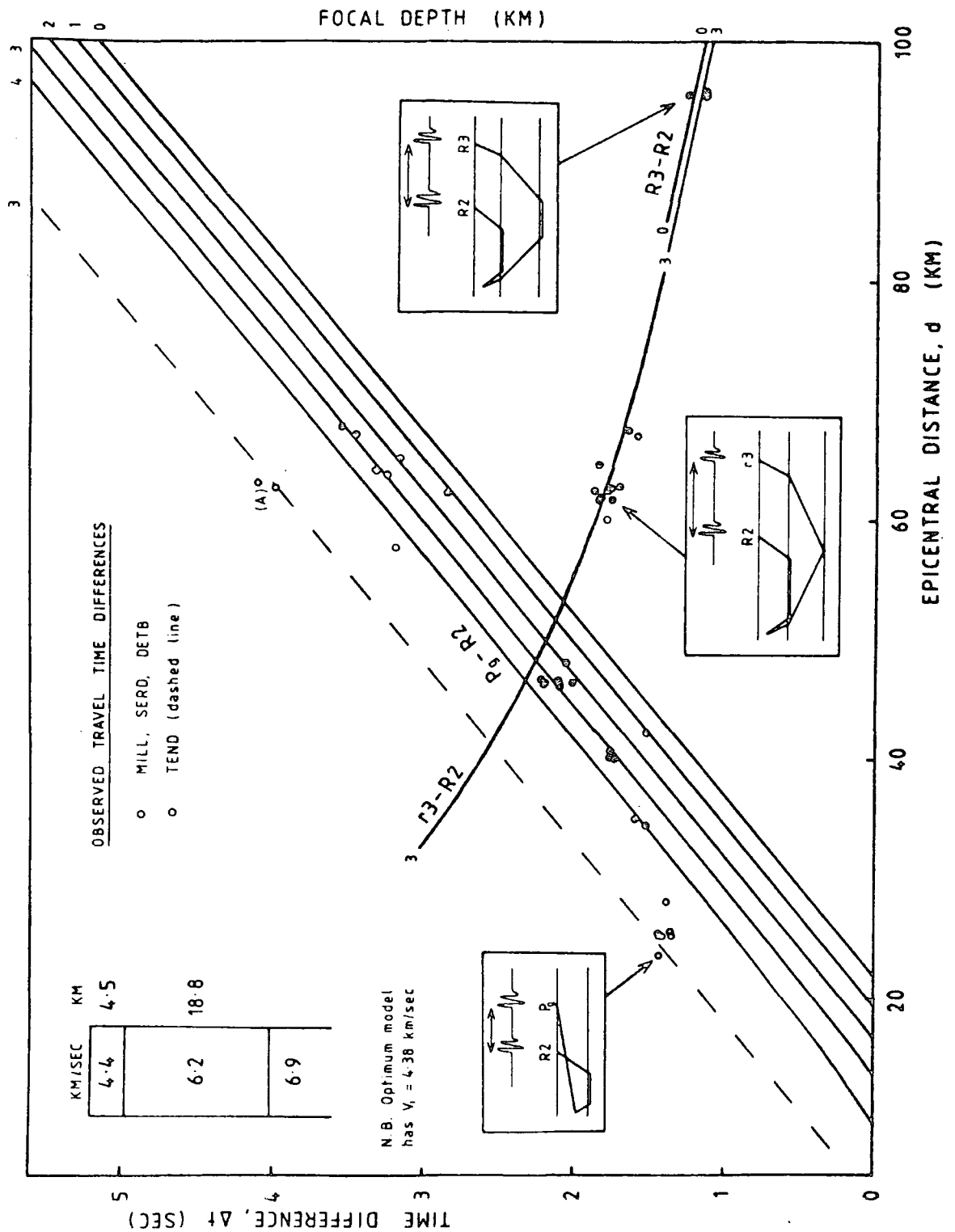

Using the preferred set of upper crustal structural parameters, the remaining parameters were varied one by one for a wide range of possible models. The lower structural parameters of Figure 4.3.2 gave Δt lower than was observed. Clearly, Δt is increased by increasing h_2 or h_3, but this also increases $\partial\Delta t/\partial d$ to exceed the observed gradient. $\partial\Delta t/\partial d$ can only be decreased by decreasing V_3, and remains unacceptably high unless h_2 is less than 7.5 km. When h_2 is as thin as this, R3 replaces R2 as the first arrival at between 65 and 90 km. Within the reasonable constraints $6.5 \leqslant V_3 \leqslant 7.0$ km, $5.0 \leqslant h_3 \leqslant 17$ km, the only parameter sets to fit the observations were

h_2	h_3	V_3
4.5	16.0	6.5
6.5	15.5 to 17.0	6.7 to 7.0

In order to explain the values of Poisson's ratio determined independently (Section 4.4) without lowering V_2 or invoking an S velocity inversion requires $V_3 \geqslant 6.9$ km s^{-1}. The most probable set of structural parameters is thus $h_2 = 6.5$ km, $h_3 = 16.5$ km, $V_3 = 6.9$ km s^{-1}, giving the model adopted hereafter (Figure 4.3.6c).

(5) The three later arrivals around 95 km are much weaker than those at 60 to 65 km. If they are spurious the constraint on $\partial\Delta t/\partial d$ is removed and a wide range of structural models gives the observed values of $\Delta t = t(r4) - t(R2)$ for the remaining observations.

FIGURE 4.3.6

VELOCITY/DEPTH MODELS FOR AFAR CONSIDERED IN CHAPTER 4

a) Profile IV of BERCKHEMER et al (1975) (see Figure 1.5.1)
b) Profile Ø5 of RUEGG (1975a,b)
c) Optimized model obtained in this chapter
d) Two-layer model from subroutine HYPCTR

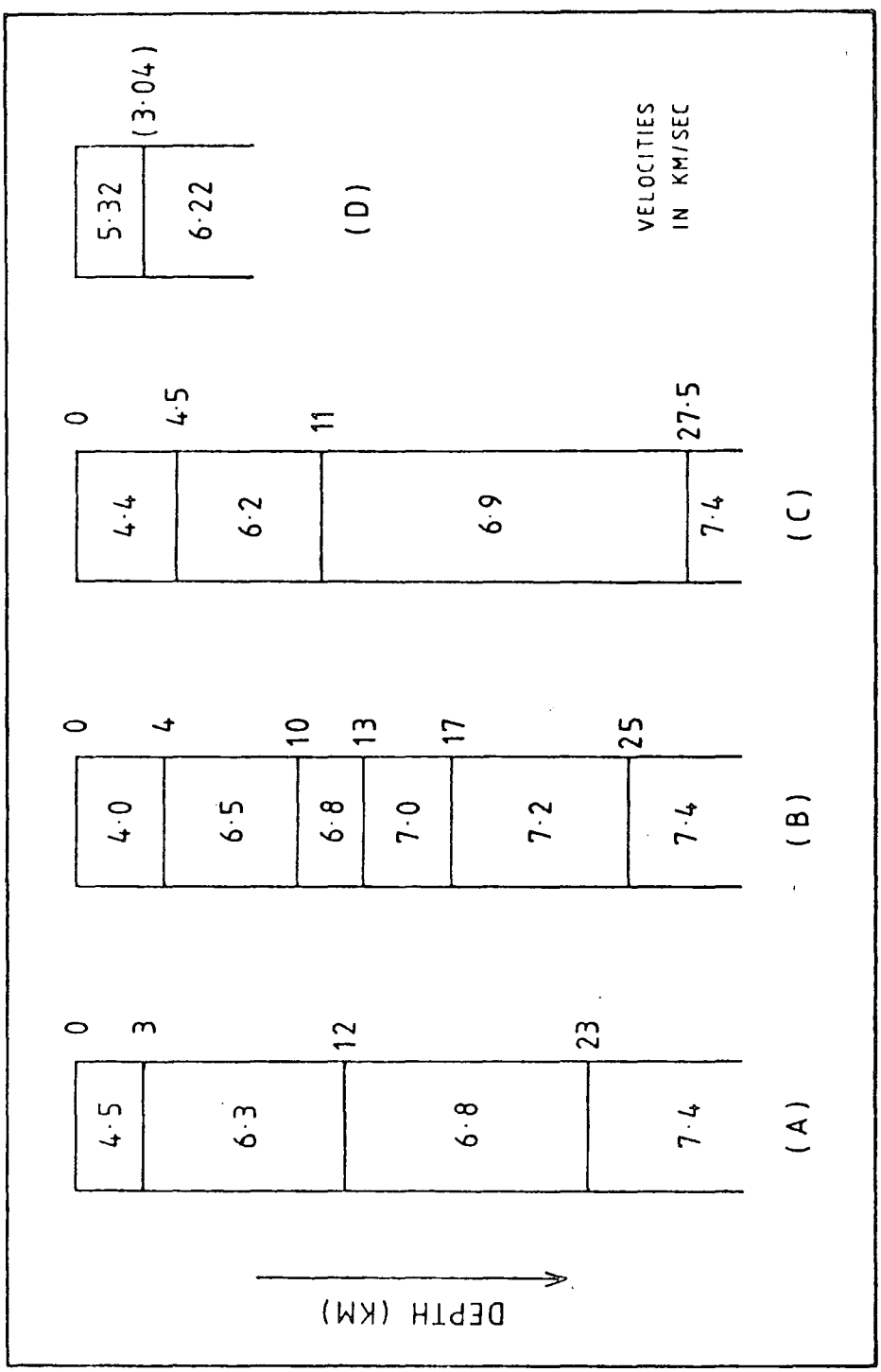

Events beyond 100 km are insufficiently well recorded for later arrivals to be picked. However, records of the cluster of earthquakes from around latitude 10.1°N on the Western Ethiopian escarpment (Section 8.3) have a significantly simpler structure than other ESP records in the same distance range (100 to 200 km). This provides indirect support for their deeper hypocentral location.

4.3.3 Deeper Velocities

In order to place constraints on the deeper velocities, and to search for possible anisotropy, the arrival time data from more distant earthquakes were processed by treating the ESP network as an array. The azimuths to events and apparent velocities across the network were computed from first arrival times.

Techniques for processing array data have been described in e.g. BIRTILL and WHITEWAY,1965, and CORBISHLEY,1969. A curved wavefront technique was used here, the epicentral distances (140 to 300 km) being too small compared to the array dimensions (Figure 2.2.1) to allow a plane wavefront approximation. The technique can be applied without *a priori* knowledge of the seismic velocities, provided they do not vary appreciably across the path traversed by the wavefront. Differences in local structure beneath individual stations may be accommodated by station residuals.

The elongate configuration of the ESP stations fundamentally limits the accuracy of the determinations.

For a wavefront crossing a linear array of length L in time t, the apparent velocity

$$V' = L/t$$

$$\therefore \Delta v'/\Delta t = -L/t^2$$

When the wavefront approaches the array at near normal incidence, t is small and small errors in t cause large uncertainties in V'. The ESP array has limited resolution perpendicular to the Mille-Serdo axis, and the problem is aggravated by the paucity of suitable earthquakes recorded at Det Bahri.

20 events were processed (Table 4.3.3). 6 of these were discarded because (1) they had azimuths within 15° of the normal to the Mille-Serdo axis, (2) they were not recorded at Det Bahri, and (3) they gave velocities with standard errors greater than 2.5 km s^{-1}. A seventh was discarded because it gave an anomalously high apparent velocity (9.68 km s^{-1}), with large station residuals indicating unacceptable arrival time errors.

For the 13 remaining events the mean apparent velocity is 6.84 ± 0.57 km s^{-1} (95% confidence limits). V' is shown as a function of distance in Figure 4.3.7, where the error bars were obtained by estimating the arrival time errors and computing the apparent velocities for the maximum and minimum errors. Many of the events processed had first arrivals which were emergent and of low amplitude, and had therefore potentially large picking errors (Section 4.6).

The dotted line on Figure 4.3.7 is the linear best fit for V' against distance (d),

TABLE 4.3.3

DETAILS OF EVENTS USED IN SECTION 4.3.3

Event	(computed from centroid) Distance (km)	Azimuth (degrees)	Arrival Times (sec) Relative to Mille Tend	Serd	Detb	Apparent Velocity (km/sec)
23	199	206	5.76	--	5.53	6.08
37	208	76	-4.67	--	8.43	6.71
163	139	283	1.38	7.17	6.18	6.73
164	142	283	0.90	6.93	5.80	6.82
173	139	277	1.54	7.70	5.95	7.17
178	140	278	1.46	7.54	5.87	7.21
274	248	209	5.39	12.60	--	6.44
395	218	80	-3.83	-10.45	--	7.71
425	150	340	-4.81	-6.04	-0.70	6.61
430	161	109	-3.38	-8.26	-7.89	6.04
431	153	87	-3.44	--	-7.74	7.39
433	194	81	-4.14	--	-8.16	6.95
443	155	236	5.40	13.21	7.39	6.39

FIGURE 4.3.7

FIRST ARRIVAL APPARENT VELOCITY AGAINST DISTANCE

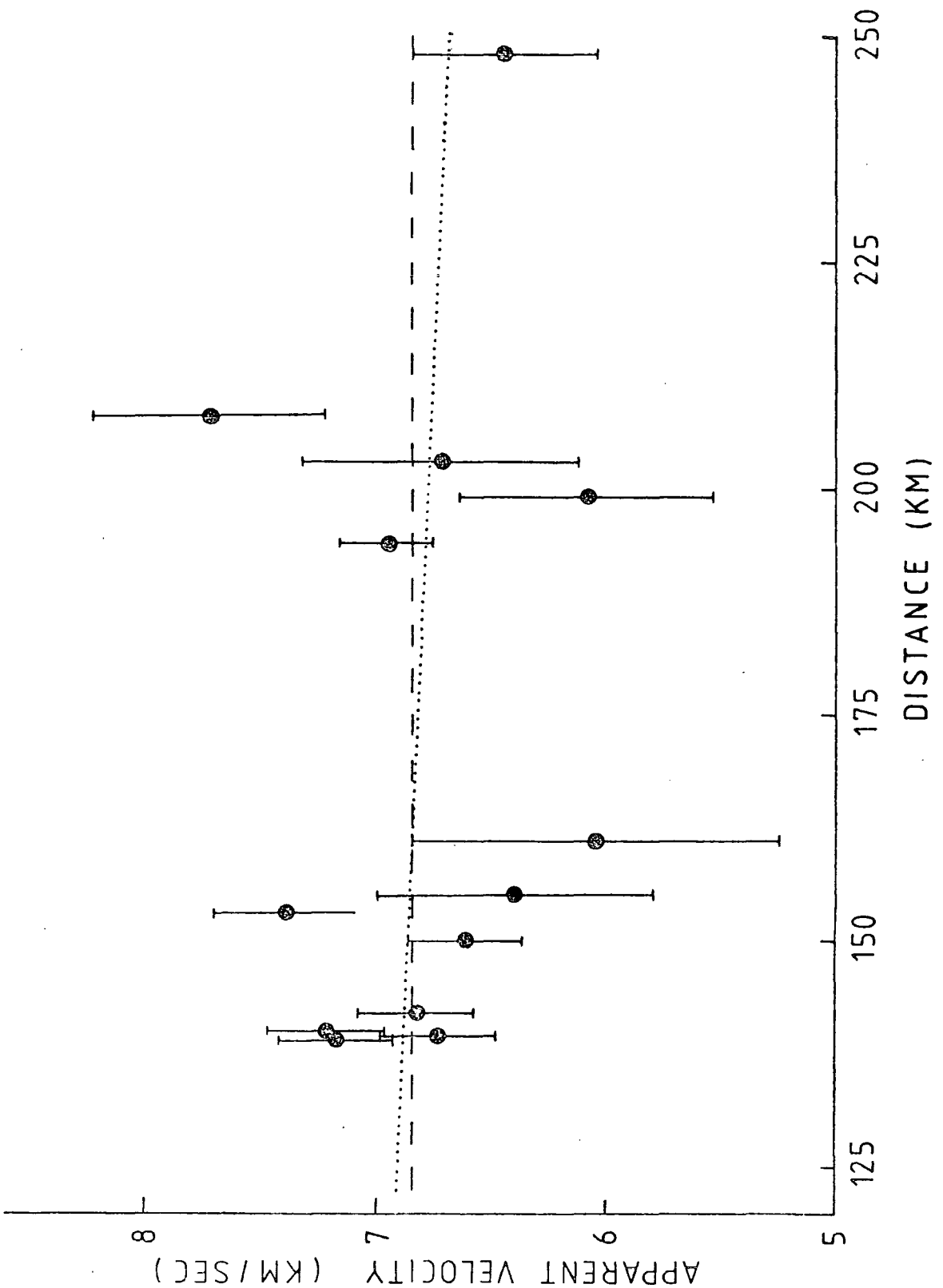

$$V' = (7.13 \pm 0.60) - (0.0018 \pm 0.0039)d \qquad (4.3.1)$$

with each point weighted by the reciprocal of its error. This indicates that within experimental error the velocity can be considered constant (an increase in V' with d might have been expected). There is no indication of a 8.0 km s^{-1} head wave over this distance raange. It follows that if 8.0 km s^{-1} mantle material exists beneath Afar it must be deeper than about 40 km (43 km for the optimized V(z) model (Figure 4.3.6c) deduced in this chapter).

To investigate the possibility of a dipping layer the apparent velocities are plotted as a function of azimuth, θ (Figure 4.3.8). This involves obtaining the weighted best fit to the sinusoid

$$V' = V_0 + V_1 \cos(\theta) + V_2 \sin(\theta) \qquad (4.3.2)$$

The fit gives

$V_0 = 6.84 \quad 0.57, \quad V_1 = 0.27 \quad 0.13, \quad V_2 = 0.14 \quad 0.13,$

which is equivalent to

$$V' = 6.84 + 0.31\cos(\theta - 27.5^{o})$$

This indicates a boundary dipping to the NNE at an angle of approximately 5° to 6°. The indication is weaker than it appears, since the statistics take no account of the absolute size of the errors in V'. It is inconsistent with BERCKHEMER et al's (1975) seismic refraction results, which indicate that this layer dips to the south, and it finds no support elsewhere in this study.

The apparent velocities are therefore interpreted in the simplest possible manner: that the arrivals all result from head waves refracted in the same layer, and that this

FIGURE 4.3.8

FIRST ARRIVAL APPARENT VELOCITY AGAINST AZIMUTH

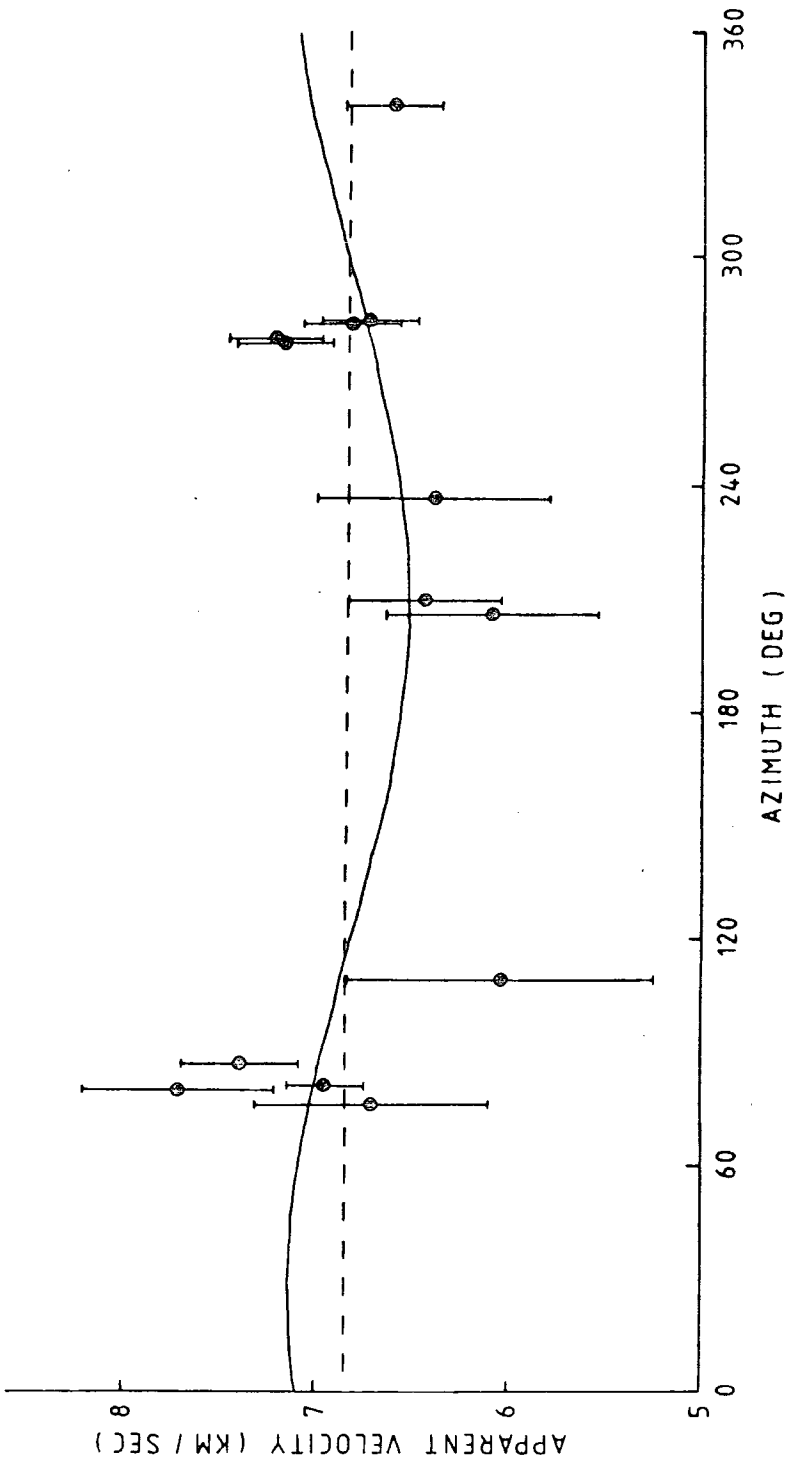

layer is horizontal and homogeneous. The apparent velocity across the array is then the true refractor velocity, and is consistent with the 6.9 km s^{-1} velocity found in Section 4.3.2.

4.3.4 The Upper Mantle

Events beyond 300 km cannot be satisfactorily located by the ESP network. ESP travel time data cannot therefore provide structural information below about 30 km. Two regional events with weak first arrivals as recorded by ESP are also listed in ISC bulletins*. Using the observed arrival times at the ESP stations and the ISC origin data, and correcting for the effect of the 4.4, 6.2 and 6.9 km s^{-1} structural layers (Figure 4.3.6c), the mean travel velocities were calculated for first arrivals to each station.

The velocities were found to be 7.8 0.7 km s^{-1}. Notable sources of error are uncertainties in the ISC epicentres and in ESP arrival times, and ignorance of the focal depths of the events and of the crustal structure in the source regions.

4.3.5 Summary

In order to locate the earthquakes recorded by ESP it has been necessary first to construct a V(z) model for South-Central Afar. The model requirements and other

---

*1974 OT Jun 21 16.03:56 ±1.6 s 12.63N±0.087 46.96E±0.071
1974 OT Jun 30 13.26:25.7±0.59s 15.97N±0.075 39.61E±0.098

scientific results obtained in this section are summarised as follows:

(1) Earthquakes originating within Afar have upper crustal foci (Ø to 5 km).

(2) The head wave R2 is the first arrival from all earthquakes with epicentral distances in the range 25 to 7Ø km.

(3) A V(z) model of not less than 4 laterally homogeneous layers is required to satisfy the later arrival observations. The preferred model is shown in Figure 4.3.6c.

(4) Parameters for the upper two structural layers are well-determined. Observations at all recording stations are satisfied by the same upper crustal velocity structure.

(5) The deeper structure is uncertain. No firm evidence is available for the depth of the layer 3/4 interface, or the velocity below it, since only the most distant earthquakes have first arrivals from layer 4. The distribution of these earthquakes is poor, their first arrivals are emergent, and later arrivals cannot satisfactorily be picked.

(6) This section has provided no conclusive evidence for or against dipping layers or lateral variations in seismic velocity within the deeper structure.

(7) Assuming the structural model of Figure 4.3.6c, 8.Ø km s^{-1} upper mantle material cannot exist at shallower depth than about 43 km.

4.4 Hypocentral Locations using Programme LEADL

Sections 4.4.1 and 4.4.2 describe the initial location of selected earthquakes using programme LEADL. The programme is tested with a number of different $V_{p(z)}$ models and values for Poisson's ratio, and is shown to yield stable, well-defined epicentres for well-recorded earthquakes. Earthquake RMS residuals with a given V(z) model provide a criterion for model evaluation.

Final hypocentral estimates are discussed in Section 4.4.3.

4.4.1 Use of the Programme and Initial Results

A sample of 91 earthquakes was located using two initial $V_{p(z)}$ structures: Model A, after BERCKHEMER et al (1975, profile IV); and Model B, after RUEGG (1975a,b) (Figures 4.3.6a,b). Model C (Figure 4.3.6c) was subsequently preferred to both initial models.

P and S arrivals were weighted according to probable picking time errors. Clean, impulsive P onsets were given a weight of 1.Ø. S onsets and poorer P onsets were given less weight, such that the weightings were approximately inversely proportional to probable picking errors. The maximum weight assigned to S onsets was Ø.5. The weighting method is subjective. However, for events from which five or more arrivals were available, the hypocentral estimates were insignificantly changed by altering the weightings of individual arrivals beyond the limits of possible subjective inconsistency.

Computed epicentres are relatively insensitive to vertical variations of velocity structure. However, 82% of the sample locations had lower, often much lower, RMS residuals with model A than with model B, irrespective of the Poisson's ratio used. Model A was therefore preferred to Model B. It has fewer layers than B, so that locations are obtained more rapidly and are less liable to computational instability.

26 earthquakes, recorded at 3 or 4 stations and chosen to cover a wide range of azimuth and distance, were processed in order to assess the behaviour of the programme. The chosen earthquakes were located for a range of values of r, where $r = V_P/V_S$ and V_P was kept constant. The earthquakes (Table 4.4.1 and Figure 4.4.1) were divided into two groups according to distance. Group A earthquakes have first arrivals which have travelled solely in the top two structural layers of Model A. First arrivals of Group B earthquakes are from the 6.8 or 7.4 km s^{-1} P-velocity layers.

It is found that:

(1) Group A earthquake RMS residuals are strongly dependent on focal depth when both P and S arrivals are used (Table 4.4.2, (1)). This enables an optimum focal depth to be determined. Group B RMS residuals become increasngly independent of focal depth, implying that beyond 150 km there is no longer any focal depth resolution.

(2) Many earthquakes show a trade-off of origin time against focal depth, without significant alteration of the

TABLE 4.4.1.

EVENTS USED IN PRELIMINARY HYPOCENTRAL LOCATIONS

	EVENT NUMBER	RECORDING STATIONS	DATE 1974	-ORIGIN TIME- HRS	MINS	SEC	LATITUDE (°N)	LONGITUDE (°E)	DEPTH (KM)
GROUP A	12 *	MTSD	23 FEB	20	31	24.82	11.8145	41.1204	3.0
	26 *	MTSD	26 FEB	11	37	19.19	11.9105	41.0310	3.0
	27	MTSD	26 FEB	11	37	39.65	11.9083	41.0329	3.0
	171 *	MTSD	2 APR	23	52	30.23	11.4201	41.4974	3.5
	270 *	MTS	23 JUN	9	55	16.00	11.1959	40.9285	1.0
	352	MTSD	26 JLY	21	33	50.09	11.8763	41.3300	0.0
	434 *	MTSD	23 SEP	8	20	42.80	11.9923	40.8726	0.5
	437	MTSD	23 SEP	10	2	36.59	11.9976	40.7681	0.75
	455 *	MTSD	24 SEP	17	38	8.02	11.8622	41.5077	0.0
	467	MTSD	24 SEP	18	48	3.97	11.8622	41.5089	0.0
	481	MTSD	24 SEP	20	25	51.74	11.8689	41.5093	0.0
	494 *	MTSD	25 SEP	1	41	37.43	11.9296	41.2058	1.75
	503 *	MTSD	25 SEP	20	19	26.89	11.9876	41.3616	5.0
GROUP B	75	MTS	26 MAR	10	20	25.36	13.2315	41.0264	
	78	MTS	26 MAR	11	28	25.19	13.2377	41.0170	
	79	MTS	26 MAR	11	57	15.51	13.2375	41.0320	
	162	MTSD	2 APR	9	2	1.00	11.9146	39.9022	7.5
	163	MTSD	2 APR	9	11	7.81	11.9339	39.9373	3.5
	164 *	MTSD	2 APR	9	49	3.86	11.8976	39.8821	8.5
	173	MTSD	3 APR	2	43	46.66	11.8650	39.8544	13.0
	178	MTSD	3 APR	5	34	57.36	11.9135	39.9015	5.5
	425 *	MTSD	17 SEP	13	26	19.94	12.7994	40.7137	
	430	MTSD	20 SEP	0	1	37.16	11.5106	42.3429	
	431	MTD	20 SEP	0	17	20.03	11.5980	42.3708	
	433	MTD	21 SEP	12	3	56.88	11.8746	42.7816	
	439	MTSD	23 SEP	13	51	22.39	11.8334	39.8983	3.0
	443 *	MTSD	23 SEP	19	54	54.07	10.8405	40.0564	

* These events were also located using subroutine HYPCTR

In this and subsequent tables,
M (or MILL) = Mille
S (or SERD) = Serdo
T (or TEND) = Tendaho
D (or DETB) = Det Bahri

FIGURE 4.4.1

LOCATION OF EARTHQUAKES DISCUSSED IN CHAPTER 4

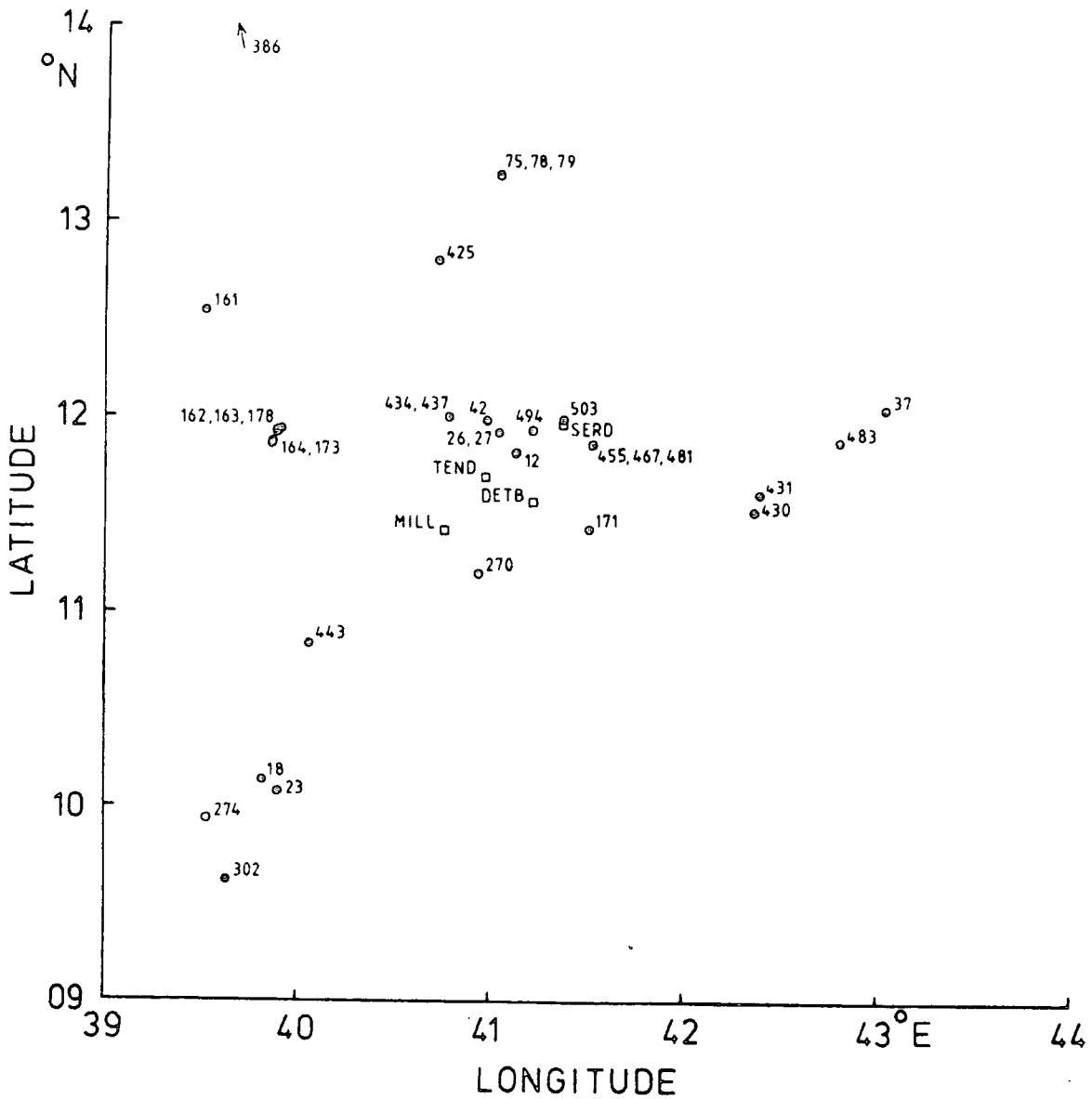

TABLE 4.4.2

VARIATION OF ORIGIN TIME AND RMS RESIDUAL WITH FOCAL DEPTH

(typical Group A earthquakes)

(1) FOR EVENT 12, BOTH P AND S PHASES USED IN SOLUTIONS

Focal Depth (km)	Origin Time (s)	----Epicentre---- Latitude (°N)	Longitude (°E)	RMS Residual (s)
0	24.21	11.814	41.122	0.163
1	24.41	11.814	41.121	0.120
2	24.61	11.814	41.121	0.081
3	24.82	11.814	41.120	0.049
4	24.81	11.815	41.120	0.051
6	24.77	11.815	41.120	0.062
8	24.70	11.815	41.120	0.084
10	24.61	11.815	41.122	0.139
12	24.51	11.815	41.125	0.231
15	24.37	11.817	41.125	0.287
20	23.98	11.811	41.141	0.430
25	23.55	11.811	41.154	0.618
30	23.01	11.812	41.168	0.789

(2) FOR EVENT 434, P ARRIVALS ONLY

0	42.88	11.9845	40.7795	0.001
1	43.04	11.9845	40.7796	0.001
2	43.19	11.9844	40.7796	0.001
3	43.34	11.9844	40.7796	0.002
4	43.34	11.9844	40.7795	0.002
5	43.34	11.9841	40.7797	0.003

epicentral estimates (Table 4.4.2). This is the phenomenon discussed in Section 4.1. The behaviour of the RMS residuals in Table 4.4.2 demonstrates the value of including S arrivals.

(3) Increasing r decreases the epicentral distance estimates (Figure 4.4.2), and increases focal depth estimates (Figure 4.4.3). For example, changing r from 1.72 to 1.82 alters the depth of event 494 from 0 to 10 km.

(4) Using both P and S arrivals, LEADL reached the same solution from every trial epicentre within 200 km of the network. When only P arrivals were used, all the group A earthquakes and 9 from group B converged without any trial epicentre being supplied. The remaining 5 earthquakes of group B converged only when a starting epicentre was used close to the solution previously computed from both P and S data.

In summary, LEADL gave stable and well-defined epicentres for all the test earthquakes. Focal depth information was obtained for earthquakes less than about 150 km from the network.

4.4.2 Determination of Poisson's Ratio

Using Model C (Figure 4.3.6c), each earthquake of Group A was located for 8 values of r, varied between 1.70 and 1.84 in steps of 0.02. The best value for r was assumed to correspond to the lowest RMS residual, at whatever focal depth this occurred. Sample plots of minimum residual against r are shown in Figure 4.4.4, and a

FIGURE 4.4.2

VARIATION OF EPICENTRE (OPEN CIRCLES) WITH P/S VELOCITY RATIO (NUMERICAL SUPERSCRIPTS) FOR A TYPICAL GROUP B EVENT

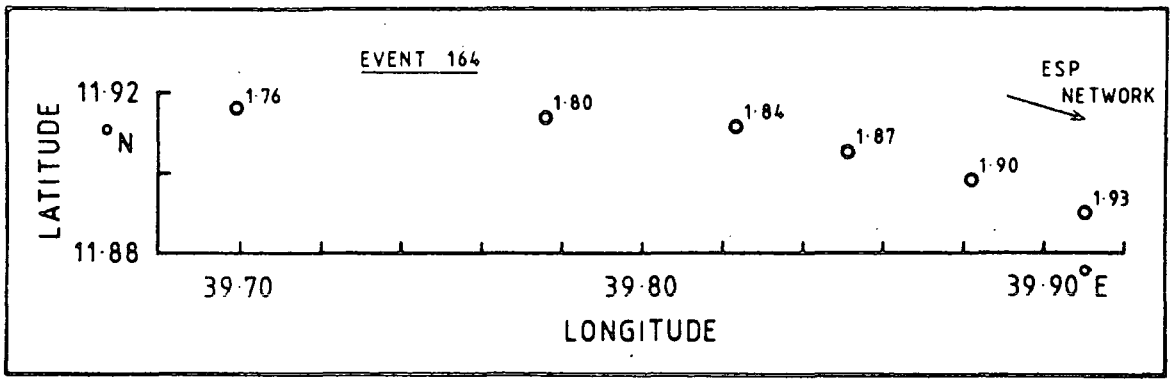

FIGURE 4.4.3

VARIATION OF OPTIMUM FOCAL DEPTH WITH P/S VELOCITY RATIO

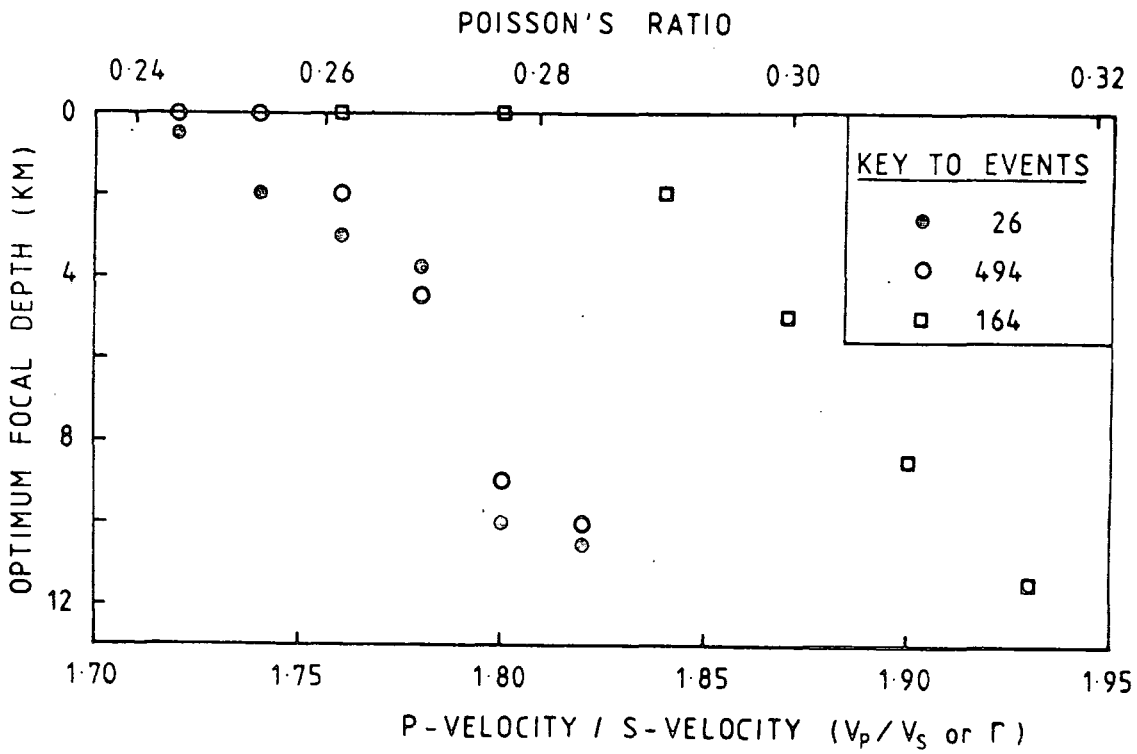

FIGURE 4.4.4

PLOTS OF MINIMUM RESIDUAL AGAINST P/S VELOCITY RATIO

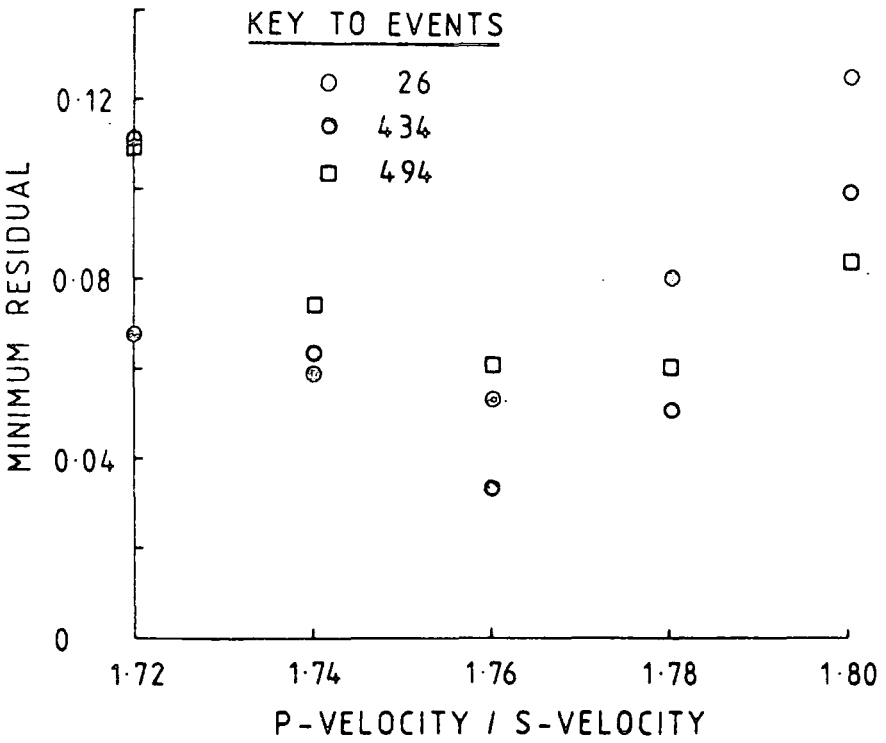

FIGURE 4.4.5

HISTOGRAMS OF OPTIMUM P/S VELOCITY RATIOS

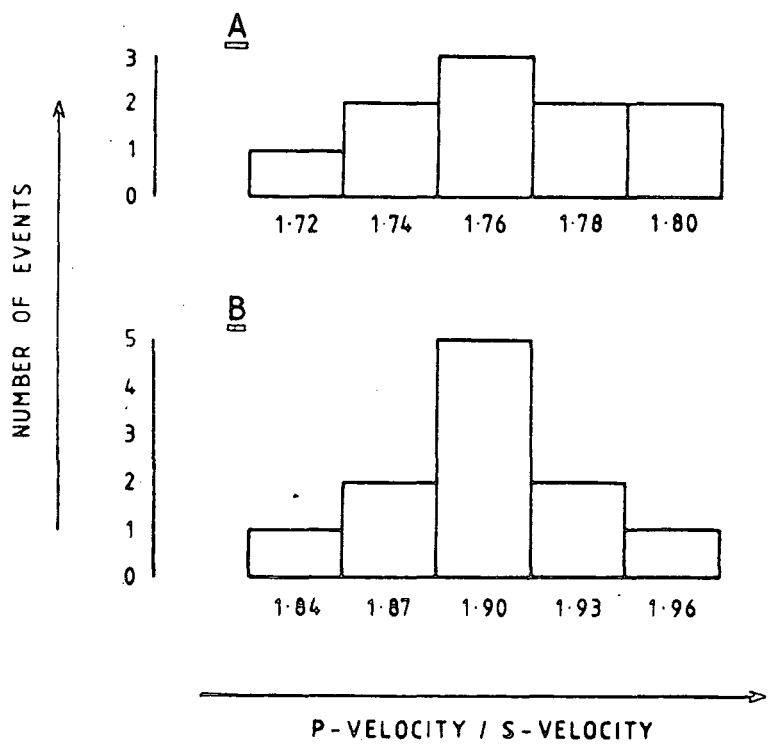

histogram of the results in Figure 4.4.5a. The mean value is r = 1.76. Hypocentral parameters of Group A earthquakes giving the minimum residual for the set of estimates with r = 1.76 were therefore taken as the best estimates.

Figure 4.4.6 shows the variation of epicentral estimate with r for two earthquakes from group A. Event 27 was recorded at all four stations, event 42 at three stations. The increased stability due to the fourth station is evident. The same figure also shows the solutions obtained from P arrivals only. They occur close to the solutions for r = 1.76, suggesting that the estimate of 1.76 is good and that LEADL is reliable when S data are not available.

Further confidence in the value r = 1.76 is obtained by plotting S travel times against P travel times (Figure 4.4.7), both calculated with reference to the origin times computed from P arrivals only. If the origin time is correctly determined, and the measured P and S correspond to the same phase, the gradient of the graph will be t(S)/t(P) = r. A linear fit to 37 data points gave r = 1.76 ± 0.012.

The velocity ratio at greater depth was determined in the same way, using the more distant group B earthquakes. The S velocities of the two upper structural layers were held at the values constrained by r = 1.76, while those of the lower layers were varied in steps of 0.03 from r = 1.81 to r = 1.99. The result was a mean value of r = 1.90 (Figure 4.4.5b). Assuming a perfectly elastic, isotropic

FIGURE 4.4.6

EPICENTRE AS A FUNCTION OF P/S VELOCITY RATIO

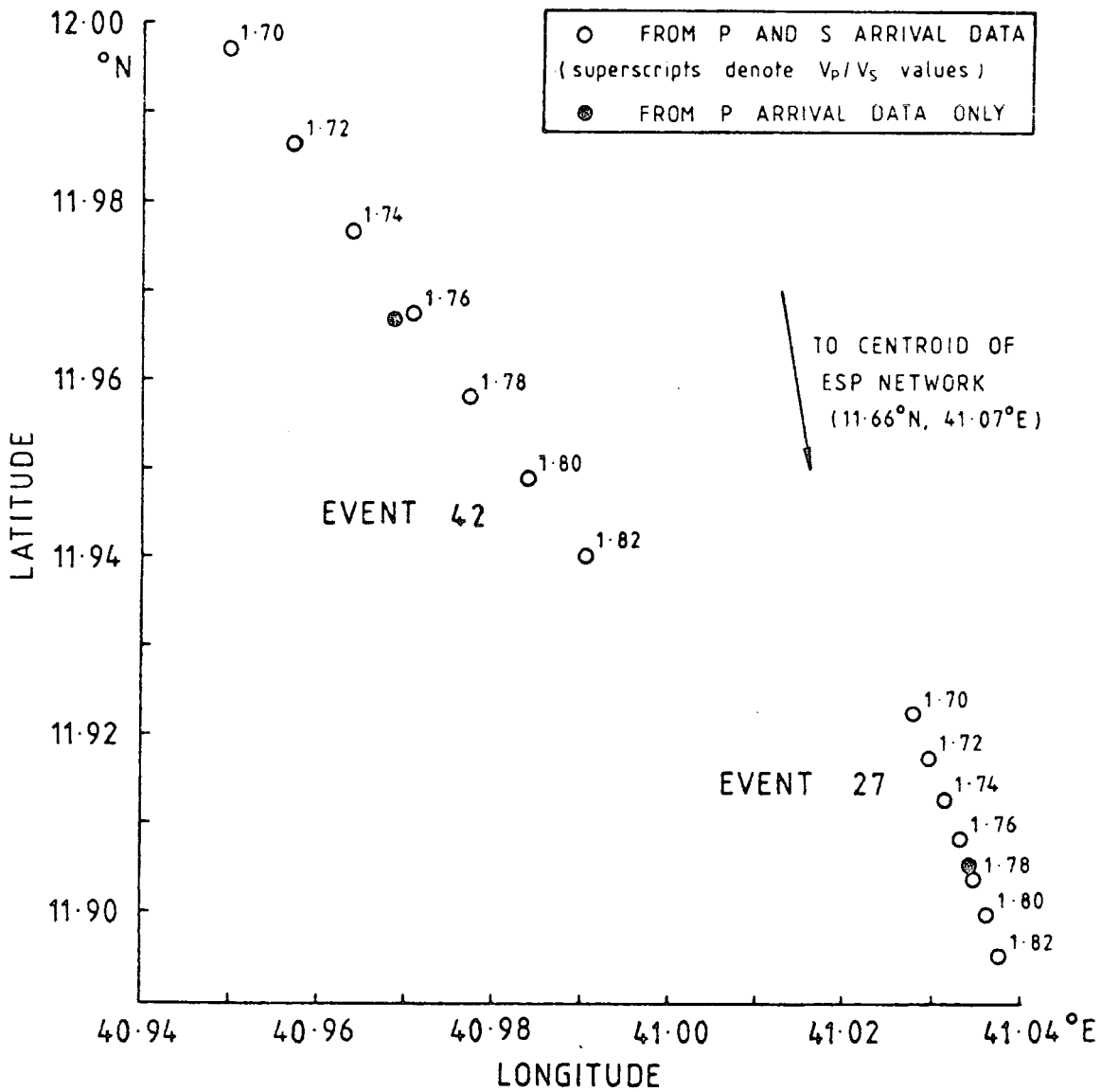

FIGURE 4.4.7

GRAPH OF P AGAINST S ARRIVAL TRAVEL TIMES

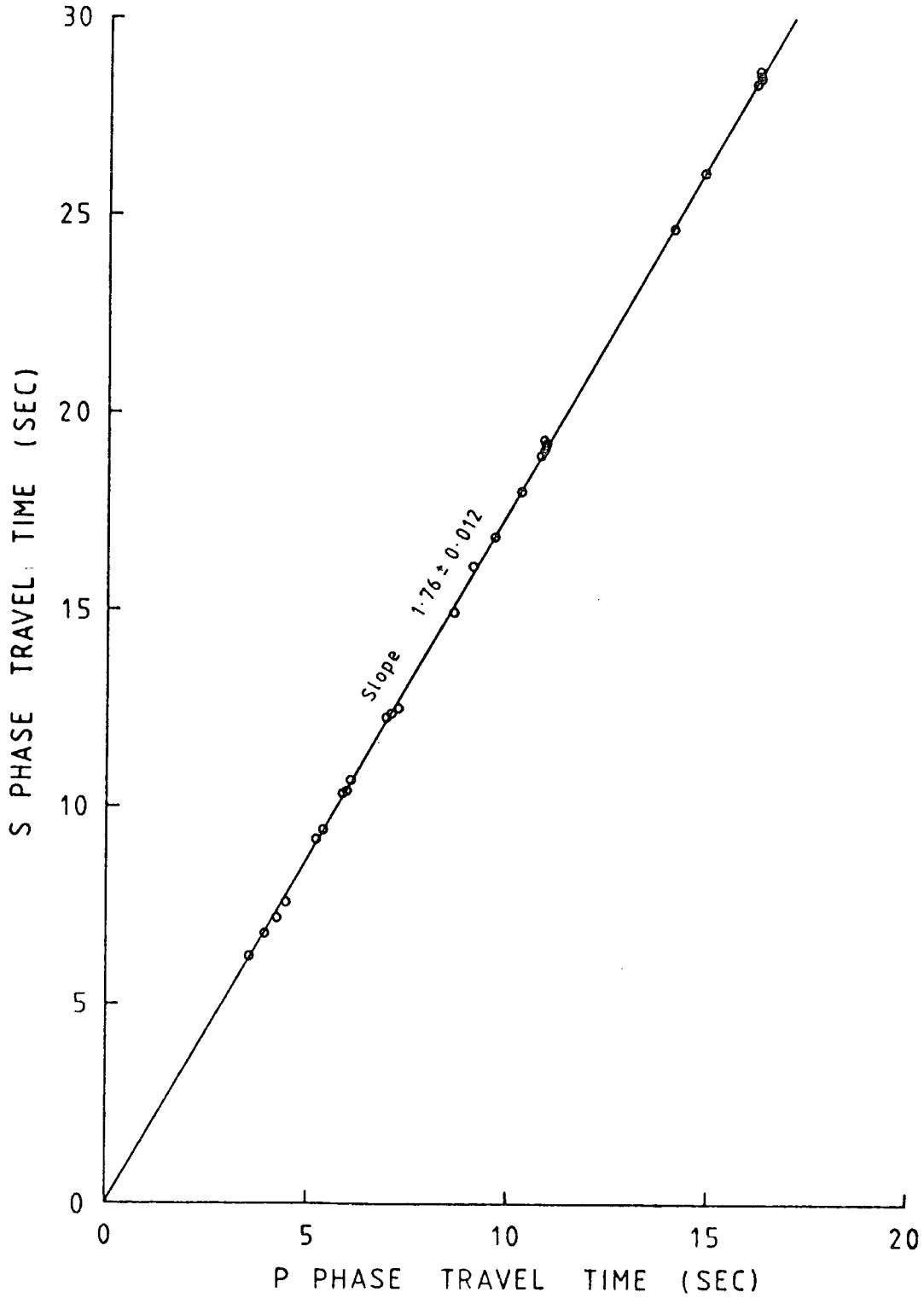

medium, r is related to Poisson's ratio, σ, by

$$\sigma = (r^2 - 2)/[2(r^2 - 1)]$$

(e.g. BULLEN,1965, p.213). r = 1.76 gives σ = Ø.26 for the upper crust, and r = 1.9Ø gives σ = Ø.31. The significance of these values is discussed in Chapter 9.

It should be noted that the sample sizes are small, since the only useful earthquakes were those for which both P and S arrivals could be accurately picked at 3 or 4 stations. Other earthquakes from similar locations were not used for fear of biasing the sample. There was no evidence for azimuthal variation of Poisson's ratio.

4.4.3 Final Hypocentral Locations

LEADL was used with the optimized model C to locate as many earthquakes as possible. The focal depth interval used was Ø.25 km from Ø to 3 km; Ø.5 km from 3 to 1Ø km; and 1 km from 1Ø to 15 km. Individual arrivals giving anomalously large residuals were assessed, and occasionally discarded. Earthquake location was usually a routine procedure, but certain cases require comment.

Earthquakes recorded at only two stations have two possible epicentres, one of which is the reflection of the other in the vertical plane including the stations. Since most earthquakes occurred in sequences one solution could usually be unambiguously preferred. A reasonable choice was possible in a few further cases. A small remainder of earthquakes could not be uniquely located.

A second problem when LEADL is used for earthquakes

recorded at only two stations is that the RMS residuals are not depth dependent i.e. there is no focal depth information. It was necessary to assume a focal depth for these earthquakes, since origin time and epicentral co-ordinates are depth dependent. Earthquakes which formed part of a sequence were assumed to have occurred at the mean of the calculated depths for that sequence. In all other instances the arbitrary focal depth 3 km was assigned, this being the mean depth of all the calculated hypocentres. 3 km was also the depth assigned to earthquakes originating 150 km or farther from the network.

LEADL would not always converge for earthquakes at epicentral distances greater than 200 km. To treat these, the programme was modified to give the RMS residuals at a grid of pre-selected points. The initial grid was defined to enclose all the intersections of the S-P circles for each recording station. The modified programme was run with grids of progressively finer mesh until the global minimum of RMS values had been found. This procedure was only necessary for poorly recorded earthquakes and those with very emergent arrivals, where the high RMS residual at the global minimum indicated large relative arrival timing errors. For a few earthquakes which were recorded at AAE or ART, approximate epicentres were obtained by incorporating arrival times at these stations. Such locations are subject to large errors, since no correction was made for the inapplicability of V(z) model C beyond Afar.

The 504 earthquakes identified by ESP are listed in

Appendix 6, 226 of these being recorded at one station only. It was possible to locate 250 of the remaining 278 using LEADL (the epicentres are mapped and discussed in CHapter 8). RMS solution residuals are included in Appendix 6 to indicate the internal consistency of the arrival data, but they should not be regarded as representing the errors on the determinations.

4.5 Hypocentral Locations using Subroutine HYPCTR

As explained in Section 4.2, the use of Subroutine HYPCTR was confined to a small number of well-recorded earthquakes. Subroutine HYPCTR was initially run using the 8 asterisked earthquakes of Group A, Table 4.4.1. V(z) structural parameters were not constrained (except for the upper layer velocity gradient, VG, which had to be positive to avoid a velocity inversion), and the initial trial values assigned to them were found not to be critical. Initial trial earthquake epicentres were as determined using LEADL. All focal depths were restrained to 3 km.

The resultant epicentres were insensitive to the parameters of the upper crustal layer, and in particular to VG. The programme was therefore rerun with VG fixed at a very low value (10^{-4} s^{-1}) to simulate a 2-layer, constant velocity model. The resultant model is shown in Figure 4.3.6d.

Table 4.5.1 compares the epicentral estimates from HYPCTR (Solution C) with those found using LEADL and the V(z) model of Figure 4.3.6c, with and without S arrivals

TABLE 4.5.1

COMPARISON OF COMPUTED EPICENTRES FOR SELECTED EVENTS

SOLUTION	(A) LEADL, for model of Fig.4.3.6c		(B) LEADL, P phases only, Fig.4.3.6c		(C) HYPCTR, optimized model, Fig.4.3.6d		(D) HYPCTR, fixed model, upper two layers of Fig.4.3.6c	
Event Number	Latitude	Longitude	Latitude	Longitude	Latitude	Longitude	Latitude	Longitude
12	11.814	41.120	11.812	41.121	11.810	41.121	11.812	41.120
26	11.910	41.031	11.907	41.032	11.901	41.037	11.901	41.037
171	11.420	41.497	11.380	41.551	11.448	41.459	11.443	41.464
270	11.196	40.928	11.189	40.928	11.181	40.933	11.196	40.926
434	11.992	40.773	11.985	40.779	11.985	40.778	11.983	40.779
455	11.862	41.508	11.859	41.462	11.858	41.456	11.863	41.470
494	11.930	41.206	11.926	41.209	11.932	41.206	11.930	41.210
503	11.988	41.362	11.985	41.360	11.985	41.351	12.005	41.371

(Solutions A and B). Also tabulated is the set of solutions (D) obtained by running HYPCTR with the constrained V(z) structure of the upper two layers of Figure 4.3.6c. All four parameter sets are in good agreement. The epicentres estimated from Solutions A, B and D are within 2 km of those estimated from Solution C in all but 4 cases (event 171, Solutions A and B; event 455, Solution A; event 503, Solution D). Otherwise, the mean distance from the Solution C estimates is 0.96 km, 0.66 km and 0.74 km for Solutions A, B and D respectively.

Adding to the data set the 3 asterisked earthquakes of group B, Table 4.4.1, a further HYPCTR solution set was obtained. The influence of the 3 more distant earthquakes was shown by an increase in the refractor velocity of the optimized V(z) model from 6.22 to 6.56 km s^{-1}, and by a two-fold increase in the minimum value of the objective function (Equation 4.2.1) (i.e. a poorer fit). As located by LEADL, these 3 earthquakes have first arrivals that are head-waves from layer 3 of model C (velocity 6.9 km s^{-1}), so both these results were to be expected.

4.6 Sources of Location Errors

Four sources of random error are identified, and two of systematic error. The random errors arise from (1) gross reading errors, (2) misidentified arrivals, (3) residual reading errors, and (4) seismogram timing errors. Seismogram timing errors, typically $\pm$ 0.02s, have already been discussed (Section 3.11). Systematic errors are caused

by (1) errors in the geographical co-ordinates assumed for the ESP recording stations and (2) inaccuracies in the assumed V(z) model.

Random Errors

4.6.1 Gross Reading Errors

A paper on errors in the first onset readings of seismograms (FREEDMAN,1966) reported that at least 5% of all onsets were picked with gross errors, generally of integral numbers of hours, minutes or seconds. The errors were usually caused by misreading the timecode.

In this study, all seismograms were reread 18 months after the onsets had originally been picked (Section 3.7), minimizing the possibility of gross reading errors. Gross errors introduced during the transcription of the data on to computer files normally became apparent when LEADL failed to converge or gave large residuals, but the arrival times of all spatially isolated hypocentral estimates were rechecked. The data are believed to be free of gross errors.

4.6.2 Misidentified Arrivals

Errors arise when either (1) the first P or S phase is totally missed or mistaken, or (2) the correct phase is read but the first cycle of the waveform overlooked. Errors are most likely to occur when the signal to noise ratio is low.

For earthquakes from 100 km or closer, most P onsets were impulsive and of comparable amplitude to the rest of

the P coda (see e.g. Figure 4.3.3). Such onsets were unmistakable. Many S arrivals were also picked with confidence (Section 3.7), and some were differentiated from later P coda arrivals by polarization analysis (Section 6.3). Others may have been mispicked by up to one cycle (giving a worst-case error of ±0.2 s for a typical frequency of 5 Hz) because of contamination by later P coda arrivals.

Comparison of the original and later readings of 30 sample earthquakes from 150 km or beyond showed onset time differences of < 0.05 s in 16 cases; between 0.05 and 0.2 s in 8; and between 0.3 and 1.5 s in the remaining 6. Neglecting these six, the mean time difference was 0.04 s. The repeatability of a set of results does not of course guarantee their accuracy, but does indicate the magnitude of likely errors.

P and S onsets of earthquakes from beyond 150 km were often of low amplitude and may sometimes have been missed, or picked early. For typical P onset frequencies of 1 to 5 Hz, arrivals mispicked by one cycle will have time errors of 1.0 to 0.2 s. A few such errors were revealed when waveform matching was used for the later set of onset picks. S onsets of distant earthquakes are liable to larger errors, because of their generally lower frequencies and the possibility of interference from earlier phases.

4.6.3 Residual Reading Errors

This section considers errors caused by misreading the exact part of the first cycle of the first arrival that constitutes the onset. For impulsive arrivals residual errors should not exceed a quarter of a cycle, i.e. Ø.Ø25 to Ø.25 s over the observed frequency range 1Ø to 1 Hz. For over 9Ø% of fair or well recorded earthquakes from 75 km or closer the time difference between the two independent seismogram onset readings (which includes timecode measuring errors, Section 3.11.4) was Ø.Ø3 s or less.

4.6.4 Discussion of Random Errors

The last squares treatment of ESP arrival times has tacitly assumed that the probability density of travel-time residuals is normal (Gaussian). This assumption is valid only if the expectation of the travel-time error is zero (see e.g. JEFFREYS, 1948; FREEDMAN,1968). The sample mean may not otherwise be an appropriate estimate for the population mean.

In this study, clock drift and measurement errors are independent from station to station, and data contamination has been eliminated as a significant cause of sample bias. P arrival time errors may, however, be biased in one direction, because undetected first arrivals are more likely than spurious early picks of background noise. Errors in picking an arrival are not independent, because of the correlation between the waveforms at different stations; but all seismograms have been read by the same person, so

maximum uniformity and internal consistency have been ensured. Correlated waveforms may result in a constant picking error at each station (especially when waveform matching is used), with no effect on the hypocentral estimates except through systematic errors in the S-P time. These errors do not significantly alter the distribution of residuals, and for the large majority of earthquakes the assumption of normality is justified.

In summary, seismogram timing errors and residual reading errors each contribute random errors of about 0.02 s to most arrivals from epicentral distances of 100 km or less. More distant (or very weak) earthquakes may have misidentified arrivals, giving rise to significantly larger errors.

One problem with the small number of available arrivals in this study is that there is little redundancy in the data, so that errors in individual travel times are not always apparent from the station residuals of the corresponding hypocentral estimates.

Systematic Errors

4.6.5 Station Co-ordinate Errors

Geographical co-ordinates of any given point within Afar vary from map to map, commonly by 1 to 2 km in latitude and up to 3 km in longitude. This is the consequence of cartography based on aerial photographs with very limited ground control. German workers have conducted a geodetic

survey in Central Afar, determining geographical co-ordinates of about 120 stations by astronomic position lines (TORGE,1975), but details have not been published. Fortunately, in the present study the absolute accuracy of the station co-ordinates is unimportant.

In order to minimise relative errors all stations were located with respect to a single set of maps (UNDP,1973, figs.29,53*), compiled during geothermal exploration. Since these are the most detailed geotectonic maps of the area they have also been used in Chapter 8 for referring seismic epicentres to local geological features. Mille is located from a map at the scale 1.5:1,000,000, the other stations from 7.5:1,000,000 scale maps.

The author was led to believe that the ESP stations had been surveyed when they were set up in 1973. Only after his final return from Ethiopia did he discover that no proper station co-ordinates existed. He was obliged to relate the station positions to adjacent landmarks featured on available maps, and on his own photographs.

Tendaho station was located to ±20 m on a 1:1000 scale map of boreholes at the proposed dam site (GIBB, Sir ALEXANDER and PARTNERS,1973), and Serdo station to ±175 m from fig.1 of SEARLE and GOUIN (1971b). Det Bahri and Mille were located directly with respect to the UNDP maps.

Estimated station locations and their errors relative

---

*This document is restricted and the maps otherwise unpublished. The author is indebted to Ato Seife Berhe of the Ethiopian Ministry of Mines, who kindly sent him copies of the maps.

to the UNDP maps are given in Table 4.6.1.

TABLE 4.6.1

ESP STATION CO-ORDINATES

	Latitude °N	Longitude °E	Elevation (metres)
Mille	11.420 ± 0.0035	40.752 ± 0.0035	505 ± 25
Tendaho	11.690 ± 0.0008	40.958 ± 0.0008	417 ± 5
Serdo	11.957 ± 0.0020	41.359 ± 0.0020	398 ± 10
Det Bahri	11.561 ± 0.0025	41.208 ± 0.0025	405 ± 25

The figures for Tendaho and Serdo include the additional uncertainty involved in transferring the locations from Gibb's and Searle's maps to the smaller scale UNDP maps. The UNDP maps are themselves distorted. They are based on aerial photographs of varying scales, and ground control is limited to geothermal areas. To allow for this a further possible error of ±0.0025° (approximately 250 m) in latitude and longitude should be assumed for the other stations relative to Tendaho. The estimated absolute error is 1 to 2 km.

Station elevations have been calculated relative to the Assab-Combolcia highway, which passes through Mille, Tendaho and Serdo and has USCGS benchmarks at intervals of 5 to 50 km. Gravity profiles along the highway have involved frequent elevation measurements made by altimeter (estimated error ±2 m) or by precise levelling (MOHR and ROGERS,1964; SEARLE and GOUIN,1971b).

The elevations of Mille and Serdo stations relative to the highway were estimated to ±20 m and ±5 m respectively, and the relative height of Tendaho station was shown on the Gibb map. Because of the extreme flatness of the Recent sediments flooring the Tendaho graben the elevation of Det Bahri could be estimated from MOHR and ROGERS'(1964) measurements east of Dubti.

A relative horizontal station location error of 'ϵ' metres, along a line having angle α to an event azimuth, is equivalent to a travel time error $E = (10^{-3}\epsilon \cos(\alpha))/V$ seconds for head wave arrivals from a horizontal crustal layer of V km s^{-1}. If ϵ = 500 m, V = 6.2 km s^{-1} and $\alpha = 0^{o}$, E = 0.08 s. This is a worst-case error. Similarly, for an arrival with angle of incidence 'i' an elevation error of ϵ metres corresponds to a travel time error of $E' = (10^{-3}\epsilon \cos(i))/V_0$ seconds, where V_0 is the near-surface velocity; with a worst-case error of $E' \approx 0.004$ s for ϵ = 25 m.

4.6.6 The Structural Model

Any V(z) structural model is only an approximation to true Earth structure. Errors will arise because of the over-simplified form of the model, and also because within the form adopted the parameter estimates may not be optimal. The effect on the hypocentre estimates of varying the model parameters is shown in Section 4.7.

In such a complex tectonic province, velocity inhomogeneities are expected from dipping layers, faults and

igneous intrusions. The effects of such lateral inhomogeneities, low-velocity layers and other structural complexities excluded from the model cannot be estimated. However, the lateral inhomogeneities are not so large as to have been revealed either by the methods of Section 4.3 or by particle motion analysis (Chapter 6).

Equation 4.3.1 may be rewritten

$$t(R2) = (1/V_o)[d \sin(i_c) + (2h_1 - z)\cos(i_c)] \quad (4.6.1)$$

where i_c is the critical angle, since $\sin(i_c) = V_\emptyset/V_1$. If the $V_\emptyset$ to V_1 layer interface dips at an angle θ^o, it is easily shown that along the direction of dip Equation 4.6.1 becomes

$$t(R2) = (1/V_\emptyset)[d \cos(\theta)\sin(i_c) + (D_E+D_R) \cos(\theta)\cos(i_c) - z \cos(i_c-\theta)] \quad (4.6.2)$$

where D_E, D_R are the depths to the dipping interface below the crust and the receiver. Substituting the crustal parameters of Figure 4.3.6c, with z = 3 km, reveals that for an epicentral distance of 50 km (where R2 is likely to be the first arrival) a 5° dip will alter the travel time by about 0.8 s. For a 10° dip the figure is about 2.2 s. The effect of undetected dips on hypocentral estimates will depend on the number of recording stations and their distribution about the hypocentres.

It is well known from laboratory experiments (e.g. TOCHER,1957) that in rock samples subject to uniaxial stress the velocity parallel to the stress axis exceeds the velocity normal to the axis. NUR (1971) has discussed this result in terms applicable to tensional and shear faulting.

Observations of such a velocity anisotropy in Afar might yield valuable information concerning the regional stress pattern (although it could also be caused by other phenomena, such as oriented dyke swarms).

ROTHMAN et al (1974) have demonstrated through a computational experiment that undetected velocity anisotropy can cause large errors in hypocentral locations. For Afar, however, velocity inhomogeneities due to deviatoric stress, major faults and intrusive bodies are likely to be less pronounced than those due to dipping layers. To find seismic evidence for such inhomogeneities, unless their location has been precisely determined from other data, normally requires analysis of azimuthal variations in the station residuals of a large and well-distributed network, together with a search for any reflected, refracted or diffracted arrivals generated by the inhomogeneities.

4.6.7 Discussion of Systematic Errors

It has been shown that the errors due to recording station mislocations do not exceed 0.08 s, whereas the errors due to undetected dips may be much larger than this and will increase with increasing epicentral distance, d. The error in t(R2) for d = 50 km and a 5° dip is about 1.3%.

Inaccuracies in the V(z) model velocities cause the largest errors. For example, considering for simplicity the V(z) model as replaced by an equivalent half-space of velocity V, the time error caused by a velocity error of ΔV will be $\Delta t = x\Delta V/V^2$, where x is the hypocentral distance.

For ΔV = 0.2 km s^{-1} and V = 5 km s^{-1}, Δt = 4%.

4.7 Estimation of Location Errors

Small RMS travel-time residuals for a hypocentral location do not necessarily imply that the parameter estimates are accurate. This has been demonstrated explicitly by JAMES et al (1969).

Where the solution has been achieved by minimization of an objective function, F, confidence regions bounded by contours of constant F are computed assuming a quadratic form for F around F_{MIN}. This approach (Section 4.7.1) is valuable in determining the shape of the confidence regions, but it is shown that the absolute size of the errors is better determined by the more direct methods employed in Section 4.7.2.

4.7.1 Method of Obtaining Confidence Regions with HYPCTR

The magnitude of the minimum value of the objective function (F_{MIN}) for an optimized model is a measure of the inconsistency between the data and the V(z) model. The value $F_{MIN} = 6.17*10^{-3}$ s^2, obtained from HYPCTR in Section 4.5 when deriving the optimum 2-layer model of Figure 4.3.6d, is greater than would be expected from the likely errors in the arrival time measurements discussed in the previous section. This could be explained by underestimation of the arrival time errors, or by failure to find the true minimum of F (unlikely, in view of the good agreement between HYPCTR and LEADL solutions demonstrated in

Table 4.5.1). The most obvious explanation is that the structural model used is too crude.

Subroutine HYPCTR was modified to allow the variations of $F(u_1,u_2,...,u_n)$ with pairs of hyperspace co-ordinates u_1, u_2 to be plotted as contour diagrams. Each contour is a fiducial confidence ellipse bounding a surface of constant F about F_{MIN} (a horizontal plane in Figure 4.7.1), i.e. enclosing a confidence region (AL-CHALABI,1972).

Sample contour diagrams are shown in Figures 4.7.2 and 4.7.3. They indicate semi-quantitatively the relative magnitudes of errors in each pair of variables, and how errors in the determination of the parameter values are inter-related. It has been shown (FLINN,1965a) that the orientation and eccentricity of the confidence ellipses for latitude and longitude (Figure 4.7.2) depend solely on the distribution in azimuth and distance of the recording stations, and not on the travel time residuals.*

The prevalent, approximately NW-SE elongation of the confidence ellipses most effectively demonstrates the deficiencies of the ESP stations for seismic event location. The four ESP stations formed an approximately elliptical network (Figure 2.2.1), with major axis at 048o and consequent poor resolution normal to this direction. The difficulty is most clearly shown by those earthquakes (12,494,26) (Figure 4.4.1) closest to the centroid of the

---

*Flinn's result assumes that the variance of the random errors is the same at all stations. Where reading errors differ from station to station, this condition is approximated by suitably weighting the observations.

FIGURE 4.7.1

DIAGRAMMATIC REPRESENTATION OF THE OBJECTIVE FUNCTION, F, IN THE REGION OF ITS MINIMUM VALUE

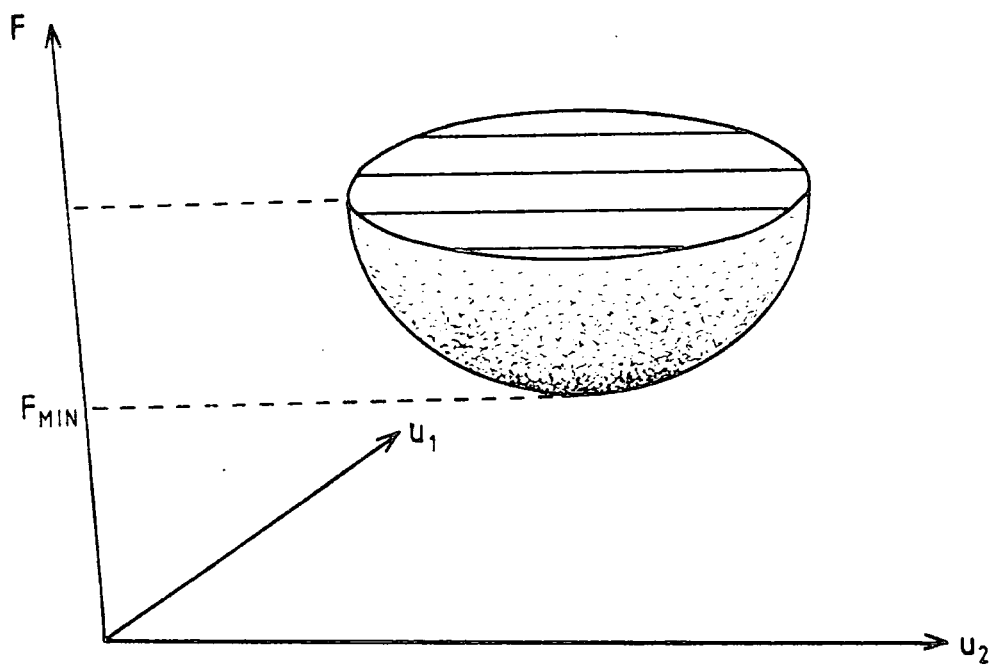

FIGURE 4.7.2

CONFIDENCE ELLIPSES FOR LATITUDE AND LONGITUDE

Length and orientation of arrows indicate
distance and direction to centroid of station network

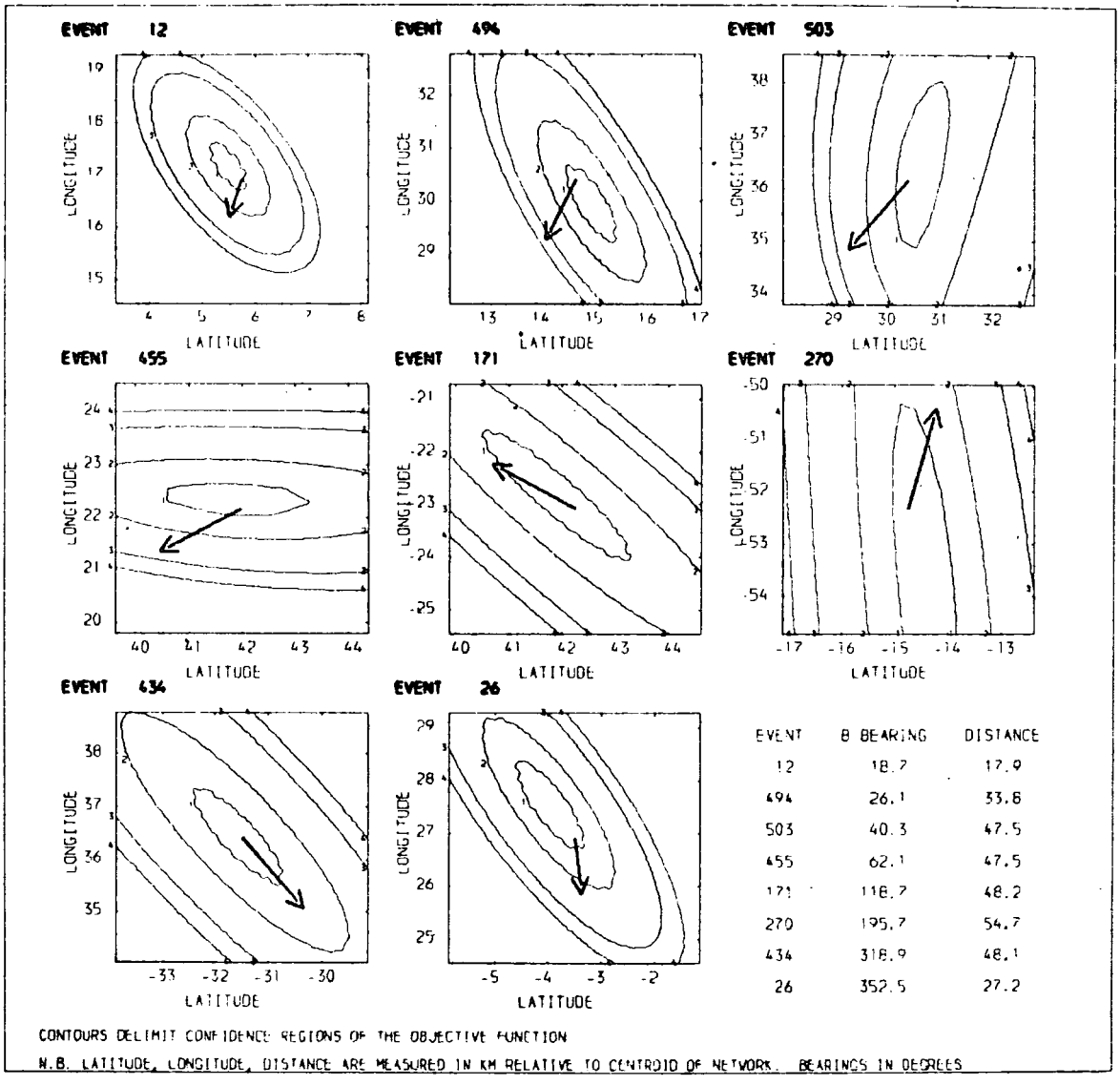

EVENT	B BEARING	DISTANCE
12	18.7	17.9
494	26.1	33.8
503	40.3	47.5
455	62.1	47.5
171	118.7	48.2
270	195.7	54.7
434	318.9	48.1
26	352.5	27.2

CONTOURS DELIMIT CONFIDENCE REGIONS OF THE OBJECTIVE FUNCTION

N.B. LATITUDE, LONGITUDE, DISTANCE ARE MEASURED IN KM RELATIVE TO CENTROID OF NETWORK. BEARINGS IN DEGREES

FIGURE 4.7.3

CONFIDENCE ELLIPSES FOR VELOCITY AND DEPTH OF CRUSTAL REFRACTOR FOR OPTIMIZED 2-LAYER MODEL

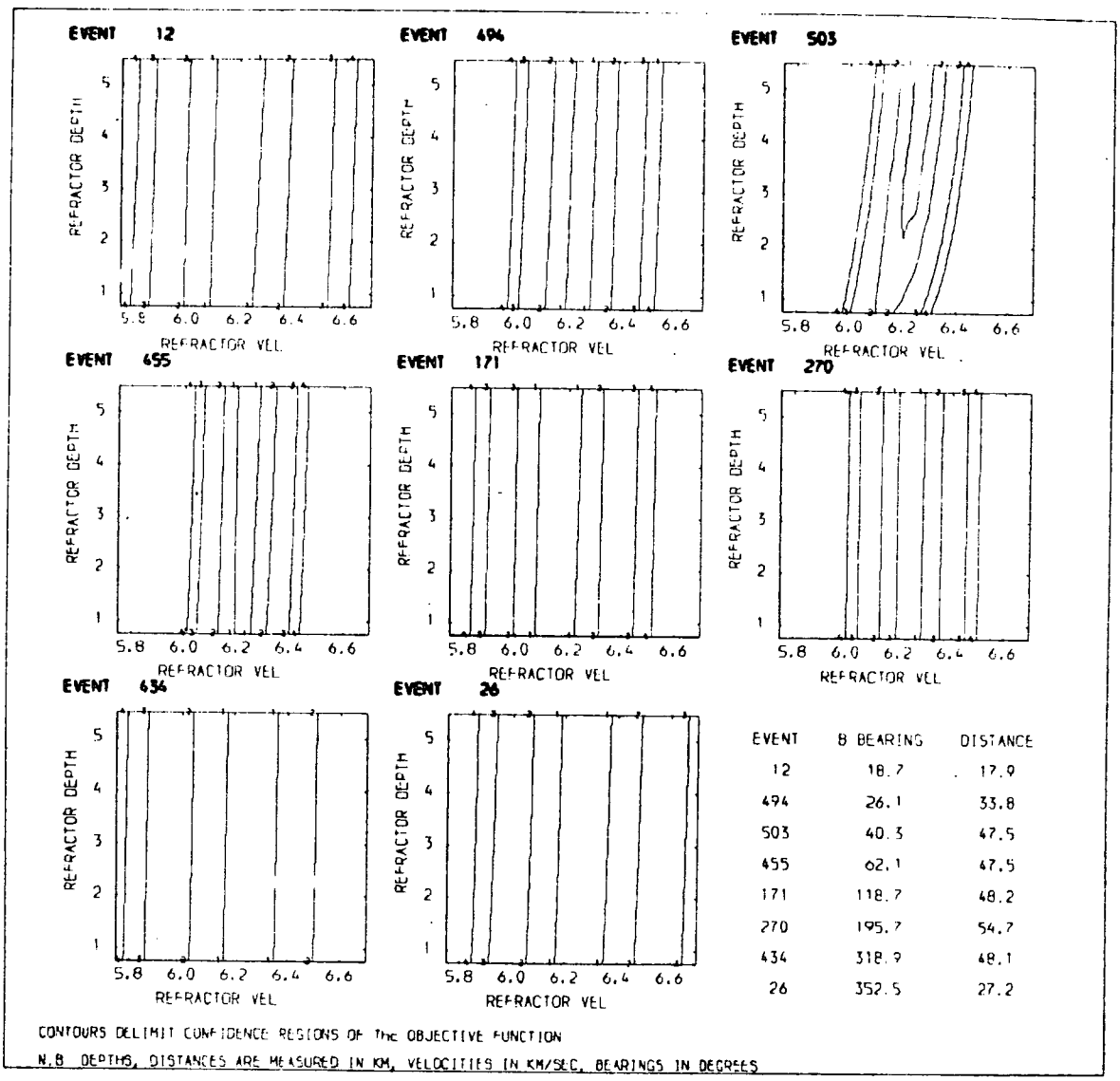

EVENT	B BEARING	DISTANCE
12	18.7	17.9
494	26.1	33.8
503	40.3	47.5
455	62.1	47.5
171	118.7	48.2
270	195.7	54.7
434	318.9	48.1
26	352.5	27.2

CONTOURS DELIMIT CONFIDENCE REGIONS OF THE OBJECTIVE FUNCTION

N.B DEPTHS, DISTANCES ARE MEASURED IN KM, VELOCITIES IN KM/SEC, BEARINGS IN DEGREES

network. More distant earthquakes (503,455,270) show the superimposed effect of elongation of the ellipses in the direction of the network centroid, the consequence of their location well outside the network. The closer the epicentre to the network centroid, the better the station distribution and the more accurate the location, as demonstrated by the relative sizes of the confidence ellipses.

F was found to be a sensitive function of refractor velocity but insensitive to the other structural parameters (e.g. refractor depth, Figure 4.7.3). The method thus gives little structural information. F was also insensitive to focal depth. This provides a justification for the focal depth constraint applied when using HYPCTR, and for fixing the value of the upper layer velocity gradient (Section 4.5).

To examine further the focal depth sensitivity, one additional set of solutions was obtained by running HYPCTR with the focal depths unrestrained, but fixing the upper crustal layer parameters and two of the event epicentres (in order that the solution be overdetermined). F remained insensitive to focal depth, and only for one event (171) did the optimized depth differ from the previously fixed depth by more than 1 km. This set of solutions may be unreliable, however, because of the minimal redundancy in the data: 31 equations in 30 unknowns.

It should be noted that it is convenient but not necessarily accurate to vary pairs of parameters in isolation, neglecting their dependence on other variables.

More rigorous analysis requires knowledge of the covariance matrix, $\underline{B}$, from whose off-diagonal elements the correlation coefficient between the ith and jth parameters is obtained as

$$c_{ij} = b_{ij}(b_{ii}b_{jj})^{-1/2}$$

where the square roots of the variances b_{ii} and b_{jj} are included as normalising factors. Where confidence boundaries for $F(u_1, u_2,\ldots,u_i,\ldots,u_n)$ are calculated from the expression for the variance, written

$$V(F) = \sum_{i=1}^{n} (\partial F/\partial u_i)^2 V(u_i) + 2\sum_{i>j}^{n}\sum_{j=1}^{n} (\partial F/\partial u_i)(\partial F/\partial u_j)c(u_i,u_j)$$

(plus higher order terms which will be insignificant in the neighbourhood of the computed epicentre), the assumption of independent variables is equivalent to combining the variances, $V(u_i)$, while ignoring the covariances, $c(u_i,u_j)$.

Applying SHUEY's (1974) statistical formulation, the 95% confidence level is calculated as $F_{\emptyset.95} = 39.8\ F_{MIN}$ from the equation

$$F_{\emptyset.95} = F_{MIN}[1 + (n/(N - n))f_{n,N-n}(\emptyset.95)] \qquad (4.7.1)$$

where n is the number of variable parameters, N the number of arrival time observations and $f_{n,N-n}(\emptyset.95)$ the appropriate fractile of the F-distribution at the 95% confidence level. By contrast, in Figures 4.7.2 and 4.7.3,

$F = 1.1F_{MIN}$ at contour 1

$F = 2.\emptyset F_{MIN}$ at contour 2

$F = 2.7F_{MIN}$ at contour 3

$F = 3.\emptyset F_{MIN}$ at contour 4

EVERNDEN (1969) has discussed the unreasonably large confidence areas given by SHUEY's method. He shows that, if

the variance of the arrival times can be assumed known (σ^2) from previous data, the extremely conservative statistic f_n can be replaced by the χ_n^2 statistic, with a pronounced reduction in the predicted area of the confidence ellipses (by the factor $(\sigma^2/S2)(\chi_n^2/2f_n)$). The drawback of Evernden's analysis is that satisfactory a priori estimation of variance, σ^2, may not be feasible.

Although contour diagrams such as Figures 4.7.2 and 4.7.3 have proved valuable in defining the shapes of the confidence regions they are uninformative as to their size, since the statistical analysis depends heavily on the quantity of data used. Alternative statistical methods (e.g. JACKSON,1976) have the same limitation. In view of the paucity of stations and earthquakes in the present study, it is better to estimate the size of the confidence ellipses more directly, as below.

4.7.2 Confidence Estimates from Perturbation Experiments

The effect of errors was also examined by perturbation experiments. Arrival times and structural parameters for 9 representative ESP earthquakes were perturbed by their likely errors, as detailed in Table 4.7.1. Station mislocations were also considered. The distribution of epicentres computed from the perturbed parameters is shown in Figure 4.7.4a for a representative event (434). The ellipse defined by the travel time errors is very similar in orientation and eccentricity to the fiducial confidence ellipse for the same event shown in Figure 4.7.2.

TABLE 4.7.1

PARAMETER PERTURBATIONS USED TO DERIVE FIGURES 4.7.4 AND 4.7.5

Event Number	-Arrival Times- at all Stations P wave (sec)	S wave (sec)	P/S Wave Velocity Ratio	P Velocity of Layer 2 (km/sec)	P Velocity of Layer 3 (km/sec)	Depth to Layer 3 (km)
12	0.03	0.2	0.02	0.2	---	---
164	0.2	0.2	0.03	0.2	0.3	3.0
171	0.05	0.2	0.02	0.2	---	---
2701	0.05	0.2	0.02	0.2	---	---
425	0.2	0.2	0.03	0.2	0.3	3.0
4332	0.2	0.5	0.03	0.2	0.3	3.0
434	0.03	0.2	0.02	0.2	---	---
455	0.03	0.2	0.02	0.2	---	---
503	0.03	0.2	0.02	0.2	---	---

Structural parameters are varied from those of Figure 4.3.6c. In addition, station location errors of 500 m north, south, east and west were considered for Mille, Serdo and Det Bahri stations.

[1]Not recorded at Det Bahri.
[2]Not recorded at Serdo.

FIGURE 4.7.4

A. EPICENTRAL DISTRIBUTIONS OBTAINED FOR EVENT 434 BY VARYING THE PARAMETERS LISTED IN TABLE 4.7.1

B,C. RESULTS FROM SUB-SETS OF ARRIVAL TIME DATA

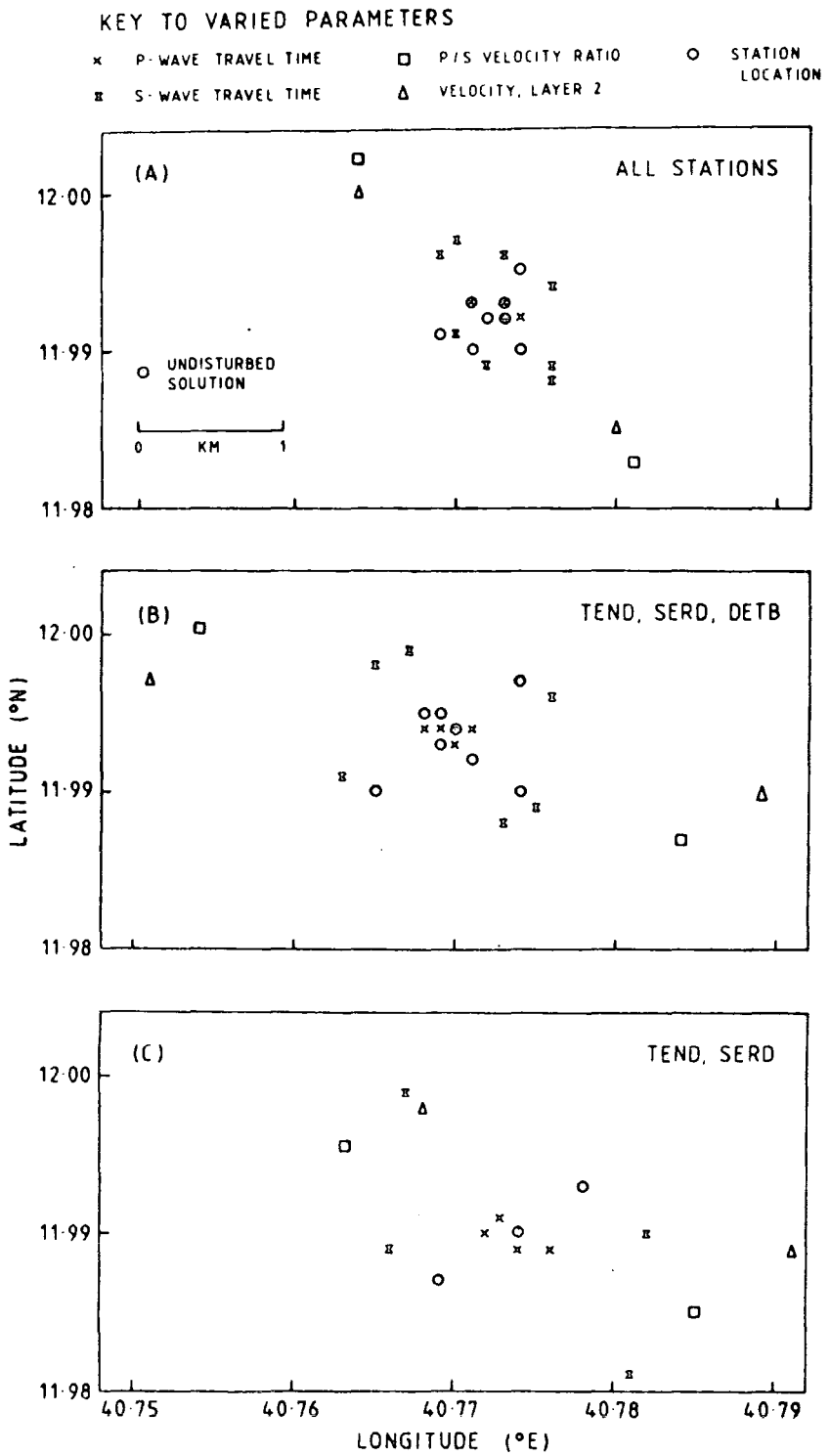

Figures 4.7.4b,c show the equivalent epicentral distribution for two sample sub-sets of the recording stations. Figure 4.7.4 confirms the intuitive expectations that

(1) for a given set of arrival time errors, events recorded at fewer stations are subject to larger epicentral uncertainties. Where only two recording stations can be used it is also possible that abnormally large arrival time errors may go undetected, causing large errors in the computed epicentres.

(2) the magnitude of the errors caused by inaccuracies in the V(z) model is little dependent on the number of recording stations.

(3) the unperturbed epicentral estimate for event 434 is little dependent on the station sub-set used to determine it.

The dispersion of the epicentres calculated from sub-sets of the total arrival data has itself been used as an estimate of location uncertainty (FLINN,1965a). The different epicentres are of course not independent, since they are influenced by arrival times that are common to more than one sub-set.

Sets of perturbed epicentres for two more distant earthquakes are shown in Figure 4.7.5. Note the increased perturbation of the epicentres due to structural parameter variations. The increase in the area of the arrival time error ellipses is caused by the assumption of larger P phase arrival time errors (Table 4.7.1).

FIGURE 4.7.5

EPICENTRAL DISTRIBUTIONS OBTAINED FOR EVENTS 164, 425 BY VARYING THE PARAMETERS LISTED IN TABLE 4.7.1

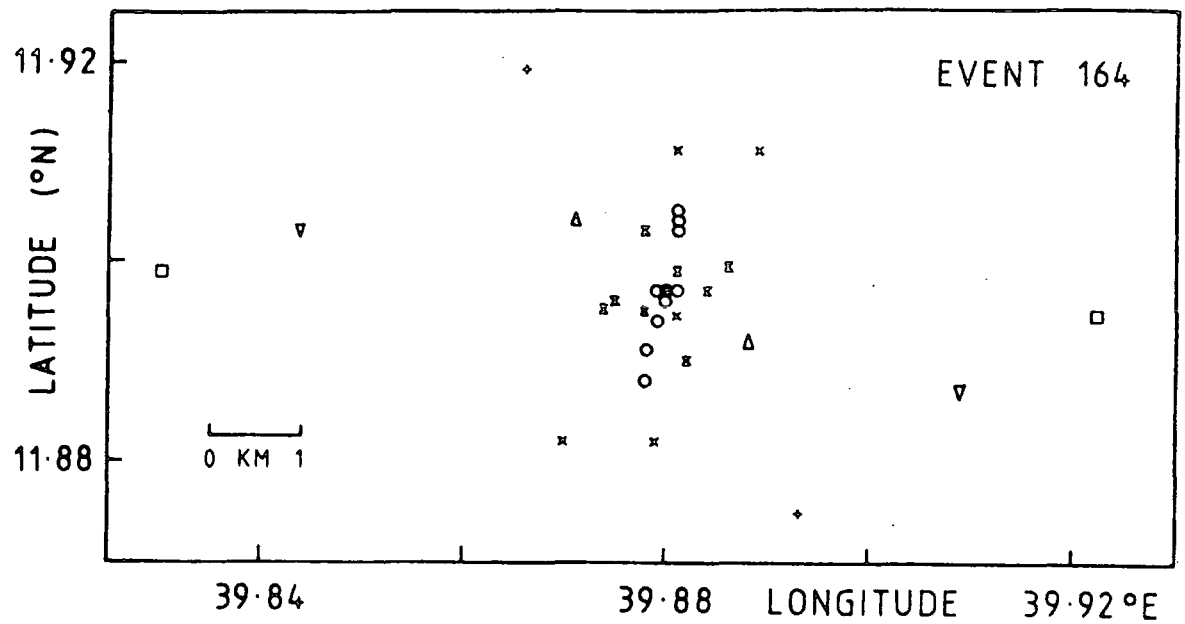

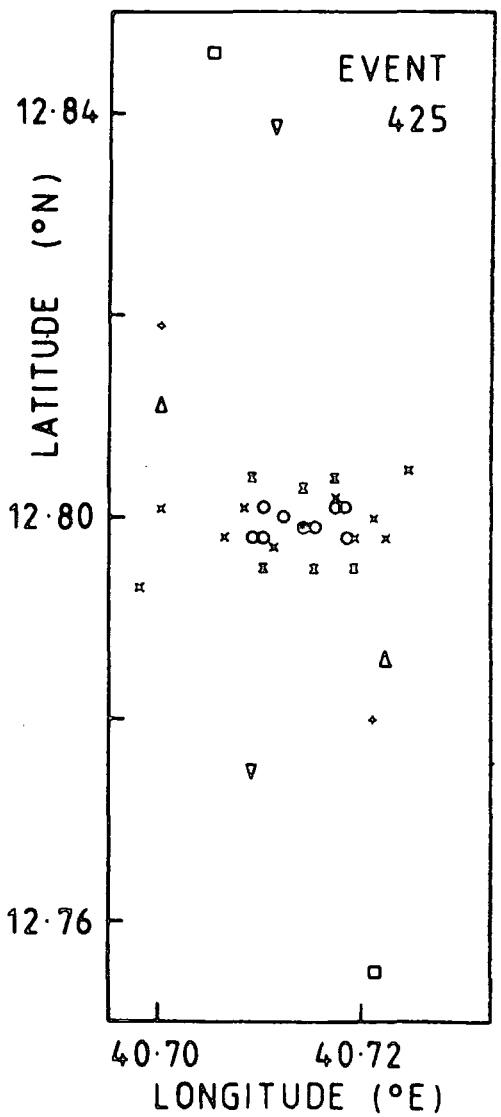

KEY TO VARIED PARAMETERS

- × P-WAVE TRAVEL TIME
- ⧖ S-WAVE TRAVEL TIME
- o STATION LOCATION
- □ P/S WAVE VELOCITY RATIO
- Δ CRUSTAL VELOCITY, LAYER 2
- ▽ CRUSTAL VELOCITY, LAYER 3
- ◈ DEPTH TO CRUSTAL LAYER 3
- ⊕ UNDISTURBED SOLUTION

EVENT	AZIMUTH	DISTANCE
164	283°	142 km
425	340°	150 km

Figure 4.7.6 shows freehand ellipses drawn around the epicentres determined from perturbation experiments on the 9 earthquakes of Table 4.7.1. Note their exaggerated scale. Spotted ellipses circumscribe epicentres perturbed by P and S arrival time errors and recording station mislocations (the former are usually much larger than the latter). Open ellipses surround epicentral perturbations due to errors in structural parameters. They degenerate into lines for the closer earthquakes, where only the two uppermost structural layers are involved.

The spotted areas are not equivalent to the confidence ellipses of Figure 4.7.2, since they depend directly on the magnitude of the errors given in Table 4.7.1. However, their orientation is in all cases very similar, emphasizing that the distribution of recording stations is the dominant factor governing their shape, whatever method is used to obtain them. The spotted ellipse for event 270 should pass through the two crosses, which have been plotted explicitly to show the anomalously large effect of altering the S phase arrival time at Tendaho. This arises because only at Tendaho does the S arrival carry significant weight in the solution (and in particular, S cannot be picked at Mille since the record is saturated by the first arrival).

Structural errors cannot operate on individual earthquakes in isolation. They may be considered as distance scaling factors operating on the full set of computed epicentres, with little azimuthal effect. They are usually substantially greater than the errors due to other

FIGURE 4.7.6

EPICENTRAL ERROR ESTIMATES FOR REPRESENTATIVE EARTHQUAKES

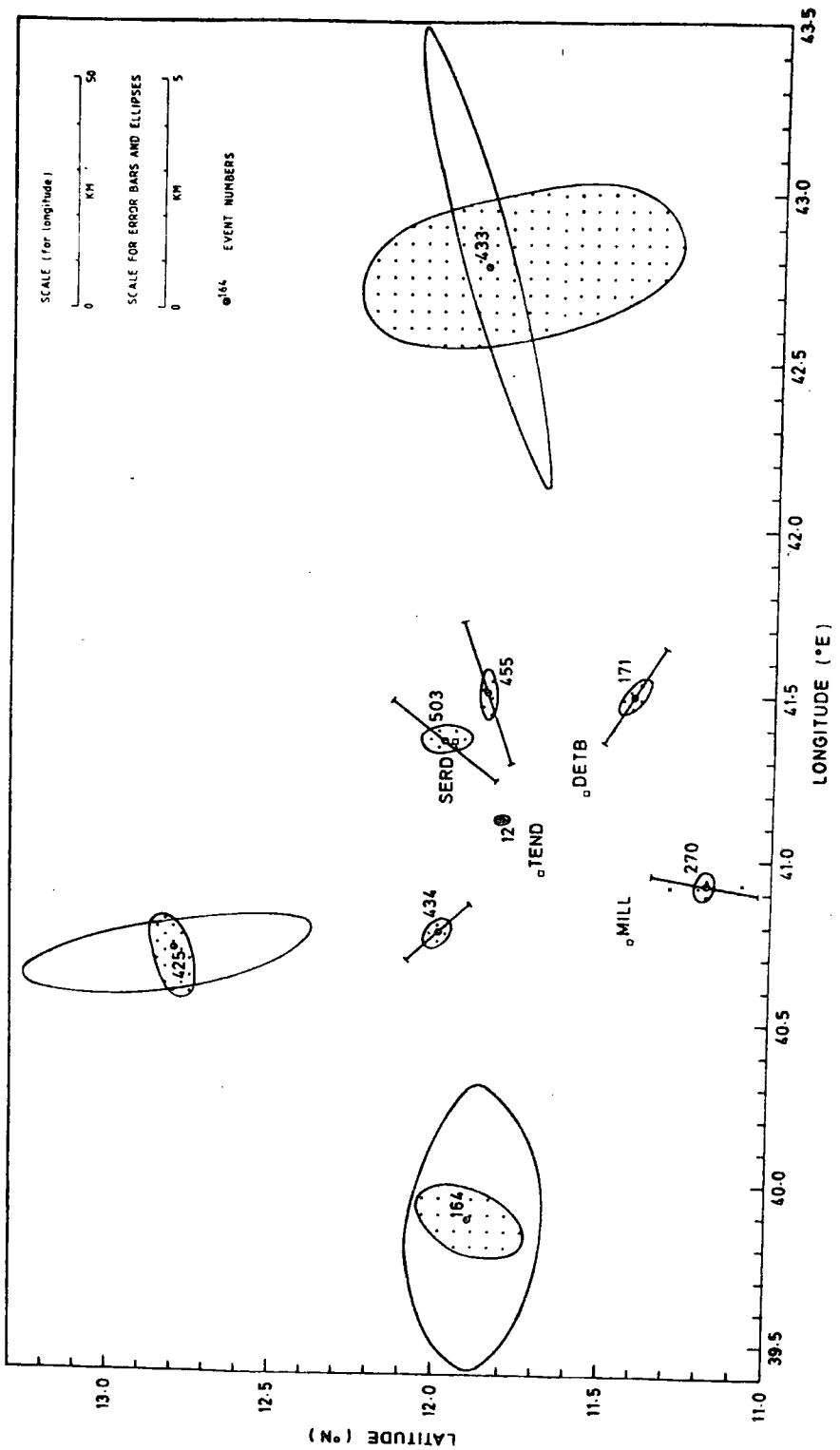

causes. The tectonic structure of the seismic area, if sufficiently well known, may be used as an additional structural determinant, structural parameters being selected to give maximum correlation of the computed epicentres with known fault patterns (see Chapter 8).

For most ESP earthquakes the distribution of recording stations is poor. The importance of an adequate station network is demonstrated by the best placed well-located event (number 12, Figure 4.7.6), for which the spotted ellipse has a major semi-axis of less than 300 m*. The structural error bar falls entirely within the spotted ellipse, and has been omitted for clarity. LANGENKAMP and COMBS (1974) have given a fuller demonstration that for events within or on the margin of a seismic recording network the epicentres are not critically dependent on the structural parameters chosen for a laterally homogeneous model.

On the basis of the data presented in Figure 4.7.6, the estimated probable error in the location of earthquakes from 85 km or less (whose first arrivals will have travelled only in the upper two layers of model C, Figure 4.3.6c), well recorded at 4 stations, is approximately ± 2.5 in distance and $\pm 1.5^{o}$ in azimuth. For more distant earthquakes the corresponding figures are $\pm 4\%$ in distance and $\pm 2.5^{o}$ in azimuth. For earthquakes recorded at fewer

---

*Its shape is determined by the effect of station mislocation errors. The smaller ellipse due to arrival time errors alone has the NW-SE orientation found in Figure 4.7.2.

stations the azimuthal error may be doubled.

The epicentral distributions of Figures 4.7.4 to 4.7.6 were computed with focal depths constrained to 3 km. Focal depths of shallow earthquakes are difficult to determine even for earthquakes within the station network, unless they have occurred very close to a particular station.

JAMES et al (1969) have shown that the theoretical sensitivity of arrival times to changes in focal depth is greatest when the station is vertically above the source, and drops rapidly to zero at a small distance, which for shallow earthquakes may be less than the network spacing. The sensitivity of focal depth to V(z) model changes has been demonstrated by LANGENKAMP and COMBS (1974). Both these previous results are confirmed by the findings of Section 4.4 (e.g. Figure 4.4.3).

All earthquakes located within Afar have upper crustal foci. For the majority of events, more exact focal depths cannot be assigned. Where exact figures are given, they may be in error by several kilometres.

4.8 Earthquake Locations: a Summary

Epicentres of 250 earthquakes (listed in Appendix 6) have been estimated using programme LEADL. A number of scientific results, obtained in the process of developing the earthquake location procedures, have already been summarised in Section 4.3.5. Subsequent sections have yielded additional interesting results:

(8) Earthquakes from Waldia, on the Western Ethiopian escarpment, also have upper crustal foci. Greater focal depths (24 to 26 km) are indicated only for one group of earthquakes farther south along the escarpment. ESP focal depth information is summarised in Figure 4.8.1.

(9) V_P/V_S has the approximate value 1.76 for the two upper layers of the preferred structural model, rising to 1.90 at greater depths, where the velocity structure is less certain. There is no evidence for azimuthal variations of these figures.

(10) For earthquakes within about 60 km of the network centroid, recorded at 3 or more stations, the epicentral estimates are insensitive to details of the V(z) model. The only exception is the second layer velocity, well established as 6.2 ± 0.1 km s^{-1}. For earthquakes outside the ESP network, the largest surce of error in the epicentral estimates is the uncertainty in the structural model. The effects of possible errors in the recording station co-ordinates are shown to be unimportant.

(11) Fiducial confidence and perturbation ellipses, computed to show the effects of random errors, have their orientation and eccentricity controlled by the network's geometry, and emphasise its relatively poor resolution along the NW-SE axis.

The significance of the earthquake locations is discussed in Chapter 8, where epicentral maps are given.

FIGURE 4.8.1

HISTOGRAM OF EARTHQUAKE FOCAL DEPTHS

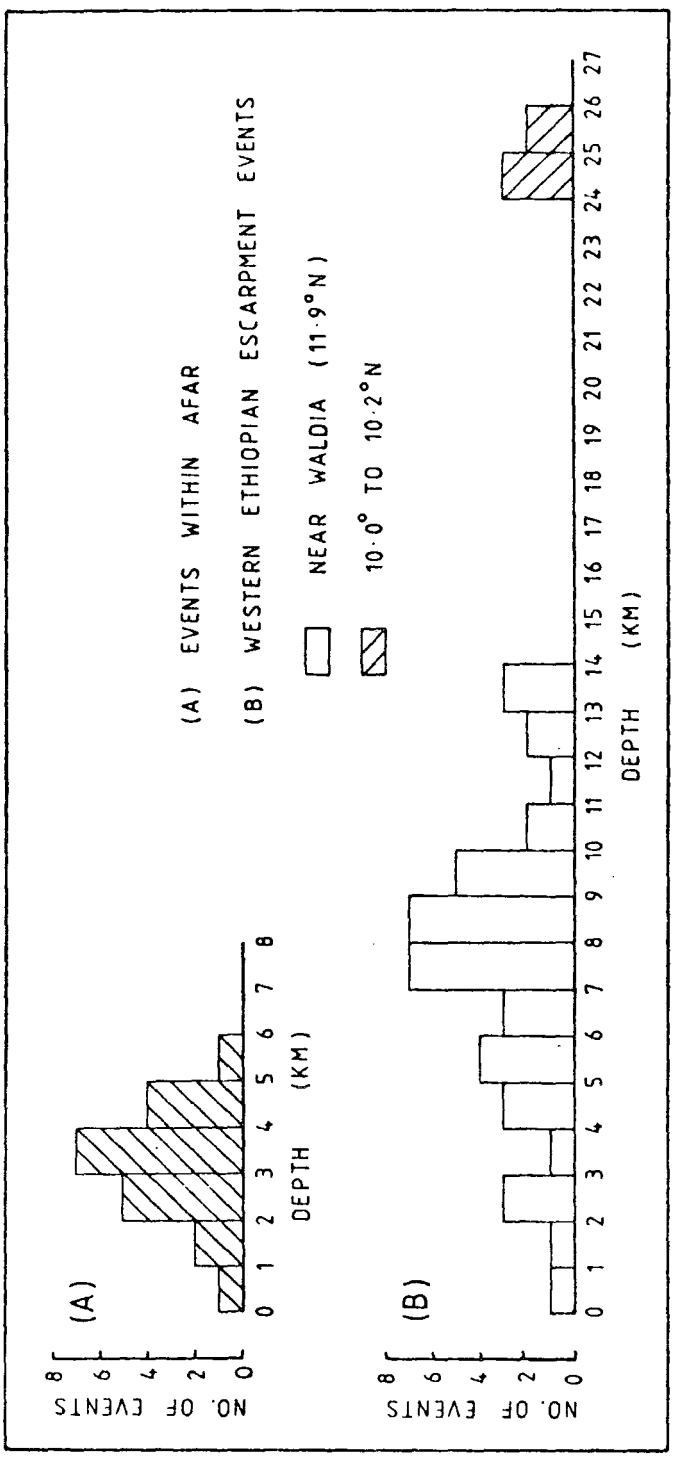

CHAPTER 5

MAGNITUDES

5.1 Introduction

The object of this chapter is to derive a local magnitude scale for Afar. The requirement is not merely a rating of ESP earthquakes according to their size or strength, but a basis for comparing them with other earthquakes recorded in Afar and elsewhere. Two quantities are used to obtain estimates of ESP earthquake magnitudes: the maximum seismogram trace amplitude, and the duration of the seismic signal.

In the frequency domain the received seismic body wave spectrum at a seismometer may be factorised as

$$X(w,r,\theta) = S(w)\ B(r,\theta)\ C_S(w)\ P(w,r)\ G(r)\ C_R(w,r)\ I(w) \qquad (5.1.1)$$

where

$X(w,r,\theta)$ = received spectrum at hypocentral distance r

$S(w)$ = source spectrum, corresponding to the far field source time function

$B(r,\theta)$ = source radiation function, with θ as azimuth

$C_S(w)$ = source crust effect on spectrum

$P(w,r)$ = path effect on spectrum

$G(r)$ = geometrical spreading

$C_R(w,r)$ = receiver crust effect on spectrum

$I(w)$ = instrumental response

Here and throughout this chapter a laterally homogeneous earth is assumed (as these factors are also functions of

position). Equation 5.1.1 is considered further in Chapter 7. Its complexity warns that earthquake magnitude, as defined by any single quantity, will be only a crude indicator of earthquake size. As RICHTER (1935) stated when first introducing the concept of earthquake magnitude:

"Precision...was neither expected nor required. What was looked for was a method of segregating large, moderate and small shocks [in a particular area], which should be based directly on instrumental indications."

Richter defined local magnitude, M_L, for Southern Californian earthquakes, by the relation

$$M_L = \log_{10}A(d) - \log_{10}A_0(d) \qquad (5.1.2)$$

where A was the maximum trace amplitude on a Wood-Anderson seismogram of an earthquake at epicentral distance d, and $A_0(d)$ was an empirical normalisation function. The zero magnitude was arbitrarily defined as that for which the maximum trace amplitude at 100 km was 1 μm.

Equation 5.1.2 is used in the present study, and is still widely used in seismological observatories throughout the world (ADAMS,1977). The normalisation function, $A_0(d)$, must be adapted for use with different instruments, different phases and different parts of the world. The difficulties involved are discussed in the next section.

A series of papers by GUTENBERG (e.g.1945a,b; also GUTENBERG and RICHTER,1956) have related the amplitude of the ground vibration to its predominant period, T, leading to formulae of the form

$$m_b = \log_{10}(A/T) + Q(d,h) \qquad (5.1.3)$$

where Q is the normalisation function, which depends also on the focal depth of the earthquake, h. m_b is the body wave magnitude, often measured for ground motion at a particular period. Any specified body wave phase may be used. Many regional empirical formulae in use currently are of the form

$$m_b = \log_{10}(A/T) + c \log_{10} d + b \qquad (5.1.4)$$

$$\text{or } M_S = \log_{10}(A/T) + C \log_{10} d + B \qquad (5.1.5)$$

Equation 5.1.5 is the corresponding formula for surface waves, of which the most widely used version is the 'Moscow-Prague' or 'IASPEI' formula (KARNIK et al,1962). NUTTLI (1972) has pointed out that the 'constants' b, c, B, C, should theoretically be written as functions $b(m_b,T)$, $c(d,T)$, $B(M_S,T)$, $C(d,T)$.

More recently, a short-range body wave magnitude (m_b^*), based on maximum P coda ground velocity, A_V, has been defined by the formula

$$m_b^* = \log_{10} A_V + 2.3 \log_{10} \Delta - 2 \qquad (5.1.6)$$

(NAVARRO and BROCKMAN,1970), where Δ = hypocentral distance. At the end of this chapter the ESP data are fitted to a local magnitude formula of this form.

In this study the parameter A has been preferred to (A/T), and M_L to m_b, because of the difficulty of isolating any particular period or phase on a local earthquake record. Whichever parameter is used, the major difficulty is the assignation of an appropriate regional normalisation function. Use of signal duration (D) as the parameter for earthquake magnitude determination (Section 5.2), eases this problem. Since the magnitude against $\log_{10} D$

relationship is closely linear its constant and gradient can be determined from a few events whose magnitudes are independently available.

26 events recorded by ESP were also received by the WWSSN station at Addis Abeba (AAE), which determined their magnitudes and normalised them to m_b as teleseismically determined by USGS (Gouin, pers. comm). These events enable ESP m_b values to be tied into the world-wide m_b scale (Section 5.2).

ESP M_L values cannot be related to m_b in this way, since 21 of the 26 events saturated the Durham recorders. Consequently, Section 5.3 presents an ESP M_L scale, based directly on the calculated gain of the Durham instruments, which assumes that Richter's $A_o(d)$ curve is applicable to Afar. Globally-linked M_D and independently-derived M_L are then compared in order to obtain the explicit regional normalisation function for Afar, $A_o(d,Afar)$. Finally, the differences between $A_o(d,S.Calif)$ (i.e. Richter's curve) and $A_o(d,Afar)$ are discussed.

5.2 Earthquake Magnitudes from Signal Duration

The use of signal duration for earthquake magnitude estimation was proposed by BISZTRICSANY (1958), who measured the duration of the surface-wave train of teleseisms recorded in Eastern Europe. Only during the past ten years has the method been widely applied to local earthquakes. Not only may it be applied to saturated records, but it is simpler to apply than the trace amplitude method; the signal

duration is often the only quantity that need be measured to obtain the magnitude estimate. It is now customary to use the total duration, D, of the seismic record measured from the initial P onset to the point at which the signal level falls below a given threshold value, or alternatively to the point at which it returns to the background noise level.

Empirical formulae relating M_L and D have the form

$$M_L = a_0 + a_1 \log_{10} D + a_2 d \qquad (5.2.1a)$$

where a_0, a_1, a_2 are constants; or simply

$$M_L = a_0 + a_1 \log_{10} D \qquad (5.2.1b)$$

since a_2 is small, and has always been found to be negligible for epicentral distances $d < 200$ km. Equation 5.2.1a might be expected to contain an additional term expressing focal depth dependence. However, for the small and shallow earthquakes to which the signal duration method is normally applied, focal depth is much less accurately determined than epicentral distance and no conclusive dependence of duration on focal depth has yet been established.

Equation 5.2.1b has been obtained theoretically by HERRMANN (1975), subject to the restrictive assumptions that the events considered have "the same source location and focal parameters with respect to the recording station"; and that their codas are monochromatically filtered and have an envelope represented by a simple power law in time. In practice, several studies have observed that the gradient, a_1, of the M_L versus $\log_{10} D$ curve increases with increasing amplitude. To account for this, some authors

(HERRMANN,1975; BAKUN and LINDH,1977) have quoted two equations of the form of Equation 5.2.1a or 5.2.1b, with different coefficients for different magnitude ranges; while others (e.g. REAL and TENG,1973) have fitted equations of the form

$$M_L = b_\emptyset + b_1 \log_{10}\emptyset D + b_2 (\log_{10}\emptyset D)^2 + b_3 d \qquad (5.2.2)$$

In all cases where Equation 5.2.2 has been fitted, b_1 has been found to be negligible. REAL and TENG (1973) attributed the curvature of the M_L versus $\log_{10}\emptyset D$ relationship to an intrinsic feature of the M_L scale. However, similar curvature is observed when $\log_{10}\emptyset D$ is plotted against m_b or $\log_{10}M\emptyset$ ($M\emptyset$ is the seismic moment). HERRMANN (1975) has derived a theoretical relationship between $\log_{10}\emptyset D$ and $\log_{10}M\emptyset$, showing that the curvature results from the effect of decreasing corner frequency with increasing event size, causing a corresponding decrease in the amplitude of the coda and hence a relatively smaller duration. The very rapid fall-off of $\log_{10}\emptyset D$ with M_L found by BAKUN and LINDH (1977) for $M_L < 1$ can probably be explained by these small events having corner frequencies above the pass band of the instruments.

The spectral content of the recorded ground motion will depend not only on the instrumental response but also on the earth filtering quality factor, Q, which characterises the effects of wave attenuation and scattering. SUTEAU and WHITCOMB (1979) have quantified these dependences in deriving a theoretical magnitude relationship of the form

$$M_L = a_\emptyset + a_1 \log_{10}\emptyset D' + a_2 D'^{1/3} + f(D') \qquad (5.2.3)$$

where the constants a_0, a_1, a_2 depend on the effective Q and on geometric spreading, and f(D') is a function of the instrumental response and, weakly, of the scattering process. Both Herrmann and Suteau and Whitcomb follow AKI's (1969) theory that the later portions of the coda are composed of backscattering surface waves, originating at large distances from the source and the receiver and due to lateral crustal inhomogeneity. Both theoretical relationships show good agreement with observational data. It should be noted that D' in Equation 5.2.3 is the total signal duration measured from the origin time, which is not necessarily known.

Figure 5.2.1 shows the plot of $\log_{10}D$ against M_L(AAE) obtained in this study using 25 of the 26 ESP events whose magnitudes were also determined at AAE*. M_L(AAE) was obtained by staff of the Geophysical Observatory, Addis Abeba, from Equation 5.1.2, through measurement of S_g or L_g (Gouin, pers. comm). Adopted values of M_L(AAE) are the mean of the magnitudes obtained from the N-S and E-W seismometers, as copied by the author from preliminary determinations on file at the Observatory. Their accuracy is approximately $\pm$ 0.3 magnitude units.

D^* is the duration, in seconds, of ESP seismic records, measured from the P onset until the time at which the signal amplitude returns to the background seismic noise level.

---

*The remaining event occurred as part of an aftershock sequence, so that its duration could not be satisfactorily measured. This is the most notable disadvantage of the signal duration method.

FIGURE 5.2.1

PLOT OF MAGNITUDE AGAINST SIGNAL DURATION FOR EARTHQUAKES RECORDED BOTH AT ESP STATIONS AND AT AAE

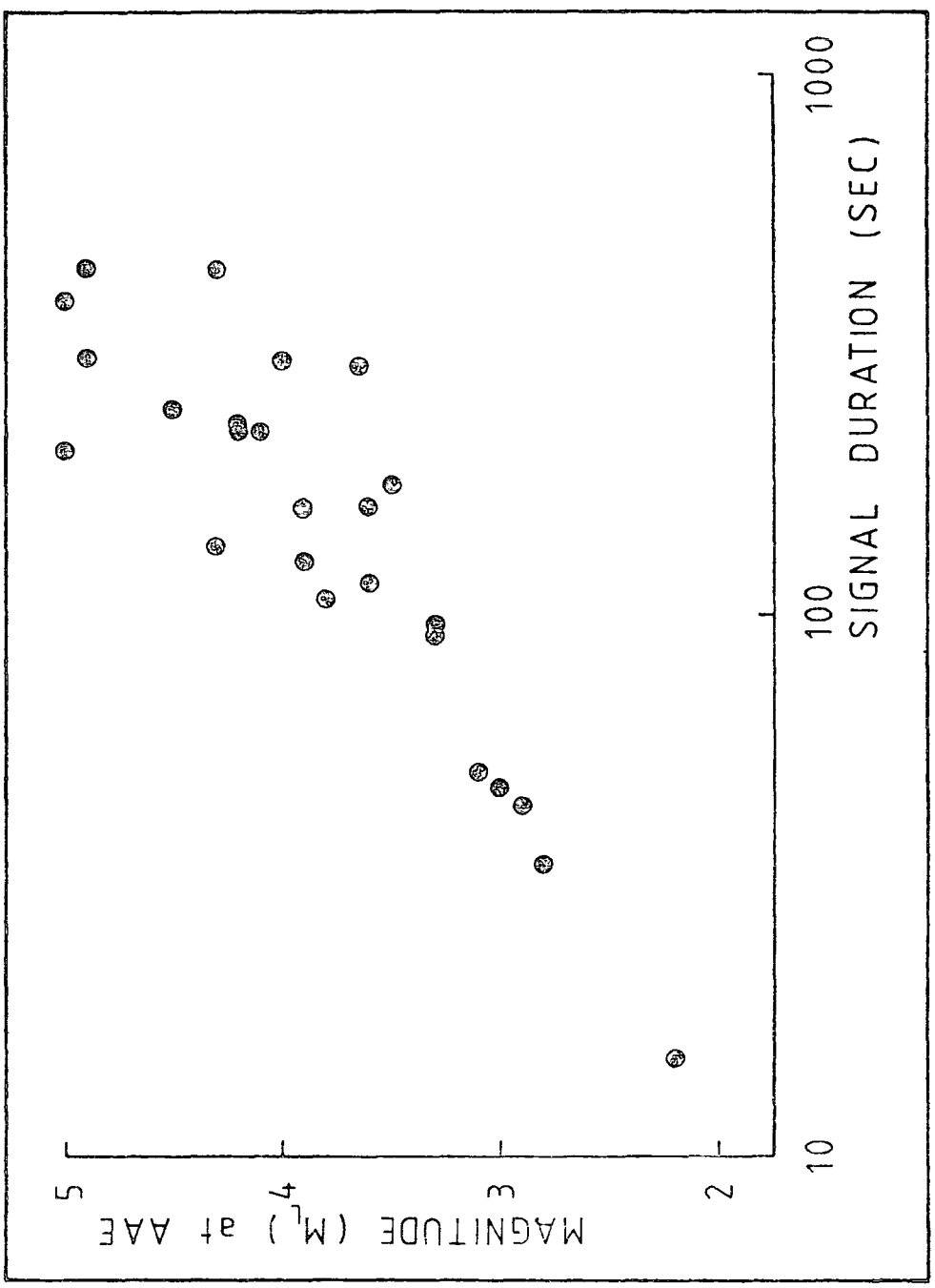

This method of defining the end of the coda has an advantage over the alternative criterion of taking the time at which the signal level falls below a given threshold value (LEE et al,1972; BAKUN and LINDH,1977), in that it is independent of the recording device and its gain on playback. The disadvantage is that measured durations will be anomalously short if the background noise level is high. HERRMANN (1975) has shown that measurements made with signal cut-offs at different amplitudes differ only in the constant term a_0 in Equation 5.2.1. a_0 increases for higher cut-off amplitudes.

Differences in signal duration, D^*, between stations may be expected because of uncertainties in measuring D^*, varying local geology and varying background noise levels. The latter two factors will cause systematic differences in D^*, which may be expressed as station corrections. In this study (using Equation 5.2.1b) a station correction ratio, S_I, referred to Tendaho station, was defined by the relationship

$$S_I = (1/n) \sum_{i=1}^{n} ((D^*_I)_i / (D^*_{Tend})_i)$$

where $(D^*_{Tend})_i$, $(D^*_I)_i$ are the signal durations at Tendaho and at station I respectively of the i^{th} of n well-recorded events. The results were

$$S_{Mill} = 1.06 \pm 0.17 \quad (n = 32)$$

$$S_{Serd} = 1.34 \pm 0.26 \quad (n = 29)$$

$$S_{Detb} = 1.22 \pm 0.21 \quad (n = 23)$$

$$(S_{Tend} = 1.00)$$

where the standard errors indicate the uncertainties in

measuring D^*, which are largely caused by the difficulty in determining the signal cut-off point. The S_I are almost negligible. They are all greater than 1.0, supporting the observation that Tendaho is generally the noisiest station.

The duration used for determining the magnitude of each event was the simple mean of the corrected durations

$$D_I = D^*_I / S_I$$

Any duration D_I which was shorter by 35% or more than the mean of the corrected durations at the other stations recording the event was attributed to high noise level, and was discarded. For all such occurrences the abnormal noise was clearly visible on the seismic records. All durations were measured on the vertical seismometer traces.

The data plotted in Figure 5.2.1 were fitted to linear and quadratic $\log_{10}D$ dependencies by least squares regression. For event 134, the difference between observed and calculated values of M_L(AAE) exceeded 2. This event was removed from the data set. The re-evaluated results, based on 24 events, were

$$M_L(AAE) = (0.10 \pm 0.35) + (1.73 \pm 0.16)\log_{10}D \qquad (5.2.4)$$

with correlation coefficient, $r = 0.92$, standard deviation, $\sigma = 0.29$,

and $$M_L(AAE) = (1.77 \pm 0.20) + (0.43 \pm 0.04)(\log_{10}D)^2 \qquad (5.2.5)$$

with $r = 0.91$, $\sigma = 0.29$.

These equations cover the magnitude range $2.2 \leqslant M_L \leqslant 5.0$.

When the data were sub-divided according to magnitude to fit two lines of the form of Equation 5.2.4 the results were

$M_L(AAE) = (0.80 \pm 0.19) + (1.28 \pm 0.10)\log_{10}D$ (5.2.6)

with $r = 0.97$, $\sigma = 0.10$, $2.2 \leqslant M_L \leqslant 3.6$, 10 events,

and $M_L(AAE) = (1.12 \pm 1.08) + (1.33 \pm 0.46)\log_{10}D$ (5.2.7)

with $r = 0.65$, $\sigma = 0.32$, $3.6 \leqslant M_L \leqslant 5.0$, 14 events,

or $M_L(AAE) = (0.67 \pm 0.29) + (1.39 \pm 0.15)\log_{10}D$ (5.2.8)

with $r = 0.94$, $\sigma = 0.18$, $2.2 \leqslant M_L \leqslant 4.0$, 15 events,

and $M_L(AAE) = (1.64 \pm 1.70) + (1.15 \pm 0.70)\log_{10}D$ (5.2.9)

with $r = 0.50$, $\sigma = 0.34$, $4.0 \leqslant M_L \leqslant 5.0$, 10 events.

Neither pair of equations represents the data as usefully as Equation 5.2.4, which is preferred to Equation 5.2.5 by virtue of its greater simplicity. The lines represented by Equations 5.2.7 and 5.2.9 are unsatisfactory because of the large scatter in the data for the larger events. They have very low correlation coefficients, and lower gradients than the full data set line of Equation 5.2.4. The scatter is probably largely caused by errors in $M_L(AAE)$. The difference in the M_L values obtained from reading the N-S and E-W seismometers at AAE was sometimes considerable (1.4 magnitude units in one case), whereas the variation in $\log_{10}D$ between different stations of the ESP network was 0.15 or less.

Table 5.2.1 compares the magnitude/duration relationships obtained in this study with those previously published. The present results are fully consistent with the earlier work. Detailed comparisons are not valid, because of the variety of instruments and magnitude ranges that have been used. Furthermore, $M_L(AAE)$ is not necessarily equivalent to Richter's M_L. These differences

TABLE 5.2.1

SUMMARY OF EMPIRICAL MAGNITUDE/DURATION RELATIONSHIPS

(A) to fit Equation 5.2.1

REFERENCE	MAGNITUDE RANGE	a_0	a_1	$10^3 a_2$	RMS ERROR	r
TSUMURA (1967)	3.2-5.0	-2.53	2.85	1.4	0.2-0.3	---
CROSSON (1972)	1.8-4.1	-2.46	2.82	---	0.21	---
LEE et al (1972)	0.5-4.0	-0.87	2.00	3.5	0.22	---
REAL and TENG (1973)	2.0-5.1	-1.01	1.89±0.05	0.9±0.2	0.16	---
	2.0-5.1	0.08	1.63±0.04	---	0.14	---
LANGENKAMP and COMBS (1974)	1.1-3.2	-1.9	2.0	---	---	---
HERRMANN (1975) *	3.0-4.4	1.13±0.24	1.22±0.11	0.51±0.66	---	0.91
**	3.0-4.4	0.34±0.36	1.31±0.13	0.74±0.76	---	0.87
*	4.3-5.5	-1.23±1.04	2.19±0.38	0.88±0.36	---	0.92
**	4.3-5.5	-4.22±1.82	2.99±0.60	0.57±0.45	---	0.89
*	2.5-4.5	0.48±0.32	1.27±0.18	1.88±1.50	---	0.92
**	2.5-4.5	-1.68±0.78	1.96±0.37	1.90±1.88	---	0.88
BAKUN and LINDH (1977)	0.5-1.5	0.28±0.01	0.71±0.01	---	0.19	---
	1.5-4+	-3.59±0.37	3.32±0.19	---	0.21	---
	1.5-4+	-3.26±0.29	2.92±0.13	---	0.16	---
	3.0-5.8	0.31±0.24	1.76±0.11	---	0.13	---
This Study	2.2-5.0	0.10±0.35	1.73±0.16	---	0.29	0.92
	2.2-4.0	0.67±0.29	1.39±0.15	---	0.18	0.94
	2.2-3.6	0.80±0.19	1.28±0.10	---	0.10	0.97

(B) to fit Equation 5.2.2

REFERENCE	MAGNITUDE RANGE	b_0	b_2	$10^3 b_3$	RMS ERROR	r
REAL and TENG (1973)	2.0-5.1	1.03	0.43±0.01	0.9±0.2	0.15	---
	2.0-5.1	1.60	0.42±0.01	---	0.14	---
BAKUN and LINDH (1977)	0.5-4+	0.16±0.09	0.70±0.04	---	0.28	---
	0.5-4+	0.20±0.01	0.60±0.002	---	0.22	---
This Study	2.2-5.0	1.77±0.20	0.43±0.04	---	0.29	---

*Amplitude cut-off 5 mm.
**Amplitude cut-off at noise level.
Otherwise, different relationships for the same reference and magnitude range imply different instruments.

mask the regional variations of the coefficient a_1 (of Equation 5.2.1) which should reflect geographical variations in the scattering process (Afar being a structurally complex region, a relatively large number of scatterers would be expected).

For proper comparison with the magnitudes of earthquakes elsewhere, the ESP signal durations must be related to a magnitude scale which has world-wide validity. Workers at AAE have obtained an empirical correction formula between M_L(AAE) and m_b(CGS), based on more than 100 events (Gouin, pers. comm),

$$M_L(AAE) = 0.24 + 1.05m_b(CGS) \qquad (5.2.10)$$

Combining Equations 5.2.4 and 5.2.10,

$$M_D \equiv m_b(CGS) = -0.13 + 1.65\log_{10}D \qquad (5.2.11)$$

Unless otherwise stated, all magnitudes quoted in subsequent chapters are calculated from Equation 5.2.11. Note that the smallest earthquake for which M_L(AAE) is available has m_b = 1.9. Magnitudes of smaller events have been obtained by extrapolation, and should be treated with caution. There is a distance-dependent lower limit to the smallest event which can be classified, since the minimum duration is by definition the P to S time.

5.3 Earthquake Magnitudes from Maximum Trace Amplitude

Before earthquake magnitudes can be determined from Richter's equation (5.1.2) three major problems must be considered. Firstly, the response characteristics of the Willmore Mk II seismometers and Durham playback electronics

used in this study differ from those of the Wood-Anderson seismometer. The Wood-Anderson is no longer considered suitable for studying small earthquakes. It has relatively low sensitivity, and records only horizontal motion.

Secondly, the dynamic range of the Durham seismic recording and playback equipment does not exceed 36 dB (Appendix 3). Thus, for any given epicentral distance (again, neglecting azimuthal effects), earthquake magnitude determinations are restricted to a range of 1.8 magnitude units or less. Smaller earthquakes will not be observed; larger ones will saturate the recording equipment.

Thirdly, Richter's normalisation function was intended for Southern California, and does not necessarily apply to other regions even if Wood-Anderson seismometers are used. It is dependent on the structure, attenuation and elastic properties of the crust and upper mantle, which vary widely from region to region (EVERNDEN,1967; MITCHELL,1973). It is for historical reasons that this study compares a dilation zone with much volcanism (Afar) to a shear zone with little volcanism (Southern California). We expect the result (Section 5.4) that the normalisation function for Afar will differ from Richter's function.

The definition of M_L is more difficult to generalise world-wide than that of m_b or M_S, which are normally measured using particular phases. Local earthquakes cannot usually be resolved into their component phases, and the phases which have greatest amplitude in any given distance range vary with structure.

The problem of instrument response should ideally be overcome by taking the Fourier displacement spectrum of the recorded seismic trace, correcting it for instrumental response, shaping it by the theoretical response of the Wood-Anderson seismometer and transforming the resultant spectrum back to the time domain, where the maximum trace amplitude is read. The present study does not use this approach, which is excessively laborious for large numbers of events where distortions such as clipping are present, and which is not justifiable in terms of the precision expected of magnitude measurements.

The overall gain, G, of the Durham seismic recording and playback equipment is calculated in Appendix 7 as

$$G = 2.74 \times 10^4$$

The natural period of the seismometers was 1.0 s. The system gain was approximately constant over the frequency range 2 to 10 Hz (the frequencies at the half-power (-3dB) points were 0.04 Hz and 15 Hz (Figure A3.1, Table A3.1)). On all the ESP seismic records the phases giving rise to the maximum trace amplitude have frequencies within this range.

As operated by Richter, the Wood-Anderson seismometer has natural period 0.8 s, damping factor 0.8, and a gain of 2800 which is also constant over the frequency range 2 to 10 Hz. Consequently, in this study the factor for conversion from ESP trace amplitude to the equivalent Wood-Anderson trace amplitude has been approximated by the ratio of the system gains. A trace amplitude A on the ESP instruments thus corresponds to

$(2800A/2.74x10^4w) = A/9.96w$ on the Wood-Anderson. The factor w (dominant frequency of the phase giving rise to A) is included because the ESP instruments measure velocity whereas the Wood-Anderson measures displacement. Equation 5.1.2 may now be written

$$M_L = \log_{10}(A/9.96w) - \log_{10}A_0(d)$$

$$= \log_{10}(A/w) - \log_{10}A_0(d) - 1.00 \qquad (5.3.1)$$

(to 2 significant figures), where A is the maximum trace amplitude and $A_0(d)$ the normalisation function.

For events of the same swarm, having approximately the same focal mechanism and recorded at the same set of seismometers, the factors on the right hand side of Equation 5.1.1 might be so equalised that each event would be a scaled version of every other, both in the frequency and the time domain. It might then be possible to alleviate the difficulty of limited dynamic range by measuring, wherever possible, both the maximum trace amplitude, A, of an event and the trace amplitude, A', of any other point on the coda that could be consistently recognised from event to event. Since the ratio A/A' would then be constant, A could be inferred from A' for larger events where A saturated the record. In practice, the only ratio that could be conveniently measured was A_S/A_P, where A_P, A_S are respectively the maximum trace amplitudes of the P and S wave codas. One set of results is shown in Figure 5.3.1. The first motions of the events shown are very similar (Chapter 8). The lack of a linear relationship between A_S and A_P ($r = 0.71$ for the best straight line in the least

FIGURE 5.3.1

MAXIMUM S CODA AMPLITUDE AGAINST MAXIMUM P CODA AMPLITUDE FOR EVENTS FROM NW TENDAHO GRABEN RECORDED AT MILLE

(distance ≈ 60 km, azimuth ≈ 30°)

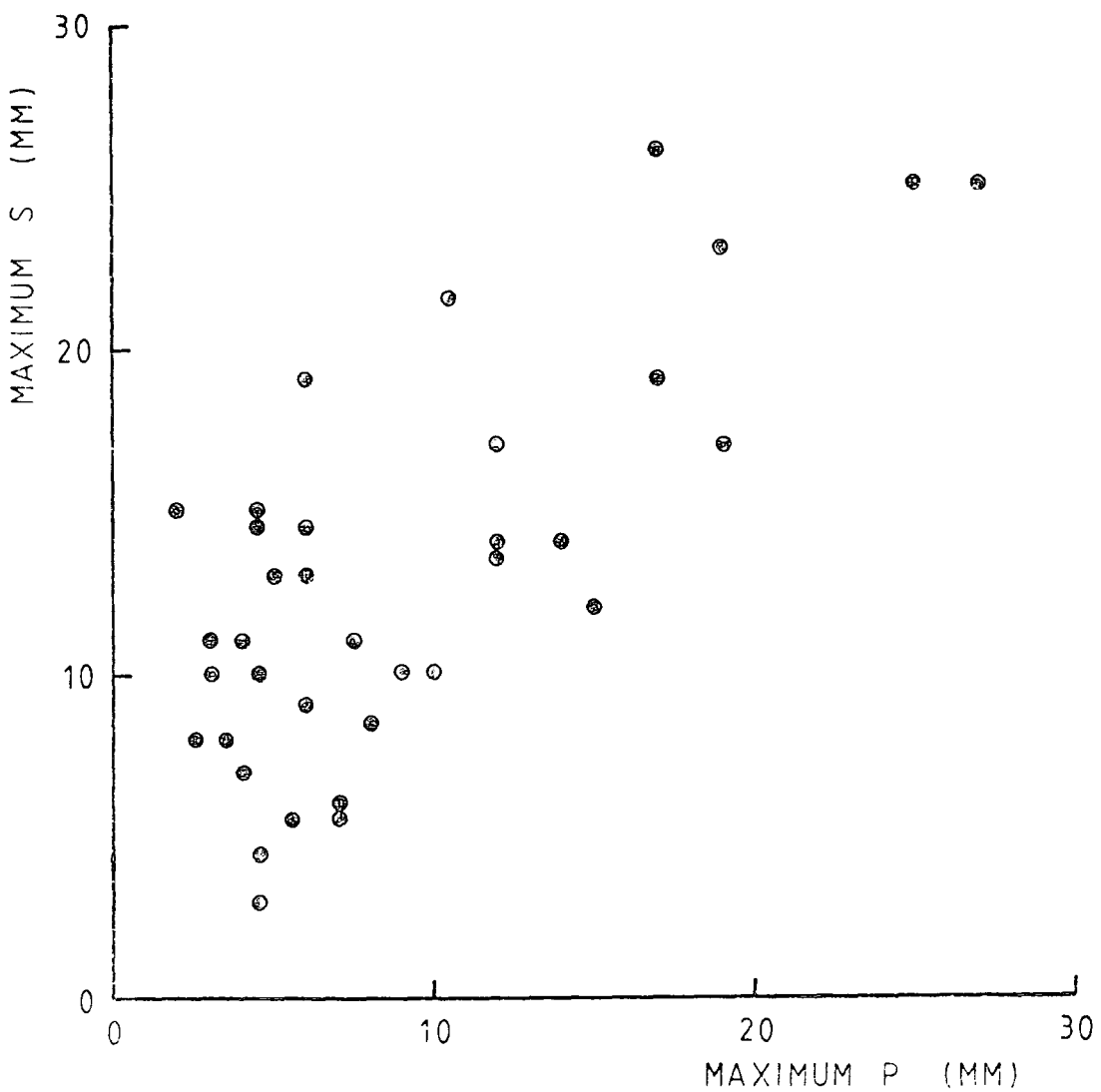

squares sense) shows the effect on coda amplitudes of even small variations in the focal mechanism or propagation path. M_L cannot therefore be reliably determined from saturated records by this method.

We now consider the problem of the normalisation function, $A_\emptyset(d)$. RICHTER (1935) obtained $A_\emptyset(d)$ for Southern California by plotting $\log_{10}A_\emptyset$ against d for a representative group of earthquakes recorded at several stations. Curves were drawn through the several points referring to each shock and were found to be approximately parallel, demonstrating the validity of the method. The curves were combined into the single $A_\emptyset(d)$ curve, parallel to the individual curves and passing through an arbitrarily selected point. EATON et al (1970) and DOUGLAS and RYALL (1972) have assumed the equivalent attenuation relation $A \propto d^{-k}$, where k is a constant attenuation factor. It corresponds to the same distance correction implicit in the definition of magnitude by such equations as 5.1.2, 5.1.4.

The ESP stations are too few for the above method to be used satisfactorily. As a first approximation Richter's $A_\emptyset(d)$ curve was therefore applied directly to the ESP data. Such a crude approach is partially justified by a previous study of East African local seismicity (ARNOLD,1974), which demonstrated that the $A_\emptyset(d)$ curves for events recorded at Nairobi and at the Durham University Kaptagat array had very similar shapes to Richter's curve. This is equivalent to saying that the difference in structure between Southern California and East Africa can be

largely represented by a constant, k', inserted into Equation 5.1.2.

Trace amplitudes were obtained from 267 records at Mille and Tendaho. In each case the maximum trace amplitude was measured from the 5 mm per recorded second 16-channel jet pen oscillograph trace (Section 3.7), and the frequency at the maximum amplitude from the 50 mm per recorded second trace. The epicentral distance used was that computed using programme LEADL (Sections 4.2.2, 4.4.3), and the corresponding value of $A_0(d)$ was read from table 1 of RICHTER (1935)*. M_L was then calculated from Equation 5.3.1.

5.4 Comparison of M_D and M_L: Results and Discussion

Ideally, every value of M_L obtained in Section 5.3 should differ from the previously determined magnitude M_D for the same event by a factor, k(d), which represents the difference between the normalisation functions for Afar and Southern California, i.e.

$$k(d) = \log_{10}A_0(d,\text{Afar}) - \log_{10}A_0(d,\text{S.Calif}) \quad (5.4.1)$$

Non-zero k(d) values will reflect structural differences between the two regions. If the normalisation functions have the same distance dependence (i.e. shape), k(d) will be a constant equivalent to ARNOLD's (1974) k'.

In practice, for a sample of 247 events the mean difference $\overline{M_L - M_D}$ was 0.19, with standard deviation 0.38

---

*It should be noted that this table, which defines the widely-used Richter curve, "presents ... the results of studying a comparatively small group of shocks", all occurring during one month (RICHTER,1935,p.7).

magnitude units. The close overall agreement between M_L and M_d shows that the error introduced by applying Richter's $A_o(d)$ to Afar is small.

The M_D values, given by Equation 5.2.11, have been calculated to be consistent with world-wide m_b results. A definitive $A_\emptyset(d,Afar)$ curve may thus be generated from the expression

$$Af_\emptyset(A/w) = \log_{10}(A/w) - M_D \qquad (5.4.2)$$

where $Af_\emptyset(A/w) = \log_{10}A_\emptyset(d,Afar)$. Combining Equations 5.2.1, 5.4.1 and 5.4.2,

$$\overline{M_L - M_D} = k - 1 = m$$

m is the mean difference due to structure between the Afar and Southern California normalisation factors, whereas k (here taken to be constant) includes also the difference in response between the instruments used to determine them. The $Af_o(A/w)$ curve is plotted on Figure 5.4.1. Points on the curve, denoted by short horizontal bars, are generated over intervals of 5 km of epicentral distance. By grouping together all events occurring within 5 km distance ranges an estimate is obtained of the scatter of the $Af_\emptyset(A/w)$ values. Vertical error bars show standard deviations for each group of events, while the thickness of each horizontal line indicates the size of the data group. Open circles denote single values. Richter's curve is plotted for comparison, displaced by k = 1.19 to optimize the fit with the $Af_\emptyset(A/w)$ curve. In other words, the relation

$$M_L(A) = \log_{10}(A/w) - \log_{10}A_o(d,S.Calif) - 1.19 \qquad (5.4.3)$$

produces maximum consistency between $M_L(A)$ and magnitude as

FIGURE 5.4.1

PLOT OF THE AFAR CALIBRATION FUNCTION $Af_{\emptyset}(A/w)$

FOR LOGARITHMIC AMPLITUDE AGAINST DISTANCE

RICHTER'S CALIBRATION FUNCTION IS SHOWN FOR COMPARISON

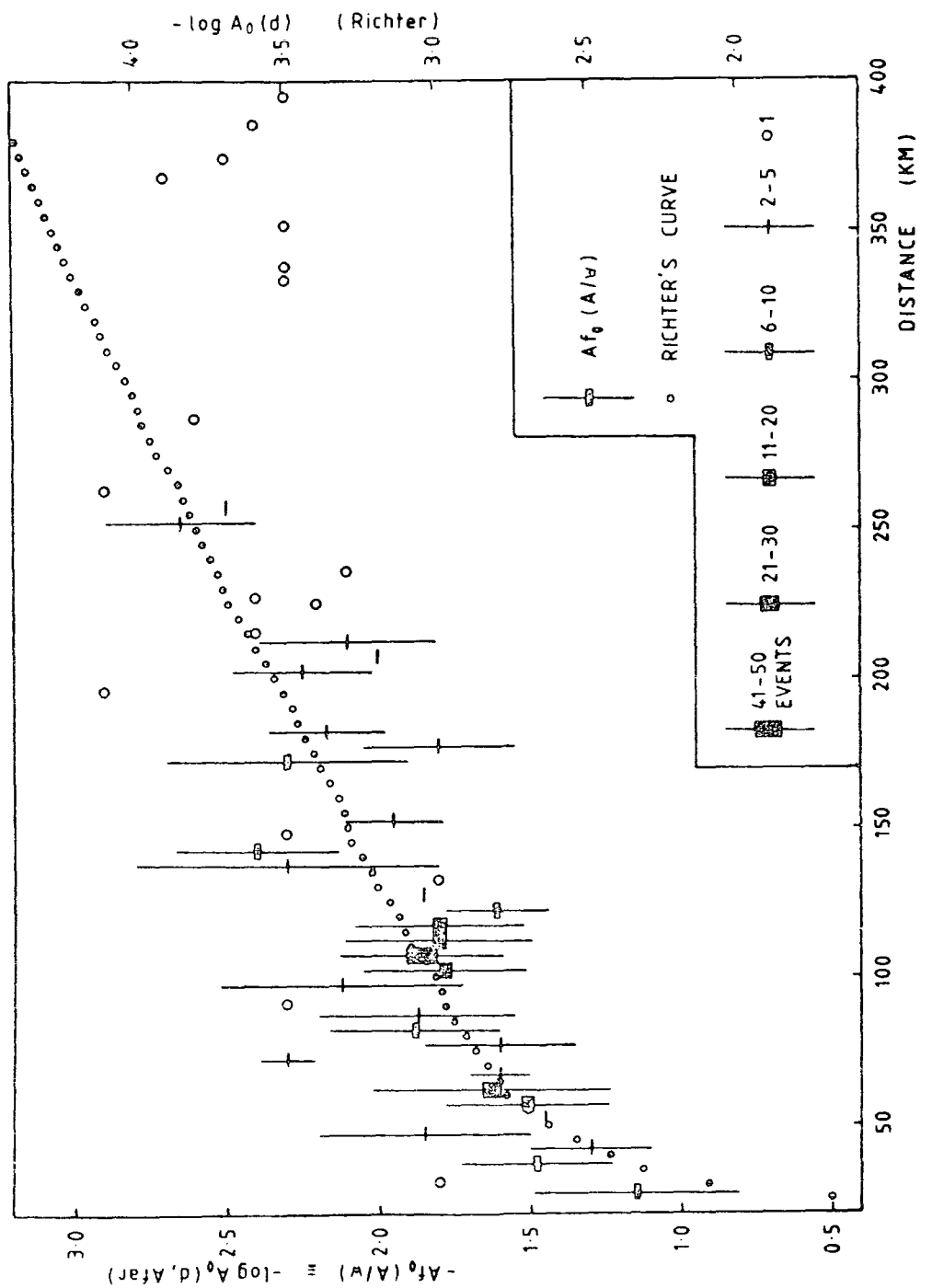

determined from Richter's curve.

Several conclusions may be drawn from the $Af_o(A/w)$ curve. However, although the validity of the M_D scale has been implicitly assumed there are no absolute measurements: the conclusions are based solely on the consistency of data from duration and amplitude measurements.

(1) The insignificant value $m = 0.19 \pm 0.38$ shows that Equation 5.2.1 may be applied directly to Afar without modification of $Af_o(d)$ by a significant constant to allow for structural differences between Afar and Southern California. However, Figure 5.4.1 demonstrates that the $Af_o(A/w)$ curve is a poor fit to Richter's curve, so that $k(d)$ is not well represented by a constant. The $Af_o(A/w)$ curve has smaller gradient than Richter's curve, reflecting a lower rate of attenuation of amplitude with distance, so that when Richter's curve is assumed magnitudes are underestimated at distances below 60 km and consistently and increasingly overestimated beyond 140 km, relative to world-wide data.

The indication is that significantly greater attenuation exists below Afar than below Southern California at lower crustal and uppermost mantle depths. This result is fully consistent with the low seismic velocities and raised Poisson's ratios found for the lower crust and uppermost mantle in the previous chapter, and with the results of other studies reviewed in Chapter 1.

(2) The standard deviations of the points of the $Af_o(A/w)$ curve from Richter's curve are of the same order as

the scatter of the individual data points, and a significantly better fit to the bulk of the data ($60 \leqslant d \leqslant 140$ km) should not be expected. The data scatter is not decreased when all the events in a given distance range originate from the same swarm, and cannot therefore be attributed to differences in focal mechanism or in attenuation as a function of azimuth. Possible azimuthal variations arising from crustal inhomogeneity are more logically examined in the frequency domain (Chapter 7).

(3) For events at epicentral distances of 100 km or greater, where $Af_{\emptyset}(A/w)$ is less strongly a function of distance, the mean difference between estimates of M_L at Mille and at Tendaho is 0.01 ± 0.12. As for the signal duration method, no station correction need be applied. The magnitudes of near events are relatively underestimated at the closer station, for example:

EVENTS FROM NW TENDAHO GRABEN	NUMBER OF EVENTS	APPROXIMATE EPICENTRAL DISTANCES
M_L(Mill) - M_L(Tend) = 0.67 ± 0.19	9	(Mill: 60-65 km (Tend: 25-30 km
M_L(Mill) - M_L(Serd) = 0.40 ± 0.05	4	(Serd: 35-40 km
EVENTS FROM SE OF SERDO		
M_L(Mill) - M_L(Tend) = 0.20 ± 0.13	4	(Mill: 93-96 km (Tend: 62-64 km

Overall figures in this distance range are statistically significant. They suggest that the prominent 'knee' on the

Richter curve (at 50 to 60 km) is much less pronounced, perhaps absent, for Afar. It also appears to be absent for Kenya (GURBUZ,1973,fig.27; ARNOLD,1974). In other words, the abnormally high rate of increase of attenuation with distance found by Richter in this distance range appears to be a peculiarity of the Southern Californian crust not exhibited by Afar. More data are required to substantiate this conclusion.

(4) (M_L-M_D) is independent of M_D for events in a given distance range. There is thus no indication that the linear extrapolation of the M_D curve below $M_D = 1.9$ is in any way invalid.

Note that the value of m depends on the computed gain of the ESP instruments. If the gain is in error by a factor 2, m will be altered by $\log_{10}2 = 0.3$.

The scatter of the data points in this section is of similar magnitude to that found in other trace amplitude magnitude studies (e.g. EATON et al,1970), and is a consequence of the initial simplifying assumption that earthquake size can be characterised by a single parameter. The imprecision of local magnitude estimates is one explanation for the multiplicity of empirical relations that have been used to fit experimental results.

The apparent absence of the Richter 'knee' suggested that the ESP data might be fitted to a simpler, analytic distance normalisation function. The equation chosen was analogous to Equation 5.1.6, but the measured trace amplitude was M_L rather than m_b. Since all the ESP events

in the data set have upper crustal foci, epicentral distance (d) was used instead of hypocentral distance. For the optimum fit,

$$M_L = \log_{10}A_V + 1.8\log_{10}d - 2.03 \qquad (5.4.4)$$

with $\sigma = 0.32$. This is a better fit than Equation 5.4.3. It is valid for the whole distance range 20 to 400 km, as shown in Figure 5.4.2.

That Equations 5.4.3, 5.4.4 and 5.2.11 (signal duration) all give consistent magnitudes for the ESP data demonstrates the unity of the three forms of relationship currently most widely used in the calculation of local magnitudes. Analytical relationships such as Equation 5.4.4 are preferable to those based on Richter's curve because they are simpler to derive and to apply.

FIGURE 5.4.2

FIT OF MAGNITUDE DATA TO EQUATION 5.4.4

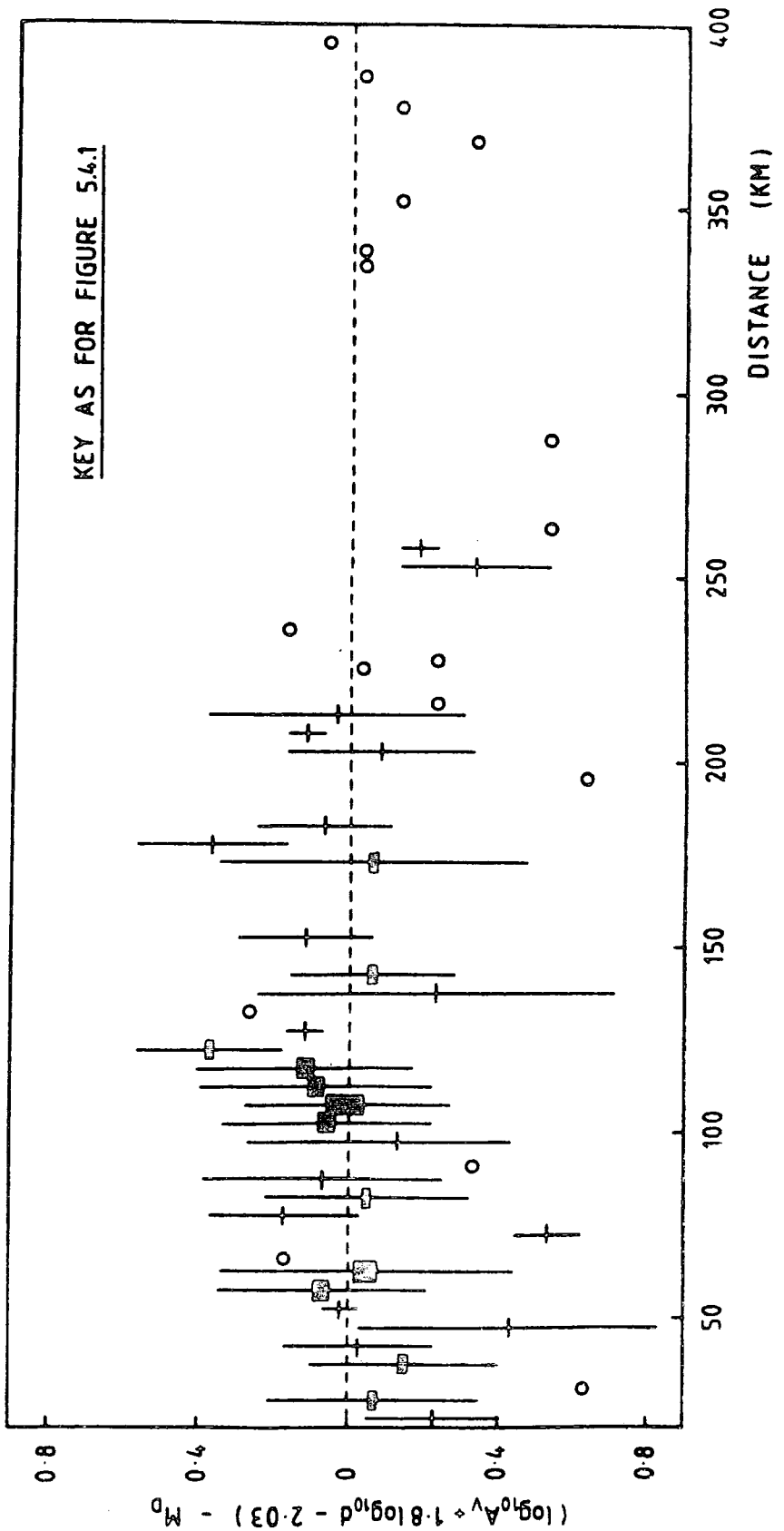

CHAPTER 6

THREE-COMPONENT ANALYSIS

6.1 Introduction

The three-component sets of seismometers used by the ESP have recorded the complete particle motion of incoming signals and noise. The various body and surface wave arrivals which constitute the seismic record have different polarization properties. Many authors have described polarization filters which will discriminate in favour of particular phases. They have been widely used in the analysis of teleseisms, but have not hitherto been applied to local earthquake records.

This chapter contains a discussion of the theory of such filters, and a review of the pertinent literature, followed by a description of their application to the ESP data. A method is developed for finding the azimuth and angle of incidence of ESP events recorded by a single three-component set of seismometers. Invoking a crustal model, the event hypocentres are determined by ray tracing. Finally, the hypocentres are compared with those obtained in Chapter 4.

The polarization properties of seismic waves within a body are well known, and may be calculated directly from infinitesimal strain theory assuming a homogeneous, elastic medium (e.g. BULLEN,1965). Despite the idealised conditions, the theory is a good approximation to real earth

conditions. This analysis concerns detectors on the earth's surface, where the incident body wave amplitudes are modified because of the P-SV interaction which occurs at the free surface. The modifications have been given by KNOPOFF et al (1957), and were first applied to the design of polarization filters by WHITE (1964).

Radial and transverse horizontal components of motion, R and T (Figure 6.1.1), are obtained from the original north-south (N) and east-west (E) horizontal seismic channels by co-ordinate rotation through an angle θ:

$$\left.\begin{aligned} R &= N\cos(\theta) + E\sin(\theta) \\ T &= N\sin(\theta) - E\cos(\theta) \end{aligned}\right\} \qquad (6.1.1)$$

where θ is the event azimuth.

The vertical component of motion, V, and R have the same waveform for P waves, and are in phase (KNOPOFF et al,1957). This is shown diagrammatically in Figure 6.1.2. For SV motion, V and R have a relative phase shift of 180°, provided the angle of incidence is less than the critical angle, $i_c = \sin^{-1}(V_S/V_P)$, where V_S, V_P are S, P wave velocities respectively. For $i \geqslant \sin^{-1}(V_S/V_P)$, the wave motion is no longer rectilinear. Incident SV is totally internally reflected as SV, undergoing a phase shift. Reflected P is also out of phase with incident SV.

Figure 6.1.2 demonstrates that the product of vertical and radial (horizontal) components of ground motion, V(t)R(t), is always positive for P arrivals and negative for S arrivals. Elliptical motion, with V phase shifted by $\pi/2$ with respect to R, gives V(t)R(t)values which may be either

FIGURE 6.1.1

COMPONENTS OF MOTION FOR A SEISMIC RAY

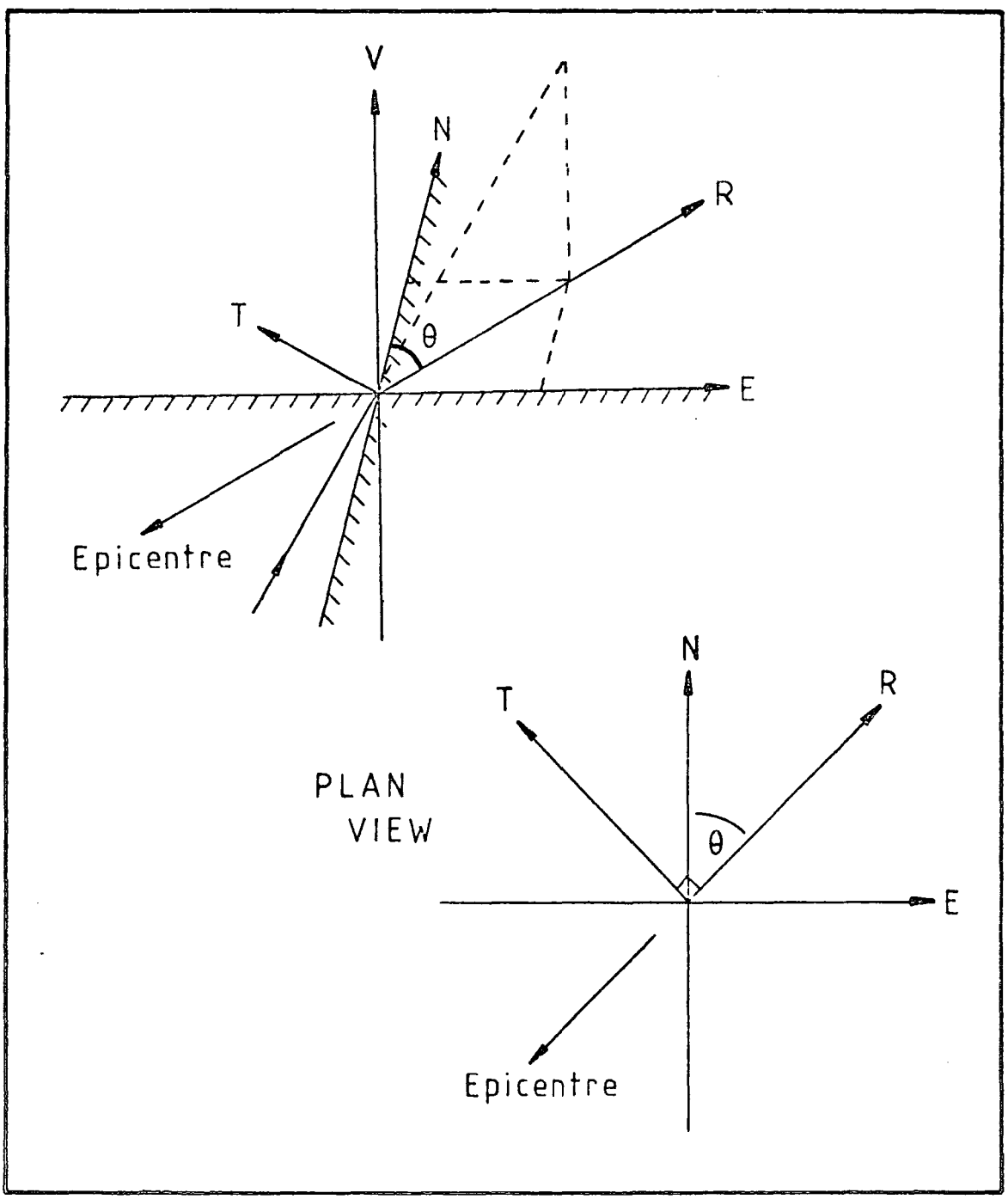

FIGURE 6.1.2

DIAGRAMMATIC REPRESENTATIONS OF THE FUNCTION VxR

(after ARMOUR, 1977)

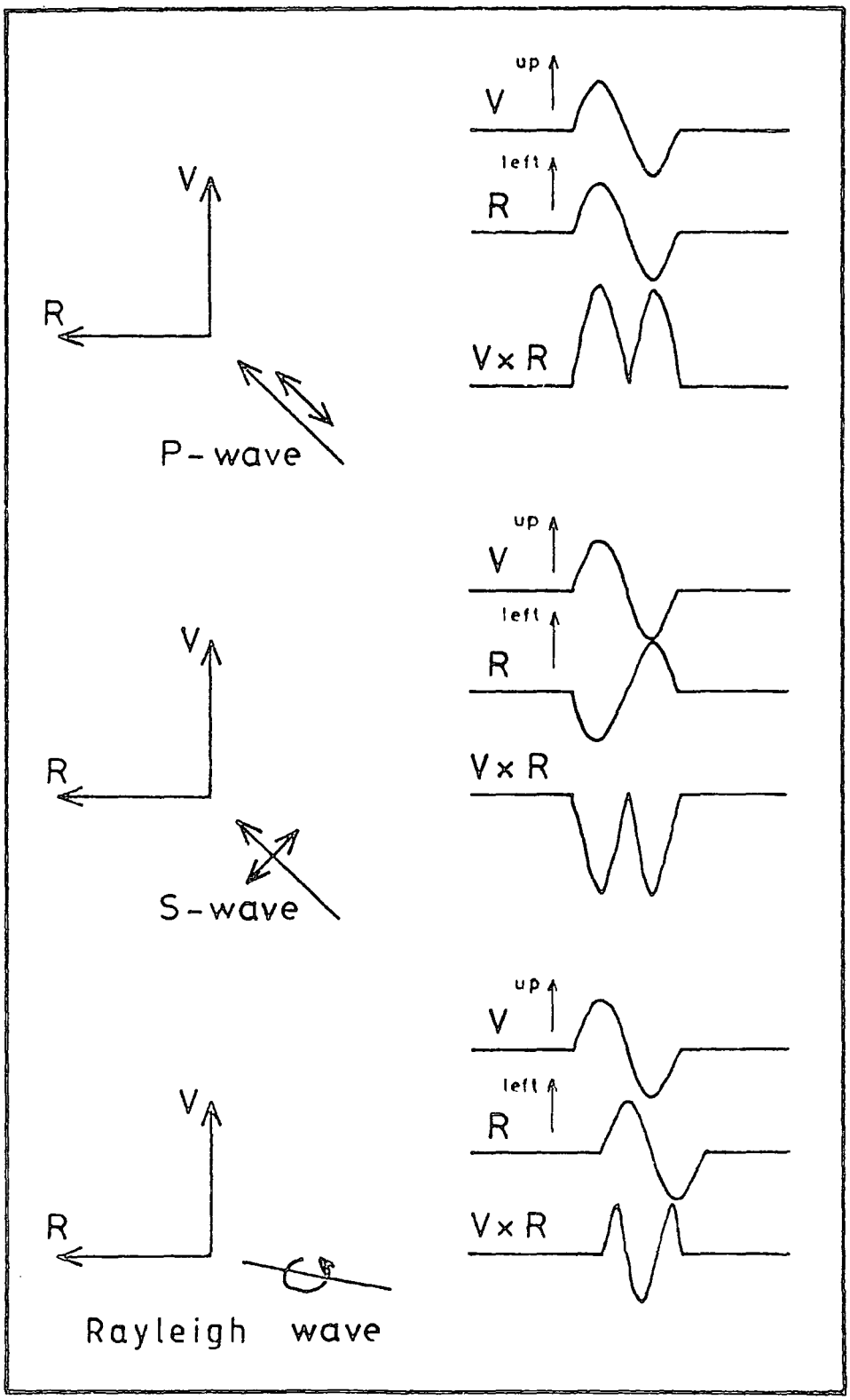

positive or negative, but which average to zero over one cycle.

A smoothing filter is usually applied to V(t)R(t) to reduce the effects of noise. For digitized data, a very simple filter may be realised by forming a moving window average over a range of n samples either side of the time corresponding to the output sample value, k. Thus

$$\overline{VR} = (1/(2n+1))\sum_{i=k-n}^{k+n} V_i R_i \quad , \qquad (6.1.2)$$

time averaged over (2n + 1) samples, can be used as a filter to enhance rectilinear wave motions. Summation over a cycle of the waveform is equivalent to

$$1/\pi\int_{-\pi}^{\pi} \cos(\theta)\cos(\theta + \epsilon)d\theta = \begin{cases} 1 \text{ if } \epsilon = 0 & \text{(P-waves)} \\ -1 \text{ if } \epsilon = \pi & \text{(S-waves, } i < i_c\text{)} \\ 0 \text{ if } \epsilon = \pi/2 & \text{(elliptically polarized waves)} \end{cases}$$

The more general equations are given by WHITE (1964).

The $\overline{VR}$ filter tends to suppress all non-rectilinear wave motions, including Rayleigh surface waves (Figure 6.1.2). Since background noise consists primarily of fundamental and higher mode Rayleigh waves, the filter has the important property of improving the signal to noise ratio. This is valuable in the present study, where signal generated noise is often substantial and cannot be removed by frequency band-pass filtering (Section 3.5). Note also that SH and Love waves do not contribute to $\overline{VR}$, since they are polarized orthogonally to V and R.

SHIMSHONI and SMITH (1964) developed the $\overline{VR}$ filter independently of WHITE (1964), and applied it to teleseismic records. The application to the ESP data of a modified version of their filter is described in Section 6.3. A

series of more general 'REMODE' (Rectilinear Motion Detector) filters, based on the correlation functions for two components of motion, was originated in the time domain by SAX and MIMS (1965) and in the frequency domain by ARCHAMBEAU and FLINN (1965), with further development by GRIFFIN (1966). Operators which enhance surface waves are generally designed in the frequency domain (although the Hilbert transform (e.g. BRACEWELL,1978,p.267) could be used), since surface wave trains are dispersive. A somewhat different polarization filter, in which both the rectilinearity and direction of the particle motion are considered, was described by FLINN (1965b) and modified by MONTALBETTI and KANASEWICH (1970). It is this filter which is developed in the present study.

REMODE filters have been applied to teleseisms by BASHAM and ELLIS (1969); and have been used in explosive-source upper mantle investigations by LEWIS and MEYER (1968) and ARCHAMBEAU et al (1969). The pertinent results of all these papers may be summarised as follows:

(1) Filtered traces are 'cleaner' than the original seismic traces. Late-arriving portions of the P coda are discriminated against (they are largely composed of upper crustal reverberations) and noise prior to the first P arrival is virtually eliminated. Filtered arrivals may confidently be picked when the original signal to noise ratio is as low as unity (SHIMSHONI and SMITH,1964).

(2) Although ARCHAMBEAU et al (1969) and MONTALBETTI and KANASEWICH (1970) have applied polarization filtering to

elucidate multiple P phases, LEWIS and MEYER (1968) found their REMODE filtered traces reliable for SV arrivals only. For P arrivals at near-vertical incidence the amplitude ratio of vertical/horizontal seismometer records will be very large. If the horizontal motion is not resolvable the P motions will be rejected by REMODE.

(3) Polarization filters are non-linear. Initial P motion is often reduced in amplitude on filtered records relative to later-arriving larger phases. The polarity of the first P motion is preserved on all records illustrated in the literature, but later arrivals are often distorted.

(4) REMODE filters have sometimes given poor results, with phases difficult to identify, when the seismic records have contained noise at the signal frequencies (i.e. not removed by band-pass filtering) (BASHAM and ELLIS,1969).

The next sections of this chapter examine to what extent these results are true for the polarization filtered records of local earthquakes detected by ESP. The large majority of ESP records used were frequency band-pass filtered in the range 2 to 10 Hz (1 to 10 Hz for Waldia events) prior to three-component analysis. When unfiltered records were used (due to faults with the KEMO filters at the time of digitization), the d.c. signal components were subtracted. Undetected residual d.c. will invalidate the results obtained with the polarization filters.

6.2 Particle Motion Plots

The particle orbits of orthogonal pairs of components of ground motion were examined visually as functions of time by inputting the components from the digital tape to the X and Y axes of the 12-channel oscilloscope or HEWLETT-PACKARD X-Y plotter. Figures 6.2.1a-f show particle motion plots of approximately the first 0.5 s of the first P and S arrivals of events with epicentres NW of the Tendaho graben. They have been traced from the X-Y plotter. The events illustrated were selected for their large signal to noise ratio. The heavy line at 45° on Figure 6.2.1a is a calibration line obtained by inputting the same signal to the plotter X, Y axes to check that their gains were equal. Its displacement from the 'preceding noise' trace on the figure is for clarity only, and does not indicate a d.c. shift.

Rectilinearity of the records is largely confined to the first cycles of the first P arrival. Note from Equations 6.1.1 that on the plots of N against E the direction of particle motion for the P onset should define the event azimuth (provided the crust is horizontally layered), while for pure SH arrivals originating from the event the direction of motion should be transverse to this azimuth. The event azimuths determined in Chapter 4 are marked on Figures 6.2.1a,e. The large transverse component seen on Figure 6.2.1a arrives so early on the record that it must be a converted phase from a shallow source. Early transverse motion has also been found in particle motion

FIGURES 6.2.1a-d

PARTICLE MOTION PLOTS FROM TENDAHO STATION

(T29, T55 are closely similar events)

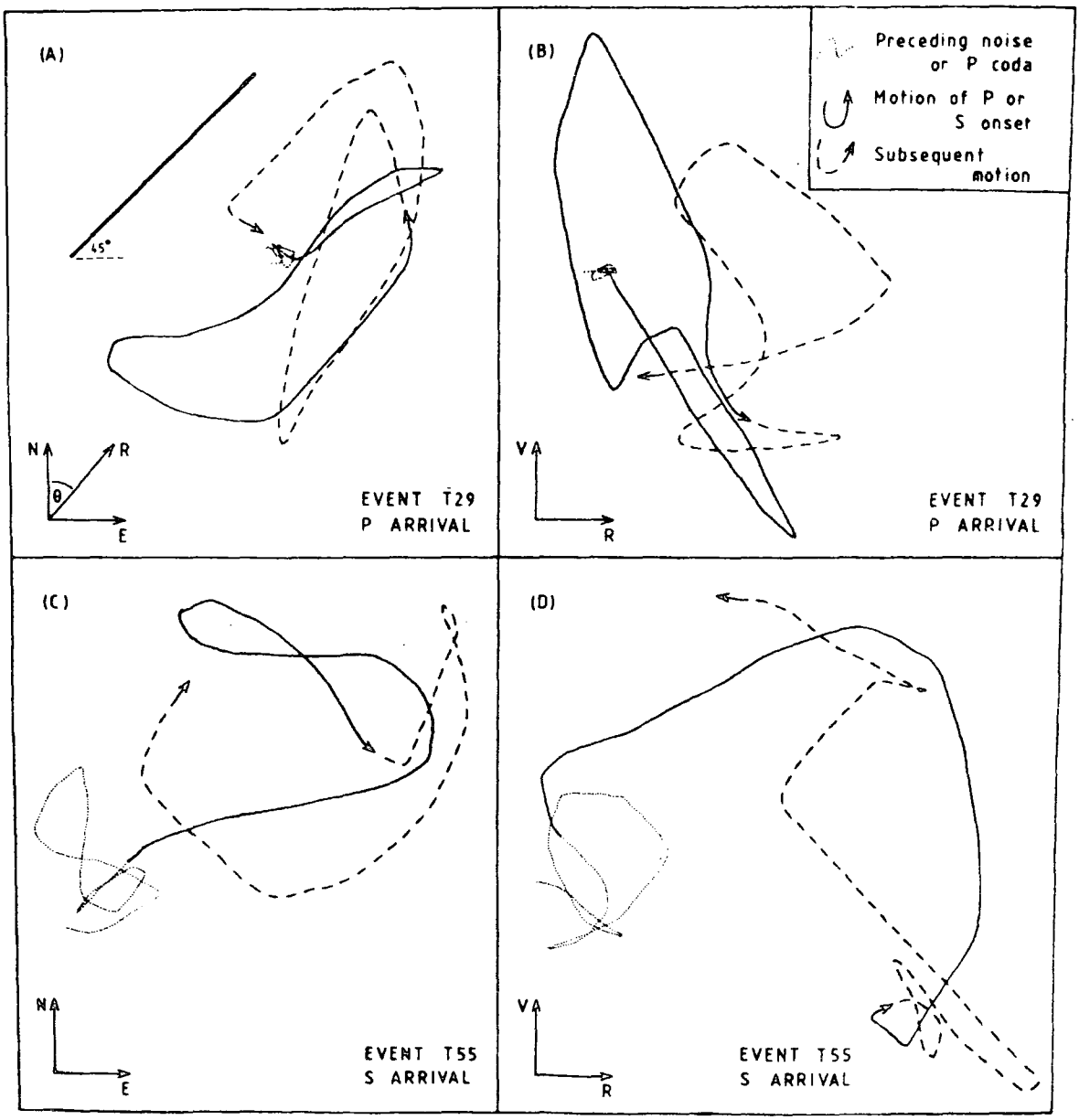

FIGURES 6.2.1e,f

PARTICLE MOTION PLOTS FROM MILLE STATION

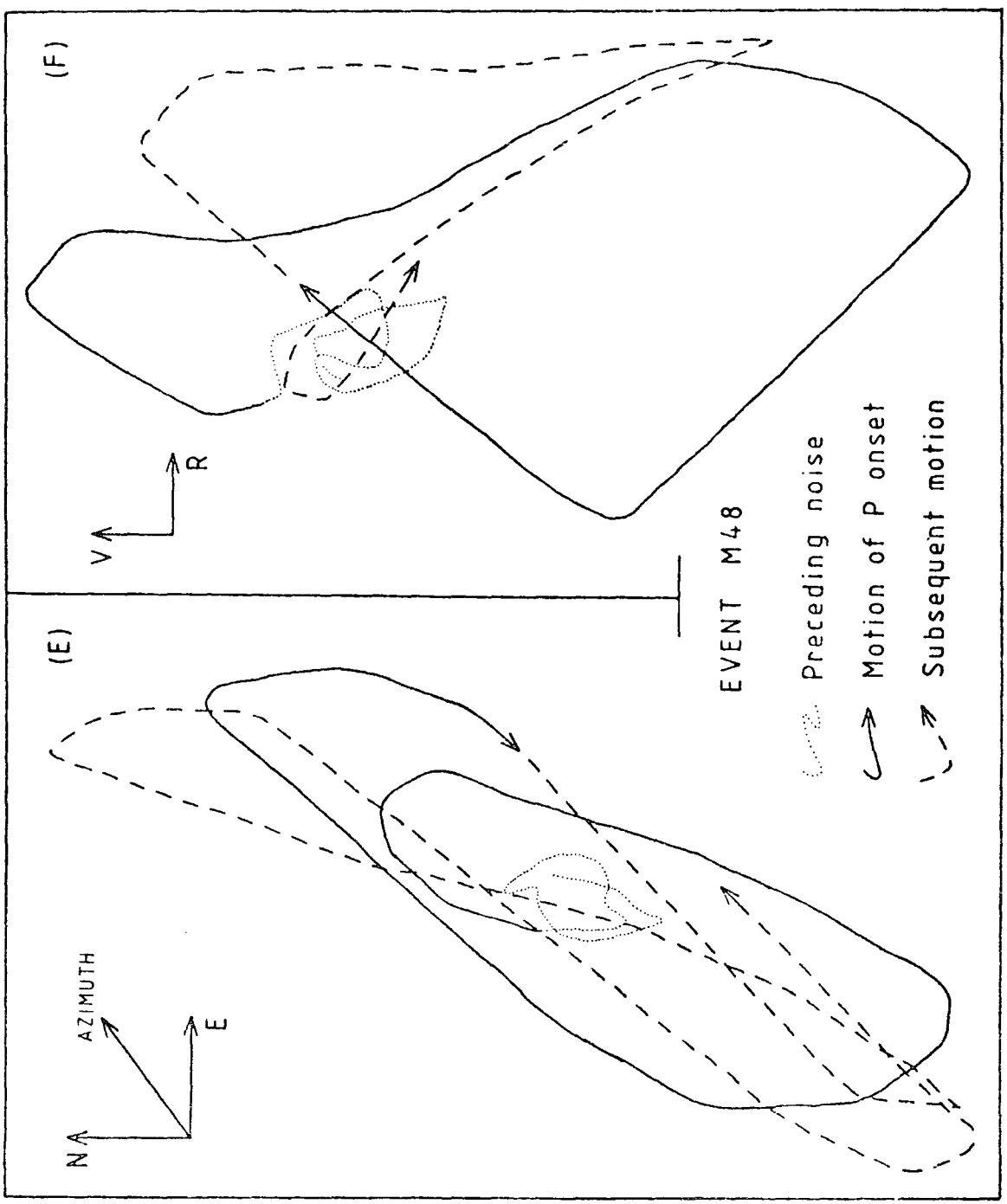

plots of teleseismic signals (ELLIS and BASHAM,1968) and was not unexpected in this study, where the near-surface geological structure is complex (Section 2.3 and Chapter 7).

Components of motion I and J, having the directions of pure P and SV arrivals, respectively, may be determined from the components V and R by

$$\left.\begin{aligned} I &= V\cos(i') + R\sin(i') \\ J &= V\sin(i') - R\cos(i') \end{aligned}\right\} \qquad (6.2.1)$$

These equations represent a co-ordinate rotation of i', the apparent angle of incidence of the event (Figure 6.2.2). i' differs from the true angle of incidence because of P-S wave conversion (KNOPOFF et al,1957). Figure 6.2.1f shows near-vertical apparent incidence which is a consequence of the very small horizontal energy observed on the seismic records for approximately Ø.Ø5 s following recognition of P on the vertical. It is typical of Mille records of Tendaho graben events, but is not observed at other stations or from other azimuths.

Many S arrivals of ESP records show very little rectilinearity (Figures 6.2.1c,d). This can be explained by interference from P coda arrivals, which occurs particularly for close events where the P to S time is short.

6.3 A Body Wave Discriminator

This section examines the performance of a simple filter which uses the time-averaged product $\overline{VR}$ (Equation 6.1.2) to discriminate between P and S body wave arrivals.

FIGURE 6.2.2

COMPONENTS OF MOTION IN THE INCIDENT PLANE OF A SEISMIC RAY

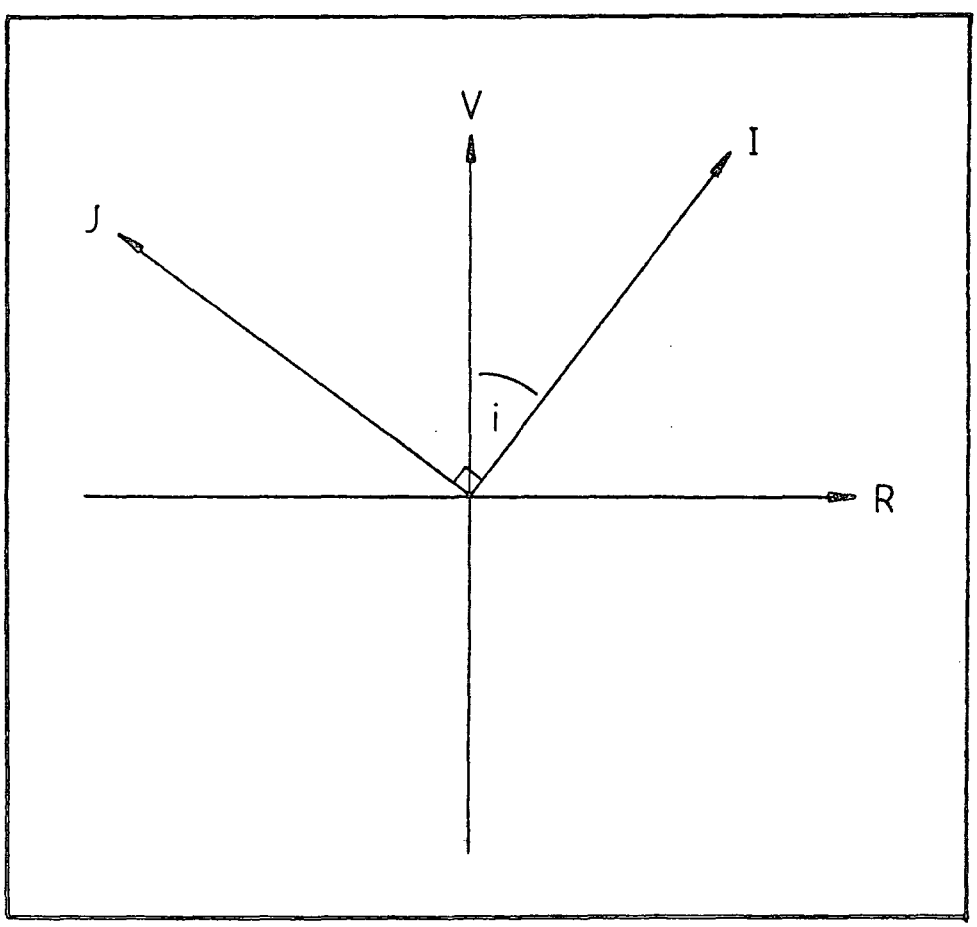

Following SHIMSHONI and SMITH (1964), 'half wave rectified' $\overline{VR}$ is multiplied by the original signals V, R in order to obtain output in a form where the seismic phases can be recognised.

The calculations are performed on the MODULAR 1 computer. The length of the time window is critical, and should be approximately equal to one cycle of the wave motion. A longer window improves the suppression of arbitrarily polarized noise, but increases the time uncertainty of the output traces. Examples of the computed output are shown in Figures 6.3.1, 6.3.2, where

$$V \times \overline{VR}^{+} = V \times \overline{VR} \quad (\overline{VR} > 0)$$
$$= 0 \quad (\overline{VR} \leqslant 0),$$

and similarly for traces 6 to 8 on Figure 6.3.1. This form of display separates P from S phases. Traces 5 to 8 on Figure 6.3.1, and 2 to 6 and 7 to 10 on Figure 6.3.2, had the same gains. The product functions were not normalised.

The following observations are made:

(1) The P coda is greatly 'cleaned' by the suppression of reverberations and other noise. Rectilinear P motion dominates the record for not longer than the first two cycles.

(2) The groups of waves marked B, C in Figure 6.3.1 do not represent rectilinearly polarized particle motion, since $\overline{VR}$ has both polarities.

(3) Event T481 (Figure 6.3.2) shows a second P arrival, indicated at D on trace 9, becoming very clear about 2 s after the first arrival. This arrival is evident on other events of this swarm. The similarity of its

FIGURE 6.3.1

BODY WAVE DISCRIMINATOR, SAMPLE OUTPUT, EVENT M289

(window length Ø.1 s, azimuth 140°, distance ≈35 km)

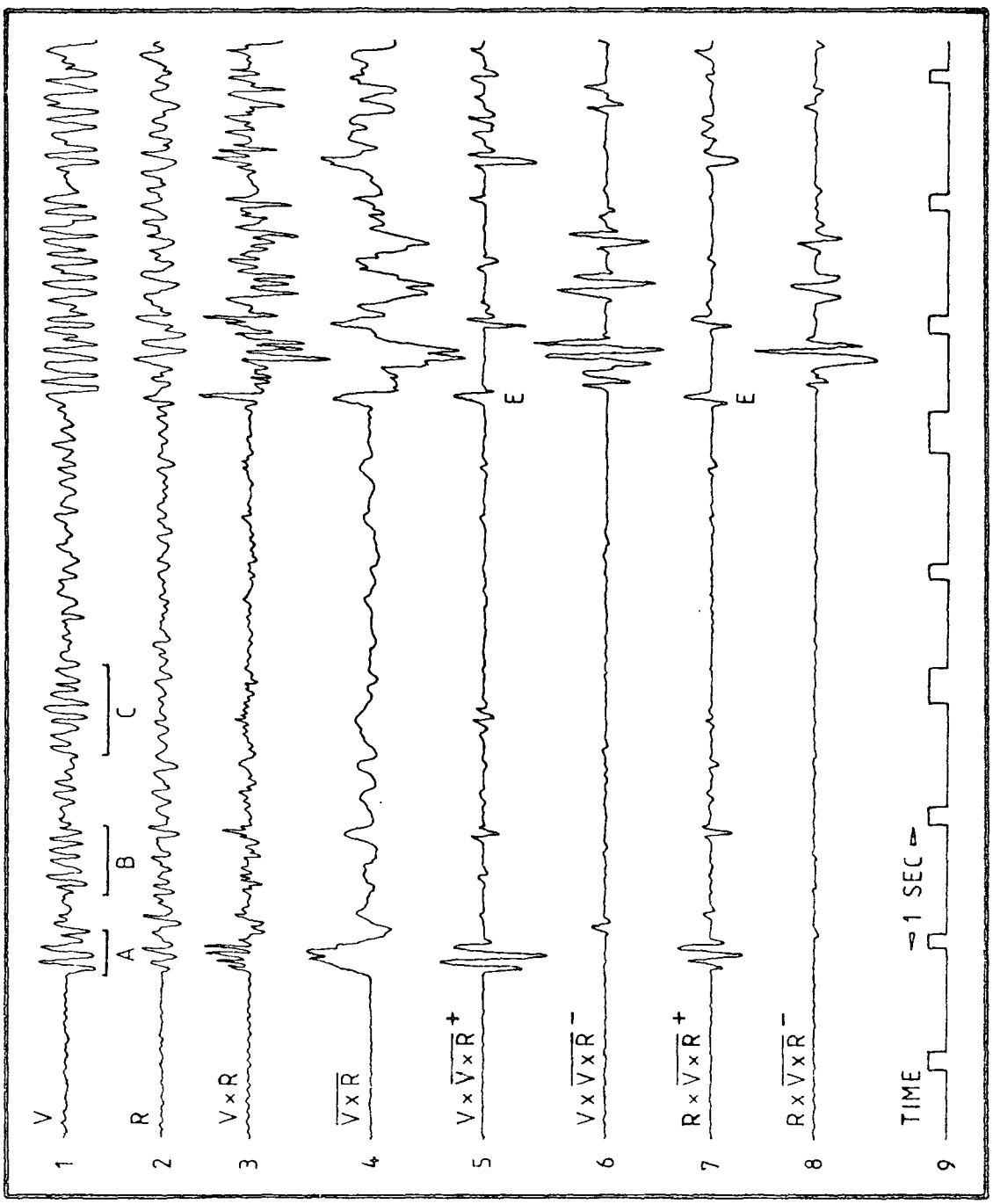

FIGURE 6.3.2

BODY WAVE DISCRIMINATOR, SAMPLE OUTPUT, EVENT T481

(window length Ø.1 s, azimuth 72°, distance ≈ 63 km)

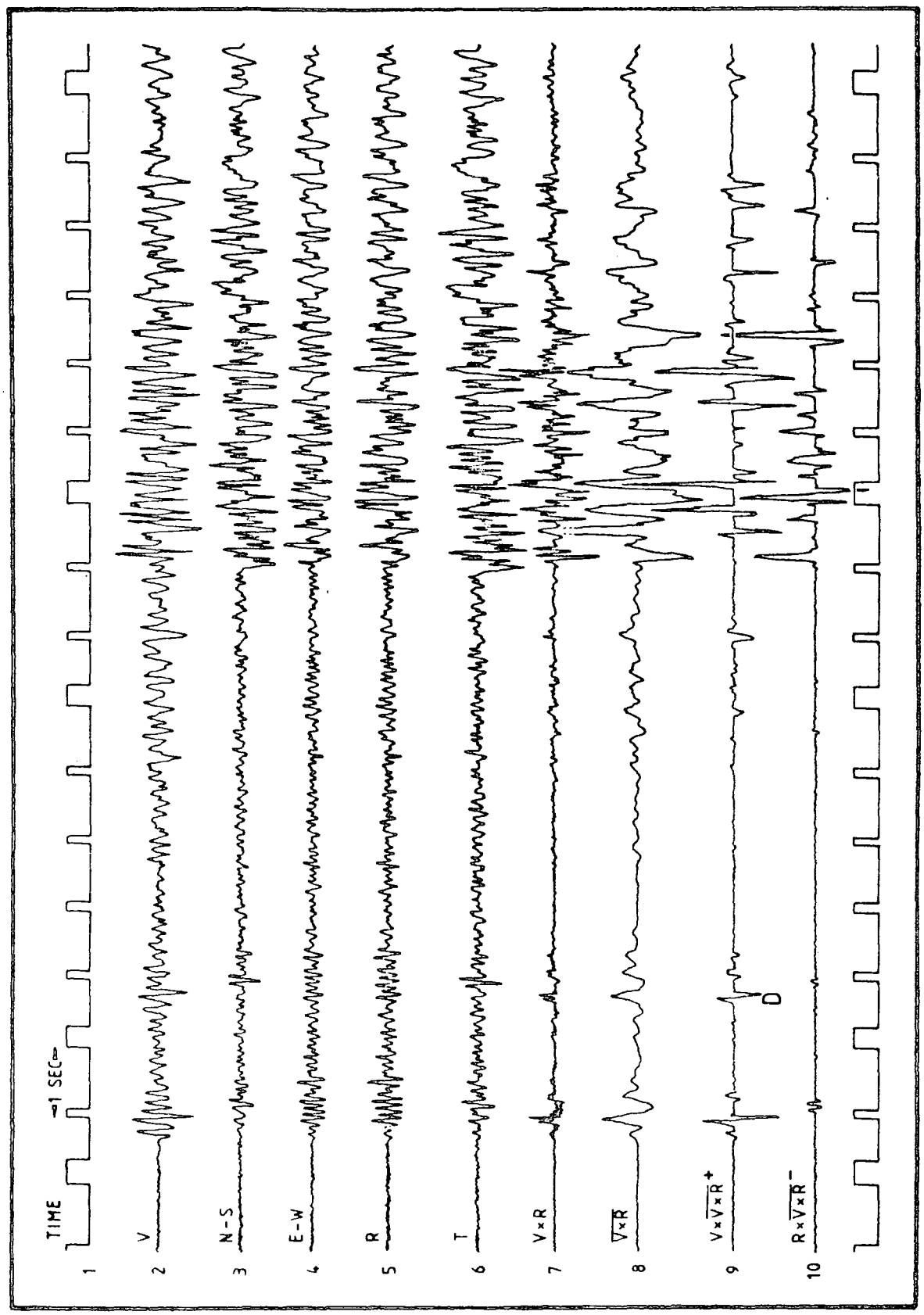

waveform with that of the first P arrival is emphasised on the filtered traces, although its onset is not evident. If present, the onset would have very low amplitude, since the output on trace 9 is roughly proportional to the cube of the input signal. For this event the initial horizontal energy is small, resulting in poor discrimination of the initial P onset on trace 9, relative to the subsequent cycle (which might represent a different phase). The horizontal energy is initially concentrated on the E-W seismic channel, as would be predicted from the event azimuth (72°). The transverse component (trace 6) builds up rapidly from zero at the first onset, and transverse energy briefly dominates the record as soon as 0.4 s after the first arrival.

(4) Event M289 (Figure 6.3.1) is atypical in suggesting the possibility of significant S-P conversion, shown at E on traces 5 and 7. Where the S arrival to P coda amplitude is large the S onset is apparent on the filtered records (as on Figure 6.3.2, trace 10), but typically shows rectilinearity for less than a cycle and is distorted in shape. These effects may be caused by slight clipping.

The body wave discriminator was used to check the validity of S onset picks (Sections 3.7 and 4.5); and to verify the existence of the later P coda arrivals described in Section 4.3. P coda second arrivals were picked later on the polarization-filtered traces than on the originals by 0.15 $\pm$ 0.2 s, and S arrivals showed a similar trend. As illustrated by point (3) above, it was concluded that the REMODE filtered traces were more likely to be late than the

original picks to be early. The former were not used for timing. It should be emphasised that the records chosen for illustration are unusually quiet.

6.4 Azimuthal Dependence of R and T

For the $\overline{VR}$ filter to be used as above, the event azimuth, θ, must be known in order to form R. The sensitivity of the filter to azimuth errors is now considered. If the filter is insensitive to small errors in azimuth, θ, such errors will be unimportant. If it proves sensitive, it may be used for determination of θ values by trial sweeps over a range of values. Part of the output of one such trial sweep is shown in Figure 6.4.1.

From Equations 6.1.1,

$$dR'/d\theta' = -N\sin(\theta') + E\cos(\theta') = -T'$$

$$dT'/d\theta' = N\cos(\theta') + E\sin(\theta') = R'$$

At the true azimuth ($\theta = \theta'$) $dT'/d\theta' = R$, its maximum value, and $dR'/d\theta' = T = 0$, i.e. $d(\overline{VR}')/d\theta' = 0$, since V is independent of θ'.

Figure 6.4.1 illustrates these points. The first onset, assumed to be pure P motion, is little affected in shape or amplitude by variations of $\pm 30^{\circ}$ from the approximately correct azimuth 183°, whereas some later arrivals are substantially altered. The figure indicates that the section of the record marked 'a' is the only other part of the P coda arriving from an azimuth similar to (or directly opposite to, since VR is simply inverted for a 180° azimuth error) that of the first arrival.

FIGURE 6.4.1

BODY WAVE DISCRIMINATOR USED FOR APPROXIMATE AZIMUTH DETERMINATION

(event T270, window length 0.15 s, distance ≈ 57 km, correct azimuth ≈ 183°)

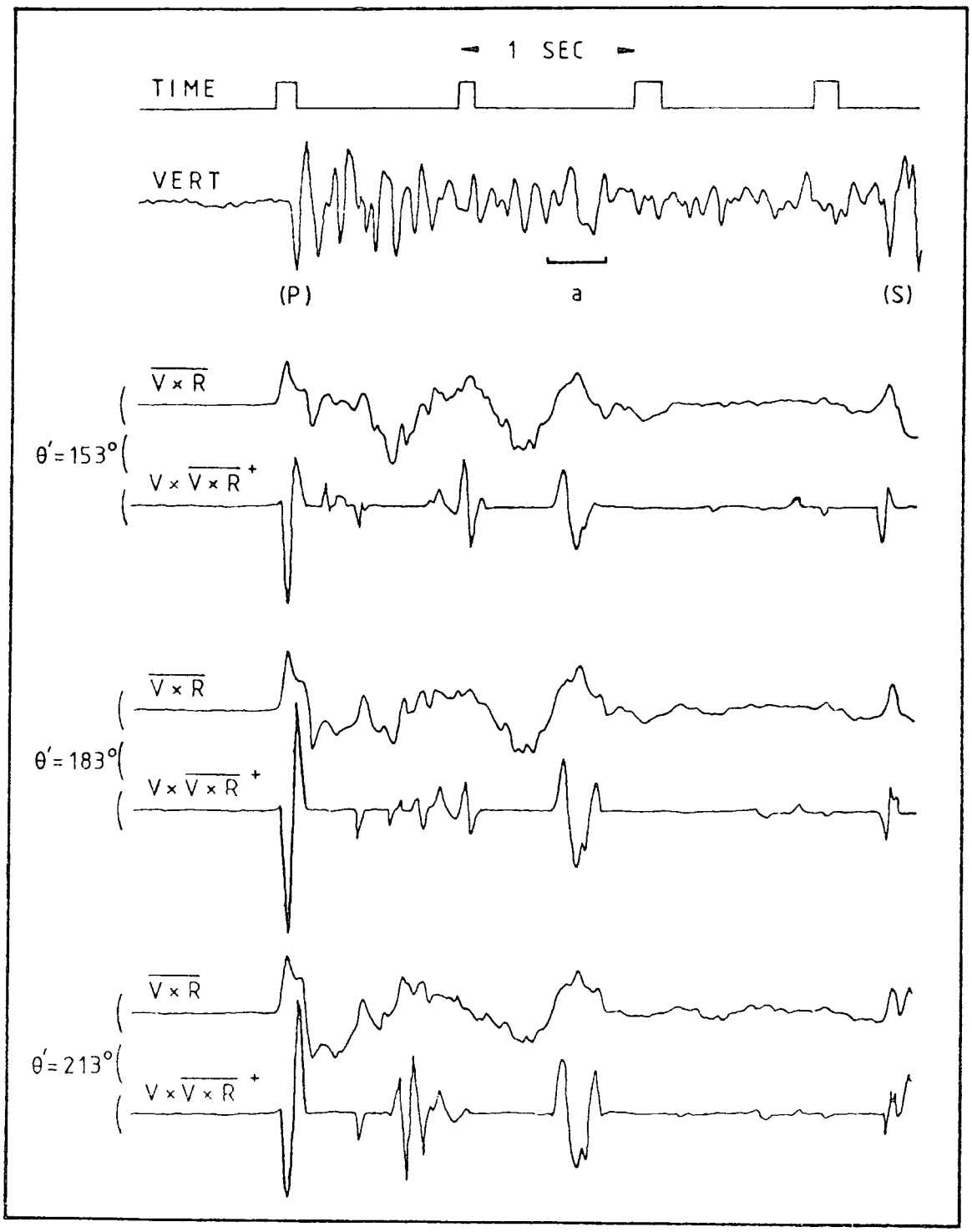

Azimuth, θ, is not accurately determined by the $\overline{VR}$ filter. It will be better determined as the value of θ' for which $\sum_{i=1}^{n} T_i = 0$ and $\sum_{i=1}^{n} VR_i > 0$ (the condition on $\sum_{i=1}^{n} VR$ is necessary to exclude the value $\theta' = \theta + \pi$). Figure 6.4.2 is a graph of the output of a programme written for the MODULAR 1 computer to calculate the quantities $\bar{R}$, $\bar{T}$, $\overline{VR}$, time averaged over the first 10 samples of event T481. The event azimuths calculated in Chapter 4, and by three-component analysis in Section 6.7, are indicated by single and double arrows, respectively.

These simple numerical methods are of limited usefulness in calculating azimuth and apparent angle of incidence as time functions along the record. They give no estimate of the coherence between the seismic components, and the parameters used are not normalised (hence the different azimuths for the peaks of $\bar{R}$ and $\overline{VR}$ in Figure 6.4.2). Further programme development was beyond the storage capacity of the MODULAR 1, so attention was turned to NUMAC for the development of a more versatile polarization filter.

6.5 Determination of Azimuth and Angle of Incidence

6.5.1 The Theory of the Polarization Filter

The covariance between n observations of two variables X, Y is in general given by

$$\mathrm{Cov}[X,Y] = (1/n)\sum_{i=1}^{n}(X_i - m_x)(Y_i - m_y),$$

where

FIGURE 6.4.2

AZIMUTH DETERMINATION USING THE MODULAR 1 COMPUTER

(Event T481, window length 0.1 s, distance ≈ 63 km, azimuth 72°)

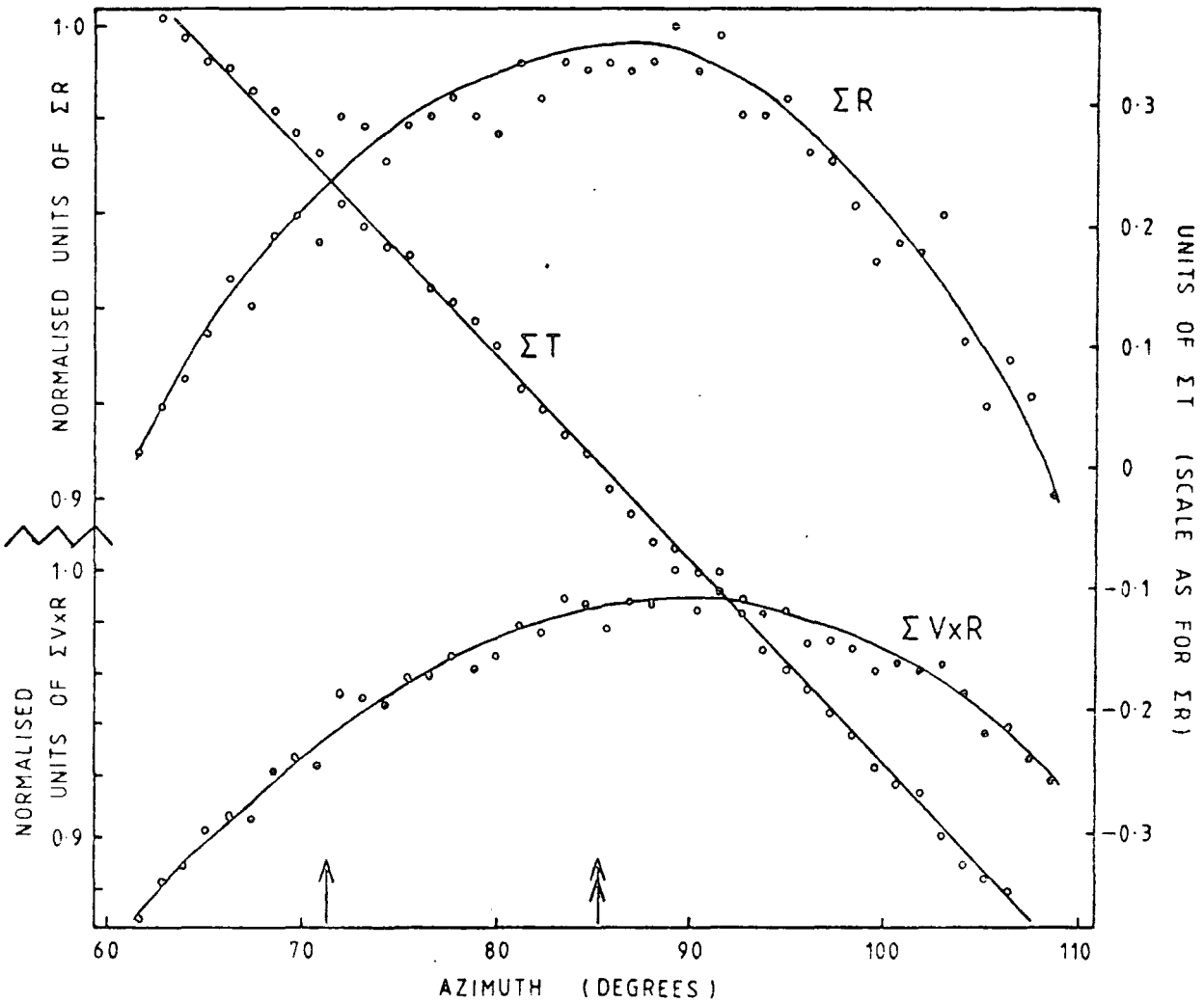

$$m_x = (1/n)\sum_{i=1}^{n} X_i \; ; \qquad m_y = (1/n)\sum_{i=1}^{n} Y_i$$

For the seismic records under consideration we have ensured that m_x and $m_y = \emptyset$ (Equation 6.1.3), therefore

$$\mathrm{Cov}[X,Y] = (1/n)\sum_{i=1}^{n} X_i Y_i \qquad (6.5.1)$$

Section 6.4 considered the determination of Θ from the relation

$$\sum_{i=1}^{n} T_i = \cos(\Theta)\sum_{i=1}^{n} E_i - \sin(\Theta)\sum_{i=1}^{n} N_i = \emptyset \, , \qquad \text{for}$$

arbitrary n, or

$$\Theta = \tan^{-1}\left(\sum_{i=1}^{n} E_i / \sum_{i=1}^{n} N_i\right)$$

Since it is only the coherent portions of the record that are of interest, Θ might be better defined by

$$\Theta = \tan^{-1}(\mathrm{Cov}[E,F]/\mathrm{Cov}[N,F]) \qquad (6.5.2)$$

(MONTALBETTI and KANASEWICH,1970), where F is any of the components V, N, E.

The coherence function between X and Y is defined by

$$B_{XY} = \frac{\mathrm{Cov}[X,Y]}{(\mathrm{Var}[X].\mathrm{Var}[Y])^{1/2}} \qquad (6.5.3)$$

Note that B_{XY} is the square root of the 'correlation efficiency' or 'correlation coefficient' defined by SAX and MIMS (1965) and used by MONTALBETTI and KANASEWICH (1970). The present definition preserves the distinction between pure P motion (for which $B_{EN} = 1$) and pure S motion ($B_{EN} = -1$). $B_{EN} = \emptyset$ for elliptically polarized phases.

Following FLINN (1965b), a measure of the rectilinearity of particle motion over an n-sample time window is given by the covariance matrix

$$C = \begin{pmatrix} \mathrm{Var}[E] & \mathrm{Cov}[E,N] & \mathrm{Cov}[E,V] \\ \mathrm{Cov}[E,N] & \mathrm{Var}[N] & \mathrm{Cov}[N,V] \\ \mathrm{Cov}[E,V] & \mathrm{Cov}[N,V] & \mathrm{Var}[V] \end{pmatrix} \qquad (6.5.4)$$

for the set of n samples (E_k, N_k, V_k), $k = 1,2,...,n$. Equation 6.5.4 is no more than a generalisation of Equation 6.5.2, and of the analogous relation for the apparent angle of incidence. C defines an ellipsoid whose shape and orientation best fit the data points in the least-squares sense. Its largest principal axis has the direction of the wave polarization. The degree of rectilinearity is measured by the ratio of the principal axes. If L_1, L_2 are the largest and intermediate eigenvalues of the covariance matrix, the function

$$RL = 1 - (L_2/L_1) \qquad (6.5.5)$$

will be close to unity if the motion is highly rectilinear (that is, when the ellipsoid is highly elongated); and to zero when it is unpolarized (Figure 6.5.1a).

6.5.2 Method for Computing Azimuth and Angle of Incidence

As used by FLINN (1965b) and by MONTALBETTI and KANASEWICH (1970), polarization filters of the type described above have been tuned to enhance arrivals from a particular desired direction, normally with R corresponding to the known great circle azimuth from source to receiver.

Flinn defined a 'directionality factor', D, by the relation

$$D = \underline{d}_1 \cdot \underline{l}_1$$

where $\underline{l}_1$, $\underline{d}_1$ are respectively unit vectors along the largest principal axis and along any chosen direction $\underline{d}_1$ (Figure 6.5.1b). Flinn used D as a gain factor to tune the filter in the direction $\underline{d}$. RL was used as a rectilinearity gain

FIGURE 6.5.1

GEOMETRICAL REPRESENTATIONS OF RECTILINEARITY AND DIRECTIONALITY FUNCTIONS

(after FLINN, 1965b)

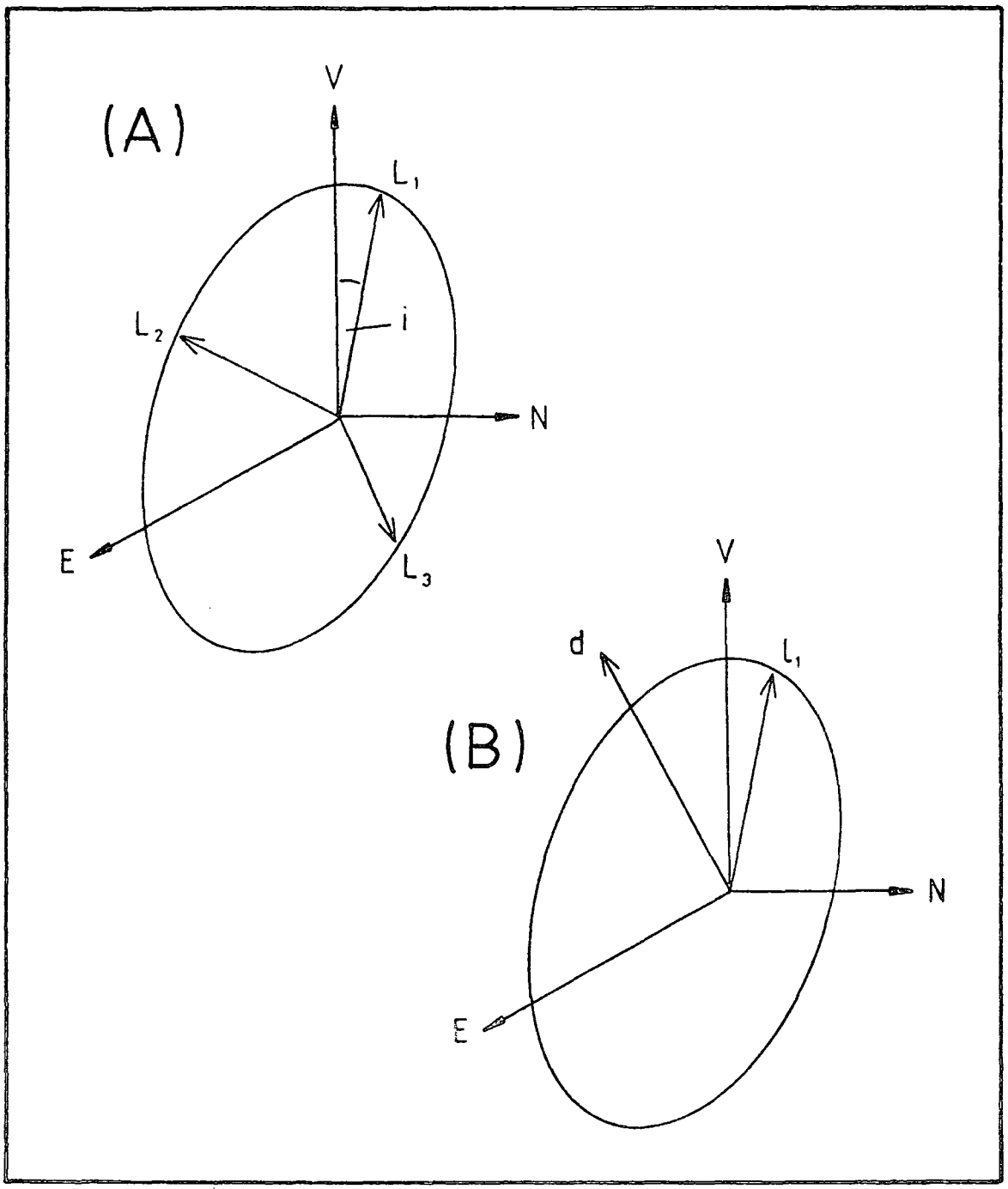

factor. The original seismic records were modulated by gain control products of the form RL^aD^b, where a, b were small integral powers controlling the sensitivity of the tuning.

In the present study the filter is adapted to determine the azimuth, θ, and apparent angle of incidence, i', of the ESP events. Attention is concentrated on the first few cycles of the first arrival, which have been shown in Section 6.2 to be the most linearly polarized section of the record and are expected to approximate to pure P motion. Their polarization direction will be that of the azimuth, and l_1 will thus have this direction. If the eigenvector of the largest principal axis is $v = (v_E, v_N, v_V)$,

$$\theta = \tan^{-1}(v_E/v_N) \qquad (6.5.6)$$

$$i' = \cos^{-1}(|v_V|) \qquad (6.5.7)$$

The true angle of incidence, i, is related to i' by

$$i = \sin^{-1}[(V_S/V_P)\sin(i'/2)]$$

(KNOPOFF et al,1957).

The behaviour of the filter is monitored by the functions RL (Equation 6.5.5) and B_{EN} (Equation 6.5.3), both of which should be close to unity if the seismic signal is truly P.

Programme MOTION, listed in Appendix 8, has been written in FORTRAN for NUMAC to calculate and solve the covariance matrix, C (Equation 6.5.4), so as to obtain θ and i' from Equations 6.5.6, 6.5.7. The elements $c_{i,j}$ are calculated over a window of length w such that

$$(c_{i,j})_r = \sum_{k=r}^{r+w-1} (S_i S_j)_k$$

for the window beginning at sample r. The computation

proceeds by moving window integration, using the relation

$$(c_{i,j})_{r+1} = (c_{i,j})_r + (S_iS_j)_{r+w} - (S_iS_j)_r$$

Each window yields values θ_r, i'_r of azimuth and apparent angle of incidence. The output values, averaged over n windows, are

$$\left.\begin{aligned} \bar{\theta} &= (1/n)\sum_{r=1}^{n}\theta_r \\ \bar{i} &= \sin^{-1}[(V_S/V_P)\sin(\overline{i'}/2)] \end{aligned}\right) \qquad (6.5.8)$$

where

$$\overline{i'} = (1/n)\sum_{r=1}^{n} i_r$$

95% confidence limits on θ, i' are calculated by Fisher statistics (FISHER,1953). Values of θ, i' are rejected for any window over which the solution for C has rectilinearity RL < 0.85 (as computed from Equation 6.5.5).

Note that Equation 6.5.6 is not single-valued. It has two solutions in the range $0° < \theta < 360°$, differing by 180°. The degeneracy is removed by considering the sign of $\overline{VR}$, which must be positive for the correct azimuth (see Section 6.1). MOTION effects this by taking the value of θ for which $v_V > 0$.

Programme MOTION has as input the digitised seismic records stored on half-inch magnetic tape (Section 3.8). On these records the event onset is preceded by approximately 150 samples of noise, of which MOTION uses the first 100 to compute the noise powers

$$P_{i,j} = 0.01\sum_{k=1}^{100} S_{i,k}S_{j,k} \qquad \text{for } i = 1 \text{ to } 3,\ j = i \text{ to } 3$$

where 1 = E-W component, 2 = N-S, 3 = Vertical.

On many records the rectilinearity of these initial samples is high. This does not invalidate the earlier

statement that background noise is likely to be unpolarized, since on quiet records the background traces are dominated by residual flutter. It does however preclude automatic recognition of the event onset by a sudden increase in the rectilinearity function, RL. The criterion for event onset used by MOTION is the signal to noise power ratio on the vertical channel,

$$SNR_3 = Var[V]/nP_{3,3}$$

where Var[V] is defined over a window of length n samples.

Values of θ, i' computed by MOTION begin to be used in the formulation of the output means $\bar{\theta}$, $\bar{i}$ only at the first window over which $SNR_3 > 50$, and provided the rectilinearity criterion is also satisfied.

It is useful to have an estimate of that part of the azimuth error caused by correlated noise or flutter. This is obtained by differentiation of Equation 6.5.2,

$$\theta = \tan^{-1}(E.V/N.V)$$

where the implied summation signs have been omitted for simplicity and F = V; whence

$$d\theta = \frac{(N.V)d(E.V) - (E.V)d(N.V)}{(E.V)^2 + (N.V)^2} \qquad (6.5.9)$$

Now E, N, V consist of the superposition of seismic signal and noise. Thus we may write

$$E.V = (E_S + E_N).(V_S + V_N)$$
$$= (E_S.V_S) + (E_N.V_N)$$

the cross terms being zero since we assume that the noise is uncorrelated with the signal. d(E.V) can be identified with the correlated noise component $(E_N.V_N)$, i.e. the

correlation E.V when no signal is present.

In terms of the covariance matrix, C, the error estimate equivalent to Equation 6.5.9 is

$$d\theta_{noise} = \frac{w(C_{23}P_{13} + C_{13}P_{23})}{C_{13}C_{13} + C_{23}C_{23}} \qquad (6.5.10)$$

This quantity is also evaluated by MOTION.

As a comprehensive check on the phases of arrivals the functions θ, i', RL, B_{EN}, B_{EV}, B_{NV}, $d\theta_{noise}$ may be output for each successive window down the record. A typical section of output is discussed in the next sub-section. The variations of θ and i' as functions of time are of particular interest, and may allow arrivals to be picked later in the P coda.

6.5.3 Application of MOTION to ESP Seismic Records

About a hundred seismic records were processed using programme MOTION. Reliable values of azimuth and angle of incidence were obtained only for events where the signal to noise ratio exceeded 6 on both V and R components. For less well recorded events (for which the event onset criterion was relaxed) the rectilinearity condition was seldom satisfied, and where values of θ, i were output they had excessively large confidence limits of 50° or greater. Results were obtained for 57 events recorded at Mille, Tendaho and Serdo. 9 events from Det Bahri were also processed, but had insufficient rectilinearity because of high background noise on the horizontal seismometer traces.

Window lengths of approximately one cycle of the first

arrival (10 to 15 samples) were used for evaluating the covariance matrix. Too long a window will soon begin to sample phase arrivals other than the first P onset, and will be less likely to pick out later rectilinear phases. Too short a window will not adequately smooth the data. Two determinations of $\bar{\Theta}$, $\bar{I}$ were made, with window lengths (n) of 10 and 25 samples. The pair of values giving the lower errors was accepted. The azimuth values Θ were found to begin to drift (indicating that unwanted phases were being encountered) after 10 to 25 successive windows following recognition of the event onset. After 15 to 30 windows (spanning 0.25 to 0.4 s after the first arrival for window length 10) the rectilinearity of the record would drop sharply. A simultaneous increase in the angle of incidence indicated the arrival of scattered waves. High (i.e. shallow) angles of incidence were found throughout most of the P coda of each event, suggesting its dominance by seismic energy scattered at shallow depths beneath the receiving stations.

The above points are apparent in Figure 6.5.2, a graph of the output from MOTION for the first 1.8 s of a well-recorded event. The figure shows the values of the angle of incidence, azimuth, rectilinearity (RL) and E-N coherence function (B_{EN}) for all windows having RL > 0.85. The first arrival is highly rectilinear over 15 successive windows, all of which give $\Theta = 28 \pm 7^{\circ}$. Note the azimuth discontinuities of $\pm\pi$ before and after the windows which sample the first P phase. As explained in Section 6.5.2,

FIGURE 6.5.2

EXAMPLE OF INFORMATION OUTPUT FROM PROGRAMME MOTION

(Event T55: window length Ø.1 s,
3-component azimuth 28°, distance ≈ 35 km)

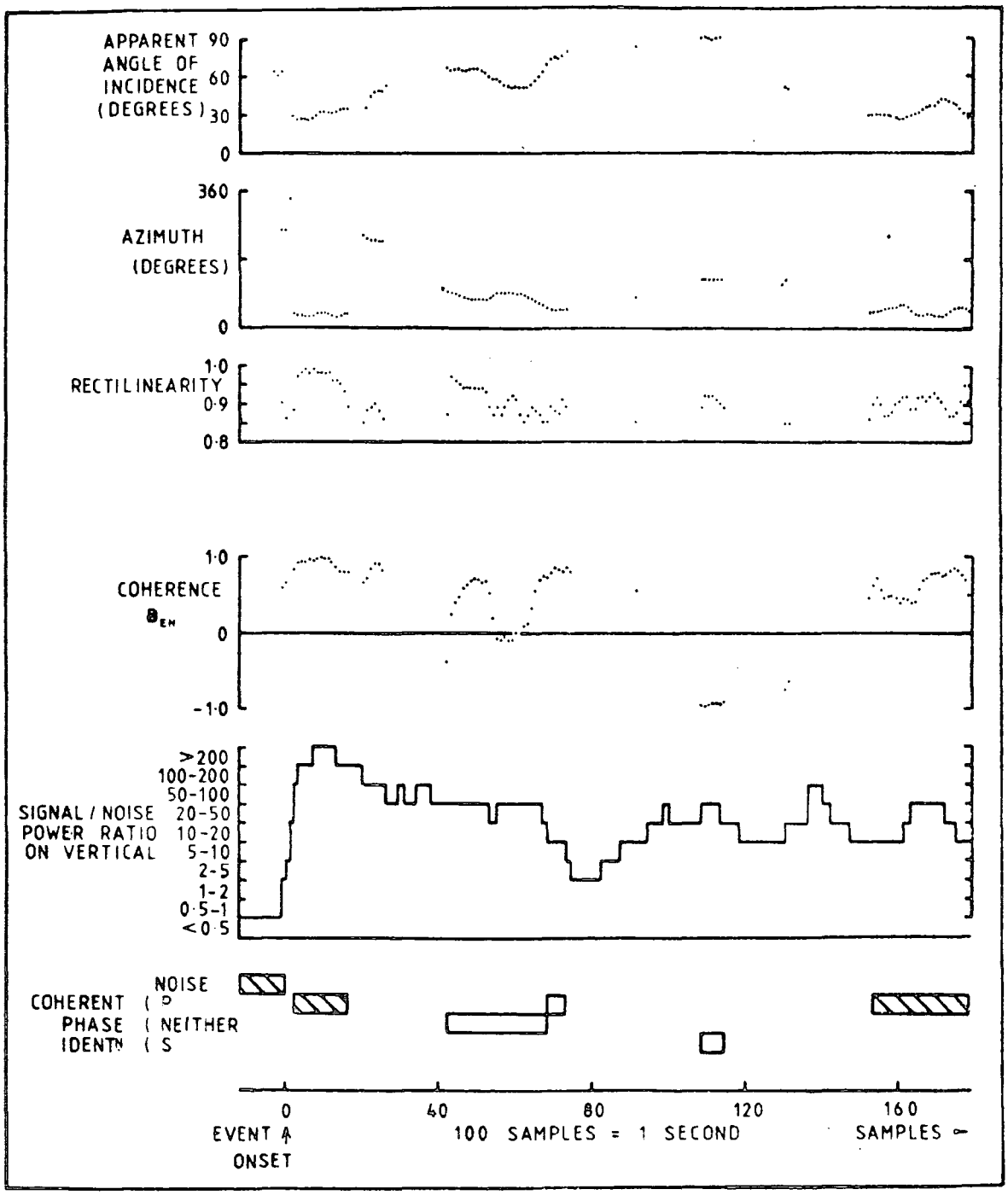

these correspond to changes in the sign of the eigenvector component v_V, which is used by MOTION to distinguish between the two azimuths, θ and $\theta + \pi$, which satisfy Equation 6.5.6.

The filter has the ability to detect later arrivals. The rectilinear section of record beginning at about 1.55 s is identified from B_{EN} as a longitudinal phase arrival. It has the same azimuth as the first arrival and a very similar angle of incidence. The arrival is unclear on the original seismic traces (Figure 6.5.3), but has been picked as a distinct onset on other records of the same earthquake sequence and is used in the analysis of Section 4.3.

The coherent section of record at about 115 samples is identified as transverse from the large negative value of B_{EN} and the apparent azimuth, which differs from the first arrival azimuth by approximately 90°. However, it cannot be directly associated with the first arrival (for example, as a P-S conversion) because it has a near-horizontal angle of approach. The same applies to the other unshaded coherent phases identified in Figure 6.5.2.

Several of the later onsets discussed in Section 4.3 were verified as P phases using programme MOTION. Others did not satisfy the rectilinearity criterion, because of perturbation due to other components of the P coda. For detecting S arrivals, MOTION was more successful for events recorded at lower amplitudes or greater distances. Any clipping of the signal waveforms will evidently invalidate the results. The majority of events used for azimuth determination had S-P times of 10 s or less. At these small

FIGURE 6.5.3

ORIGINAL SEISMIC TRACES, EVENT T55

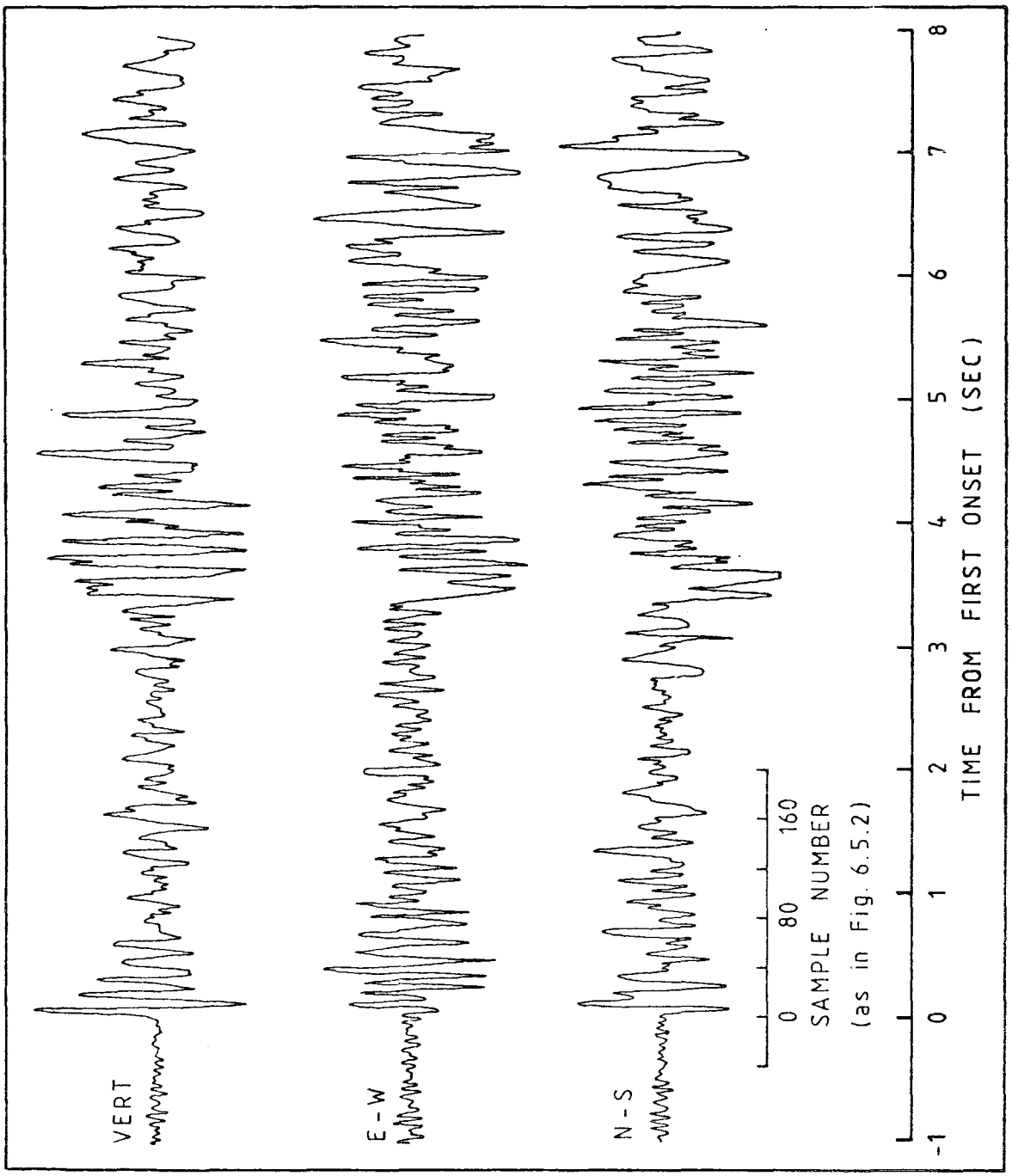

distances, many records with adequate signal to noise ratios for azimuth determination had (S arrival) to (tail of P coda) amplitude ratios of 3 or less.

6.6 Results, with Discussion of Possible Sources of Inaccuracy

6.6.1 Introduction

Azimuths (θ_3) and angles of incidence output from MOTION are listed, with error estimates, in Table 6.6.1. For comparison, the multi-station azimuths (θ_S) obtained in Chapter 4 are also given. The table shows azimuth deviations, $\Delta\theta = \theta_S - \theta_3$, which consistently exceed the calculated error estimates. In addition, the standard errors for the angles of incidence for groups of events (Table 6.6.2) are greater than the errors calculated for individual events (Table 6.6.1).

These discrepancies may result from one or more of the following factors:

(a) Local effects of superficial crustal structure beneath the recording stations;

(b) Effects on the wave paths of deeper structural inhomogeneities;

(c) Instrumental effects;

(d) Perturbation by noise;

and, in the case of $\Delta\theta$,

(e) Errors in θ_S.

Factors (c) to (e) are considered briefly in Sections

TABLE 6.6.1

AZIMUTHS AND ANGLES OF INCIDENCE

FROM THREE-COMPONENT ANALYSIS

EVENT	MULTI-STATION AZIMUTH θ_S	3-COMPONENT AZIMUTH θ_3	INCIDENT ANGLE	COMMENTS
M5	33.8	1.4+/- 9.9	18.8+/- 3.6	
M11	102.6	57.7+/- 6.8	22.8+/- 2.5	
M26	29.1	21.5+/- 6.5	16.6+/- 2.1	
M27	29.4	--- ---	--- ---	IN TAIL OF M26
M48	44.2	29.3+/- 5.8	19.5+/- 2.5	
M125	299.2	312.1+/- 4.9	14.6+/- 1.4	
M144	300.4	311.0+/-14.8	19.0+/- 4.2	
M145	298.9	319.0+/- 6.7	18.8+/- 2.5	
M153	300.1	318.4+/- 6.0	26.3+/- 3.0	
M270	142.3	181.0+/- 5.5	33.7+/- 3.3	SATURATED RECORD
M281	---	173.4+/- 5.8	18.6+/- 2.1	RECORDED AT M ONLY
M283	---	175.4+/- 4.8	24.6+/- 2.2	RECORDED AT M ONLY
M289	---	167.0+/- 4.7	26.1+/- 2.3	RECORDED AT M ONLY
M434	2.0	10.6+/-10.1	17.0+/- 3.4	
M464	57.6	51.9+/- 3.8	45.0+/- 2.4	SATURATED RECORD
M467	59.2	62.1+/-11.7	11.4+/- 2.7	
M481	58.8	65.7+/- 9.0	17.6+/- 3.1	
T26	18.0	74.3+/- 9.2	15.4+/- 2.8	SLIGHTLY SATURATED
T27	18.6	--- ---	--- ---	IN TAIL OF T26
T29	36.4	41.6+/- 3.7	23.7+/- 1.7	
T42	2.5	18.3+/- 4.2	17.2+/- 1.4	
T47	57.4	29.5+/- 7.6	17.4+/- 2.6	
T52	14.1	35.2+/- 4.2	24.5+/- 1.9	
T63	12.1	31.4+/- 2.8	25.3+/- 1.3	
T293	26.2	17.4+/- 7.4	21.4+/- 3.1	
T125	280.9	305.3+/- 3.6	21.0+/- 1.5	
T145	280.9	289.2+/- 5.4	28.4+/- 2.8	
T154	280.8	302.6+/- 4.8	18.6+/- 1.8	
T164	281.1	313.3+/- 6.5	39.9+/- 6.0	
T434	329.0	359.0+/- 3.9	23.2+/- 1.7	
T437	328.9	347.2+/- 6.7	19.8+/- 2.6	
T455	72.3	100.0+/-15.6	10.5+/- 3.3	
T467	72.3	84.3+/- 3.3	13.3+/- 0.9	
T481	71.7	85.6+/- 7.2	11.0+/- 1.6	
T494	45.4	83.0+/- 8.2	16.0+/- 2.6	
S3	262.0	250.2+/-11.6	27.4+/- 5.9	
S4	253.6	261.0+/- 7.6	32.7+/- 4.5	
S8	265.4	256.0+/- 5.7	32.8+/- 3.4	
S26	261.8	247.8+/-13.5	29.0+/- 8.5	
S27	261.4	--- ---	--- ---	IN TAIL OF S26
S293	255.0	284.0+/-10.5	17.5+/- 3.6	
S294	255.0	253.2+/-10.9	25.4+/- 5.2	
S125	267.4	237.8+/- 4.2	18.2+/- 1.5	
S126	268.8	154.6+/- 8.2	27.6+/- 4.2	SATURATED RECORD
S129	268.3	245.5+/-13.1	22.4+/- 5.6	SATURATED RECORD
S170	165.8	201.1+/-48.4	13.5+/-12.9	
S171	165.8	181.9+/-42.6	9.3+/- 7.9	
S180	---	209.2+/-19.3	16.0+/- 6.1	RECORDED AT S ONLY
S182	---	208.8+/-13.6	19.9+/- 5.3	RECORDED AT S ONLY
S455	123.0	98.5+/-22.6	6.7+/- 3.0	SATURATED RECORD, CLOSE
S452	121.9	--- ---	--- ---	CLOSE EVENT
S457	260.1	--- ---	--- ---	CLOSE EVENT
S464	135.9	--- ---	--- ---	SATURATED RECORD, CLOSE
S477	111.6	88.7+/-20.8	14.0+/- 5.8	CLOSE EVENT
S466	349.7	343.3+/-15.2	7.6+/- 2.3	CLOSE EVENT
S467	122.8	--- ---	--- ---	SATURATED RECORD, CLOSE
S496	256.0	250.7+/-16.8	23.7+/- 7.6	CLOSE EVENT

Multi-station azimuths have probable errors of approximately +/-1.5° (Sections 4.7, 6.6.4).

TABLE 6.6.2

ANGLE OF INCIDENCE DATA BY EVENT GROUPS

Station	Group	Mean angle of Incidence (Degrees)	Approximate Azimuth* (Degrees)	Approximate P to S Time (Sec)
Mille	a	19.4+/- 2.6	020-045	7.8-8.2
Mille	c	22.7+/-13.1	058	12.3
Mille	d	23.1+/- 4.0	170	4.7
Mille	e	19.9+/- 5.9	299	15.3
Tendaho	a	21.2+/- 3.8	012-057	2.9-4.1
Tendaho	b	21.5+/- 2.4	329	5.3
Tendaho	c	11.6+/- 1.5	072	8.4
Tendaho	e	19.9+/- 9.2	281	17.2
Serdo	a	27.5+/- 5.7	253-265	4.2-5.0
Serdo	c,g	13.0+/- 7.8	various	2.5-3.3
Serdo	f	14.2+/- 5.3	166	8.1
Serdo**	e	18.2	238	22.1

*This column gives the ranges of multi-station azimuths, θ_s, for the events of each group.

**Only one reliable event in this group. Not included in Figure 6.6.3.

Key to event groups (see also Figure 6.7.2).

(a) NW Tendaho graben.
(b) N of Mille
(c) SE of Serdo.
(d) Allallobeda graben.
(e) Waldia (W Ethiopian escarpment).
(f) S of Serdo.
(g) Kurub volcano area.

6.6.2 to 6.6.4. Section 6.6.5 discusses the more important points relating to geological structure. It is shown that the poor correlation between the results of this chapter and those of Chapter 4 is caused by the unrealistic assumption of laterally homogeneous structure below Afar; and in particular to local scattering effects, to which the three-component method is extremely sensitive.

6.6.2 Perturbation by Noise and Flutter

The azimuth error due to noise and flutter, $d\theta_{noise}$, computed by MOTION (Equation 6.5.1Ø) is less than 5° for all events used in this section. The signal to noise amplitude ratios exceed 6 on R and 9 on V. The observed variations in azimuth and angle of incidence cannot be attributed to noise or to residual flutter.

6.6.3 Instrumental Effects

Mis-match between the seismic traces of any three-component set of instruments will cause systematic errors in the azimuth and/or angle of incidence. For example, if one vertical seismometer gain is anomalously high, angles of incidence computed at that station will be systematically too low; or if an E-W seismometer is outputting a low amplitude signal, azimuths will be deviated towards the N-S axis.

Tests reported in Chapters 2 and 3 have shown no indication of differential instrumental response. Furthermore, the present data set shows that no individual

station exhibits anomalous behaviour.

6.6.4 Errors in the Multi-Station Azimuth

Most of the events used here have been well recorded at 3 or 4 stations. Their absolute azimuth error has been estimated in Section 4.7 as 1.5°. Systematic variations in $\Delta\theta$ might derive from errors in the multi-station azimuth arising from the unjustified assumption of a laterally homogeneous crust. However, within each group the waveforms of events are so strikingly similar that they strongly support the tight clustering of epicentres found in Chapter 4. The scatter in $\Delta\theta$ is very largely caused by the three-component values.

6.6.5 Structural Considerations

Sections 6.6.2 to 6.6.4 have eliminated non-structural sources as major causes of the observed fluctuations in azimuth and angle of incidence. We now examine the structural effects, factors (a) and (b) in the introduction to this section, by reference to Figures 6.6.1 to 6.6.3, which show graphically the important features of Tables 6.6.1 and 6.6.2. Figure 6.6.1 shows a scatter of angle of incidence as a function of S-P time that, if it is caused by real structural effects, implies a highly three-dimensional structure.

Theoretical plots of angle of incidence against distance (or S-P time) are shown in Figure 6.6.4. For a crust of constant velocity (Figure 6.6.4a),

FIGURE 6.6.1

PLOT OF ANGLE OF INCIDENCE AGAINST S-P TIME

FOR EVENTS RECORDED AT ESP STATIONS

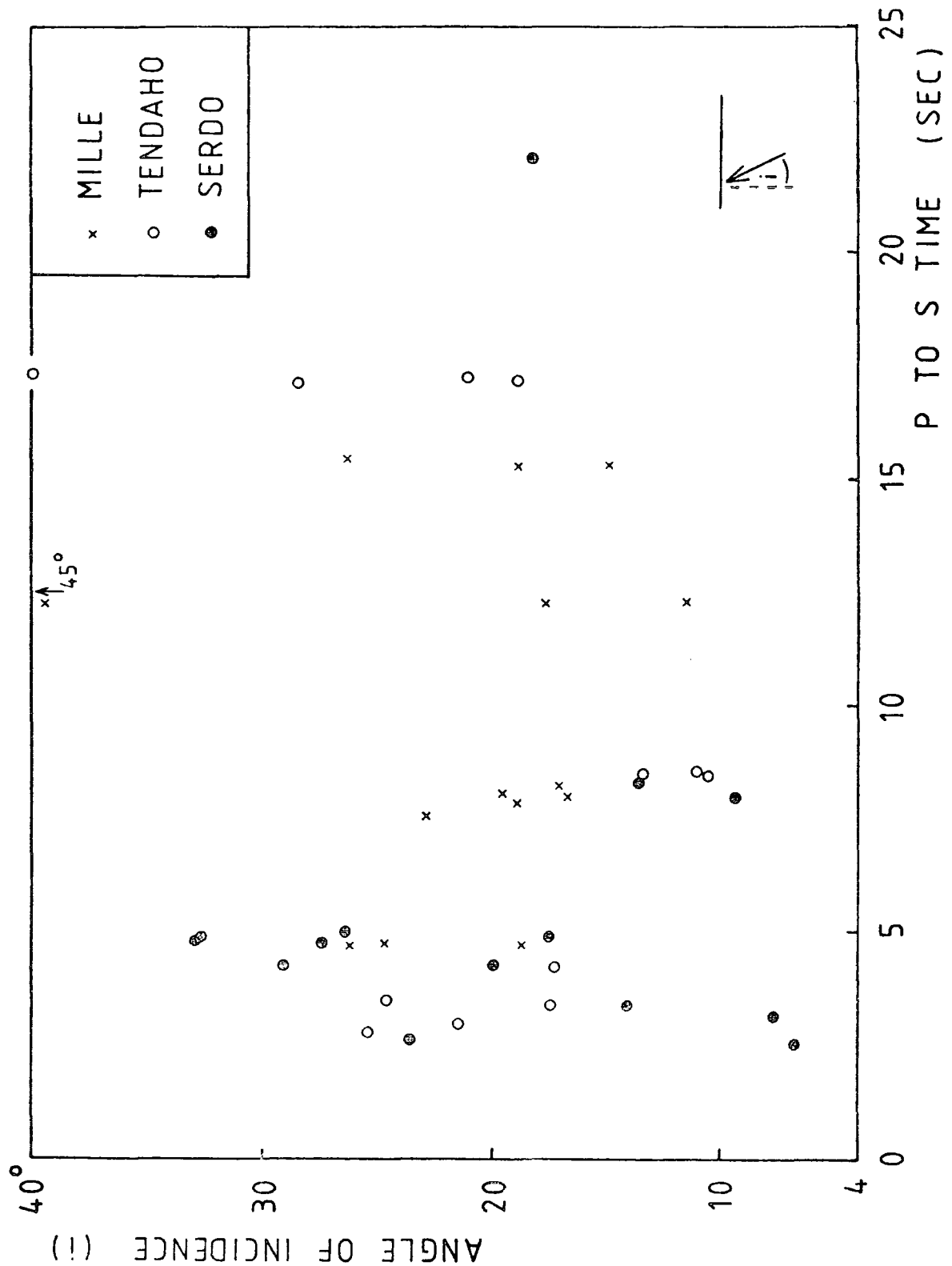

FIGURE 6.6.2

PLOT OF $\Delta\theta = \theta_S - \theta_3$, AGAINST θ_S, FOR EVENTS RECORDED AT ESP STATIONS

θ_S is azimuth obtained from P and S arrivals at more than one station

θ_3 is azimuth from particle motion at a single station Full circles represent Waldia swarm events (epicentral distance greater than 100 km). All other events (open circles) are closer than 100 km).

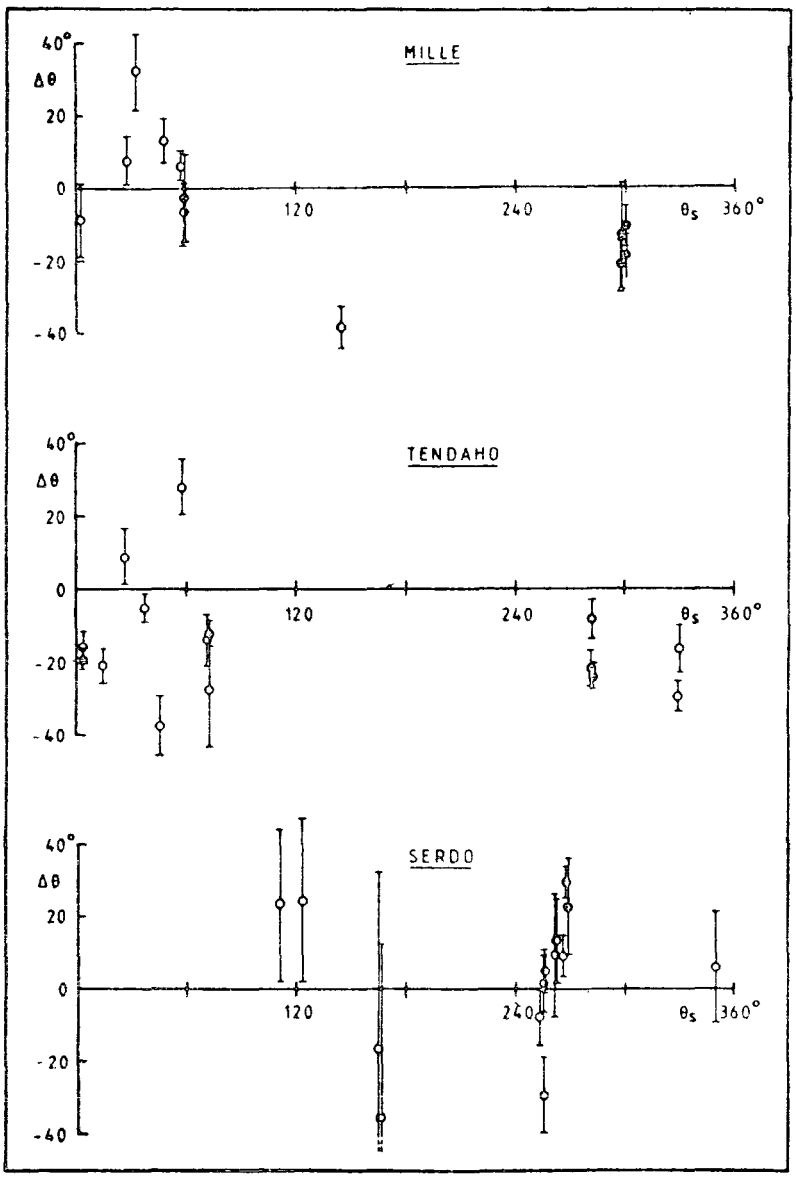

FIGURE 6.6.3

PLOT OF ANGLE OF INCIDENCE AGAINST MULTI-STATION AZIMUTH FOR GROUPS OF EVENTS

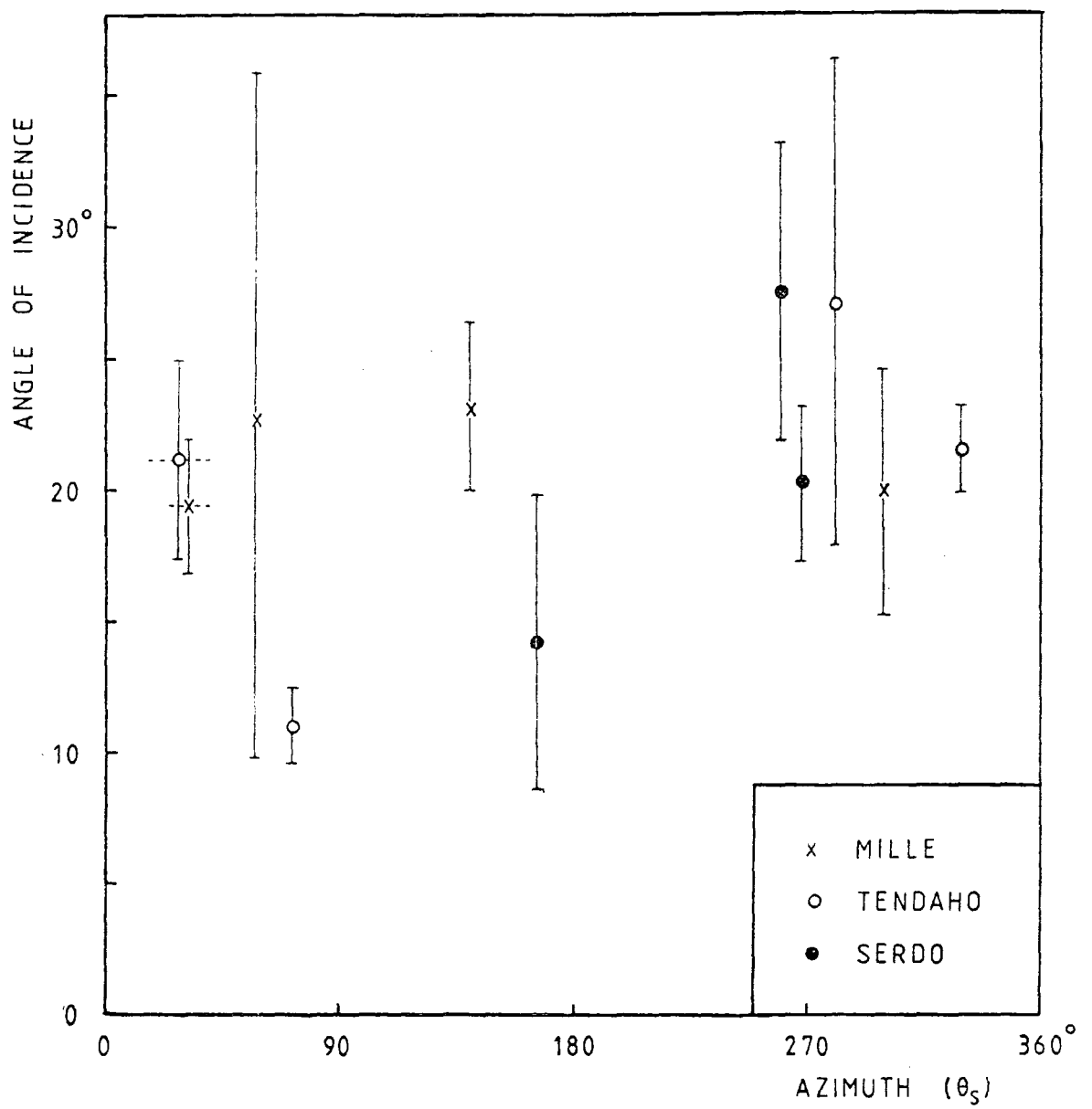

FIGURE 6.6.4

THEORETICAL PLOTS OF ANGLE OF INCIDENCE AGAINST DISTANCE FOR LATERALLY HOMOGENEOUS STRUCTURAL MODELS

(a) constant velocity structure
(b) diagram to clarify the text
(c) layered structure

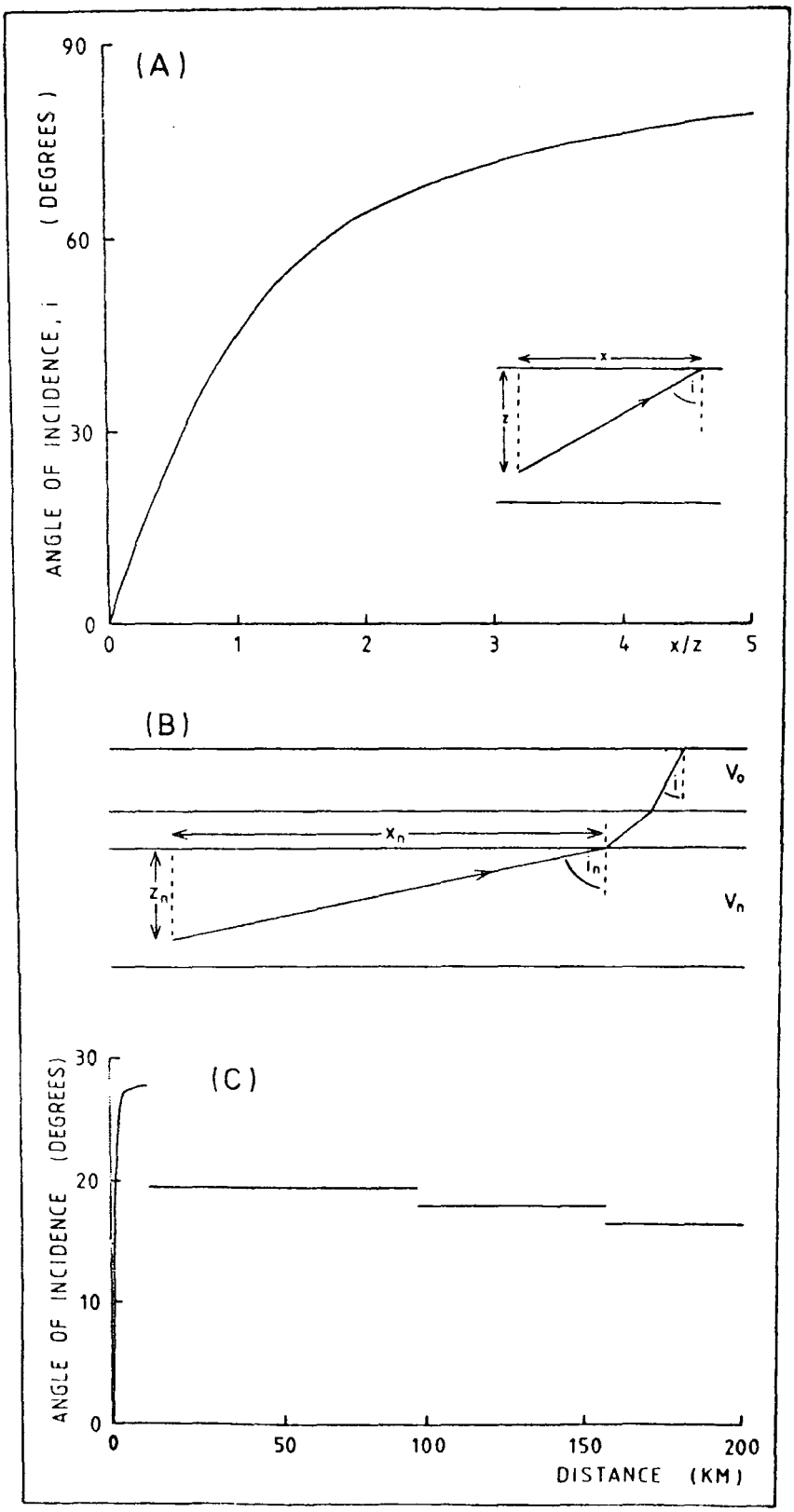

$$i = \tan^{-1}(x/z)$$

For a layered V(z) model, with the focus in layer n,

$$\sin(i)/\sin(i_n) = V_\emptyset/V_n \qquad \text{(Figure 6.6.4b)}$$

But $\tan(i_n) = x_n/z_n$,

$$\therefore i = \sin^{-1}[(V_o/V_n)(x_n/(x_n^2 + z_n^2)^{1/2})] \qquad (6.6.1)$$

tending to $\sin^{-1}(V_\emptyset/V_n)$ for $x_n >> z_n$. Equation 6.6.1 is illustrated in the distance range below 12 km in Figure 6.6.4a, which is drawn for an event with 1.Ø km focal depth using the preferred structural model of Chapter 4, overlain by a superficial layer of velocity 2.1 km s^{-1}. For increasing distances beyond 12 km the first arrival is a head wave in progressively deeper layers of the structure. Over the distance range that the first arrival is a head wave in a given layer, the angle of incidence is distance-independent (Figure 6.4.4c) and has the appropriate value given in Table 6.6.3, row 3. Figure 6.6.4 is easily modified for a structure where the velocity increases continuously with depth, since such a structure is equivalent to many thin layers each having a discrete velocity.

Figure 6.6.1 does not resemble the simple theoretical form for a layered V(z) model shown in Figure 6.6.4c. Some scatter in angle of incidence (i) as a function of epicentral distance (or S-P time) is to be expected due to the different focal depths (z) of ESP events. For very close events, where the direct wave is the first arrival, the dependence of i on z is given by Equation 6.6.1. i is independent of z for head waves, but Figure 6.6.1 will

still show scatter at larger S-P times because crossover distances (or S-P times) diminish with increasing z. Using the preferred V(z) model of Figure 4.3.6c, overlain by a superficial layer with velocity 2.1 km s^{-1} and arbitrary thickness 300 m, Figure 6.6.5 shows the theoretical scatter due to the observed focal depth variations (0 to 5 km) for events within Afar. This is much less than the observed scatter (Figure 6.6.1), which must therefore largely be caused by superficial scattering and/or deeper structural inhomogeneities. If the latter is the primary cause, systematic azimuthal variations of $\Delta\theta$ and angle of incidence are to be expected.

TABLE 6.6.3

CRITICAL ANGLES: THEIR DEPENDENCE ON SURFACE VELOCITY

Velocity of Surface Layer (km/sec)	Critical Angle in Degrees for Refraction at Deeper Boundaries of Given Velocities (km/sec)			
	4.4	6.2	6.9	7.4
4.4		45.2	39.6	36.5
3.0	43.0	28.9	25.8	23.9
2.1	28.5	19.8	17.6	16.5
1.5	19.9	14.0	12.6	11.7

$\Delta\theta$ (Figure 6.6.2) has no statistically significant azimuthal dependence. Events arriving at the same station

FIGURE 6.6.5

THEORETICAL SCATTER IN ANGLE OF INCIDENCE AGAINST S-P TIME CAUSED BY VARIATIONS IN EVENT FOCAL DEPTHS

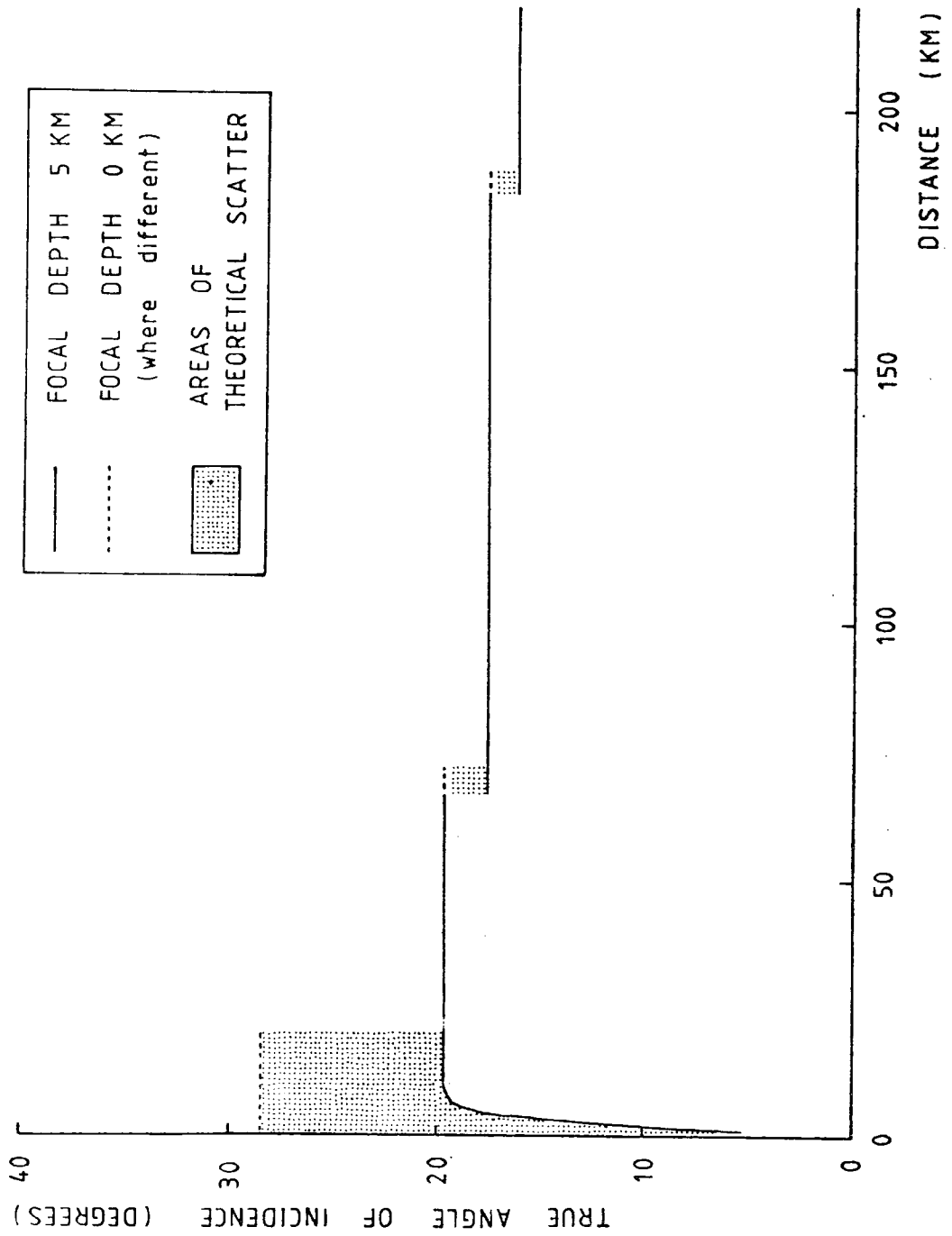

from similar azimuths show large fluctuations in $\Delta\theta$; and the Waldia swarm events (full circles), which have similar azimuths from all three stations, show negative $\Delta\theta$ at Mille and Tendaho but positive $\Delta\theta$ at Serdo. Figure 6.6.3 relates angle of incidence to azimuth, θ_s. The plotted points mark the angles of incidence for the groups of events defined by Table 6.6.2, while the error bars represent the standard deviations within these groups. The large size of the error bars of Figure 6.6.3, and the paucity of points, emphasise that three-dimensional modelling is not justified.

By excluding other sources of data scatter, it has been demonstrated that the variation in three-component estimates of azimuth and angle of incidence arises primarily from crustal inhomogeneities beneath the recording stations so local and superficial that they cannot be meaningfully modelled. They create reverberations (i.e. signal generated noise) which scatter part of the primary energy by refractions, reflections and diffractions, distorting even the first cycles of the recorded seismic arrivals. Figures 6.6.2 and 6.6.3 show that the angles of incidence are consistently and significantly smaller than those that would result from head wave arrivals on the preferred V(z) model (Figure 4.3.6c). If this model were applied directly, all the events would be located in the lower crust or the mantle. This is contrary to the findings of Chapter 4, where it was shown that all events within Afar have upper crustal foci, and that the large majority of first arrivals are likely to be head waves.

Chapter 4 did not consider thin, shallow surface layers. These have no significant effect on the multi-station locations, but affect the three-component angle of incidence profoundly. A low velocity surface layer will cause the incident waves to be deviated towards the normal, to a dramatic degree if the velocity contrast is substantial (Table 6.6.3). The observed low angles of incidence can only be satisfactorily explained by such a low velocity layer. Instrumental effects and noise perturbation have already been ruled out. A lower crustal or upper mantle source is impossible: to obtain a head wave as an arrival at an angle of 20° through a surface velocity of 4.4 km s^{-1} requires a refractor with a velocity in excess of 13 km s^{-1}. Moreover, low surface velocities are very probable for the lavas (with possible intercalated sediments) on which the ESP stations are sited.

The range of values of angle of incidence can be used to place limits on the velocity of the surface layer, which is assumed to overlie the structure of Figure 4.3.6c. If the first arrivals for event group c at Tendaho (i=11.6°, Table 6.6.2) and group a at Serdo (i=27.5°) both result from head waves in a layer of velocity 6.2 ± 0.1 km s, as deduced in Chapter 4, the corresponding surface velocities are 1.3 ± 0.1 km s^{-1} and 3.3 ± 0.2 km s^{-1}. These represent the extreme values indicated by the data (optimum values for each station are presented in Section 6.7). Note that group a at Serdo is too distant for the larger incident angles of their first arrivals to be explained as direct

waves or wide-angle reflections.

Although it has been shown that scattering is the prime cause of the form of Figures 6.6.1 to 6.6.3, we conclude this section by examining the underlying systematic variations that would be observed due to more profound lateral structural variations. The ESP network is such that it is possible, in theory, to detect lateral structural variations across the Tendaho graben. Seismic events occurring around Tendaho can be located from P and S arrivals at the trio of stations west of the graben (Figure 6.6.6). The azimuth and angle of incidence relative to Serdo of the same events can then be obtained by analysis of the complete ground motion recorded at Serdo. Systematic variations from the expected values may be attributable to lateral structural variations.

We examine briefly the consequences for θ_3 and i of two types of lateral structural inhomogeneity: a dipping layer, and a lateral velocity boundary, for instance the edge of a basaltic intrusion. Effects of lateral inhomogeneities on apparent velocity have already been mentioned in Section 4.5.

A dipping layer will have little effect on the apparent azimuth, θ_3. The effect on the angle of incidence, as a function of azimuth, is illustrated in Figure 6.6.7. It is clear that an approximately cosinusoidal relationship exists,

$$i(\theta) = i_c + d\cos(\theta - \epsilon) , \qquad (6.6.2)$$

where $i_c = \sin^{-1}(V_\emptyset/V_1)$, d is the angle of dip and ϵ the

FIGURE 6.6.6

DIAGRAMMATIC REPRESENTATION OF LOCATION OF TENDAHO GRABEN, RELATIVE TO ESP STATIONS

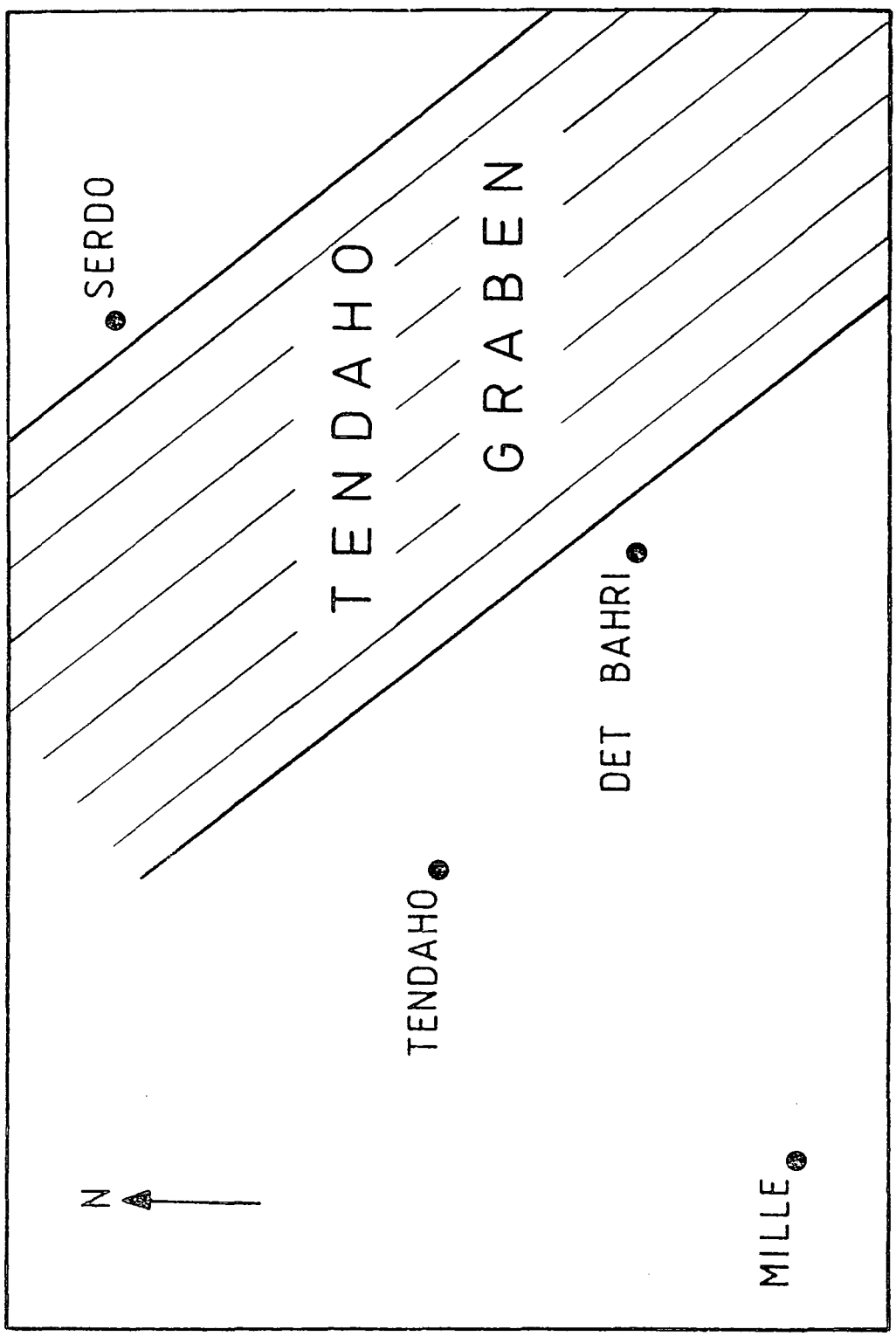

FIGURE 6.6.7

VARIATION OF ANGLE OF INCIDENCE WITH AZIMUTH FOR A LAYER DIPPING TO THE WEST

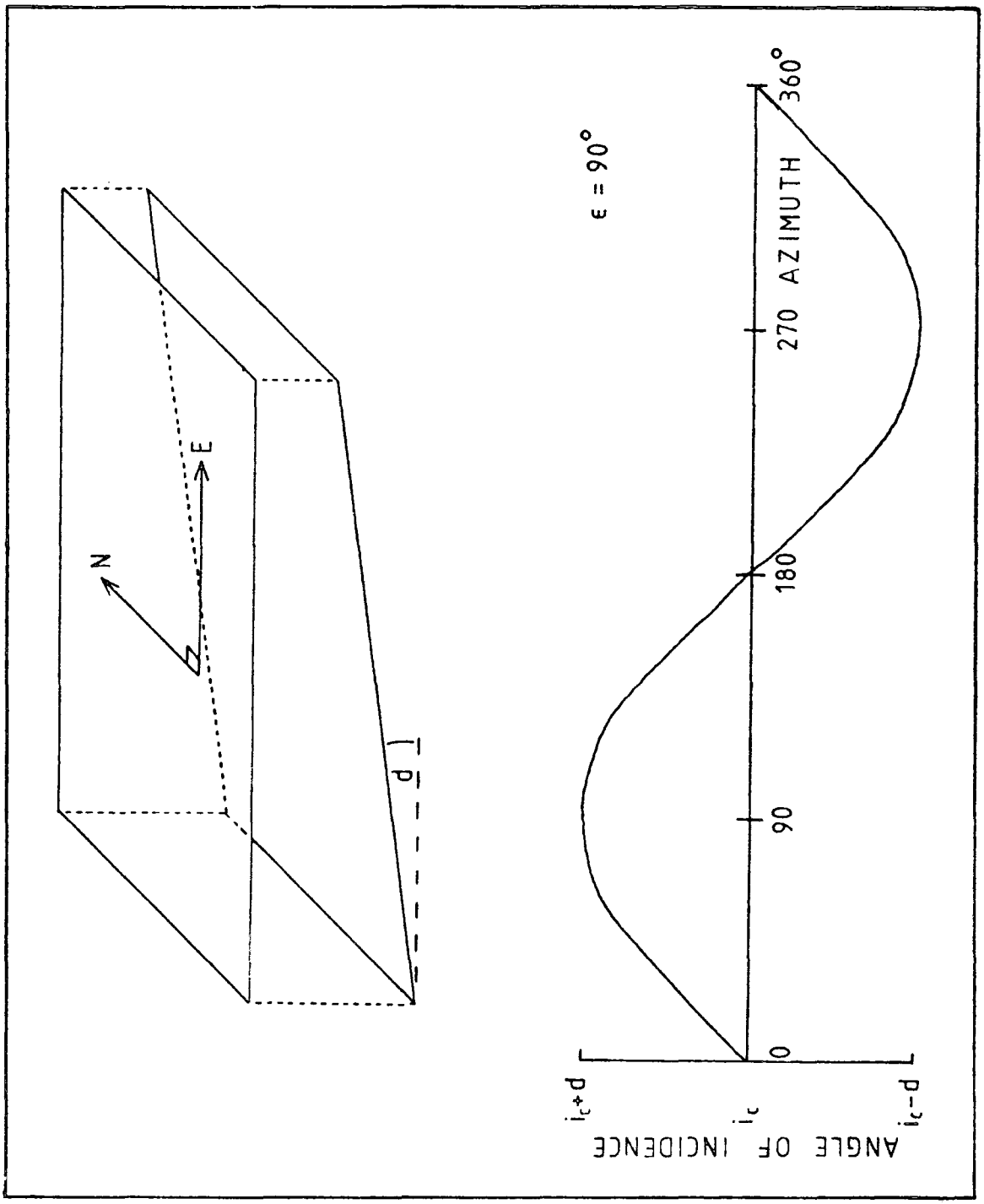

up-dip azimuth.

The consequences of lateral velocity boundaries are mathematically more complex. A simple example is given in Figure 6.6.8a, which assumes a N-S lateral velocity discontinuity. Suppose a seismic event has been located at E using Mille, Tendaho and Det Bahri station records. The true azimuth of the event from Serdo is θ_s, along SE. However, the angle of approach of the seismic waves, which is the value for azimuth that will be obtained from the ground motion at Serdo, is θ_3, along SB. With the notation of Figure 6.6.8a,

$$\theta_3 = 90^o - i_1 \qquad (6.6.3)$$

$$\tan(\theta_s) = EN/SN = \left[\frac{a\cos(i_1) + b\cos(i_2)}{a\sin(i_1) + b\sin(i_2)}\right]$$

$$\theta_s = \tan^{-1}\frac{a\sin(\theta_3) + b\cos(i_2)}{a\cos(\theta_3) + b\sin(i_2)} \qquad (6.6.4)$$

$$V_1/V_2 = \sin(i_1)/\sin(i_2) \qquad \text{(Snell's law)}$$

$$= \cos(\theta_3)/\sin(i_2)$$

$$i_2 = \sin^{-1}((V_2/V_1)\cos(\theta_3)) \qquad (6.6.5)$$

Eliminating i_2 from Equations 6.6.4 and 6.6.5, and rearranging,

$$\Delta\theta = \theta_s - \theta_3$$

$$= \tan^{-1}\left[\frac{\sin(\theta_3) + (b/a)(1 - [(V_2/V_1)\cos(\theta_3)^2]1/2]}{\cos(\theta_3)(1 + (bV_2/aV_1))}\right] - \theta_3$$

From Equation 6.6.4, $\theta_s \rightarrow \theta_3$ in the limit $(b/a) \rightarrow 0$. As $(a/b) \rightarrow 0$,

$$\theta_s \rightarrow \tan^{-1}(\cot(i_2)) = 90^o - i_2$$

and

FIGURE 6.6.8

EFFECTS OF LATERAL VELOCITY DISCONTINUITIES

ON SEISMIC WAVE TRAVEL PATHS

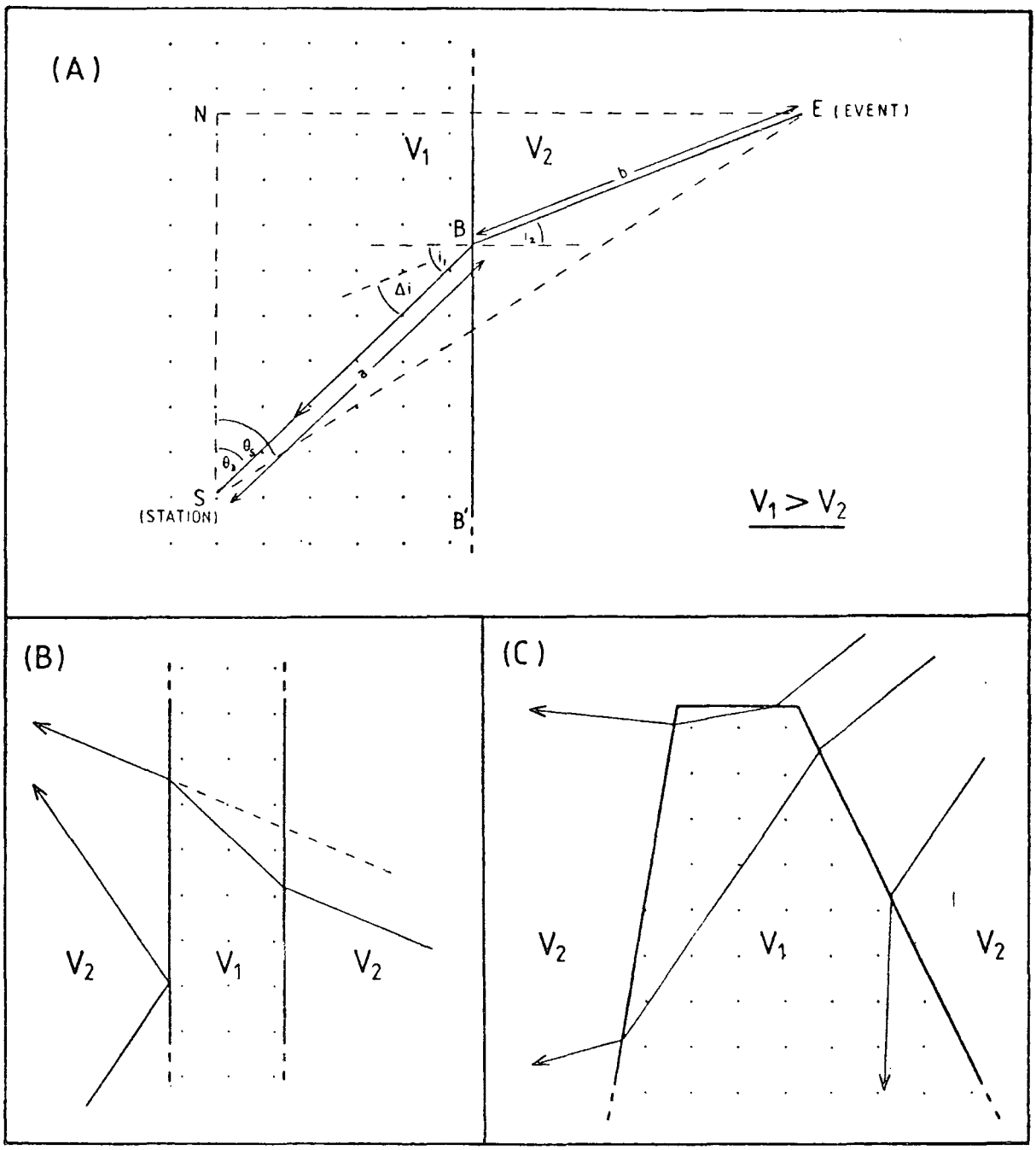

$$\Delta\theta \longrightarrow 90^\circ - i_2 - \theta_3 = i_1 - i_2 = \Delta i ,$$

its maximum value. Thus

$$\Delta\theta = 90^\circ - \theta_3 - \sin^{-1}((V_2/V_1)\cos(\theta_3)) \qquad (6.6.6)$$

For $\theta_3 = 45^\circ$ and $V_2/V_1 = 0.9$, $\Delta i = 10.5^\circ$.

In the extreme case as $a \longrightarrow 0$ and $\theta_3 \longrightarrow 0^\circ$,

$\Delta\theta \longrightarrow 90^\circ - \sin^{-1}(V_2/V_1) = 25.8^\circ$ for $(V_2/V_1) = 0.9$.

The case $a<<b$, $(V_2/V_1) = 0.9$ (Figure 6.6.9a), where the boundary has azimuth ϵ, is illustrated graphically in Figure 6.6.9b. Such a velocity contrast is geologically reasonable, and the azimuth disparity $\Delta\theta$ will be readily observable. In the case where the receiving station is in the higher velocity medium there is the possibility of head wave arrivals along the velocity discontinuity (Event 2, Figure 6.6.9c). If Figure 6.6.8a were viewed in section, instead of in plan, it would illustrate the analogous effect of a vertical velocity boundary on the angle of incidence. Figures 6.6.8b,c show further possibilities.

In general, a realistic three-dimensional structure will present a superposition of all the effects considered in this section, with the addition of the multiple reflections and/or diffractions that will arise in the models shown in Figures 6.6.8b,c. To locate events through such a three-dimensional structural model rapidly becomes a complex exercise in ray tracing.

Although the present data set is insufficient for the detection of lateral structural inhomogeneities, the method developed here has potential. The two limitations encountered are the poor distribution of naturally-occurring

FIGURE 6.6.9

EFFECTS OF LATERAL VELOCITY BOUNDARIES

(a), (c). Diagrams of a seismic station close to a lateral velocity discontinuity.
(b) Deviation ($\Delta\theta$) of azimuth caused by velocity discontinuity, for the case illustrated in (a), with $V_2/V_1 = 0.9$.

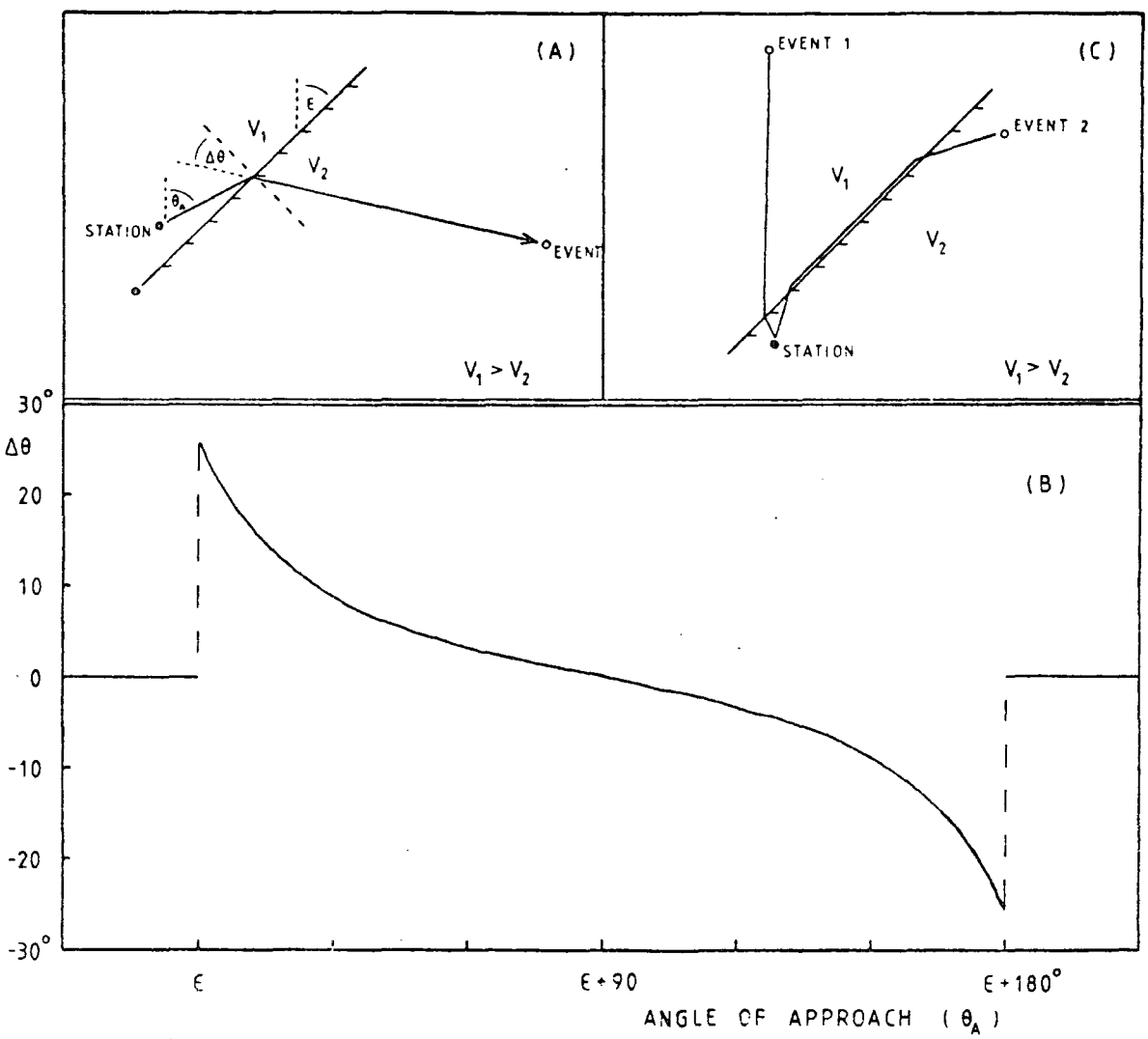

earthquakes over a comparatively short time period, and the probable errors in the hypocentres determined by other methods. These difficulties could be lessened in a future study by incorporating a network of explosive sources, and by increasing the number of seismic recorders.

6.7 Hypocentral Locations from Three-Component Analysis

Given the azimuth and angle of incidence of a seismic event at a recording station, and the S-P time, the hypocentre may be found by tracing the seismic ray back through the earth to its point of origin. For the ray tracing procedure to be successful the earth structure must be known. Erroneous structural models will give rise to systematic location errors. If the event locations are already known (as, for instance, in the case of explosions) the structural model may be optimised and refined to be consistent with them.

It is apparent from Section 6.6 that three-component hypocentral locations using the data of Tables 6.6.1 and 6.6.2 will be unsatisfactory. They are included here because they highlight the problems caused by structural inhomogeneity, especially the critical effects on the angle of incidence. There is every indication that the location method might be valuable in regions of less anomalous crustal structure.

This study has used a ray tracing programme written by Ms. Mary Rogan of Durham University for application to an n-layered ($n \leqslant 5$), laterally homogeneous earth structure.

We define

i = angle of incidence (to the vertical)

Δi = error in i

t_{PS} = S-P time

i_{cn} = critical angle for refraction at the interface between layers (n-1), n

t_n = travel time in layers Ø to n

The following ray path options are considered by the programme. They are shown diagrammatically in Figure 6.7.1.

(a) $i > i_{c1} + \Delta i$. Ray reflected at first interface.

(b) $i < i_{c4} - \Delta i$. Focus in bottom layer of structure.

(c) $i < i_{cr} - \Delta i$ and $t_{r-1} < t_{PS} < t_r$. Focus in layer n ($r < n$).

(d) $i - i_{cr} < \Delta i$. Ray is a head wave in layer r. In this case there is no unique solution. The programme computes the extreme possibilities d_1 and d_2. d_1 is the shallowest and closest possible hypocentre, such that the ray travels the minimum distance along the refractor. d_2 is the deepest, most distant solution.

The programme was applied using the azimuths and angles of incidence obtained with programme MOTION (Table 6.6.1), for all events on which S could be picked. The structural model was the preferred velocity/depth structure of Chapter 4 (Figure 4.3.6c), overlain by a Ø.1 km thick surface layer whose velocity was varied between 1.3 and 3.7 km s^{-1}, at Ø.2 km s^{-1} intervals. The value 2.1 km s^{-1} gave the set of focal depths least inconsistent with those

FIGURE 6.7.1

RAY PATHS CONSIDERED BY RAY TRACING PROGRAMME

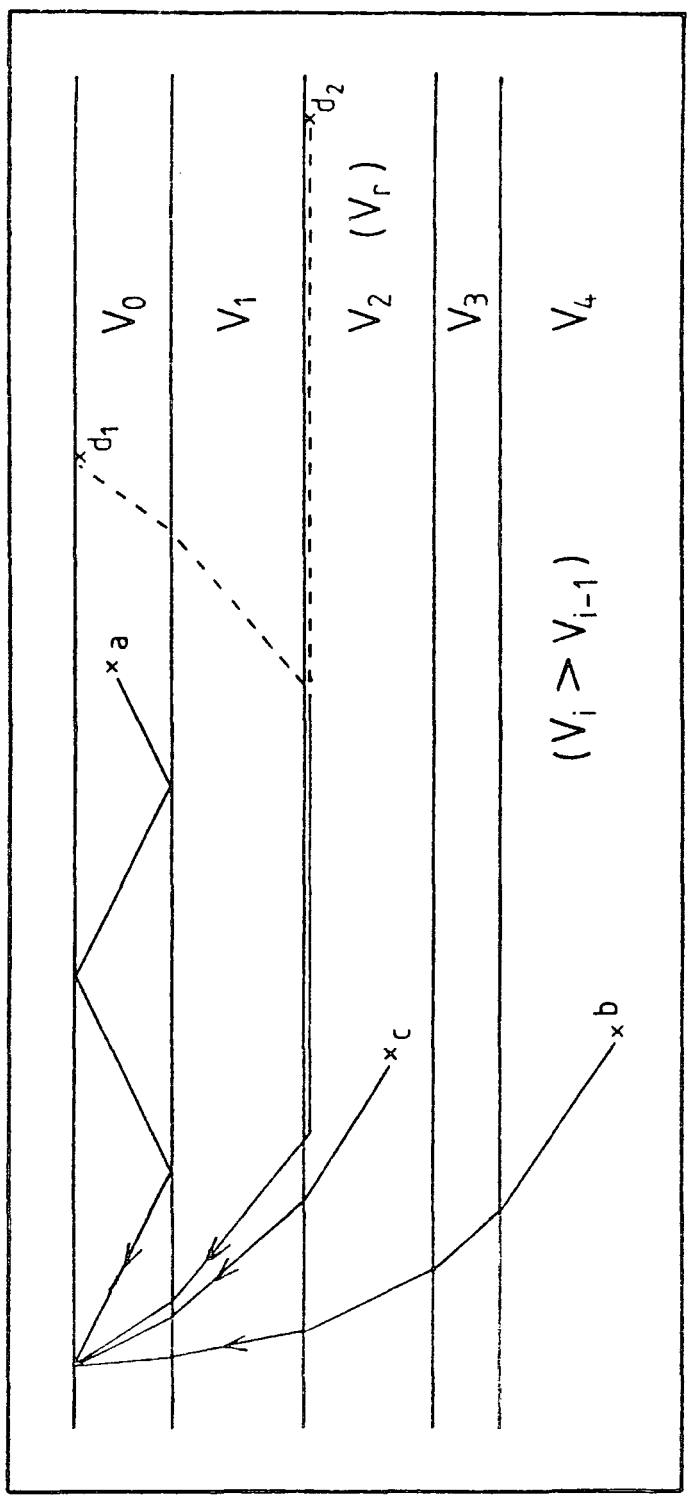

of Chapter 4. Table 6.7.1 shows that this velocity is reasonable, and demonstrates that there is no justification for using different surface velocities at different stations.

TABLE 6.7.1

MEAN DATA FOR EACH STATION, FOR EVENTS CLOSER THAN 100 KM

Station	Mean Angle of Incidence (Degrees)	Corresponding Surface Velocity (km/sec)
Mille	22.6+/-9.0	2.4+/-0.9
Tendaho	18.4+/-4.9	2.0+/-0.5
Serdo	19.7+/-9.2	2.1+/-0.9

The resulting hypocentres are listed in Table 6.7.2 and are compared in Figure 6.7.2 with those obtained in Chapter 4.

(1) The programme has effectively confirmed the assignation of the three previously unlocated events (group d) to the Allallobeda graben. This group of events is mapped in Figure 8.2.7.

(2) There is no systematic pattern to the differences between the two sets of solutions, as would be caused by lateral inhomogeneities at depth. In particular, there is no consistency between the locations of different events

TABLE 6.7.2

EARTHQUAKE HYPOCENTRES BY THREE-COMPONENT ANALYSIS

GRP	EVENT	AZIMUTH (degrees)	ANGLE OF INCIDENCE (degrees)	P TO S TIME (sec)	----HYPOCENTRE---- LAT (deg)	LONG (deg)	DEPTH (km)
a	M5	1.4	18.8	7.85	12.00	40.77	3.0
a	M26	21.5	16.8	7.93	11.94	40.96	15.0
a	M48	29.3	19.5	8.06	11.94	41.05	3.0
a	M11	57.7	22.8	7.56	11.60	41.05	2.1
b	M434	10.6	17.0	8.22	12.00	40.86	18.1
c	M464	51.9	45.0	12.28	11.56	40.93	0.0
c	M467	62.1	11.4	12.29	11.76	41.40	87.4
c	M481	65.7	17.6	12.27	11.82	41.65	12.0
d	M289	167.0	26.1	4.70	11.17	40.81	0.1
d	M281	173.4	18.6	4.72	11.10	40.79	11.0
d	M283	175.4	24.6	4.72	11.19	40.77	1.3
e	M125	312.1	14.6	15.31	12.19	39.88	74.3
e	M153	318.4	26.3	15.45	12.06	40.17	0.1
e	M145	319.0	18.8	15.31	12.30	39.97	3.0
a	T293	17.4	21.4	2.95	11.81	41.00	0.6
a	T42	18.3	17.2	4.10	11.95	41.04	15.0
a	T47	29.5	17.4	3.36	11.87	41.06	12.7
a	T63	31.4	25.3	2.74	11.81	41.03	0.9
a	T52	35.2	24.5	3.44	11.83	41.06	2.2
b	T437	347.2	19.8	5.32	12.07	40.87	3.0
b	T434	359.0	23.2	5.34	11.94	40.95	0.2
c	T467	84.3	13.3	8.49	11.74	41.52	50.6
c	T481	85.6	11.0	8.45	11.73	41.43	61.1
c	T455	100.0	10.5	8.42	11.61	41.40	62.7
e	T145	289.2	28.4	17.10	12.00	40.04	0.1
e	T154	302.6	18.6	17.14	12.36	39.90	7.6
e	T125	305.3	21.0	17.22	12.11	40.35	2.7
e	T164	313.3	39.9	17.32	11.89	40.75	0.0
a	S26	247.8	29.0	4.24	11.87	41.14	0.1
a	S3	250.2	27.4	4.75	11.87	41.11	0.1
a	S294	253.2	25.4	4.99	11.88	41.09	0.1
a	S8	256.0	32.8	4.87	11.94	41.29	0.0
a	S4	261.0	32.7	4.89	11.95	41.29	0.0
a	S293	284.0	17.5	4.89	12.04	41.03	7.1
c	S477	88.7	14.0	3.35	11.96	41.54	18.9
c	S455	98.5	6.7	2.50	11.95	41.42	19.1
e	S125	237.8	18.2	22.06	11.12	40.01	11.4
f	S171	181.9	9.3	7.95	11.59	41.35	62.9
f	S170	201.1	13.5	8.28	11.45	41.16	48.2
f	S182	208.8	19.9	4.24	11.69	41.21	3.0
g	S496	250.7	23.7	2.62	11.91	41.22	0.1
g	S466	343.3	7.6	3.10	12.05	41.33	23.8

Event groups as in Table 6.6.2.

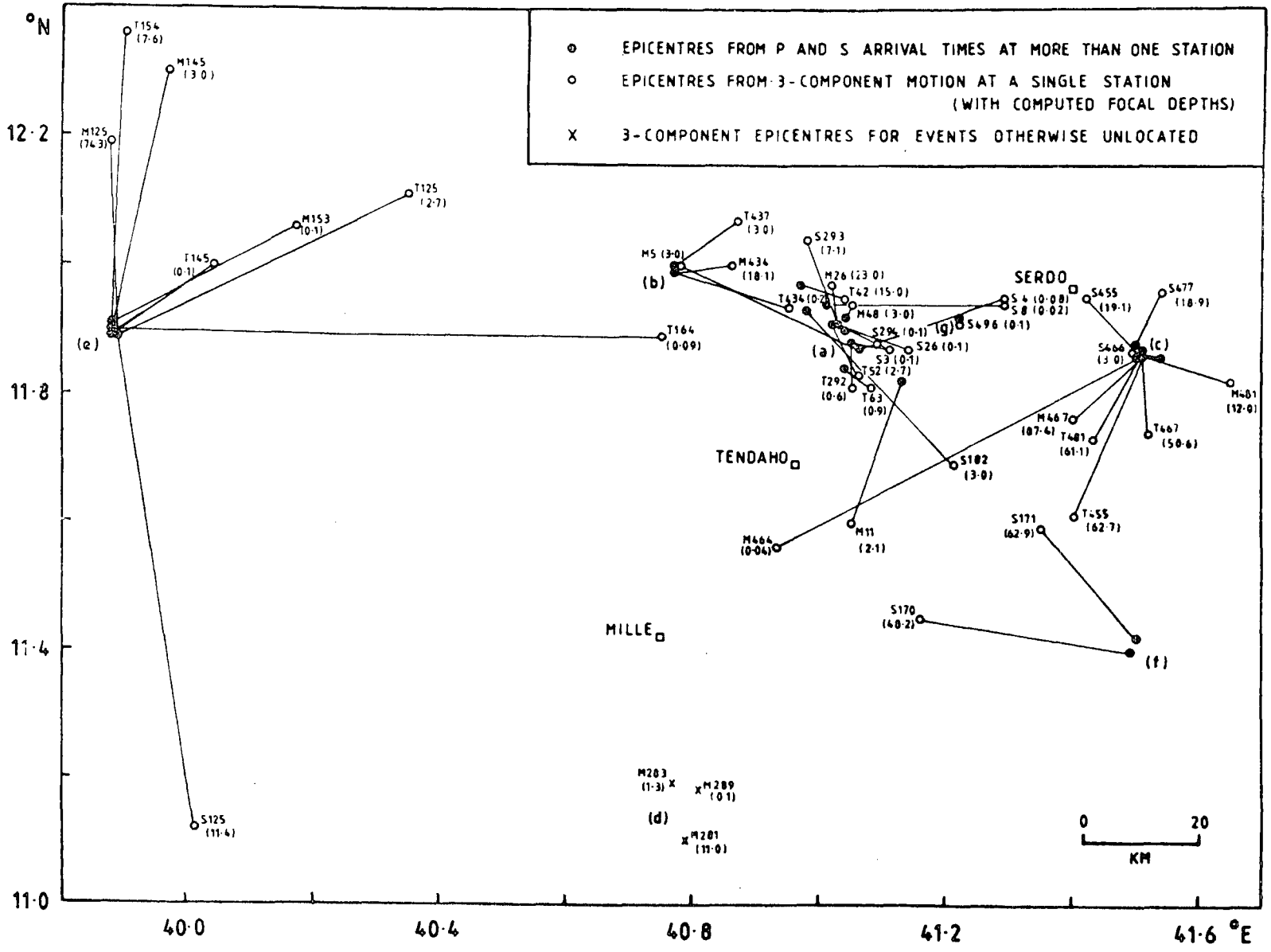

FIGURE 6.7.2

PLOT OF EARTHQUAKE HYPOCENTRES

belonging to the same earthquake sequence, which have traversed essentially the same path; or between locations for the same event (e.g. 125 in group e) recorded at different stations.

(3) Many three-component epicentral estimates lie closer to the recording stations than the corresponding multi-station estimates. This is not a real structural effect. Since any event having $i > i_{ci} + \Delta i$ is assumed to have as first arrival the wave ('a' in Figure 6.7.1) multiply reflected within the superficial (2.1 km s^{-1}) velocity layer, a grossly unrealistic hypocentral estimate will be obtained. The assumed velocity is too low, so the calculated epicentre is too close; and the focal depth cannot exceed 0.1 km. Unrealistic epicentral estimates are also obtained for events with i such that the first arrival is assumed to be the direct wave from the 4.4 km s^{-1} velocity layer, since all S-P times are sufficiently long that head waves from deeper, higher velocity layers will arrive earlier. Events located anomalously deep (e.g. S455) are also placed too close to the recording stations, because of the large proportion of the wave travel time assumed to have been spent in near-vertical ascent from the deep source.

(4) The epicentral distance of the three-component events is largely controlled by the angle of incidence, which dictates the velocity of the structural layer in which the incoming ray has travelled for the majority of its path. For instance, for group e:

T164	2.1 km s^{-1} velocity layer
T125, T145, M153	4.4 km s^{-1}
T154, M145, S125	6.2 km s^{-1}
M125	7.4 km s^{-1}

The large variation in the angle of incidence of these events, which all occurred during the Waldia swarm of 1974 April 1 and 2, is most simply explained by perturbation of the seismic traces caused by local scattering effects.

(5) Errors in the angle of incidence are critical. For the structural model used here, Table 6.6.3 shows that only 3.3° separates the angle of incidence for waves which have travelled as head waves in the upper crust (velocity 6.2 km s^{-1}) and in the lowest layer of the model (7.4 km s^{-1}).

6.8 Summary and Further Comments

The techniques developed in this chapter are most effective for the first two cycles of the first onset. The remainder of the seismic record is largely randomly polarized (as has been graphically demonstrated by particle motion plots).

A problem arises because of scattering from many structural discontinuities at shallow depths below the recording stations. The P coda can be 'cleaned' of randomly polarized motion, but phase arrivals obscured by scattered energy cannot be recovered.

Even for events recorded through a homogeneous, layered V(z) structure the bulk of the P coda will consist of the superposition of many interfering arrivals. Assuming a plane-parallel 4-layer structural model, MAGUIRE (1974)

constructed the synthetic seismogram of the first 10 s of an event from a distance of 55 km. He calculated that 60 arrivals should appear having amplitudes within three orders of magnitude of that of the first arrival. Widespread interference between arrivals is inevitable. The computation, as time functions, of coherence, rectilinearity, azimuth and angle of incidence (Figure 6.5.2), which provide a means of differentiating between unique and interfering arrivals, is shown to be of great value.

Analysis of the S onset, which should be rectilinearly polarized, is hindered because of (1) interference from the P coda and (2) waveform clipping on many records. However, three-component analysis has proved valuable for verifying the nature of certain S arrivals (Figure 6.3.2) and later phases within the P coda (Figure 6.5.2), and in some cases for checking their onset times. The results of Chapter 4 that rely on these later arrivals have been validated.

The method of MONTALBETTI and KANASEWICH (1970) has been extended to enable the azimuth and angle of incidence of events to be determined from their first arrival at a single recording station. For well recorded events the azimuth errors are normally less than 30°, which is adequate for pilot studies of local seismicity. No previously published studies have succeeded in determining azimuth to this accuracy from a single station. The method developed here will be more accurate in regions of 'normal' crust, where less scattering will occur and where the assumption of

lateral structural homogeneity is more reasonable.

It has not been possible satisfactorily to locate the hypocentres of ESP events by three-component analysis, since small errors in the computed angle of incidence critically affect the ray tracing procedure. The differences between three-component and multi-station estimates of azimuth and angle of incidence have been studied, but cannot be related to macro-structural inhomogeneities. However, the consistently small angles of incidence obtained clearly indicate the presence of a low velocity surface layer.

Three-component methods should work better for regional and teleseismic events than for locals. For more distant events the complexity and distortion of the seismic records resulting from near-surface effects is less significant, and may be clearly separated from the arrivals of interest by low-pass frequency filtering.

CHAPTER 7

SPECTRAL ANALYSIS

7.1 Introduction

This chapter describes the further analysis of ESP seismic records through spectral analysis. Its purposes are to provide additional information on the crustal and upper mantle structure beneath the receiving stations and along the wave travel path; and to obtain estimates of seismic source parameters.

The spectrum of a seismic record is influenced by a multiplicity of factors, conveniently divisible into source response, path response, receiver response and instrumental response (Equation 5.1.1). To derive meaningful conclusions from observed spectra equalization techniques are used to isolate these influences one from another.

Velocity amplitude spectra of ESP records are discussed in Section 7.3. They illustrate a fundamental problem with local events, that the predominant effect of the crust beneath the receiver tends to mask all other spectral parameters and to prevent their accurate measurement. Consequently the computed velocity amplitude spectra, and crustal transfer ratios derived from them, are first interpreted in terms of crustal structure (Sections 7.3 to 7.5). Then, in Section 7.6, seismic source parameters are estimated from ESP displacement amplitude spectra using the 'corner frequency' method.

Spectral analysis is performed using regularly sampled and digitized seismograms. The finite time series and corresponding complex spectrum are related by the well-known discrete Fourier transform pair

$$F(W) = N^{-1/2}\sum_{T=\emptyset}^{N-1} f(T)\exp(-i2\pi(v/N)t)$$

$$f(T) = N^{-1/2}\sum_{T=\emptyset}^{N-1} F(W)\exp(i2\pi(v/N)t) \qquad (7.1.1)$$

(e.g. KANASEWICH,1975, p.36), where N is the total number of points sampled. The sampling intervals in the time (ΔT) and frequency (ΔW) domains are related by

$$\Delta W = 2 / N\Delta T \qquad (7.1.2)$$

Digitization at 100 samples s^{-1} gives a Nyqvist frequency of 50 Hz (e.g. BÅTH,1974,p.146). This is adequate for accurate representation of the analogue signal (Section 3.8).

7.2 Fourier Transformation of ESP Records

All the computations required in this chapter have been carried out within the single programme TRANSF, written in FORTRAN for NUMAC and described and listed in Appendix 9. Taking sampled and digitized seismograms as input, TRANSF performs the discrete Fourier transformation using the fast Fourier transform (FFT) algorithm adopted by COOLEY and TUKEY (1965). Plotted spectra are output.

This section examines briefly some practical difficulties associated with the discrete Fourier transform.

Firstly, the choice of window length is most important, and must be a compromise. A long time series is required to give good spectral resolution: a short series to exclude

unwanted seismic phases. Velocity amplitude spectra of a typical event (M26), sampled with time data windows from 1.Ø to 2Ø.Ø s, showed that 3.Ø s was a sufficient window length for good spectral resolution. Windows of 2.5 s or shorter were not acceptable, as the sampling period in the frequency domain was then too large to resolve significant variations. Whenever possible, spectra that were to be compared were computed from equal length windows. In other cases differential smoothing was applied by TRANSF so as to maintain effectively constant spectral resolution.

Secondly, window functions (discussed by KURITA,1969) are desirable to reduce spectral distortion, unless the input waveform is a transient and the whole signal is included within the window. Failure to apply any special window shape is equivalent to imposing a rectangular window in the time domain, corresponding to the sinc function spectral window $F(w) = \sin(w/2)/(w/2)$. All FFTs in this study used the TRANSF programme facility of tapering both ends of the window by applying a Hanning (cosine) window (e.g. BÅTH,1974,p.159).

TRANSF also incorporates a subroutine to remove the physically unrealistic d.c. component which arises through the arbitrary truncation of the seismogram. If not removed, this d.c. component would "leak" across to other components, corrupting the spectral estimate. It is equivalent to a rectangular window convolved with the time series.

One further source of loss of spectral resolution is specific to ESP. Variations in analogue tape speed on

playback have given rise to fluctuations in the digitization rate of 1% to 2% (Chapter 3), which will cause spectral broadening of a 10 Hz frequency by ±0.1 or ±0.2 Hz.

It should be noted that differences in instrumental response might cause errors when comparing the spectra of records from different stations. Seismometer calibration pulses routinely recorded at the ESP stations were so closely similar that a common instrumental response curve, I(w), was assumed. I(w) is independent of w (to -3 dB) over the frequency range of interest (Figure A3.1). Only in Section 7.6 has I(w) sometimes been included to correct the trace amplitude spectrum, F(w), to the true ground amplitude spectrum, $F_\emptyset(w)$, according to the relation

$$F_\emptyset(w) = F(w)/I(w) \qquad (7.2.1)$$

7.3 Velocity Amplitude Spectra

An expression for the received body wave frequency spectrum, X(w,r,Θ), was given in Section 5.1 as

$$X(w,r,\Theta) = S(w)\ B(\Theta)\ C_S(w)\ P(w,r)\ G(r)\ C_R(w,r)\ I(w) \qquad (5.1.1)$$

Equation 5.1.1 can be re-written as

$$X(w,r,\Theta) = X_o(w,r,\Theta)\ C_R(w,r) \qquad (7.3.1)$$

where $X_o(w,r,\Theta)$ represents the spectrum at arbitrary depth h in the upper crust beneath the receiver (Figure 7.3.1). The instrumental response factor, I(w), has been omitted from Equation 7.3.1 as explained in Section 7.2.

Equation 7.3.1 is strictly valid only when an infinitely long seismogram is used, so that the whole

FIGURE 7.3.1

DIAGRAM TO ILLUSTRATE MODIFICATION OF BODY WAVE SIGNAL SPECTRUM BY RECEIVER UPPER CRUSTAL STRUCTURE

(C_{Ri} represents that element of C_R due to layer i)

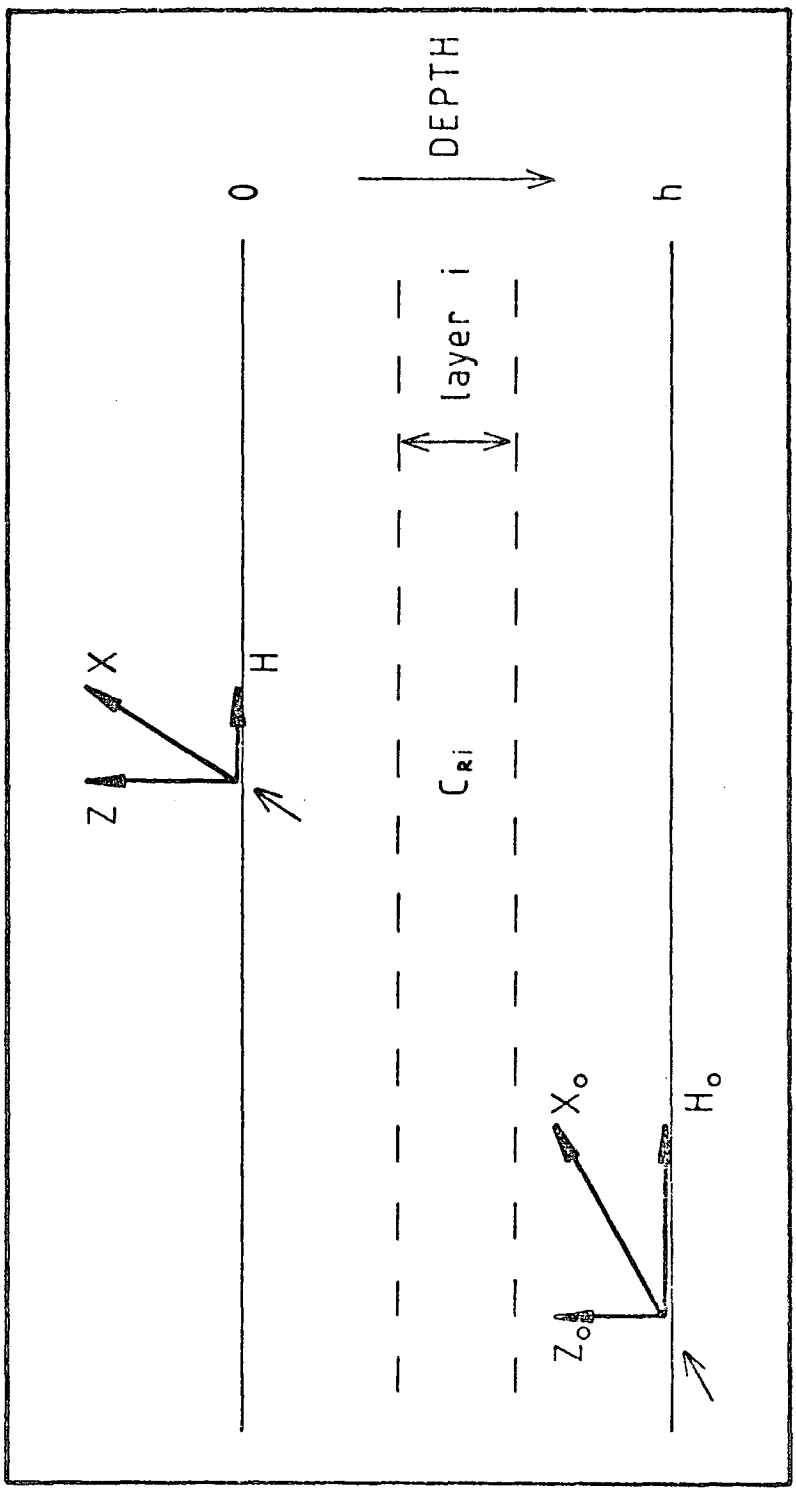

crustal effect is included. The effect of a time window of length T s can be expressed in the frequency domain by convolution with the equivalent window function, W(w), i.e.

$$X(w,r,\theta) = [X_o(w,r,\theta)\ C_R(w,r)] * W(w) \qquad (7.3.2)$$

LEBLANC (1967) has shown that, under certain conditions, this is equivalent to

$$X(w,r,\theta) = X_o(w,r,\theta)\ [C_R(w,r) * W(w)]$$
$$= X_o(w,r,\theta)\ C_{RT}(w,r) \qquad (7.3.3)$$

$C_{RT}(w,r)$ is known as the truncated crustal transfer function.

7.3.1 P Waves

P coda velocity amplitude spectra were obtained for 140 ESP records, using programme TRANSF. Time window lengths for the Fourier transformation were chosen so as to include the full P coda, with the 0.5 s of background noise immediately preceding the first P onset, but exclude the S onset. Window lengths ranged from 3.0 to 20.0 s, depending on P to S time. The sampling rate was 100 samples s^{-1} (Section 3.8). Time windows were corrected to mean baseline and cosine tapered, with trailing zeros added to bring the sample size to 512, 1024 or 2048 for the discrete Fourier transform.

As a first stage in spectral analysis the spectra were examined qualitatively to assess their relative dependence on the receiver upper crustal factor ($C_{RT}(w,r)$ in Equation 7.3.3) and on source and path effects ($X_o(w,r,\theta)$). Spectra of typical events are shown in Figures 7.3.2 to 7.3.4, and their epicentres in Figure 7.3.5. Details of azimuths,

FIGURE 7.3.2

PV VELOCITY AMPLITUDE SPECTRA AT MILLE

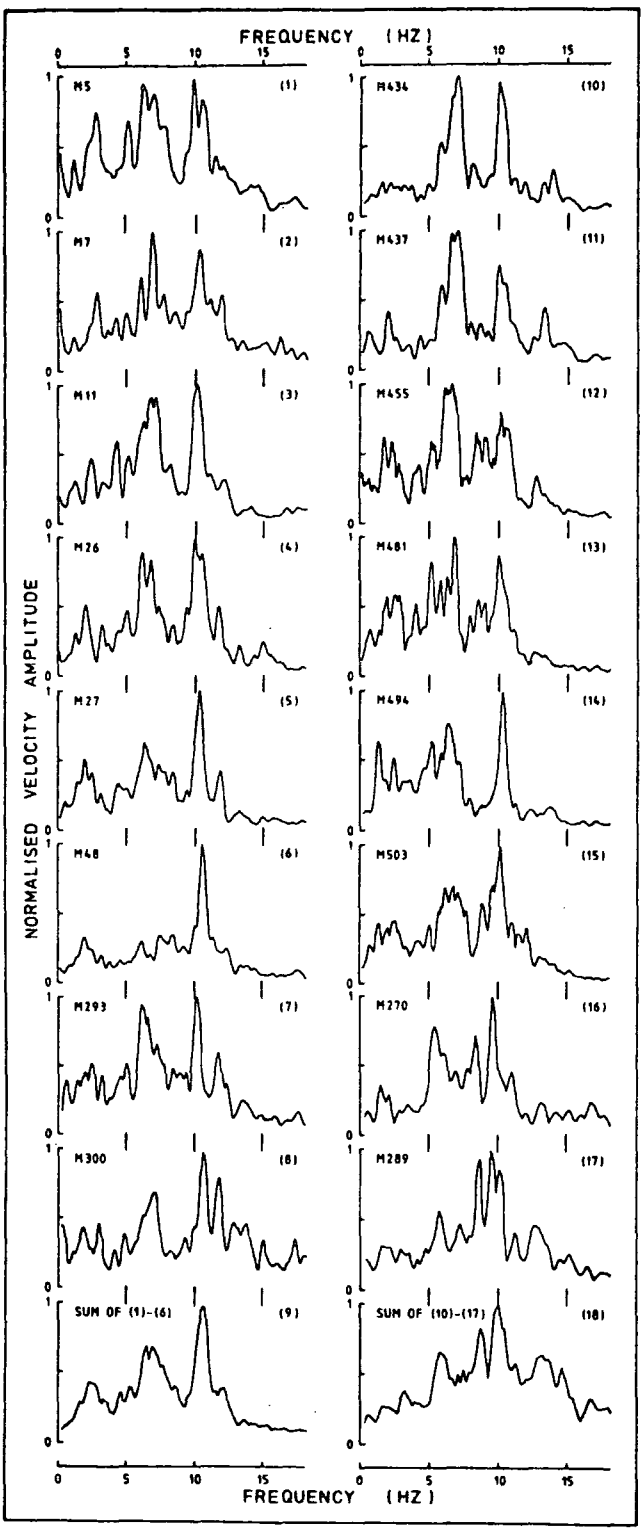

FIGURE 7.3.3

PV VELOCITY SPECTRA OF TYPICAL EVENTS

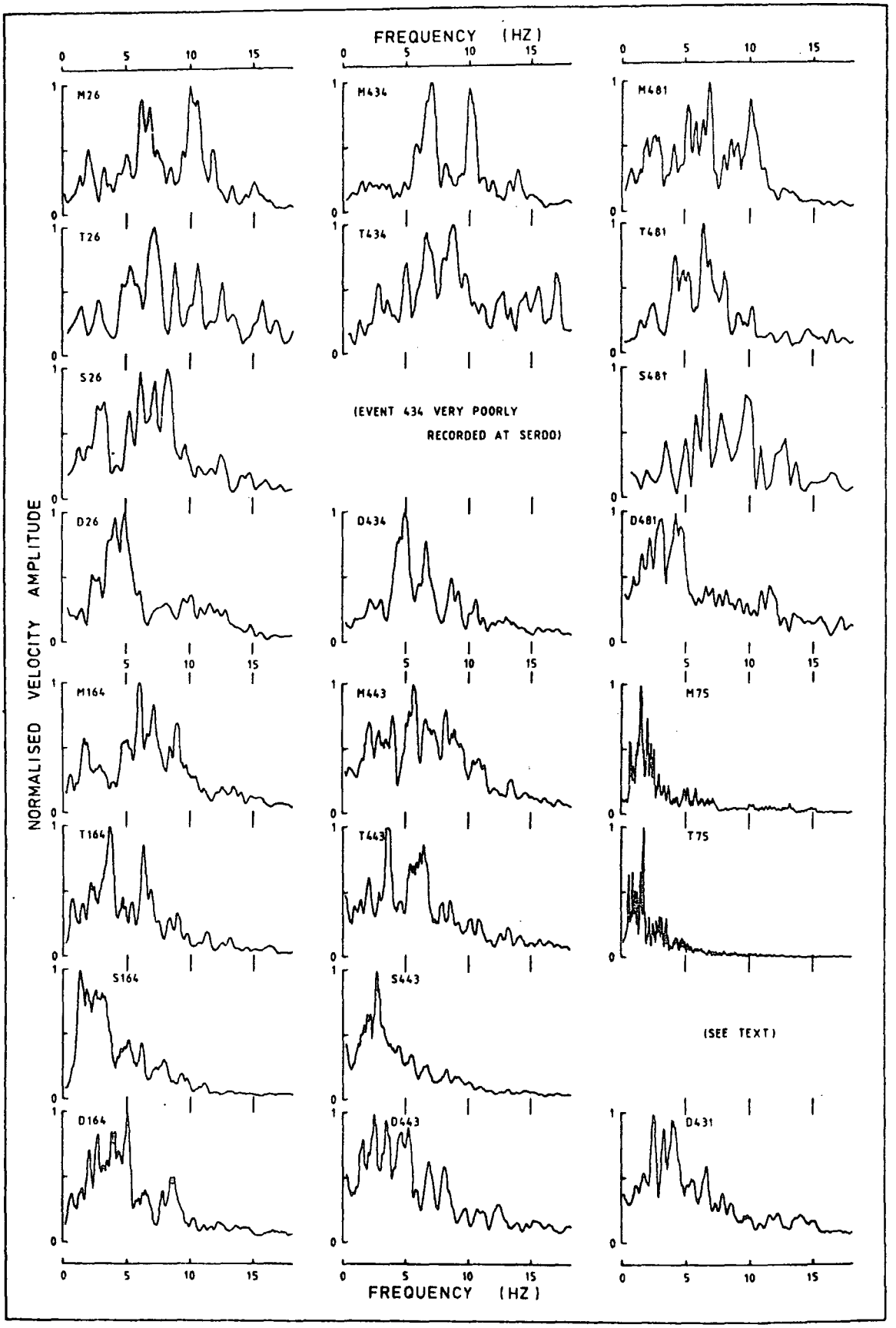

FIGURE 7.3.4

SUMMED PV VELOCITY SPECTRA

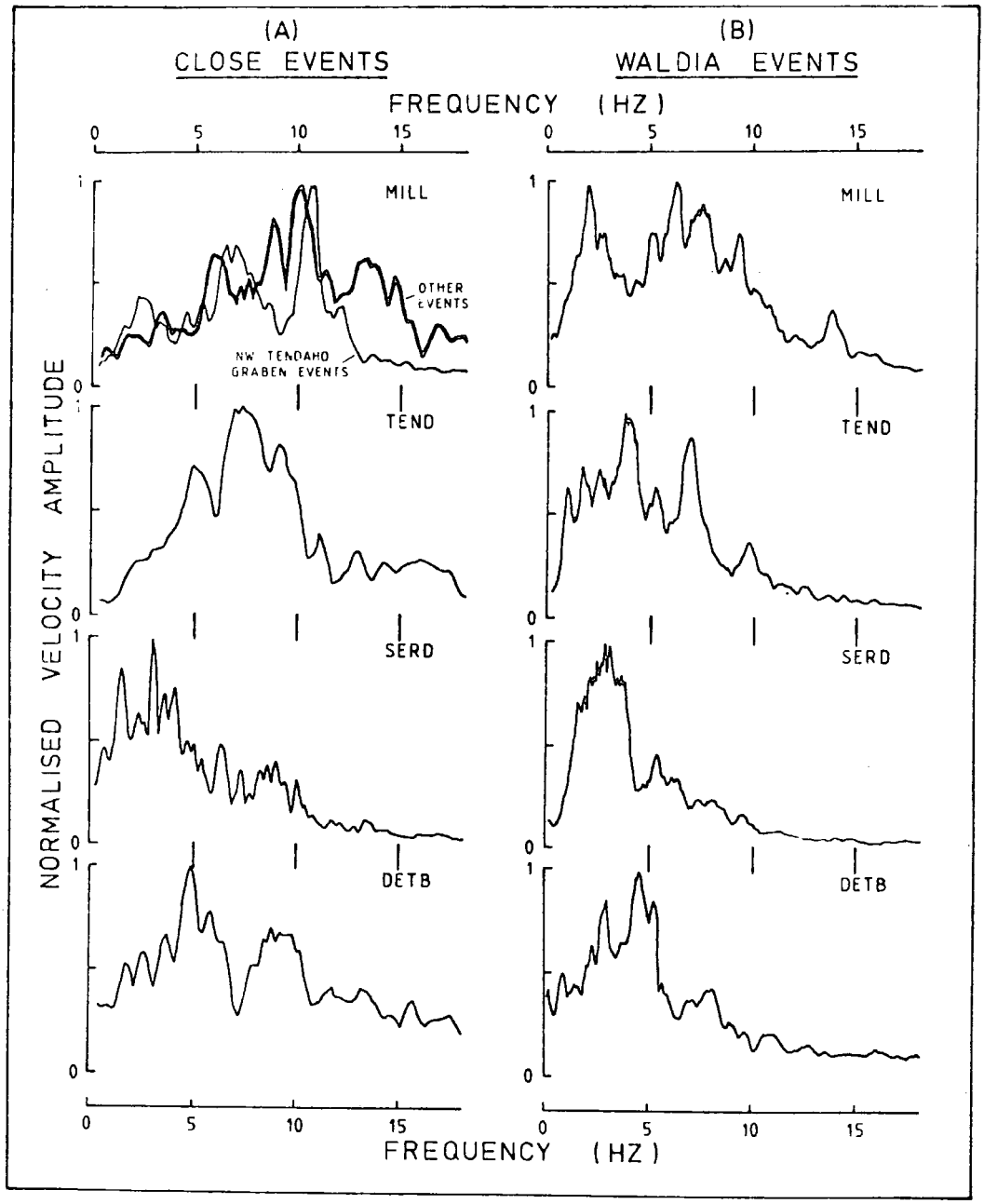

FIGURE 7.3.5

EPICENTRES OF EVENTS CITED IN CHAPTER 7

AND REGIONS OF INFERRED LOW Q

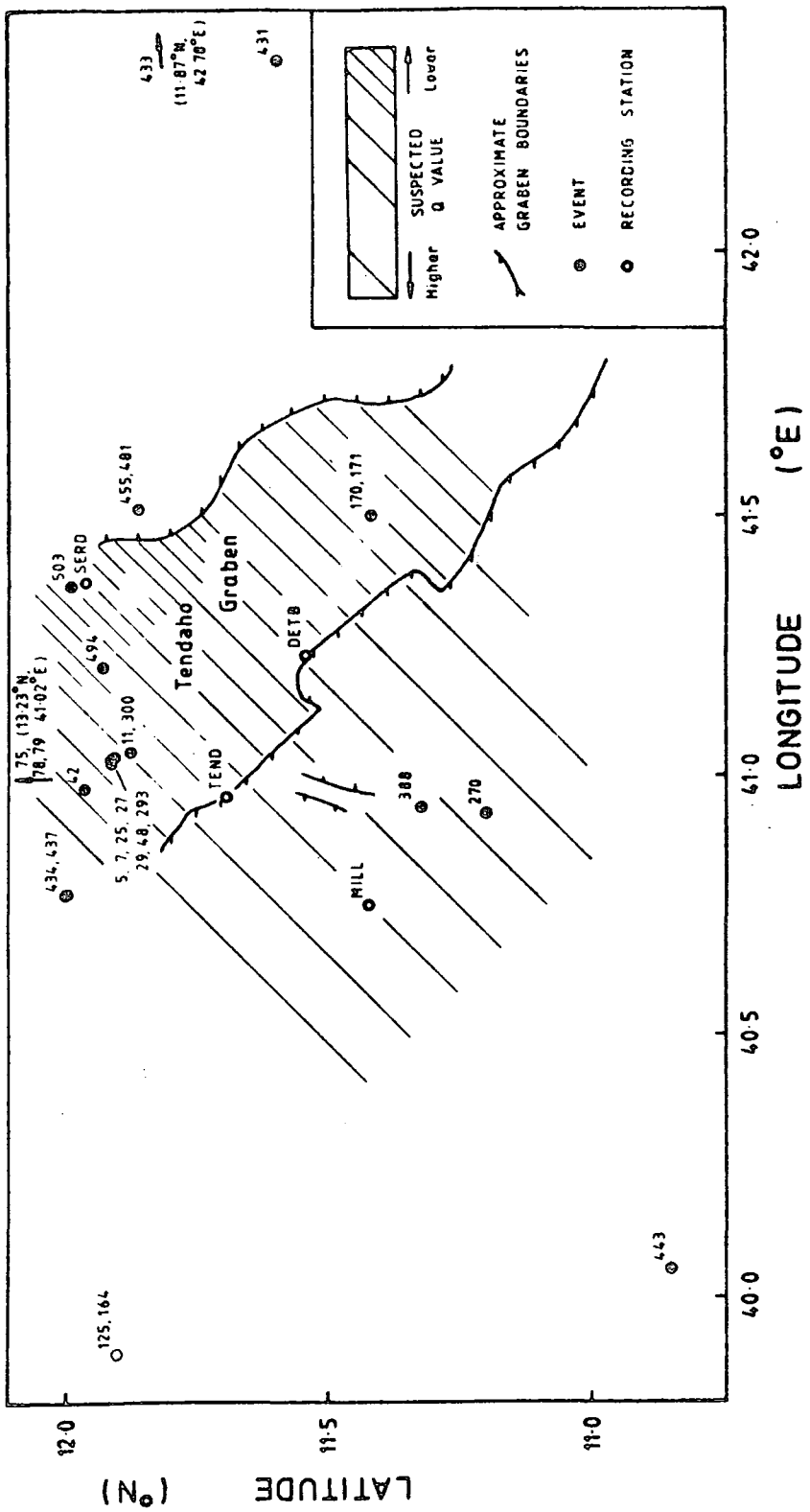

epicentral distances and time window lengths are given in Table 7.3.1. All the spectra reproduced here are from the vertical component of seismic motion, although the same conclusions can be drawn from spectra from the horizontal components. It is seen that:

(1) Events from adjacent hypocentres, observed at the same station, have similar velocity amplitude spectra (e.g. records 1-8, 10-11, Figure 7.3.2). These events thus do not have such radically different source spectra or source space functions (e.g. as a result of different focal mechanisms) as to dominate the observed spectra. Furthermore, the spectra are not so sensitive to small differences in the wave path as to make further analysis meaningless.

(2) Spectra from the same events, recorded at different stations, are substantially different, even when the azimuths are similar (Figure 7.3.3). This emphasises the predominant influence on the spectra of the receiver crustal structure rather than the source function.

(3) Events from different locations, in the same distance range, observed at the same station, have similar spectra. The events shown in Figure 7.3.2, records 1 to 15, cover a distance range of 55 to 100 km and an azimuth range of 57°. These events have different $X_o(w,r,\theta)$, but will have similar $C_{RT}(w,r)$ (the restriction to comparison of events from similar distances implies similar angles of incidence) unless the upper crust below the station is very inhomogeneous. Figure 7.3.2 therefore reinforces the

TABLE 7.3.1

DETAILS OF EVENTS ILLUSTRATED IN CHAPTER 7

Event	Azimuth (degrees)	Epicentral Distance (km)	FFT Time Window (sec)*	Illustrated In Figures
M5	31	60	7.0	7.3.2;7.5.3
M7	30	62	7.0	7.3.2
M11	27	60	7.0	7.3.2
M26	29	62	7.0	7.3.2;7.3.3;7.5.2; 7.5.3;7.5.2;7.5.3
T26	18	26	3.0	7.3.3;7.5.3
S26	262	36	4.0	7.3.3
D26	334	43	5.5	7.3.3
M27	29	62	7.0	7.3.2
T29	36	26	3.0	7.6.3
T42	3	31	3.0	7.5.3;7.6.3
M48	30	63	7.0	7.3.2;7.5.3
M75	8	174	20.0	7.3.3
T75	2	142	20.0	7.3.3
M125	299	107	15.0	7.5.3
M164	299	108	15.0	7.3.3;7.3.6;7.5.3
T164	281	119	15.0	7.3.3;7.3.6
S164	268	161	20.0	7.3.3;7.3.6;7.6.3
D164	284	149	20.0	7.3.3;7.3.6
S170	166	61	7.0	7.6.3
S171	166	61	7.0	7.6.3
M270	142	31	4.0	7.3.2;7.5.3
M289	(142)**	(31)**	4.0	7.3.2
M293	30	62	7.0	7.3.2;7.3.6;7.5.3
T293	19	25	3.0	7.3.6
S293	260	36	4.0	7.3.6
M300	36	55	7.0	7.3.2
D388	228	39	4.5	7.3.6
D431	88	126	15.0	7.3.3
M434	2	63	7.0	7.3.2;7.3.3;7.3.6; 7.5.3
T434	329	39	4.0	7.3.3;7.3.6;7.5.3; 7.6.3
D434	315	67	8.0	7.3.3;7.3.6
M437	2	64	7.0	7.3.2
M443	230	99	11.0	7.3.3;7.3.6;7.6.3
T443	226	136	15.0	7.3.3;7.3.6
S443	229	188	20.0	7.3.3;7.3.6;7.6.3
D443	237	148	20.0	7.3.3;7.3.6
M455	59	95	11.0	7.3.2
T455	72	63	4.0	7.5.3
M481	59	96	11.0	7.3.2;7.3.3;7.6.3
T481	72	63	4.0	7.3.3
S481	121	19	3.0	7.3.3
D481	44	47	6.0	7.3.3
M494	41	75	9.0	7.3.2
M503	46	91	11.0	7.3.2;7.5.3
T503	53	55	6.0	7.5.3

*Not applicable to Figure 7.3.6.
**Approximate figures. This event was located at Mille only.

observation that the observed spectrum is being dominated by the receiver crustal factor, $C_{RT}(w,r)$. The very small dependence on azimuth of the spectral frequency peaks provides further evidence for the small angles of incidence deduced for ESP events in Section 6.6. Records 16 and 17 on Figure 7.3.2 are less similar. They derive from events at much shorter distances (about 30 km) from Mille, and having abnormally complex P codas.

(4) It is possible to sum the velocity amplitude spectra of different events recorded at the same station without destroying the prominent peaks (Figure 7.3.2, records 9 and 18; Figure 7.3.4). Traces on Figure 7.3.4 each represent stacks of 5 to 8 records. "Close" on Figure 7.3.4a indicates events from epicentral distances less than 100 km, covering a wide range of azimuths and distances. It is now clear that the dominant, oscillatory nature of the spectra is due to receiver crustal effects. This conclusion corroborates results in other areas (e.g. LEBLANC and HOWELL,1967; HELMBERGER and JOHNSON,1977). For a given station, maxima and minima are observed at the same frequencies for the stacks of Figures 7.3.4a and b, although modified by the envelope of overall spectral shape.

(5) Fourier transformation of successive 3.0 s window lengths along the P coda of sample events yielded almost identical frequency spectra. The spectra illustrated are thus representative of both the first arrival and the P coda as a whole.

7.3.2 S and Surface Waves

For the 140 events discussed above, spectra were also obtained for time windows commencing with the S phase arrival. No attempt was made to separate S from other body and surface wave phases within the time windows, which therefore contain some surface waves.

Typical velocity amplitude spectra of the horizontal component of wave motion are shown in Figure 7.3.6, which should be compared with Figure 7.3.3. The same events have been used in both figures, except in the case of the NW Tendaho graben event, 26, for which S was clipped by the recorders. The similarity in overall shape between the two sets of spectra is very marked. Maxima and minima are not necessarily at the same frequencies, since differences in the wave paths of different wave types will result in differences in the pattern of their reverberations.

7.3.3 Noise

Samples of background noise, and of unidentified noise bursts, yielded approximately flat velocity amplitude spectra at all stations. Superimposed on these 'white' spectra a prominent peak at 12 ± 1 Hz was sometimes seen on quiet records at Tendaho. A smaller peak at the same frequency was seen on a sample of background noise from Det Bahri, promoting the speculation that it might be related to the Allallobeda graben geothermal area (Figure 2.3.1) close to these two stations. The peak has low amplitude relative to the signal spectra of well-recorded events (it does not

FIGURE 7.3.6

SH VELOCITY AMPLITUDE SPECTRA OF TYPICAL EVENTS

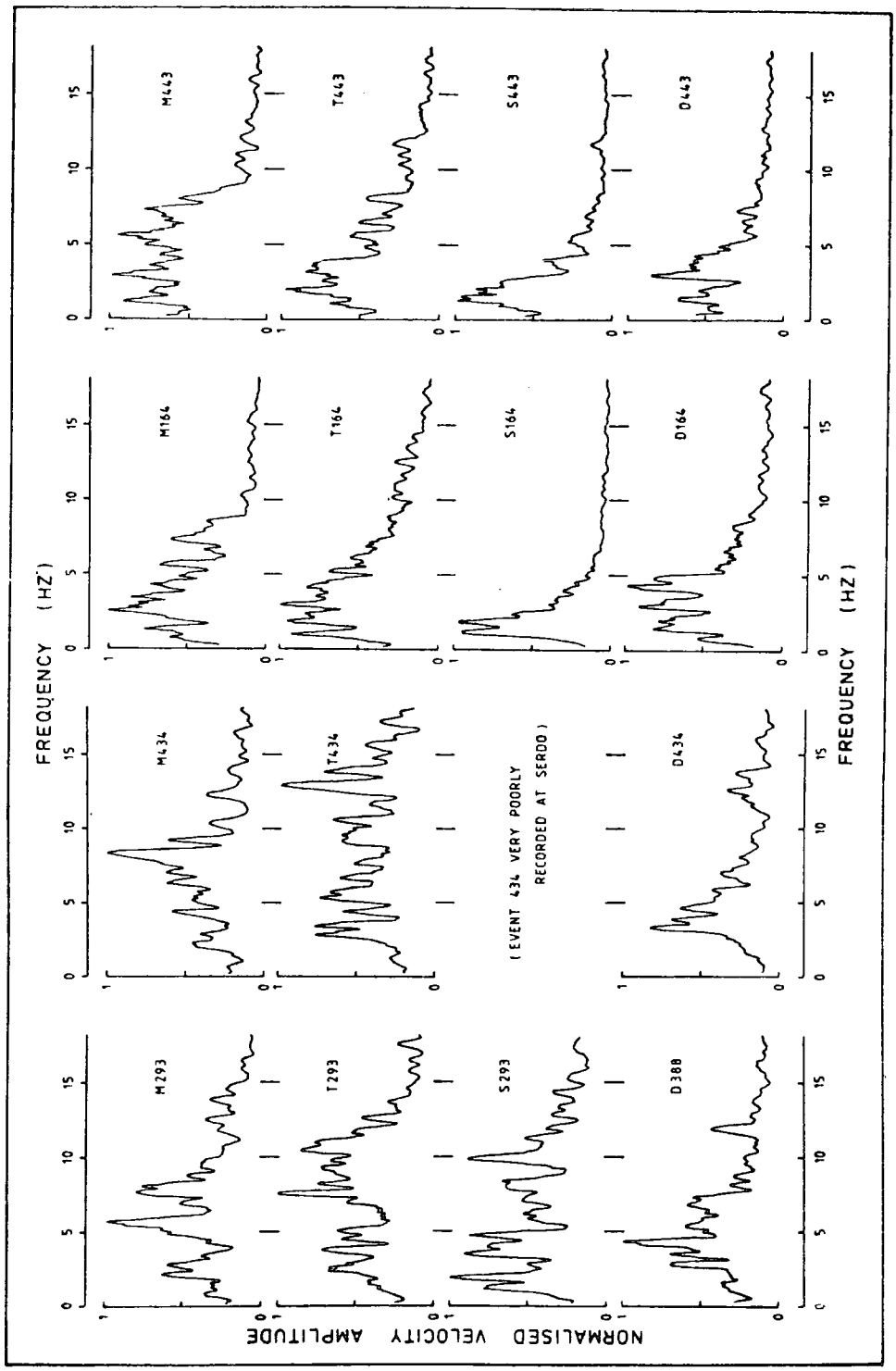

appear on any of the spectra in Figures 7.3.2 to 7.3.4) and seems to have no structural significance.

Consecutive time windows (length 70 s) of background noise at a recording station showed quasi-stationarity (i.e. very similar frequency spectra). It was thus considered permissible to correct for noise by subtracting from an event signal spectrum the spectrum of the background noise immediately preceding the event onset. For all events considered in this chapter the signal to noise ratio is so large that the influence of noise on the signal spectra is negligible.

7.4 Seismic Wave Attenuation related to the Tendaho Graben

The expected effect of attenuation with distance is a decrease in the relative magnitude of higher frequencies. This is seen for results from the Western Ethiopian escarpment (Figure 7.3.4b; Figures 7.3.3 and 7.3.6, events 164 and 443), where arrivals at Serdo (epicentral distance $\approx$ 158 km for Waldia events) and Det Bahri (146 km) show much greater attenuation than those at Tendaho (117 km) and Mille (107 km). This effect is unexpectedly pronounced, and comparison of Figures 7.3.4a, 7.3.4b shows that close events at Serdo station are also severely attenuated at higher frequencies. (See Figure 7.3.5 for station and event locations relative to the Tendaho graben).

The simplest explanation is a region of low Q (high attenuation) in the upper crust below Serdo. Close events at Mille, 40 km west of the Tendaho graben, are less

attenuated than those at Tendaho and Det Bahri on its western margin. This implies higher upper crustal Q below Mille than below either flank of the graben. During the period of this study no seismic events were recorded from areas within Afar (e.g. west of Mille) such that wave paths wholly unaffected by the Tendaho graben could be studied.

Fourier transformation of events from Afar marginal areas other than the Western Ethiopian escarpment would provide important additional information on the distribution of Q in the region below the Tendaho graben. Few such events occurred of suitable magnitude to be well recorded at the ESP stations. Those that did were recorded on to half-inch digital tape for Fourier analysis, but the digital tape was subsequently erased in Newcastle and could not be re-recorded, since the Durham CTL MODULAR 1 and associated half-inch tape drive had by then (1980) been dismantled. The only events to be Fourier transformed were 431 and 433, at Det Bahri; and 75, 78 and 79, at Mille and Tendaho (Figure 7.3.3. Records for event 75 are unsmoothed). The wave path giving the highly attenuated waveform for event 75 passes directly below the seismically active NW Tendaho graben area, while that of the less attenuated D431 waveform has traversed the graben farther south.

Direct study of the time domain records shows that events 431 and 433 are more attenuated at Tendaho station than at Det Bahri, and still more attenuated at Mille. Serdo station was not functioning at the time of these events. Events 75, 78 and 79 were recorded with similar

attenuation at Mille, Tendaho and Serdo (Det Bahri was inoperative).

All the records indicate an area of low Q beneath the Tendaho graben, extending to shallow depth below Serdo. Further data are required to quantify this result.

7.5 The Spectra and their Relation to Crustal Structure

7.5.1 Reverberations

The geological structure below the ESP station sites is beds of hard basalts with relatively high seismic velocity, intercalated with softer, lower velocity rocks formed of tuffs and volcanic ash. This superficial structure presents a series of layer boundaries with high reflectivity to seismic waves. The crustal frequency response is therefore likely to show strong peaks caused by resonances, and in the time domain the signal will be prolonged. These effects have been remarked previously.

While complicating the observed seismic signals, reverberations caused by superficial structure themselves theoretically provide a method of examining the structural layers. Some semi-quantitative observations on the ESP spectra are presented here. The data were not considered to warrant a thorough quantitative study.

Amplitude spectra will exhibit maxima and minima corresponding to constructive and destructive interference between waves reflected from the upper and lower surfaces of each structural layer. The case of a single, plane,

parallel, homogeneous, intercalated sub-surface layer is depicted in Figure 7.5.1. It is straightforward to show that the frequency separation between adjacent maxima will be

$$\Delta f = \frac{V_n}{2h}\left(\frac{\cos(i_n)}{1 + \sin^2(i_n)}\right) \qquad (7.5.1)$$

with the first maximum at $\Delta f/2$. The complexity of the theoretical spectra increases rapidly when two or more layers are considered, and has usually been investigated following the Thomson-Haskell matrix formulation (e.g.HASKELL,1953,1962).

The principal weakness of exact solutions for the transfer function for elastic or viscoelastic layered models (e.g. MURPHY et al,1971) is that they rigorously apply only to layers of constant thickness and infinite extent. Numerical methods, such as the finite element technique (DESAI and ABEL,1972), are required to treat laterally heterogeneous models. A further problem with the spectra of local earthquakes is that their dominant wavelengths are of the same order as the thicknesses of the superficial crustal layers under investigation.

The spectral oscillations observed at Mille, with strong maxima at approximately 2.Ø, 6.Ø and 1Ø.Ø Hz (Figures 7.3.2, 7.3.4), can be explained in terms of a single resonant layer. Taking V = 2.5 km s^{-1} and i = 2Ø° in Equation 7.5.1 gives 262 m as an estimate for the layer thickness. Assuming normal incidence, the thickness is 312.5 m.

FIGURE 7.5.1

AN ILLUSTRATION OF REVERBERATION FROM A SUB-SURFACE LAYER

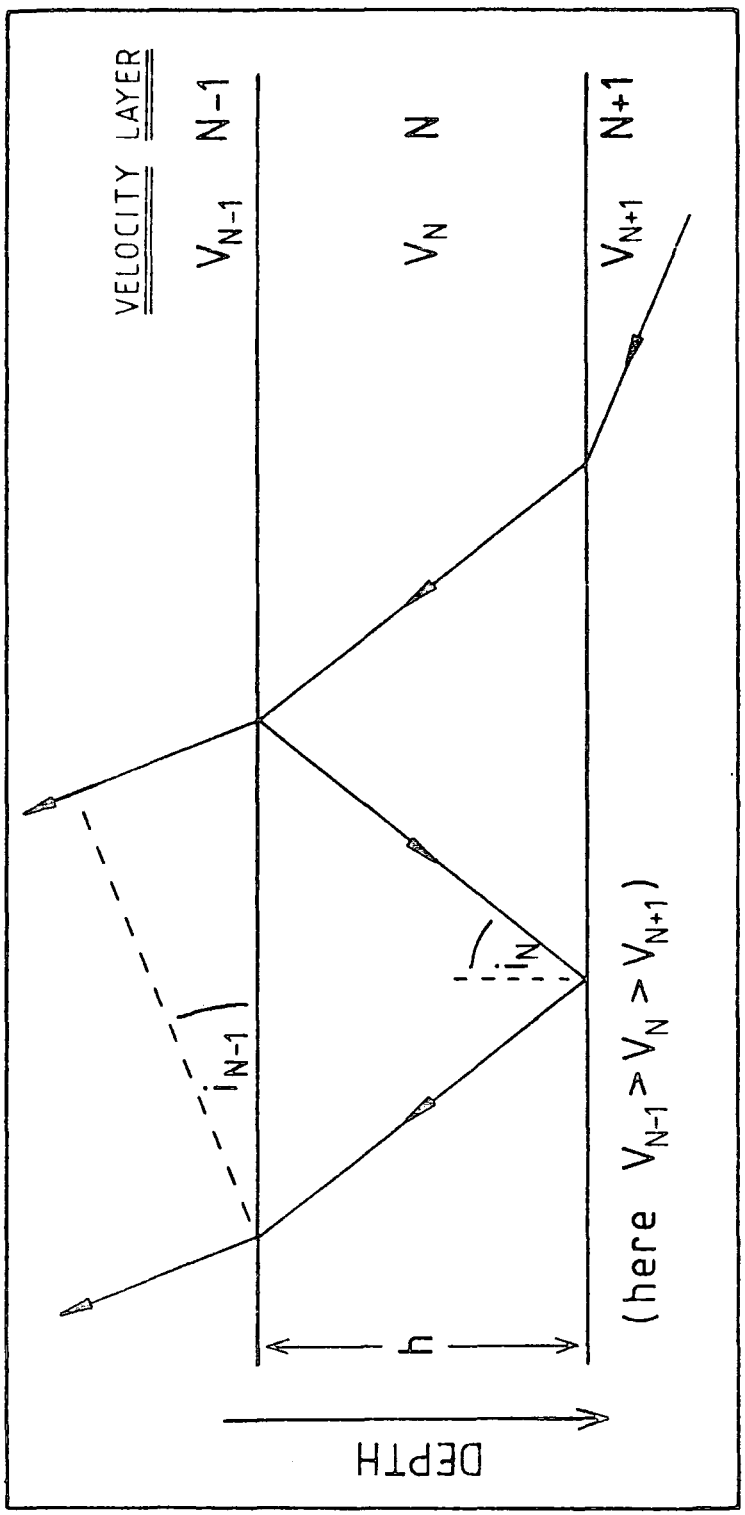

Amplitudes of recorded seismic signals will clearly also be affected by reverberation and resonance effects. Fundamental to much literature on this subject is the theoretical paper of TSAI (1970), who defined spectral amplitude, AMP(w), as the ratio of the surface motion to twice the motion of the bedrock (i.e. AMP(w) = 1 in the case of no superficial layering). Tsai showed the particular dependence of the limits of AMP(w) on the acoustic impedance ratio at the bedrock, such that for n layers

$$\rho_n V_n/\rho_{n-1}V_{n-1} \leqslant \text{AMP}(w) \leqslant \rho_n V_n/\rho_1 V_1 \qquad (7.5.2)$$

where ρ = density, V = seismic velocity. Thus for a single layer

$$\text{AMP}(w) = \rho_2 V_2/\rho_1 V_1.$$

No attempt has been made in this work to calculate AMP(w). Equation 7.5.2 is included for its relevance to the time-domain signal amplitude measurements discussed in Chapter 5. Magnitude estimates based on signal amplitudes at different stations would be grossly inconsistent if AMP(w) varied widely from station to station. This was found not to be the case.

7.5.2 Crustal Transfer Ratios

Equation 7.3.1 may be split into vertical and horizontal components $Z(w,r,\theta)$ and $H(w,r,\theta)$, as defined in Figure 7.3.1, and re-written

$$\left.\begin{aligned} Z(w,r,\theta) &= X_o(w,r,\theta)\ C_{RZ}(w,r) \\ H(w,r,\theta) &= X_o(w,r,\theta)\ C_{RH}(w,r) \end{aligned}\right\} \qquad (7.5.3)$$

where $C_{RZ}(w,r)$, $C_{RH}(w,r)$ represent vertical and horizontal

components of the receiver crustal structure factor, $C_R(w,r)$.

The crustal transfer ratio, the frequency-dependent tangent of the apparent angle of emergence, is obtained by complex division, $Z(w,r,\theta)/H(w,r,\theta)$; or, taking the amplitudes,

$$T(w,r) = |Z(w,r,\theta)|/|H(w,r,\theta)| = |C_{RZ}(w,r)|/|C_{RH}(w,r)| \quad (7.5.4)$$

This equation is independent of the incident signal spectrum, $X_o(w,r,\theta)$. $T(w,r)$, normally calculated for a homogeneous layered structural model using the Thomson-Haskell matrix formulation (see HASKELL,1962), depends solely on the receiver crustal structure.

The crustal transfer method was developed by PHINNEY (1964) with application to long-period (Ø to Ø.Ø2 Hz) body waves, and has been used in this form in lower crustal and upper mantle studies. Its extension to shorter-period body waves, for crustal studies, requires replacement of $T(w,r)$ by the truncated crustal transfer ratio $T_T(w,r)$, defined from Equation 7.3.3 instead of from Equation 7.3.1.

The spectral ratio method for short-period P waves from teleseismically recorded events has been applied by LEBLANC and HOWELL (1967), ELLIS and BASHAM (1968), HASEGAWA (1971) and others; and has been extended to treat dipping layers by ROGERS and KISSLINGER (1972). It has had limited success in resolving gross crustal features, primarily because the shorter period waves are scattered to a greater extent by small-scale inhomogeneities within the crust. P to S

conversion and signal generated noise may also limit its applicability. It has, however, been shown to be capable of resolving thin, low-velocity layers (HASEGAWA,1971).

Examples of observed crustal transfer ratios computed from ESP seismic records using programme TRANSF are shown in Figures 7.5.2 and 7.5.3. This is the first application of the method to local events. The broadness of the spectral peaks does not derive from excessive smoothing, but probably reflects the thinness of the layers which are causing them. The simplicity of the spectra compares extremely favourably with those obtained from teleseismically observed events (e.g. LEBLANC and HOWELL,1967).

In the frequency range 2 to 12 Hz, within which most of the seismic energy is concentrated (Figure 7.3.3), all the crustal transfer ratio spectra at a station are markedly similar. This is shown for Mille events from a wide range of azimuths and distances in Figure 7.5.3, records 1 to 9; and for Tendaho events on records 11 to 15.

The typical background noise spectrum (record 10) is flat. Section 6.1 has asserted that this noise consists primarily of Rayleigh waves. The absence of reverberation and resonance effects caused by receiver crustal structure indicates no one predominant noise source, but rather many sources at different azimuths and depths. The illustrated result that $Z(w,r,\theta)/H(w,r,\theta) < 1.0$ at all frequencies is general for background noise from all ESP stations.

Event spectra show equal frequency separation of their spectral peaks. There is a marked similarity between these

FIGURE 7.5.2

EXAMPLE OF A CRUSTAL TRANSFER RATIO SPECTRUM

COMPUTED USING PROGRAMME TRANSF

(channels 1 and 2 are Z(w,r,θ) and H(w,r,θ) respectively)

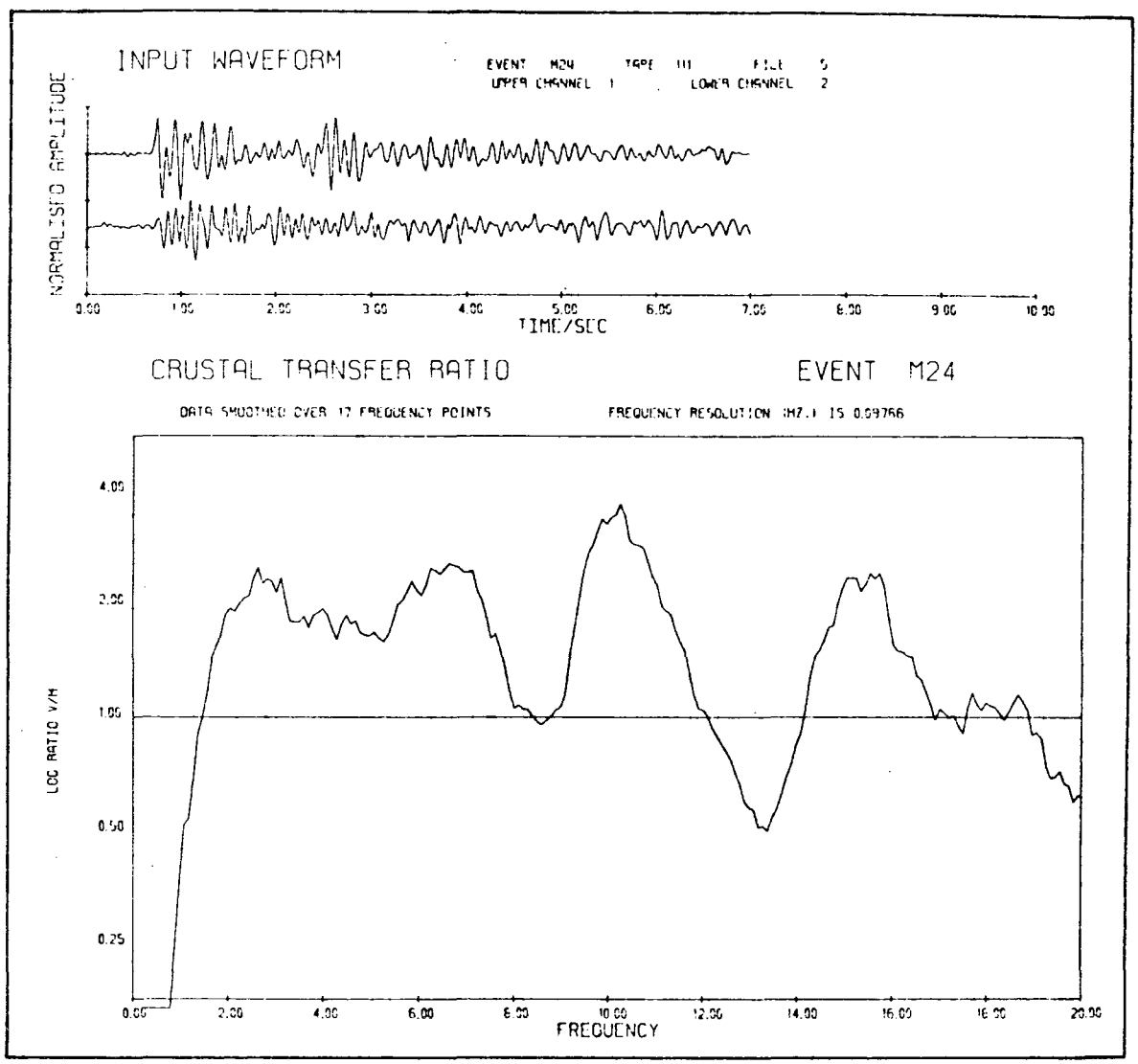

FIGURE 7.5.3

SAMPLE CRUSTAL TRANSFER RATIO SPECTRA FOR EVENTS RECORDED AT MILLE AND TENDAHO STATIONS

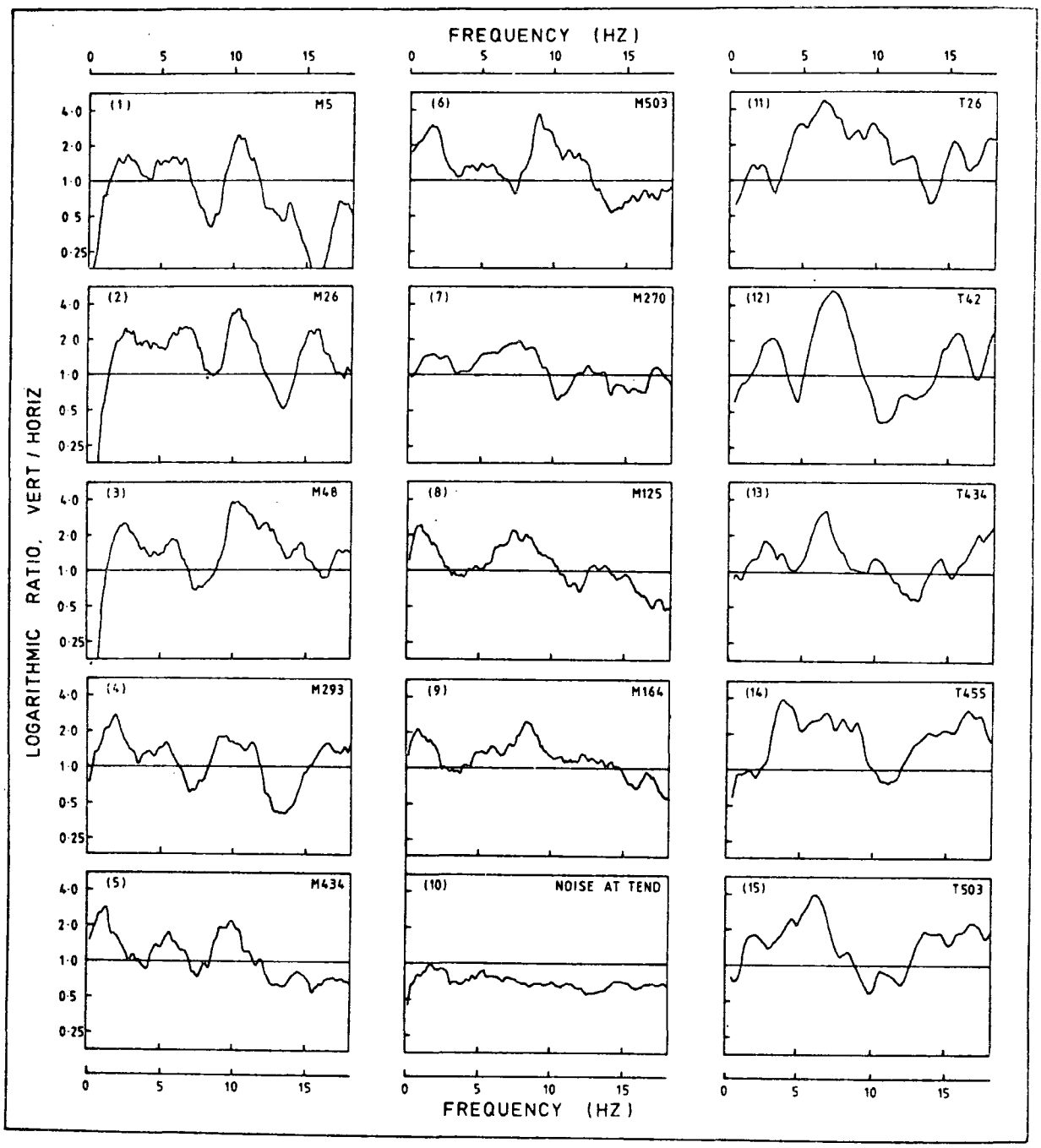

spectra (from which non-crustal influences have theoretically been removed) and those of Figures 7.3.2 and 7.3.3. This emphatically reinforces the conclusion of Section 7.3 that the large oscillations on the velocity amplitude spectra derive from the receiver crustal effect. It also indicates that the observed spectra could be approximated by a computed truncated crustal transfer function based on a single resonant layer.

7.6 Earthquake Source Parameters

7.6.1 The Corner Frequency Method

The vast literature pertaining to seismic source properties and associated spectral studies has been generally reviewed by BÅTH (1974) and by JOHNSON (1979). This section presents one technique, the 'corner frequency' method, by means of which seismic source parameters of some ESP events have been estimated from their P wave displacement amplitude spectra. The method involves the construction of a theoretical spectrum, normally an amplitude-frequency spectrum in a log-log plot, against which the observed spectra are matched. The shape of the theoretical spectrum depends on the details of the mathematical source model from which it is derived. The observed spectra are corrected so as to try to eliminate all influences other than the source response.

Theoretical calculations of the near-field and/or far-field radiation spectra from a seismic source have been

made by HASKELL (1964,1966); SAVAGE (1966,1972,1974); AKI (1967); BERCKHEMER and JACOB (1968); BRUNE (1970, corrected in BRUNE,1971); HANKS and WYSS (1972); KNOPOFF and MOUTON (1975); MADARIAGA (1976,1979); DAS and AKI (1977); ARCHULETA and FRAZIER (1978); HARTZELL et al (1978); BOATWRIGHT (1980); and others. The far-field radiation spectrum is appropriate to the study of ESP events, whose hypocentral distances are in all cases very large compared with their source dimensions.

The corner frequency method provides for the calculation of the source parameters (seismic moment, M_o; fault length, L; stress drop, $\Delta\sigma$) of an event from its acceleration spectral parameters (d.c. level, W_o; corner frequency, w_c; and negative logarithmic slope of the high frequency response envelope, γ) (Figure 7.6.1). The two sets of parameters are related by equations of the form

$$M_o = P_1 \mu W_o / K \qquad (7.6.1)$$

$$L = P_2 c / w_c \qquad (7.6.2)$$

$$\Delta\sigma = \frac{P_3 M_o}{L^3} = \frac{P_1 P_3}{P_2{}^3} \frac{w_c{}^3 \mu W_o}{K c^3} \qquad (7.6.3)$$

(KNOPOFF and MOUTON,1975), where μ is the rigidity of the medium, K is a factor to take account of geometrical spreading of seismic energy, c is the seismic wave velocity and P_1, P_2, P_3 are dimensionless numbers whose numerical values depend on the postulated model of fault rupture and healing.

Equations of the form of 7.6.1 to 7.6.3 are approximations. The dangers of forming direct relationships

FIGURE 7.6.1

ASYMPTOTES OF THEORETICAL FREQUENCY SPECTRA (A) AND THE CORRESPONDING OBSERVED SPECTRA FOR THE SUM OF 6 EVENTS FROM WALDIA RECORDED AT SERDO STATION (B)

The observed spectra are smoothed and corrected for geometrical spreading, and for attenuation with Q=600

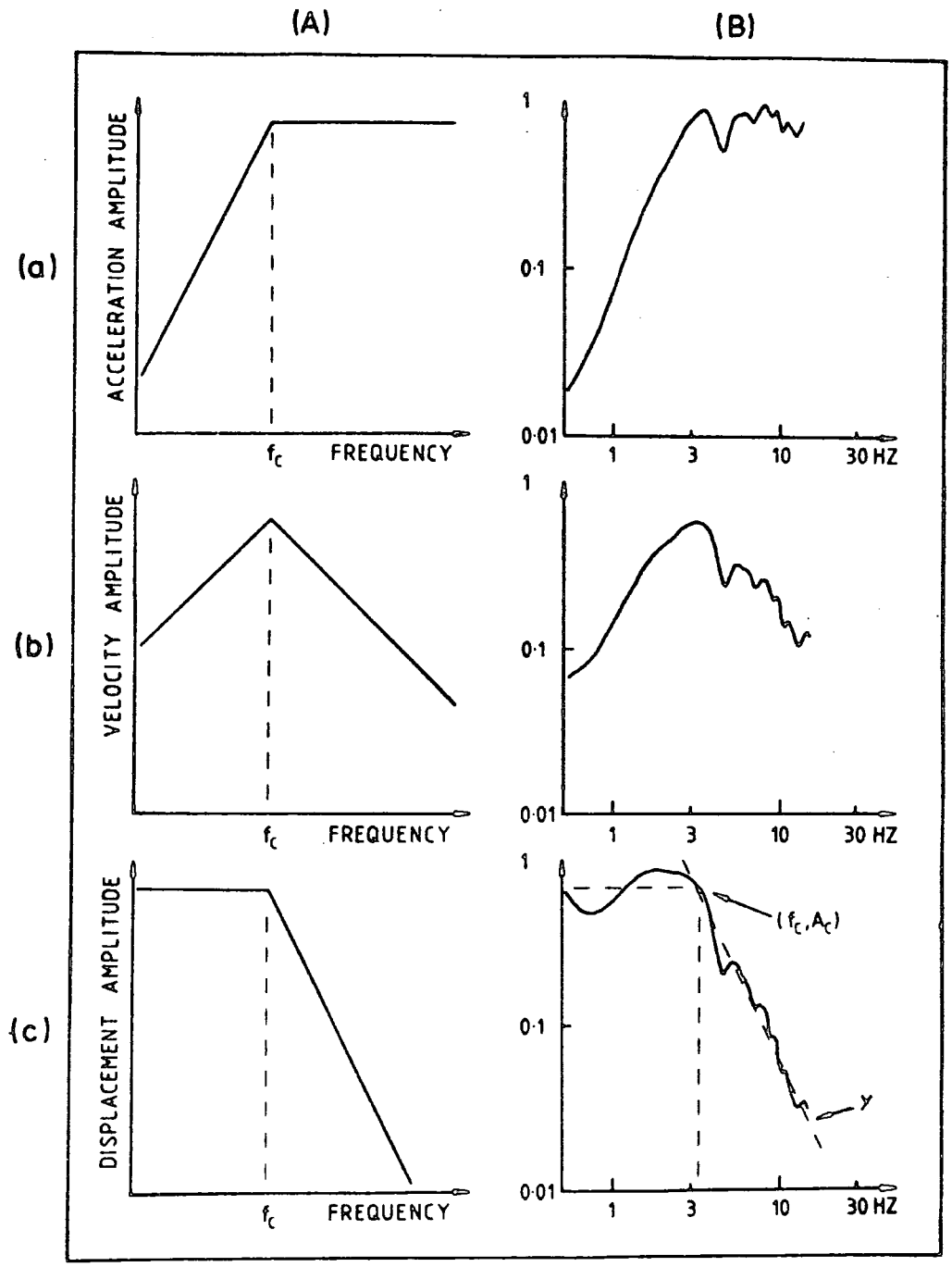

between source and spectral parameters, without regard for the tectonic prestress and frictional stress environment of the ruptured fault segment, have been emphasised by KNOPOFF and MOUTON (1975). In particular, the implication of Equation 7.6.2 that w_c^{-1} is essentially the pulse duration (or, equivalently, that w_c is a measure of the spectrum width, since pulse width and spectrum width are inversely proportional), is dubious (SAVAGE,1972); while intuitively a relationship between fault length and pulse duration should depend on the rupture and healing velocities.

The value of γ may also vary with details of the model, since the asymptotic behaviour of the spectrum of a pulse is determined by the order of the discontinuities of the pulse shape. The models of HASKELL (1964), BERCKHEMER and JACOB (1968), BRUNE (1970) and (except for one case) KNOPOFF and MOUTON (1975) all have $\gamma = 2$ for high frequencies. The statistical models of HASKELL (1966) and AKI (1967), where corner frequency is related to coherence length rather than to fault length, also yield $\gamma = 2$. SAVAGE (1972) argues for $\gamma = 3$ for coherent radiation, while MADARIAGA (1976) has $\gamma = 2.5$. HASKELL (1964), BERCKHEMER and JACOB (1968) and SAVAGE (1972) derive two corner frequencies bounding an intermediate-frequency $\gamma = 1$ trend, and circular fault models sometimes show greater complexity at intermediate frequencies (SAVAGE,1974; MADARIAGA,1976; BOATWRIGHT,1980). Even in theory an intermediate trend may not necessarily be visible on the spectra of seismic events, as the two corner frequencies may be very close together.

Most applications of the corner frequency method have used BRUNE's (1970) model for S waves and its semi-empirical extension to P waves (HANKS and WYSS,1972; DAHLEN,1974), although the foundation of Brune's model has been questioned (see Section 7.6.4). The theoretical value $\gamma = 2$ has been found to be quite well obeyed, with some irregularities, for teleseisms (HANKS and THATCHER,1972; HANKS and WYSS,1972; MAASHA and MOLNAR,1972; MOLNAR and WYSS,1972; WYSS and HANKS,1972; THATCHER and HANKS,1973), and for locally recorded events (DOUGLAS and RYALL,1972; MOLNAR et al,1973); and the values obtained for the source parameters have been in good agreement with those found by other methods (e.g. WYSS and HANKS,1972).

7.6.2 Corrections to the Received Signal Spectrum

ESP P coda velocity amplitude spectra were converted to displacement or acceleration amplitude spectra by respectively dividing or multiplying by frequency. Before numerical estimates of source parameters could be attempted, a number of other factors affecting the received spectra had to be considered:

(1) Attenuating and scattering. There exist several more or less equivalent measures of the dimensionless attenuation factor, Q (KNOPOFF,1969). The most applicable here is that $2\pi/Q$ is equal to the fraction of the total strain energy dissipated per cycle. Unless Q is excessively small, the logarithmic decrement is approximately equal to π/Q. Following DOUGLAS and RYALL (1972) and MOLNAR et al

(1973), this study corrects effects of attenuation and scattering by multiplying the spectral amplitudes by the factor exp(w/2QV), where V is the P phase velocity. The form of this expression is readily justified from theoretical consideration of the effect of departures of seismic waves from perfect elasticity (e.g. BULLEN,1965, p.81).

(2) Spherical spreading. To correct for this, spectral amplitudes were multiplied by the hypocentral distance, R. This is the correction factor used by BRUNE (1970), and it has been applied without comment by DOUGLAS and RYALL (1972) and by MOLNAR et al (1973). However, for a layered earth a correction factor R^k with k = 1 is not necessarily correct, since different wave types have theoretically different k.

(3) Instrumental response. For a few of the closest events, where spectral energies at and above 15 Hz may be significant, the spectra have been corrected according to Equation 7.2.1. For the large majority of events the instrumental response is effectively flat (Figure A3.1).

(4) Crustal effect. The very significant crustal effect described in Sections 7.3 and 7.5 appears as a perturbation on the spectra illustrated in this section. Crustal resonance is equivalent to a filtering effect, so it would be desirable to use a deconvolution technique to reduce it before attempting to study seismic source spectral properties. Sections 7.3 and 7.5 have gone some way towards deriving a suitable inverse filter, since the major

spectral oscillations have been explained in terms of a resonant layer. However, the filter will be sensitive to small structural changes (e.g. LEBLANC,1967) and is also a function of angle of incidence. No previous study has succeeded in applying such a filter, even when the crustal structure has been well known from independent observations. Consequently, in this study the spectra have simply been smoothed, as in previous work (e.g. DOUGLAS and RYALL,1972).

The effect of the additional smoothing subroutine, LOGSMO, used with programme TRANSF for this purpose is illustrated in Figure 7.6.2. In all applications the parameter FLOG (Appendix 9) was set equal to 1.1. This corresponds to smoothing each frequency, w_i, over a moving window extending from $w_i/1.1$ to $1.1w_i$ Hz.

(5) Radiation pattern and azimuthal effects. No correction has been made for these. Observations of ESP-recorded events were too sparse for the determination of fault-plane solutions (Section 8.4). The same problem has occurred in other applications of the corner frequency method to local events. MOLNAR et al (1973) make no correction. DOUGLAS and RYALL (1972) make an implicit crude correction by quoting source parameters for each event that are the average of records at two or three stations. A much greater number of stations is required for effective azimuthal averaging.

7.6.3 Calculation of Seismic Source Parameters

From BRUNE's (1970) formulation for the S wave far-field radiation spectrum, the value of P_2 in Equation 7.6.2 is 2.34/2 . Following HANKS and WYSS (1972, Equn.7), Equation 7.6.2 is applied to P waves simply by writing $c = V_P$. Taking r as the source dimension (radius) of an equivalent circular dislocation surface, Equation 7.6.2 becomes

$$r = 0.37V_P/w_c \qquad (7.6.4)$$

Again following Brune and DOUGLAS and RYALL (1972), Equation 7.6.3 yields

$$\Delta\sigma = (27.5\,\mu V_S A_c)/r^3 \qquad (7.6.5)$$

and $$M_o = (16/7)\Delta\sigma r^3 \qquad (7.6.6)$$

The factor 16/7 in Equation 7.6.6 is BRUNE's (1971) correction to his originally published value of 18/7 (BRUNE,1970, Equn.31). A_c in Equation 7.6.5 is the 'corner amplitude', read directly from the observed spectrum as shown in Figure 7.6.1Bc. The amplitudes, A(w), of the observed spectra have already been corrected for geometrical spreading as explained above, so that $A_c = RW_c$. The observed displacement amplitude spectra are not in general flat (i.e. $A(w) = A_o(w)$) for all $w < w_c$, as predicted from simple theory, so A_c is required in Equation 7.6.5 rather than A_o.

For P waves, Equation 7.6.5 becomes

$$\Delta\sigma = [27.5(k + (4/3)\mu)V_P A_c]/r^3 \qquad (7.6.7)$$

where k is the bulk modulus. It is well known that for elastic waves

FIGURE 7.6.2

THE EFFECT OF SMOOTHING ON A TYPICAL CRUSTAL TRANSFER RATIO SPECTRUM (M26)

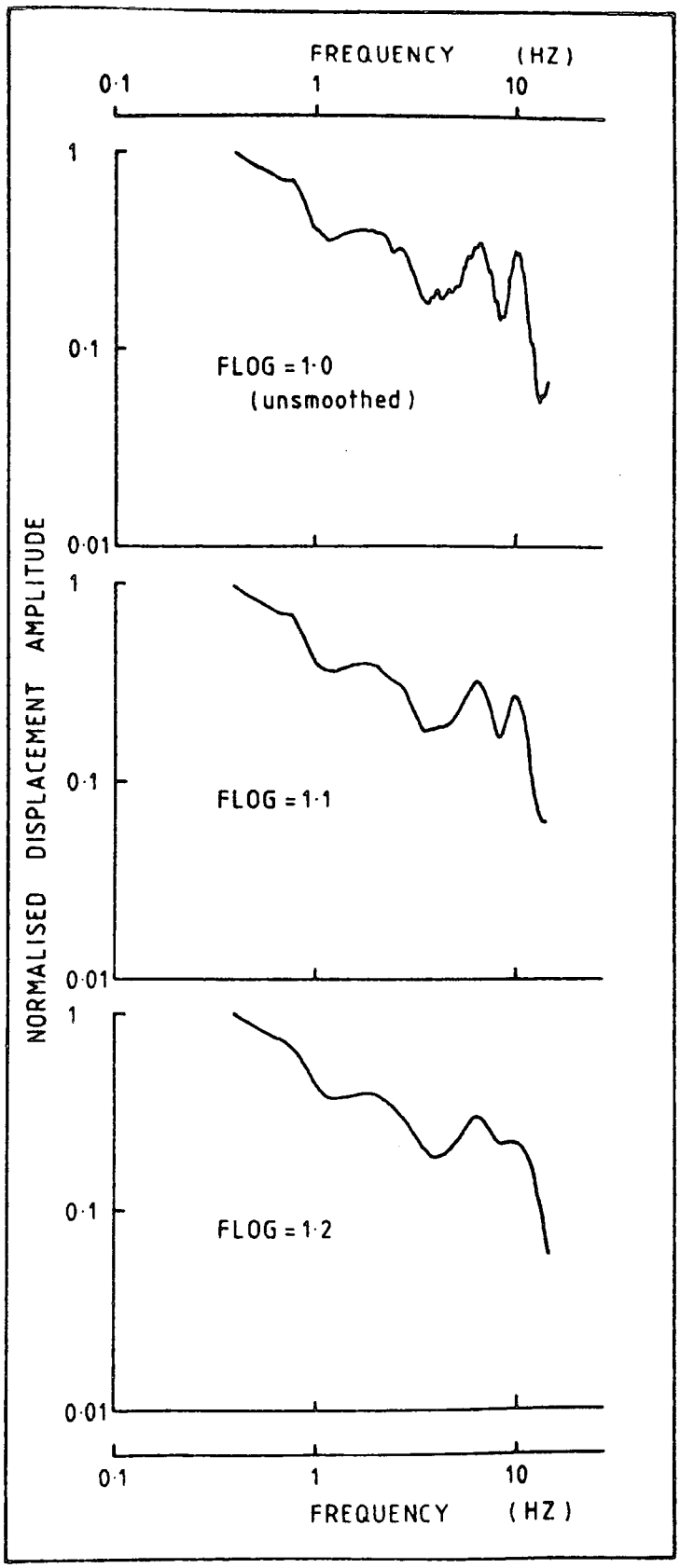

$$V_P^2 = [k + (4/3)\mu]/\rho \qquad \text{(e.g. BULLEN,1965)}$$

Assuming V_P = 6.2 km s^{-1} and ρ = 2.65 gm cm^{-3}, and substituting these values in Equations 7.6.4, 7.6.6 and 7.6.7,

$$r = 2.31/w_c \qquad (7.6.8)$$

$$\Delta\sigma = 1.43*10^{-3}A_c w_c^3 \text{ bar} \qquad (7.6.9)$$

$$M_o = 3.95*10^{19}A_c \text{ dyn cm} \qquad (7.6.10)$$

where w_c is measured in Hz and A_c in cm^2 s. CGS units are used here where they are customary in published work.

Representative ESP displacement amplitude spectra are illustrated in Figure 7.6.3, where the upper, middle and lower curves show the spectra corrected for spherical spreading and for attenuation with Q = 200, 400 and 800 respectively. The spectral parameters A_c, w_c and γ of 24 events were estimated by fitting the observed spectra to the theoretical asymptotes shown in Figures 7.6.1Ac and Bc. The resultant values are given in Table 7.6.1, together with the corresponding source parameter values calculated from Equations 7.6.8 to 7.6.10. The curve for Q = 400 was used except where otherwise stated. A further 4 spectra (of which Figure 7.6.3, record 1, is one) are not represented in Table 7.6.1, since they differed too greatly from the theoretical form for their spectral parameters to be estimated.

FIGURE 7.6.3

REPRESENTATIVE ESP DISPLACEMENT AMPLITUDE SPECTRA

(numbered in order of increasing epicentral distance)

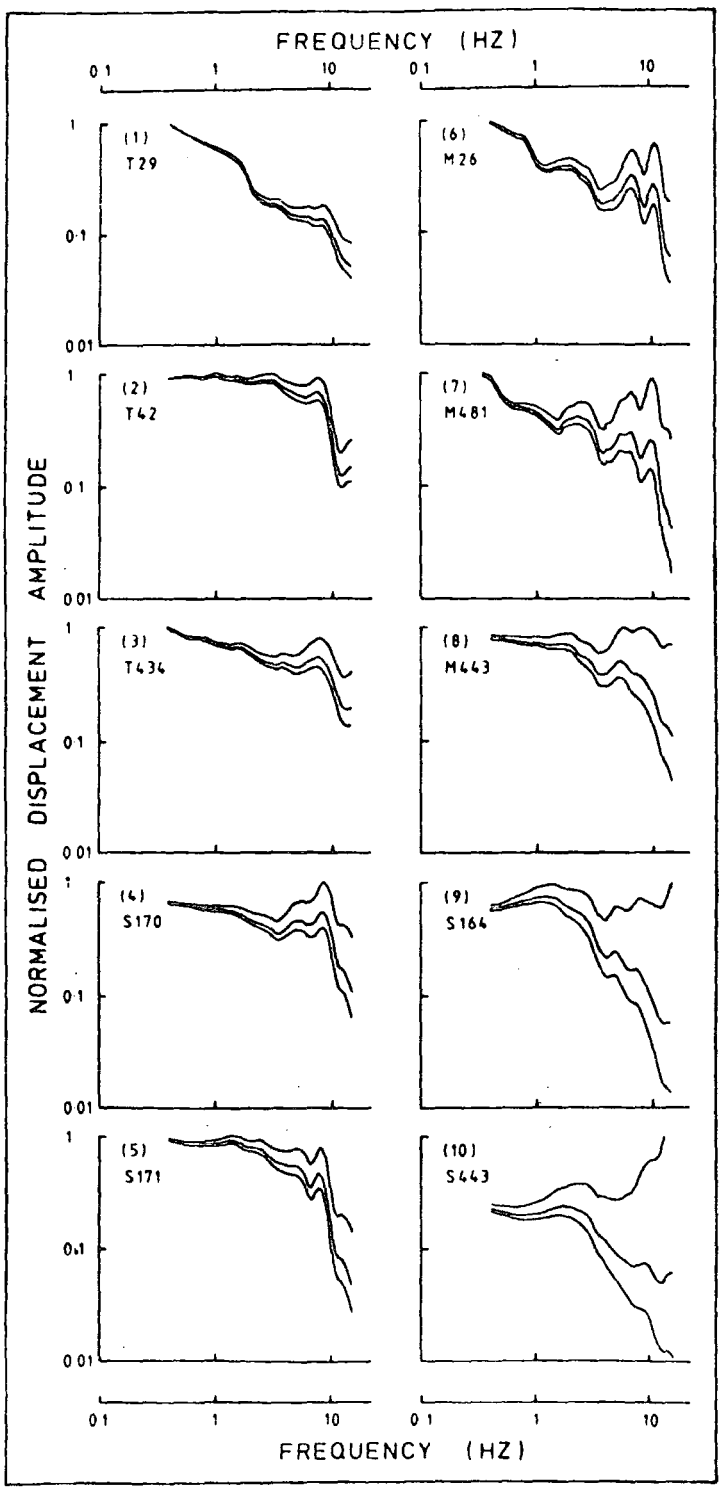

TABLE 7.6.1

SPECTRAL AND SOURCE PARAMETERS OF ESP EVENTS

Event	Epicentral Distance (km)	Duration Magnitude (M_D)	---SPECTRAL PARAMETERS-- Corner Amplitude (cm^2 sec)	Corner Freq (Hz)	Log Slope	-----SOURCE PARAMETERS---- Source Radius (km)	Stress Drop (bar)	Seismic Moment*10^{19} (dyn cm)
M5	60	2.3	0.71	8.2	2.5	0.28	0.56	2.8
M7	62	2.2	0.52	8.6	2.2	0.27	0.47	2.1
S8	38	1.4	0.26	7.0	2.2	0.33	0.13	1.0
M11	60	2.4	1.24	8.0	3.3	0.29	0.91	4.9
M26	62	2.5	1.10	8.2	2.5	0.28	0.98	4.3
T26	26	2.5	0.92	6.2	2.0	0.37	0.37	3.6
S26	36	2.5	1.00	6.5	2.6	0.35	0.39	4.0
M27	62	2.5	1.32	8.0	2.8	0.29	0.97	5.2
T42	31	2.1	0.60	7.2	2.4	0.32	0.32	2.4
T48	25	1.2	0.21	8.1	2.3	0.28	0.16	0.8
T63	17	1.7	0.34	7.7	2.8	0.30	0.22	1.3
M125	107	3.3	9.03	1.9	1.7	1.22	0.09	35.7
T125	117	3.3	7.66	2.2	1.8	1.05	0.12	30.3
S125	159	3.3	9.26	2.0	2.4	1.16	0.11	36.6
S164	161	3.3	8.88	2.1	2.0	1.10	0.13	35.1
D164	149	3.3	10.51	4.0	2.0	0.58	0.96	41.5
S170	61	1.9	0.72	6.8	2.4	0.34	0.32	2.8
S171	61	1.6	0.38	7.5	3.8	0.31	0.23	1.5
M281	(31)*	2.3	0.59	7.2	2.2	0.32	0.31	2.3
M289	(31)*	2.3	0.85	7.4	1.8	0.25	0.49	3.4
M434	63	1.6	0.77	7.6	2.0	0.30	0.48	3.0
T434	39	1.6	0.61	8.4	2.0	0.27	0.52	2.4
M437	64	1.6	0.54	7.4	1.8	0.31	0.31	2.1
M443	99	2.9	3.16	1.9	1.3	1.22	0.03	12.5
T443	136	2.9	3.46	2.4	1.2	0.96	0.07	13.7
S443	188	2.9	3.91	2.2	1.4	1.05	0.06	15.4
D443	148	2.9	5.20	2.2	1.4	1.05	0.08	20.5
M455	95	2.8	1.10	7.2	2.0	0.32	0.59	4.3
T455	63	2.8	1.14	6.8	1.7	0.34	0.51	4.5
M467	96	2.8	1.04	7.4	2.1	0.31	0.60	4.1
M481	96	2.9	1.23	8.0	2.7	0.29	0.90	4.9
T481	63	2.9	2.01	6.1	1.9	0.38	0.65	7.9
M494	75	2.8	1.04	8.0	2.5	0.29	0.76	4.1
M503	91	2.9	1.43	8.3	2.3	0.28	1.17	5.6

*These events were recorded at Mille only. Epicentral distances have been obtained by three-component analysis.

7.6.4 Discussion

Referring to Figure 7.6.3, it is apparent that several factors limit the accuracy with which the spectral parameters can be picked. For the closer events, w_c occurs close to the high-frequency end of the logarithmic frequency axis, which cannot be extended to higher frequencies because of the limited bandwidth of the recorder/playback system. At frequencies above 10 Hz the spectra are not well defined, and it is unclear whether their shape is most affected by the seismic source, crustal reverberations or uncorrected effects of attenuation. For example, it is impossible to know what significance to attach to the sharp increase in spectral amplitude at the high-frequency limit of records 2 and 3. At 15 Hz and above, noise generated in the recorder/playback system may also be considerable. The consequence is increased uncertainty in the estimates of corner frequency.

Since the correction factor for attenuation and scattering is an exponential function of R and w, the choice of Q becomes increasingly critical at greater epicentral distances and higher frequencies. For 23 records where $R < 100$ km, taking $Q = 400$, the mean value obtained for γ was 2.25 ± 0.18 (records of M11 and S170 gave excessively high γ values (Table 7.6.1), which were rejected). Note that if the value assumed for Q were grossly in error, w_c and γ would be expected to vary as functions of R. This was not the case. For $R > 100$ km (records 9 and 10) the correction factor dominated the spectral shape, and little

significance should be attached to the result that Q = 800 was found to give more acceptable values for γ. However, it remained possible to obtain estimates for w_c and A_c which were not critically dependent on Q.

Values of γ are in fact less accurately determined than is implied by the quoted standard deviation. Apart from an incorrect estimate of attenuation, unconsidered ground filtering effects at the station sites is another possible source of systematic error. The observed values of γ are therefore consistent with $\gamma = 2$ as predicted by the Brune model. Although γ does not occur in the equations (7.6.4 to 7.6.6) for the source parameters, γ values widely differing from 2 would imply measured w_c values inconsistent with w_c in these equations.

The receiver crustal effect, considered in Sections 7.3 and 7.5, masks the shape of the source-derived spectrum, and particularly the position of w_c. This is most pronounced for Mille spectra (records 6 to 8). When an attempt was made to remove the crustal effect from these spectra they became substantially smoother, but the difficulty in determining the extent of the crustal contribution to the spectrum led to increased uncertainty in overall spectral shape.

The observed spectra are not flat at low frequencies. The spectra illustrated in Section 7.3 have shown little energy below 1.0 Hz, where it is possible that spectral amplitudes may be affected by uncompensated flutter and other mechanical effects in the recorders (Chapter 3).

Consequently the observed spectra may also be unreliable in the low-frequency limit.

The overall shape of the observed spectra is in fair agreement with theory. Estimates of A_c and w_c may be in error by a factor of 2, implying errors of the same factor in seismic moment, M_o, and source radius, r. The resultant error in stress drop, $\Delta\sigma$, may be an order of magnitude, since $\Delta\sigma \propto A_c w_c^3$ through Equation 7.6.9. This is much larger than the error arising from the total stress drop assumption made earlier (i.e. assuming $\epsilon = 1$ in Brune's equations).

Values of $\Delta\sigma$ for events within Afar do not positively indicate any geographical stress variations. They are consistent with the results of DOUGLAS and RYALL (1972), who used the corner frequency method to obtain stress drops in the range 0.07 to 0.60 bar from 7 Central Nevada events of magnitude 1.0 to 2.0. For the remaining ESP events (125,164,443), all of which are located below the Western Ethiopian escarpment, the much lower stress drops, if correct, would indicate a markedly different source mechanism. However, they may derive from erroneous estimates of corner frequency, as suggested by the anomalous results obtained from the T164 and D164 records.

MAASHA and MOLNAR (1972) used BRUNE's (1970) theory to calculate source parameters for the 1969 April 05 Serdo earthquake (Section 8.2), which had magnitude $m_b = 6.2$ (CGS) or 5.8 (ISC). They obtained the low value for of 3.4 bar. Low stress drop is considered to be characteristic

of earthquakes caused by tectonic rifting along plate boundaries (Chapter 8). Their results for seismic moment were $M_o(P) = 1.96*10^{25}$ dyn cm and $M_o(S) = 1.18*10^{25}$ dyn cm, from P and S wave spectra respectively; and for corner frequency, $w_c(P) = 1.95*10^{-1}$ Hz and $w_c(S)=1.18*10^{-1}$ Hz.

The relationship between seismic moment, M_o, and duration magnitude, M_D, is shown graphically in Figure 7.6.4. ESP M_o values agree well with those obtained by DOUGLAS and RYALL (1972), which are shown also for comparison, but it should be remembered that Douglas and Ryall's magnitudes are measurements of M_L rather than M_D. The regression line

$$\log_{10}(M_o) = (0.61 \pm 0.03)M_D + (18.16 \pm 0.05) \quad (7.6.11)$$

for 23 ESP events may be compared with BAKUN and LINDH's (1977) relationship for 28 Californian events ($0 \leqslant M_D \leqslant 6$),

$$\log_{10}(M_o) = (1.21 \pm 0.03)M_D + (17.02 \pm 0.07)$$

and with recent M_o versus M_L relationships for small ($0 \leqslant M_L \leqslant 2.2$) earthquakes, e.g.

$$\log_{10}(M_o) = (1.06 \pm 0.11)M_L + (16.9 \pm 0.1))$$

(PEPPIN and BUFE,1980)

and $$\log_{10}(M_o) = (0.957 \pm 0.062)M_L + (17.6 \pm 0.072)$$

(SOMERVILLE et al,1980)

In possible explanation of the low slope given by Equation 7.6.11 it should be remembered that M_o has here been obtained from the P wave spectrum, rather than from S waves as in the other studies cited. However, extrapolation of Equation 7.6.11 to magnitude 6 gives a seismic moment three orders of magnitude less than MAASHA and MOLNAR's (1972)

FIGURE 7.6.4

GRAPH OF SEISMIC MOMENT AGAINST MAGNITUDE

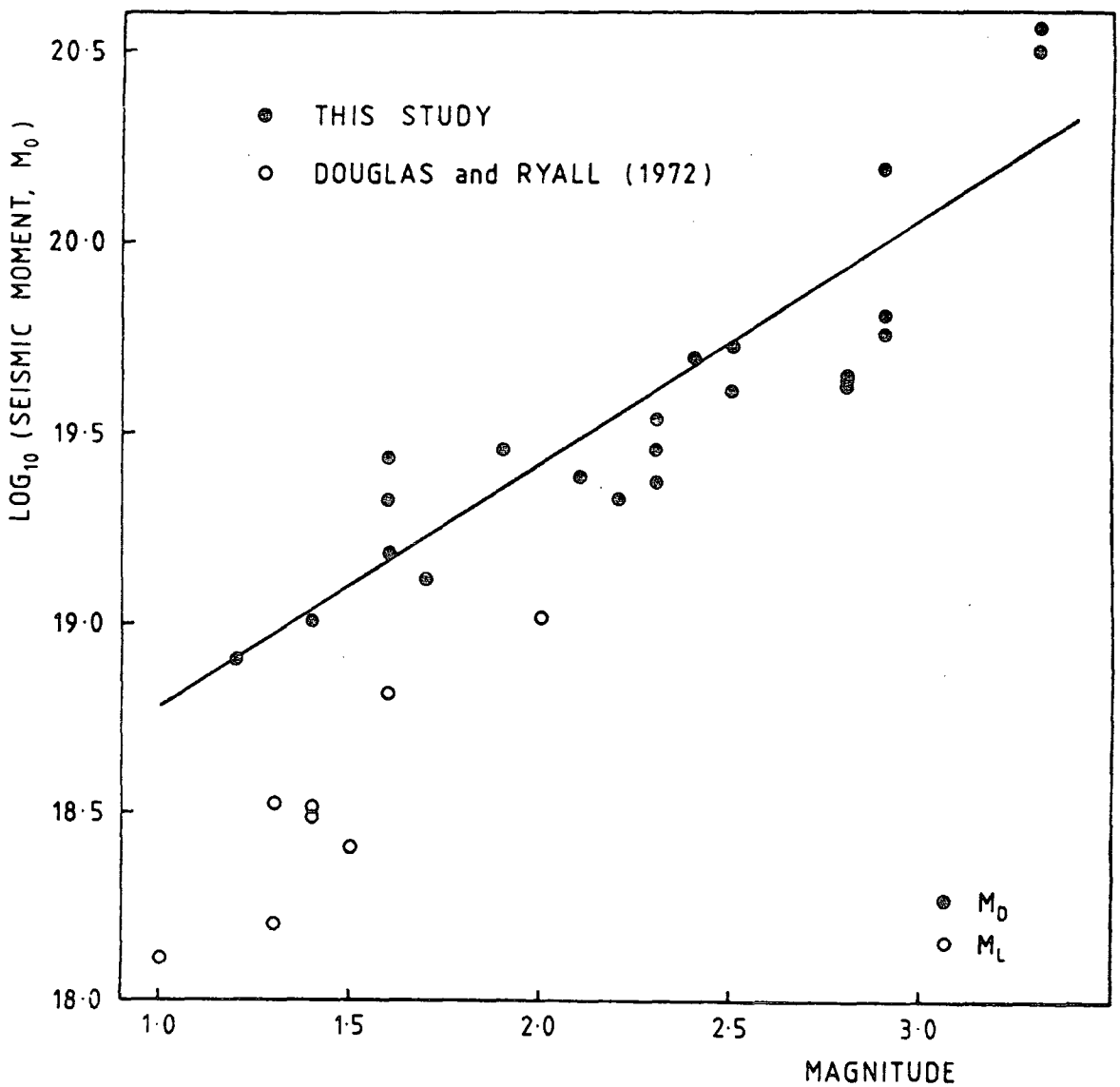

values for the Serdo earthquake.

Within the magnitude range ($1.2 \leqslant M_D \leqslant 2.9$) of studied events within Afar, source radii (r) range from 0.25 to 0.38 km (Table 7.6.1). Douglas and Ryall obtained $0.18 \leqslant r \leqslant 0.25$ km for 6 of 7 events with $1.0 \leqslant M_L \leqslant 2.0$ (the seventh had $r = 0.40$ km, $M_L = 1.6$). Assuming $V_P/V_S = 1.73$, and applying Equation 7.6.4, PEPPIN and BUFE's (1980) P arrival data for events in the Geysers area, California, give $0.05 \leqslant r \leqslant 0.25$ km for $-0.4 \leqslant M_L \leqslant 2.3$.

None of these studies shows any increase of source radius with magnitude, as might be expected. Source radii for Afar events are a little larger than those obtained by the corner frequency method in the Western United States (it has not found application elsewhere). It is not clear whether this is a consequence of the difference in tectonic regime, or whether it simply reflects the greater magnitude of the ESP events.

It is necessary to consider the validity of BRUNE's (1970) theory as applied here. Calculated values for $\Delta\sigma$, in particular, depend critically on the value assumed by P_2 in Equation 7.6.2; and it is desirable to find some justification for Equation 7.6.4. The value of P_2 has been the subject of much discussion. Reviewing the results for various earthquake source models, BRUNE et al (1979) have concluded that P_2 could range between 0.16 and 0.49, or

$$P_2 = 0.33 \pm 0.5 * 0.33$$

A 50% variation in P_2 corresponds to an error factor of 3.3

in the inferred stress drop.

The immediate consequence of applying Equation 7.6.2 directly to P waves, to obtain Equation 7.6.4, is the prediction that $w_c(P)/w_c(S) = V_P/V_S$. Although Brune's theory does not treat P waves, a number of later models have predicted theoretical ratios for $w_c(P)/w_c(S)$. These are summarised in the following two paragraphs.

Dislocation models with bilateral rupture (e.g. SAVAGE,1972) predict $w_c(P) < w_c(S)$, as do models where the source is a long, thin fault along which a dislocation propagates (e.g. EATON et al, 1970). DAHLEN's (1974) self-similar three-dimensional kinematic model also predicts $w_c(P) < w_c(S)$. Dislocation models with unilateral rupture (e.g. HASKELL,1964) give $w_c(P) \approx w_c(S)$. Theoretical ratios of $w_c(P)/w_c(S) > 1$ may be derived by resorting either to volume source models (those that assume boundary conditions in or on the surface of a finite volume instead of on a plane surface, e.g. ARCHAMBEAU,1968); or to statistical models (e.g. HASKELL,1966; AKI,1967), where the corner frequencies are defined by the coherence lengths. HANKS and WYSS's original justification for Equation 7.6.4 was a statistical one, although it was applied to a faulting model.

To obtain $w_c(P) > w_c(S)$ for faulting models it is not necessary to assume instantaneous stress release, as argued by IDA and AKI (1972) against the Brune model. Rather MOLNAR et al (1973) have demonstrated the less stringent requirement that both the duration of slip on the fault and

the time for the rupture area to develop must be small compared to the time for seismic waves to cross the source area, and for which most of the radiation is generated by essentially simultaneous slip over most of the rupture area. MADARIAGA (1976) has obtained $w_c(P) > w_c(S)$ at azimuths (θ) of more than 30^o, measured from the normal to the fault, for a model of a circular fault which expands at a constant velocity and stops suddenly. Here the width of the far-field spectrum is controlled by the stopping phases radiated when the fault stops expanding, which have longer duration for S pulses than for P pulses when $\theta > 30^o$.

It has been observed that $w_c(P) > w_c(S)$ for almost all observed seismic spectra, whether of teleseisms (HANKS and WYSS,1972; WYSS and HANKS,1972; LINDE and SACKS,1972), strong-motion accelerograms (TRIFUNAC,1972), or local events (MOLNAR et al,1973; SOMERVILLE et al,1980). This is true for the ESP events also. Although no attempt was made to determine $w_c(S)$ from ESP data, because of the greater problem of contamination by other phases (particularly by P, for close events with large signal-to-noise ratio), it was clear from inspection of P and S arrivals in the time domain that P contained more high frequency energy than S.

The conclusion from this review is that the assumption of effectively-instantaneous stress release, as in the Brune model, will give acceptable results; and that such a model is less physically unrealistic than some have suggested. Within the accuracy claimed for the observations, the theoretical procedure is quite justified.

7.7 Summary

The frequency spectra of ESP seismic records are dominated by the effect of the shallow crustal structure beneath the seismic recorders. The frequencies of the resultant spectral maxima and minima are little dependent on azimuth, indicating that arrivals from different azimuths have sampled the same or very similar crustal structures. This implies (for a laterally heterogeneous crust) that the arrivals have been received at near-vertical incidence, in accordance with the conclusions of Chapter 6. At Mille station, where the spectral oscillations are especially pronounced, they have been explained in terms of a single shallow layer of approximate thickness 250 to 300 m.

The spectra support the hypothesis that Q is lower directly beneath the Tendaho graben than beneath either of its flanks. The pronounced attenuation evident on Serdo records of relatively close earthquakes indicates that the low Q region reaches shallower depth below Serdo station, on the eastern margin of the graben, than below Tendaho and Det Bahri on the west. The shapes of ESP P-wave displacement amplitude spectra are consistent with Q values of 400 below the Tendaho graben and 800 below Western Afar.

Crustal transfer ratio spectra of ESP events show a simplicity, and a similarity from event to event over wide ranges of distance and azimuth, that indicate that the crustal transfer ratio method is applicable to local events, and that the spectra could be modelled using a comparatively simple truncated crustal transfer ratio function. This

would not only provide a model for the upper crust, but would enable deconvolution of the receiver crust effect on the observed seismic spectrum to facilitate subsequent studies of the seismic source.

Despite the perturbation caused by the receiver crustal effect, and the uncertainties involved in correcting for path effects, ESP displacement spectra have overall shapes in accordance with theory, permitting the calculation of seismic source parameters for events within Afar as follows: source radius, 0.25 to 0.38 km; stress drop, 0.13 to 1.17 bar; seismic moment, $0.8*10^{19}$ to $7.9*10^{19}$ dyn cm. These figures are in good agreement with previous evaluations for similar sized events elswhere.

CHAPTER 8

SPATIO-TEMPORAL CHARACTERISTICS OF ESP EVENTS, AND THEIR RELATION TO REGIONAL TECTONIC PROCESSES

8.1 Introduction

504 seismic events, listed in Appendix 6, were detected by the ESP local network between 1974 Feb 20 and 1974 Sept 27. For 23% of this period the network was inoperative (Figure 8.1.1). The majority of events occurred in sequences of between 1 and 7 days' duration. Longer term variations in the intensity of seismicity were difficult to observe because of the network's intermittent operation.

Epicentres were determined for 250 events, and focal depths for 79 (Chapter 4). Approximate positions of a further 195 events, mostly recorded at one station only, were established from the very close similarity of their waveforms with those of already located earthquakes, and/or their occurrence within well-defined sequences. In a few instances these approximate locations were confirmed by three-component analysis (Chapter 6).

Epicentres of ESP-recorded events are shown on Figure 8.1.2. For comparison, Figure 8.1.3 shows teleseismically-located events which have occurred in the same area during the period 1955 to 1980 (Appendix 2). Events prior to 1955 are not included, since their epicentres have large uncertainties which cannot easily be represented by error bars. Teleseisms have been discussed

FIGURE 8.1.1

HISTOGRAM OF LOCAL EVENTS RECORDED BY ESP (1974)

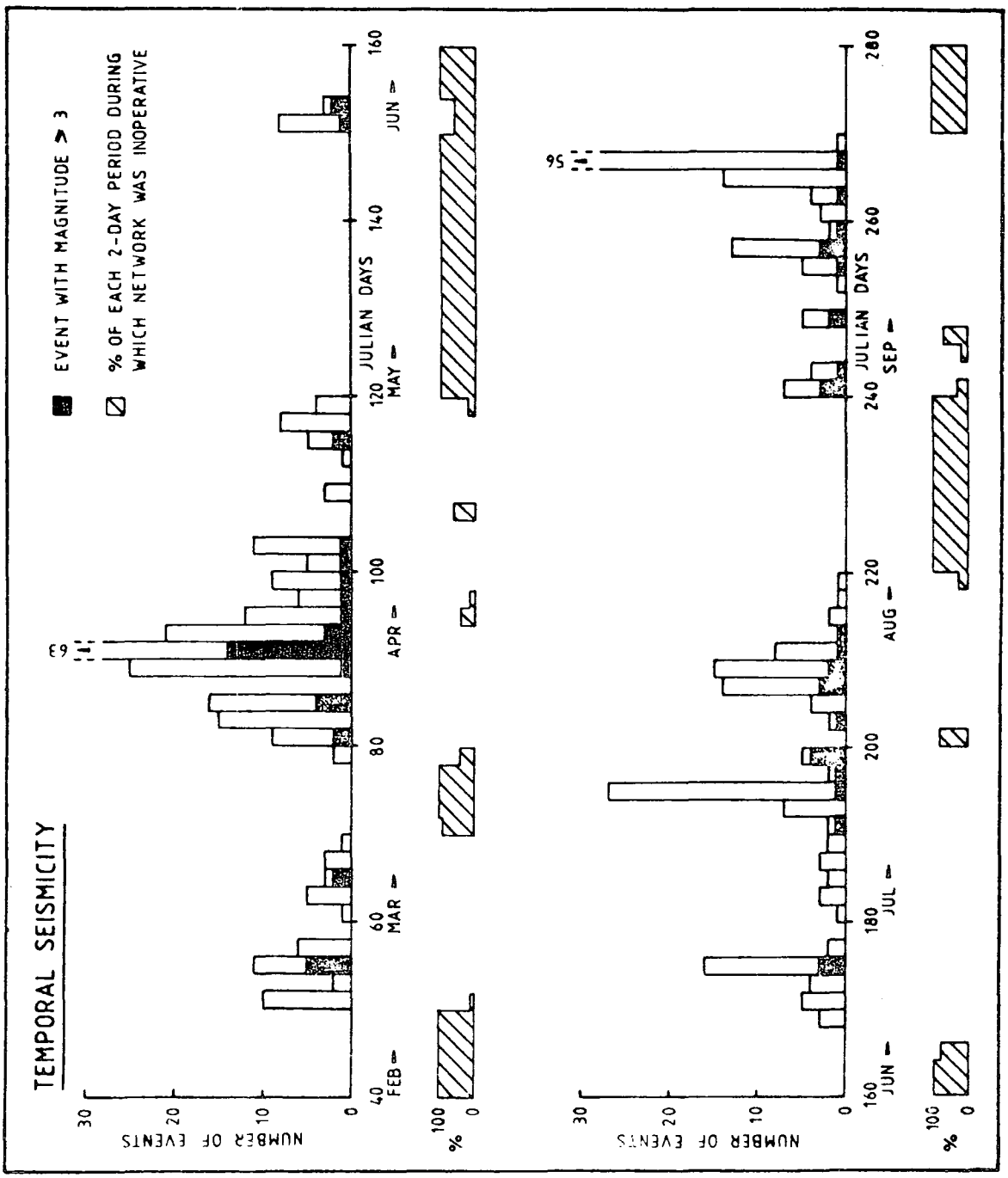

FIGURE 8.1.2

EPICENTRES OF LOCAL EVENTS RECORDED BY ESP

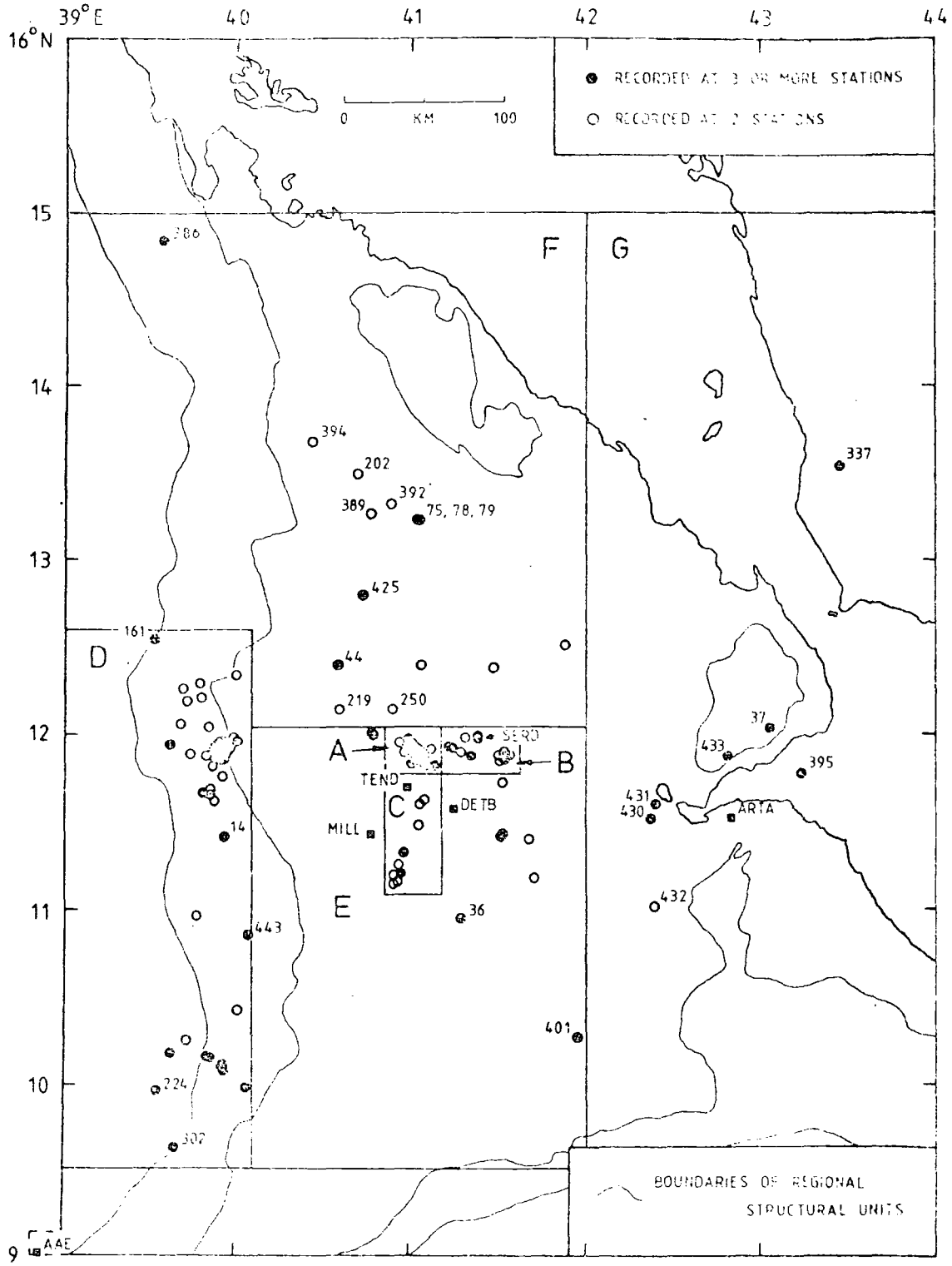

FIGURE 8.1.3

EVENTS TELESEISMICALLY LOCATED WITHIN THE AREA OF FIGURE 8.1.2 DURING THE PERIOD 1955 TO 1980

(sources are given in Appendix 2)

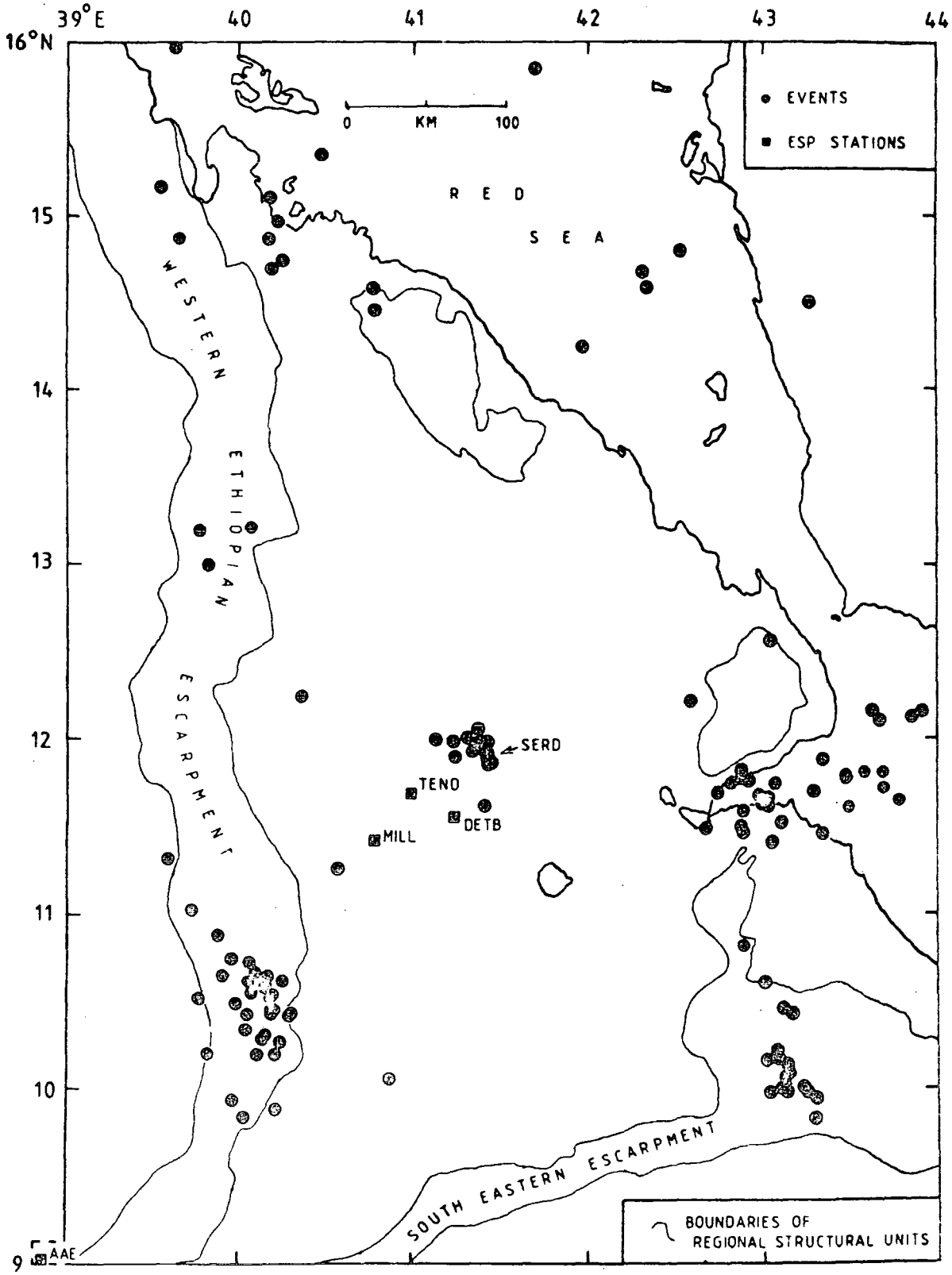

in a regional context in Section 1.4. The destructive 1969 events teleseismically located near Serdo are described more specifically in Section 8.2, since they occurred only just outside the ESP station network. ESP local records can consequently provide additional information on such important parameters as focal depth and fault plane for seismic activity around Serdo, which cannot be determined beyond dispute from the 1969 teleseismic data.

Section 8.3 describes the spatial relationship of ESP-located events to local tectonics. In this respect the sense of first motions recorded by ESP is important, and this is the subject of Section 8.4. The stations are too few for focal mechanisms to be determined, but some types of faulting can be excluded as incompatible with the observed first motions. Certain sequences of events are of particular interest, and are considered in Section 8.5 in terms of their magnitude-time relationships and magnitude-frequency b-coefficients.

A possible explanation of the ESP seismicity observations is given in Section 8.6. Finally, in Section 8.7, the 1969 Serdo earthquakes are re-examined, and three models for spreading within Afar considered, in the light of the new ESP seismicity data.

8.2 The 1969 Serdo Earthquakes

On 1969 Mar 29 the village of Serdo (11.97°N, 41.31°E) was completely destroyed by an earthquake with the loss of 40 lives (Figure 8.2.1). Initial horizontal motion to the

FIGURE 8.2.1

RUINS OF SERDO FOLLOWING THE 1969 SEQUENCE OF EARTHQUAKES

(photographs taken 1974)

north east is suggested by the present inclination to the south west of the reinforced concrete water tower (Figure 8.2.1a), and of a steel flag pole at Serdo; and is corroborated by survivors' reports of being thrown in an eastward direction (DAKIN et al,1971). A second major shock occurred on 1969 Apr 05, opening three large faults near Serdo trending 130° to 140°, and many small tensional fissures up to 50 km from the epicentre (DAKIN et al,1971). Dakin et al also found that weathered boulder fields 15 km north of Serdo had been disturbed by sudden vertical motion.

12 shocks were reported by international agencies and 253 aftershocks were recorded at AAE over 39 days (DAKIN,1975). Four sets of epicentres for the teleseismically-observed events are given in Figure 8.2.2 and Table 8.2.1, where 'JED' refers to FAIRHEAD and GIRDLER's (1970,1971) relocations by joint epicentral determination (the restrained sub-master event was located at 13.00°N, 48.35°E) and 'GOUIN' to GOUIN's (1975) south-eastward translation and clockwise rotation of the JED epicentres based on field observations. Gouin concluded that "it is evident that the 12 events belong to a common NW-SE active tectonic zone about 50 km wide at the 12°N latitude". These events have also been discussed by SEARLE and GOUIN (1971a) and by GIRDLER (in preparation).

Identical fault plane solutions for the two major events (2 and 6, Table 8.2.1) have been computed by McKENZIE et al (1970) (Figure 8.2.3). One nodal plane strikes 063° with a 70° dip to the SE, the other 333° with a

FIGURE 8.2.2

EPICENTRES OF TELESEISMICALLY-RECORDED EVENTS

OF THE 1969 SERDO SEQUENCE

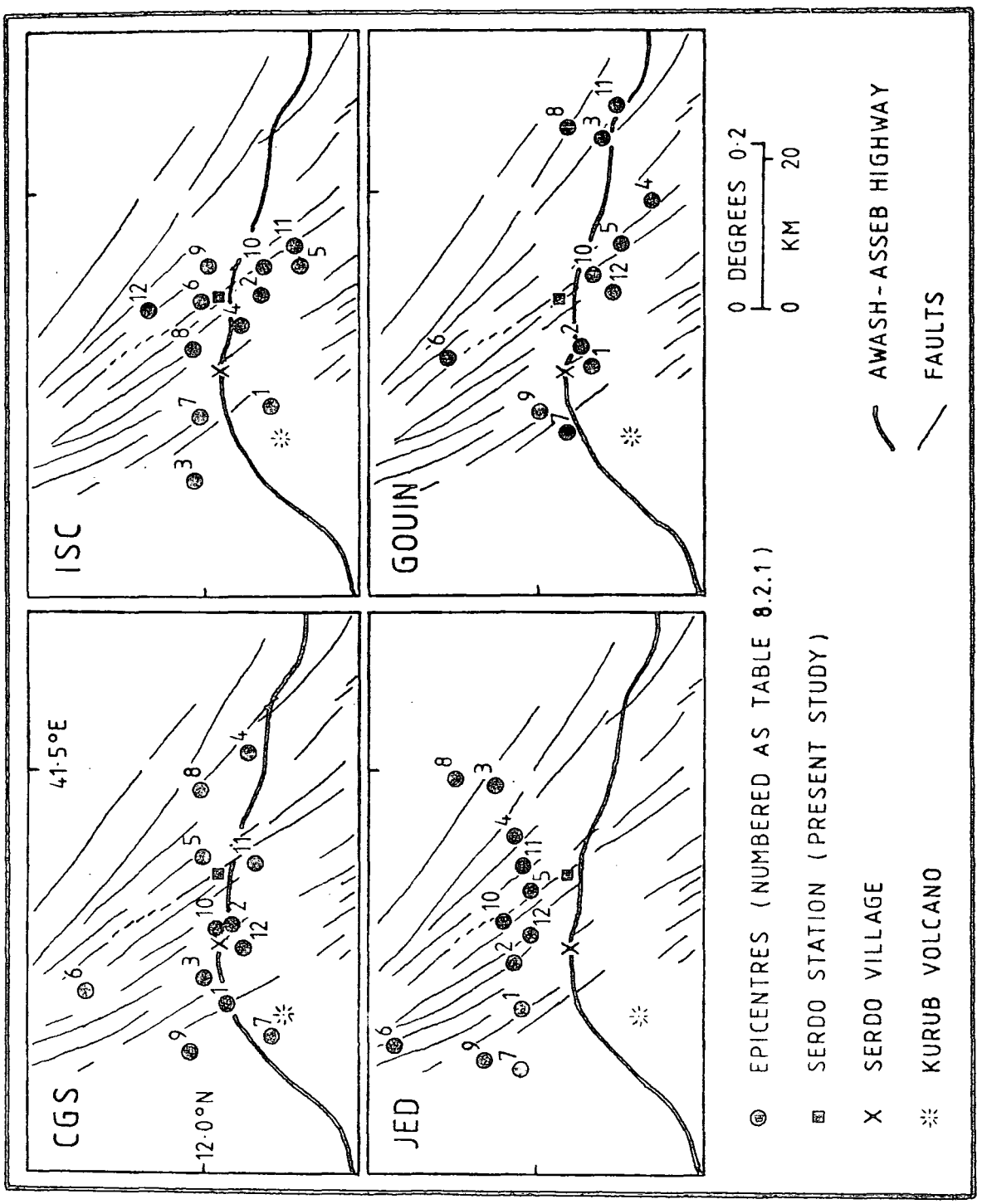

TABLE 8.2.1

PARAMETERS OF TELESEISMICALLY-RECORDED EVENTS OF THE 1969 SERDO SEQUENCE

Event Number	Date	Agency	Origin Time	Latitude (°N)	Longitude (°E)	Focal Depth (KM)	Magnitude m_b	Magnitude M_S	Number of Recording Stations
1	MAR 29	CGS	09:15 54.1±0.17	11.97±.03	41.18±.03	33	5.8	6.3	72
		ISC	09:15 54 ±1.0	11.91±.03	41.21±.03	35±10	5.9		204
		JED		12.02	41.18				
		GOUIN		11.93	41.27				
2	MAR 29	CGS	11:04 47.9±3.7	11.96±.04	41.29±.055	4±22	5.6		54
		ISC	11:04 52 ±1.1	11.92±.03	41.36±.032	35	5.5		166
		JED		12.03	41.24				
		GOUIN		11.94	41.30				
3	MAR 29	CGS	11:07 30.0±0.3	11.99±.03	41.21±.85	33	5.3	5.8	21
		ISC	11:07 45 ±6.0	12.01±.07	41.1 ±.141	64±56	4.9		55
		JED		12.06	41.48				
		GOUIN		11.91	41.57				
4	MAR 29	CGS	13:08 11.4±3.9	11.94±.03	41.52±.09	4±23	5.1		23
		ISC	13:08 17 ±1.2	11.94±.04	41.31±.05	43±12	5.1		88
		JED		12.03	41.41				
		GOUIN		11.85	41.49				
5	MAR 29	CGS	18:30 42.2±0.4	12.00±.08	41.38±.12	33	4.6		8
		ISC	18:30 49 ±5	11.87±.09	41.40±.13	95±52			19
		JED		12.01	41.34				
		GOUIN		11.89	41.43				
6	APR 05	CGS	02:18 29.9±1.9	12.15±.03	41.20±.04	17±14	6.2	6.1	46
		ISC	02:18 30 ±2.8	12.00±.04	41.35±.04	19±20	5.8		175
		JED		12.19	41.13				
		GOUIN		12.12	41.26				
7	APR 05	CGS	20:06 23.8±0.4	11.91±.08	41.14±.11	33	4.3		6
		ISC	20:06 24 ±2.8	12.0 ±.15	41.2 ±.20	32±33			13
		JED		12.02	41.10				
		GOUIN		11.95	41.19				
8	APR 05	CGS	20:14 35.9±0.4	12.03±.04	41.47±.07	33	4.9	5.2	19
		ISC	20:14 41 ±1.3	12.02±.05	41.28±.07	70±14	4.8		35
		JED		12.11	41.49				
		GOUIN		11.96	41.59				
9	APR 06	CGS	16:51 45.5±2.0	12.03±.04	41.12±.06	20±15	5.2	5.4	39
		ISC	16:51 47 ±1.1	11.99±.03	41.40±.039	41±11	5.1		104
		JED		12.07	41.11				
		GOUIN		12.00	41.21				
10	APR 07	CGS	06:23 53.4±1.2	11.98±.10	41.28±.08	33	4.6		14
		ISC	06:23 55 ±1.8	11.92±.10	41.40±.09	58±20			24
		JED		12.04	41.30				
		GOUIN		11.93	41.29				
11	APR 08	CGS	02:13 58.7±1.3	11.93±.06	41.37±.07	34±13	4.8		18
		ISC	02:14 01 ±1.1	11.88±.05	41.42±.05	56±12	4.8		52
		JED		12.02	41.37				
		GOUIN		11.90	41.62				
12	MAY 05	CGS	02:45 38.0±1.3	11.94±.08	41.26±.06	35±15	5.2	5.0	20
		ISC	02:45 40 ±1.5	12.07±.04	41.34±.06	38±15	4.9		83
		JED		12.01	41.28				
		GOUIN		11.90	41.37				

FIGURE 8.2.3

FAULT PLANE SOLUTIONS FOR 1969 SERDO EVENTS

(McKenzie et al,1970)
(the labels 2 and 6 are event numbers as in Table 8.2.1)

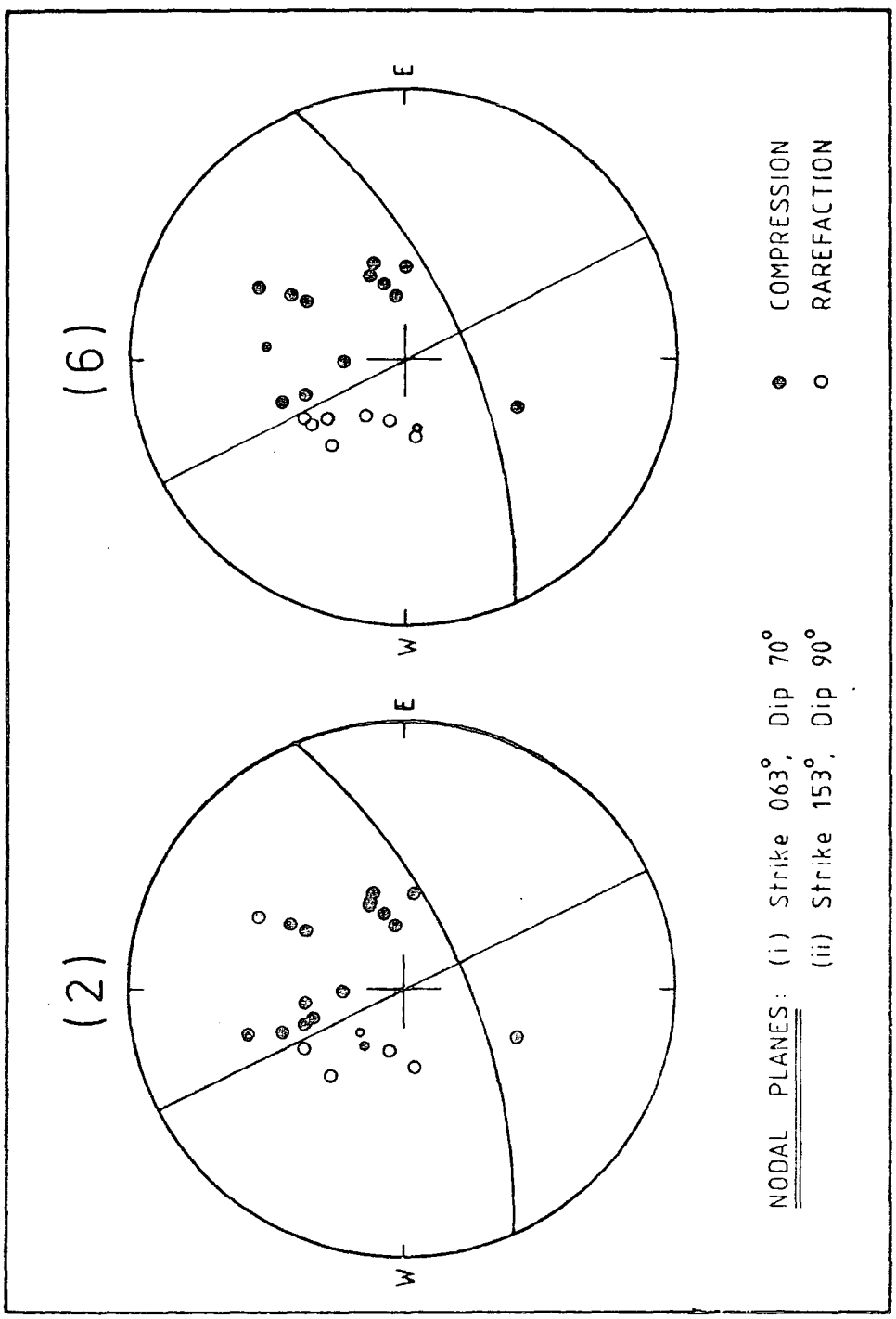

90° dip. McKENZIE et al (1970) and GOUIN (1975) have chosen the 333° plane as the fault plane on the basis of field observations of sinistral strike-slip along 320° fractures (DAKIN et al,1971), and of the general trend of surface faulting.

FAIRHEAD and GIRDLER (1971) and GIRDLER (in preparation) have adopted the alternative (063°) fault plane on the basis of the 080° alignment of JED epicentres. This plane gives dextral motion consistent with the anticlockwise rotation of the Danakil block and with a postulated ENE-WSW transform fault beneath the Bidu-Hanish volcanic line (Figure 1.4.2). The surface phenomena are held to be second order effects which could have been induced by ENE-WSW dextral motion at depth. Laboratory experiments with freezing wax (OLDENBURG and BRUNE,1972) and wet clay (COURTILLOT et al,1974; TAPPONNIER and VARET,1974) suggest this possibility. Two intersecting sets of surface faults would be expected (as seen over the Mak'arrasou transform fault in SE Afar to which Courtillot et al applied their model). Faults near Serdo trend almost exclusively NW-SE (Figure 8.3.3), but in adjacent areas of Afar faulting is complex and GIRDLER (in preparation) maintains that the fault trends are broadly as predicted by COURTILLOT et al's (1974) model.

Source parameters and frequency-magnitude b-coefficient values for the 1969 Serdo events are discussed below in the light of fresh information provided by this study.

8.3 Regional Description of Local Seismicity

Figure 8.1.2 should not be interpreted as showing the distribution of seismicity within the whole of Afar, since the station network is too compact for a large scale seismicity study. Its location capability decreases rapidly with distance, not only because the network aperture to epicentral distance ratio is decreasing (Chapter 4), but also because arrivals from 150 km or farther have emergent onsets which cannot be so accurately timed (Section 3.7). Location thresholds of M_L = 1.4 at 50 km and 1.9 at 100 km were estimated from Equation 5.4.3. These thresholds are for a typical background noise level of 3 mm peak-to-peak trace amplitude, and assume that for an event to be located requires signal to noise ratio > 1.5.

In this section ESP-located events are geographically grouped for clarity into the seven regions, A to G, indicated on Figure 8.1.2.

8.3.1 Region A

(11.75°N to 12.0°N, 40.83°E to 41.15°E, Figure 8.3.1)

The 86 events recorded in this region occur at the margin of the Tendaho graben. They are referred to as "NW Tendaho graben" events. 45 epicentres were computed, and 14 focal depths (mean depth 2.5 ± 0.98 km). The NW Tendaho graben area was active throughout the period of study. Two events occurred with $M_D \geq 3.0$: event 49 (M_D = 3.0), associated with a sequence of 2 foreshocks and 9 aftershocks in a 60 hr period; and event 319 (M_D = 3.2), with 5

FIGURE 8.3.1

ESP EPICENTRES: NW TENDAHO GRABEN, REGION A

(adjacent areas of Regions B and C are shown also)

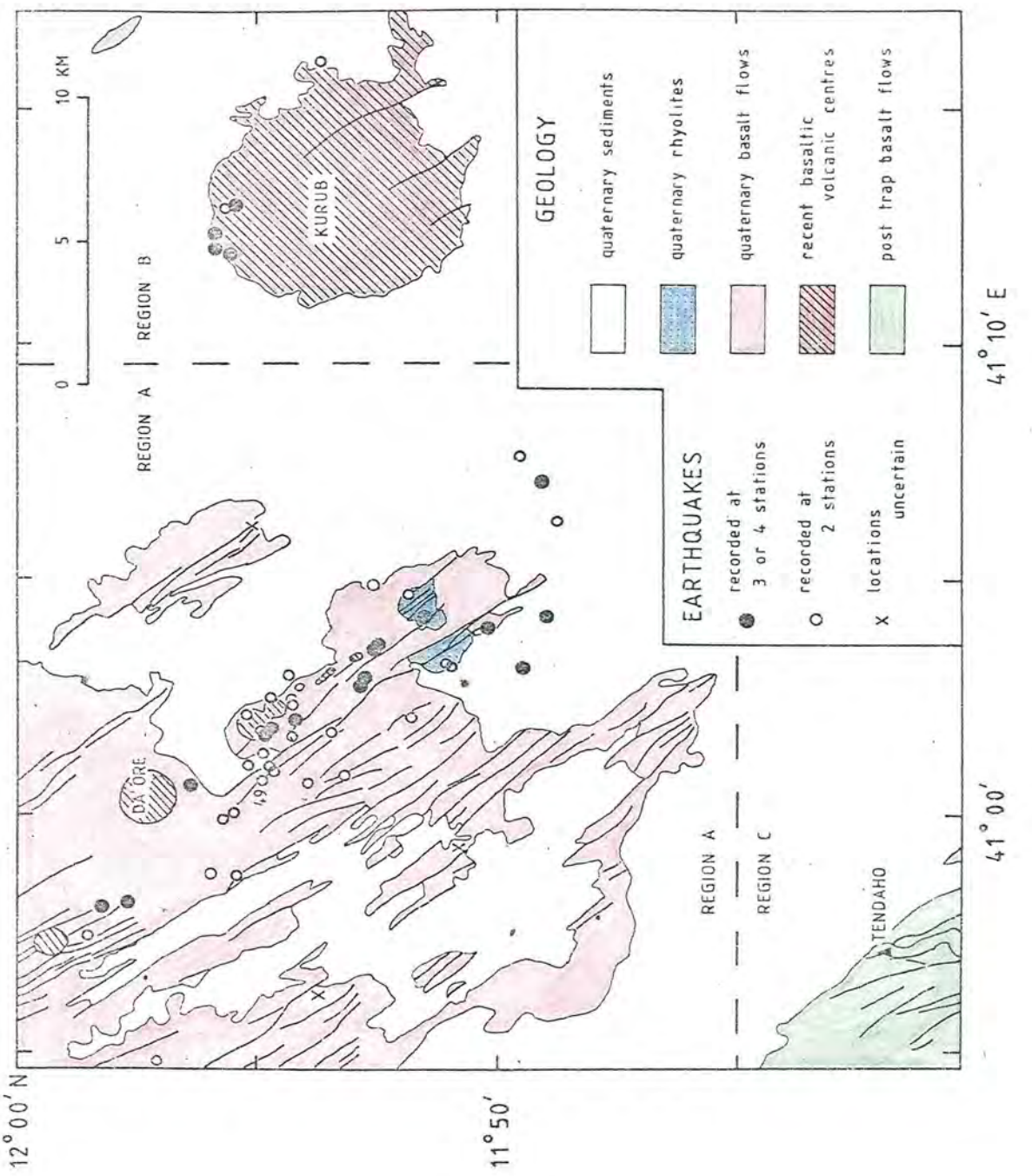

foreshocks and 20 aftershocks in 27 hr. The larger sequence (see Section 8.5) was recorded at Tendaho only, so no epicentres could be determined. Otherwise, no event was recorded with $M_D > 2.6$ and no sequence contained more than 5 events.

The western margin of the Tendaho graben exhibits intense NW-SE extensional faulting of Quaternary flood basalts and occasional Quaternary rhyolites. All exposures are probably younger than 0.34 Myr (Section 2.3). The set of NW Tendaho graben epicentres is remarkably linear along a NW-SE axis (also the axis of the Tendaho graben itself), and follows a NW-SE line of volcanic centres including Da'Ore volcano. These centres post-date the Lower Holocene Tendaho lake, but are cut by NW- and NNW-trending faults (Section 2.3). There is thus a very strong correlation of current seismicity with Recent volcanic activity and surface faulting, but the consistency of recorded first motions (Section 8.4) suggests that the events should be classified as tectonic rather than volcanic.

It was shown in Section 4.7 that error ellipses for NW Tendaho graben epicentres are elongated along a NW-SE axis, especially for events not recorded at Det Bahri. However, confidence ellipses are small for all events recorded at 3 or more stations (e.g. event 12, Figure 4.7.6), since the events lie near the centroid of the ESP station network. Events recorded at 2 stations only may be subject to errors of as much as $\pm$ 2 km along the NW-SE axis. The linearity of the NW Tendaho graben epicentres over more than 25 km is

undoubtedly real.

Figure 8.3.2 is a plot against time of the position of NW Tendaho graben epicentres along the 134° axis of activity. Distance on the y-axis increases towards the south east from zero at 11.98°N, 40.95°E. It was possible that the seismic activity might have shown a linear migration with time along the axis of activity, analogous to LONG, R.'s (1974a) tentatively proposed 7.5 km yr^{-1} migration of seismicity. Figure 8.3.2 shows no evidence for any such migration. During the period of greatest seismicity (Julian days 50 to 120) the whole area was active.

8.3.2 Region B

(11.75°N to 12.0°N, 41.15°E to 41.6°E, Figure 8.3.3)

Had field recording terminated three days earlier, Region B would have appeared seismically almost inactive. One event (223, M_D = 2.3) had been poorly recorded at Mille and Tendaho and located 3 km WNW of Serdo village, and another (272, M_D = 1.9) tentatively located just east of Kurub volcano. A single, relatively large event (352, M_D = 2.9) had occurred south of Serdo (11.88°N, 41.33°E) at the northern end of a ridge of Holocene to Recent basalt flows, extending NW above the sediments of the Tendaho graben and cut by NW-SE faulting. One event (224, M_D = 2.7) had been observed SE of Serdo.

During the period Sep 24 13.00 hr to Sep 25 06.00 hr 35 events were detected SE of Serdo, 18 of which were

FIGURE 8.3.2

POSITION OF NW TENDAHO GRABEN EPICENTRES ALONG A 134° AXIS AS A FUNCTION OF ORIGIN TIME

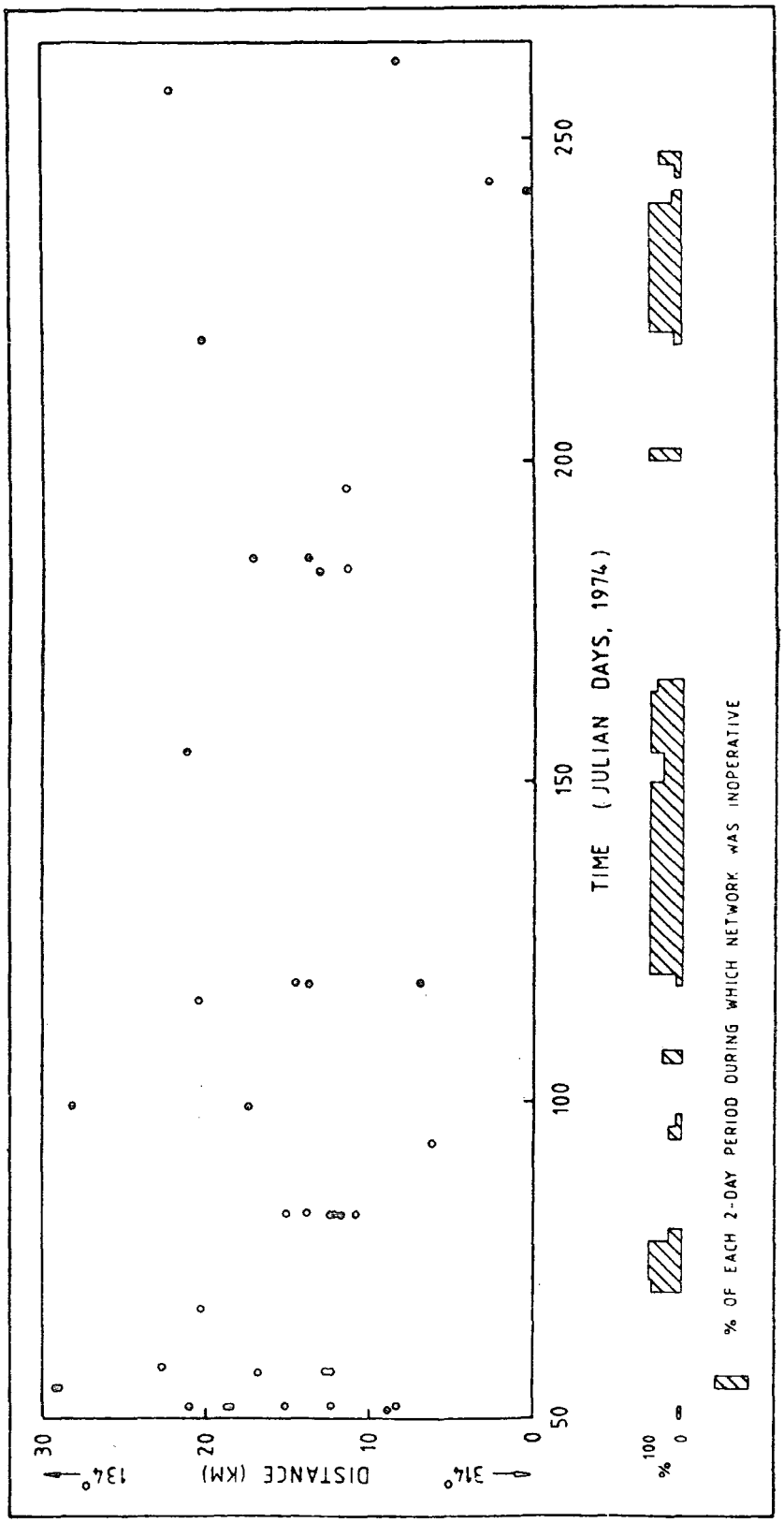

FIGURE 8.3.3

ESP EPICENTRES: REGION B

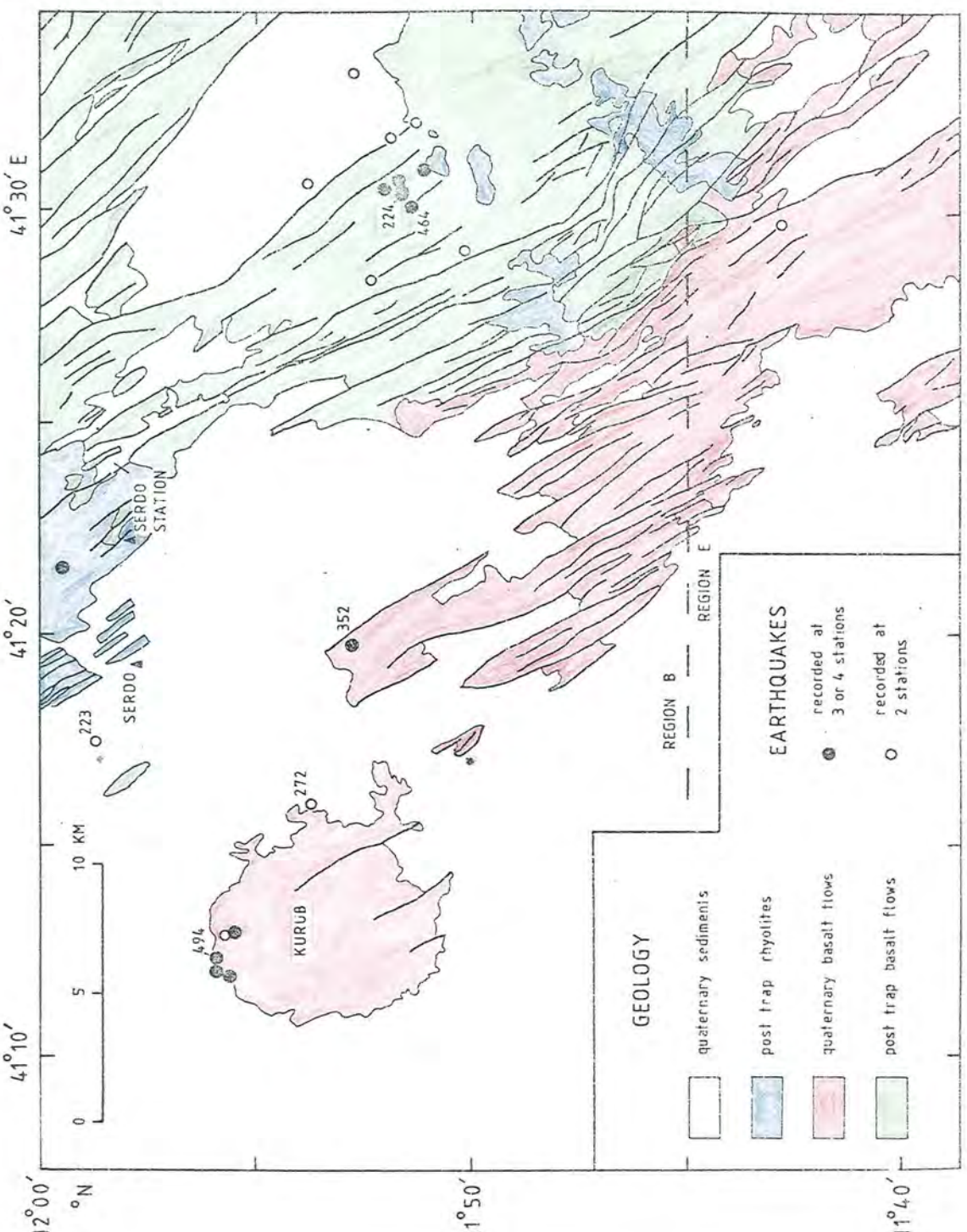

located (Figure 8.3.3). 20 events, of which 6 were located, occurred under the northern edge of Kurub volcano during the same period. The relationship between these sequences is considered in Section 8.7.

SE of Serdo the main shock (464, M_D = 3.9) saturated all the ESP recorders, and was recorded at ART (Ruegg, pers.comm) and at AAE. One foreshock and two aftershocks attained M_D = 2.8 or 2.9, all three having computed surface foci. 7 other foreshocks and 23 other aftershocks, whose focal depths could not be determined, had $M_D < 2.5$. All four principal shocks were located within 0.6 km of 11.863°N, 41.505°E, and all the others within 3 km. This point is 18.9 km SE of Serdo station and lies directly on the SE prolongation of the fresh faults observed following the 1969 Apr 05 Serdo earthquake, in a region of stratoid basaltic lavas (undated, probably Quaternary, marked as 'post trap' basalts on Figure 8.3.3) associated with smaller areas of rhyolites of similar age. The ubiquitous NW-SE faults cut these rocks also.

The largest shock of the Kurub sequence (494) had M_D = 2.8. 14 foreshocks were recorded over a period of 8 hr, and 5 aftershocks within 5 min of the main shock. The largest were the first two aftershocks (M_D = 2.5, 2.3). All the located epicentres are within about 1 km of 11.923°N, 41.206°E (17 km from Serdo station at azimuth 257°), and the estimated focal depths for the two largest are 1.75 km and 3.0 km. Kurub volcano is composed of basaltic lavas known to have been extruded since the

Lower Holocene (Section 2.3), although no volcanic activity is known in historical times. The lavas are cut by NW-SE faults.

8.3.3 Region C

(11.0°N to 11.75°N, 40.83°E to 41.15°E, Figure 8.3.4)

23 events were detected from Region C, of which 14 were recorded at Mille station only. The epicentres of the other 9 are shown on Figure 8.3.4. The most northerly located event (233, M_D = 1.6) was on the W margin of the Tendaho graben on 1974 Apr 20. A single event (388, M_D = 2.7) took place on Aug 04 at an estimated 4 km depth. All the remaining events occurred during June, including 16 in a sequence between Jun 23 09.00 hr and Jun 26 01.00 hr (Section 8.5) that contained one shock with M_D = 3.4 and four with $M_D \geqslant 2.8$. Depths of these events could not be determined.

The most northerly located events coincide with the Allallobeda graben, where intersecting systems of NW-SE and NNE-SSW faults have been active in Recent times. Hot springs exist around Allallobeda and have been investigated for their geothermal potential (MARRIOTT,1969; UNDP,1973). An aerial infra-red photomosaic of the area exists (Ato Seife Berhe, pers.comm.) but is not generally available.

The remarkable NNE-SSW linearity of the ESP epicentres, continuing as far north as the Tendaho graben western (Magenti Ale) marginal escarpment, demonstrates the significance of the NNE-SSW faults in this area and strongly

FIGURE 8.3.4

ESP EPICENTRES: REGIONS C AND E

(Region C is bordered in red)

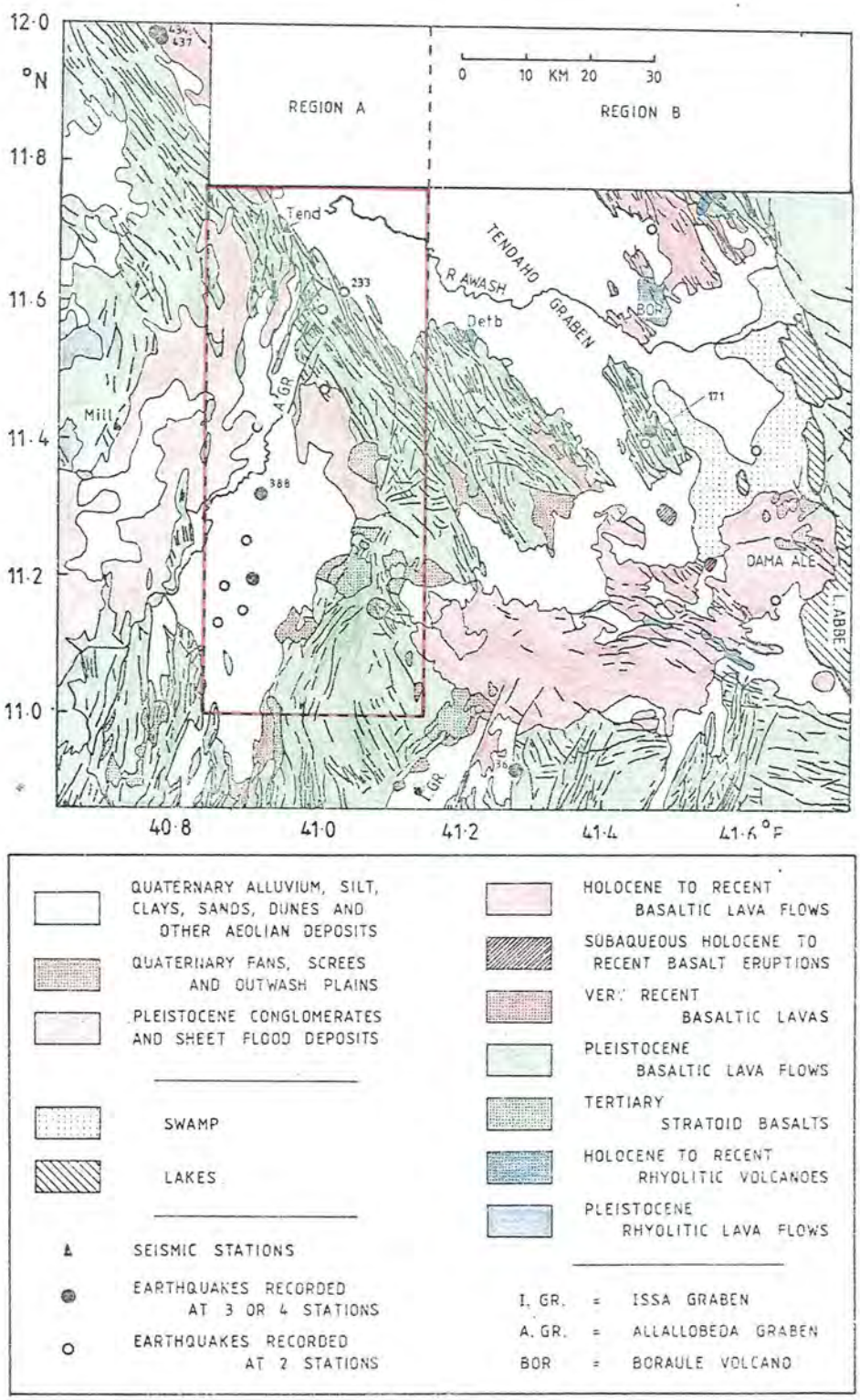

suggests that the Allallobeda graben is a more important structure than is indicated by its limited surface expression, continuing beneath Quaternary sedimentary cover at least as far south as the most southerly located epicentre (11.13°N). The sediments are probably underlain by recently active NNE-SSW faults contiguous with those observed from 10.7°N to 11.0°N and 40.6°E to 41.0°E.

8.3.4 Region D

(9.5°N to 12.6°N, and west of 40.1°E, Figure 8.3.5)

All ESP events located within Region D occur along the Western Ethiopian escarpment, the most teleseismically active land area of Ethiopia. Activity is associated with continuing development of the Afar marginal graben, and has been recorded along most of the length of the escarpment. However, it had been thought that a seismicity gap might exist between 11°N and 13°N (GOUIN,1979).

ESP identified two loci of activity on the escarpment, centred at approximately 10.0°N and 11.9°N. Only one, isolated event (443) was recorded from the area of the 1961 Kara Kore swarm (Section 1.4.1). The time period of this study is too short for this quiescence to be significant.

The majority of events from about 10°N occurred on 1974 Feb 25 (the Debre Sina sequence, Table 8.3.1). The main shock was reported by ISC and USGS, but was recorded by only Mille and Det Bahri of the ESP stations. It occurred during a period of heavy contractors' noise at Tendaho, and while a tape was being changed at Serdo. 5 of 8 aftershocks

FIGURE 8.3.5

ESP EPICENTRES: REGION D

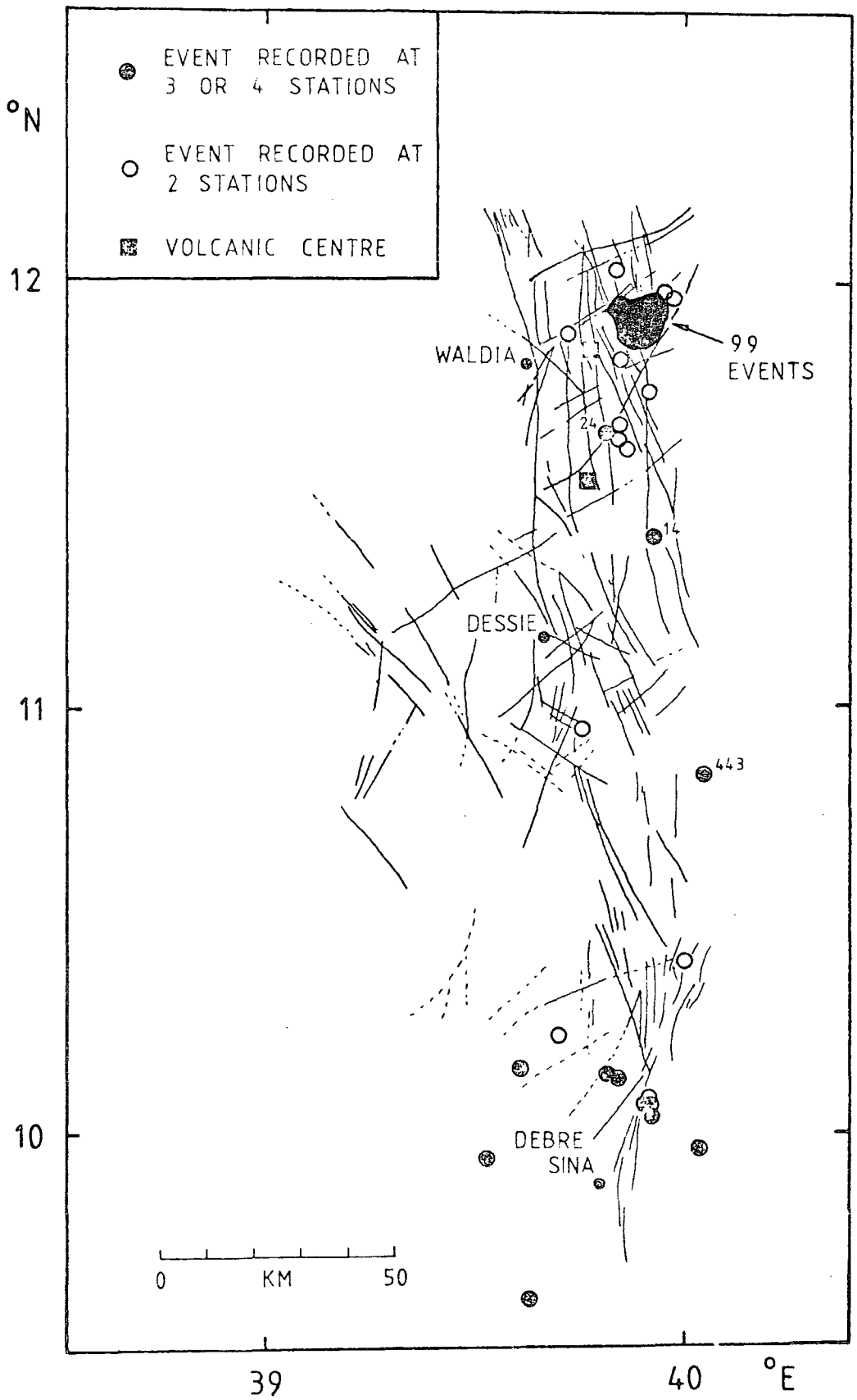

TABLE 8.3.1

PARAMETERS OF DEBRE SINA SEQUENCE EVENTS

ESP PARAMETERS

Event Number	Date	Origin Time hr min sec	Latitude (°N)	Longitude (°E)	Depth (km)	M_L	M_D	Recording Stations
15	Feb 25	16:05 15.59	10.07	39.92			4.4	MD
16	Feb 25	16:10 46.05	10.09	39.91				MD
17	Feb 25	16:12 32.81	10.16	39.61			3.4	MSD
18	Feb 25	19:22 54.87	10.14	39.82	24	3.1	3.3	MTSD
19	Feb 25	20:47 29.25					2.7	MD
20	Feb 25	21.58 30.94	10.13	39.84	24	2.6		MTD
21	Feb 25	21.59 01.69	9.96	40.04	25		3.9	MTSD
22	Feb 25	22.09 27.60	10.06	39.92	24		4.1	MTD
23	Feb 25	22.37 19.18	10.08	39.91	25	2.8	2.4	MTD
193	Apr 05	00.31 59.86	10.23	39.70		2.8	2.8	MT
274	Jun 24	10:34 59.86	9.94	39.53		3.3	3.5	MT
302	Jul 10	13:29 30.01	9.62	39.64		3.6	4.1	MTS

INTERNATIONAL AGENCY PARAMETERS FOR ESP EVENT 15

Agency	Origin Time	Latitude (°N)	Longitude (°E)	M_b	Number of Recording Stations
ISC	16:05 18.0 ±1.3	10.20 ± 0.13	39.80 ± 0.23	4.6	9
CGS	16:05 15.7 ±1.4	09.84 ± 0.17	40.03 ± 0.19	4.5	6

recorded by ESP were received at 3 or more stations, and all gave focal depths of 24 or 25 km (± 10 km). These are the greatest depths obtained during this study. The NW-SE alignment of this sequence suggests a possible active geological structure at depth whose orientation is not that of local surface faulting.

AAE local earthquake data files* list 36 events recorded between Feb 24 18.00 hr and Feb 26 09.00 hr. GOUIN (1979) has assigned all of these to the Debre Sina sequence. ESP locations for two of these events (numbers 14 and 24, Figure 8.3.5) are well determined and show them to have occurred more than 100 km farther north. The main event had no recorded foreshocks.

The greatest concentration of events recorded by ESP occurred NE of Waldia, around 11.9°N, 39.9°E. Epicentral co-ordinates were computed for 109 of 181 events detected. 124 events were recorded in the period from Mar 31 to Apr 14, most as aftershocks of three main events ($M_D > 4.0$) occurring on Mar 31 and Apr 01. Another major event ($M_D = 4.2$) occurred in the same area on Jly 27, as part of a sequence of 24 (1 foreshock, 22 aftershocks) over a 4-day period. Characteristics of these 'Waldia' sequences are discussed in Section 8.5. 33 further events, recorded in sequences of three or less, demonstrate that the Waldia area was active throughout the study period.

Focal depths were computed for 42 Waldia area events,

---

*Kindly made available by Professor Gouin to the author on his visits to the Geophysical Observatory, Addis Abeba.

giving a range from Ø.5 to 13.Ø km with mean depth of 7.Ø km and standard deviation 3.49 km. First motions were compressional at all stations (Section 8.4). The events are clearly associated with marginal faulting towards the base of the Western Ethiopian escarpment (Figure 8.3.5), and possibly with the volcanic centre east of Waldia. They provide conclusive confirmation that there is no significant seismicity gap along the escarpment between 1Ø° and 12°N.

8.3.5 Region E (the remaining area west of 42°E and south of 12°N, Figure 8.3.4)

Four events occurred near 11.99°N, 4Ø.77°E, in the extreme north west of Region E, within a 2 hr period on Sep 23 and having M_D between 1.3 and 1.6. The two larger events (434 and 437) were recorded at all the ESP stations and had computed depths of Ø.5 km and Ø.75 km. Like the NW Tendaho graben events (Region A, to the east), these four events occurred in an area of Holocene to Recent basaltic lava flows. They were all within 1 km of a small, isolated volcanic centre (obscured on FIgure 8.3.4 by the earthquake symbols) at the southern end of the Manda Hararo axial volcanic range. Since they occurred only three days before the end of field recording, it is not known whether they were isolated events or may have marked the initiation of an episode of activity in this area.

In the east of this region a sequence of 3 small events was observed, 2 of which were located near 11.42°N, 41.5Ø°E. A focal depth of 3.5 km was obtained for the best recorded

event (171). These events occur below a NW-SE trending block of stratoid basaltic lavas, much affected by NW-SE faults, standing out from the southern Tendaho graben sediments S of Boraule and NW of Dama Ale. Boraule is a rhyolitic volcano, elongated along a NW-SE axis, with lavas probably extruded from a NW-SE fault now concealed by younger sediments (UNDP,1973). A further sequence of 3 events was detected adjacent to Dama Ale, but their epicentres are poorly determined. Dama Ale is a large, Quaternary basaltic massif intersected by WNW-ESE normal faults.

These two small bursts of seismicity, one lying SE or ESE of the other and both associated with geological structures having these trends, are insufficient to suggest a NW-SE or WNW-ESE axis of seismic activity between Asayita and Dama Ale. However, a NW-SE line of events has been located in this area by the IPG Gulf of Tadjoura network (Ruegg, pers.comm, epicentral co-ordinates not available).

Two events were observed south of 11°N. Event 36 was well recorded from near the northern end of the Issa graben, which trends NNE-SSW and is actively spreading (SCHAEFER,1975). Event 401 (10.26°N, see Figure 8.1.2) is a poor location beneath the sediments of the Buren plain in Southern Afar.

8.3.6 Region F (the remaining area west of 42°E and north of 12°N, Figure 8.1.2)

15 events are located in this region. Their epicentres are all either based on only 2 records, or are so distant compared with the ESP network aperture (long axis, 88.6 km; short axis, 28.8 km: Figure 2.2.1) that accurate locations are impossible.

The most northerly event (386, M_D = 4.5, Figure 8.1.2) is plotted at 14.84°N, 39.56°E on the Western Ethiopian escarpment. This is close to the computed position of a large (M_b = 6.2) earthquake teleseismically recorded by 191 stations on 1950 Aug 02. More recent activity has also been reported in the area (GOUIN,1979). ESP arrival times for this event were poorly recorded, and the epicentre may be in error by up to 30 km.

Events 394 and 202 lie on the Erta Ale volcanic range (Figure 1.4.2), and the 3 clustered events 75, 78 and 79 on the Tat Ali range. Events 389 and 392 lie along the offset between these two "en échelon" axial ranges, both of which consist of Recent basalts and are actively spreading (Section 1.4.2).

Events 44 and 250 lie along the axis of the active NW-SE Manda Hararo axial range, and event 219 (an uncertain location) at the western extremity of associated NW-SE faulting. Event 425 was relatively well recorded at all four ESP stations and is slightly north of the Tertiary granitic Affara Dara massif, on the line of BARBERI and VARET's (1977) postulated transform fault connecting Tat Ali

and Manda Hararo.

Epicentres for the three remaining events are uncertain. Event 296 has been located on the southern margin of Gad'Elu, a silicic volcano, and 402 on a line running NW from Manda Inakir axial volcanic range to the silicic centre Oyma. Pronounced NW-SE faulting in this region suggests a possible NW continuation of the Manda Inakir line of activity.

The overall correspondence between ESP epicentres and Recent volcanic and tectonic activity is impressive. It is weakened by any significant variation of the structural model parameters used to generate the epicentres (Chapter 4), thus providing indirect support for the model. In particular, the NW-SE linearity of events 75, 78, 79, 392, 202 and 394 makes it unlikely that they are not associated with the Erta Ale and Tat Ali ranges.

8.3.7 Region G (east of 42°E, Figure 8.1.2)

7 events were located in Region G, but their azimuthal resolution is particularly poor as they are almost in line with the major axis of the ESP network. All have $M_D > 2.5$ and should have been observed by the IPG network, but only events 395 and 337 are included on preliminary IPG bulletins kindly supplied by Professor Ruegg. Event 395 has a provisional IPG location 15 km east of its ESP location. Event 337 was very poorly recorded by ESP and almost certainly originates beneath the Red Sea, as located by IPG. Events 430 and 431 are associated with the active Asal rift

(Figure 1.4.2). An increase in azimuth of 9° (within the possible ESP error) brings events 37 and 433 on to the axis of maximum seismicity in the Gulf of Tadjoura, which is offset towards its northern shoreline (e.g. RUEGG, 1975a).

During 1973 Mar-Apr a major episode of seismic activity occurred in the Gulf of Tadjoura around 11.7°N, 43.0°E. 14 teleseismic locations were computed by ISC and CGS. Approximately 13,000 shocks, attaining a maximum frequency of 80 to 100 hr^{-1}, were detected by the IPG network (LÉPINE and RUEGG,1973), which at that time consisted of only 3 stations. The activity (see also Sections 8.5, 8.7) was largely confined to spreading ridge segments and connecting transform faults, with some clustering around submarine volcanoes known from bathymetric soundings (RUEGG,1975a; LÉPINE and RUEGG,1976).

8.4 Focal Mechanisms

8.4.1 Sense of First Motions of ESP Events

Tectonic earthquakes occur, according to Reid's elastic rebound theory (see e.g. BOTT,1971, pp.258-262), as the sudden reduction of accumulated strain energy by faulting. Part of this energy is converted into the elastic waves which are recorded at seismic stations. By analysing the recorded wave motions it should therefore be possible to make deductions about the nature of the faulting, and thence about the stresses within the earth that caused it. This is the underlying rationale of focal mechanism studies, which

were initiated by Byerly in 1926 and developed by him over many years (see BYERLY,1955), and independently by other investigators (STAUDER,1962, review).

Reid's elastic rebound theory predicts a quadrantal pattern of compression and rarefaction for the first motion of P, whether a single- or double-couple mathematical model is assumed for equivalent body forces acting at the earthquake focus. In theory, the two models can be distinguished by their S radiation patterns, but the sense of S first motion cannot usually be determined (HODGSON,1957). Dislocation theory predicts other possible schemes of faulting at a point source, which produce different radiation patterns (e.g. KNOPOFF and GILBERT,1960).

The concept of a point source is an idealisation, equivalent to the assumption that fault movement is synchronous over the fault face. Chapter 7 investigated the size of the focal volume, which for mathematical convenience was taken to be spherical. In this chapter we consider the focus as determined by first motion studies as the very small region, approaching a point, in which failure originates.

The practical problem of focal mechanism studies is to fit two orthogonal planes, separating regions of compression and dilatation on a spherical surface, to the observed P first motions. There are two possibilities for the orientation of the fault and the direction of movement along it, since the far-field P radiation pattern alone cannot

establish which of the two P nodal planes is the fault and which the auxiliary.

The sense of first motions of well-recorded earthquakes from within Afar is given in Table 8.4.1 and summarised in Figure 8.4.1 for groups of events. Each section of Figure 8.4.1 is the stereographic projection of the lower hemisphere of the focal sphere (Wulff net). The lower hemisphere is used because the rays leave the source downwards, unless the first arrival is P_g. In Figure 8.4.2,

θ = event azimuth,

$d = r \tan(i/2)$, (8.4.1)

where r = radius of circle, i = angle at which ray leaves the focus ($\emptyset^o$ = vertically downwards).

The distribution of recording stations is insufficient for nodal planes to be accurately fitted. Furthermore, i is calculated from the structural model of Figure 4.3.6c and is the same for all the events shown in Figure 8.4.1, since all have head wave first arrivals from the 6.2 km s^{-1} layer of the model. If the structural model is wrong the angle of declination, and hence d in Equation 8.4.1, will be in error. Within these limitations, Section 8.4.2 considers possible focal mechanisms for events within Afar.

8.4.2 Discussion of Possible Focal Mechanisms

Hypothetical fault plane models for the ESP events are shown in Figure 8.4.3a-h. They have been chosen as likely "solutions" on the basis of the known geology, tectonics and patterns of seismicity in the study area, as follows:

TABLE 8.4.1

SENSE OF VERTICAL SEISMOMETER FIRST MOTIONS FOR ESP EVENTS

('+' = compression, '-' = rarefaction)

	STATION	DIRECTION OF MOTION	NUMBER OF EVENTS
(A)	NW Tendaho Graben Group		
	Mille	+	31
	Mille	-	5
	Tendaho	+	22
	Tendaho	-	2
	Serdo	+	20
	Det Bahri	+	3
(B)	SE of Serdo Group		
	Mille	+	4
	Tendaho	+	4
	Tendaho	-	2
	Serdo	+	1
	Serdo	-	8
	Det Bahri	+	7
(C)	Kurub Volcano Group		
	Mille	+	2
	Tendaho	+	3
	Serdo	-	4
	Det Bahri	+	8
(D)	Allallobeda Graben Group*		
	Mille	+	5
	Mille	-	2
	Serdo	-	3
	Det Bahri	+	1

*Poor records at Tendaho during this period.

FIGURE 8.4.1

LOWER HEMISPHERE STEREOGRAPHIC PROJECTIONS OF VERTICAL SEISMOMETER FIRST MOTIONS FOR GROUPS OF ESP EVENTS

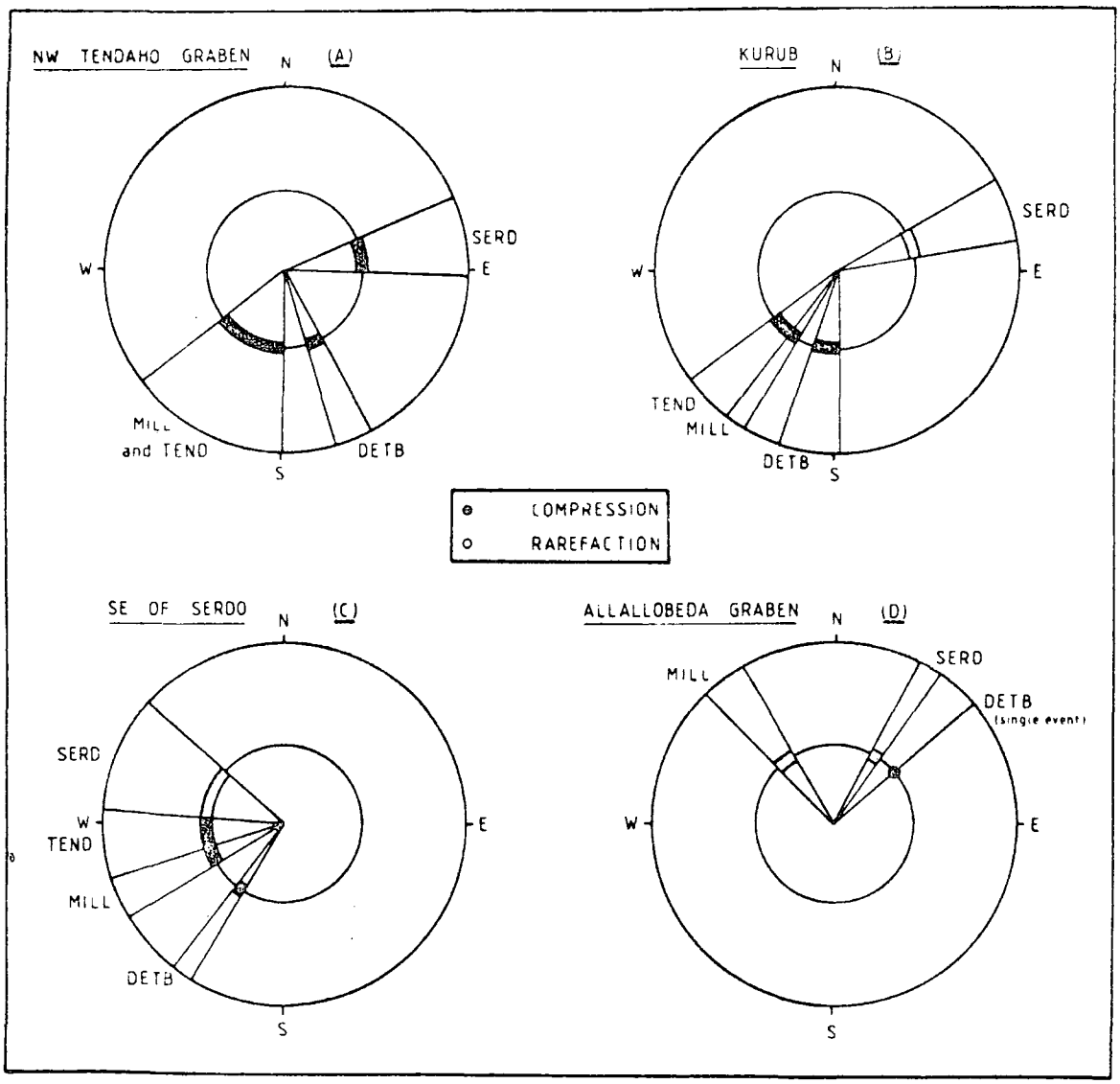

FIGURE 8.4.2

DIAGRAM TO ILLUSTRATE THE LOWER HEMISPHERE STEREOGRAPHIC PROJECTION

(a) Vertical section through focal sphere

(b) Horizontal equatorial plane (Wulff net)

F is focus. S, a point on the focal sphere, projects to S'. Nodal plane FS projects to shaded area on (b). P is point of projection. d = tan(i/2) on a unit sphere.

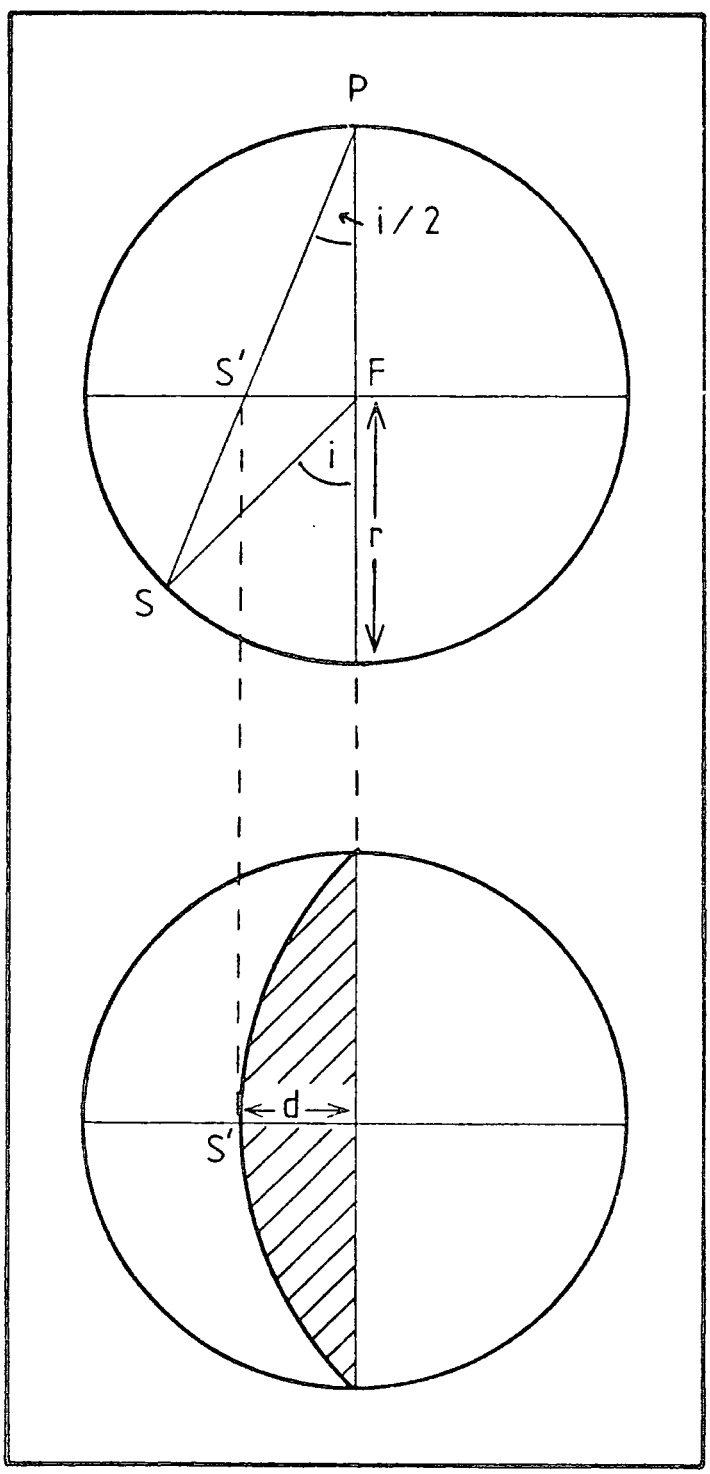

FIGURE 8.4.3

HYPOTHETICAL FAULT PLANE MODELS FOR ESP EVENT GROUPS

(model (a) is McKENZIE et al's (1970) solution for the 1969 Serdo earthquakes)

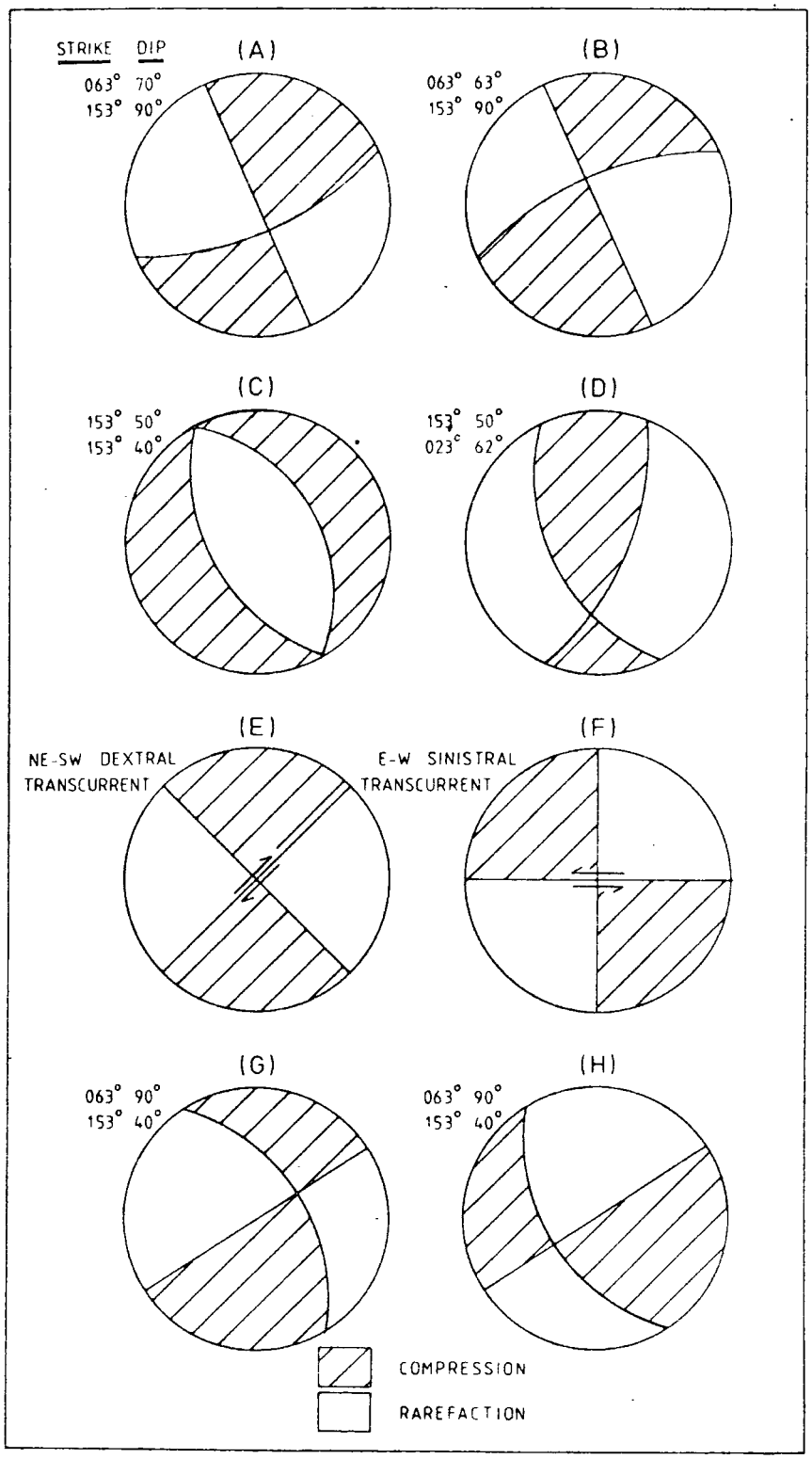

(a) This is McKENZIE et al's (1970) fault plane solution for the 1969 Serdo earthquakes (see Figure 8.2.3).

(b) The 153° vertical plane of (a) is retained, but the direction of dip of the Ø63° plane is reversed for compatibility with the first motions of ESP events SE of Serdo (Figure 8.4.1c).

(c) This is a normal faulting solution, compatible with the fist motions of Figure 8.4.1c, retaining the 153° fault plane suggested by the intense surface faulting. Since the ESP events are so shallow, the surface faulting is expected to reflect the direction of the fault plane.

(d) The auxiliary plane of (c) is altered. This plane is little constrained by the data of Figure 8.4.1c, and may be drawn at any angle λ to the fault plane, provided its dip is such that the normal lies in the fault plane. It is easily shown that this condition may be written

$$\cot(\theta) = \tan(\theta_p)\cos(\lambda) \qquad (8.4.2)$$

where θ, θ_p are the dips of the focal and auxiliary planes respectively.

(e) This shows NE-SW dextral transcurrent faulting, as proposed by BARBERI and VARET (1977) along a hypothetical NE-SW transform fault passing through Kurub and Serdo.

(f) E-W sinistral transcurrent faulting. CHRISTIANSEN et al (1975) have found field evidence for sinistral movement on E-W faults 1Ø km north of Kurub (farther south, the movement on E-W faults is dextral), but these faults are not shown on detailed tectonic maps of the area (GEOMAP,1969; UNDP,1973).

(g,h) Two solutions compatible with the first motions of ESP NW Tendaho graben events (Figure 8.4.1a), having the 153° plane suggested by surface faulting but showing opposite senses of strike-slip motion.

Table 8.4.2 summarises the degree of compatibility of the eight "solutions" of Figure 8.4.3 with the first motions of the four groups of ESP events shown in Figure 8.4.1. None of the ESP event groups shows first motions compatible with McKENZIE et al's (1970) solution for the 1969 Serdo earthquakes, nor are the observed 1969 Serdo first motions compatible with any of the hypothetical "solutions" of Figure 8.4.3. Retaining McKenzie et al's 153° nodal plane as fault plane, however, the strike-slip and normal faulting models of Figures 8.4.3b,c are compatible with the first motions of the ESP events SE of Serdo.

The ESP Kurub events (Figure 8.4.1b) occurred contemporaneously with those SE of Serdo and may have the same fault plane. They too are consistent with Figure 8.4.3b. A pure normal faulting solution along the direction of the surface faulting is only possible if the dip to the WSW is 80° or greater, whereas for the ESP events SE of Serdo the dip was constrained to be 50° WSW.

The Kurub events are also consistent with NE-SW dextral faulting, which might be expected if Kurub lay on the hypothetical transform fault suggested by BARBERI and VARET (1977), connecting the Manda Hararo and Manda Inakir axial volcanic ranges (Figures 1.4.2, 8.7.2). No other ESP event

TABLE 8.4.2

COMPATIBILITY OF OBSERVED FIRST MOTIONS

WITH HYPOTHETICAL FAULT PLANE MODELS OF FIGURE 8.4.3

(yes = compatible, no = incompatible)

Fault Plane Model (Fig.8.4.2)	-------ESP Event Group (as in Figure 8.4.1)------- A NW Tendaho Graben	B Kurub	C SE of Serdo	D Allallobeda Graben	1969 Serdo Earthquake Sequence
A	no	no	no	no	yes
B	no	yes	yes	no	no
C	no	no	yes	marginal	no
D	no	marginal	yes	no	no
E	no	yes	no	no	no
F	no	no	no	no	no
G	yes	yes	no	marginal	no
H	yes	no	marginal	marginal	no

groups show first motions consistent with NE-SW dextral movement. E-W sinistral movement, which would accord with CHRISTIANSEN et al's (1975) field observations, is not compatible with any ESP event group first motions.

The compressional first motions of ESP NW Tendaho graben events (Figure 8.4.1a) prohibit any pure normal faulting mechanism. Thrust faulting is consistent with the observed motions, but is highly unlikely within a region of active extension. Intense NW-SE and NNW-SSE surface faulting again suggests this direction for the fault plane. Two solutions compatible with the data, with opposite senses of strike-slip motion, are shown in Figures 8.4.3g,h. However, since these events are associated with the line of volcanic centres running NW-SE through Da'Ore (Figure 8.3.1), the first motions may not reflect the regional stress pattern.

The Allallobeda events (Figure 8.4.1d) lie in an area of intersecting NNE-SSW and NNW-SSE to NW-SE surface faults. Their first motion data place few constraints on possible focal mechanisms.

In summary, although it is not possible to fit the same nodal planes to all the event groups of Figures 8.4.1, all the observed motions are compatible with movement along the observed NNW-SSE to NW-SE direction of local surface faulting. Left-lateral movement with an element of dip-slip is suggested. The data are not incompatible with the hypothesis that a NE-SW dextral fault passes under Kurub volcano. They are totally incompatible with E-W sinistral movement.

8.5 Characteristics of Earthquake Sequences

8.5.1 Magnitude-Time Relationships

DAKIN (1975) studied 26 episodes of local seismic activity (sequences or single shocks) which were well recorded at AAE between 1958 and 1973. The majority occurred within the area shown in Figure 8.1.2. She concluded that every earthquake with $m_b > 5.9$ had occurred as part of an event sequence, but that every event but one with $m_b < 5.0$ had occurred as a single shock.

The three largest events recorded by ESP as single shocks, and located within 150 km of the ESP network, had $M_D = 2.9$. Two of them occurred near Serdo, the other on the Western Ethiopian escarpment. 45 larger events were located within 150 km, all belonging to one of 8 sequences (4 within Afar, 4 on the Western Ethiopian escarpment). All but one (with $M_D = 3.0$) occurred within 24 hr of another shock belonging to the same sequence and having $M_D > 2.7$.

Since there is no reason why the period of the ESP study should be anomalous, it is concluded that most if not all of the seismic activity within the area occurs in sequences, and that Dakin's contrary result was due to the limited detection capability of a single station at a greater distace from the activity. Dakin's conclusion also contradicts FRANCIS and PORTER's (1971) result for the Mid-Atlantic Ridge, that the smaller an event the more likely it is to be part of a sequence.

Earthquake time sequences have been classified into

three types (MOGI,1963): type 1, a clearly defined main shock with aftershocks but no foreshocks; type 2, a foreshock-mainshock-aftershock sequence; and type 3, a swarm sequence having no distinct main shock. To these Dakin added type 4, comprising several main shocks each accompanied by its own aftershock sequence. Into this last category she placed the three largest, most destructive sequences recorded by AAE: Kara Kore 1961, Serdo 1969 and Gulf of Tadjoura 1973. She showed that renewals of activity in type 4 sequences may be associated with movements along different, but coupled, tectonic lines. This is particularly evident for the Gulf of Tadjoura 1973 events (LÉPINE and RUEGG,1973).

Magnitude-time histograms of the larger sequences recorded by ESP are shown in Figures 8.5.1 to 8.5.3. A frequency-time histogram of Serdo 1969 aftershocks recorded at AAE is added for comparison (Figure 8.5.4). The 1969 earthquakes are of course very much larger ($4.6 \leqslant m_b \leqslant 6.2$) than the 1974 ESP events, and this is reflected in the much longer duration of the 1969 sequence.

Like the 1969 sequence, the largest ESP-recorded sequences (from Waldia, Figures 8.5.1, 8.5.3c) are clearly of type 4. The smaller sequences (Figures 8.5.2, 8.5.3a,b), observed within Afar close to the ESP network, have the form of type 3 sequences (swarms) with very rapid type 2 sequences superposed. The mainshock-aftershock sequence occurs after a period of foreshocks that is long relative to the total duration of the activity.

FIGURE 8.5.1

MAGNITUDE-TIME HISTOGRAM FOR WALDIA MARCH-APRIL SEQUENCE

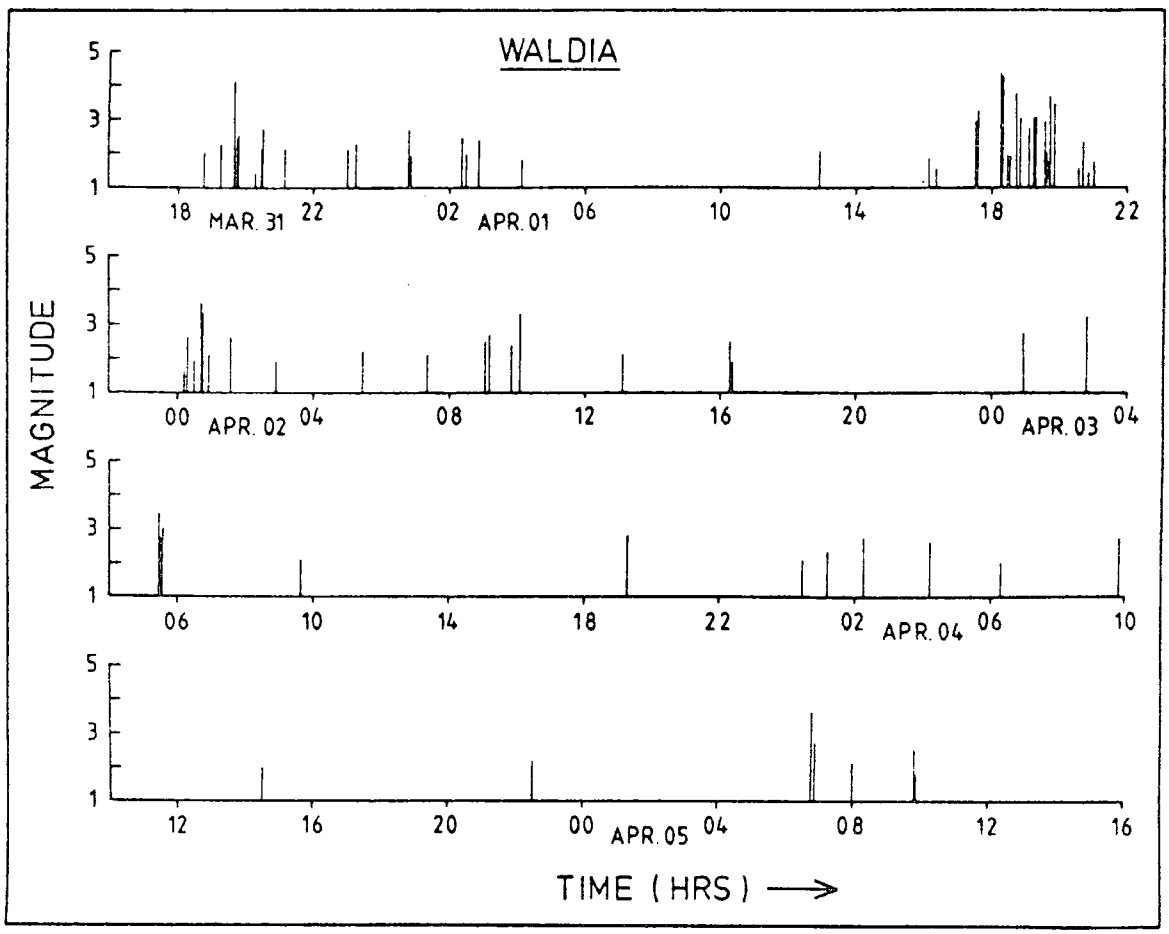

FIGURE 8.5.2

MAGNITUDE-TIME HISTOGRAM FOR SERDO SEQUENCES

(SE of Serdo and north edge of Kurub volcano)

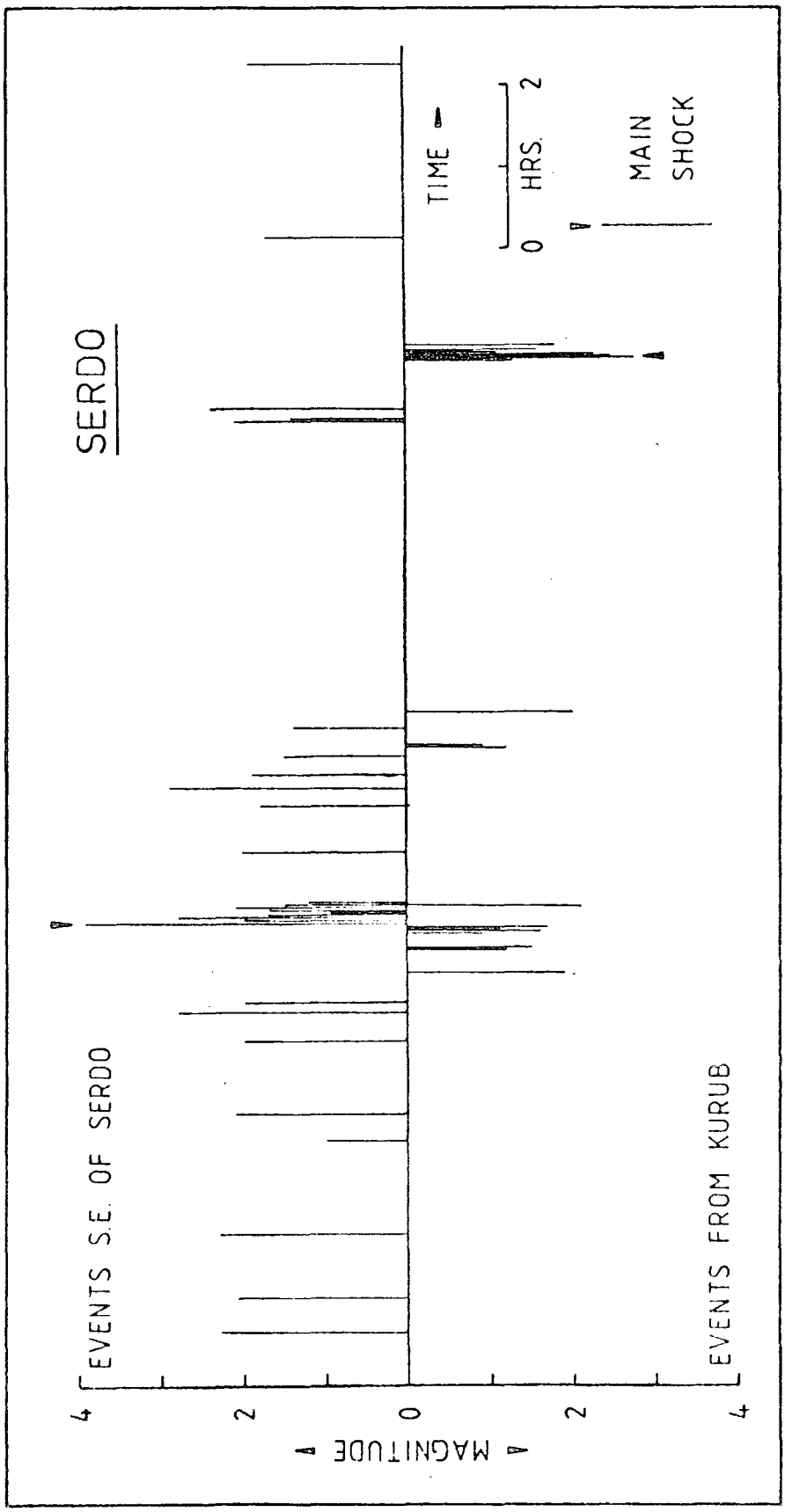

FIGURE 8.5.3

MAGNITUDE-TIME HISTOGRAMS FOR: (A) ALLALLOBEDA GRABEN; (B) NW TENDAHO GRABEN; (C) WALDIA (JULY SEQUENCE)

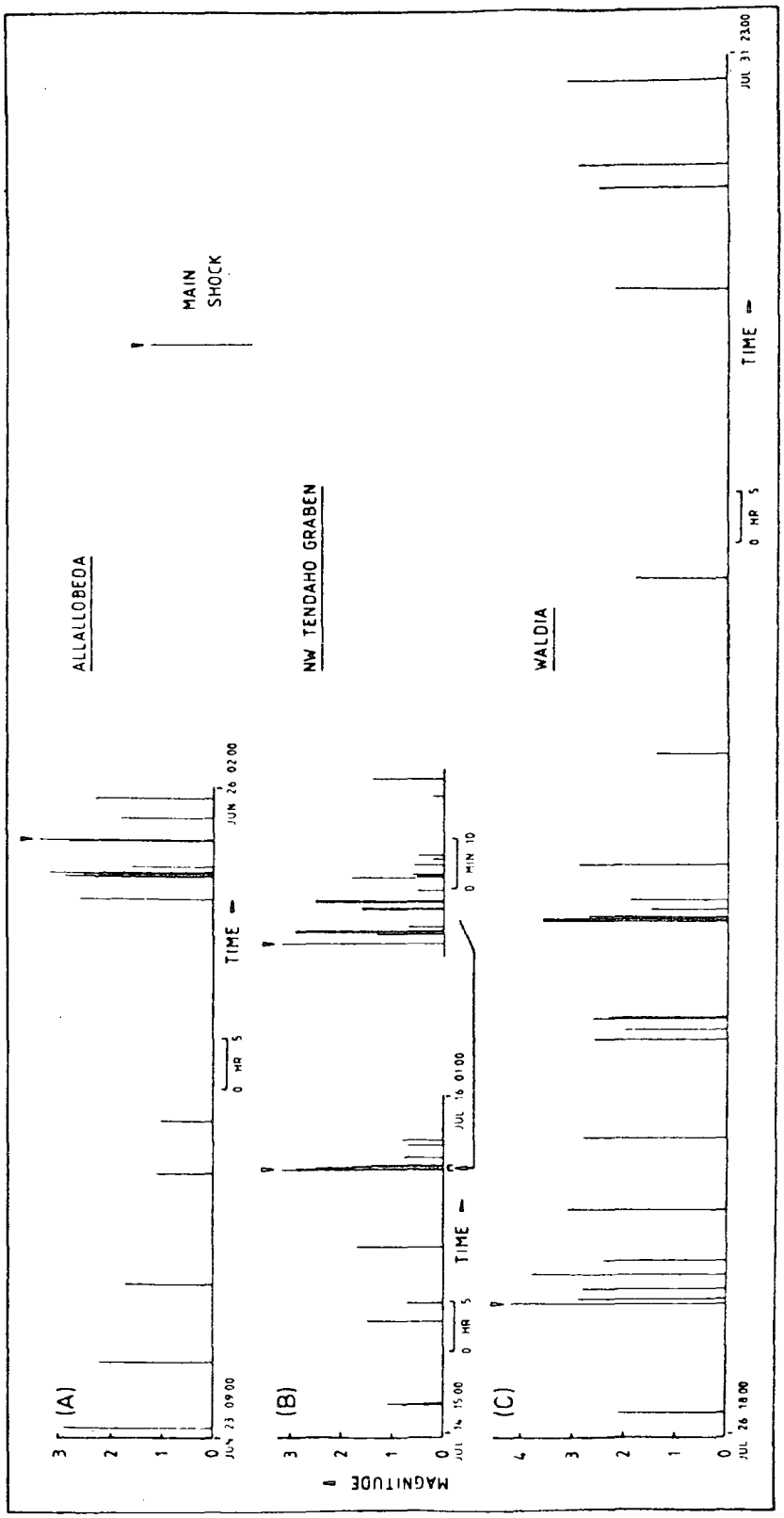

FIGURE 8.5.4

FREQUENCY-TIME HISTOGRAM FOR SERDO 1969 SEQUENCE

(after DAKIN et al, 1971)

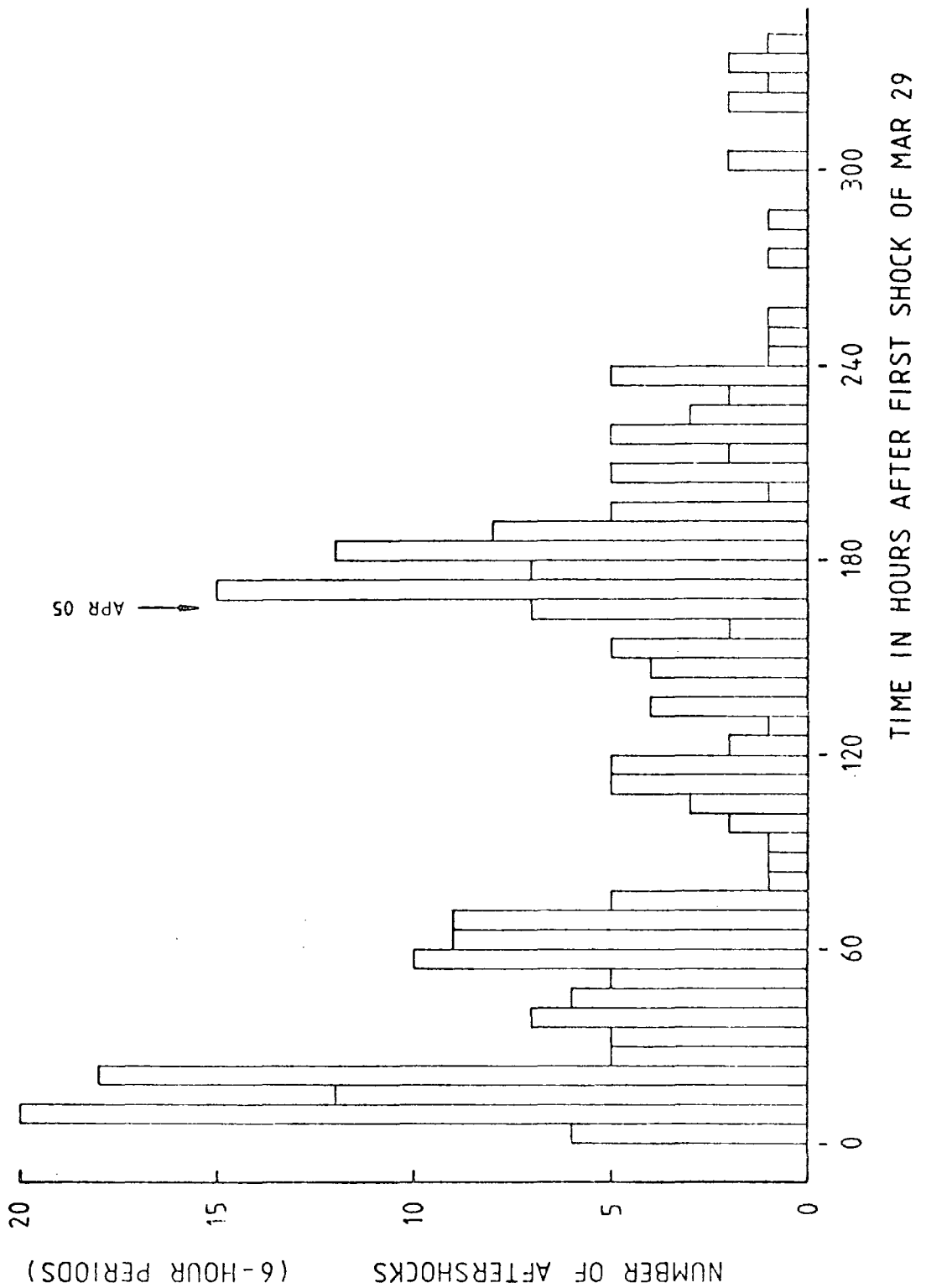

Earthquake sequences are found not to occur at depths below about 20 km (e.g. PAGE,1968). The type of sequence observed is considered to depend on the tectonic, magmatic and hydrothermal state of the crust (SYKES,1970). FOULGER and EINARSSON (1980) have summarised some suggested associations (Table 8.5.1), although they emphasise that exceptions are known.

TABLE 8.5.1

PHYSICAL ASSOCIATIONS OF EARTHQUAKE SEQUENCES

(after FOULGER and EINARSSON,1980)

Swarm sequences	Mainshock-aftershock sequences
Inhomogeneity of crust	Homogeneity of crust
Inhomogeneity of stress	Homogeneity of stress
High fluid pressure	Low fluid pressure
Normal faulting	Strike-slip faulting
Short, shallow faults	Long, deep faults
Spreading ridge crests	Transform faults
Areas of recent volcanism	Tectonic earthquakes
Geothermal areas	

Iceland and Afar invite geophysical comparison (e.g. MAKRIS,1975), since both offer sub-aerial sites for the observation of first-order processes of crustal extension and generation. Published earthquake sequences for Iceland often show great complexity (e.g. EINARSSON et al,1977). There is a pronounced similarity to Afar sequences (TRYGGVASON,1973; EINARSSON,1974; BRANDSDÓTTIR and

EINARSSON,1979; FOULGER and EINARSSON,1980), with a greater tendency towards the type 3 sequences found on mid-ocean ridges (e.g. SYKES,1970). This is consistent with comparisons of crustal structure below Afar (BERCKHEMER et al,1975), the Gulf of Tadjoura (RUEGG,1975a) and Iceland (PÁLMASON,1971; FLÖVENZ,1980), which show a variation from largely attenuated continental (according to Berckhemer's interpretation) towards oceanic-type crust; and towards greater attenuation of seismic waves of local earthquakes in the Gulf of Tadjoura ($Q < 80$,* perhaps about 30, in actively spreading zones, PONTOISE et al,1976) than in the present study, indicating greater volumes of magma at shallow depths in these areas.

8.5.2 Recurrence Relationships

The magnitude and frequency of events of an earthquake sequence are commonly related empirically by

$$\log_{10}N = a - bM \qquad (8.5.1)$$

where N is the number of earthquakes of magnitude M and greater, and a and b are constants (GUTENBERG and RICHTER,1944).

Laboratory rock deformation studies (SCHOLZ,1968) and theoretical considerations (WYSS,1973) have shown that the value of b is related to the effective stress in the source region. GIBOWICZ (1973) found the empirical relationship

$$b = 0.84 + k \log_{10}(\Delta\sigma_o/\Delta\sigma_M) \qquad (8.5.2)$$

---

*Figures are presumed to be for S waves, although this is not stated.

for tectonic earthquakes, where $\Delta\sigma_o$ is the stress drop associated with the main shock and $\Delta\sigma_M$ the stress drop of an average earthquake of the same magnitude. k is a constant whose value is close to unity.

GIBOWICZ (1973) concluded that b-values and other physical characteristics of aftershock sequences are determined by the source parameters of the main shock. A low stress drop in the main shock leads to a low value for b. If the low stress drop implies that high stress remains in the region after the main event, b varies inversely with the logarithm of stress.

Recurrence relationships have been related to stress drop, $\Delta\sigma$, and source radius, r, by WYSS (1973), HANKS (1977) and CAPUTO and CONSOLE (1980). HANKS (1979) shows that

$$N' \propto \Delta\sigma^{-2/3}\, r^{-2} \qquad (8.5.3)$$

where N' is the number of earthquakes with source radius > r.

Magnitude-frequency relationships for some sequences discussed in Section 8.5.1 are shown in Figure 8.5.5. Limiting magnitudes above which all events were assumed to be detected are marked by dashed vertical lines. They were calculated on the same basis as the locatability thresholds given in Section 8.1. The magnitude interval (ΔM) between points on the 'all events' curves is 0.3. For the other curves, $\Delta M = 0.5$. ESP b-values are listed in Table 8.5.2. They are compared in Table 8.5.3 with values found elsewhere in East Africa and in Iceland. b-values obtained in different studies are less strictly comparable than is

FIGURE 8.5.5

MAGNITUDE-FREQUENCY RELATIONSHIPS FOR ESP EVENTS

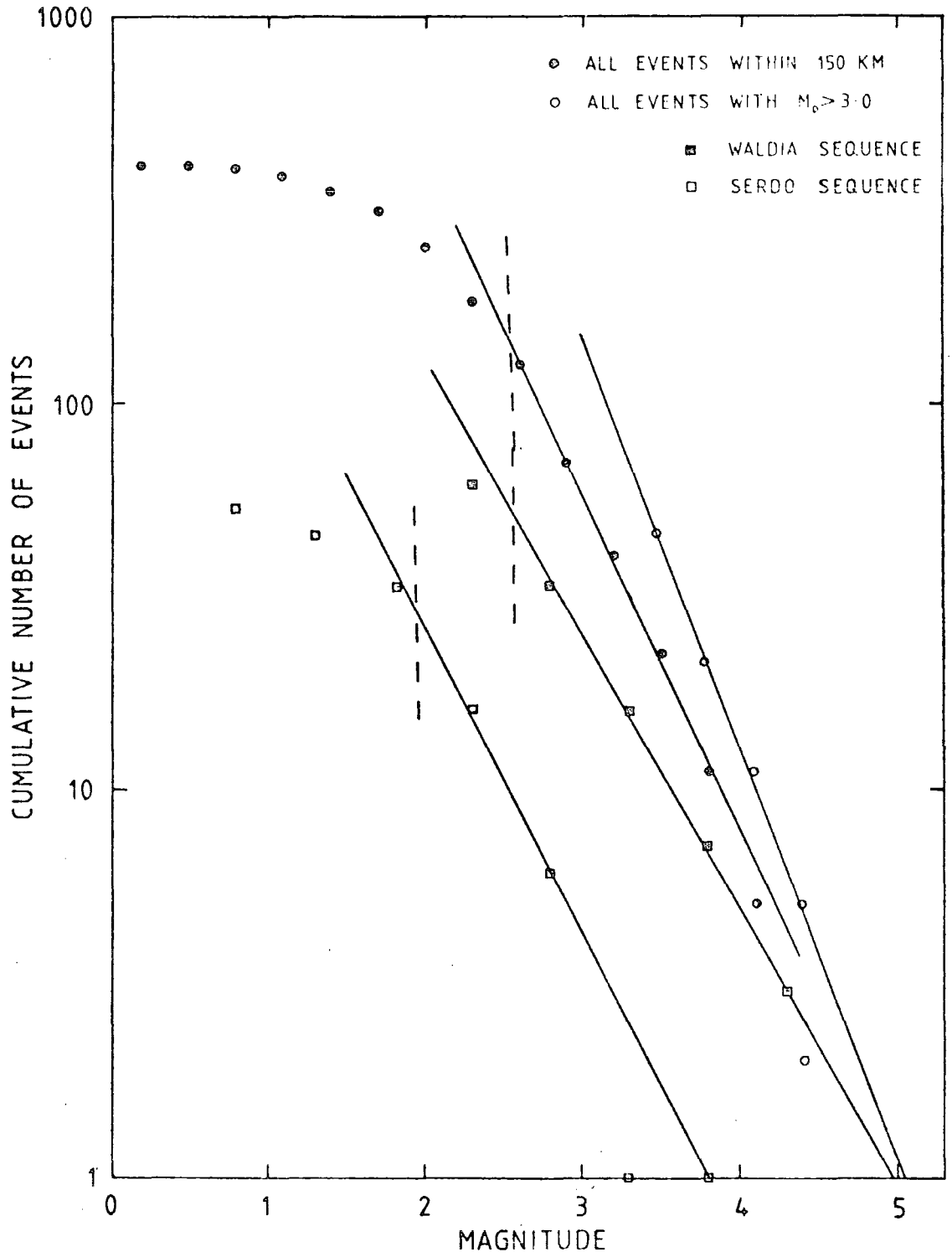

TABLE 8.5.2

FREQUENCY-MAGNITUDE b-COEFFICIENTS: THIS STUDY

Event Group	b-Value
Waldia Sequence (March - April 1974)	0.71 ± 0.05
Serdo Sequence (events SE of Serdo and near Kurub volcano)	0.78 ± 0.04
All events located within 150 km of network	0.87 ± 0.05
All events with magnitudes greater than 3.0	1.05 ± 0.03

TABLE 8.5.3

A SYNTHESIS OF FREQUENCY-MAGNITUDE b-COEFFICIENTS

Approx. Location of Events	b-value	Source
East Africa		
Ethiopia, Sudan, Northern Kenya, Northern Uganda	0.95	Fairhead and Girdler,1971
East Africa overall	0.87	Kaila and Narain,1971
Ethiopia and Horn of Africa		
60 yr observation period	0.84*	Gouin,1979
100 yr observation period	0.62*	Gouin,1979
343 yr observation period	0.71*	Gouin,1979
East African Rift	0.79	Wohlenberg,1968
Western Rift	0.65	Wohlenberg,1968
ESP-located events		
within 150 km of network	0.87±0.05	This study
with magnitude > 3.0	1.05±0.03	This study
Debre Berhan, W.Eth.Escarp.		
1968 (≈ 09.7°N,39,5°E)	3.0,1.19,0.66,0.55# (0.60)**	Gouin,1979
Waldia 1974 (≈ 11.9°N,39.9°E)	0.71±0.02	This study
Serdo 1969 (≈ 12.0°N,41.3°E)		
AAE data (251 events)	0.73	Gouin,1979
Teleseismic data (12 events)	0.76	Fairhead and Girdler,1970
Serdo 1974 (Section 8.2.4)	0.80±0.05	This study
Gulf of Tadjoura		
1963 (≈ 11.6°N,42.8°E)	0.73±0.04	Gouin,1979
1966 (≈ 12.0°N,43.5°E)	1.55, 0.92±0.02#	Gouin,1979
1973 (≈ 11.7°N,43.0°E)	0.65**	Gouin,1979
Iceland		
Iceland overall	0.93 to 0.76#	Tryggvason,1973
Borgarfjördur, W Iceland	1.06±0.06	Einarsson et al,1977
Krafla volcano, NE Iceland		
1977 deflation	3.1±0.9, 2.7±0.9	Brandsdóttir and Einarsson,1979
1978 deflation	1.7±0.2	Einarsson and Brandsdóttir,1980

*Based on frequency-intensity relationships.
#Decreasing values for decreasing magnitudes.
**By method of maximum likelihood.
Other results are by least squares.

often supposed, since they depend on the method used to evaluate them, the kind of magnitude measured, and other factors (BÅTH,1978a,b). The applicability of Equation 8.5.1 is limited towards higher magnitudes by the limited duration of observations, and towards lower magnitudes by insufficient seismometer detection capability.

There is some controversy (e.g. CAGNETTI and PASQUALE,1979) over the relative merits of measuring b-values by maximum likelihood (UTSU,1966) or by least squares. The method of least squares unjustifiably assumes that there is no uncertainty in M and that the event magnitudes are normally distributed. It tends to over-weight the relatively few high-magnitude events. The maximum likelihood method is generally preferable, although in the approximate form in which it is usually applied it gives b-values systematically too low when, as here, $bM <$ about Ø.25 (GIBOWICZ,1963). This study follows the majority of workers cited in Table 8.5.3 in using least squares.

The overall b-value, Ø.87 ± Ø.Ø5, obtained in this study agrees with FAIRHEAD and GIRDLER (1971), with KAILA and NARAIN (1971) and with GOUIN's (1979) 6Ø yr period figures, all calculated for larger magnitude events over a wider area. The magnitude detection level in Fairhead and Girdler's study, for example, was $m_b = 4.8$. The lower b-values of Gouin's longer-period figures (Table 8.5.3), based on frequency-intensity relationships, may be at least partially due to incompleteness and inaccuracy of his data

file. Older entries are based on felt reports, and the reported intensities are not epicentral values. The reporting of felt events decreases as their amplitudes become of less importance to the observer, so that higher intensity events are over-weighted and the inferred value for b is unrealistically low.

ESP b-values within Afar are slightly higher than those for the Western Ethiopian escarpment, but much lower than values for Icelandic sequences. This can be explained in terms of the correlation of high b-values and swarm sequences with spreading ridge crests and other actively volcanic and geothermal areas (SYKES,1970 and Table 8.5.1); and with normal faulting. FRANCIS (1968) has demonstrated a significantly higher b-value for normal than for strike-slip faulting. The higher value $b = 1.05 \pm 0.03$ is obtained for ESP events having $M_D > 3.0$.

According to Equation 8.5.2, the overall ESP b-value of $b = 0.87 \pm 0.05$ indicates sequences whose main shocks have average (i.e. typical) values of $\Delta\sigma_o$. Stress drops of smaller ESP events, obtained directly in this study, have also shown typical values (Section 7.5). ESP shocks show characteristics intermediate between the low $\Delta\sigma$, large r earthquakes associated by WYSS and BRUNE (1971) with (Californian) earthquakes occurring in zones of weakness along existing major faults; and high $\Delta\sigma$, low r events found where fresh breaks are occurring in virgin rock.

ESP has manifestly not detected volcanic earthquakes associated with deflation, as at Krafla volcano in Iceland

(Table 8.5.3). However, TRYGGVASON's (1973) b-values for Iceland overall are in the same range as the Afar values, and Tryggvason also observed b to decrease with decreasing magnitude. Until the theoretical basis of Equation 8.5.1 is better understood it is unwise to put forward a tectonic cause for its invalidity. LONG, L. (1974) found an apparent increase in b-value with decreasing magnitude for the South Eastern United States, but he attributed this to instrumental effects.

The conclusions of this section may be summarised as follows:

(1) The b-values obtained in this study are 0.87 ± 0.05 for all events within 150 km of the ESP epicentres, and 1.05 ± 0.03 for all events with magnitude $M_D > 3.0$.

(2) These b-values are very comparable with those previously obtained for East Africa. They imply stress drops, for principal ESP-recorded shocks of a given magnitude, of close to the world average.

(3) The b-values are consistent with predominantly strike-slip rather than normal faulting, and with mainshock-aftershock sequences rather than swarm sequences. This is in accordance with the findings of Sections 8.4 and 8.5.1, respectively.

(4) b-values apparently decrease with decreasing magnitude. The same behaviour has been found previously on the Western Ethiopian escarpment, in the Gulf of Tadjoura and in Iceland (Table 8.5.3).

8.6 An explanation for the ESP Seismicity Observations

Several theories have been advanced to explain the mechanism of earthquake sequences (BENIOFF,1951; MOGI,1963; NUR and SCHULTZ,1973). Mogi considers earthquake sequences to be the result of random fracturing in a heterogeneous brittle material in response to an external stress. When this stress exceeds the strength of the material most of it is released by movement along a major fracture. The disturbance resulting from this movement produces a number of random subsidiary fractures in the surrounding region. The remaining stress becomes locally concentrated at these fractures and is released gradually by their random slippage, giving rise to aftershocks. The more brittle or inhomogeneous the material the greater the number of subsidiary fractures, and hence the greater the number of aftershocks.

Icelandic studies suggest that Icelandic rifting episodes start near a magma chamber and propagate away, with lateral injection of magma into the fissure swarm. Epicentral migration is related to subsidence of the top of the magma chamber (LARSEN et al,1979; EINARSSON and BRANDSDÓTTIR,1980). The existence of a similar magma chamber below the Asal rift in Djibouti, causing the Ghoubbet al Kharab 1978 seismic activity, is suggested by the observed fissure volcanism (ALLARD et al,1979) and the bulging of the inner floor of the rift (STIELTJES,1973). A broad-band magnetotelluric experiment (Van NGOC et al,1981) has recently revealed this chamber, and has shown it to have

a depth of 2 to 4 km and a probable melt volume of order 1Ø km^3. It underlies Ardoukôba volcano, which was built during the 1978 activity.

No volcanism has been observed in Central Afar associated with seismicity, although the Serdo 1969 Apr Ø5 earthquake produced fissures (DAKIN et al,1971). The tectonic situation is different from Iceland and from Djibouti, but it is probable that for a rifting episode to occur there must be liquid magma present under hydrostatic pressure (as proposed for Djibouti by TARANTOLA et al,198Ø). The liquid is in contact with a stretched lithosphere where the minimum stress is less than the magma pressure, and fracturing will be induced perpendicular to the minimum stress direction, i.e. parallel to the rift axis.

TARANTOLA et al (198Ø) argue that if the magma were not present the elastic-brittle threshold would not be reached until the elastic stretching reached higher values. The brittle mechanism would be very different from the magmatic fissuring just described, and would involve normal faulting and crustal thinning without dyke or fissure formation.

One possible explanation of the ESP sequences observed within Afar is that the earthquakes are triggered by magma pressure, but that magma injection is performed essentially vertically from a magma source in the lower crust below the level of seismic activity, rather than by lateral injection from a very shallow chamber. This explains the absence of epicentral migration and of marked S wave attenuation for local events. Although occurring in response to magmatic

activity, the seismicity is itself tectonic and does not therefore give rise to the very high b-values associated with volcanic swarms.

The magma pressure will cause increasing strain on the overlying brittle crustal rocks (with small foreshocks occurring during this period) until heterogeneous brittle fracture suddenly occurs (main shock), with aftershocks following rapidly according to MOGI's (1963) hypothesis. For larger episodes of activity, such as the Serdo 1969 sequence of Figure 8.5.4, the same process involves a larger area, leading to major brittle fracture along more than one fault and giving rise to the observed type 4 sequences.

Potential spreading centres within the ESP study area are underlain by intermittent magma chambers intruding the upper crust and elongated NW-SE in response to the regional stress field associated with the separation of Danakil and Nubia. Further intrusion may lead to axial basaltic ranges with fissural volcanism, underlain by a continuous upper crustal magma source, as already observed elsewhere in Afar along the Erta Ale and Asal ranges. This magma chamber elongation is the immediate cause of the linearity of the ESP epicentres along the trends of surface faulting.

8.7 Discussion

8.7.1 The 1969 Serdo Earthquakes

Were the 1969 Serdo earthquakes associated with right lateral shear along a NW-SE or WNW-ESE transform fault zone between Nubia and Danakil (FAIRHEAD and GIRDLER,1971; GIRDLER, in preparation), or with tectonic activity along the NW-SE trend of surface faulting (DAKIN et al,1971; GOUIN,1975,1979)? This major unresolved question is examined here in the light of the present study. GIRDLER (in preparation) has summarised as follows the evidence from the 1969 Serdo earthquakes for a WSW-ENE transform:

(1) Ø8Ø° alignment of JED epicentres.

(2) Fault plane solutions with steeply dipping nodal planes at Ø63°, 153° (McKENZIE et al,197Ø).

(3) Model studies (e.g. COURTILLOT et al,1974) indicating that WSW-ENE shear at depth could produce NW-SE surface faults as "second-order" effects.

(4) Low b-value (Ø.76, FAIRHEAD and GIRDLER,197Ø), indicating possible shear motion. (Note also that the low stress drops calculated for the two major events (MAASHA and MOLNAR,1972; Section 7.6) imply a low b-value for the sequence, through Equation 8.5.2).

(5) "Surprisingly large" ISC focal depths, ranging from 19 to 164 km (weighted mean depth 45 ± 21 km).

In support of Girdler's theory it could be argued that obliqueness of transform faults linking slowly spreading ridge segments has commonly been observed (ATWATER and

MACDONALD,1977), and may be shown to be energetically favourable (STEIN,1978).

Points (1) to (3) have been considered in Section 8.2. No 080° alignment is seen on GOUIN's (1975) revised epicentres, and it is not necessary to choose the 063° nodal plane. However, with regard to point (3) it is in favour of Girdler's interpretation that COURTILLOT et al's (1974) model predicts strike slip and some dip slip of the "second-order" faults. This type of faulting has been inferred above for ESP events in the vicinity, on the basis of relatively low observed b-values (0.78 ± 0.04 for the ESP Serdo sequence, Table 8.5.2) and the occurrence of mainshock-aftershock sequences.

GIRDLER's (in preparation) interpretation becomes untenable unless the 1969 Serdo earthquakes had foci in a major transform structure below (and obscured by) the upper crustal lava flows. The shallowness of all ESP hypocentres within Afar casts doubt on the 1969 Serdo ISC focal depths. Foci at 45 km or below are also not easily reconciled with an upper mantle having low seismic velocity and raised Poisson's ratio (Chapter 4). Furthermore, 1973 events from the Gulf of Tadjoura (where teleseismic evidence shows that the upper mantle anomaly is no greater than below Serdo (Ebbutt, pers. comm)) were located by ISC at depths of up to 187 km. The three most widely reported events were placed at 70 ± 13 km, 52 ± 9.8 km and 65 ± 14 km. Focal depth determinations from the IPG local network have shown these and all subsequent events in the vicinity to have had depths

of less than 10 km (Ruegg, pers. comm).

Overestimation of depths of teleseismically-recorded events in this area appears to be general. The 1971 April 15 Gulf of Aden earthquake (ISC co-ordinates 12.79°N, 48.56°E, h = 61 ± 13 km; m_b = 4.7) has focal depth 5.4 ± 1.5 km as determined from the time difference between P and sea-surface reflections (PEARCE,1981). Pearce positively identifies this event, which is located very close to the median ridge axis, as having occurred within layer 3 of a 3-layer oceanic crust similar to that deduced by LAUGHTON (1966a) from seismic refraction profiles.

If the 1969 Serdo earthquakes, like the ESP-recorded events, had foci within the upper crust (0 to 5 km), it is impossible to argue that the associated surface features observed by DAKIN et al (1971) are merely second-order effects. Their NW-SE trend must be interpreted as a direct expression of the faulting direction, as maintained by GOUIN (1975,1979). The ESP-recorded events are, however, some three orders of magnitude smaller than the principal 1969 earthquakes. It may therefore be argued that both the ESP events and the surface faults are second-order phenomena, occurring within the lavas that obscure the hypothetical underlying major transform structure with which the 1969 earthquakes are (according to this hypothesis) associated. PEARCE's (1981) accurate focal depth occurs within oceanic layer 3, not in the surface layer.

It is concluded that, in the absence of any large magnitude event near Serdo during this study, the ESP data

cannot resolve the ambiguity in the interpretation of the 1969 Serdo earthquakes.

8.7.2 Implications for Tectonic Models

Detailed plate tectonic models for the development of Afar over the past 1 Myr have been presented by SCHAEFER (1975) and by BARBERI and VARET (1977). Although the present study covers only 7 months, it may help to test the models.

Schaefer's model (Figure 8.7.1) is largely based on detailed field observations south of 12.5°N. In Southern Afar most spreading has occurred perpendicular to the NNE-SSW trend of the Issa and Herta Ale graben (Figure 1.4.2). Schaefer's interpretation is in terms of a sinking, attenuated continental crust, following BERCKHEMER et al's (1975) explanation of seismic refraction data and MAKRIS et al's (1975) gravity data interpretation. These studies were reviewed in Chapter 1.

It is widely accepted that the (North) Danakil block is a crustal platelet, rotating anticlockwise between the Nubia and Arabia plates (e.g. LE PICHON and FRANCHETEAU,1978; and Section 1.2). Schaefer considers the Dobi block (NE of 'Tendaho spreading zone' on Figure 8.7.1) also to be an area of continental crust, so that "the Tendaho graben and Manda (Inakir) zone are the only areas [in South-Central Afar] where major dilatation can take place". The Dobi block lies between these two areas. Its tensional features are a result of its break-up "while swimming between two

KEYS TO FIGURES 8.7.1 AND 8.7.2

(reproduced from SCHAEFER et al, 1975, and BARBERI and VARET, 1977, respectively)

Figure 8.7.1

ERTA ALE RANGE

ALAITO RANGE

AMARTI RANGE

TENDAHO SPREADING ZONE

MANDA (INAKIR) SPREADING ZONE

HERTALE and ISSA SPREADING ZONE

28 MOHO DEPTH [km]

On Schaefer's key, Alaito and Amarti ranges correspond to Alayta and Tat Ali on Figures 1.4.2 and 8.7.2.

Figure 8.7.2

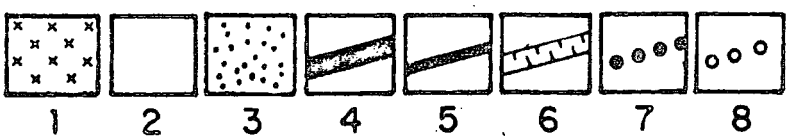

(1) Outcropping continental basement.
(2) Continental rift material.
(3) Oceanic crust formed since 4 Myr ago.
(4) Spreading axes of axial volcanic ranges.
(5) Transform faults, with inferred directions of motion.
(6) Manifestations of extensional tectonics, without development of axial volcanic ranges.
(7) Transverse volcanic structures.
(8) Central volcanoes.

FIGURE 8.7.1

A MODEL FOR AFAR SPREADING (SCHAEFER et al,1975)

(overlay shows seismic epicentres located by ESP)

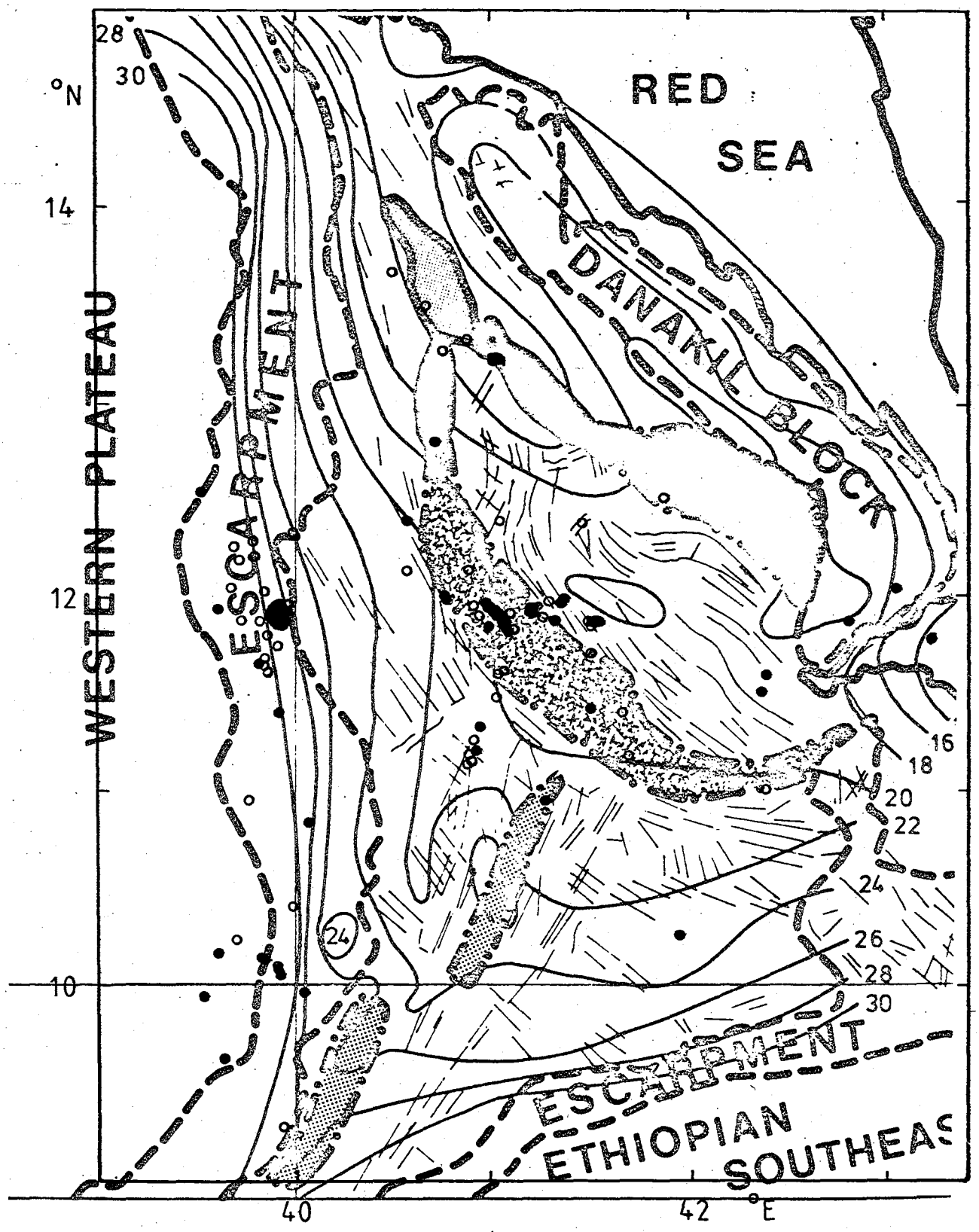

FIGURE 8.7.2

A SCHEMATIC STRUCTURAL MODEL FOR AFAR

(BARBERI and VARET,1977)

(overlay shows seismic epicentres located by ESP)

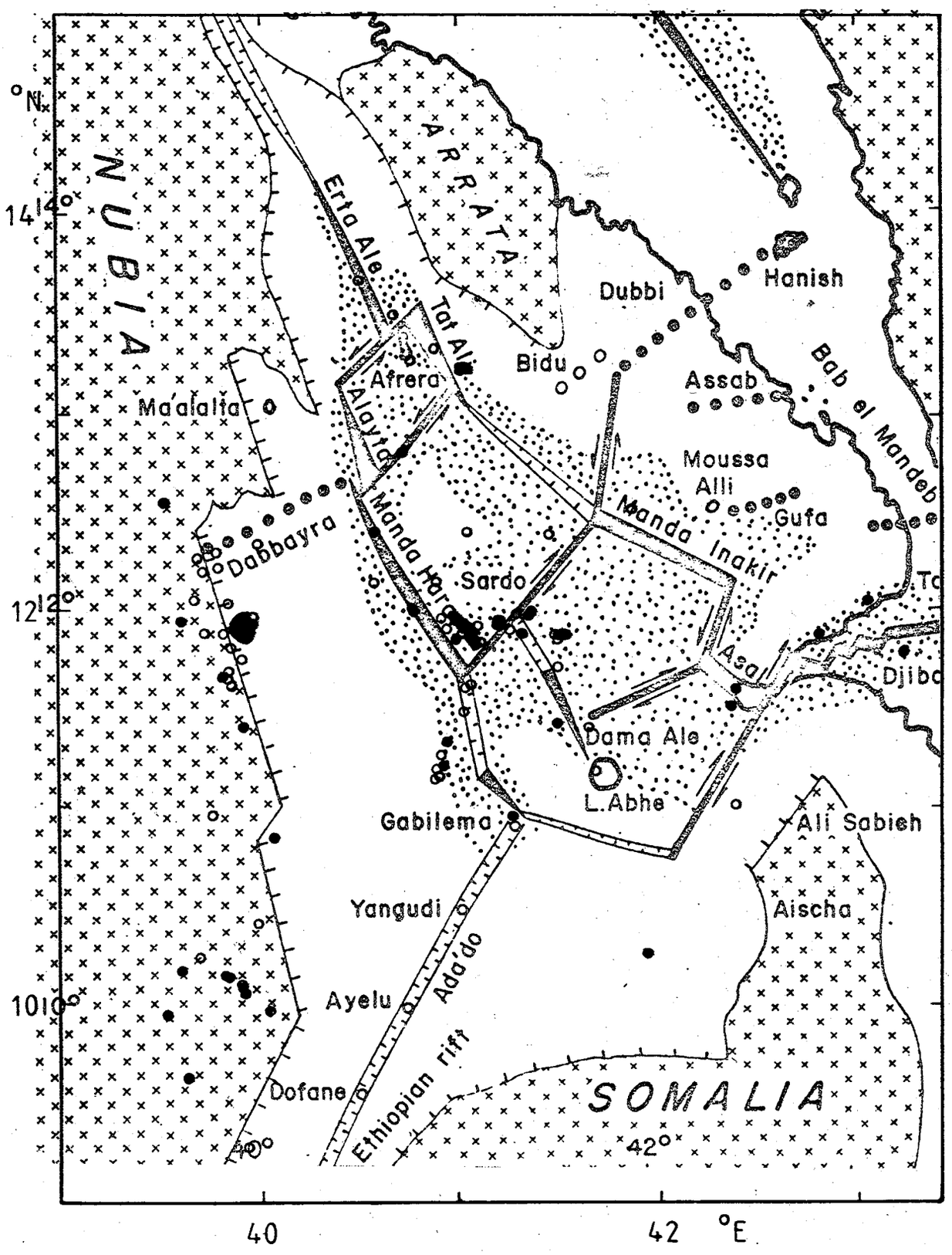

zones of major crustal attenuation".

In contrast, BARBERI and VARET (1977) conclude that "geophysical and petrological data are consistent in suggesting an oceanic nature for large parts of internal Afar". Their schematic structural map (Figure 8.7.2) is based on volcanological and geochemical data (Section 1.4) as well as on observations of surface faulting. They find it necessary to introduce five microplates, some of which are wholly made up of oceanic crust formed during the past 4 Myr, in addition to the continental Nubia, Arabia and Somalia plates.

ESP epicentres are displayed as overlays on the models of Figures 8.7.1 and 8.7.2. Conclusions are limited by the short duration of the ESP study, during which active regions may have been temporarily aseismic. However, it is observed that:

(1) Seismicity is largely confined to the flanks of the Tendaho graben. There is no indication that the graben (or the Manda Inakir zone) is currently active as a major spreading zone, as proposed by Schaefer.

(2) No seismicity has been detected in SW Afar. This concords with the sparsity of events recorded at AAE from the Main Ethiopian rift (DAKIN,1975), and with the absence of microseismic activity along the rift farther south (7°N to 9°N) during a 1969 survey (MOLNAR et al,1970).

(3) Seismicity in N Afar coincides with the Erta Ale and Tat Ali axial volcanic ranges and demarcates their NW-SE to NNW-SSE trend.

(4) Continuous seismicity has been observed on the NW flank of the Tendaho graben at the southern end of the Manda Hararo range. This activity is localised along the NW-SE axis of the range, following a line of volcanic centres. Activity has also been found SE of Serdo such as to support Barberi and Varet's postulated axis of activity linking Serdo and Dama Ale. No activity has been observed along the postulated link between Manda Hararo and Gabilema.

(5) Tectonic activity has occurred at Kurub volcano, which might lie on a hypothetical NE-SW transform fault through Serdo (Figures 8.3.3, 8.7.2). The remarkable temporal relationship between sequences of events located at Kurub and SE of Serdo (Figure 8.5.2) suggests that the former were triggered by the latter, or that both had a common cause. It is conceivable that NW-SE faulting SE of Serdo might provoke NE-SW dextral faulting at Kurub, although the Kurub events are so shallow that some surface evidence of a NE-SW fault plane would be expected.

In view of the Recent NW-SE surface faulting observed at Kurub, and of the similarity of the two sequences of Figure 8.5.2, it is more likely that both sequences were caused by NW-SE faulting. If this is the case, ESP has detected three parallel NW-SE axes of active seismicity (NW Tendaho graben, Kurub, SE of Serdo)(Figure 8.7.3). This is far more consistent with the idea of widespread crustal attenuation than with Barberi and Varet's plate tectonic scheme.

(6) The line of NNE-SSW ESP epicentres coincident with

FIGURE 8.7.3

A MODEL FOR SPREADING IN CENTRAL-SOUTHERN AFAR BASED ON THE SPATIAL DISTRIBUTION OF ESP EPICENTRES

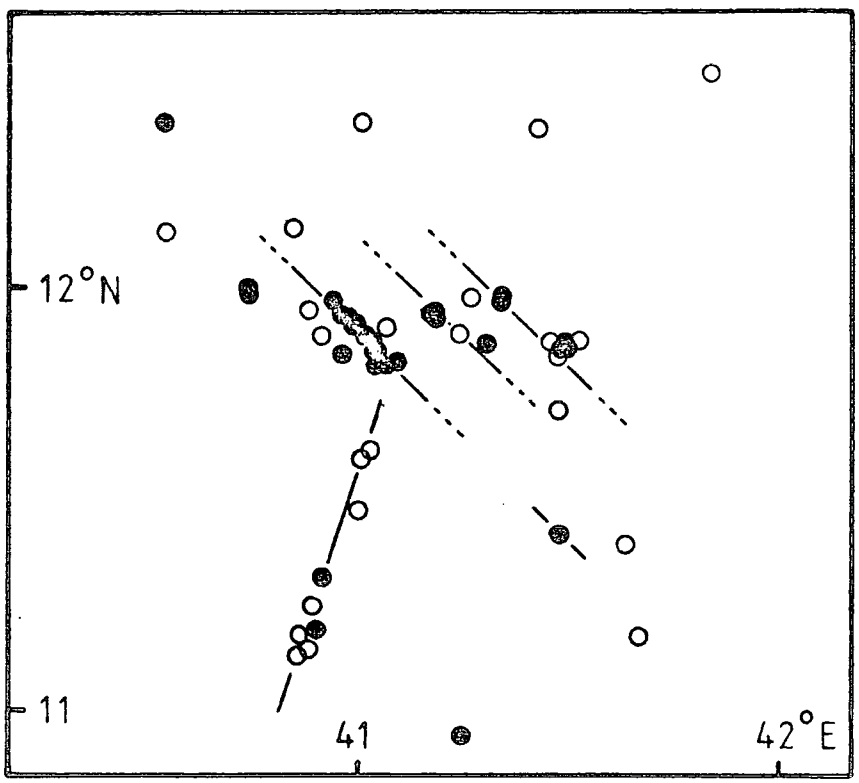

● RECORDED AT 3 OR 4 STATIONS

○ RECORDED AT 2 STATIONS

and south of the surface expression of the Allallobeda graben has been remarked on in Section 8.3.3. The epicentres run parallel to the Issa and Herta Ale graben in Southern Afar (Figure 1.4.2) (Gabilema - Dofane axis on Figure 8.7.2), which are the most northerly well-defined sections of the Main Ethiopian rift. This seismic line strongly suggests that the Main Ethiopian rift continues north from the Issa graben as far as the western margin of the Tendaho graben through the Allallobeda graben (Figure 2.3.2), the latter having greater structural significance than hitherto supposed. MOHR and WOOD (1976) have suggested that the rift terminates at Dama Ale, which is dextrally offset from the Issa graben. Pronounced NNE-SSW surface faulting is seen SSW of Dama Ale, and it is quite possible that the complex Afar tectonic regime permits the existence of two parallel NNE-SSW rift segments, analogous to NW-SE trending Alayta and Tat Ali (Figures 1.4.2, 8.7.2).

There is no geological or geochemical evidence for the existence of a NW-SE or WNW-ESE transform fault through Serdo. Except for the NNE-SSW line of epicentres (Figure 8.7.3) south west of the station network in Southern Afar (where a different plate pair is involved (Nubia - Somalia instead of Nubia - Danakil)), the present study has yielded no positive evidence for tectonic activity within Afar with any other direction than NW-SE to NNW-SSE.

CHAPTER 9

DISCUSSION

9.1 Crustal and Upper Mantle Structure of Afar

9.1.1 The Structural Model

Ignoring superficial layers of volcanics and sediments, the Afar crust and uppermost mantle have been modelled by a plane-parallel, homogeneous velocity-depth (V(z)) structure (Figure 9.1.1a). This has been shown to be the simplest geologically feasible layered model consistent with all the arrival time data. The layer 2 velocity (6.2 ± 0.1 km s^{-1}) is the best constrained model parameter, since the majority of well recorded events have epicentral distances (d) in the range 20 to 70 km, giving head waves in layer 2 for first arrivals.

Other V(z) parameters are not well constrained by P and S arrival data, because of the small number of recording stations and their poor distribution in relation to the epicentres. A maximum of 8 arrivals is available (4 P, 4 S), while for each earthquake there are 4 unknowns (3 positional co-ordinates and origin time). However, identification of the direct arrival P_g, and/or the simple reflection r2, on records from d = 25 to 65 km has enabled V_1 and h_1 to be estimated with some certainty (Section 4.3.2). V_1 and V_2 appear to be the same beneath all recording stations, but there is some indication of

KEY TO FIGURE 9.1.1

COMPARISON OF PREFERRED STRUCTURAL MODEL FOR AFAR (A) WITH PREVIOUS MODELS FOR AFAR (B TO G) AND WITH A GENERALISED MODEL FOR ICELAND (H)

(A) This study. Inferred structure beneath ESP station network.

(B) to (G) BERCKHEMER et al, 1975

(B) Profiles II and III.

(C) Profile IV.

(D) Profile V.

(E) RUEGG (1975a,b): Profiles 2 and 5.

(F) and (G) SEARLE (1975)

(F) Model 130N.

(G) Model 125G.

(H) Generalised model for Iceland (after PÁLMASON and SAEMUNDSSON, 1974).

Models (B) to (G) have been discussed in Section 1.5. Their locations within Afar are shown in Figure 9.1.2.

The model for Iceland is interpreted as follows: layer 1 - basalt lavas, sometimes containing intercalated sediments and clastic volcanics; layer 2 - mainly basaltic lavas, with some basic and acid intrusions; layer 3 - basalt layer, equivalent to oceanic layer 3; layer 4 - upper mantle.

FIGURE 9.1.1

COMPARISON OF PREFERRED STRUCTURAL MODEL FOR AFAR (A)

WITH PREVIOUS MODELS FOR AFAR (B TO G)

AND WITH A GENERALISED MODEL FOR ICELAND (H)

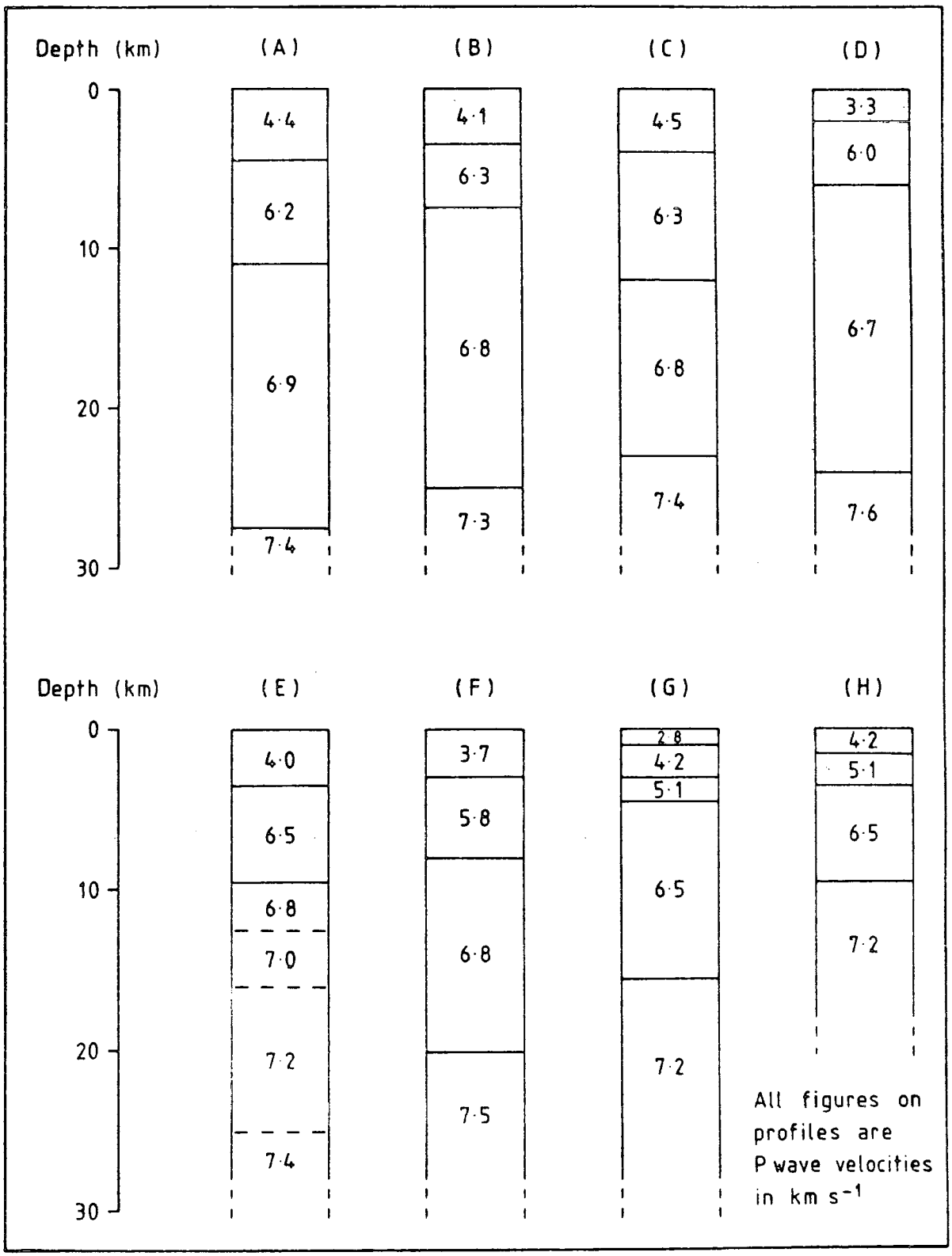

FIGURE 9.1.2

LOCATION MAP REFERRING PROFILES (B) TO (G) OF FIGURE 9.1.1 TO THE ESP STATION NETWORK

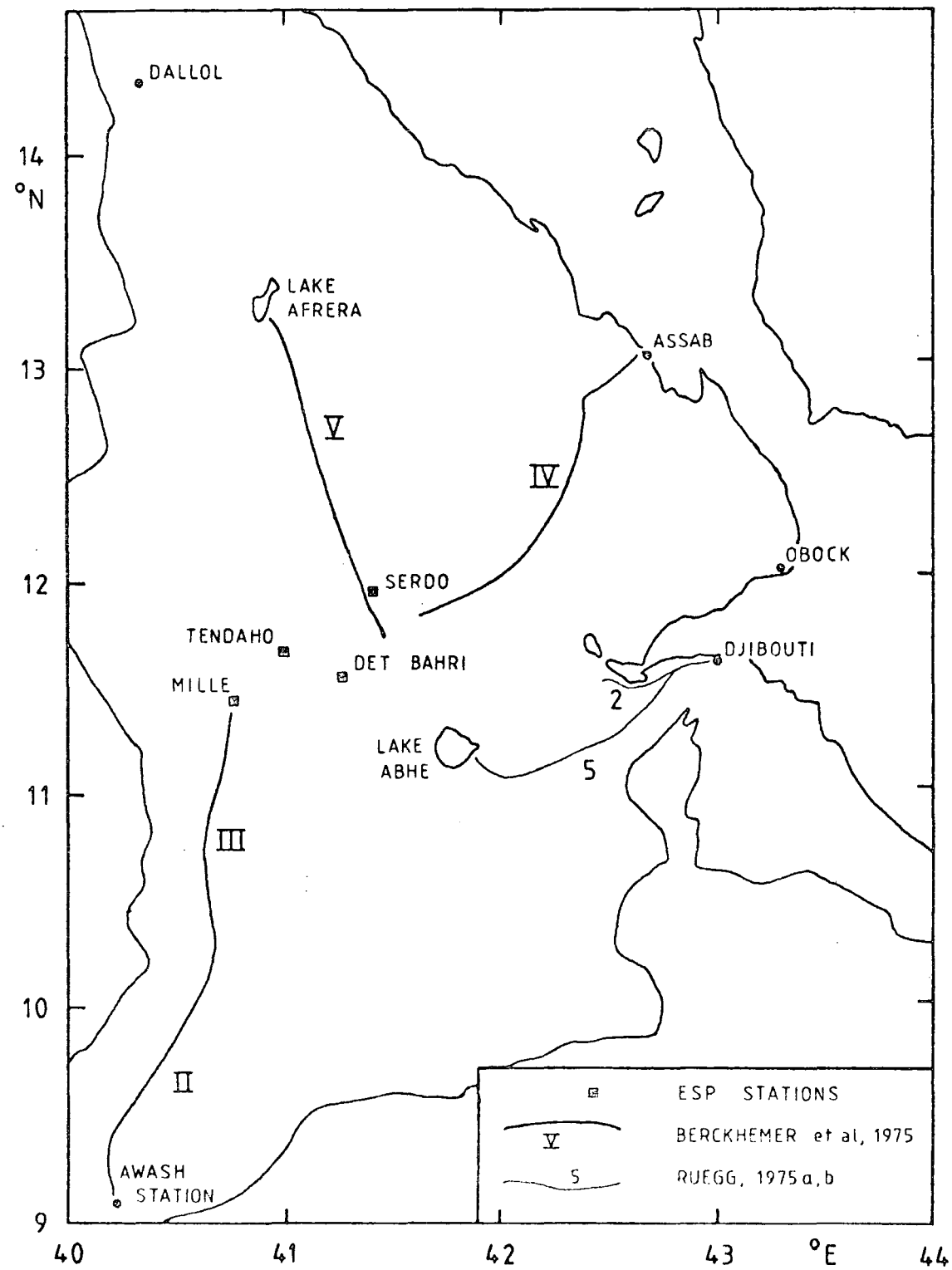

shallower h_1 below Tendaho.

This 2-layer upper crust is not the only laterally homogeneous model that could be derived from the P and S arrival data. For a network of four ocean-bottom recorders on the Mid-Atlantic Ridge FRANCIS et al (1978) have shown that two-gradient, two-layer and even single layer models yield very similar RMS residuals of individual hypocentral solutions. A layered structure is chosen as best explaining the later arrivals within the P coda, and is directly comparable with the structural models of BERCKHEMER et al (1975) and RUEGG (1975a,b).

P and S arrival data give little information on the deeper layers. A value of $V_3 = 6.84 \pm 0.57$ km s^{-1} was calculated, and it was shown that normal (8.0 km s^{-1}) upper mantle could not exist above about 40 km depth (43 km for the preferred structural model). The adopted parameters h_2, V_3, h_3 depend critically on the interpretation of the later arrivals from events in the distance range 60 to 95 km as head waves in layer 4. V_4 is essentially unconstrained, but the presence of later arrivals suggests a well-defined 3/4 layer interface rather than the quasi-continuous increase of velocity with depth favoured by RUEGG(1975a,b). RUEGG's (1975a,b) profiles 2 and 5 for Djibouti (Figure 9.1.1e) are quite inconsistent with these arrivals and have V_2 outside the error range in this study. They also give consistently and significantly larger RMS residuals than the ESP model. SEARLE's (1975) models (Figure 9.1.1f,g) also lack any layer with velocity close to 6.2 km s^{-1}.

V_P/V_S has been calculated as approximately 1.76 for V_1 and V_2, with 1.90 at greater depths. These figures correspond to Poisson's ratios of 0.26 and 0.31, respectively. RUEGG (1975a, Fig.6c) has also found raised V_P/V_S values, ranging from 1.8 to 2.0 and increasing with depth.

The ESP model, although differing in detail from Ruegg's, is similar to BERCKHEMER et al's (1975) seismic refraction profile IV for East-Central Afar (Figures 9.1.1c, 9.1.2), just east of the ESP network. The layer 2 velocities obtained by BERCKHEMER et al (1975) and RUEGG et al (1975a,b) are only apparent velocities (although the majority of refraction lines were reversed). Lateral homogeneity was assumed because of the lack of evidence to the contrary.

No lateral velocity inhomogeneities have been detected in this study. Any gross structural inhomogeneity associated with the Tendaho graben should have been observable, and it is concluded that no such inhomogeneity exists. This is consistent with the flat local gravity field (SEARLE and GOUIN,1971a; MAKRIS et al, 1973) observed over this region. However, the spectral analysis has enabled greater P and S wave attenuation to be detected beneath the Tendaho graben. This attenuation extends to shallower depth (5 km or less) below Serdo on the eastern margin of the graben than below Tendaho and Det Bahri on the west. There is also an indication that attenuation may increase from south to north of the ESP network.

It was not possible to detect any lateral inhomogeneities from the P and S arrival times because of the paucity of recording stations, and 3-component analysis suffered from the effects of local scattering caused by superficial geology.

9.1.2 Interpretation of the Model

Each layer of the ESP model (Figure 9.1.1a) is discussed in turn. Velocities given in brackets are those obtained for Afar by BERCKHEMER et al (1975).

LAYER 4: V_p = 7.4 km s^{-1} (7.3 to 7.6 km s^{-1})

Layer 4 is interpreted as anomalous upper mantle. This study has demonstrated: (1) the absence of normal upper mantle seismic P-velocities; (2) elevated Poisson's ratios; and (3) significantly greater attenuation than below California.

This interpretation is consistent with previous gravity, magnetotelluric, petrochemical and seismic refraction results (Chapter 1) which have implied the existence of low-velocity, high-temperature upper mantle material. Local seismicity does not yield information on the depth of this material or the velocity distribution within it. This will be provided by ESP teleseismic observations (Ebbutt, in preparation).

LAYER 3: V_p = 6.9 km s^{-1} (6.7 to 6.8 km s^{-1})

Layer 3 has been variously interpreted as: (1) equivalent to the lower continental crustal layer

(V_P = 6.6 km s^{-1}) found below the Ethiopian plateau by BERCKHEMER et al,1975 (see also GEHLEN et al,1975); (2) partially melted upper mantle (BARBERI and VARET,1975,1977); and (3) "equivalent to oceanic layer '3A', composed of serpentinized and amphibolitized gabbro, resting on fresh gabbro of the 7.3 - 7.6 km s^{-1} layer '3B'" (MOHR,1978). We consider these hypotheses in turn in the light of the evidence provided by this study.

Identification of layer 3 as equivalent to lower continental crust is hindered by the higher velocity obtained here. It is also incompatible with Poisson's ratios as high as 0.31, as found in this study (e.g. HYNDMAN,1979). Moreover, if layer 3 is attenuated continental crust, its thickness (16.5 km according to this study, 11 to 18 km according to Berckhemer et al) is too great to allow for the degree of crustal extension across Afar required for consistency with the oceanic nature of the Gulf of Aden; or for any explanation of the Yemen overlap on pre-drift reconstructions (Section 1.2.2). The 6.9 km s^{-1} velocity found here also makes it less plausible directly to compare layer 3 with the equivalent layer below Iceland (6.5 km s^{-1}, Figure 9.1.1b), as attempted by MAKRIS (1975).

(2) If structural layer 3 were partially molten upper mantle, S waves would be severely attenuated. This is contrary to the observations of this and previous (e.g. SEARLE and GOUIN,1971a,1972) studies of Southern and Central Afar. Furthermore, on this hypothesis Berckhemer's seismic refraction profiles imply a total crustal thickness

of only 6 to 7 km below much of Afar and Djibouti. This is as thin as the crust of the Gulf of Aden axial trough (LAUGHTON,1966a; LAUGHTON et al,1970) and other young 'normal' oceanic crust (e.g. CHRISTENSEN,1970), and many geological and geophysical data reviewed in Chapter 1 are irreconcilable with a 'normal' oceanic crust for Afar. 6.7 to 6.9 km s^{-1} is also a very low velocity for anomalous upper mantle (c.f. 7.2 km s^{-1} in the Red Sea and Gulf of Aden).

(3) MOHR's (1978) identification of layer 3 with oceanic layer 3A is the interpretation most consistent with the results of this study. 0.31 is a typical Poisson's ratio for young gabbroic lower oceanic crust (mostly sampled from the Mid-Atlantic Ridge (HYNDMAN,1979)). MOHR (1978) attempts to explain the great thickness of layer 3 as due to the slow rate of crustal extension in Afar, leading to more protracted and episodic magmatic processes at the spreading axes.

LAYER 2: V_p = 6.2 km s^{-1} (6.0 to 6.3 km s^{-1})

Interpretation of layer 2 is also contentious. If it is attenuated continental crust, equivalent to the 6.2 km s^{-1} layer below the Western Ethiopian plateau (BERCKHEMER et al,1975) (Figure 1.5.1a), it is difficult to explain its increase in thickness from south to north (found by Berckhemer et al), since gravity (MAKRIS et al,1972,1973,1975; BROWN and GIRDLER,1980) and seismic refraction results suggest increasing crustal attenuation from south to north. However, interpretation as oceanic

layer 2B ("a sheeted dike complex that has been metamorphosed to greenschist facies, having usual seismic velocity 5.8 to 6.0 km s^{-1}" (MOHR,1978)), or oceanic layer 3 (RUEGG,1975a,b, with the anomalously low velocity explained in terms of a presumed higher geothermal gradient), is hardly reconciled with Poisson's ratios as low as 0.26 ± 0.005 (this study). HYNDMAN (1979) shows that no layers of the oceanic crust (except for "uncommon late stage differentiates containing quartz") have ratios lower than 0.28.

Despite the absence in this study of any evidence for lateral inhomogeneity, it has to be concluded that both these interpretations are probably too simple. Magnetic data reveal two distinct styles of magnetic anomaly: short-wavelength, high-amplitude, typically 'oceanic' linear anomalies, which have nowhere been found over attenuated continental crust; and longer-wavelength, low-amplitude anomalies. Laterally homogeneous structural models are insufficiently detailed to shed much light on this problem.

LAYER 1: V_p = 4.4 km s^{-1} (3.3 (for N.Afar) to 4.5 km s^{-1})

Layer 1, as determined in this study, is fully consistent with BERCKHEMER et al's (1975) layer 1. It is comparable to, but somewhat thicker than, layer 1 for Iceland (4.2 km s^{-1}, Figure 9.1.1h)). It corresponds to the thick stratoid volcanic pile, which is intercalated with sediments originating from the Afar marginal plateau escarpments. MOHR (1978) has estimated that about $3*10^4$ km^3 of rock has been denuded from the plateau margins.

The present study has not solved the conundrum of the Afar crust. If the crust and uppermost mantle are reasonably laterally homogeneous, it is evident that they do not conform to any recognized structural type. In particular, although Afar and Iceland are commonly compared as sites of crustal extension and generation, they show greatly dissimilar V(z) structures (Figure 9.1.1).

ESP was conceived as a pilot study. Any further local seismicity study to elucidate the fine structure of Afar should use a larger number of more densely spaced recording stations, and should include the firing of explosive shots to constrain the inferred V(z) model.

9.2 The Evolution of Afar

Some form of two-stage sea-floor spreading origin for the Red Sea and Gulf of Aden (e.g. GIRDLER and STYLES,1976,1978) is now widely accepted, since it is a feasible model for their common evolutionary history (Section 1.2). This implies that at least three-quarters of the width of Afar must have been formed during the first stage (i.e. before 5 Myr ago).

An attenuated continental crust below the ESP study area cannot explain this degree of extension (except in the unlikely event that large amounts of extension have been taken up below the marginal plateaux). An attenuated continental crust punctured by massive intrusions of anomalous upper mantle material to shallow depths should have led to the presence of lateral structural

inhomogeneities, which are not indicated by the local gravity and aeromagnetic data. A largely oceanic crust in the study area, maintained above sea level by excessive magmatism, is irreconcilable with the autochthonous position of the Aisha spur (CHRISTIANSEN et al,1975), with published gravity profiles (MAKRIS et al,1975) and with the observed propagation of L_g and R_g (SEARLE and GOUIN,1971a; DAKIN et al,1971).

Models of SCHAEFER (1975) and BARBERI and VARET (1977) for the current (second) stage of separation have been considered in Section 8.7 in the light of current seismicity observed in this study. ESP provides no support for Schaefer's model. Barberi and Varet's model, which is partly based on their interpretation of Girdler and Hall's aeromagnetic survey (GIRDLER,1970; GIRDLER and HALL,1972), is weakened by its inconsistency with subsequent, more detailed aeromagnetic results (COURTILLOT et al,1980). It requires microplates 100 km or less in length, with boundaries of comparable width. It is difficult to accept that these microplates are sufficiently rigid for plate tectonic analyses to be viable.

COURTILLOT (1980) and COURTILLOT et al (1980) have interpreted GIRDLER and STYLES's Western Gulf of Aden magnetic profiles in terms of a single spreading phase with a half-spreading rate of about 0.8 cm yr^{-1}. COCHRAN (1981), analysing marine magnetic profiles over the entire Gulf of Aden, reaches a similar conclusion. Courtillot proposes that the Western Gulf of Aden has developed since the Upper

Miocene by means of a westward-propagating lithospheric crack. Positions of the crack tip, based on the inferred age of the interface between Gulf of Aden oceanic magnetic anomalies and the bounding magnetic quiet zones, are: 45.7°E at 12 Myr ago; 45.0°E at 10 Myr ago; Gulf of Tadjoura < 2.5 Myr ago; Asal rift < 1 Myr ago; close to Lake Asal (42.5°E) at present. Courtillot supports these dates by radiometric age determinations of tholeiitic basalts on either side of the Gulf of Tadjoura. They represent a constant crack propagation velocity of approximately 3 cm yr^{-1}.

Courtillot interprets deformation within Afar as being "analogous to the region of anelastic deformation that usually occurs in front of a propagating crack tip" (COURTILLOT et al,1980). Such deformation would presumably have given rise to the 'quiet' magnetic anomalies observed in Southern and Central Afar. Localised and well-defined plate boundaries are only observed behind the propagating crack tip, as exemplified by the recent initiation of oceanic-type spreading in the Asal rift (HARRISON et al,1975; NEEDHAM et al,1976; ABDALLAH et al,1979). Courtillot's model well explains the pattern of local seismicity revealed by this study, which has been most simply explained in terms of diffuse extension in South-Central Afar across several discrete NW-SE axes, rather than concentration at a single spreading axis; and which provides no evidence for the NE-SW or ENE-WSW transform faults required by Barberi and Varet's model.

According to Courtillot, the continuing passage across Afar of the propagating crack will define the future Nubia - Somalia (Africa - Arabia) plate boundary. Whether it will propagate via the Manda Inakir range to Tat Ali (Figure 1.4.2), or via the Goba'ad and Tendaho graben to Manda Hararo and Alayta (as suggested by SCHAEFER's (1975) model, Figure 8.7.1a), is a matter for conjecture. Noting the correspondence of Figure 8.7.1a with Figure 1.4.3 and other geochemical indicators (see e.g. BARBERI and VARET,1977), the present author suggests the latter. Crack propagation northward to north-westward from Central Afar, or southward to south-eastward from the Red Sea, will be complicated by the presence of the 'hinged' North Danakil block (Section 1.2.2).

Whatever evolutionary model is favoured for Afar, it is volcanically, geochemically and physiographically evident (Chapter 1) that the Recent volcanic ranges represent current sea-floor spreading within Afar under the influence of the regional NE-SW stress system. The evidence of local seismicity presented here supports this view. As Arabia and Africa continue to separate, the spreading axis within Afar will become clearly defined. Some presently active Afar axial volcanic ranges will become identified as 'fossil' spreading axes.

The tendency of recent authors to regard Afar merely as the "elbow" of the Red Sea - Gulf of Aden spreading system is an oversimplification. The discovery in this study of a NNE-SSW axis of seismic activity, coupled with evidence for

Recent spreading across the 'en échelon' Issa and Herta Ale graben (SCHAEFER,1975), shows that the NNE-SSW trending Main Ethiopian rift of the East African rift system continues to exert at least a major perturbation on the established Red Sea - Gulf of Aden system.

APPENDIX 1

PUBLISHED POTASSIUM-ARGON ROCK AGES

WITHIN AND SURROUNDING AFAR

LOCATION	AGE	ROCK TYPE	AREA (OR COORDINATES WITHIN AFAR)	SOURCE
E of Batie	66	Basaltic Dyke	W Plateau Margin	MNS
Nr. Ambo	58	Basaltic Dyke	W Plateau	MNS
E of Batie	57	Basaltic Dyke	W Plateau Margin	MNS
E of Batie	55	Basaltic Dyke	W Plateau Margin	MNS
E of Batie	48.5	Basaltic Dyke	W Plateau Margin	MNS
SE of Debre Markos	42	Basaltic Dyke	W Plateau	MNS
Wolkefit Pass	36.0	Flood Basalt	W Plateau	J
E of Batie	36	Basaltic Dyke	W Plateau Margin	MNS
Miesso	35.5	Basaltic Dyke	SE Plateau	MNS
E of Batie	35	Basaltic Dyke	W Plateau Margin	MNS
Nr. Harar	35	Basaltic Dyke	SE Plateau	MNS
SE of Debre Markos	32	Basaltic Dyke	W Plateau	MNS
E of Batie	32	Basaltic Dyke	W Plateau Margin	MNS
Wolkefit Pass	31.6	Flood Basalt	W Plateau	J
SE of Debre Markos	31.5	Basaltic Dyke	W Plateau	MNS
Nr. Ambo	31	Basaltic Dyke	W Plateau	MNS
E of Batie	31	Basaltic Dyke	W Plateau Margin	MNS
E of Batie	30	Basaltic Dyke	W Plateau Margin	MNS
Nr. Harar	30	Basaltic Dyke	SE Plateau	MNS
Nr. Goba	30	Basaltic Dyke	Ethiopian Rift Margin	MNS
Afar	29.1	Basalt	not given	KKM
Afar	28.2	Trachyte	not given	KKM
E of Batie	28	Basaltic Dyke	W Plateau Margin	MNS
Nr. Harar	28	Basaltic Dyke	SE Plateau	MNS
Miesso	28	Basaltic Dyke	SE Plateau	MNS
Cinina	28	Basalt	Ethiopian Rift	MNPP
Blue Nile Gorge	27.4	Basalt	W Plateau	MMW
Blue Nile Gorge	27.2	Basalt	W Plateau	MMW
Wolkefit Pass	27.0	Flood Basalt	W Plateau	J
Ali Sabieh	26.7	Basalt	Aisha Block	CDMW
Afar	26.3	Basalt	not given	KKM
Maichew	26.2	Flood Basalt	W Plateau	J
E of Batie	26	Basaltic Dyke	W Plateau Margin	MNS
Dawanlle	25.9	Trap Series Basalt	Aisha Block	BMR
S Danakil	25.9	Hawaiite	S Danakil	CDGGLL
Maichew	25.7	Flood Basalt	W Plateau	J
Dawanlle	25.5	Trap Series Basalt	Aisha Block	BMR
E of Batie	25.5	Basaltic Dyke	W Plateau Margin	MNS
Ali Sabieh	25.2	Rhyolite	Aisha Block	CDMW
Affara Dara	25.0	Peralkaline Granite	12.5N 41.0E	BBFMSTV
N of Omo	25	Porphyritic Basalt	Eth. Rift Margin	GMM
E of Batie	25	Basaltic Dyke	W Plateau Margin	MNS
E of Batie	25	Basaltic Dyke	W Plateau Margin	MNS
E of Batie	25	Basaltic Dyke	W Plateau Margin	MNS
E of Batie	24.5	Basaltic Dyke	W Plateau Margin	MNS
Garamulatta	24.3	Flood Basalt	Ethiopian Rift Margin	J
E of Batie	24.2	Basaltic Dyke	W Plateau Margin	MNS
Blue Nile Gorge	24.2	Basalt	W Plateau	MMW
E of L. Giulietti	24.0	Basalt	14.0N 41.0E	BBFMSTV
Waldia	24	Basalt	W. Eth. Escarpment	BBKKKM
Ali Sabieh	23.8	Ignimbrite	Aisha Block	CDMW
E of Batie	23.5	Basaltic Dyke	W Plateau Margin	MNS
Blue Nile Gorge	23.5	Basalt	W Plateau	MMW
Limmo	23.3	Porphyritic Rhyolite	W. Eth. Escarpment	BMRS
Afar	23.3	Basalt	09.1N 40.9E	KKM
Asa Ale	23.0	Rhyolite	Danakil Block	BBKKKM
S Danakil	23.0	Mugearite	S Danakil	CDGGLL
Blue Nile Gorge	23.0	Basalt	W Plateau	MMW
Anfila Bay	23	Basalt	Red Sea W Margin	F
Afar	22.9	Basalt	09.3N 41.1E	KKM
Afar	22.9	Basalt	09.0N 40.9E	KKM
Limmo	22.8	Peralkaline Granite	W. Eth. Escarpment	BMRS
Wolkefit Pass	22.8	Flood Basalt	W Plateau	J
Jijiga	22.6	Flood Basalt	SE Plateau	J
E of Batie	22.6	Basaltic Dyke	W Plateau Margin	MNS

Ali Sabieh	22.6	Basalt	Aisha Block	CDMW
Nr. Ambo	22.5	Basaltic Dyke	W Plateau	MNS
Afar	22.5	Basalt	09.3N 41.1E	KKM
Adigrat	22.4	Flood Basalt	W Plateau Margin	J
Ali Sabieh	22.3	Microsyenite	Aisha Block	CDMW
Afar	22.2	Basalt	09.0N 40.8E	KKM
Asa Ale	22.0	Granite	Danakil Block	BBKKKM
Guga Mt.	22	Basalt	Ethiopian Rift	MNPP
S Danakil	21.8	Granite	S Danakil	CDGGLL
Mugher	21.6	Flood Basalt	W Plateau	J
E of Batie	21.6	Basaltic Dyke	W Plateau Margin	MNS
Mugher	21.5	Flood Basalt	W Plateau	J
E of Batie	21.2	Basaltic Dyke	W Plateau Margin	MNS
Ali Sabieh	21.0	Ignimbrite	Aisha Block	CDMW
E of Batie	21	Basaltic Dyke	W Plateau Margin	MNS
Nr. Goba	21	Basaltic Dyke	Ethiopian Rift Margin	MNS
Din Din	21	Basalt	Ethiopian Rift	MNPP
Cassam Gorge	20.9	Basalt	Ethiopian Rift Margin	RGD
Garamulatta	20.8	Flood Basalt	Ethiopian Rift Margin	J
Garamulatta	20.7	Flood Basalt	Ethiopian Rift Margin	J
Ali Sabieh	20.5	Ignimbrite	Aisha Block	CDMW
E of Batie	20.5	Basaltic Dyke	W Plateau Margin	MNS
Adigrat	20.1	Flood Basalt	W Plateau	J
Jijiga	20.1	Flood Basalt	SE Plateau	J
Ali Sabieh	20.0	Hawaiite	Aisha Block	BFSV
S Danakil	19.9	Rhyolite	S Danakil	CDGGLL
Aisha	19.9	Flood Basalt	Aisha Block	J
Mugher	19.8	Flood Basalt	W Plateau	J
Aisha	19.8	Flood Basalt	Aisha Block	J
Dawanlle	19.7	Trap Series Basalt	Aisha Block	BMR
S Danakil	19.6	Rhyolite	S Danakil	CDGGLL
Ali Sabieh	19.6	Dolerite	Aisha Block	CDMW
Afar	19.6	Basalt	09.3N 41.1E	KKM
E of Batie	19.4	Basaltic Dyke	W Plateau Margin	MNS
SE of Debre Markos	19.3	Basaltic Dyke	W Plateau	MNS
Ali Sabieh	19.1	Rhyolite	Aisha Block	CDMW
S Danakil	19.0	Obsidian	S Danakil	CDGGLL
E of Batie	19	Basaltic Dyke	W Plateau Margin	MNS
Nr. Goba	19	Basaltic Dyke	Ethiopian Rift Margin	MNS
Nr. Goba	19	Basaltic Dyke	Ethiopian Rift Margin	MNS
Adigrat	18.8	Flood Basalt	W Plateau	J
Ali Sabieh	18.7	Microgranite	Aisha Block	CDMW
E of Batie	18.5	Basaltic Dyke	W Plateau Margin	MNS
Miesso	18	Basaltic Dyke	SE Plateau	MNS
Afar	17.9	Trachyte	09.1N 40.9E	KKM
Afar	17.9	Basalt	09.2N 41.1E	KKM
Afar	17.7	Basalt	08.9N 40.6E	KKM
Ali Sabieh	17.5	Microgranite	Aisha Block	CDMW
Ali Sabieh	16.3	Dolerite	Aisha Block	CDMW
Afar	16.3	Basalt	09.2N 41.1E	KKM
Nr. Goba	16	Basaltic Dyke	Ethiopian Rift Margin	MNS
Adigrat	15.5	Flood Basalt	W Plateau	J
E of Batie	15.5	Basaltic Dyke	W Plateau Margin	MNS
Nr. Goba	15.5	Basaltic Dyke	Ethiopian Rift Margin	MNS
Dawanlle	15.3	Rhyolite	Aisha Block	BMR
Miesso	15	Basaltic Dyke	SE Plateau	MNS
Nr. Goba	15	Basaltic Dyke	Ethiopian Rift Margin	MNS
Nr. Goba	15	Basaltic Dyke	Ethiopian Rift Margin	MNS
Baka Island	15	Basalt	Red Sea W Margin	F
Simbileyta	14.6	Basalt	12.0N 43.0E	BFSV
Afar	14.4	Basalt	09.1N 40.9E	KKM
Ali Sabieh	14.3	Rhyolite	Aisha Block	CDMW
Ali Sabieh	14.2	Rhyolite	Aisha Block	CDMW
Coursa	14.2	Basalt	12.5N 43.0E	BFSV
Ali Sabieh	14.1	Rhyolite	Aisha Block	CDMW
Afar	14.1	Basalt	09.1N 40.8E	KKM
Afar	14.1	Basalt	08.6N 40.2E	KKM
Afar	13.8	Trachyte	09.1N 40.9E	KKM
Afar	13.6	Trachyte	08.8N 40.4E	KKM
E of Batie	13.5	Basaltic Dyke	W Plateau Margin	MNS
Afar	13.5	Basalt	09.1N 40.8E	KKM
Afar	13.3	Trachyte	09.1N 40.8E	KKM
Ali Sabieh	13.3	Obsidian	Aisha Block	CDMW
Afar	13.2	Trachyte	09.1N 40.8E	KKM
Afar	13.1	Basalt	08.6N 40.2E	KKM
Afar	12.9	Trachyte	09.1N 40.8E	KKM

Vofi	12.6	Acidic	Ethiopian Rift	MNPP
Ali Dalaha	12.5	Rhyolitic Ignimbrite	12.0N 43.0E	BFSV
At'Anda	12.4	Comendite	12.5N 43.0E	BFSV
Afar	12.3	Basalt	08.8N 40.6E	KKM
Goursa	12.1	Basalt	12.5N 43.0E	BFSV
Simbililu	12.1	Basalt	12.0N 43.0E	BFSV
Celaleca	11.7	Acidic	Ethiopian Rift	MNPP
Bia Andt	11.5	Basalt	Aisha Block	BMR
Akkaba	11.4	Comendite	12.0N 43.0E	BFSV
Afar	11.2	Trachyte	08.8N 40.4E	KKM
Afar	11.1	Trachyte	08.9N 40.4E	KKM
E of Batie	11.1	Basaltic Dyke	W Plateau Margin	MNS
Afar	11.05	Trachyte	09.0N 40.8E	KKM
Miesso	11	Basaltic Dyke	SE Plateau	MNS
Ali Sabieh	10.8	Obsidian	Aisha Block	CDMW
E of Batie	10.8	Basaltic Dyke	W Plateau Margin	MNS
Afar	10.5	Basalt	09.1B 40.7E	KKM
Cassam	9.8	Flood Basalt	Ethiopian Rift Margin	J
Simbileyta	9.7	Dark Trachyte	12.0N 43.0E	BFSV
Ali Sabieh	9.6	Tuff	Aisha Block	CDMW
Afar	9.6	Basalt	09.0N 40.8E	KKM
Afar	9.5	Basalt	08.9N 40.4E	KKM
Afar	9.3	Basalt	09.7N 40.7E	KKM
Afar	9.05	Basalt	08.9N 40.4E	KKM
Afar	9.0	Trachyte	09.0N 40.3E	KKM
Cassam Gorge	9.0	Basalt	Ethiopian Rift	RGD
Cassam Gorge	8.9	Flood Basalt	Ethiopian Rift Margin	J
Cassam Gorge	8.7	Flood Basalt	Ethiopian Rift Margin	J
Unda Hemed	8.0	Basalt	11.5N 42.5E	BFSV
Ali Sabieh	7.9	Basalt	Aisha Block	CDMW
Aisha	7.7	Afar Flood Basalt	Aisha Block	BMR
Faracassa	7.7	Acidic	Ethiopian Rift	MNPP
Sakolol	7.5	Basalt	12.0N 42.5E	BFSV
Aisha	7.5	Afar Flood Basalt	Aisha Block	BMR
Mille River	7.4	Basalt	11.5N 40.5E	BFSV
Afar	7.4	Basalt	11.2N 40.2E	KKM
Ali Sabieh	7.3	Basalt	Aisha Block	CDMW
S Adda'do	7.1	Basalt	Ethiopian Rift Margin	BFSV
Danakil	7.0	Rhyolite	Danakil Block	BBKKKM
Mat Ala	6.7	Basalt	13.0N 41.0E	BBKKKM
E Mogorros	6.7	Basalt	13.0N 42.0E	BBKKKM
E Batie	6.6	Basalt	W Margin	BFSV
Afar	6.50	Trachyte	08.9N 40.3E	KKM
Hedalou	6.5	Basalt	S Gulf of Tadjoura	BFSV
Arba Dima	6.5	Acidic	Ethiopian Rift	MNPP
Aisha	6.4	Afar Flood Basalt	Aisha Block	BMR
Ali Sabieh	6.3	Basalt	Aisha BLCOK	CDMW
Aisha	6.3	Afar Flood Basalt	Aisha Block	BMR
Afar	6.1	Trachyte	09.0N 40.2E	KKM
Afar	6.1	Basalt	11.2N 40.2E	KKM
Afar	6.0	Basalt	09.2N 40.7E	KKM
Ali Sabieh	5.6	Basalt	Aisha Block	CDMW
Afar	5.50	Basalt	09.1N 40.5E	KKM
E of L. Giulietti	5.4	Basalt	14.0N 41.0E	BBKKKM
Mannhars River	5.3	Acidic	Ethiopian Rift	MNPP
Ali Sabieh	5.1	Basalt	Aisha Block	CDMW
Ali Sabieh	5.0	Basalt	Aisha Block	CDMW
Afar	5.0	Basalt	09.2N 40.6E	KKM
Afar	4.95	Basalt	09.1N 40.4E	KKM
Ali Sabieh	4.9	Basalt	Aisha Block	CDMW
Ali Sabieh	4.8	Basalt	Aisha Block	CDMW
Ali Sabieh	4.6	Trachyte	Aisha Block	CDMW
S of Arba Station	4.6	Acidic	Ethiopian Rift	MNPP
Din Din	4.4	Acidic	Ethiopian Rift	MNPP
Dulul Graben	4.3	Hawaiite	10.5N 42.0E	BFSV
S of Guna	4.3	Acidic	Ethiopian Rift	MNPP
Guna	4.1	Acidic	Ethiopian Rift	MNPP
Afar	4.0	Basalt	10.3N 40.7E	KKM
Gamari Fault	3.9	Basalt	11.5N 41.5E	BFSV
Garab	3.8	Basalt	12.0N 42.5E	BFSV
Abomsa	3.8	Acidic	Ethiopian Rift	MNPP
Dima Bridge	3.8	Acidic	Ethiopian Rift	MNPP
Sandera	3.6	Trachyte	11.5N 43.0E	BFSV
Adda'do Graben	3.6	Basalt	10.5N 41.0E	BFSV
SE of Sifa Bridge	3.6	Acidic	Ethiopian Rift	MNPP
Afar	3.50	Basalt	11.4N 40.7E	KKM

Ribta	3.5	Comendite	12.0N 43.0E	BFSV
E Magenti Ale	3.5	Basalt	11.5N 41.0E	BFSV
Afar	3.5	Basalt	07.8N 40.4E	KKM
Dire Dawa	3.4	Rhyolite	Aisha Block	BMR
Dire Dawa	3.3	Rhyolite	SE Plateau	BMR
Mt. Ayelu	3.3	Pantelleritic ignimbrite	09.7N 40.4E	S
Asal Graben	3.3	Basalt	12.0N 42.0E	BFSV
Asal Graben	3.3	Basalt	12.0N 42.0E	BFSV
Gamari Fault	3.3	Basalt	11.5N 41.5E	BFSV
Aibta	3.2	Comendite	12.0N 43.0E	BFSV
E of Batie	3.2	Basaltic Dyke	W Plateau	MNS
Askola Graben	3.2	Basalt	11.0N 41.5E	BFSV
Afar	3.11	Basalt	11.1N 40.8E	KKM
Afdera Volcano	3.1	Basalt		BFSV
S Magenti Ale	3.0	Comendite	11.0N 41.0E	BFSV
E Magenti Ale	3.0	Basalt	11.5N 41.0E	BFSV
W of Sire	3.0	Acidic	Ethiopian Rift	MNPP
Askola Graben	2.6	Basalt	11.0N 41.5E	BFSV
Afar	2.52	Basalt	07.8N 39.5E	KKM
Am'adu Graben	2.4	Basalt	11.0N 42.0E	BFSV
Engheda	2.4	Acidic	Ethiopian Rift	MNPP
N of Serdo	2.3	Hawaiite	12.0N 41.5E	BFSV
Adda'do Graben	2.3	Hawaiite	10.5N 41.0E	BFSV
Babba Alou	2.3	Comendite	11.5N 42.0E	BFSV
Afar	2.3	Basalt	11.9N 40.7E	KKM
Det Bahri	2.2	Hawaiite	11.5N 41.0E	BFSV
Babba Alou	2.2	Basalt		BBFMSTV
Dobi Graben	2.1	Basalt	12.0N 42.0E	BFSV
SW of Dagaba Plain	1.9	Basalt		BFSV
Sire	1.9	Acidic	Ethiopian Rift	MNPP
Meayle Lake	1.6	Basalt	11.5N 41.0E	BFSV
Boseti Gudda	1.6	Acidic	Ethiopian Rift	MNPP
Sifa Bridge	1.5	Acidic	Ethiopian Rift	MNPP
Dire Dawa	1.4	Flood Basalt	SE Plateau	BMR
NE Affara Dara	1.4	Basalt	13.0N 41.0E	BFSV
S of Gad'elu	1.4	Basalt	12.5N 41.0E	BFSV
Magenti Ale	1.4	Basalt	11.5N 41.0E	BFSV
Alu (Erta Ale)	1.2	Basalt	14.0N 40.5E	BBFMSTV
Babba Alou	1.2	Basalt		BBFMSTV
S of Gad'elu	1.1	Rhyolite	12.5N 41.0E	BFSV
North Ali Mela Ale	1.0	Basalt	13.0N 41.5E	BBKKKM
N of Serdo	0.62	Hawaiite	12.5N 41.5E	BFSV
Afar	0.59	Basalt	09.7N 40.6E	KKM
Gad'elu	0.56	Obsidian	12.5N 41.0E	BBFMSTV
Ma'alalta (Pruvost)	0.55	Rhyolite	13.0N 40.0E	BBFMSTV
Gad'elu	0.37	Obsidian	12.5N 41.0E	BBFMSTV
North Alu (Erta Ale)	0.35	Dark Trachyte	14.0N 40.5E	BBFMSTV
Afar	0.29	Basalt	10.1N 40.7E	KKM
South Pruvost	0.12	Obsidian		BBFMSTV
Gada Ale*	0.069	Apatite	14.0N 40.5E	BBFMSTV
Boina Centre*	0.044	Obsidian	12.5N 40.5E	BBFMSTV
Afar	0.04	Basalt	09.0N 40.3E	KKM
Boina Centre*	0.01	Obsidian	12.5N 40.5E	BBFMSTV

*Dating by fission track.

Key to Sources:

BBFMSTV	BARBERI et al (1972b)
BBKKKM	BANNERT et al (1970)
BFSV	BARBERI et al (1975a)
BMR	BLACK et al (1975)
BMRS	BLACK et al (1972)
CDGGLL	CIVETTA et al (1975)
CDMW	CHESSEX et al (1975)
GMM	GRASTY et al (1963)
F	FRAZIER (1970)
J	JONES (1976)
KKM	KUNZ et al (1975)
MMW	McDOUGALL et al (1975)
MNPP	MORBIDELLI et al (1975)
MNS	MEGRUE et al (1972)
RGD	REX et al (1971)
S	SPIES (1975)

APPENDIX 2

LISTING OF ALL EVENTS TELESEISMICALLY LOCATED WITHIN THE AREA

05°N TO 20°N, 36°E TO 48°E

(N = number of recording stations)

YEAR	MON	DAY	HR	MIN	SEC	LAT	LONG	MAG (m_b)	N	SOURCE
1906	8	25	13	47	36	09	39	6.7		GR
191[illegible]	[illegible]	27	16	22	54	17.5	39	5.7		GR
1913	3	27	03	13	00	16.5	39	5.5		GR
1913	9	16	11	56	42	06	36.5	6.2		GR
1915	9	23	08	14	48	16	39	6.7		GR
1921	8	14	13	15	28	15.5	40.5			GR
1921	9	21	11	01	31	14	39			GR
1926	10	30	01	38	10	11	44			GR
1928	10	04	18	22	58	07	38			GR
1929	1	22	14	43	05	11.5	43.5	6		GR
1929	5	18	01	02	12	11.5	41.5	6		GR
1930	10	24	10	47	21	10.5	43			GR
1930	10	25	17	41	55	11.5	44			GR
1930	10	27	23	28	41	12.5	43.5			GR
1937	11	30	12	57	46	05	36	6.2		GR
1938	5	12	21	31	35	18.5	37.5			GR
1938	9	27	02	31	49	11	41	6		GR
1938	10	20	13	14	58	10	39.5			GR
1938	10	23	02	25	14	10	39.5			GR
1941	1	11	08	31	56	17	43	6.2		GR
1941	2	04	09	17	44	16	43			GR
1941	3	19	01	31	52	12	43.5			GR
1942	11	18	12	01	20	12	40			GR
1944	9	06	13	27	55	06	38	6		GR
1945	10	28	00	17	10	11	42.5			GR
1946	9	29	20	22	10	13	48			GR
1955	1	17	15	35	13.2	12.23	46.02		5	SL
1955	2	04	05	21	00.9	05.80	36.62		13	SL
1955	3	03	00	43	44.8	16.54	41.25		4	FG
1955	10	17	20	08	53.1	17.16	43.65		12	SL
1957	3	14	00	11	38.5	14.97	40.19		13	FG
1957	4	12	15	58	47.3	11.47	43.30	5.0	12	FG
1958	1	09	07	56	27.2	17.71	40.12		7	SL
1958	2	13	10	23	36.5	14.26	41.92		20	FG
1958	5	24	22	25	32.6	12.17	43.58		9	SL
1958	5	24	23	53	42.7	12.13	43.82	5.5	44	FG
1958	5	25	02	53	53.1	12.16	43.88	5.0	37	FG
1958	6	28	17	05	24.5	12.26	45.13		9	FG
1959	8	16	13	31	15.1	14.52	43.21		9	FG
1960	1	04	06	08	00.7	11.83	42.84		8	FG
1960	1	04	06	16	35.3	11.51	42.84		22	FG
1960	3	25	09	45	46.0	12.26	46.61		21	FG
1960	7	14	18	39	49.1	07.18	38.82	6.3	38	FG
1960	8	08	12	28	12.4	12.06	44.49		41	FG
1960	8	13	22	28	13.6	14.70	40.16		5	SL
1960	8	13	22	28	19.4	15.11	40.15		5	FG
1960	9	12	03	13	48.0	11.80	46.72		6	FG
1960	10	23	19	21	07.7	17.50	40.07		8	SL
1960	12	16	16	49	20.5	14.81	42.48		28	FG
1961	3	11	08	41	07.9	11.71	43.25	5.9	85	FG
1961	5	29	04	59	42.1	10.43	40.03	5.0	21	FG
1961	5	29	10	51	49.4	10.43	40.16	5.5	55	FG
1961	5	29	11	39	56.2	10.62	40.03		11	FG
1961	5	29	19	23	53.9	10.46	40.18	5.0	46	FG
1961	5	29	19	40	29.0	10.46	40.16		22	FG
1961	5	30	13	11	19.4	10.58	40.12		16	FG
1961	6	01	21	07	21.7	10.75	39.94		11	FG
1961	6	01	23	29	21.7	10.53	40.17	6.4	147	FG
1961	6	01	23	56	52.0	10.65	39.89		10	FG
1961	6	02	00	01	47.3	10.49	39.96		32	FG
1961	6	02	00	08	57.6	10.42	40.26		46	FG

1961	6	02	00	21	19.4	09.84	40.01		13	FG
1961	6	02	00	57	55.3	09.89	40.19		16	FG
1961	6	02	02	35	41.6	11.27	40.54		17	FG
1961	6	02	03	19	39.5	09.94	39.95		9	FG
1961	6	02	03	49	11.1	10.06	40.84		11	FG
1961	6	02	04	51	04.8	10.31	40.13	6.2	142	FG
1961	6	02	05	22	19.1	10.20	40.08		72	FG
1961	6	02	05	44	36.9	10.27	40.22	5.8	82	FG
1961	6	02	06	17	15.8	10.67	40.07		26	FG
1961	6	02	07	02	47.1	10.20	40.19	5.5	62	FG
1961	6	02	07	21	49.8	10.73	40.04		26	FG
1961	6	02	22	19	34.5	10.43	40.28		9	FG
1961	6	02	23	32	39.7	10.52	40.15		34	FG
1961	6	03	02	05	36.1	10.29	40.11		11	FG
1961	6	03	15	20	28.7	10.43	40.16		33	FG
1961	6	03	15	23	03.6	10.62	40.23	5.8	68	FG
1961	6	03	16	25	56.0	10.59	40.13		15	FG
1961	6	04	00	41	43.1	10.34	40.02		9	FG
1961	6	06	17	46	43.4	10.88	39.86		8	FG
1961	6	07	15	01	16.5	10.54	40.17		11	FG
1961	6	14	20	32	10.1	10.55	40.05	5.7	89	FG
1961	6	19	04	34	14.3	10.44	40.21		8	FG
1961	6	20	03	21	28.8	12.17	44.37	6.1	77	FG
1961	6	24	15	04	34.2	10.65	40.14		5	FG
1962	8	25	00	54	17.5	17.12	40.14	4.8	11	FG
1962	11	11	15	15	33.9	17.22	40.58	5.6	95	FG
1963	10	05	14	57	47.8	11.60	42.85	5.3	21	FG
1963	10	05	17	18	25.6	11.70	42.71		7	FG
1964	7	13	19	18	33.0	11.32	39.57	5.0	9	FG
1964	8	03	10	45	14	15.2	39.0		4	I
1965	3	07	07	39	39.4	12.19	46.34	4.9	19	FG
1965	3	07	07	42	32.2	12.17	46.38	5.3	26	FG
1965	5	16	00	45	58.0	11.07	45.61		7	FG
1965	6	07	13	43	59.0	11.63	41.38		8	FG
1965	7	19	15	49	37.0	12.22	42.56		5	FG
1965	12	30	08	54	14	18.7	39.3	4.1	10	I
1965	12	30	08	54	14.5	18.87	39.71	4.1	5	FG
1966	1	21	12	39	44.9	12.11	43.64	4.7	6	FG
1966	4	09	19	11	12.0	14.46	40.74	4.7	6	FG
1967	3	10	13	41	06	19.9	38.9		11	I
1967	3	10	19	46	55	19.78	38.5		9	I
1967	3	11	19	33	49.6	19.65	38.92	4.9	6	FG
1967	3	11	19	38	22.3	19.73	38.80	5.2	12	FG
1967	3	12	10	01	50.7	19.90	38.88		6	FG
1967	3	12	21	44	34.2	19.82	38.86		11	FG
1967	3	12	22	39	09	19.48	39.07		7	I
1967	3	13	07	28	06.3	19.74	38.82	5.3	14	FG
1967	3	13	08	10	57.4	19.70	38.81	5.0	13	FG
1967	3	13	11	46	29.9	19.77	38.98	5.0	11	FG
1967	3	13	19	22	16.3	19.79	38.82	5.8	60	FG
1967	3	14	21	52	06.6	19.49	38.76	4.6	11	FG
1967	3	16	02	41	42	19.55	38.96	5.5	16	I
1967	3	16	03	12	00.3	19.61	38.87	5.4	12	FG
1967	3	16	11	41	29.8	19.80	38.91		6	FG
1967	3	16	14	45	13.6	19.63	38.87	5.1	12	FG
1967	3	16	16	00	17.9	19.96	38.85	5.0	11	FG
1967	3	21	23	39	24.2	19.7	38.9		7	I
1967	3	22	22	59	51.7	19.77	38.74		7	EG
1967	5	17	17	50	39.6	19.78	38.84	5.3	28	FG
1967	5	19	15	52	40.5	14.87	40.14	5.1	26	FG
1967	7	14	03	11	28.3	19.80	38.91	4.7	18	FG
1967	9	18	02	03	01.8	15.80	38.93	4.8	14	FG
1967	9	21	18	36	27.0	18.05	40.13	4.4	7	FG
1967	11	16	02	22	06.2	15.17	39.53	5.1	7	FG
1967	12	17	18	03	43	05.8	37.1	4.9	12	I
1968	1	23	19	18	14.7	08.74	37.56	5.1	20	FG
1968	3	14	09	57	05	17.1	42.0		4	I
1968	5	23	23	36	06.4	14.75	40.22	4.8	13	?I
1968	12	12	17	30	30	12.11	46.05	4.5	53	I
1968	12	12	17	30	30.2	12.09	45.87	4.6	15	FG
1969	3	29	09	15	54	11.91	41.21	5.9	204	I
1969	3	29	11	04	52	11.92	41.36	5.5	166	I
1969	3	29	11	07	45	12.01	41.1	4.9	55	I
1969	3	29	13	08	17	11.94	41.31	5.1	88	I

1969	3	29	18	30	49	11.87	41.4		19	I
1969	4	05	02	18	30	12.00	41.35	5.8	175	I
1969	4	05	20	06	24	12.0	41.2		13	I
1969	4	05	20	14	41	12.02	41.28	4.8	35	I
1969	4	06	16	51	47	11.99	41.40	5.1	104	I
1969	4	07	06	23	55	11.92	41.40		24	I
1969	4	08	02	14	01	11.88	41.42	4.8	52	I
1969	5	05	02	45	40	12.07	41.34	4.9	83	I
1969	9	26	04	54	38	16.41	41.02	5.0	94	I
1969	10	24	10	12	42.3	11.85	44.96	4.6	25	I
1969	12	20	07	51	33	10.8	37.6		1	I
1970	5	14	18	45	39	13.0	39.8		7	I
1970	7	16	07	13	47	8.8	39.5		5	I
1971	4	25	17	42	15	11.82	43.85	4.3	35	I
1971	11	13	15	47	44	11.03	39.71	5.1	124	I
1972	3	03	07	30	53	11.7	45.7		17	I
1973	1	07	12	17	12	05.14	36.78	4.8	107	I
1973	3	28	10	45	29.3	11.47	42.85	4.6	46	I
1973	3	28	13	35	05	11.53	43.07	4.9	72	I
1973	3	28	13	42	11	11.77	42.89	5.0	164	I
1973	3	28	14	00	32	11.5	42.64	4.0	17	I
1973	3	28	14	18	55	11.69	42.93	5.2	151	I
1973	3	28	14	59	07	11.76	42.78	5.1	126	I
1973	4	01	06	29	31	11.42	43.01	4.5	56	I
1973	4	01	07	12	41	11.63	43.00	5.0	199	I
1973	4	01	07	38	41.2	11.76	43.03	4.9	52	I
1973	4	01	07	41	22	11.9	43.3	4.5	12	I
1973	4	04	21	52	00	12.10	46.16		39	I
1973	4	05	01	59	08	12.09	46.41	4.9	77	I
1973	4	07	17	36	43.3	11.64	42.95	4.7	83	I
1973	4	07	19	17	38.3	11.78	42.84		7	I
1973	4	11	02	09	33.3	11.68	43.0		16	I
1973	4	13	14	13	57.0	11.93	43.83	4.8	75	I
1974	2	25	16	05	18	10.2	39.8	4.6	9	I
1974	4	17	18	27	34	17.30	40.30	5.1	179	I
1974	4	26	18	08	18	17.10	40.44	4.4	37	I
1974	6	21	16	03	56	12.63	46.96	4.4	48	I
1974	6	30	13	26	25.7	15.97	39.61	4.5	20	I
1975	4	16	02	55	09.2	14.59	40.73	4.3	25	I
1975	6	04	16	37	28.0	11.9	43.8	4.8	16	I
1975	6	28	18	12	18	17.2	39.8		9	I
1975	6	29	13	16	57	18.7	40.5		7	I
1975	6	29	15	01	15	18.8	39.5	4.8	19	I
1975	6	29	21	45	58.9	18.57	39.78	4.8	43	I
1975	6	30	04	20	52	18.0	40.2	4.6	21	I
1975	8	07	22	43	13.7	15.36	40.44	4.7	48	I
1975	8	23	21	35	21.2	10.52	39.75	4.9	75	I
1975	12	14	23	16	49	14.60	42.29	5.3	131	I
1975	12	14	23	27	27.2	14.69	42.26	5.2	144	I
1976	1	31	02	36	10.2	18.97	39.23	4.3	15	I
1976	3	18	17	39	44	19.7	39.0	4.4	11	I
1976	3	19	00	50	02.5	19.77	38.98	4.3	11	I
1976	4	22	16	29	25	19.80	38.66	4.0	21	I
1976	8	06	20	32	26.3	13.14	39.71	4.7	31	I
1976	11	07	05	53	07	15.86	41.36	4.8	23	I
1976	11	07	20	21	47.4	15.99	41.43	4.7	15	I
1976	11	16	12	53	34.2	15.86	41.8	4.6	31	I
1976	12	01	05	03	41	15.77	41.9	4.8	32	I
1977	7	08	06	23	03.1	11.08	39.62	5.0	144	I
1977	10	17	21	46	44.0	11.80	42.94	5.0	5	I
1977	12	05	10	02	59	12.7	40.8	4.5	11	I
1977	12	05	10	06	09	11.4	42.1	4.9	14	I
1977	12	28	02	45	33.1	16.54	40.32	5.9	339	I
1978	1	04	05	04	43.0	16.6	40.9	4.4	28	I
1978	1	17	15	00	31	16.52	40.28	5.1	169	I
1978	2	09	05	00	43.4	11.63	42.46		8	I
1978	2	17	12	52	06.1	12.7	40.4	4.4	9	I
1978	2	21	22	04	42.2	16.32	40.45	4.7	42	I
1978	3	12	23	29	15	13.2	41.4		7	I
1978	3	25	02	55	04.2	16.51	40.19	4.9	113	I
1978	5	12	06	20	10	12.7	40.31	4.6	35	I
1978	6	10	19	07	41.3	12.05	46.51	4.6	6	I
1978	10	16	20	34	57	11.9	43.6		5	I
1978	11	07	00	23	27	10.3	42.8	4.2	10	I

1978	11	07	06	44	18.5	11.64	42.58	4.5	18	I
1978	11	07	12	05	52.7	11.53	42.6	5.3	235	I
1978	11	07	17	05	52.7	11.5	42.7	4.2	8	I
1978	11	07	19	54	03	11.5	42.8	4.2	11	I
1978	11	08	05	08	01.7	11.48	42.54	4.9	160	I
1978	11	08	07	42	21.4	11.67	42.5	4.7	25	I
1978	11	08	08	44	45	11.5	42.7	4.2	7	I
1978	12	21	04	03	54.0	11.54	42.96	5.1	145	I
1979	5	13	20	48	00.3	18.759	39.295	4.8	53	PDE
1979	5	13	20	55	40.3	18.864	39.190	4.5	25	PDE
1979	9	09	16	47	23.3	12.059	46.120	4.6	9	PDE
1979	9	10	20	57	25.0	12.022	46.032	4.9	18	PDE
1979	9	19	18	48	12.8	12.239	40.359	5.0	59	PDE
1979	10	16	13	18	50.5	11.843	43.613	5.1	20	PDE
1979	10	16	15	57	50.8	11.825	43.578	5.1	92	PDE
1979	10	16	18	11	32.1	11.818	43.692	5.1	35	PDE
1979	10	16	20	34	59.0	11.799	43.474	5.2	24	PDE
1979	10	16	20	45	54.4	11.610	43.858	5.3	32	PDE
1979	10	16	20	54	46.1	11.659	43.786	5.5	85	PDE
1979	10	16	21	14	49.7	11.730	43.693	5.1	29	PDE
1979	10	16	22	14	07.9	10.817	42.888	5.1	13	PDE
1979	10	16	23	41	38.7	11.782	43.465	5.2	38	PDE
1979	11	10	17	42	44.8	14.880	39.640	4.3	5	PDE
1979	11	13	17	01	36.7	13.221	40.046	4.2	5	PDE
1980	1	14	04	10	54.0	16.518	40.268	5.3	159	PDE
1980	1	14	04	21	49.2	16.551	40.083	4.5	35	PDE
1980	1	14	12	28	22.6	16.453	40.232	5.3	126	PDE
1980	1	14	12	57	15.4	16.323	40.173	4.7	28	PDE
1980	1	26	06	15	30.4	16.372	40.137	4.6	22	PDE
1980	3	05	03	12	05.2	16.610	40.239	4.9	88	PDE
1980	4	29	18	54	25.2	10.081	43.148	4.6	11	PDE
1980	4	29	21	05	22.7	10.162	43.012	4.4	13	PDE
1980	4	30	03	44	45.8	9.975	43.249		10	PDE
1980	5	03	03	30	55.6	10.013	43.125	5.3	128	PDE
1980	5	03	07	46	30.1	9.941	43.296	4.5	12	PDE
1980	5	03	09	25	20.3	10.135	43.131	4.1	15	PDE
1980	5	03	18	37	01.0	10.425	43.163		9	PDE
1980	5	07	11	17	33.3	10.459	43.111		9	PDE
1980	5	13	05	35	30.6	10.165	43.078	4.6	9	PDE
1980	5	16	17	40	42.3	9.980	43.035	4.9	37	PDE
1980	5	30	08	02	50.4	10.000	43.102	5.2	64	PDE
1980	5	30	11	03	22.8	9.821	43.294		7	PDE
1980	5	30	11	43	14.0	10.007	43.226	4.3	9	PDE
1980	6	23	18	03	16.0	10.609	43.003	4.4	12	PDE
1980	7	11	23	31	45.9	9.980	43.133	4.5	18	PDE
1980	7	12	12	59	04.5	17.193	40.266	4.3	18	PDE
1980	7	16	23	14	56.7	17.245	40.435	4.8	43	PDE
1980	7	17	00	08	19.1	16.633	40.465	4.6	18	PDE
1980	7	17	00	12	50.9	17.411	39.965	4.3	10	PDE
1980	8	15	02	41	53.0	10.066	43.118	4.4	11	PDE
1980	8	15	02	44	48.9	10.216	43.076		9	PDE
1980	8	31	22	05	33.3	12.128	46.006	4.7	35	PDE
1980	11	28	02	11	31.3	12.562	43.039		7	PDE

KEY TO SOURCES:
- GR GUTENBERG and RICHTER (1954)
- SL SYKES and LANDISMAN (1964)
- FG FAIRHEAD and GIRDLER (1970)
- I ISC Biannual Regional Catalogues of Earthquakes, and Monthly Bulletins
- PDE USGS Preliminary Determination of Epicentres

APPENDIX 3

A NOTE ON THE DURHAM UNIVERSITY SEISMIC RECORDING AND PLAYBACK EQUIPMENT

This note describes the results of standard tests to determine the frequency response and dynamic range of the Durham three channel portable seismic recording equipment and associated playback electronics. The set tested has been used in the field in Iceland, Ethiopia and elsewhere, and is still in use.

A theoretical explanation is given for the observed poor flutter compensation of large amplitude signals played back at Durham.

Recording

Tests were carried out on a seismic recording set chosen at random after reconditioning by Departmental technical staff. The tape recorder was operated at Ø.1 in sec-1, the faster of its two design speeds. Correct operation of the set was verified by monitoring of its own comprehensive built-in checking facilities.

A sinusoidal voltage from an ADVANCE VLF function generator, type SG88, was input via an attenuator to the central seismic channel of the recorder. The amplified and frequency modulated signal was recorded on to the same quarter inch Agfa triple-play tape as is used in the field. Also recorded was encoded time from the internal clock; and a standard, 1ØØ Hz, clock-derived reference frequency. The

latter is used to control tape speed on playback, and for flutter compensation. To test the frequency response an input voltage was selected to give approximately 75% at 1 Hz of the maximum signal obtainable without saturation. A one minute length of tape was recorded at each of a range of input frequencies varied between 0.01 Hz and 40 Hz. The dynamic range of the equipment was tested by recording a 1 Hz input over a range of voltage amplitudes. Both procedures were carried out at five different gain settings of the recorder's amplifier. Additionally, an input voltage was recorded to test the dynamic range at 8 Hz and a gain of 12,800 (gain setting, n=7). This was the gain used in Ethiopia, and the frequency was selected to represent the P phases of recorded Ethiopian local earthquakes.

Playback

The test tape was played back in the Durham seismic processing laboratory. Here the tape transport unit is the shell of a commercial NAGRA IV deck, modified to run at ten times the recording speed (i.e. 1 in sec^{-1} in this case). This speed is obtained directly from the standard reference frequency recorded on the tape, the deck motor being incorporated in a feedback loop to allow automatic compensation on playback for fluctuations of recording speed in the field. Demodulation is carried out by electronics designed and built within the Department.

The playback system was set up for optimum flutter compensation by adjusting the tape head of the NAGRA deck

and the gain of the seismic signal demodulator. These adjustments must be made whenever a tape is to be processed. In this case they were facilitated by using a section of the test tape specifically recorded with no input to the seismic channel under test. The demodulated output was displayed on paper by means of a jet pen recorder. Paper records were made of the output signal both unfiltered and after various degrees of band-pass filtering accomplished by KEMO dual variable filters type VBF/8K.

Performance

To determine the frequency response the jet pen trace amplitude, A_f, was measured at each recorded frequency. The response in decibels, D_f, relative to the response at 1 Hz (trace amplitude A_1), was then calculated from the relation

$$D_f = 20 \log_{10}(A_f/A_1)$$

The resultant curves are shown in Figures A3.1a, A3.1b, and bandwidths in Table A3.1. Attenuation rates at low and high frequencies are approximately 13 dB/Oct and 27 dB/Oct respectively. In the field the recording equipment is normally operated at a gain of 1280Ø or 2560Ø (n=7 or 8). At quiet sites gain 5120Ø (n=9) has been used. At high gains in particular the results shown here fall short of the published amplifier frequency response for the portable seismic recorder (LONG, 1974, p.94 and fig.2a).

The dynamic range was found by measuring the lowest voltage 1 Hz input (V_L) for which the output signal was visible above system noise on playback; and the voltage

FIGURE A3.1a

LOW FREQUENCY RESPONSE OF THE SEISMIC PROCESSING EQUIPMENT

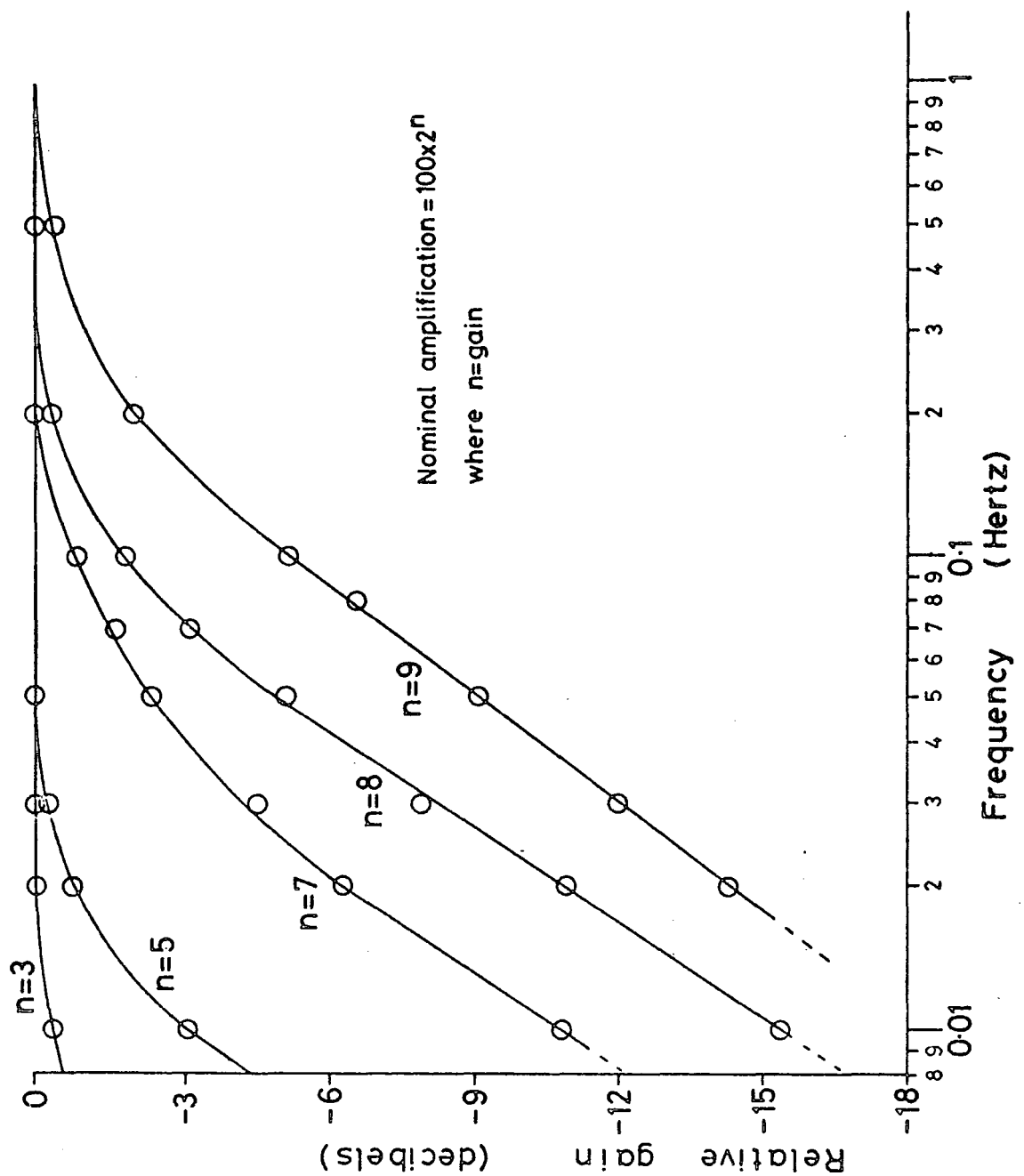

FIGURE A3.1b

HIGH FREQUENCY RESPONSE OF THE SEISMIC PROCESSING EQUIPMENT

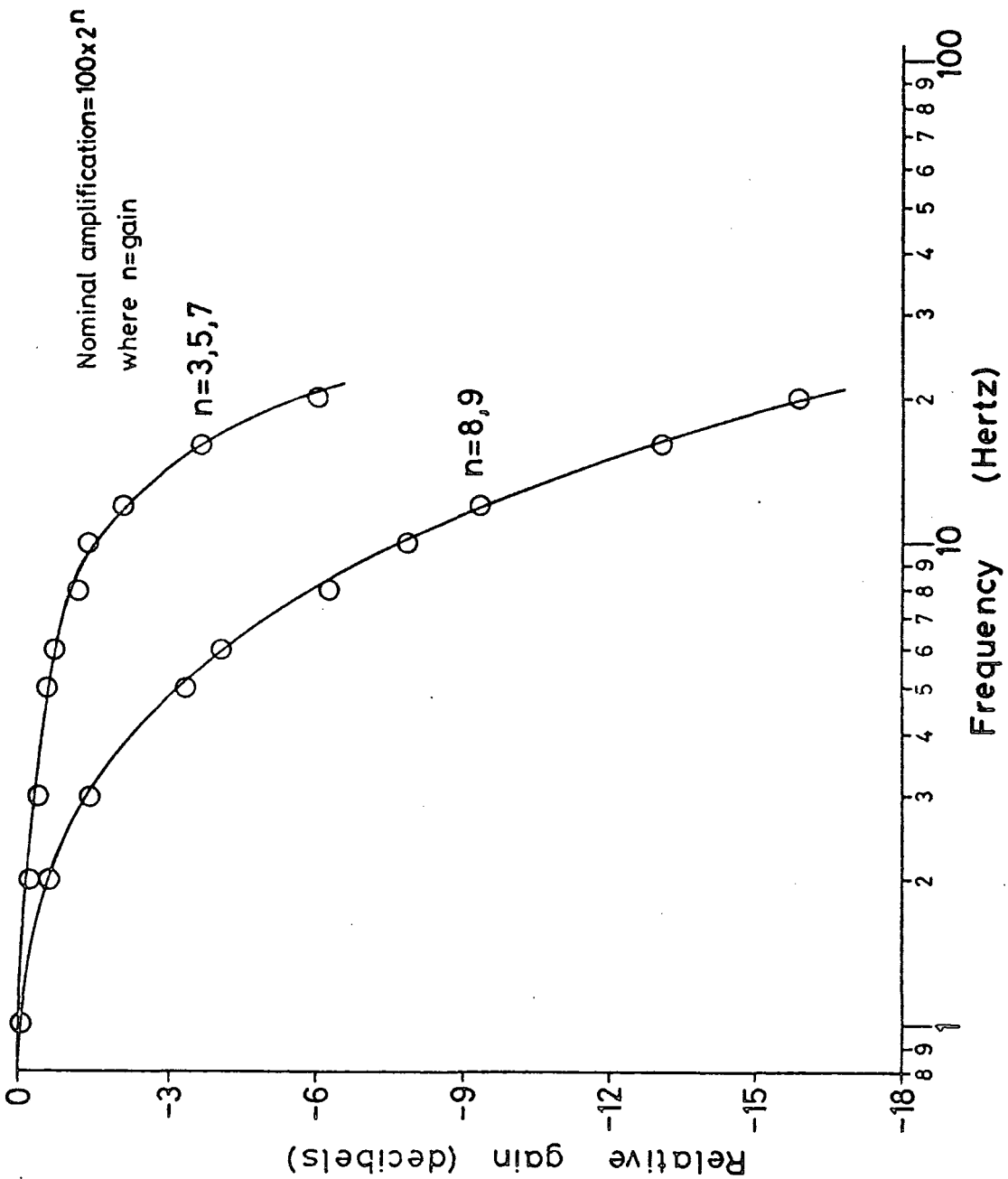

TABLE A3.1

BANDWIDTH

This table gives half-power (-3db) frequency points at various gains

Gain Setting	Nominal Gain	Low Frequency (Hz)	High Frequency (Hz)
9	51200	0.15	5
8	25600	0.07	5
7	12800	0.04	15
5	3200	0.01	15
3	800	<0.01	15

TABLE A3.2

DYNAMIC RANGE AT 1 Hz

Accuracy ± 3 dB

Gain Setting	9	8	7	5	3
Nominal Gain	51200	25600	12800	3200	800
Dynamic Range	32	36	36	37	37

input (V_U) at which the output waveform began to saturate. The dynamic range is then expressed in decibels as $20 \log_{10} (V_U/V_L)$. The results are given in Table A3.2. They were not significantly improved by narrow-band (0.5-2Hz) filtering. At 8 Hz and a gain of 12800 the dynamic range did not exceed 30 dB.

It should be noted that the dynamic range figures "in excess of 50 dB" reported by Long were achieved using a standard set of E.M.I. frequency demodulation electronics that has now been superceded by the equipment described above. Accepting Long's specification for the portable seismic recorder, it must be concluded that this demodulation equipment is much inferior to commercially available systems.

Flutter Compensation

During play-out of low frequency sinusoids to assess the frequency response, incomplete flutter compensation of large amplitude signals was unusually evident (Figure A3.2). For simplicity, the following explanation of this observation omits consideration of other types of noise generated during the modulation/demodulation process.

Consider the effect on a seismic signal, S, of the successive operations of frequency modulation, speed compensation by the tape transport unit, frequency demodulation and flutter compensation (Figure A3.3a).

After modulation, the seismic signal is represented by the frequency ($f_S + kS$), where f_S is the carrier centre

FIGURE A3.2

INCOMPLETE FLUTTER COMPENSATION OBSERVED ON THE JET PEN RECORDER

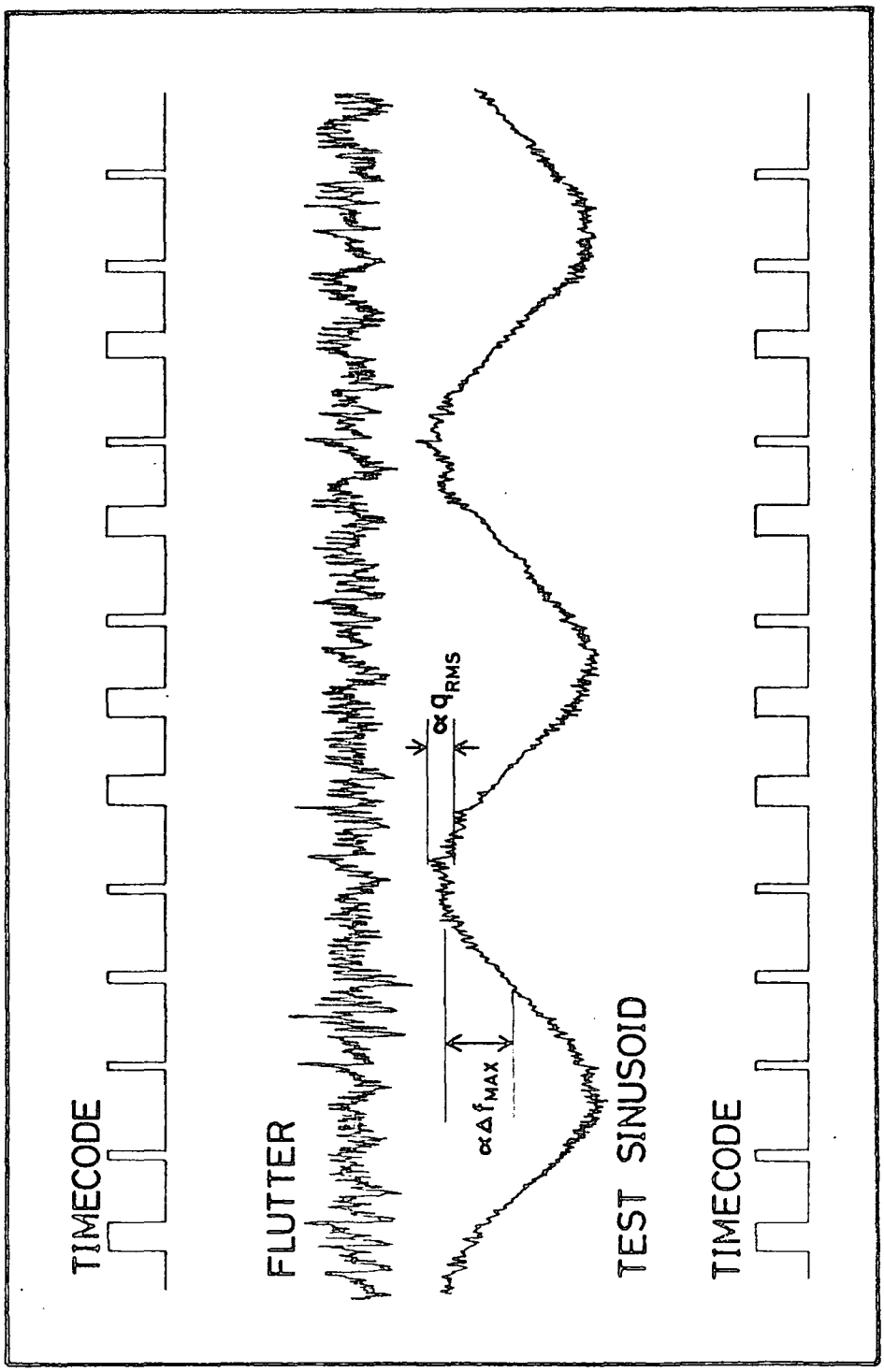

FIGURE A3.3

BLOCK DIAGRAMS OF THE PROCESSING EQUIPMENT

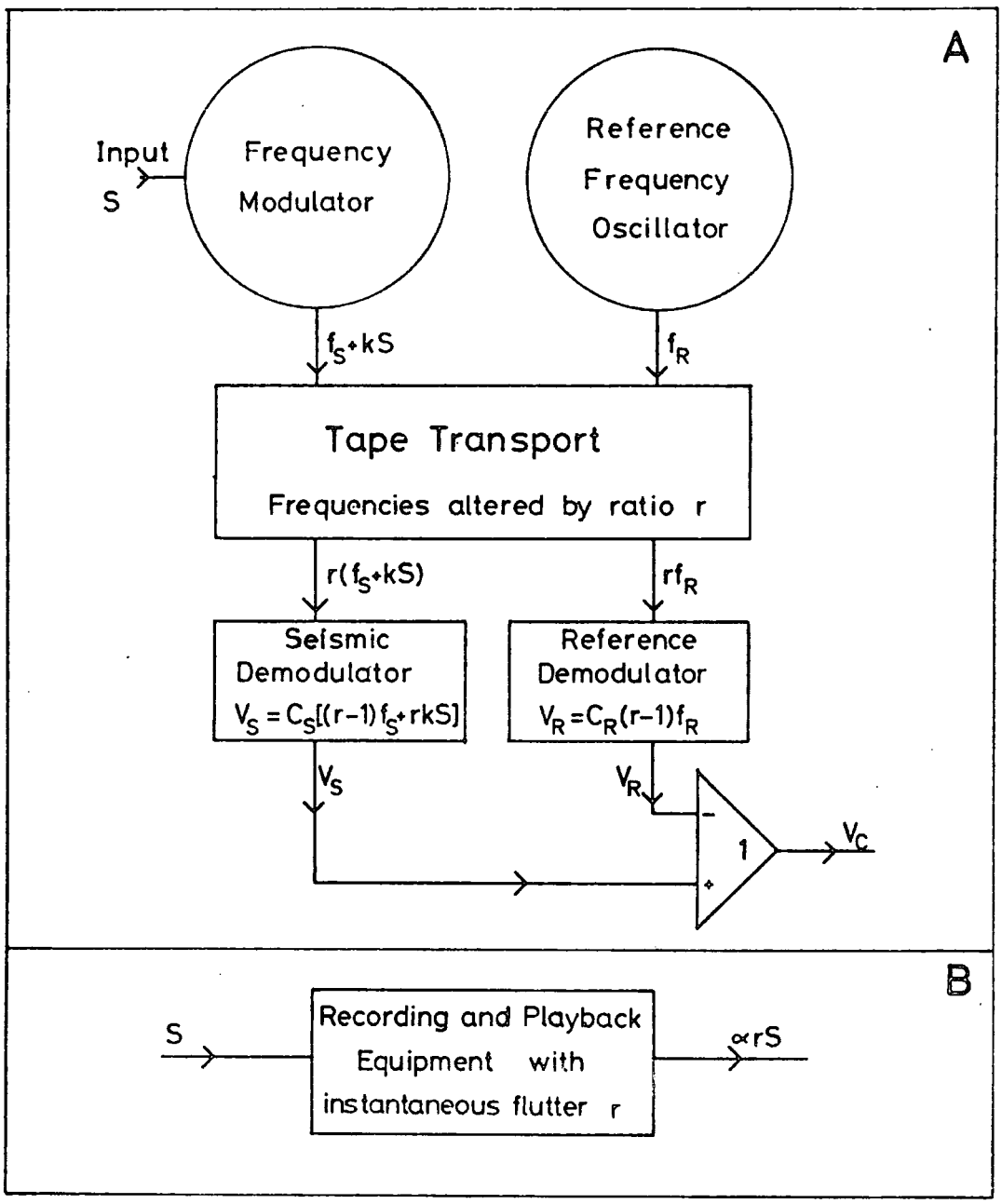

frequency and k is a constant.

At any instant, let r be the ratio of the tape playback speed to the expected value of ten times the recording speed. r will vary from unity because of the effect of flutter on the speed of the deck. The effect of the tape transport unit is to impose a multiplication by r on both the modulated seismic signal and the frequency, f_R, recorded on the reference channel. These become, respectively, $r(f_S + kS)$ and rf_R.

After demodulation, the carrier frequency has been subtracted and the voltage, V_S, on the seismic channel is given by

$$V_S \propto r(f_S + kS) - f_S$$

$$\therefore V_S = C_S((r - 1)f_S + rkS)$$

Similarly, the voltage, V_R, on the reference channel is

$$V_R \propto rf_R - r$$

$$\therefore V_R = C_R(r - 1)f_R,$$

where C_S, C_R are demodulator gain constants.

The seismic channel output voltage is then flutter compensated by subtracting from it the reference channel output voltage. The resultant seismic voltage is

$$V_C = V_S - V_R$$

$$= C_S((r - 1)f_S + rkS) - C_R(r - 1)f_R \qquad \text{(A3.1)}$$

To achieve full flutter compensation the constants C_S and/or C_R are so adjusted as to give zero output voltage on the seismic channel in the absence of a seismic signal, whatever the value of r. Writing $V_C = 0$ when $S = 0$ in

Equation 1 yields the condition $C_{Sf_S} = C_{Rf_R}$, whence Equation 1 may be rewritten

$$V_C = C_S r k_S$$

Thus the modulation/demodulation process has the effect of multiplying the original seismic signal by the ratio r. This is represented schematically in Figure A3.3b. The result is a noise voltage, V_N, due to uncompensated flutter,

$$V_N = C_S r k_S - C_S k_S$$

Writing $k_S = \Delta f$, where Δf is the change in the carrier frequency, f_S, due to the seismic signal, S, and setting $q = r - 1$, the r.m.s. noise due to flutter is

$$V_N = C_S q_{RMS} \Delta f$$

This reaches a maximum value of $C_S q_{RMS} f_{MAX}$, where Δf_{MAX} represents the frequency deviation caused by a seismic signal on the point of saturation. The dynamic range is consequently reduced to

$$-20 \log_{10} \left(\frac{q_{RMS} \Delta f_{MAX}}{2 \Delta f_{MAX}} \right) = -20 \log_{10} \left(\frac{q_{RMS}}{2} \right) \text{ (Figure A3.2)}$$

Measurements on the low frequency sinusoidal output indicate not less than 15% flutter at maximum signal amplitude. The dynamic range at maximum amplitude is therefore only $-20 \log_{10} (0.15/2) = 22.5$ dB.

This compensation problem has become apparent only because of the very high level of flutter generated by the current electronics. The wow and flutter characteristic of the commercial NAGRA IV deck, running at its lowest design speed of 3.75 in sec^{-1}, is about 0.11%. The recommended solution is to remodify the electronics that allow the NAGRA

deck to run so slowly, in such a way as drastically to reduce the flutter level. Should this not prove feasible a different deck must be used.

W.G. Rigden &
J.E.G. Savage
25 April 1977

APPENDIX 4

PROGRAMME TIMFIT

This programme fits polynomials to station clock errors measured relative to G.M.T. pips. The programme is fully explained by comment cards within the listing. An option exists to read, correct for clock errors and print out the arrival times of earthquake phases.

Programme TIMFIT uses the NAG Mk IV library subroutine E02ABF for polynomial curve fitting, and the NUMAC plotting library *PLOTSYS if plotted output is requested. *PLOTSYS routines are called from SUBROUTINE PLTIME. An example of plotted output is reproduced at a modified scale as Figure A4.1.

INPUT

Unit 4. Earthquake arrival data, one card for each arrival. Input is terminated by a card having LEVENT = 999.

```
LEVENT,LLINE,PHASE,LM,LD,LH,LMI,LS
                          2X,I3,1X,I4,1X,A4,4(3X,I2),F10.2
```

LLEVENT Event number.

LLINE Station/line coding. This is a 4-digit number. The most significant digit identifies the station, as described in lines 20 to 23 of the programme listing. The remaining digits identify the polynomial to be used in making the time correction.

PHASE Used to describe phase of arrival.

LM,LD,LH,LMI,S Phase arrival time in months, days, hours, minutes and seconds.

FIGURE A4.1

SAMPLE OUTPUT, PROGRAMME TIMFIT, SERDO STATION

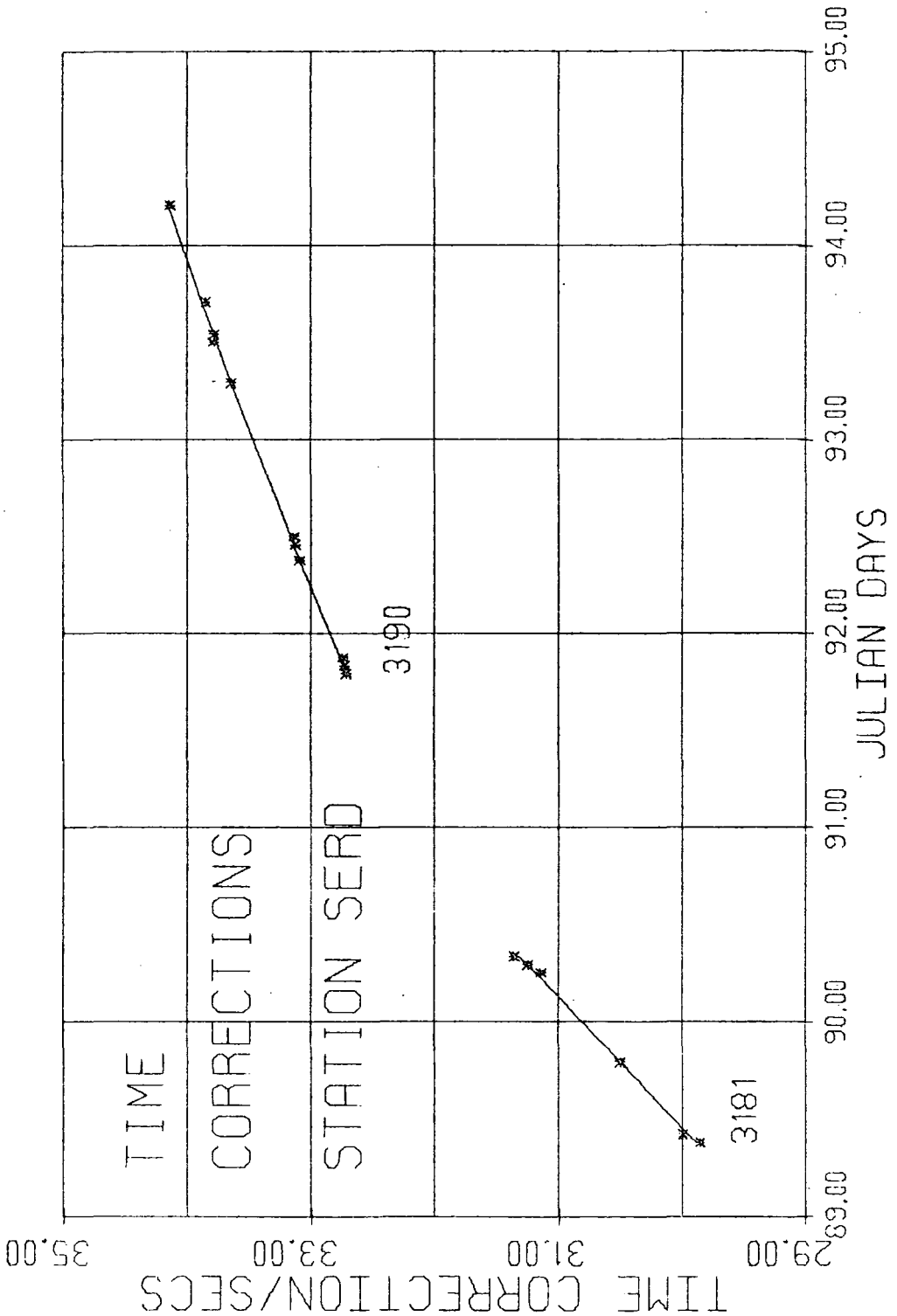

Unit 5. All other input, including times of G.M.T. pips and the corresponding clock errors. One card, programme option controls

M(I),ID(I),IH(I),Y(I),LINE(I)		3(3X,I2),F9.2,2X,I4
M(I),ID(I),IH(I)	Time of G.M.T. pips in months, days and hours.	
Y(I)	Corresponding measured clock error.	
LINE(I)	Station/line coding.	

OUTPUT

Unit 6. All printed output appears here, and is fully explained in the programme listing.

Unit 9. Outputs a standard plotfile for *PLOTSYS.

```
>                          PROGRAMME TIMFIT
>
>
>C      PROGRAMME TIMFIT          W.G.RIGDEN        JULY 1977
>C        **********
>C      PROGRAMME FITS A POLYNOMIAL TO STATION CLOCK ERRORS OBTAINED FROM
>C      MEASUREMENTS OF G.M.T. PIPS.  TIME ERROR DATA ARE PRINTED ON
>C      TELETYPE AND/OR PLOTTED ON I.B.M. 11-INCH PLOTTER.  APPROPRIATE
>C      TIME CORRECTIONS ARE APPLIED TO EARTHQUAKE ARRIVAL DATA.
>C        **********
>C      THE COMPILED PROGRAMME MUST BE RUN WITH THE NUMAC PACKAGES '*NAG'
>C      (FOR THE POLYNOMIAL FITTING SUBROUTINE) AND '*PLOTSYS' (FOR THE
>C      GRAPHICS).
>C      TIME DATA IS INPUT FROM I/O DEVICE 5.  THE FIRST CARD CONTAINS
>C      THE VALUES OF THE PROGRAMME OPTION SWITCHES (SEE LINE 38 AND
>C      FORMAT STATEMENT LABEL 500).  THE REMAINING CARDS CONTAIN THE TIME
>C      CORRECTION DATA, AND MAY BE READ IN ANY ORDER OF TIME AND STATION
>C      (SEE LINE 66 AND FORMAT LABEL 501).  REMEMBER TO TERMINATE WITH
>C      THE FLAG.
>C      EVENT DATA IS INPUT FROM I/O DEVICE 4.  (SEE LINE 233 AND FORMAT
>C      LABEL 400).
>C
>C      N.B. THE MOST SIGNIFICANT DIGIT OF THE STATION/LINE CODING
>C      IDENTIFIES THE STATION:-
>C         1 = MILLE            2 = TENDAHO
>C         3 = SERDO            4 = DET BHARI
>C
>C        **********
>C
>       IMPLICIT REAL*8(A-H,O-Z)
>       DIMENSION M(3000),ID(3000),IH(3000),LINE(3000),KD(3000),ISTATN(4)
>       DIMENSION IS2(300),IS3(300),IS4(300),LIT(100),III(100),MONTH(10)
>       REAL*8 A(10,100),Y(3000),XD(3000),ALINE(3000),S1(300),S5(300)
>       REAL*8 W(300),RERR(100),SI(10),P(10),KALC(3000)
>       REAL*4 STA,PHASE
>       LOGICAL L
>       L=.TRUE.
>       DATA MONTH/'JAN ','FEB ','MAR ','APR ','MAY ','JUN ','JUL ','AUG '
>      %,'SEP ','OCT '/,ISTATN/'MILL','TEND','SERD','DETB'/
>C
>C      READ I-VALUES.  THESE CONTROL PROGRAMME OPTIONS.  EXCEPT FOR I1,
>C      THEY SHOULD BE SET TO 1 IF CORRESPONDING ROUTINE IS REQUIRED,
>C      OTHERWISE LEFT BLANK
>C        I1   ORDER OF POLYNOMIAL TO BE USED FOR CURVE FITTING
>C        I2   WRITE OUT DETAILS OF TIME ERROR DATA AND BESTFIT POLYNOMIAL
>C        I3   APPLY TIME CORRECTIONS TO EARTHQUAKE ARRIVAL DATA
>C        I4   PLOT TIME DATA FOR MILLE       )
>C        I5   PLOT TIME DATA FOR TENDAHO     )  OUTPUT TO
>C        I6   PLOT TIME DATA FOR SERDO       )  11-INCH PLOTTER
>C        I7   PLOT TIME DATA FOR DET BHARI   )
>C        I8   PRINT WARNING IF OBSERVED AND CALCULATED CLOCK ERRORS
>C           DIFFER BY MORE THAN 0.04 SECS.
>C
>C      N.B. BECAUSE OF PRESENT LIMITS ON PLOTTER X-AXIS LENGTH, THE
>C      PLOTTING SUBROUTINE IS SO WRITTEN THAT IT CAN BE CALLED ONLY
>C      ONCE PER PROGRAMME RUN.
>C
>C      WRITE PROGRAMME HEADING
>C        **********
>C
>       READ (5,500) I1,I2,I3,I4,I5,I6,I7,I8
> 500 FORMAT (2X,I2,1X,7I1)
>       WRITE (6,600)
> 600 FORMAT (1H1,1X,'PRINT-OUT OF PROGRAMME TIMFIT, TO FIT BEST CURVE T
>      %O STATION CLOCK ERROR DATA'/2X,'AND COMPUTE CORRECTED EARTHQUAKE A
>      %RRIVAL TIMES')
>C
>C        **********
>C      READ TIME DATA
>C        M,ID,IH   TIMES OF RECORDED G.M.T. PIPS (MONTH,DAY,HOUR)
>C              Y   STATION CLOCK ERRORS
>C           LINE   STATION/LINE CODING
#
```

```
>C      TERMINATE DATA WITH CARD HAVING LINE = 9999
>C        **********
>C
>      DO 10 I=1,3000
>      READ (5,501) M(I),ID(I),IH(I),Y(I),LINE(I)
> 501  FORMAT (3(3X,I2),F9.2,2X,I4)
>      ALINE(I)=DFLOAT(LINE(I))
>C
>C      CHECK STATION/LINE CODING FOR FLAG OR FAULTY DATA
>C
>      IF (LINE(I).EQ.9999) GO TO 100
>      ICHECK=LINE(I)/1000
>      IF (ICHECK.GT.4) GO TO 111
>      IF (ICHECK.LT.1) GO TO 111
>C
>      GO TO 10
> 111  WRITE (6,611) I
> 611  FORMAT (/2X,'INPUT DATA FAULT AT CARD ',I4)
>   10 CONTINUE
> 100  LL=I
>C
>      WRITE (6,612) LL
> 612  FORMAT (/2X,'DATA INPUT TERMINATED. ',I4,' CARDS READ')
>C
>C        **********
>C      SORT DATA ACCORDING TO STATION/LINE CODING
>C      CONVERT TIMES TO JULIAN DAYS (XD)
>C        **********
>C
>      CALL SORT (ALINE,M,ID,IH,Y,LL)
>      DO 11 I=1,LL
>      KD(I)=0
>      LINE(I)=ALINE(I)
>      CALL CONV (M(I),KD(I),ID(I))
>   11 XD(I)=KD(I)+IH(I)/24.0
>C
>      IC=I1+1
>      NUM=1
>      JJJ=1
>      DO 12 I=1,LL
>      IF (LINE(JJJ).EQ.9999) GO TO 102
>      SERR=0.0
>      NUMO=NUM
>      LIT(I)=LINE(NUMO)
>      NUM1=NUMO+1
>      DO 13 JJJ=NUM1,LL
>      NUM=NUM+1
>      IF (LIT(I).NE.LINE(JJJ)) GO TO 101
>   13 CONTINUE
> 101  III(I)=NUM-NUMO
>      II=III(I)
>C
>C      THE 'I'TH' LINE (REFERRED TO AS 'LINE (NUMO)') HAS NOW BEEN
>C      IDENTIFIED AS HAVING 'II' POINTS.  THESE POINTS ARE FOUND ON TIME
>C      CARDS 'NUMO' TO 'NUM-1'.  DATA CARD 'NUM' CONTAINS THE FIRST POINT
>C      ON THE NEXT LINE, UNLESS THIS IS A FLAG IN WHICH CASE THE LOOP
>C      LABELLED 12 IS TERMINATED BY LINE 110 AFTER CALCULATION OF THE
>C      CURRENT LINE.
>C
>C      MANIPULATE DATA PREPARATORY TO SUBROUTINE CALLS
>C
>      DO 14 K=1,II
>      IN=K+NUMO-1
>      S1(K)=XD(IN)
>      IS2(K)=M(IN)
>      IS3(K)=ID(IN)
>      IS4(K)=IH(IN)
>      S5(K)=Y(IN)
>   14 W(K)=1.0
>C
>C      IN THIS VERSION OF THE PROGRAMME THE WEIGHTS (W) OF ALL READINGS
>C      OF G.M.T. PIPS ARE SET EQUAL TO UNITY.
#
```

```
>C
>C      DATA IS CHECKED TO ENSURE THAT THE NUMBER OF POINTS ON THE LINE
>C      LIES WITHIN THE RANGE PERMITTED BY SUBROUTINE E02ABF.  IF
>C      NECESSARY THE SUBROUTINE IS SKIPPED AND AN ERROR MESSAGE PRINTED.
>C
>      IF (II.GT.200) GO TO 112
>      IF (II.LE.IC) GO TO 113
>C
>C      FOR EACH LINE, SORT DATA ACCORDING TO TIME AND CALCULATE BEST
>C      FITTING POLYNOMIAL USING SUBROUTINE E02ABF FROM THE *NAG LIBRARY.
>C        N.B. ROUTINE WILL FAIL IF TWO EQUAL TIME VALUES OCCUR ON THE
>C      SAME LINE.  THE ERROR MESSAGE IS 'IFAIL = 4'.
>C
>      CALL SORT (S1,IS2,IS3,IS4,S5,III(I))
>      CALL E02ABF (III(I),S1,S5,W,IC,IO,SI,P,L)
>      IO=IO+1
>      DO 20 IX=1,IC
>   20 A(IX,I)=P(IX)
>C
>C      WRITE HEADING FOR LINE INFORMATION
>C
>      IF (I2.EQ.1) WRITE (6,601) LINE(NUMO),III(I)
>  601 FORMAT (/////2X,'LINE ',I4,' HAVING ',I3,' POINTS'/32X,'CORRECTION
>     %',2X,'CORRECTION'/2X,'DAY',2X,'MONTH',2X,'HOUR',2X,'JULIAN DAY',2X
>     %,'FROM PIPS',3X,'CALCULATED',2X,'RESIDUAL')
>C
>      DO 15 K=1,II
>      IN=K+NUMC-1
>      XD(IN)=S1(K)
>      M(IN)=IS2(K)
>      ID(IN)=IS3(K)
>      IH(IN)=IS4(K)
>      Y(IN)=S5(K)
>      CALC=0.0
>      DO 16 J=1,IO
>      CALC=CALC+P(J)*S1(K)**(J-1)
>   16 KALC(IN)=CALC
>      ERR=CALC-S5(K)
>      IF (I8.NE.1) GO TO 106
>C
>C      'CALC' IS CLOCK ERROR CALCULATED FROM THE FITTED POLYNOMIAL
>C
>C      DATA IS CHECKED FOR UNUSUALLY LARGE RESIDUALS, INDICATING
>C      POSSIBLY FAULTY READINGS OF CLOCK ERROR (Y).
>C
>      IF (DABS(ERR).GE.0.04) WRITE (6,616) XD(IN),ERR
>  616 FORMAT (2X,'WARNING: RESIDUAL AT ',F7.3,' JULIAN DAYS IS ',F7.3,'
>     %SECS.')
>  106 SERR=SERR+ERR**2
>      IMONTH=MONTH(M(IN))
>      IF (I2.EQ.1) WRITE (6,602) ID(IN),IMONTH,IH(IN),XD(IN),Y(IN),CALC,
>     %ERR
>  602 FORMAT (3X,I2,2X,A4,4X,I2,4X,F7.3,6X,F5.2,7X,F5.2,5X,F7.3)
>   15 CONTINUE
>      DIII=DFLOAT(III(I))
>      RMS=DSQRT(SERR/DIII)*1.D3
>      RERR(I)=RMS
>C
>C      PRINT OUT CALCULATED LINE DATA
>C        RMS      ROOT MEAN SQUARE OF TIME ERROR RESIDUALS FOR EACH LINE
>C        P(J)     POLYNOMIAL COEFFICIENTS
>C        SI(J)    ...AND THEIR STANDARD ERRORS
>C
>      IF (I2.EQ.1) WRITE (6,603) LINE(NUMO),RMS
>  603 FORMAT (//2X,'LINE ',I4/2X,'R.M.S. OF TIME ERROR RESIDUALS (MSEC.)
>     % IS ',F5.1/4X,'A POLYNOMIAL HAS BEEN FITTED OF THE FORM'/7X,'P(1)+
>     %P(2)*X+...+P(N)*X**(N-1)'/2X,'COEFFICIENTS ARE AS FOLLOWS:'/11X,'C
>     %OEFFICIENT',10X,'STD. ERROR')
>      DO 17 J=1,IO
>      SI(J)=DSQRT(SI(J))
>      IF (I2.EQ.1) WRITE (6,604) J,P(J),SI(J)
>  604 FORMAT (2X,'P(',I1,') =',F14.7,9X,F11.7)
#
```

```
>  17 CONTINUE
>     GO TO 12
> 112 WRITE (6,614) LINE(NUMO),III(I)
> 614 FORMAT (/2X,'LINE ',I4,' HAS ',I4,' POINTS'/2X,'POLYNOMIAL FITTING
>    % ROUTINE CANNOT HANDLE MORE THAN 200 POINTS PER LINE')
>     GO TO 12
> 113 WRITE (6,615) LINE(NUMO),III(I)
> 615 FORMAT (/2X,'LINE ',I4,' HAS ONLY ',I2,' POINTS'/2X,'POLYNOMIAL FI
>    %T IS INDETERMINATE')
>C
>C     CONTINUE TO NEXT LINE
>C
>  12 CONTINUE
> 102 IF (I3.NE.1) GO TO 105
>     JI=I-1
>     LLN=0
>C
>C       **************************************************
>C
>C     READ EARTHQUAKE DATA FROM I/O DEVICE 4
>C       LEVENT   EVENT NUMBER
>C        LLINE   STATION/LINE CODING
>C        PHASE   DESCRIPTION OF ARRIVAL
>C       LM,LD,LH,LMI,S  ARRIVAL TIME (MONTH,DAY,HOUR,MINUTE,SECOND)
>C     TERMINATE DATA WITH CARD HAVING LEVENT = 999
>C
>C     DATA IS CORRECTED FOR TIME ERRORS AND PRINTED OUT.  'ERROR' IS THE
>C     R.M.S. OF TIME ERROR RESIDUALS (SECS) FOR THE APPROPRIATE LINE
>C       **********
>C
>     WRITE (6,607)
> 607 FORMAT (1H1,1X,'PRINT-OUT OF CORRECTED ARRIVAL TIMES.  ERROR IS TH
>    %E '/2X,'R.M.S. OF THE TIME RESIDUALS (SEC) FOR THE APPROPRIATE LIN
>    %E'/)
>     WRITE (6,605)
> 605 FORMAT (////1X,'EVENT',3X,'STATION',5X,'PHASE',2X,'DAY MONTH HOUR
>    %MIN SEC',2X,'CORRECTION',2X,'ERROR')
> 103 READ (4,400) LEVENT,LLINE,PHASE,LM,LD,LH,LMI,S
> 400 FORMAT (2X,I3,1X,I4,1X,A4,4(3X,I2),F10.2)
>C
>C     CHECK FOR FLAG.
>C     FIND STATION (ISTA) FROM MOST SIGNIFICANT DIGIT OF 'LLINE'.  IF
>C     THE REMAINING DIGITS OF 'LLINE' ARE ZEROS THE LINE CODING IS A
>C     DUMMY AND A WARNING MESSAGE IS PRINTED OUT.
>C
>     IF (LEVENT.EQ.999) GO TO 105
>     IST=LLINE/1000
>     ISTA=ISTATN(IST)
>     IREM=LLINE-IST*1000
>     IF (IREM.EQ.0) GO TO 110
>C
>C     CONVERT TO JULIAN DAYS AND APPLY TIME CORRECTION (C)
>C     LOOP 18 IDENTIFIES THE TIME CORRECTION LINE ON WHICH THE EVENT
>C     FALLS, AND HENCE THE APPROPRIATE POLYNOMIAL COEFFICIENTS
>C     A(IZ,IP) FOR CALCULATING C.   JI = TOTAL NUMBER OF LINES.
>C       **********
>C
>     CALL CONV (LM,KDD,LD)
>     XLD=KDD+LH/24.0+LMI/1440.0
>     DO 18 J=1,JI
>     IF (LLINE.EQ.LIT(J)) GO TO 104
>  18 CONTINUE
>     WRITE (6,608) LEVENT,LLINE
> 608 FORMAT (2X,'EVENT ',I3,' LINE ',I4,'.  THIS LINE DOES NOT OCCUR IN
>    % TIME DATA')
>     GO TO 103
> 104 IP=J
>     C=0.0
>     DO 21 IZ=2,IC
>  21 C=C+A(IZ,IP)*XLD**(IZ-1)
>     C=C+A(1,IP)
>     S=S+C
#
```

```
>      IF (S.GE.60.0) LMI=LMI+1
>      IF (S.GT.60.0) S=S-60.0
>      IF (S.LT.0.0) LMI=LMI-1
>      IF (S.LT.0.0) S=S+60.0
>      JMONTH=MONTH(LM)
>C
>C      WRITE OUT CORRECTED EARTHQUAKE PHASE ARRIVAL TIMES,
>C      LEAVING A BLANK LINE BETWEEN EACH EVENT.
>C
>      IF (LEVENT.NE.LLN) WRITE (6,609)
> 609 FORMAT (1H )
>      LLN=LEVENT
>      RERROR=RERR(IP)/1000.0
>      WRITE (6,606) LEVENT,ISTA,PHASE,LD,JMONTH,LH,LMI,S,C,RERROR
> 606 FORMAT (2X,I3,2(6X,A4),3X,I2,3X,A4,2X,I2,2X,I2,F6.2,3X,F5.2,5X,F5.
>     &3)
>      GO TO 103
> 110 IF (LEVENT.NE.LLN) WRITE (6,609)
>      LLN=LEVENT
>      WRITE (6,610) LEVENT,ISTA
> 610 FORMAT (2X,I3,6X,A4,6X,'LINE NOT ASSIGNED')
>      GO TO 103
>C
>C      PERFORM PLOTTING ROUTINES
>C        **********
>C
> 105 IF (I4.EQ.1) CALL PLTIME (LINE,XD,Y,LL,KALC,IC,1,&800)
>      IF (I5.EQ.1) CALL PLTIME (LINE,XD,Y,LL,KALC,IC,2,&800)
>      IF (I6.EQ.1) CALL PLTIME (LINE,XD,Y,LL,KALC,IC,3,&800)
>      IF (I7.EQ.1) CALL PLTIME (LINE,XD,Y,LL,KALC,IC,4,&800)
> 800 STOP
>      END
>C       ***************************************************
>C       ***************************************************
>      SUBROUTINE SORT (AI,KJ,KK,KL,AM,N)
>C
>C      SHUFFLES THE 'N' VALUES OF ARRAY 'AI' INTO ORDER OF INCREASING
>C      MAGNITUDE.  THE CONTENTS OF THE OTHER ARRAYS ARE SHUFFLED IN THE
>C      SAME WAY.  THE ROUTINE IS ADAPTED FROM J.T. GOLDEN, PP.87-8.
>C
>      DIMENSION KJ(N),KK(N),KL(N)
>      REAL*8 AI(N),AM(N)
>      LIM=N-1
> 100 INT=1
>      DO 10 I=1,LIM
>      IF (AI(I+1).GE.AI(I)) GO TO 10
>      AAI=AI(I+1)
>      KKJ=KJ(I+1)
>      KKK=KK(I+1)
>      KKL=KL(I+1)
>      AAM=AM(I+1)
>      AI(I+1)=AI(I)
>      KJ(I+1)=KJ(I)
>      KK(I+1)=KK(I)
>      KL(I+1)=KL(I)
>      AM(I+1)=AM(I)
>      AI(I)=AAI
>      KJ(I)=KKJ
>      KK(I)=KKK
>      KL(I)=KKL
>      AM(I)=AAM
>      INT=I
>   10 CONTINUE
>      IF (INT.EQ.1) GO TO 101
>      LIM=INT-1
>      GO TO 100
> 101 RETURN
>      END
>C      ***************************************************
>C      ***************************************************
>      SUBROUTINE CONV (M,KD,ID)
>C
#
```

```
>C     CONVERSION FROM MONTHS AND DAYS TO JULIAN DAYS (NOT FOR LEAP YEARS)
>C        **********
>C
>      IF (M.EQ.2) KD=ID+31
>      IF (M.EQ.3) KD=ID+59
>      IF (M.EQ.4) KD=ID+90
>      IF (M.EQ.5) KD=ID+120
>      IF (M.EQ.6) KD=ID+151
>      IF (M.EQ.7) KD=ID+181
>      IF (M.EQ.8) KD=ID+212
>      IF (M.EQ.9) KD=ID+243
>      IF (M.EQ.10) KD=ID+273
>      RETURN
>      END
>C     ************************************************
>C     ************************************************
>      SUBROUTINE PLTIME (LINE,XD,C,LL,KALC,IC,ISIG,*)
>C
>C      TIME DATA PLOTTED.
>C        XD     TIME IN JULIAN DAYS
>C         C     ASSOCIATED CLOCK ERROR
>C      KALC     CLOCK ERROR PREVIOUSLY CALCULATED BY SUBROUTINE E02ABF
>C      ISIG     DEFINES STATION FOR WHICH DATA IS TO BE PLOTTED
>C        **********
>C
>      DIMENSION LINE(LL),NLINE(1000),LIT(1000)
>      REAL*8 X(400),Y(400),Z(400),XD(LL),C(LL),KALC(LL)
>      REAL*4 STATN(4)
>      DATA STATN/'MILL','TEND','SERD','DETB'/
>C        **********
>C      DRAW AXES AND WRITE SPECIAL SYMBOLS
>C        **********
>      CALL PLTXMX (125.0)
>      CALL PAXIS (0.5,0.5,11HJULIAN DAYS,-11,120.0,0.0,40.0,2.0,1.0)
>      IF (ISIG.EQ.1) CALL PAXIS (0.5,0.5,20HTIME CORRECTION/SECS,20,10.0
>     %,90.0,-4.0,2.0,1.0)
>      IF (ISIG.EQ.2) CALL PAXIS (0.5,0.5,20HTIME CORRECTION/SECS,20,10.0
>     %,90.0,-4.0,4.0,1.0)
>      IF (ISIG.EQ.3) CALL PAXIS (0.5,0.5,20HTIME CORRECTION/SECS,20,10.0
>     %,90.0,-5.0,5.0,1.0)
>      IF (ISIG.EQ.4) CALL PAXIS (0.5,0.5,20HTIME CORRECTION/SECS,20,10.0
>     %,90.0,-6.0,3.0,1.0)
>      CALL PSYMB (1.0,9.7,-0.3,4HTIME,0.0,4)
>      CALL PSYMB (1.0,7.7,-0.3,7HSTATION,0.0,7)
>      CALL PSYMB (3.25,7.7,-0.3,STATN(ISIG),0.0,4)
>      CALL PSYMB (8.85,9.85,-0.3,5HDGP02,0.0,5)
>      CALL PSYMB (1.0,9.0,-0.3,11HCORRECTIONS,0.0,11)
>C        **********
>C      DRAW RECTANGULAR GRID
>C        **********
>      DO 10 I=1,10
>      A=0.5+1.0*I
>      CALL PENUP (0.5,A)
>   10 CALL PENDN (120.5,A)
>      DO 11 I=1,60
>      B=0.5+2.0*I
>      CALL PENUP (B,0.5)
>   11 CALL PENDN (B,10.5)
>C        **********
>C     PLOT TIME DATA AS A DISCONTINUOUS LINE (X AGAINST Y)
>C     PLOT CALCULATED TIME CORRECTIONS AS CONTINUOUS LINES (X AGAINST Z)
>C        **********
>      N=0
>      DO 12 I=1,LL
>C
>C      OMIT POINT DEFINED BY FLAG.
>C      OMIT POINTS FROM STATIONS OTHER THAN THAT NOMINATED BY 'ISIG'.
>C
>      IF (LINE(I).EQ.9999) GO TO 12
>      IS=LINE(I)/1000
>      IF (IS.NE.ISIG) GO TO 12
>      N=N+1
#
```

```
>      X(N)=(XD(I)-40.0)/2.0+0.5
>      IF (ISIG.EQ.1) Y(N)=(C(I)+4.0)/2.0+0.5
>      IF (ISIG.EQ.2) Y(N)=(C(I)+4.0)/4.0+0.5
>      IF (ISIG.EQ.3) Y(N)=(C(I)+5.0)/5.0+0.5
>      IF (ISIG.EQ.4) Y(N)=(C(I)+6.0)/3.0+0.5
>      IF (ISIG.EQ.1) Z(N)=(KALC(I)+4.0)/2.0+0.5
>      IF (ISIG.EQ.2) Z(N)=(KALC(I)+4.0)/4.0+0.5
>      IF (ISIG.EQ.3) Z(N)=(KALC(I)+5.0)/5.0+0.5
>      IF (ISIG.EQ.4) Z(N)=(KALC(I)+6.0)/3.0+0.5
>      NLINE(N)=LINE(I)
>C
>C      DELETE POINT IF IT FALLS OUTSIDE RANGE OF Y-AXIS.
>C
>      IF (Y(N).GT.10.1) N=N-1
>   12 CONTINUE
>C
>C      PLOT THE DISCONTINUOUS LINE.  DATA POINTS REPRESENTED BY ASTERISKS
>C
>      CALL PLINE (X(1),Y(1),N,2,-1,11,0.0)
>C
>C      DIVIDE DATA INTO LINES, SINCE A SEPARATE CONTINUOUS LINE PLOT IS
>C      TO BE MADE FOR EACH LINE.  THE METHOD USED IS SIMILAR TO THAT OF
>C      THE MAIN PROGRAMME.
>C
>      NUM=1
>      DO 13 J=1,N
>      NUMO=NUM
>      LIT(J)=NLINE(NUMO)
>      NUM1=NUMO+1
>      DO 14 K=NUM1,N
>      NUM=NUM+1
>      IF (LIT(J).NE.NLINE(K)) GO TO 101
>   14 CONTINUE
>      NUM=NUM+1
>  101 II=NUM-NUMO
>      DO 15 KK=1,II
>      IN=KK+NUMO-1
>      X(KK)=X(IN)
>   15 Z(KK)=Z(IN)
>C
>C      DO NOT PLOT LINES FOR WHICH SUBROUTINE E02ABF WAS NOT CALLED IN
>C      THE MAIN PROGRAMME.
>C
>      IF (II.GT.200) GO TO 13
>      IF (II.LE.IC) GO TO 13
>C
>C      PLOT A CONTINUOUS LINE.
>C      WRITE CORRESPONDING LINE CODE, GIVEN BY 'LIT(J)'.
>C
>      CALL PLINE (X(1),Z(1),II,2,0,0,0.0)
>      P=Z(1)-0.5
>      IF (Z(1).LT.1.0) P=P+1.0
>      CALL PNUMBR (X(1),P,-0.2,LIT(J),0.0,'I4*')
>      IF (K.EQ.N) GO TO 102
>   13 CONTINUE
>  102 CALL PLTEND
>  100 RETURN 1
>      END
#
```

APPENDIX 5

NON-LINEAR OPTIMIZATION USING MINUIT

The non-linear optimization package MINUIT (JAMES and ROOS,1974), available on NUMAC, incorporates three minimization methods, which may be used singly or in combination depending on the properties of the function, F, to be minimised. Variable parameter starting values, step sizes and upper and lower bounds are assigned to MINUIT at the start of the minimization, which is controlled by a user-supplied command sequence. At each iteration, MINUIT calls the user-written subroutine, in this case HYPCTR, which returns the F value calculated from the current MINUIT parameters.

The three minimization methods available are a Monte Carlo search subroutine (JAMES,1967); a simplex minimization method (NELDER and MEAD,1964); and a minimum gradient (MIGRAD) method using an algorithm devised by FLETCHER (1970), based on the Davidon-Fletcher-Powell algorithm (FLETCHER and POWELL,1963).

The Monte Carlo routine is essentially a trial and error method, whose principal use is to establish a starting point for the other routines. In this application it was not required, since the input hypocentral parameters were those output from LEADL and the V(z) model was adequately constrained by geological feasibility. Fletcher's variable matrix method estimates the quadratic part of F variations by calculating an approximate covariance matrix. From

samples of F in hyperspace, both the estimated position of F_{min} and the covariance matrix are updated at each iteration.

In this study the simplex minimization method was chosen. For the minimization of a function of n variables, the method depends on the comparison of F values at the (n + 1) vertices of a general simplex.

At each iteration, F is evaluated at a new point, $\underline{P}^*$, found by reflecting the worst point, $\underline{P}_H$, of the simplex in the centre of gravity, $\bar{P}$, of the remaining points. Depending on how good $F(\underline{P}^*)$ is, relative to the known simplex points, the programme either replaces $\underline{P}_H$ by $\underline{P}^*$, or evaluates F at a new point, $\underline{P}^{**}$, on the line $(\underline{P}_H, \underline{P})$. Depending on how good $F(\underline{P}^*)$ and $F(\underline{P}^{**})$ are, relative to the known simplex points, the programme may then either replace $\underline{P}_H$ by $\underline{P}^*$, $\underline{P}^{**}$ or the point where a parabola through $\underline{P}_H$, $\underline{P}^*$ and $\underline{P}^{**}$ has a minimum; or reduce the simplex linearly in every direction by a factor Ø.5, retaining only the best point; or use the best point, $\underline{P}_L$, as a starting point and evaluate a new starting simplex. The simplex thus adapts itself to the local F landscape, contracting in to the minimum along the line of steepest gradient.

The simplex method does not require estimates of either first- or second-order derivatives. Only (n + 1) F values are retained at any stage, and no account is taken of past positions. Although slower than Fletcher's method in nearly quadratic regions, it is very stable and converges rapidly farther from the minimum.

APPENDIX 6

CHRONOLOGICAL LISTING OF ALL EVENTS RECORDED BY ETHIOPIAN LOCAL NETWORK

Key to Stations: M = Mille, T = Tendaho, S = Serdo, D = Det Bahri, R = Arta (IPG network), A = AAE (WWSSN station at Addis Abeba). Arta arrival times were included for a few locations.

Asterisks in columns for latitude, longitude, focal depth or magnitude indicate that these parameters could not be determined.

N.B. When the epicentral coordinates are undetermined the time given is the arrival time at the closest station recording the event. Otherwise it is the event origin time.

A plus sign following an event number indicates that the location is unreliable.

M_D is based on signal duration, M_L on P coda maximum trace amplitude.

EVENT NUMBER	RECORDING STATIONS	DATE	---TIME--- HRS	MINS	SECS	LATITUDE	LONGITUDE	FOCAL DEPTH	MAGNITUDES M(D)	M(B)	COMMENT ON LOCATION
1	MS	20 Feb	10	53	32.90	11.9216	41.0041	**	1.3	1.3	NW Tendaho Graben
2	S	20 Feb	21	34	18.51	****	****	**	2.1	2.3	NW Tendaho Graben
3	MS	20 Feb	21	35	33.27	11.9120	41.0325	**	2.1	2.1	NW Tendaho Graben
4	MTS	20 Feb	21	40	59.28	11.8712	41.0622	**	1.6	1.7	NW Tendaho Graben
5	MTS	20 Feb	23	24	55.09	11.8725	41.0613	1.25	2.3	2.4	NW Tendaho Graben
6	MTS	20 Feb	23	27	39.88	11.8552	41.0726	0.25	1.9	1.9	NW Tendaho Graben
7	MS	21 Feb	0	5	12.32	11.9005	41.0412	**	2.2	2.3	NW Tendaho Graben
8	MTS	21 Feb	1	13	46.23	11.9362	41.0131	2.75	1.4	1.6	NW Tendaho Graben
9	S	21 Feb	4	5	31.86	****	****	**	**	**	Within 10 km of Serdo Stn
10	M	21 Feb	22	19	1.24	****	****	**	**	**	
11	MD	23 Feb	20	27	11.56	11.8222	41.1290	**	2.4	2.3	NW Tendaho Graben
12	MTSD	23 Feb	20	31	24.82	11.8145	41.1204	3.0	1.8	**	NW Tendaho Graben
13	M	24 Feb	8	23	13.78	****	****	**	**	**	
14	MTD A	24 Feb	18	11	42.05	11.4000	39.9200	**	1.9	2.4	
15	MD A	25 Feb	16	5	15.59	10.0749	39.9158	**	4.4	**	W. Eth. Escarpment
16	MD A	25 Feb	16	10	46.05	10.0943	39.9087	**	**	**	W. Eth. Escarpment
17	MSD A	25 Feb	16	12	32.81	10.1575	39.6130	**	3.4	**	W. Eth. Escarpment
18	MTSDA	25 Feb	19	22	54.87	10.1360	39.8223	24.0	3.3	3.1	W. Eth. Escarpment
19	MD A	25 Feb	20	47	29.25	****	****	**	2.7	**	W. Eth. Escarpment
20	MTD A	25 Feb	21	58	30.94	10.1323	39.8439	24.0	**	2.6	W. Eth. Escarpment
21	MTSDA	25 Feb	21	59	1.69	9.9596	40.0446	25.0	3.9	**	W. Eth. Escarpment
22	MTD A	25 Feb	22	9	27.60	10.0552	39.9232	24.0	4.1	**	W. Eth. Escarpment
23	MTD A	25 Feb	22	37	19.18	10.0753	39.9051	25.0	2.4	2.8	W. Eth. Escarpment
24	MSD A	26 Feb	3	27	7.31	11.6485	39.8066	0.5	2.5	2.3	Waldia Area
25	MTD	26 Feb	10	2	25.52	11.8772	41.0476	2.75	1.4	2.0	NW Tendaho Graben
26	MTSD	26 Feb	11	37	19.19	11.9105	41.0310	3.0	2.5	2.4	NW Tendaho Graben
27	MTSD	26 Feb	11	37	39.65	11.9083	41.0329	3.0	2.5	2.4	NW Tendaho Graben
28	M	26 Feb	14	57	19.78	****	****	**	**	**	

29	MTS	27	Feb	2	54	30.71	11.8334	41.0686	4.0	2.1	2.1	NW Tendaho Graben
30	M	3	Mar	19	25	18.34	****	****	**	**	**	
31	M	5	Mar	1	9	48.09	****	****	**	0.9	**	NW Tendaho Graben
32	M	5	Mar	17	5	10.57	****	****	**	1.2	**	Waldia Area
33	MT A	5	Mar	17	46	40.67	10.9465	39.7581	11.0	2.7	2.6	Waldia Area
34	M	5	Mar	17	47	59.56	****	****	**	1.4	**	Waldia Area
35	M	5	Mar	23	43	31.09	****	****	**	3.1	**	
36	MTD	6	Mar	13	1	29.36	10.9407	41.2662	6.0	2.4	2.4	
37	MTD	6	Mar	17	11	47.89	12.0416	43.0213	**	3.5	3.4	Distant Event (>200km)
38	M	7	Mar	7	46	25.58	****	****	**	2.1	**	South of Asayita
39	MT	8	Mar	1	30	47.48	11.3954	41.6498	**	2.4	2.4	South of Asayita
40	MS	8	Mar	10	6	48.43	11.8461	41.0551	**	2.1	2.1	NW Tendaho Graben
41+	MD	8	Mar	15	13	20.25	11.1758	41.6807	**	**	2.6	South of Asayita
42	MTS	10	Mar	2	31	9.33	11.9672	40.9704	3.0	2.1	1.9	NW Tendaho Graben
43	MD	20	Mar	7	49	3.95	11.8245	40.9734	**	2.1	2.2	NW Tendaho Graben
44	MTD	20	Mar	13	44	49.66	12.3935	40.5697	1.0	2.6	2.4	
45	MT	22	Mar	6	57	53.74	11.8820	39.8413	**	2.3	2.5	Waldia Area
46	M	22	Mar	10	7	27.31	****	****	**	3.0	**	Distant Event (>200km)
47	MT	23	Mar	6	37	12.15	11.9109	41.0246	**	1.2	1.9	NW Tendaho Graben
48	MT	23	Mar	6	45	55.24	11.9168	41.0382	**	2.3	2.3	NW Tendaho Graben
49	MT	23	Mar	7	57	57.83	11.9162	41.0206	**	3.0	**	NW Tendaho Graben
50	MT	23	Mar	8	24	23.29	11.8955	41.0142	**	1.7	2.1	NW Tendaho Graben
51+	MT	23	Mar	8	25	40.75	11.9085	41.0590	**	0.9	1.0	NW Tendaho Graben
52	MT	23	Mar	8	56	51.61	11.9113	41.0151	**	1.6	1.5	NW Tendaho Graben
53	MT	23	Mar	9	24	3.74	11.9082	41.0441	**	1.1	1.4	NW Tendaho Graben
54	S	24	Mar	6	50	0.49	****	****	**	2.1	**	NW Tendaho Graben
55	S	24	Mar	6	51	27.24	****	****	**	1.8	**	NW Tendaho Graben
56	T	24	Mar	6	57	22.68	****	****	**	1.7	**	NW Tendaho Graben
57	S	24	Mar	8	26	57.91	****	****	**	2.9	**	Distant Event (>200km)
58	S	24	Mar	17	50	31.89	****	****	**	1.8	**	Within 10 km of Serdo Stn
59	M	24	Mar	21	2	23.16	****	****	**	**	**	
60	S	24	Mar	21	40	19.94	****	****	**	1.6	**	Within 10 km of Serdo Stn
61	S	25	Mar	1	41	26.52	****	****	**	1.6	**	Within 10 km of Serdo Stn
62	S	25	Mar	1	55	28.22	****	****	**	1.1	**	Within 10 km of Serdo Stn
63+	MTS	25	Mar	5	9	32.72	11.8438	40.9917	**	1.7	1.9	NW Tendaho Graben
64	S	25	Mar	18	2	35.43	****	****	**	1.2	**	Within 10 km of Serdo Stn
65	S	25	Mar	18	45	44.97	****	****	**	1.1	**	Within 10 km of Serdo Stn
66	S	25	Mar	19	14	5.45	****	****	**	1.3	**	Within 10 km of Serdo Stn
67	S	25	Mar	19	38	33.12	****	****	**	1.5	**	Within 10 km of Serdo Stn
68	S	25	Mar	23	47	21.14	****	****	**	2.0	**	NW Tendaho Graben
69	S	26	Mar	0	23	26.55	****	****	**	**	**	
70	S	26	Mar	0	52	17.78	****	****	**	**	**	
71	S	26	Mar	5	21	11.56	****	****	**	3.7	**	Waldia Area
72	S	26	Mar	5	30	32.48	****	****	**	**	**	
73	S	26	Mar	8	40	41.85	****	****	**	2.5	**	Waldia Area
74	S	26	Mar	9	47	16.10	****	****	**	1.7	**	Within 10 km of Serdo Stn
75	MTS RA	26	Mar	10	20	25.36	13.2315	41.0264	**	3.7	3.2	Distant Event (>200km)
76	S	26	Mar	10	44	4.16	****	****	**	1.5	**	Within 10 km of Serdo Stn

77	S		26 Mar	11	9	43.04	****	****	**	**	**	
78	MTS		26 Mar	11	28	25.19	13.2377	41.0170	**	3.6	3.1	Distant Event (>200km)
79	MTS	A	26 Mar	11	57	15.51	13.2375	41.0320	**	3.9	**	Distant Event (>200km)
80	S		26 Mar	18	8	52.68	****	****	**	1.3	**	Within 10 km of Serdo Stn
81	S		27 Mar	5	25	43.79	****	****	**	2.6	**	
82	S		27 Mar	5	37	51.73	****	****	**	1.6	**	NW Tendaho Graben
83	S		27 Mar	9	26	11.79	****	****	**	2.0	**	Within 10 km of Serdo Stn
84	S		27 Mar	19	52	2.49	****	****	**	1.4	**	Within 10 km of Serdo Stn
85	S	A	31 Mar	18	47	14.80	****	****	**	2.0	**	Waldia Area
86	S	A	31 Mar	19	15	12.41	****	****	**	2.2	**	Waldia Area
87	S	A	31 Mar	19	37	46.52	****	****	**	**	**	Waldia Area
88	S	A	31 Mar	19	42	6.83	****	****	**	4.1	**	Waldia Area
89	S		31 Mar	19	47	0.83	****	****	**	**	**	Waldia Area
90	S		31 Mar	19	47	39.53	****	****	**	2.1	**	Waldia Area
91	S		31 Mar	19	52	27.73	****	****	**	2.4	**	Waldia Area
92	S	A	31 Mar	20	3	33.84	****	****	**	2.5	**	Waldia Area
93	S	A	31 Mar	20	13	18.04	****	****	**	**	**	Waldia Area
94	S	A	31 Mar	20	16	53.34	****	****	**	1.4	**	Waldia Area
95	S	A	31 Mar	20	19	18.44	****	****	**	**	**	Waldia Area
96	S		31 Mar	20	21	58.75	****	****	**	**	**	Waldia Area
97	S	A	31 Mar	20	29	17.05	****	****	**	2.1	**	Waldia Area
98	S	A	31 Mar	20	30	28.45	****	****	**	2.7	**	Waldia Area
99	S	A	31 Mar	20	41	15.06	****	****	**	2.8	**	Waldia Area
100	S		31 Mar	20	43	49.96	****	****	**	**	**	Waldia Area
101	S		31 Mar	20	47	50.66	****	****	**	**	**	Waldia Area
102	S	A	31 Mar	21	9	28.37	****	****	**	2.1	**	Waldia Area
103	S		31 Mar	21	19	26.17	****	****	**	**	**	Waldia Area
104	S	A	31 Mar	21	51	32.29	****	****	**	**	**	Waldia Area
105	S		31 Mar	22	23	34.21	****	****	**	**	**	
106	S	A	31 Mar	23	0	35.73	****	****	**	1.3	**	Waldia Area
107	S	A	31 Mar	23	1	6.13	****	****	**	2.1	**	Waldia Area
108	S	A	31 Mar	23	16	18.53	****	****	**	2.3	**	Waldia Area
109	S	A	31 Mar	23	18	29.33	****	****	**	**	**	Waldia Area
110	S		1 APR	0	32	22.87	****	****	**	**	**	Waldia Area
111	S	A	1 APR	0	49	15.18	****	****	**	2.7	**	Waldia Area
112	S		1 APR	0	54	12.38	****	****	**	1.9	**	Waldia Area
113	S	A	1 APR	0	57	32.68	****	****	**	**	**	Waldia Area
114	S	A	1 APR	2	23	9.83	****	****	**	2.5	**	Waldia Area
115	S	A	1 APR	2	31	26.23	****	****	**	2.0	**	Waldia Area
116	S	A	1 APR	2	52	1.34	****	****	**	2.4	**	Waldia Area
117	S		1 APR	4	9	24.48	****	****	**	1.8	**	Waldia Area
118	S		1 APR	4	40	16.60	****	****	**	**	**	Waldia Area
119	S		1 APR	5	29	36.32	****	****	**	**	**	
120	S	A	1 APR	5	44	37.43	****	****	**	**	**	Waldia Area
121	M		1 APR	12	56	13.37	****	****	**	2.1	**	Waldia Area
122	MT		1 APR	16	8	42.89	11.8858	39.9216	**	1.9	2.3	Waldia Area
123	MT		1 APR	16	22	20.50	11.8942	39.9219	**	1.6	2.0	Waldia Area
124	MT		1 APR	17	32	22.80	11.9084	39.8836	**	3.0	2.6	Waldia Area

125	MTS	1 APR	17	37	11.82	11.8904	39.8949	4.0	3.3	2.6	Waldia Area
126	MTS A	1 APR	18	12	55.97	11.9246	39.9013	7.5	4.4	**	Waldia Area
127+	MTS	1 APR	18	16	21.90	11.9370	39.6129	8.0	**	**	Waldia Area
128	MT	1 APR	18	18	52.80	11.9542	39.9432	**	**	**	Waldia Area
129	MTS	1 APR	18	20	3.10	11.9151	39.8938	7.5	4.3	**	Waldia Area
130	MTS	1 APR	18	23	8.68	11.9045	39.9127	8.0	**	**	Waldia Area
131	MT	1 APR	18	27	51.90	11.9329	39.9319	**	2.0	**	Waldia Area
132	T	1 APR	18	30	4.41	****	****	**	1.8	**	Waldia Area
133	MTS	1 APR	18	32	16.62	11.9123	39.8995	9.5	2.0	**	Waldia Area
134	MTS A	1 APR	18	43	35.97	11.9233	39.8996	**	3.8	**	Waldia Area
135	MT	1 APR	18	49	48.35	11.9553	39.9933	**	3.1	2.5	Waldia Area
136	MT	1 APR	18	52	36.84	11.8475	39.9143	**	2.5	2.4	Waldia Area
137	MTS	1 APR	19	6	27.27	11.9200	39.8857	7.0	2.8	2.5	Waldia Area
138	MTS	1 APR	19	15	4.68	11.9136	39.8519	13.0	3.1	**	Waldia Area
139	M	1 APR	19	18	39.18	****	****	**	**	**	Waldia Area
140	MT	1 APR	19	19	13.46	11.9004	39.8821	**	3.1	**	Waldia Area
141	MT	1 APR	19	34	8.58	11.8978	39.8834	**	3.0	2.6	Waldia Area
142	MT	1 APR	19	36	3.97	11.9018	39.8883	**	2.1	2.2	Waldia Area
143	MT	1 APR	19	37	0.95	11.8917	39.8940	**	1.8	2.1	Waldia Area
144	MTS	1 APR	19	44	30.25	11.9160	39.8911	8.5	3.7	**	Waldia Area
145	MTS	1 APR	19	50	59.76	11.8932	39.8780	9.0	3.5	**	Waldia Area
146	MT	1 APR	20	35	16.63	11.8949	39.8924	**	1.6	2.1	Waldia Area
147	MTS	1 APR	20	41	48.99	11.8991	39.8840	7.5	2.4	2.6	Waldia Area
148	M	1 APR	20	52	40.56	****	****	**	1.5	**	Waldia Area
149	MT	1 APR	21	0	51.43	11.8858	39.8817	**	1.8	2.1	Waldia Area
150	M	2 APR	0	12	35.41	****	****	**	1.6	**	Waldia Area
151	TS	2 APR	0	18	26.69	11.8959	39.8900	**	2.6	**	Waldia Area
152	T	2 APR	0	30	23.61	****	****	**	1.9	**	Waldia Area
153	MTS	2 APR	0	42	24.11	11.9141	39.8827	10.0	3.6	**	Waldia Area
154	MTS	2 APR	0	45	6.66	11.8901	39.8844	6.0	3.3	2.7	Waldia Area
155	MTS	2 APR	0	56	10.74	11.8952	39.8801	8.0	2.1	2.4	Waldia Area
156	TS	2 APR	1	34	22.81	11.9045	39.9131	**	2.6	**	Waldia Area
157	M	2 APR	2	52	9.91	****	****	**	1.9	**	Waldia Area
158	MT	2 APR	3	37	22.52	11.8983	39.8922	**	**	2.6	Waldia Area
159	S	2 APR	5	25	46.95	****	****	**	2.2	**	Waldia Area
160	MTD	2 APR	7	18	40.08	11.7489	39.9125	**	2.1	2.2	Waldia Area
161	MTS	2 APR	9	2	1.00	12.5433	39.5215	**	2.5	2.6	Distant Event (>200km)
162	MTSD	2 APR	9	11	7.81	11.9146	39.9022	7.5	2.7	2.6	Waldia Area
163	MTSD	2 APR	9	49	3.86	11.9339	39.9373	3.5	2.4	2.3	Waldia Area
164	MTSD	2 APR	10	3	3.80	11.8976	39.8821	8.5	3.3	2.7	Waldia Area
165	S	2 APR	10	58	35.14	****	****	**	2.0	**	
166	S	2 APR	12	32	22.72	****	****	**	1.7	**	NW Tendaho Graben
167	TD	2 APR	13	5	22.26	11.9769	39.9173	**	2.1	**	Waldia Area
168	MT	2 APR	16	15	38.37	11.8971	39.8831	**	2.5	2.5	Waldia Area
169	MT	2 APR	16	19	39.96	12.3354	39.9876	**	1.9	**	Waldia Area
170	SD	2 APR	18	21	6.57	11.4026	41.4912	**	1.9	**	South of Asayita
171	MTSD	2 APR	23	52	30.23	11.4201	41.4974	3.5	1.6	1.9	South of Asayita
172	MTS	3 APR	0	55	30.62	11.9112	39.9020	3.5	2.7	2.5	Waldia Area

173	MTSDA	3	APR	2	43	46.66	11.8650	39.8544	13.0	3.2	**	Waldia Area
174	S	3	APR	5	6	47.98	****	****	**	0.5	**	Within 10 km of Serdo Stn
175	S	3	APR	5	21	18.71	****	****	**	1.8	**	Within 10 km of Serdo Stn
176	MTD A	3	APR	5	25	42.24	11.8902	39.8824	6.5	3.4	**	Waldia Area
177	MTD	3	APR	5	28	8.93	11.8999	39.8879	5.5	2.7	2.6	Waldia Area
178	MTSD	3	APR	5	34	57.36	11.9135	39.9015	5.5	3.0	2.6	Waldia Area
179	S	3	APR	6	59	26.52	****	****	**	1.7	**	SOUTH of ASAYITA
180	S	3	APR	7	20	57.74	****	****	**	2.2	**	Within 10 km of Serdo Stn
181	MT	3	APR	9	37	52.07	11.8026	39.8537	**	2.1	2.1	Waldia Area
182	MS	3	APR	9	40	47.16	11.9301	40.9826	**	2.1	**	NW Tendaho Graben
183	TD	3	APR	14	28	29.33	11.8951	39.9141	**	2.0	**	Waldia Area
184	MTSD	3	APR	19	24	34.25	11.9237	39.8879	7.0	2.8	2.5	Waldia Area
185	M	4	APR	0	43	30.40	****	****	**	2.1	**	Waldia Area
186	M	4	APR	1	11	5.10	****	****	**	2.3	**	Waldia Area
187	MTD	4	APR	2	13	57.44	11.8987	39.8995	4.0	2.7	2.6	Waldia Area
188	MTD	4	APR	4	12	30.46	11.9041	39.9479	**	2.6	2.5	Waldia Area
189	MTD	4	APR	6	16	50.65	11.9161	39.9020	5.5	2.4	2.5	Waldia Area
190	MT	4	APR	9	48	33.10	11.8677	39.8165	0.0	2.7	2.5	Waldia Area
191	MTD	4	APR	22	29	46.87	11.8653	39.9391	6.5	2.2	2.5	Waldia Area
192	M	4	APR	22	30	14.03	****	****	**	**	**	Waldia Area
193	MT A	5	APR	0	31	59.86	10.2338	39.7042	**	2.8	2.8	W. Eth. Escarpment
194	MTD	5	APR	6	52	27.49	11.9289	39.9004	5.0	2.7	2.6	Waldia Area
195	MTD	5	APR	7	59	33.49	11.8610	39.8652	12.0	2.1	2.3	Waldia Area
196	M	5	APR	8	12	6.48	****	****	**	2.1	**	Waldia Area
197	M	5	APR	9	48	6.21	****	****	**	2.5	**	Waldia Area
198	MTD	5	APR	9	50	25.74	11.9165	39.8941	6.5	2.0	2.2	Waldia Area
199	MTSD	5	APR	6	46	17.95	11.9128	39.9137	**	3.6	**	Waldia Area
200	MTSDA	5	APR	6	46	20.91	11.9048	39.9125	**	**	*	
201	M	7	APR	22	23	5.52	****	****	**	1.4	**	NW Tendaho Graben
202+	MT	8	APR	2	15	58.92	13.4982	40.6775	**	3.0	3.1	Distant Event (>200km)
203	MT A	8	APR	4	56	13.83	11.9075	39.9025	**	2.3	2.7	Waldia Area
204	MT	8	APR	4	58	57.74	11.9146	39.8885	**	1.6	2.2	Waldia Area
205	MT A	8	APR	19	17	51.03	11.6439	39.8352	**	2.3	2.4	Waldia Area
206	MT	8	APR	19	34	55.39	11.6793	39.8353	**	2.4	2.6	Waldia Area
207	MT	9	APR	0	13	19.21	11.8601	41.0370	**	1.6	1.9	NW Tendaho Graben
208	MT	9	APR	0	22	26.34	11.8094	41.1061	**	1.8	2.1	NW Tendaho Graben
209	MT	9	APR	0	47	48.27	11.8470	39.8717	**	2.6	2.7	Waldia Area
210	MT	9	APR	4	10	23.82	11.8653	39.9015	**	2.5	2.6	Waldia Area
211	MTD	9	APR	20	20	11.02	11.8883	39.8957	7.0	2.6	2.6	Waldia Area
212	MTD	10	APR	3	3	5.57	11.9024	39.9226	2.0	2.4	2.5	Waldia Area
213	MTD A	10	APR	20	15	36.02	11.8791	39.9138	2.0	3.5	**	Waldia Area
214	D	10	APR	20	17	57.23	****	****	**	**	**	Waldia Area
215	MTD A	10	APR	20	34	0.48	11.9061	39.9057	4.5	2.6	2.7	Waldia Area
216	MSD	11	APR	3	47	14.42	11.8999	39.9396	**	2.7	2.6	Waldia Area
217	MTD	11	APR	11	54	57.89	11.8894	39.9129	6.0	3.3	**	Waldia Area
218	MTD	11	APR	20	34	4.92	11.8618	39.8967	12.0	2.4	2.6	Waldia Area
219	MD	11	APR	21	2	45.76	12.1354	40.5742	**	2.3	2.4	Waldia Area
220	D	12	APR	4	59	56.12	****	****	**	2.0	**	

221	M	13	APR	8	40	22.05	****	****	**	2.5	**	Waldia Area
222	M	13	APR	9	46	53.60	****	****	**	2.6	**	Waldia Area
223+	MT	13	APR	12	56	23.05	11.9759	41.2931	**	2.3	2.6	
224+	MT	13	APR	14	41	27.81	11.8612	41.5088	**	2.7	2.4	SE of Serdo
225	MT	14	APR	4	29	26.68	11.9134	39.8989	**	2.4	2.4	Waldia Area
226	MTD A	14	APR	8	40	58.48	11.8653	39.8920	9.5	3.1	2.8	Waldia Area
227	MTD A	14	APR	8	52	4.20	11.8613	39.8955	9.5	2.8	2.7	Waldia Area
228	MTD	14	APR	8	54	50.48	11.8767	39.9048	8.0	2.7	2.6	Waldia Area
229	MTD	14	APR	9	2	10.99	11.8810	39.9025	9.0	2.4	2.4	Waldia Area
230	M	14	APR	9	43	19.80	****	****	**	**	**	Waldia Area
231	M	14	APR	9	43	28.24	****	****	**	2.2	**	Waldia Area
232	MT	19	APR	23	22	40.47	12.0303	39.8318	**	2.3	2.4	Waldia Area
233+	MT	20	APR	7	28	58.82	11.6182	41.0546	**	1.6	1.9	
234+	MT	**	Feb	9	30	33.80	11.8915	40.9394	**	1.4	1.9	
235+	MT	**	Feb	**	48	57.04	12.0483	39.6667	**	2.6	2.7	
236	MT	25	APR	13	1	22.71	11.8728	41.0838	**	1.6	1.5	NW Tendaho Graben
237	M	25	APR	14	30	3.38	****	****	**	**	**	
238	M	25	APR	16	54	24.52	****	****	**	**	**	
239+	MT	26	APR	16	43	28.13	9.2715	39.9301	**	3.6	3.2	Distant Event (>200km)
240	M	26	APR	19	7	17.30	****	****	**	3.6	**	
241	T	28	APR	6	20	23.83	****	****	**	**	**	NW Tendaho Graben
242	MT	28	APR	6	20	48.23	11.8828	41.0174	**	2.1	2.2	NW Tendaho Graben
243	M	28	APR	7	28	22.05	****	****	**	1.8	**	
244	MT	28	APR	11	17	4.73	11.9204	40.9813	**	1.0	**	NW Tendaho Graben
245	MT	28	APR	11	17	23.34	11.8872	41.0322	**	2.1	2.2	NW Tendaho Graben
246	MT	28	APR	21	51	55.36	11.6106	39.8602	**	2.1	2.4	Waldia Area
247	M	29	APR	18	43	54.04	****	****	**	2.1	**	Waldia Area
248	M	29	APR	18	49	7.12	****	****	**	1.8	**	
249	M	29	APR	19	5	23.26	****	****	**	2.7	**	Waldia Area
250+	MT	30	APR	0	8	50.74	12.1422	40.8755	**	2.0	2.3	
251	MT	3	Jun	6	24	2.50	11.8607	41.0804	**	1.5	1.8	NW Tendaho Graben
252	M	3	Jun	12	6	21.64	****	****	**	**	**	
253	M	3	Jun	14	27	57.94	****	****	**	1.6	**	S Allallobeda Graben
254	M	3	Jun	15	45	12.80	****	****	**	**	**	
255	M	3	Jun	17	39	31.20	****	****	**	**	**	
256+	MT	3	Jun	18	26	43.81	11.4742	41.0278	**	1.3	0.9	S Allallobeda Graben
257	M	3	Jun	18	47	23.92	****	****	**	3.5	**	
258	M	4	Jun	1	55	57.39	****	****	**	2.0	**	
259	M	4	Jun	3	59	39.52	****	****	**	3.6	**	
260	M	4	Jun	4	33	23.55	****	****	**	4.1	**	
261+	MT	18	Jun	13	35	37.67	11.5930	41.0245	**	1.9	1.7	S Allallobeda Graben
262	M	19	Jun	2	13	27.19	****	****	**	1.5	**	
263	M	19	Jun	18	57	2.04	****	****	**	1.6	**	S Allallobeda Graben
264	MT	20	Jun	18	49	16.11	11.9719	39.9775	**	2.7	2.7	Waldia Area
265	MTS	20	Jun	23	0	6.52	11.9087	39.9776	**	2.7	2.7	Waldia Area
266	M	21	Jun	17	34	33.40	****	****	**	**	**	
267	M	21	Jun	18	53	56.76	****	****	**	1.6	**	Waldia Area
268	S	21	Jun	21	8	49.83	****	****	**	2.0	**	Within 10 km of Serdo Stn

269	M	22 Jun	22	5	59.20	****	****	**	1.6	**	Waldia Area
270	MTS	23 Jun	9	55	16.00	11.1959	40.9285	1.0	2.9	**	S Allallobeda Graben
271	MT	23 Jun	17	39	29.20	11.1848	40.8887	**	2.2	1.9	S Allallobeda Graben
272+	TS	23 Jun	23	35	18.78	11.8921	41.2665	**	1.9	1.8	SE of Serdo
273	M	24 Jun	0	32	46.47	****	****	**	1.7	**	S Allallobeda Graben
274	MTS A	24 Jun	10	34	24.50	9.9442	39.5344	**	3.5	3.3	Distant Event (>200km)
275	M	24 Jun	11	10	52.68	****	****	**	**	**	
276	M	24 Jun	11	32	18.10	****	****	**	1.1	**	S Allallobeda Graben
277	M	24 Jun	16	48	22.49	****	****	**	1.1	**	
278	M	24 Jun	16	48	42.97	****	****	**	**	**	S Allallobeda Graben
279	M	24 Jun	16	49	42.98	****	****	**	1.0	**	S Allallobeda Graben
280	MT	25 Jun	14	57	43.15	11.1324	40.8801	**	2.6	2.1	S Allallobeda Graben
281	M	25 Jun	17	11	19.44	****	****	**	2.3	**	S Allallobeda Graben
282	MS	25 Jun	17	12	37.30	11.2520	40.9197	**	2.9	**	S Allallobeda Graben
283	M	25 Jun	17	19	17.72	****	****	**	2.5	**	S Allallobeda Graben
284	MS	25 Jun	17	27	58.60	11.1500	40.9160	**	3.2	**	S Allallobeda Graben
285	M	25 Jun	18	2	48.21	****	****	**	1.6	**	S Allallobeda Graben
286	M	25 Jun	20	42	19.03	****	****	**	2.8	**	S Allallobeda Graben
287	M	25 Jun	20	45	19.02	****	****	**	3.4	**	S Allallobeda Graben
288	M	25 Jun	22	55	14.61	****	****	**	1.8	**	S Allallobeda Graben
289	M	26 Jun	0	51	36.79	****	****	**	2.3	**	S Allallobeda Graben
290	M	26 Jun	7	1	16.28	****	****	**	1.6	**	NW Tendaho Graben
291	MD	1 Jly	17	16	2.73	11.9012	41.0307	**	2.4	**	NW Tendaho Graben
292	MD	2 Jly	7	43	54.64	11.9074	41.0181	**	2.3	2.3	NW Tendaho Graben
293	MTS	3 Jly	23	3	37.12	11.8995	41.0362	2.0	1.8	2.0	NW Tendaho Graben
294	MTS	3 Jly	23	4	39.20	11.8759	41.0511	1.5	1.6	1.9	NW Tendaho Graben
295	MTS	5 Jly	13	15	0.64	11.8765	39.8685	13.0	2.6	2.6	Waldia Area
296+	MD	5 Jly	22	15	26.40	12.2295	40.9929	**	1.7	2.2	
297	M	6 Jly	1	46	40.75	****	****	**	2.1	**	Distant Event (>200km)
298	M	7 Jly	22	4	12.16	****	****	**	1.3	**	Waldia Area
299	M	7 Jly	22	4	45.70	****	****	**	1.5	**	Waldia Area
300	MTS	8 Jly	21	16	32.53	11.8214	41.0544	2.25	1.6	1.7	NW Tendaho Graben
301	M	9 Jly	8	47	29.50	****	****	**	2.0	**	
302	MTS RA	10 Jly	13	29	30.01	9.6225	39.6359	**	4.1	3.6	Distant Event (>200km)
303	M	10 Jly	16	46	15.09	****	****	**	1.4	**	Waldia Area
304	M	12 Jly	6	13	20.68	****	****	**	1.4	**	S Allallobeda Graben
305	T	12 Jly	11	47	50.93	****	****	**	**	**	
306	T	12 Jly	13	10	56.54	****	****	**	**	**	
307	S	13 Jly	9	6	32.68	****	****	**	**	**	
308	S	13 Jly	20	26	50.66	****	****	**	2.3	**	Waldia Area
309	S	13 Jly	20	53	3.72	****	****	**	1.1	**	Within 10 km of Serdo Stn
310	S	14 Jly	0	2	47.16	****	****	**	0.9	**	Within 10 km of Serdo Stn
311	MT	14 Jly	17	44	22.37	11.9086	41.0202	**	1.8	2.0	NW Tendaho Graben
312	T	14 Jly	17	48	22.16	****	****	**	0.5	**	
313	T	14 Jly	17	52	0.63	****	****	**	0.8	**	NW Tendaho Graben
314	T	14 Jly	17	55	0.90	****	****	**	1.1	**	NW Tendaho Graben
315	S	14 Jly	22	38	5.72	****	****	**	1.1	**	Within 10 km of Serdo Stn
316	S	15 Jly	2	18	48.93	****	****	**	1.2	**	NW Tendaho Graben

317	T	15	Jly	4	9	1.27	****	****	**	0.7	**	NW Tendaho Graben
318	T	15	Jly	9	46	33.84	****	****	**	1.8	**	NW Tendaho Graben
319	T	15	Jly	17	30	5.81	****	****	**	3.2	**	NW Tendaho Graben
320	T	15	Jly	17	32	4.18	****	****	**	1.3	**	NW Tendaho Graben
321	TS	15	Jly	17	32	25.07	11.8929	41.0597	**	2.9	**	NW Tendaho Graben
322	T	15	Jly	17	33	29.33	****	****	**	0.7	**	NW Tendaho Graben
323	TS	15	Jly	17	37	2.19	11.8898	41.0534	**	1.6	0.8	NW Tendaho Graben
324	TS	15	Jly	17	38	38.80	11.8600	41.0805	**	2.5	**	NW Tendaho Graben
325	T	15	Jly	17	40	46.83	****	****	**	0.5	**	NW Tendaho Graben
326	T	15	Jly	17	43	21.88	****	****	**	1.8	**	NW Tendaho Graben
327	T	15	Jly	17	43	41.67	****	****	**	0.5	**	NW Tendaho Graben
328	T	15	Jly	17	44	5.14	****	****	**	0.6	**	NW Tendaho Graben
329	T	15	Jly	17	45	51.49	****	****	**	0.6	**	NW Tendaho Graben
330	T	15	Jly	17	47	7.93	****	****	**	0.2	**	NW Tendaho Graben
331	T	15	Jly	17	47	41.29	****	****	**	0.5	**	NW Tendaho Graben
332	T	15	Jly	17	59	33.42	****	****	**	0.2	**	NW Tendaho Graben
333	T	15	Jly	18	3	34.42	****	****	**	1.4	**	NW Tendaho Graben
334	T	15	Jly	18	42	20.68	****	****	**	0.8	**	NW Tendaho Graben
335	T	15	Jly	19	51	36.66	****	****	**	0.7	**	NW Tendaho Graben
336	T	15	Jly	20	28	45.62	****	****	**	0.8	**	NW Tendaho Graben
337	MTS R	16	Jly	16	34	4.05	13.5605	43.4223	**	3.6	3.7	Distant Event (>200km)
338	T	16	Jly	17	54	17.94	****	****	**	1.8	**	
339	MT R	18	Jly	4	16	4.21	13.0684	43.6952	**	3.5	3.5	Distant Event (>200km)
340	MT R	18	Jly	7	52	15.01	13.1510	43.8379	**	3.6	3.7	Distant Event (>200km)
341	M	18	Jly	17	58	1.37	****	****	**	3.6	**	Distant Event (>200km)
342	T	19	Jly	15	19	43.17	****	****	**	1.0	**	NW Tendaho Graben
343	M	19	Jly	16	56	32.02	****	****	**	3.2	**	Distant Event (>200km)
344	M	22	Jly	10	29	20.88	****	****	**	3.4	**	Waldia Area
345	T	22	Jly	17	31	40.03	****	****	**	1.4	**	
346	S	24	Jly	2	18	17.25	****	****	**	1.4	**	
347	M	24	Jly	4	26	11.28	****	****	**	1.6	**	
348	S	24	Jly	20	40	10.12	****	****	**	1.3	**	Within 10 km of Serdo Stn
349	T	25	Jly	15	23	49.15	****	****	**	1.1	**	NW Tendaho Graben
350	MD	26	Jly	20	0	22.24	11.8917	39.8559	**	2.1	2.2	Waldia Area
351	T	26	Jly	21	18	10.07	****	****	**	**	**	
352	MTSD	26	Jly	21	33	50.09	11.8763	41.3300	**	2.9	2.4	
353+	MD	27	Jly	5	1	59.91	11.9481	40.9157	**	1.8	2.2	
354	MTSD	27	Jly	6	58	1.01	11.9466	39.8688	1.75	4.2	**	Waldia Area
355	MD	27	Jly	7	28	18.41	11.8913	39.8578	**	2.9	2.7	Waldia Area
356	MTSD	27	Jly	8	33	52.41	11.9283	39.8757	**	2.8	2.7	Waldia Area
357	TSD A	27	Jly	9	58	14.55	11.9579	39.9018	**	3.8	**	Waldia Area
358	S	27	Jly	11	21	15.88	****	****	**	1.1	**	
359	SD	27	Jly	11	22	7.25	11.9503	39.8713	**	2.4	**	Waldia Area
360	S	27	Jly	12	9	45.48	****	****	**	1.3	**	Within 10 km of Serdo Stn
361	SD	27	Jly	16	24	2.91	11.9607	39.8686	**	3.1	**	Waldia Area
362	SD	27	Jly	23	40	0.65	11.9274	39.8478	**	2.8	**	Waldia Area
363	MD	28	Jly	9	35	27.95	11.8780	39.8586	**	2.6	2.7	Waldia Area
364	M	28	Jly	10	31	54.32	****	****	**	2.0	**	Waldia Area

365	MD		28 Jly	11	41	15.83	11.8758	39.8656	**	2.6	2.7	Waldia Area
366	MD		28 Jly	11	48	0.43	11.8879	39.8712	**	2.3	2.5	Waldia Area
367	M		28 Jly	15	30	38.16	****	****	**	**	**	
368	MD	A	28 Jly	21	17	38.97	11.9080	39.8815	**	3.6	**	Waldia Area
369	MD	A	28 Jly	21	38	47.19	11.9151	39.8806	**	3.6	**	Waldia Area
370	MD		28 Jly	21	49	57.88	11.9164	39.8804	**	2.7	2.7	Waldia Area
371	M		28 Jly	22	25	42.93	****	****	**	1.5	**	Waldia Area
372	M		28 Jly	23	40	46.87	****	****	**	1.9	**	Waldia Area
373	MD		29 Jly	2	52	50.20	11.9694	39.8818	**	2.9	**	Waldia Area
374	M		29 Jly	3	14	40.20	****	****	**	**	**	Waldia Area
375	M		29 Jly	10	4	11.12	****	****	**	1.4	**	Waldia Area
376	MD		29 Jly	20	27	31.20	11.9107	39.8588	**	1.8	2.1	Waldia Area
377	S		29 Jly	21	19	11.54	****	****	**	1.4	**	
378	S		30 Jly	10	47	2.36	****	****	**	1.6	**	
379	T		30 Jly	20	44	0.85	****	****	**	1.4	**	
380	T		30 Jly	23	44	53.38	****	****	**	0.2	**	NW Tendaho Graben
381	T		30 Jly	23	46	49.14	****	****	**	1.3	**	NW Tendaho Graben
382	M		31 Jly	1	16	1.57	****	****	**	2.2	**	Waldia Area
383	M		31 Jly	10	43	15.82	****	****	**	2.5	**	Waldia Area
384	MS		31 Jly	13	3	56.79	11.9289	39.8621	**	2.9	2.8	Waldia Area
385	MTS		31 Jly	20	29	12.08	11.9314	39.8790	4.5	3.1	2.8	Waldia Area
386	MTS	RA	1 Aug	10	33	45.25	14.8491	39.5594	**	4.5	**	Distant Event (>200km)
387	MSD		3 Aug	11	59	51.35	11.8132	41.0725	1.75	1.6	**	NW Tendaho Graben
388	MTD		4 Aug	16	56	53.94	11.3209	40.9397	4.0	2.7	**	S Allallobeda Graben
389	MS		5 Aug	22	47	42.93	13.2763	40.7575	**	2.7	2.4	
390	MS		7 Aug	2	46	18.16	11.8479	41.0561	**	1.8	2.1	NW Tendaho Graben
391	M		29 Aug	20	51	56.43	****	****	**	1.6	**	Waldia Area
392	MT		29 Aug	21	16	14.68	13.3282	40.8690	**	3.1	**	
393	MT		29 Aug	23	39	24.50	11.9723	40.9599	**	1.9	1.7	NW Tendaho Graben
394+	MT		30 Aug	2	3	22.46	13.6820	40.4136	**	3.2	3.0	
395	MTS	RA	30 Aug	8	16	24.83	11.7804	43.1989	**	4.3	**	Distant Event (>200km)
396	MT		30 Aug	18	12	44.29	11.8714	39.8643	**	2.0	2.2	Waldia Area
397	M		30 Aug	20	3	59.87	****	****	**	1.8	**	
398	MTS		31 Aug	1	19	26.17	11.9182	39.8602	1.0	1.8	2.1	Waldia Area
399	MTS		31 Aug	11	26	46.08	11.9585	40.9720	4.0	1.9	1.8	NW Tendaho Graben
400	MT		31 Aug	20	25	8.98	11.9165	39.8608	**	1.5	2.1	Waldia Area
401+	MT	RA	1 Sep	13	38	30.43	10.2558	41.9288	0.0	3.7	3.0	
402+	M	R	7 Sep	14	13	31.47	12.5145	41.8515	**	2.1	2.0	
403+	M	A	7 Sep	23	15	36.43	12.2500	39.8521	**	3.5	2.8	
404	M	RA	7 Sep	23	28	40.59	11.8792	39.7255	**	4.1	**	
405	M		7 Sep	23	31	53.06	****	****	**	2.2	**	
406	M		7 Sep	23	53	54.79	****	****	**	2.7	**	
407	MT		10 Sep	11	49	24.87	10.4078	39.9976	**	1.9	2.3	
408	M		13 Sep	2	25	50.33	****	****	**	**	**	
409	M		13 Sep	20	26	9.18	****	****	**	**	**	
410	MT	A	13 Sep	21	27	58.47	12.2023	39.7918	**	3.3	2.9	Waldia Area
411	M		13 Sep	21	48	42.08	****	****	**	2.0	**	
412	MT		13 Sep	22	24	39.36	12.2863	39.7832	**	2.3	2.3	Waldia Area

413	MT	14	Sep	0	17	44.85	****	****	**	1.9	**	
414+	MT	14	Sep	0	22	20.90	12.2576	39.6848	**	2.5	2.5	Waldia Area
415	MT	14	Sep	15	46	32.92	11.8360	41.0662	**	0.9	1.8	
416	MT	14	Sep	21	46	30.05	11.8928	39.8695	**	2.8	2.6	Waldia Area
417	MT A	14	Sep	22	4	4.87	11.4185	40.9333	**	3.6	**	
418	M	14	Sep	22	16	52.93	****	****	**	1.8	**	
419	MT	14	Sep	23	4	2.62	11.8437	39.8517	**	1.8	2.0	Waldia Area
420+	MT	15	Sep	5	40	43.72	12.3800	41.4457	**	3.1	2.7	
421	MTD	15	Sep	16	16	9.05	****	****	**	**	**	
422	T	15	Sep	20	32	41.86	****	****	**	1.8	**	
423	MT RA	15	Sep	20	37	13.30	12.2157	44.5086	4.0	3.6	**	
424	M	15	Sep	21	58	14.92	****	****	**	4.0	**	
425	MTSD	17	Sep	13	26	19.94	12.7994	40.7137	**	2.6	2.5	
426	M	17	Sep	16	44	18.32	****	****	**	3.7	**	
427	S	18	Sep	7	41	58.41	****	****	**	1.8	**	
428+	MD	18	Sep	7	49	44.81	12.1849	39.7103	**	2.8	2.7	
429	MT	19	Sep	1	52	58.78	11.9252	41.0014	**	1.2	1.0	NW Tendaho Graben
430	MTSD	20	Sep	0	1	37.16	11.5106	42.3429	**	1.8	**	Distant Event (>200km)
431	MTD	20	Sep	0	17	20.03	11.5980	42.3708	**	2.8	2.8	Distant Event (>200km)
432	MT	21	Sep	1	30	33.07	11.0106	42.3650	**	2.6	2.6	Distant Event (>200km)
433	MTD	21	Sep	12	3	56.88	11.8746	42.7816	**	3.0	3.0	Distant Event (>200km)
434	MTSD	23	Sep	8	20	42.80	11.9923	40.7726	0.5	1.6	2.0	
435	M	23	Sep	8	31	22.61	****	****	**	**	**	
436	T	23	Sep	10	2	9.55	****	****	**	**	**	
437	MTSD	23	Sep	10	2	36.59	11.9976	40.7681	0.75	1.6	1.9	
438	TD	23	Sep	10	3	18.16	11.9924	40.7760	**	1.3	**	
439	MTSD	23	Sep	13	51	22.39	11.8334	39.8983	3.0	2.8	2.6	Waldia Area
440	S	23	Sep	18	54	46.35	****	****	**	1.1	**	Within 10 km of Serdo Stn
441	S	23	Sep	18	55	17.00	****	****	**	1.0	**	Within 10 km of Serdo Stn
442	S	23	Sep	18	55	33.44	****	****	**	1.0	**	Within 10 km of Serdo Stn
443	MTSD	23	Sep	19	54	54.07	10.8405	40.0564	**	2.9	**	
444	T	23	Sep	21	20	2.07	****	****	**	1.2	**	NW Tendaho Graben
445	MSD	23	Sep	21	21	48.39	11.8338	39.9261	**	2.5	2.5	Waldia Area
446	S	23	Sep	23	16	56.45	****	****	**	1.6	**	Within 10 km of Serdo Stn
447	M	23	Sep	23	36	30.99	****	****	**	1.6	**	
448	SD	24	Sep	13	40	8.80	11.8664	41.5336	**	2.3	**	SE of Serdo
449	D	24	Sep	14	6	20.63	****	****	**	2.1	**	SE of Serdo
450	TD	24	Sep	14	54	27.13	11.8990	41.5117	**	2.3	**	SE of Serdo
451	S	24	Sep	16	5	57.35	****	****	**	1.0	**	SE of Serdo
452	TSD	24	Sep	16	23	5.86	11.8631	41.5131	**	2.1	**	SE of Serdo
453	M	24	Sep	16	42	48.59	****	****	**	0.8	**	SE of Serdo
454	TS	24	Sep	17	16	5.83	11.8741	41.4736	**	2.0	**	SE of Serdo
455	MTSD	24	Sep	17	38	8.02	11.8622	41.5077	0.0	2.8	2.3	SE of Serdo
456	D	24	Sep	17	45	5.15	****	****	**	2.0	**	SE of Serdo
457	TSD	24	Sep	18	11	20.19	11.9293	41.2006	**	1.9	**	Kurub Area
458	S	24	Sep	18	25	51.56	****	****	**	1.2	**	Kurub Area
459	S	24	Sep	18	26	38.61	****	****	**	1.5	**	Kurub Area
460	S	24	Sep	18	36	7.42	****	****	**	0.9	**	Kurub Area

461	S	24 Sep	18	38	44.40	****	****	**	1.6	**	Kurub Area
462	S	24 Sep	18	39	42.76	****	****	**	1.1	**	Kurub Area
463	S	24 Sep	18	39	55.72	****	****	**	1.7	**	Kurub Area
464	MTSDRA	24 Sep	18	43	50.27	11.8586	41.5023	**	3.9	**	SE of Serdo
465	S	24 Sep	18	46	19.88	****	****	**	**	**	SE of Serdo
466	TS	24 Sep	18	46	50.64	11.8568	41.5357	**	2.0	1.8	SE of Serdo
467	MTSD	24 Sep	18	48	3.97	11.8622	41.5089	0.0	2.8	2.1	SE of Serdo
468	S	24 Sep	18	48	59.75	****	****	**	1.7	**	SE of Serdo
469	S	24 Sep	18	49	48.66	****	****	**	1.0	**	SE of Serdo
470	S	24 Sep	18	51	31.00	****	****	**	1.0	**	SE of Serdo
471	S	24 Sep	18	52	33.76	****	****	**	1.0	**	SE of Serdo
472	S	24 Sep	18	53	19.85	****	****	**	1.7	**	SE of Serdo
473	SD	24 Sep	18	54	7.25	11.8666	41.5298	**	2.1	**	SE of Serdo
474	S	24 Sep	18	54	42.55	****	****	**	0.9	**	SE of Serdo
475	S	24 Sep	18	55	10.03	****	****	**	1.5	**	SE of Serdo
476	SD	24 Sep	18	56	8.94	11.9256	41.2149	**	2.1	**	Kurub Area
477	SD	24 Sep	18	58	43.83	11.8810	41.5551	**	1.2	**	SE of Serdo
478	S	24 Sep	18	58	59.60	****	****	**	1.4	**	SE of Serdo
479	TS	24 Sep	19	36	25.77	11.8462	41.5166	**	2.0	**	SE of Serdo
480	TS	24 Sep	20	10	25.47	11.8518	41.5062	**	1.8	**	SE of Serdo
481	MTSD	24 Sep	20	25	51.74	11.8689	41.5093	0.0	2.9	2.4	SE of Serdo
482	S	24 Sep	20	33	19.63	****	****	**	1.9	**	SE of Serdo
483	S	24 Sep	20	46	17.30	****	****	**	1.5	**	SE of Serdo
484	S	24 Sep	20	53	46.03	****	****	**	1.2	**	Kurub Area
485	S	24 Sep	20	54	12.82	****	****	**	0.9	**	Kurub Area
486	S	24 Sep	20	54	32.97	****	****	**	0.9	**	Kurub Area
487	S	24 Sep	21	7	34.55	****	****	**	1.4	**	SE of Serdo
488+	TD	24 Sep	21	19	53.76	11.9145	41.1046	**	2.0	**	Kurub Area
489	M	24 Sep	23	55	47.76	****	****	**	1.0	**	NW Tendaho Graben
490+	TS	25 Sep	0	54	36.71	11.7167	41.4961	**	2.1	**	SE of Serdo
491	S	25 Sep	0	55	39.68	****	****	**	1.4	**	SE of Serdo
492	TSD	25 Sep	1	2	56.64	11.8536	41.5168	**	2.4	**	SE of Serdo
493	S	25 Sep	1	40	46.13	****	****	**	1.3	**	Kurub Area
494	MTSD	25 Sep	1	41	37.43	11.9296	41.2058	1.75	2.8	2.4	Kurub Area
495	MSD	25 Sep	1	42	18.81	11.9317	41.1974	3.0	2.5	2.0	Kurub Area
496	MSD	25 Sep	1	43	50.64	11.9219	41.2159	**	2.3	1.8	Kurub Area
497	S	25 Sep	1	44	53.95	****	****	**	1.4	**	Kurub Area
498	S	25 Sep	1	45	11.96	****	****	**	1.1	**	Kurub Area
499	S	25 Sep	1	45	33.99	****	****	**	1.6	**	Kurub Area
500	SD	25 Sep	1	50	25.33	11.8379	41.4853	**	1.8	**	SE of Serdo
501	SD	25 Sep	3	9	4.73	****	****	**	1.7	**	SE of Serdo
502	SD	25 Sep	5	17	21.18	****	****	**	1.9	**	SE of Serdo
503	MTSD	25 Sep	20	19	26.89	11.9876	41.3616	5.0	2.9	2.5	Within 10 km of Serdo Stn
504	M	26 Sep	19	59	57.38	****	****	**	1.9	**	Waldia Area

APPENDIX 7

CALCULATION OF GAIN OF RECORDING SYSTEM

The overall gain of the seismic recording and playback equipment is derived as follows.

The Willmore Mk II vertical seismometer can be considered to be a pendulating mass on a spring. The mass is constrained by five spokes, with wires at either end which form frictionless pivots. It has six degrees of freedom (3 translational, 3 rotational), and the five constraining spokes are so arranged that the remaining component of motion is predominantly vertical. With the seismometer correctly set up the spokes are all horizontal at the equilibrium position. When the mass is vertically displaced it rotates about its own axis, introducing an additional inertial component into the motion, but this can be neglected for small displacements.

In the steady state the spring supports the mass, M (Figure A7.1). Let $u = f(t)$ be the upward vertical component of ground displacement, and $x(t)$ the extension of the spring. Resolving vertically,

$$Z = bx + D\dot{x} \qquad \text{(A7.1)}$$

where

Z = the upward vertical component of the resultant force exerted on the pendulum,

b = spring constant,

D = damping coefficient (damping assumed proportional to pendulum velocity, $\dot{x}$).

FIGURE A7.1

DIAGRAMMATIC REPRESENTATION OF SEISMOMETER

AS A MASS ON A SPRING

(one constraining spoke shown)

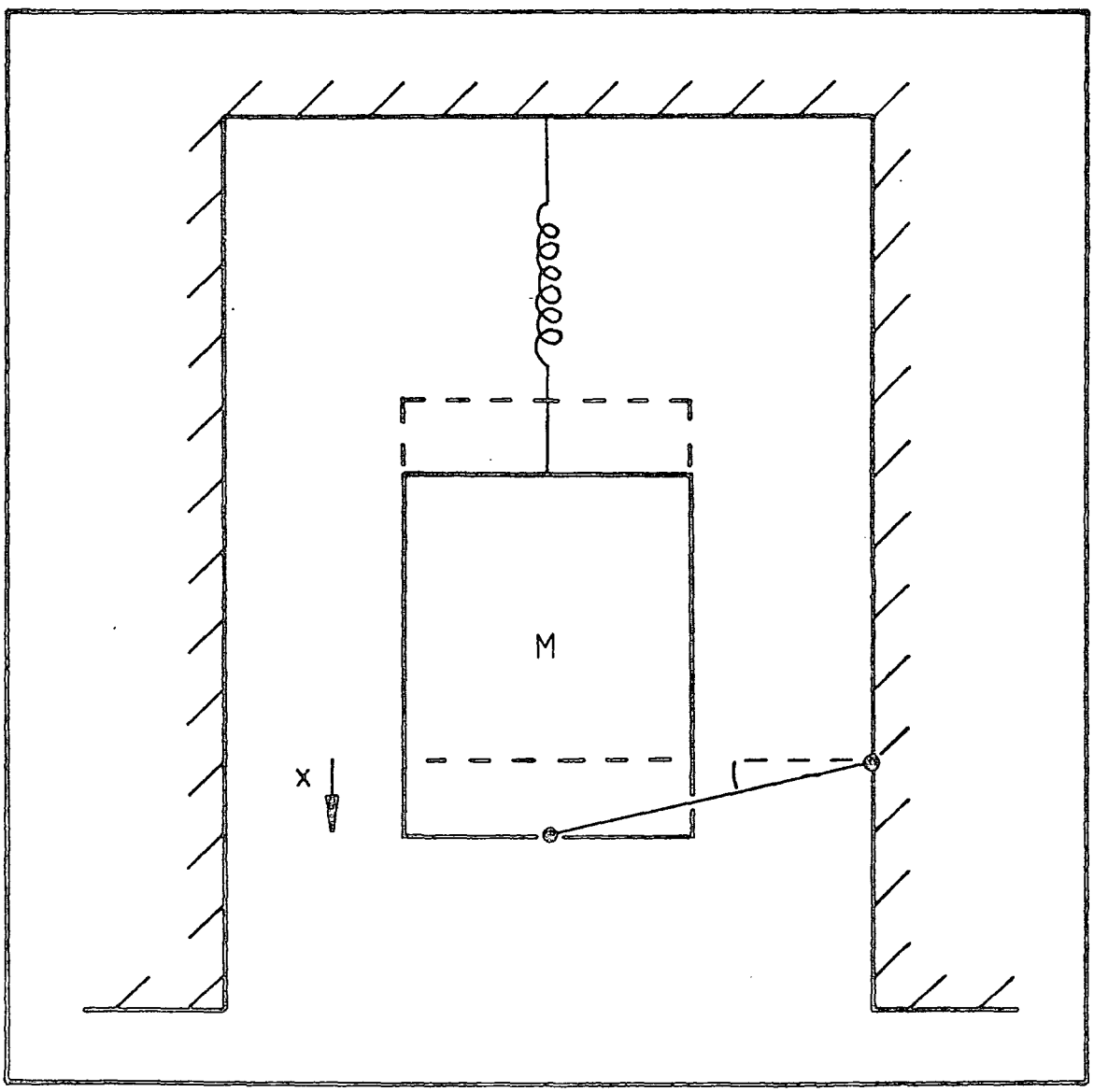

This results in an acceleration in the vertical frame of $(\ddot{u} - \ddot{x})$, whence according to Newton's second law

$$M(\ddot{u} - \ddot{x}) = Z \qquad (A7.2)$$

Eliminating Z from Equations A7.1 and A7.2,

$$\ddot{x} + DM\dot{x} + (b/M)x = \ddot{u} \qquad (A7.3)$$

which is of the same form as the indicator equation

$$\ddot{x} + 2\lambda w\dot{x} + w^2x = \ddot{u} \qquad (A7.4)$$

with

$$w^2 = b/M, \qquad (A7.5)$$

where w = the angular frequency of undamped oscillations.

The seismometer is calibrated by applying a current i, causing a force Ki, where K is the motor constant of the seismometer. This results in a steady-state extension of the spring, x_o, given by

$$Ki = bx_o \qquad (A7.6)$$

Removal of the calibration current, say at time t = Ø, may be regarded as equivalent to a step in ground displacement of $u_o = x_o$.

For $t > Ø$, $\ddot{u} = Ø$ and Equation A7.4 becomes

$$\ddot{x} + 2\lambda w\dot{x} + w^2x = Ø \qquad (A7.7)$$

with solutions of the form

$$x = \exp(-w\lambda t)[X\cos(w't) + Y\sin(w't)], \qquad (A7.8)$$

where w' is the angular frequency of oscillations, given by

$$w' = w(1-\lambda^2)^{1/2}$$

and X, Y are constants. Note that in the overdamped case, where $\lambda > 1$, w' is imaginary, and the motion is purely exponential decay.

Subject to the boundary conditions

$$x = x_o \text{ at } t = \emptyset$$

and $\dot{x} = \emptyset$ at $t = \emptyset$,

$$\left.\begin{aligned} X &= x_o \\ Y &= w\lambda x_o/w' = \lambda x_o/(1-\lambda^2)^{1/2} \end{aligned}\right\} \quad (A7.9)$$

Within the pass band of the recorder-playback system the trace amplitude, A, is approximately proportional to the seismometer E.M.F., which is in turn proportional to the rate of change of x. Thus we may write

$$A = G\dot{x}, \quad (A7.10)$$

where G is the overall system gain.

Differentiating Equation A7.8, and substituting from Equations A7.5 and A7.6, gives

$$\dot{x} = (Ki/w'M)\exp(-\lambda wt)\sin(w't) \quad (A7.11)$$

We now consider the peak trace amplitude, corresponding to the peak velocity. The time, t_p, when peak velocity is attained is determined by differentiating Equation A7.11 and putting the result equal to zero. This gives

$$t_p = (1/w')\cos^{-1}\lambda \quad (A7.12)$$

Substituting into Equation A7.11 gives the peak velocity

$$\dot{x}_p = (Ki/w'M)\exp[(-\lambda w/w')\cos^{-1}\lambda]\sin(\cos^{-1}\lambda)$$

$$= (Ki/wM)\exp[-\lambda\cos^{-1}\lambda/(1-\lambda^2)^{1/2}]$$

$$\therefore G = (A_p wM/Ki)\exp[\lambda\cos^{-1}\lambda/(1-\lambda^2)^{1/2}] \quad (A7.13)$$

Assuming negligible distortion due to recording and playback, the calibration pulse trace follows the form of Equation A7.8, sketched in Figure A7.2. Values for w' and λ may be obtained from measurements made on the calibration curves.

Consider Equation A7.11. Maxima and minima occur when

FIGURE A7.2

OSCILLATIONS OF UNDER-DAMPED SEISMOMETER

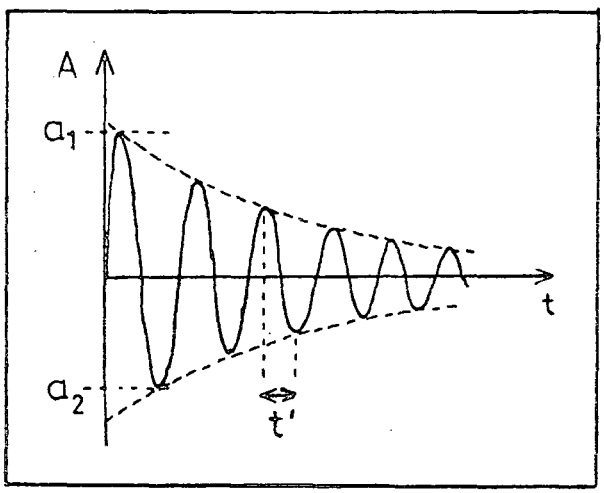

$$\log_e(a_1/a_2) = \pi\lambda/(1-\lambda^2)^{1/2}$$

$$t' = \pi / w(1-\lambda^2)^{1/2}$$

$\dot{x} = 0$, whence for peak values, denoted by suffix p, it can be shown that

$$\tan(w't_p) = (1-\lambda^2)^{1/2}/\lambda,$$

therefore

$$t_p = (1/w')\tan^{-1}(w'/w\lambda) + n\pi/w'$$

The cross-over points ($x = 0$) occur when $w't = n\pi$ (from Equation A7.11)

i.e. at time intervals

$$t' = \pi/w' = \pi/[w(1-\lambda^2)^{1/2}] \qquad (A7.15)$$

It is also easily shown from Figure A7.2 and Equations A7.8 or A7.11 that the damping coefficient, λ, is related to the ratio, $r = a_1/a_2$, of successive swings of the seismograph by

$$\log_e r = \log_e(a_1/a_2) = \pi\lambda/(1-\lambda^2)^{1/2} \qquad (A7.16)$$

In fact the seismometers were only just under-damped, so that the amplitude of the calibration pulse is very small after the first half cycle and r and t' can only be approximately measured. Values of λ calculated from typical measurements using Equation A7.16 were about 0.7.

The natural (undamped) seismometer periods were set and checked in the field as 1.0 s, giving a value for w of $2\pi s^{-1}$. Thus $t' \approx 0.7$ s and $t_p \approx 0.175$ s, from Equations A7.15 and A7.14 respectively. These values are in good agreement with measurements.

The calibration current, i, is calculated from the input circuitry, shown in Figure A7.3a. R_C is the seismometer coil resistance. Combining R_A, R_D and R_C to form an equivalent resistance, R_E, as in Figure A7.3b, the

FIGURE A7.3

INPUT CIRCUITRY, DURHAM SEISMIC RECORDING EQUIPMENT

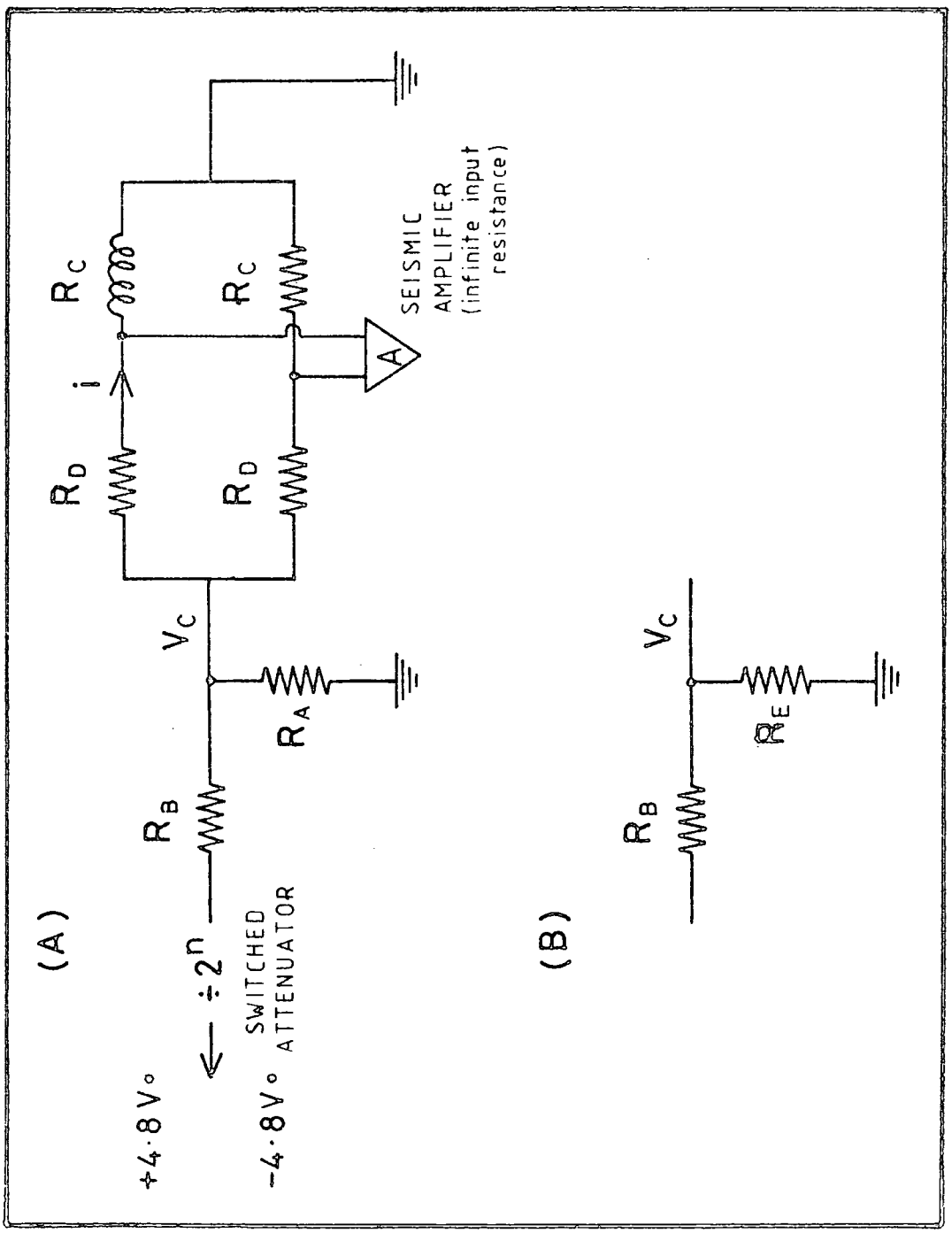

following equations result immediately:

$$1/R_E = 1/R_A + 2/(R_D + R_C)$$

$$V_C = 4.8R_E/G'(R_B + R_E) \text{ (volts)}$$

$$i = V_C/(R_D + R_E) \text{ (amps)}$$

where G' is the nominal gain of the recorder amplifier, equal to 12800 in this study.

The resistances used were:

$R_A = 6.8\ K\Omega$ $R_C = 3.3\ K\Omega$

$R_B = 100\ K\Omega$ $R_D = 3.0\ K\Omega$,

whence

$$i = 1.25*10^{-7}\ A$$

The jet pen oscillograph channels were normally adjusted so that the maximum trace amplitude, A_p, was 3 cm.

The remaining unknowns in Equation A7.13 are given in the Willmore MkII handbook (HILGER and WATTS,1964) as

$M = 4750\ g$

$K = 5.7\ V\ cm^{-1}\ s = 5.7*10^2\ N\ amp^{-1}$

Accepting these values, which could not conveniently be checked, the calculated result for the overall system gain is

$$G = 2.74*10^4\ s$$

In view of the approximations mentioned above, and the uncertainty of some numerical quantities, this figure is considered to have a possible error of a factor of two.

APPENDIX 8

PROGRAMME MOTION

This programme calculates the azimuth and angle of incidence of a seismic arrival recorded by a three-component set of seismometers. The errors in these quantities are calculated by the method of FISHER (1953). The computations are carried out by SUBROUTINE COVMAT, which constructs the covariance matrix for the three signal components according to the method of MONTALBETTI and KANASEWICH (1970). The main calculations are described in Chapter 6.

The programme has an option to print out for each sample the current values of the signal components, signal/noise ratios, signal rectilinearity, azimuth, angle of incidence, coherence factors and azimuth error due to correlated noise.

INPUT

Unit 2. The digitised seismic signal (unfiltered or frequency band-pass filtered) as stored on 8-track, half-inch magnetic tape. See Appendix 8.

Unit 5. Control information governing movement of the tape. Information concerning each tape file.

```
      IFNO,EVENT,(LC(I),I=1,6),(NP(I),I=1,6),IFILT,
      ISTART,ILEN,IWIN,IWRITE,(COMM(I),I=1.10)
            3X,I2,1X,A4,1X,6I1,1X,6I2,I1,3(I4,1X),I1,3X,10A4
```

IFNO Tape file number to be read.
EVENT Station/event number coding.
LC(I) Channel number on half inch tape to which signal component I corresponds.
I 1 - unfiltered E-W 4 - filtered E-W

2 - unfiltered N-S 5 - filtered N-S
3 - unfiltered V 6 - filtered V

NP(I) Polarity of channel I (normally 1; -1 if reversed)

IFILT If blank, read unfiltered channels. If 1, filtered channels.

ISTART First sample of tape to be read (normally 1).

ILEN Number of samples to be processed.

IWIN Number of samples over which covariance matrix is to be calculated.

IWRITE Flag. Set to 1 if full print-out required. Otherwise leave blank.

COMM(I) Reserved for user comments.

OUTPUT

All output appears on Unit 6, and is explained in the programme listing. Optional output (for IWRITE=1) is written from SUBROUTINE COVMAT, where 'azimuth error' is defined by Equation 6.5.10. Mean values of azimuth and angle of incidence for each event are written from the main programme.

```
>                              PROGRAMME MOTION
>
>
>C      PROGRAMME MOTION    W.G. RIGDEN    FEBRUARY 1980
>C      MOVING WINDOW INTEGRATION VERSION.
>C        **********
>C       THIS PROGRAMME COMPUTES THE AZIMUTH AND ANGLE OF INCIDENCE OF
>C      SEISMIC EVENTS RECORDED ON THREE-COMPONENT SETS ALIGNED
>C      VERT, N-S, E-W.
>C       SIGNAL RECTILINEARITY, COHERENCE FACTORS AND
>C      SIGNAL/NOISE RATIOS MAY ALSO BE PRINTED.
>C
>C      SIGNAL VALUES ARE READ FROM HALF INCH DIGITAL TAPES, ON UNIT 2.
>C       TAPE FORMAT AND READING ROUTINES ARE AS FOR THE AUTHOR'S
>C      PROGRAMME TRANSF.
>C
>C      TAPE FILE DATA ARE READ FROM UNIT 5.
>C      IFNO  FILE NO.          EVENT  EVENT NO.
>C    LC(I) ARE TAPE CHANNEL NOS. TO WHICH SEISMIC CHANNELS CORRESPOND.
>C    NP(I) ARE SEISMIC CHANNEL POLARITIES (+1 OR -1).
>C      IFILT=0, READ UNFILTERED CHS.; =1, READ FILTERED CHANNELS
>C      ISTART  STARTING SAMPLE.      ILEN SAMPLES ARE PROCESSED
>C      IWIN  WINDOW LENGTH FOR COMPUTING COVARIANCE MATRIX
>C        I=1,2,3   (E-W), (N-S), VERT COMPONENTS
>C    COMM(10) IS PROVIDED FOR USER COMMENTS.
>C
>C        **********
>      DIMENSION COMM(10), IS(3,300), LC(6), NP(6)
>      INTEGER*2 JIM(256), LEN
>      PI = 4.0 * ATAN(1.0)
>      RTOD = 180.0 / PI
>      WRITE (6,10)
>   10 FORMAT (2X, '**********PROGRAMME MOTION (FEB 1980)**********')
>C
>C        **********
>C   POSITION TAPE AT START OF FIRST DATA FILE.
>C   N.B. TAPE FORMAT AND READING ROUTINES ARE DESCRIBED ELSEWHERE
>      LEN = 8
>      CALL CNTRL('POSN=*2*', LEN, 2)
>      LEN = 3
>      JFNO = 1
>C
>C        **********
>C   READ TAPE FILE DATA
>   20 READ (5,30,END=220) IFNO, EVENT, (LC(I),I=1,6), (NP(I),I=1,6),
>     1IFILT, ISTART, ILEN, IWIN, IWRITE, (COMM(I),I=1,10)
>   30 FORMAT (3X, I2, 1X, A4, 1X, 6I1, 1X, 6I2, I1, 3(I4,1X), I1, 3X,
>     1       10A4)
>      WRITE (6,40) EVENT, IFNO, IWIN, ISTART, ILEN, (LC(I),I=1,6),
>     1(NP(I),I=1,6), (COMM(I),I=1,10)
>   40 FORMAT (1H1, 1X, 'EVENT ', A4, ',   FILE ', I3, ',   WINDOW', I3,
>     1       ',   STARTING SAMPLE', I4, ',   LENGTH ', I4//'UNFILTERED C
>     2HANNELS:  E ON ', I1, ',   N ON ', I1, ',   V ON ', I1/'   FILTERE
>     3D CHANNELS:  E ON ', I1, ',   N ON ', I1, ',   V ON ', I1/10X, 'PO
>     4LARITIES: UNFILTERED', 3(1X,I2), ', FILTERED', 3(1X,I2)/2X, 11A4)
>      IF (IFILT .NE. 1) WRITE (6,50)
>   50 FORMAT (3X, 'USING UNFILTERED CHANNELS'/)
>      IF (IFILT .EQ. 1) WRITE (6,60)
>   60 FORMAT (3X, 'USING FILTERED CHANNELS'/)
>      IF = 3.0 * IFILT
>C
>C        **********
>C   POSITION TAPE AT START OF REQUIRED FILE
>   70 M = 0
>   80 IF (IFNO - JFNO) 90, 110, 100
>   90 CALL CNTRL('BSF', LEN, 2)
>      JFNO = JFNO - 1
>      GO TO 70
>  100 CALL CNTRL('FSF', LEN, 2)
>      JFNO = JFNO + 1
>      M = 1
>      GO TO 80
#
```

```
> 110 IF (M .EQ. 1) GO TO 120
>     CALL CNTRL('BSF', LEN, 2)
>     CALL CNTRL('FSF', LEN, 2)
> 120 NBLK = 0
>     NSAM = 0
>     L = 1
>C
>C       **********
>C  READ REQUIRED FILE, CORRECTING POLARITY IF NECESSARY
> 130 READ (2,140,END=170) (JIM(I),I=1,256)
> 140 FORMAT (128A2/, 128A2)
>     NBLK = NBLK + 1
>     K = 2
>     IF (NBLK .EQ. 1) K = 42
>     DO 160 IK = K, 255, 8
>       NSAM = NSAM + 1
>       IF (NSAM .LT. ISTART) GO TO 160
>       DO 150 I = 1, 3
>         ILC = LC(I + IF)
>         IS(I,L) = JIM(ILC + IK - 1)
> 150   IF (NP(I + IF) .EQ. - 1) IS(I,L) = -IS(I,L)
>       IF (L .EQ. ILEN) GO TO 190
>       L = L + 1
> 160 CONTINUE
>     GO TO 130
> 170 WRITE (6,180) L
> 180 FORMAT (2X, 'END OF TAPE FILE AFTER ', I4, ' SAMPLES')
>C
>C       **********
>C     CALCULATE AZIMUTH AND ANGLE OF INCIDENCE
> 190 CALL COVMAT(ILEN, IWIN, IWRITE, IS, THETA, AI, DTH, DAI)
>     IF (THETA .EQ. 999.9) GO TO 20
>C
>C       **********
>C     PRINT AZIMUTH AND ANGLE OF INCIDENCE, AS RETURNED FROM COVMAT
>     WRITE (6,200) EVENT, THETA, DTH, AI, DAI
> 200 FORMAT (1H , 2X, 'EVENT ', A4, 1X, 'AZIMUTH:  ', F5.1, ' +/- ',
>    1       F5.1/3X, 'ANGLE OF INCIDENCE:  ', F5.1, ' +/- ', F5.1)
> 210 FORMAT (2(1X,I4,2X,F6.3,3(1X,F6.2),2(1X,F6.1),3X), I6)
>     GO TO 20
> 220 STOP
>     END
>C
>C       ************************************************************
>C        SUBROUTINE  COVMAT
>C
>C     THE SUBROUTINE DETERMINES THE AZIMUTH, THETA, AND THE DIP, AI, OF
>C     THE FIRST (P-WAVE) ARRIVAL OF AN EVENT AT THE RECORDING STATION.
>C     THE METHOD OF MONTALBETTI AND KANASEWICH(1970) IS USED.
>C     THE COVARIANCE MATRIX IS CONSTRUCTED AND THE RECTILINEARITY
>C     OF THE SIGNAL IS ESTIMATED FROM THE RATIO OF THE MAXIMUM
>C     AND INTERMEDIATE EIGENVALUES. THE DIRECTION OF THE WAVE(IF IT
>C     IS SUFFICIENTLY RECTILINEAR) IS GIVEN BY THE
>C     EIGENVECTOR CORRESPONDING TO THE LARGEST EIGENVALUE.
>C      THE ERRORS IN THETA AND AI ARE DETERMINED (USING FISHER
>C     STATISTICS) FROM THE VARIATION IN EIGENVALUES OVER A
>C     FROM THE VARIATION IN EIGENVECTORS OVER A WINDOW AROUND THE
>C     WINDOW AROUND THE FIRST ARRIVAL.
>C
>C     VARIABLES:
>C     ==========
>C     INPUT TO SUBROUTINE:
>C       LS = LENGTH OF SAMPLE
>C       IS(I,J) = DATA.  I = 1  EAST COMPONENT
>C                        I = 2  NORTH COMPONENT
>C                        I = 3  VERTICAL COMPONENT
>C                        J = 1,LS  SAMPLE NUMBER
>C
>C     OUTPUT OF SUBROUTINE
>C       THETA = AZIMUTH OF FIRST (P) ARRIVAL
>C       DTH = 95% CONFIDENCE INTERVAL FOR THETA
>C       AI = ANGLE OF INCIDENCE OF P ARRIVAL
#
```

```
>C        DAI = 95% CONFIDENCE INTERVAL FOR AI (USING FISHER STATISTICS).
>C
>C        **********
>      SUBROUTINE COVMAT(LS, NWIND, IWRITE, IS, THETA, AI, DTH, DAI)
>      DIMENSION ISUM(3), V(3,3), T(3,3), X(3), EV(3), XEV(3,3), XT(3),
>     1          IS(3,300), ANOIS2(3,3), COH(3,3), SNR(3)
>      PI = 4.0 * ATAN(1.0)
>      RTOD = 180.0 / PI
>C
>C        **********
>C      CALCULATE DC LEVEL
>C      SUBTRACT DC LEVEL FROM SIGNAL
>      DO 20 I = 1, 3
>        ISUM(I) = 0.0
>        XT(I) = 0.0
>        DO 10 J = 1, 100
>          ISUM(I) = ISUM(I) + IS(I,J)
>   10   CONTINUE
>   20 ISUM(I) = ISUM(I) / FLOAT(LS)
>      DO 30 I = 1, 3
>        DO 30 J = 1, LS
>          IS(I,J) = IS(I,J) - ISUM(I)
>   30 CONTINUE
>C      COMPUTE NOISE POWER FOR EACH CHANNEL
>      DO 50 I = 1, 3
>        DO 50 K = 1, 3
>          ANOIS2(I,K) = 0.0
>          DO 40 J = 1, 100
>   40     ANOIS2(I,K) = ANOIS2(I,K) + IS(I,J) * IS(K,J)
>   50 ANOIS2(I,K) = ANOIS2(I,K) / 100.0
>C      WRITE HEADING
>      IF (IWRITE .EQ. 1) WRITE (6,60)
>   60 FORMAT (7X, 'SIGNAL VALUES   SIGNAL/NOISE RATIOS', 19X, 'COHERENCE
>     1 FACTORS AZIMUTH'/'SAMP   E     N     V     E      N      V     RL
>     2  AZIM  AINC  (E,N) (E,V) (N,V) ERROR')
>      LMAX = LS - NWIND
>      ISTART = 0
>      JSUM = 0
>C
>C        **********
>C      FOR EACH SAMPLE, CALCULATE THE COVARIANCE MATRIX
>      DO 170 IL = 101, LMAX
>        IF (IL .GT. 101) GO TO 90
>C      FOR SUBSEQUENT VALUES OF IL, IT IS MORE EFFICIENT
>C      TO COMPUTE V(I,J) BY MOVING WINDOW INTEGRATION.
>C      SET COVARIANCE MATRIX = 0
>        DO 70 I = 1, 3
>          DO 70 J = 1, 3
>   70   V(I,J) = 0.0
>C      CALCULATE COVARIANCE MATRIX OVER A WINDOW NWIND
>        DO 80 K = 1, NWIND
>          DO 80 I = 1, 3
>            DO 80 J = I, 3
>              V(I,J) = V(I,J) + IS(I,IL + K - 1) * IS(J,IL + K - 1)
>              V(J,I) = V(I,J)
>C      CALCULATE SIGNAL/NOISE RATIOS
>C      N.B. THESE ARE NOISE POWER RATIOS
>              SNR(I) = V(I,I) / (ANOIS2(I,I)*NWIND)
>   80   CONTINUE
>        GO TO 110
>   90   DO 100 I = 1, 3
>          DO 100 J = 1, 3
>            V(I,J) = V(I,J) + IS(I,IL + NWIND - 1) * IS(J,IL + NWIND -
>     1      1) - IS(I,IL - 1) * IS(J,IL - 1)
>            V(J,I) = V(I,J)
>  100   CONTINUE
>C      CHECK FOR STARTING CRITERION
>  110   IF (ISTART .NE. 0) GO TO 120
>        CRIT = SNR(3)
>        IF (CRIT .GT. 10.0) ISTART = IL
>  120   IF (IWRITE .NE. 1) GO TO 130
>C      CALCULATE COHERENCE FUNCTIONS
#
```

```
>        COH(1,2) = V(1,2) / SQRT(V(1,1)*V(2,2))
>        COH(1,3) = V(1,3) / SQRT(V(1,1)*V(3,3))
>        COH(2,3) = V(2,3) / SQRT(V(2,2)*V(3,3))
>C      CALCULATE AZIMUTH ERROR DUE TO NOISE
>        DTHETA = RTOD * NWIND * (V(2,3)*ANOIS2(1,3) + V(1,3)*ANOIS2(2,3)
>     1  ) / (V(2,3)**2 + V(1,3)**2)
>C      DIAGONALISE V
> 130    CALL DIAG(V, XEV, EV)
>        JMAX = 1
>        JINT = 2
>        ELAM1 = ABS(EV(JMAX))
>        ELAM2 = ABS(EV(JINT))
>C      SET X EQUAL TO THE EIGENVECTOR CORRESPONDING TO THE
>C      MAXIMUM EIGENVALUE.
>        DO 140 J = 1, 3
>          X(J) = XEV(J,JMAX)
> 140    CONTINUE
>C      CALCULATE RECTILINEARITY.
>        RL = 1.0 - ELAM2 / ELAM1
>C      CALCULATE AZIMUTH AND DIP FROM EIGENVECTOR X.
>        AI = ARCOS(ABS(X(3))) * RTOD
>        IF (ABS(X(2)) .LT. 1.0E-4*ABS(X(1))) X(2) = ABS(X(1)) * 1.0E-4 *
>     1   SIGN(1.0,X(2))
>        THETA = ATAN2(X(1),X(2)) * RTOD
>        IF (X(3) .LT. 0.0) THETA = THETA + 180.
>        IF (THETA .LT. 0.) THETA = THETA + 360.
>C       PRINT SIGNAL COMPONENTS, SIGNAL/NOISE RATIOS, RECTILINEARITY,
>C      AZIMUTH, ANGLE OF INCIDENCE, COHERENCE FACTORS AND
>C      AZIMUTH ERROR.
>        IF (IWRITE .EQ. 1) WRITE (6,150) IL, (IS(I,IL),I=1,3),
>     1  (SNR(I),I=1,3), RL, THETA, AI, COH(1,2), COH(1,3), COH(2,3),
>     2  DTHETA
> 150    FORMAT (I4, 3(1X,I4), 2X, 3(F6.2,1X), 1X, F4.2, 1X, 2(1X,F5.1),
>     1          1X, 3(1X,F5.2), 1X, F5.1)
>C      CALCULATE MEAN AZIMUTH AND DIP FOR FIRST ARRIVAL
>        IF (ISTART .EQ. 0) GO TO 170
>        IF (RL .LT. 0.85) GO TO 170
>        IF (IL .GT. (ISTART + 2.0*NWIND)) GO TO 170
>        JSUM = JSUM + 1
>        DO 160 I = 1, 3
>          XT(I) = XT(I) + X(I)
> 160    CONTINUE
> 170 CONTINUE
>C
>C         **********
>      IF (IWRITE .EQ. 1) WRITE (6,180) JSUM, ISTART
> 180 FORMAT (1H , 2X, 'STATISTICS BASED ON ', I2, ' VALUES'/3X, 'STARTI
>     1NG SAMPLE ', I3)
>      IF (JSUM .EQ. 0) GO TO 190
>      IF (ABS(XT(2)) .LT. 1.0E-4*ABS(XT(1))) XT(2) = ABS(XT(1)) * 1.
>     10E-4 * SIGN(1.0,XT(2))
>      AI = ARCOS(ABS(XT(3))/FLOAT(JSUM)) * RTOD
>      THETA = ATAN2(XT(1),XT(2)) * RTOD
>      IF (XT(3) .LT. 0.0) THETA = THETA + 180.0
>      IF (THETA .LT. 0.0) THETA = THETA + 360.0
>C      CALCULATE DEVIATION OF AZIMUTH AND INCLINATION USING
>C      FISHER STATISTICS.
>      RR = SQRT(XT(1)**2 + XT(2)**2 + XT(3)**2)
>      ALPHA = 140.0
>      IF (JSUM .GT. 1.0) ALPHA = 140.0 * SQRT((JSUM - RR)/FLOAT(JSUM*(
>     1JSUM - 1)))
>      DAI = ALPHA
>      DTH = ALPHA / SIN(AI/RTOD)
>C      CONVERT MEASURED ANGLE OF INCIDENCE OF P WAVE TO TRUE ANGLE OF
>C      INCIDENCE (SEE WHITE(1964), GEOPHYSICS 29 P288).
>      AI2 = SIN(AI/2.0/RTOD)
>      IF (AI2*1.73 .GT. 1) AI2 = 1 / 1.73
>      AI = ARSIN(AI2*1.73) * RTOD
>      RETURN
> 190 WRITE (6,200)
> 200 FORMAT (2X, 'RECORDS NOT RECTILINEAR')
>      THETA = 999.9
#
```

```
>      RETURN
>      END
>C
>C        ****************************************************************
>C         SUBROUTINE  DIAG
>C
>C      SUBROUTINE DIAG DIAGONALISES THE SYMMETRIC 3*3 MATRIX A.
>C      IT RETURNS THE EIGENVALUES IN THE VECTOR EV, AND THE 3
>C      EIGENVECTORS IN THE ARRAY V, WHERE THE J'TH COLUMN IS THE
>C      EIGENVECTOR CORRESPONDING TO THE J'TH EIGENVALUE.
>C      THE JACOBI METHOD OF SUCCESIVE ROTATION ISUSED. FOR REFERENCE SEE
>C      WILKINSON AND REINSCH, 1971 "HANDBOOK FOR AUTOMATIC COMPUTATION,
>C      VOLUME II".
>C
>C          **********
>      SUBROUTINE DIAG(A, V, D)
>      DIMENSION A(3,3), V(3,3), B(3), D(3), Z(3)
>      INTEGER P, Q, P1
>      DO 10 P = 1, 3
>        DO 10 Q = 1, 3
>          V(P,Q) = 0.0
>          IF (P .EQ. Q) V(P,Q) = 1.0
>   10 CONTINUE
>      DO 20 P = 1, 3
>        B(P) = A(P,P)
>        D(P) = B(P)
>        Z(P) = 0
>   20 CONTINUE
>      D1 = D(1)
>      D2 = D(2)
>      D3 = D(3)
>      ROT = 0.0
>      DO 130 I = 1, 50
>C      START SWEEP
>        SM = 0.0
>        DO 30 P = 1, 2
>          P1 = P + 1
>          DO 30 Q = P1, 3
>            SM = SM + ABS(A(P,Q))
>   30   CONTINUE
>        IF (SM .EQ. 0) GO TO 140
>        TRESH = 0.0
>        IF (I .LT. 4) TRESH = 0.2 * SM / 9.0
>        DO 110 P = 1, 2
>          P1 = P + 1
>          DO 110 Q = P1, 3
>            G = ABS(A(P,Q)*100.)
>            IF (I .GT. 4 .AND. (ABS(D(P)) + G) .EQ. ABS(D(P)) .AND. (
>     1          ABS(D(Q)) + G) .EQ. ABS(D(Q))) GO TO 100
>            IF (ABS(A(P,Q)) .LE. TRESH) GO TO 100
>C      ROTATE A SO THAT A(P,Q)=0
>            H = D(Q) - D(P)
>            IF ((ABS(H) + G) .NE. ABS(H)) GO TO 40
>            T = A(P,Q) / H
>            GO TO 50
>   40       THETA = 0.5 * H / A(P,Q)
>            T = 1 / (ABS(THETA) + SQRT(1 + THETA**2))
>            IF (THETA .LT. 0.0) T = -T
>   50       CONTINUE
>            C = 1 / SQRT(1 + T*T)
>            S = T * C
>            TAU = S / (1 + C)
>            H = T * A(P,Q)
>            Z(P) = Z(P) - H
>            Z(Q) = Z(Q) + H
>            D(P) = D(P) - H
>            D(Q) = D(Q) + H
>            A(P,Q) = 0.0
>            IF (P .EQ. 1) GO TO 60
>            G = A(1,P)
>            H = A(1,Q)
>            A(1,P) = G - S * (H + G*TAU)
#
```

```
>            A(1,Q) = H + S * (G - H*TAU)
>            GO TO 80
>  60        IF (P .EQ. 2 .OR. Q .EQ. 2) GO TO 70
>            G = A(P,2)
>            H = A(2,Q)
>            A(P,2) = G - S * (H + G*TAU)
>            A(2,Q) = H + S * (G - H*TAU)
>            GO TO 80
>  70        IF (Q .EQ. 3) GO TO 80
>            G = A(P,3)
>            H = A(Q,3)
>            A(P,3) = G - S * (H + G*TAU)
>            A(Q,3) = H + S * (G - H*TAU)
>  80        CONTINUE
>            DO 90 J = 1, 3
>              G = V(J,P)
>              H = V(J,Q)
>              V(J,P) = G - S * (H + G*TAU)
>              V(J,Q) = H + S * (G - H*TAU)
>  90        CONTINUE
>            ROT = ROT + 1
>            GO TO 110
> 100        CONTINUE
>            A(P,Q) = 0.0
> 110    CONTINUE
>        DO 120 P = 1, 3
>          B(P) = B(P) + Z(P)
>          D(P) = B(P)
>          Z(P) = 0.0
> 120    CONTINUE
> 130 CONTINUE
>C       ORDER EIGENVALUES SO THAT EV(1)>EV(2)>EV(3).
> 140 KMAX = 1
>     KMIN = 1
>     DO 150 K = 2, 3
>       ADK = ABS(D(K))
>       IF (ADK .GT. ABS(D(KMAX))) KMAX = K
>       IF (ADK .LT. ABS(D(KMIN))) KMIN = K
> 150 CONTINUE
>     DO 160 K = 1, 3
>       KINT = K
>       IF (K .EQ. KMAX .OR. K .EQ. KMIN) GO TO 160
>       GO TO 170
> 160 CONTINUE
> 170 D1 = D(KMAX)
>     D2 = D(KINT)
>     D3 = D(KMIN)
>     D(1) = D1
>     D(2) = D2
>     D(3) = D3
>     DO 190 J = 1, 3
>       DO 180 I = 1, 3
>         B(I) = V(J,I)
> 180   CONTINUE
>       V(J,1) = B(KMAX)
>       V(J,2) = B(KINT)
>       V(J,3) = B(KMIN)
> 190 CONTINUE
>     RETURN
>     END
#
```

APPENDIX 9

PROGRAMME TRANSF

This programme performs fast Fourier transforms using the Cooley-Tukey algorithm (COOLEY and TUKEY, 1965). A number of output options are available, to enable the programme to perform all required operations with the same FFT algorithm. The options are fully described within the programme listing (lines 9-18 and 43-73). All user-supplied input parameters are also explained within the listing.

Programme TRANSF is run with the NUMAC plotting library *PLOTSYS, and contains calls to plotting library subroutines. Examples of plotter output are shown in Figures 7.5.2, A9.1 and A9.2.

INPUT

Unit 2. The digitised seismic signal as stored on 8-track, half-inch magnetic tape. Relevant comments are in lines 124-138 of the programme listing.

Tapes digitised on the MODULAR 1 consist of continuous strings of samples stored in blocks of 256. Each sample from an 8-track, field-recorded analogue tape is digitised as 8 digits. The format of samples on digital tape is shown in Figure A9.3. Note that the final digit of samples 27+n (n=0,1,2,...) appears as the first digit of the following block. This complicates the tape reading process (lines 240-253). Programme TRANSF positions tapes remotely to the start of the desired files by CNTRL commands (lines

FIGURE A9.1

EXAMPLE OF NORMALISED VELOCITY AMPLITUDE SPECTRUM OBTAINED USING PROGRAMME TRANSF

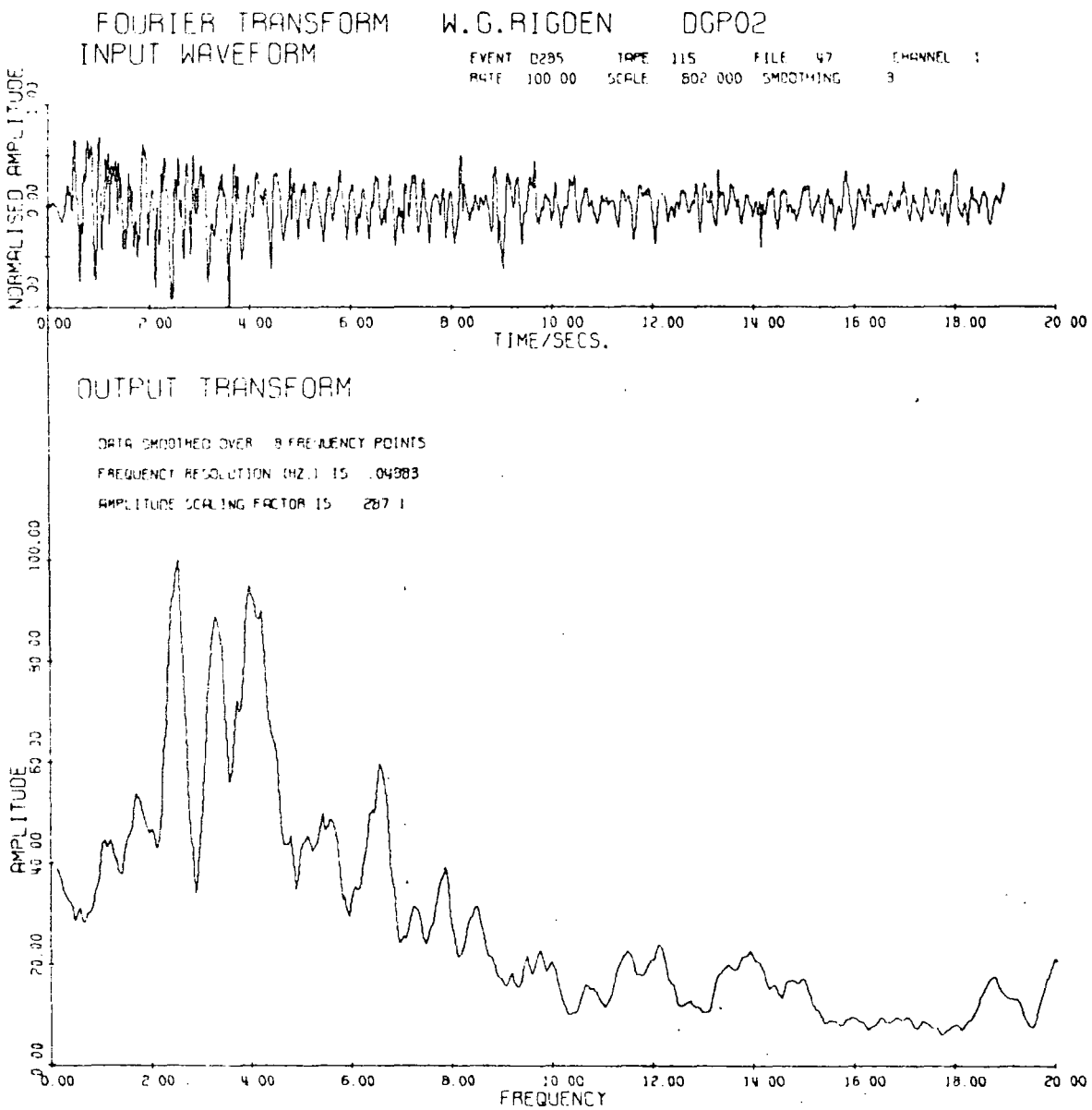

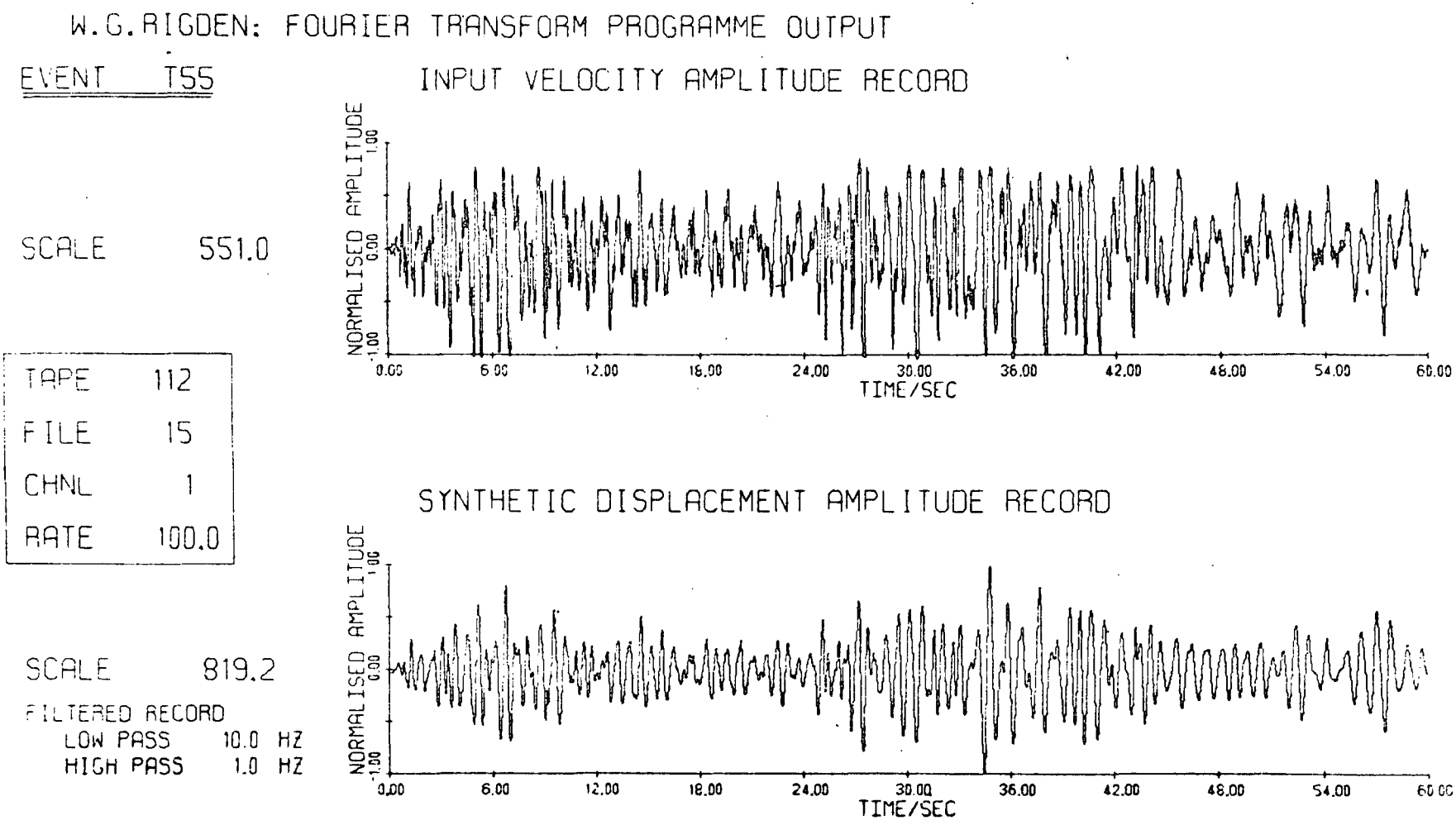

FIGURE A9.2

EXAMPLE OF SYNTHETIC DISPLACEMENT AMPLITUDE RECORD OBTAINED USING PROGRAMME TRANSF

FIGURE A9.3

FORMAT OF MODULAR 1 DIGITAL MAGNETIC TAPE FILES

(modified from ARMOUR, 1977)

BLOCK 1

TRACK NUMBER		DIGIT NUMBER
	TAPE HEADER INFORMATION	1 2 3 41
1 2 3 4 5 6 7 8	1st SAMPLE	42 43 44 45 46 47 48 49
1 2 3 4 5 6 7 8	2nd SAMPLE	50 51 52 53 54 55 56 57
1 2 8		58 59 249
1 2 3 4 5 6 7	27TH SAMPLE	250 251 252 253 254 255 256

BLOCK 2
etc

TRACK NUMBER		DIGIT NUMBER
8		1
1 2 3 4 5 6 7 8	28TH SAMPLE	2 3 4 5 6 7 8 9
1 2 3 4 5 6 7 8	29TH SAMPLE	10 11 12 13 14 15 16 17
1 2 3 4 5 6 7 8	30TH SAMPLE	18 19 20 21 22 23 24 25
1 2 8		26 27 249
1 2 3 4 5 6 7	59TH SAMPLE	250 251 252 253 254 255 256

218-238).

An option exists for reading input data from file on Unit 4, instead of from digital tape. Small data sets can then be accessed without the necessity of having a tape mounted remotely in Newcastle.

Unit 3. Option to read additional data from file. These take the form of other spectra in the frequency domain (comments, lines 382-389). This option is chiefly intended for the removal of noise from velocity amplitude spectra.

```
AIMAX,INOUT,(W(K),K=1,INOUT)    F10.5,5X,I5/(8(3X,F7.2))
```

Unit 4. Option to input digitised seismic signal from file. In this case IFLAG is negative and Unit 2 is not used. This option is explained in lines 35-40.

```
(X(I),I=1,N)                                    8(3X,F7.2)
```

Unit 5. Control data for positioning and reading the magnetic tape, and processing the input seismic signal channels.

One card: programme option controls

```
IWRIT1,IWRIT2,IWRIT3,...IWRIT9,IWRI10          2X,10I1
```

One card: information common to all events to be processed during one run of the programme

```
ITAPE,NFRQSM,FLOG,LATER,NSF,ITAPER,NT,FLOW,FHIGH
 7X,I3,8X,I2,1X,F4.2,4X,I1,1X,I2,6X,I1,7X,I3,2(6X,F4.1)
```

Two cards: titles for plotter display

TLIN(L)/TLOG(L) 20A4/20A4

One card for each input file (10 is a recommended maximum if plotter output is required); or NSF cards if NSF 1.

```
STEV,VC,IFNO,RKM,J,J2,SRATE,NSKIP,TIME,NSKIP2,TIME2
 6X,A4,1X,F4.2,2X,I3,1X,F5.1,2(1X,I1),5X,F5.2,6X,I4,5X,
                                    F5.2,6X,I4,5X,F5.2
```

OUTPUT

Unit 6. All printed output is normally routed here.

Unit 7. The FFT frequency spectrum may be output here in a condensed format, for temporary storage and later re-input from Unit 3 during subsequent programme runs.

Unit 9. Outputs a standard plotfile for *PLOTSYS.

```
>                          PROGRAMME TRANSF
>
>
>C      PROGRAMME TRANSF     W.G.RIGDEN
>C      NEW VERSION OF FAST FOURIER TRANSFORM PROGRAMME, JUNE 1980
>C        **********
>C      THIS PROGRAMME WILL CARRY OUT A NUMBER OF OPERATIONS INVOLVING
>C      THE FAST FOURIER TRANSFORMATION (USING THE COOLEY-TUKEY ALGORITHM)
>C      OF A SEISMIC RECORD INPUT FROM DIGITAL TAPE (I/O DEVICE 2) OR
>C      FROM AN EXTERNAL DATA FILE (I/O DEVICE 4).
>C        **********
>C      OUTPUT OPTIONS ARE:
>C      (1)  DISPLACEMENT, VELOCITY OR ACCELERATION AMPLITUDE SPECTRUM
>C        IN THE FREQUENCY DOMAIN.
>C      (2)  VELOCITY PHASE SPECTRUM.
>C      (3)  SYNTHETIC DISPLACEMENT, VELOCITY OR ACCELERATION SEISMIC
>C        RECORDS OBTAINED FOLLOWING INVERSE FOURIER TRANSFORMATION,
>C        WITH OR WITHOUT BAND PASS FILTERING.
>C      (4)  DIVISION OF ONE SPECIFIED FOURIER TRANSFORMED SEISMIC CHANNEL
>C        BY ANOTHER, WITH OUTPUT GIVING CRUSTAL TRANSFER RATIO.
>C      (5)  PRINT-OUT OF VELOCITY AMPLITUDE, PHASE AND ENERGY SPECTRA.
>C        **********
>C      OUTPUT IS ROUTED TO THE I.B.M. 11-INCH PLOTTER.  SUBROUTINES
>C      NEWSMO AND LOGSMO ALLOW SMOOTHING OF THE TRANSFORMED DATA.
>C      SUBROUTINE BASE CORRECTS THE INPUT DATA TO MEAN BASELINE, AND
>C      SUBROUTINE TAPER PERMITS COSINE WINDOW TAPERING OF THE INPUT
>C      WAVEFORM.  SUBROUTINE COOL IS SUBSTANTIALLY THE SUBROUTINE
>C      WRITTEN BY I.MACLEOD, DEPT. OF PHYSICS, A.N.U.  AN ALTERNATIVE
>C      FFT ROUTINE, WRITTEN BY W.G.RIGDEN, IS ALSO AVAILABLE.
>C        **********
>C        **********
>C        **********
>C      DATA INPUT
>C        **********
>C      READ UP TO 10 INFORMATION CARDS.
>C        INFORMATION SHOULD BE WRITTEN IN COLUMNS 4 TO 80.  TERMINATE
>C        FINAL INFORMATION CARD BY WRITING IFLAG>0 IN COLUMN 3.
>C      N.B. IF IFLAG<0 DATA WILL BE READ FROM I/O DEVICE 4 INSTEAD
>C      OF FROM MAGNETIC TAPE.  THIS OPTION IS INTENDED CHIEFLY FOR
>C      TESTING PURPOSES AND THEREFORE HAS APPARENT PECULIARITIES.
>C      THE NUMBER OF SAMPLES READ IN ON I/O 4 IS FIXED AT 1040,
>C      WHEREAS THE NUMBER ACTUALLY PROCESSED IS STILL CONTROLLED
>C      BY I/O 5 (BUT CLEARLY CANNOT EXCEED 1040).
>     CONTINUE
>C
>C      READ IWRIT-VALUES.  THESE CONTROL PROGRAMME OPTIONS.  THEY SHOULD
>C      BE SET TO 1 IF CORRESPONDING ROUTINE IS REQUIRED.  OTHERWISE LEAVE
>C      BLANK.
>C        IWRIT1     PRINT EVENT AND DIGITAL TAPE DATA.
>C        IWRIT2     PRINT INPUT DATA.    )    WARNING: THESE
>C        IWRIT3     PRINT OUTPUT DATA.   )    MAY BE LENGTHY
>C        IWRIT4     WRITE FILE NUMBER AT WHICH DIGITAL TAPE IS POSITIONED.
>C        IWRIT5     CORRECT DATA TO MEAN BASELINE (SUBROUTINE BASE).
>C        IWRIT6     CORRECT SPECTRUM (E.G.FOR MEAN CRUSTAL RESPONSE)
>C           IF IWRIT6=1 (2), SPECTRAL OUTPUT IS DIVIDED (SUBTRACTED)
>C           BY SPECTRUM READ IN FROM I/O DEVICE 3 (FORMAT STMT. 300).
>C        IWRIT7     OUTPUT AMPLITUDE DATA TO I/O DEVICE 7, FOR USE
>C           AS INPUT FOR OTHER FOURIER ROUTINES.
>C        IWRIT8     OVERRIDE SPECIFIED VALUE OF 'NFRQSM'.  IN THIS CASE
>C           DATA ARE AUTOMATICALLY SMOOTHED SO AS TO GIVE STANDARD
>C           OUTPUT FREQUENCY RESOLUTION.
>C        IWRIT9     PLOT INPUT WAVEFORM WITH AMPLITUDE SPECTRUM.
>C         IWRI10     CONTROLS FORM OF PLOTTED OUTPUT.  AVAILABLE OPTIONS
>C      ARE:
>C           IWRI10=0 TO 3: OUTPUT IN FREQUENCY DOMAIN,
>C           0  VELOCITY PHASE SPECTRUM
>C           1  VELOCITY AMPLITUDE SPECTRUM (LINEAR PLOT).
>C           2  DISPLACEMENT AMPLITUDE SPECTRUM (LOG-LOG PLOT).
>C           3  ACCELERATION AMPLITUDE SPECTRUM (LOG-LOG PLOT).
>C           IWRI10=4 TO 6: OUTPUT IN TIME DOMAIN AFTER INVERSE FFT,
>C           4  SYNTHETIC DISPLACEMENT AMPLITUDE RECORD.
>C           5  SYNTHETIC VELOCITY AMPLITUDE RECORD.
#
```

```
>C          6  SYNTHETIC ACCELERATION AMPLITUDE RECORD.
>C          OTHER OPTIONS,
>C          8  NO PLOTTER OUTPUT.
>C          9  CRUSTAL TRANSFORM RATIO.
>C
>      CONTINUE
>C      READ CARD HAVING:-
>C          ITAPE   MAGNETIC TAPE FROM WHICH FILES ARE TO BE READ
>C        NFRQSM    NO. OF FREQUENCY POINTS OVER WHICH TRANSFORMED DATA IS
>C            TO BE SMOOTHED.  WRITE 0 IF SMOOTHING NOT REQUIRED.
>C          FLOG    LOGARITHMIC SMOOTHING FACTOR.
>C         LATER    IF LATER=1, 'NSKIP' AND 'TIME' ARE REPLACED BY 'NSKIP2'
>C            AND 'NTIME2', CORRESPONDING TO ONSETS FARTHER DOWN MAGNETIC
>C            TAPE FILE RECORD.
>C           NSF    THIS IS AN IMPORTANT PARAMETER.  IF NSF>1,
>C            PROGRAMME SUMS NSF TRANSFORMED VELOCITY AMPLITUDES,
>C            TAKES THEIR MEAN AND PLOTS THE RESULTANT AVERAGE
>C            SPECTRUM, AFTER WHICH IT TERMINATES.  THIS OPTION
>C            IS ONLY AVAILABLE FOR VELOCITY AMPLITUDE IN THIS
>C            VERSION OF THE PROGRAMME, AND WILL TREAT A MAXIMUM
>C            OF 1024 INPUT SAMPLES.  NOTE THAT SOME OF THE
>C            'IWRITN' PROGRAMME OPTIONS ARE AUTOMATICALLY OVERRIDEN.
>C        ITAPER    COSINE TAPERING OPTION:-
>C            IF ITAPER=1, DATA IS TAPERED AT BOTH ENDS
>C            IF ITAPER=2, DATA IS FRONT TAPERED
>C            IF ITAPER=3, DATA IS END TAPERED
>C            IF ITAPER=0, DATA IS NOT TAPERED
>C            NT    NO. OF SAMPLES TO BE COSINE TAPERED.
>C          FLOW    HIGH PASS FREQUENCY LIMIT FOR BAND PASS FILTERING
>C            APPLIED.
>C            BEFORE TAKING INVERSE FOURIER TRANSFORM.  WHEN SYNTHETIC
>C            DISPLACEMENT RECORD IS TO BE PLOTTED, DEFAULT VALUE IS
>C            0.5 HZ.
>C         FHIGH    LOW PASS FREQUENCY LIMIT FOR BAND PASS FILTERING.
>C
>C      READ 2 CARDS HAVING TITLES FOR PLOTTER DISPLAY:-
>C        TLIN(L)    TITLE FOR OUTPUT FROM SUBROUTINE OPLOT.
>C        TLOG(L)    TITLE FOR OUTPUT FROM SUBROUTINE OLGPLT.
>C
>C      READ CARD HAVING:-
>C          STEV    STATION AND EVENT NUMBER IDENTIFIER.
>C            VC    SEISMIC WAVE VELOCITY (KM/SEC).
>C          IFNO    TAPE FILE TO BE READ.
>C           RKM    DISTANCE OF EVENT (KM).
>C             J    TAPE CHANNEL TO BE READ.
>C            J2    SECOND TAPE CHANNEL TO BE READ.  THIS IS THE
>C            DIVIDEND IN THE CRUSTAL TRANSFER RATIO OPTION.
>C         SRATE    SAMPLING RATE (SAMPLES/SEC.).
>C         NSKIP    NO. OF SAMPLES TO BE NEGLECTED AT START OF RECORD.
>C          TIME    LENGTH OF RECORD TO BE TRANSFORMED (SEC.).
>C      N.B. VC, RKM ARE NOT REQUIRED UNLESS IWRI10=1 OR 3.
>C      N.B. NSKIP2, TIME2 REPLACE NSKIP, TIME IF LATER=1.
>      CONTINUE
>C        **********
>C      READ DIGITAL TAPE:-
>C          THE FIRST 41 SAMPLES OF THE FIRST BLOCK OF EACH DIGITAL TAPE
>C        ARE TAPE HEADER INFORMATION.  THEY ARE IGNORED.  ON SUBSEQUENT
>C        BLOCKS, THE FIRST SAMPLE OF THE FIRST CHANNEL OCCURS IN POSN. 2.
>C          EACH SAMPLE OF EVERY BLOCK IS READ INTO 'JIM'.  EACH SAMPLE
>C        OF THE SELECTED DATA CHANNEL (J) IS TRANSFERRED FROM 'JIM' TO
>C        'X', EXCEPTING THE FIRST 'NSKIP' SAMPLES WHICH ARE NEGLECTED.
>C        THUS THE R-TH REQUIRED SAMPLE IS READ INTO X(R).
>C
>C          AMAX, A2MAX ARE SCALING FACTORS USED IN PLOTTING SUBROUTINES.
>C
>C          'CALL CNTRL' ROUTINES CAUSE DIGITAL TAPE TO BE WOUND FORWARD
>C        OR BACKWARD TO NEXT TAPE FILE FROM WHICH DATA ARE REQUIRED.
>C        TAPE IS INITIALLY POSITIONED AT START OF FILE 1, WHICH CONTAINS
>C        TAPE INITIALISING DATA ONLY.
>C        **********
>      COMPLEX CS, CS2, CDI
>      DIMENSION X(16400), CS(16400), FREQ(8200), AMP(8200), ENERGY(8200)
#
```

```
>      DIMENSION PHASE(8200), ACC(8200), DIS(8200), W(8200), SAMP(8200)
>      DIMENSION RT(4), X2(16400), CS2(16400), AMP2(8200), RATIO(8200)
>      DIMENSION EDISX(8200), TLIN(20), TLOG(20), DI(4), VE(4), AC(4)
>      DIMENSION PH(4), BL(4)
>      INTEGER*2 JIM(256), LEN
>      PI = 4.0 * ATAN(1.0)
>      RTOD = 180.0 / PI
>      KNS = 0
>      DO 10 I = 1, 1024
>   10 SAMP(I) = 0.0
>      SAMAX = 0.0
>C        **********
>C       POSITION TAPE AT START OF FIRST FILE
>      LEN = 3
>      CALL CNTRL('REW', LEN, 2)
>C        **********
>C       READ INFORMATION CARDS AND PROGRAMME OPTIONS
>      WRITE (6,20)
>   20 FORMAT (1H1)
>      DO 40 I = 1, 10
>        READ (5,30) IFLAG
>        WRITE (6,30)
>   30   FORMAT (I3, 77H
>     1                              )
>        IF (IFLAG) 50, 40, 50
>   40 CONTINUE
>   50 READ (5,60) IWRIT1, IWRIT2, IWRIT3, IWRIT4, IWRIT5, IWRIT6,
>     1IWRIT7, IWRIT8, IWRIT9, IWRI10
>   60 FORMAT (2X, 10I1)
>C        **********
>C       READ INFORMATION COMMON TO ALL EVENTS TO BE PROCESSED
>C       ON THIS RUN.
>      READ (5,70) ITAPE, NFRQSM, FLOG, LATER, NSF, ITAPER, NT, FLOW,
>     1FHIGH
>   70 FORMAT (7X, I3, 8X, I2, 1X, F4.2, 4X, I1, 1X, I2, 6X, I1, 7X, I3,
>     1        2(6X,F4.1))
>      IF (NSF .LT. 2) GO TO 90
>      WRITE (6,80) NSF
>      IWRIT2 = 0
>      IWRIT3 = 0
>      IWRIT9 = 0
>      IWRI10 = 1
>   80 FORMAT (2X, 'AVERAGING OPTION IN EFFECT OVER ', I2, ' RECORDS')
>   90 IF (ITAPER .GT. 3) WRITE (6,100)
>  100 FORMAT (2X, 'ERROR IN DATA FORMAT FOR ITAPER'/2X, 'DATA WILL NOT B
>     1E COSINE TAPERED')
>      IF (ITAPER .GT. 3) ITAPER = 0
>      IF (LATER .EQ. 1) WRITE (6,110)
>  110 FORMAT (5X, 'DATA TO BE READ FROM LATER PORTIONS OF TAPE FILES')
>      JFNO = 0
>      IOPT = IWRI10 / 4
>  120 READ (5,130) (TLIN(L),L=1,20), (TLOG(L),L=1,20)
>  130 FORMAT (20A4/20A4)
>C        **********
>C       RE-ENTRY POINT.
>C       READ INFORMATION FOR NEXT EVENT TO BE PROCESSED.
>  140 READ (5,150,END=650) STEV, VC, IFNO, RKM, J, J2, SRATE, NSKIP,
>     1TIME, NSKIP2, TIME2
>  150 FORMAT (6X, A4, 1X, F4.2, 2X, I3, 1X, F5.1, 2(1X,I1), 5X, F5.2,
>     1        6X, I4, 5X, F5.2, 6X, I4, 5X, F5.2)
>      IF (IFNO .LT. 0) GO TO 650
>      IF (IFNO .LT. 0) WRITE (6,160)
>  160 FORMAT (2X, 'ERROR IN FILE NUMBER READ FROM I/O DEVICE 2'/2X, 'FIL
>     1E CANNOT REPRESENT A TAPE FILE CONTAINING EVENT DATA')
>      IF (LATER .EQ. 1) NSKIP = NSKIP2
>      IF (LATER .EQ. 1) TIME = TIME2
>      IF (TIME .EQ. 0.0) GO TO 140
>      IF (NSKIP .GT. 20) NSKIP = NSKIP - 20
>      KNS = KNS + 1
>      AMAX = 0.0
>      A2MAX = 0.0
>      IF (IFLAG .LT. 0) GO TO 280
#
```

```
>      IF (IWRIT1 .EQ. 1) WRITE (6,170) ITAPE
> 170 FORMAT (////3X, 'DIGITAL TAPE NUMBER  ', I3)
>C       **********
>C      POSITION TAPE AT START OF REQUIRED FILE.
> 180 M = 0
> 190 IF (IFNO - JFNO) 200, 230, 210
> 200 CALL CNTRL('BSF', LEN, 2)
>      JFNO = JFNO - 1
>      IF (IWRIT4 .EQ. 1) WRITE (6,220) JFNO
>      GO TO 180
> 210 CALL CNTRL('FSF', LEN, 2)
>      JFNO = JFNO + 1
>      M = 1
>      IF (IWRIT4 .EQ. 1) WRITE (6,220) JFNO
> 220 FORMAT (1H , I3)
>      GO TO 190
> 230 IF (M .EQ. 1) GO TO 240
>      CALL CNTRL('BSF', LEN, 2)
>      CALL CNTRL('FSF', LEN, 2)
> 240 NBLK = 0
>      NSAM = 0
>      N = 1
>      IEND = SRATE * TIME
>      IF (NSF .GE. 2 .AND. N .EQ. 1024) GO TO 330
>C       **********
>C      READ DIGITAL TAPE.
> 250 READ (2,260,END=310) (JIM(I),I=1,256)
> 260 FORMAT (128A2/, 128A2)
>      NBLK = NBLK + 1
>      K = 2
>      IF (NBLK .EQ. 1) K = 42
>      DO 270 I = K, 255, 8
>        NSAM = NSAM + 1
>        IF (NSAM .LE. NSKIP) GO TO 270
>        X(N) = JIM(I + J - 1)
>        IF (IWRI10 .EQ. 9) X2(N) = JIM(I + J2 - 1)
>        IF (N .EQ. IEND) GO TO 330
>        N = N + 1
> 270 CONTINUE
>      GO TO 250
>C       **********
>C       **********
> 280 IF (KNS .LT. 2) WRITE (6,290)
> 290 FORMAT (////3X, 'DATA READ FROM I/O DEVICE 4')
>      N = SRATE * TIME
>      READ (4,300) (X(I),I=1,N)
> 300 FORMAT (8(3X,F7.2))
>      GO TO 330
>C       **********
> 310 TIME = N / SRATE
>      WRITE (6,320) TIME
> 320 FORMAT (2X, 'END OF TAPE FILE ENCOUNTERED AFTER ', F5.2, ' SECS.')
>C       **********
>C      WRITE PROGRAMME INFORMATION.
> 330 IF (IWRIT1 .NE. 1) GO TO 350
>      WRITE (6,340) STEV, JFNO, J, SRATE, NSKIP, TIME, N
> 340 FORMAT (1H0, 2X, 'DIGITAL TAPE DATA'/5X, 'STATION AND EVENT NUMBER
>     1', 3X, A4/18X, 'FILE NUMBER', 4X, I3/15X, 'CHANNEL NUMBER', 6X,
>     2       I1/16X, 'SAMPLING RATE', 4X, F6.2/7X, 'NO. OF SAMPLES SKIPP
>     3ED', 3X, I4/6X, 'LENGTH OF RECORD (SECS)', 5X, F5.2/15X, 'NO. OF S
>     4AMPLES', 2X, I5)
> 350 IF (IWRI10 .EQ. 2 .OR. IWRI10 .EQ. 3) WRITE (6,360) RKM, VC
> 360 FORMAT (7X, 'DISTANCE OF EVENT (KM)', 4X, F5.1/4X, 'ASSUMED VELOCI
>     1TY (KM/SEC)', 6X, F4.2/)
>      IF (IWRIT2 .EQ. 1) WRITE (6,370) N, (I,X(I),I=1,N)
> 370 FORMAT (//2X, 'INPUT DATA'/10X, 'NO. OF SAMPLES =', I5//5(4X,'SAMP
>     1LE',3X,'AMPLITUDE',1X)/(5(4X,I5,5X,F7.2,2X)))
>      IF (IWRI10 .EQ. 9) WRITE (6,380) J2
> 380 FORMAT (2X, 'CHANNEL ', I1,' READ FOR CRUSTAL TRANSFER RATIO')
>      IF (IWRIT5 .EQ. 1) CALL BASE(X, N)
>      DO 390 I = 1, N
>        AL = ABS(X(I))
#
```

```
>       IF (AL .GT. AMAX) AMAX = AL
> 390 CONTINUE
>     IF (IWRI10 .NE. 9) GO TO 410
>     DO 400 I = 1, N
>       AL2 = ABS(X2(I))
>       IF (AL2 .GT. A2MAX) A2MAX = AL2
> 400 CONTINUE
> 410 SAMAX = SAMAX + AMAX
>     IF (IWRIT1 .EQ. 1) WRITE (6,420) AMAX
> 420 FORMAT (2X, 'MAXIMUM AMPLITUDE OF INPUT WAVEFORM IS', F6.1, ' UNIT
>    1S')
>     IF (ITAPER .NE. 0) CALL TAPER(X, N, NT, ITAPER)
>C       **********
>C      FOURIER TRANSFORMATION
>C         NUMBER OF SAMPLES IS RAISED TO  NEAREST POWER OF 2, DENOTED
>C       BY 'NRAISE'.
>C         FOURIER TRANSFORM IS EXECUTED BY SUBROUTINE COOL, WHICH USES
>C       THE COOLEY-TUKEY ALGORITHM.  THE RESULTING SPECTRUM IS COMPUTED
>C       AT 'NOUT' FREQUENCY POINTS.
>C       **********
>     AN = N
>     ANLOG2 = ALOG10(AN - 1) / ALOG10(2.0)
>     N2 = ANLOG2 + 1.0
>     IF (IWRIT8 .EQ. 1) NFRQSM = 2 ** (N2 - 8)
>     NRAISE = 2 ** N2
>     NOUT = NRAISE / 2 + 1
>     NPLUS = N + 1
>     DO 430 I = NPLUS, NRAISE
>       X2(I) = 0.0
> 430 X(I) = 0.0
>     ANRAIS = FLOAT(NRAISE)
>     DO 440 I = 1, NRAISE
>       CS2(I) = CMPLX(X2(I),0.0)
> 440 CS(I) = CMPLX(X(I),0.0)
>     CALL COOL(N2, CS, -1.0)
>     IF (IWRI10 .EQ. 9) CALL COOL(N2, CS2, -1.0)
>     DO 450 I = 1, NRAISE
>       IF (IWRI10 .EQ. 9) CS2(I) = CS2(I) / SQRT(ANRAIS)
> 450 CS(I) = CS(I) / SQRT(ANRAIS)
>     DO 460 I = 1, NOUT
>       FREQ(I) = (I - 1) * SRATE / NRAISE
>       AMP(I) = CABS(CS(I))
>       IF (IWRI10 .EQ. 9) AMP2(I) = CABS(CS2(I))
>       SAMP(I) = SAMP(I) + AMP(I)
>       ACC(I) = AMP(I) * FREQ(I)
>       IF (FREQ(I) .GT. 0.0) DIS(I) = AMP(I) / FREQ(I)
>       ENERGY(I) = 2 * AMP(I) ** 2
>       RCS = REAL(CS(I))
>       ACS = AIMAG(CS(I))
>       IF (RCS .EQ. 0.0) RCS = 0.0001
>       IF (ACS .EQ. 0.0) ACS = 0.0001
>       PHASE(I) = ATAN2(ACS,RCS) * RTOD
> 460 CONTINUE
>     DO 470 I = 2, NOUT
> 470 FREQ(NRAISE - I + 2) = FREQ(I)
>     IF (KNS .LT. NSF) GO TO 140
>     IF (NSF .LT. 2) GO TO 490
>     DO 480 K = 1, NOUT
> 480 AMP(K) = SAMP(K) / NSF
>     AMAX = SAMAX / NSF
> 490 DIS(1) = DIS(2)
>     IF (NFRQSM .EQ. 0) WRITE (6,500)
> 500 FORMAT (2X, 'OUTPUT DATA IS UNSMOOTHED')
>     IF (NFRQSM .EQ. 0) GO TO 520
>C       **********
>C      CALL SMOOTHING ROUTINES (SIMPLE MOVING WINDOWS)
>     CALL NEWSMO(AMP, NOUT, NFRQSM)
>     IF (IWRI10 .EQ. 9) CALL NEWSMO(AMP2, NOUT, NFRQSM)
>     IF (IWRI10 .EQ. 2) CALL NEWSMO(DIS, NOUT, NFRQSM)
>     IF (IWRI10 .EQ. 3) CALL NEWSMO(ACC, NOUT, NFRQSM)
>     IF (IWRIT3 .EQ. 1) CALL NEWSMO(ENERGY, NOUT, NFRQSM)
>     IF (IWRIT3 .EQ. 1) CALL NEWSMO(PHASE, NOUT, NFRQSM)
#
```

```
>      IF (IWRIT1 .EQ. 1) WRITE (6,510) NFRQSM
> 510 FORMAT (////2X, 'OUTPUT DATA HAS BEEN SMOOTHED OVER ', I2, ' FREQU
>     1ENCY POINTS')
>C         **********
> 520 FRES = FREQ(2) - FREQ(1)
>      IF (IWRIT3 .EQ. 1) WRITE (6,530) FRES, (FREQ(I),AMP(I),PHASE(I),
>     1ENERGY(I),I=1,NOUT)
> 530 FORMAT (/2X, 'FREQUENCY RESOLUTION = ', F8.5//6X, 'FREQUENCY',
>     1        11X, 'AMPLITUDE', 13X, 'PHASE', 14X, 'ENERGY'/7X,
>     2        '(HERTZ)', 32X, '(DEGREES)'/(7X,F5.2,14X,F7.2,13X,F7.2,13X,
>     3        F8.2))
>      IF (IWRI10 .NE. 9) GO TO 550
>C         **********
>C      COMPUTE AND PLOT CRUSTAL TRANSFER RATIO.
>      DO 540 I = 1, NOUT
>        IF (AMP2(I) .LT. 0.001) AMP2(I) = 0.001
> 540 RATIO(I) = AMP(I) / AMP2(I)
>      IF (IWRI10 .EQ. 9) CALL IPINP(X, X2, TIME, STEV, ITAPE, IFNO, J,
>     1     J2, SRATE, AMAX, A2MAX, N, LATER, 1)
>      CALL PLOTO(RATIO, FREQ, NOUT, NFRQSM, STEV)
>      GO TO 140
> 550 IF (IWRIT6 .EQ. 0) GO TO 600
>C         **********
>C      READ ADDITIONAL DATA FROM I/O DEVICE 3:-
>C          DATA TAKE THE FORM OF OTHER AMPLITUDE SPECTRA IN THE FREQUENCY
>C        DOMAIN (E.G. A NOISE SPECTRUM) WHICH MAY BE SUBTRACTED FROM, OR
>C        USED FOR DIVISION OF, THE FOURIER TRANSFORMED INPUT SEISMIC
>C        RECORD.
>C             W    ARRAY HOLDING SPECTRAL VALUES.
>C          AIMAX   MAXIMUM AMPLITUDE VALUE IN W.
>C          INOUT   NUMBER OF SAMPLES IN W.
>C         **********
>      READ (3,560) AIMAX, INOUT, (W(K),K=1,INOUT)
> 560 FORMAT (F10.5, 5X, I5/(8(3X,F7.2)))
>      CSCALE = AMAX / AIMAX
>      DO 580 K = 2, INOUT
>        W(K) = W(K) * CSCALE
>        IF (IWRIT6 .EQ. 2) GO TO 570
>        IF (W(K) .EQ. 0.0) W(K) = 0.001
>        AMP(K) = AMP(K) / W(K)
>        ACC(K) = ACC(K) / (W(K)*FREQ(K))
>        DIS(K) = (DIS(K)*FREQ(K)) / W(K)
>        GO TO 580
> 570    AMP(K) = AMP(K) - W(K)
>        ACC(K) = (ACC(K) - W(K)*FREQ(K)) + 100
>        DIS(K) = (DIS(K) - W(K)/FREQ(K)) + 100
> 580 CONTINUE
>      WRITE (6,590) IWRIT6, CSCALE
> 590 FORMAT (2X, 'THIS SPECTRUM HAS BEEN CORRECTED USING CORRECTION OPT
>     1ION ', I1, '.  ADDITIONAL DATA READ FROM I/O DEVICE 3'/2X, 'CORREC
>     2TION SCALING FACTOR IS', F6.3)
>C         **********
>C      CALL LOGARITHMIC SMOOTHING AND PLOTTING ROUTINES
> 600 IF (FLOG .GT. 1.0 .AND. IWRI10 .EQ. 2) CALL LOGSMO(DIS, FREQ,
>     1     NOUT, FLOG)
>      IF (FLOG .GT. 1.0 .AND. IWRI10 .EQ. 3) CALL LOGSMO(ACC, FREQ,
>     1     NOUT, FLOG)
>      IF (IWRIT9 .EQ. 1 .AND. IWRI10.LT.2) CALL IPINP(X, X2, TIME, STEV,
>     1     ITAPE, IFNO, J, J2, SRATE, AMAX, A2MAX, N, LATER, 0)
>      IF (IWRI10 .EQ. 1) CALL OPLOT(AMP, FREQ, NOUT, NFRQSM, TLIN, STEV,
>     1     NSF, 2)
>      IF (IWRI10 .EQ. 0) CALL OPLOT(AMP, FREQ, NOUT, NFRQSM, TLIN, STEV,
>     1     NSF, 0)
>      IF (IWRI10 .EQ. 2) CALL OLGPLT(DIS, FREQ, NOUT, NFRQSM, FLOG,
>     1     TLOG, RKM, VC, STEV, 2)
>      IF (IWRI10 .EQ. 3) CALL OLGPLT(ACC, FREQ, NOUT, NFRQSM, FLOG,
>     1     TLOG, RKM, VC, STEV, 3)
>      IF (IWRIT7 .EQ. 1) WRITE (7,560) AMAX, NOUT, (AMP(K),K=1,NOUT)
>      IF (IOPT .NE. 1) GO TO 640
>C         **********
>C          THIS SECTION OF THE PROGRAMME PERFORMS THE INVERSE FOURIER
>C        TRANSFORM.  THE OUTPUT PRODUCED IS A PLOT OF THE SYNTHETIC
#
```

```
>C        DISPLACEMENT, VELOCITY OR ACCELERATION AMPLITUDE RECORD IN
>C        THE TIME DOMAIN.
>C        **********
>      IF (FHIGH .EQ. 0.0) FHIGH = 100.0
>      IF (IWRI10 .EQ. 4 .AND. FLOW .EQ. 0.0) FLOW = 0.5
>      EMAX = 0.
>      ANSCA = NRAISE
>      DO 610 ID = 2, NRAISE
>        CDI = CMPLX(0.0,FREQ(ID))
>        IF (IWRI10 .EQ. 4) CS(ID) = CS(ID) / CDI
>        IF (IWRI10 .EQ. 6) CS(ID) = CS(ID) * CDI
>        IF (FREQ(ID) .LT. FLOW) CS(ID) = (0.0,0.0)
>        IF (FREQ(ID) .GT. FHIGH) CS(ID) = (0.0,0.0)
>        IF (REAL(CS(ID)) .EQ. 0.0 .AND. AIMAG(CS(ID)) .EQ. 0.0)
>     1  ANSCA = ANSCA - 1
> 610 CONTINUE
>      CALL COOL(N2, CS, 1.0)
>      WRITE (6,620) ANSCA, N, NRAISE
> 620 FORMAT (2X, 'DUMMY SCALE', F6.0/2X, 'N', I6/2X, 'NRAISE', I6)
>      ANRAIS = FLOAT(NRAISE)
>      DO 630 ID = 1, N
>        EDISX(ID) = REAL(CS(ID)) / SQRT(ANRAIS)
>        EDM = ABS(EDISX(ID))
>        IF (EDM .GT. EMAX) EMAX = EDM
> 630 CONTINUE
>      IF (IWRIT9 .EQ. 1) CALL IPINV(X, TIME, STEV, ITAPE, IFNO, J,
>     1      SRATE, AMAX, N, LATER, 7.0, 0.0, 0.0, IWRI10)
>      CALL IPINV(EDISX, TIME, STEV, ITAPE, IFNO, J, SRATE, EMAX, N, 2,
>     1      3.0, FLOW, FHIGH, IWRI10)
> 640 IF (NSF .GT. 2) GO TO 650
>      GO TO 140
> 650 STOP
>      END
>C
>C
>C     ***************************************************************
>      SUBROUTINE IPINP(XX, XX2, T, S, IT, IF, J, J2, RATE, AMAX,A2MAX,N,
>     1            LATER, IK)
>      DIMENSION XX(N), XX2(N)
>C        **********
>C          THE INPUT WAVEFORM IS PLOTTED, NORMALISED AMPLITUDE
>C        AGAINST TIME.  THE TIME AXIS IS SCALED AS NECESSARY.
>C        LABELS IDENTIFY THE STATION AND EVENT NUMBER, TAPE NUMBER,
>C        FILE NUMBER, CHANNEL NUMBER, SAMPLING RATE AND SCALING FACTOR.
>C        BOTH INPUT CHANNEL WAVEFORMS ARE PLOTTED IF THE CRUSTAL
>C        TRANSFER OPTION HAS BEEN CHOSEN.
>C        N.B.  THIS SUBROUTINE CONTAINS NO 'CALL PLTEND', SINCE IT
>C        IS USED ONLY WITH SUBROUTINES OPLOT, PLOTO AND OTRANS.
>C        **********
>      ISCALE = (T - 0.01) / 10.0 + 1.0
>      SCALE = FLOAT(ISCALE)
>      IF (IK .EQ. 1) GO TO 10
>      AK = 0.0
>      SK = 2.0
>      CALL PSYMB(8.9, 10.4, -0.1, 7HCHANNEL, 0.0, 7)
>      CALL PSYMB(4.7, 10.2, -0.1, 22HRATE              SCALE, 0.0, 22)
>      CALL PNUMBR(9.7, 10.4, -0.1, J, 0.0, 'I1*')
>      CALL PNUMBR(5.0, 10.2, -0.1, RATE, 0.0, 'F5.2*')
>      CALL PNUMBR(6.3, 10.2, -0.1, AMAX, 0.0, 'F7.1*')
>      GO TO 20
>   10 AK = 0.5
>      SK = -2.0
>      CALL PSYMB(4.7, 10.2, -0.1, 38HUPPER CHANNEL            LOWER CHAN
>     1NEL,0.0, 38)
>      CALL PNUMBR(6.0, 10.2, -0.1, J, 0.0, 'I1*')
>      CALL PNUMBR(8.05, 10.2, -0.1, J2, 0.0, 'I3*')
>   20 CALL PAXIS(0.5, 8.0, 8HTIME/SEC, -8, 10.0, 0.0, 0.0, SCALE,1.0)
>      CALL PAXIS(0.5, 8.0, 20HNORMALISED AMPLITUDE, 20, SK, 90.0, -1.0,
>     1      1.0, 0.5)
>      CALL PSYMB(0.8, 10.4, -0.2, 14HINPUT WAVEFORM, 0.0, 14)
>      CALL PSYMB(4.7, 10.4, -0.1, 37HEVENT            TAPE            FI
>     1LE, 0.0, 37)
#
```

```
>      CALL PSYMB(5.3, 10.4, -0.1, S, 0.0, 4)
>      IF (LATER .EQ. 1) CALL PSYMB(0.8, 10.2, -0.1, 15HN.B.LATER ONSET,
>     1      0.0, 15)
>      CALL PNUMBR(6.7, 10.4, -0.1, IT, 0.0, 'I3*')
>      CALL PNUMBR(8.05, 10.4, -0.1, IF, 0.0, 'I3*')
>      AK1=9.0-AK
>      CALL PENUP(0.5, AK1)
>      DO 30 I = 1, N
>        X = (I - 1) / (RATE*SCALE) + 0.5
>        Y = XX(I) *(1.0-AK)/ AMAX + 9.0 + AK
>   30 CALL PENDN(X, Y)
>      IF (IK .EQ. 0) GO TO 50
>      CALL PENUP (0.5,8.5)
>      DO 40 I = 1, N
>        X = (I - 1) / (RATE*SCALE) + 0.5
>        Y = XX2(I) *0.5/ A2MAX + 8.5
>   40 CALL PENDN (X, Y)
>   50 RETURN
>      END
>C
>C
>C     ************************************************************
>      SUBROUTINE IPINV(XX, T, S, IT, IF, J, RATE, AMAX, N, ICALL, ORIG,
>     1            FL, FH, IW)
>      DIMENSION XX(N)
>C        **********
>C          IF ICALL<2, THE INPUT RECORD IS PLOTTED IN A SIMILAR MANNER
>C        TO SUBROUTINE IPINP.  IF ICALL=2, THE SYNTHETIC OUTPUT RECORD
>C        IS PLOTTED.  AMPLITUDES OF BOTH PLOTS ARE NORMALISED.
>C        **********
>      ISCALE = (T - 0.01) / 10.0 + 1.0
>      SCALE = FLOAT(ISCALE)
>      CALL PAXIS(4.0, ORIG, 8HTIME/SEC, -8, 10.0, 0.0, 0.0, SCALE, 1.0)
>      CALL PAXIS(4.0, ORIG, 20HNORMALISED AMPLITUDE, 20, 2.0, 90.0,
>     1      -1.0, 1.0, 0.5)
>      IF (ICALL .EQ. 2) GO TO 10
>      CALL PSYMB(1.0, 10.0, -0.2, 46HW.G.RIGDEN: FOURIER TRANSFORM PROGR
>     1AMME OUTPUT, 0.0, 46)
>      CALL PSYMB(4.3, 9.5, -0.2, 31HINPUT VELOCITY AMPLITUDE RECORD,
>     1      0.0, 31)
>      CALL PSYMB(0.5, 9.5, -0.2, 5HEVENT, 0.0, 5)
>      CALL PSYMB(1.7, 9.5, -0.2, S, 0.0, 4)
>      IF (ICALL .EQ. 1) CALL PSYMB(6.5, 9.5, -0.1, 15HN.B.LATER ONSET,
>     1      0.0, 15)
>      CALL PSYMB(0.5, 6.65, -0.2, 4HTAPE, 0.0, 4)
>      CALL PSYMB(0.5, 6.15, -0.2, 4HFILE, 0.0, 4)
>      CALL PSYMB(0.5, 5.65, -0.2, 4HCHNL, 0.0, 4)
>      CALL PSYMB(0.5, 5.15, -0.2, 4HRATE, 0.0, 4)
>      CALL PNUMBR(1.76, 6.65, -0.2, IT, 0.0, 'I3*')
>      CALL PNUMBR(1.7, 6.15, -0.2, IF, 0.0, 'I3*')
>      CALL PNUMBR(1.7, 5.65, -0.2, J, 0.0, 'I3*')
>      CALL PNUMBR(1.6, 5.15, -0.2, RATE, 0.0, 'F3.1*')
>      CALL PENUP(0.5, 9.45)
>      CALL PENDN(2.34, 9.45)
>      CALL PENUP(2.34, 9.42)
>      CALL PENDN(0.5, 9.42)
>      CALL PENUP(0.3, 7.0)
>      CALL PENDN(0.3, 5.0)
>      CALL PENDN(2.51, 5.0)
>      CALL PENDN(2.51, 7.0)
>      CALL PENDN(0.3, 7.0)
>   10 CALL PSYMB(0.5, (ORIG + 0.9), -0.2, 5HSCALE, 0.0, 5)
>      CALL PNUMBR(1.7, (ORIG + 0.9), -0.2, AMAX, 0.0, 'F5.1*')
>      IF (ICALL .LT. 2) GO TO 20
>      IF (IW .EQ. 4) CALL PSYMB(4.3, 5.5, -0.2, 39HSYNTHETIC DISPLACEMEN
>     1T AMPLITUDE RECORD, 0.0, 39)
>      IF (IW .EQ. 5) CALL PSYMB(4.3, 5.5, -0.2, 35HSYNTHETIC VELOCITY AM
>     1PLITUDE RECORD, 0.0, 35)
>      IF (IW .EQ. 6) CALL PSYMB(4.3, 5.5, -0.2, 39HSYNTHETIC ACCELERATIO
>     1N AMPLITUDE RECORD, 0.0, 39)
>      IF (FL .EQ. 0.0 .AND. FH .EQ. 100.0) GO TO 20
>      CALL PSYMB(0.5, (ORIG + 0.5), -0.15, 15HFILTERED RECORD, 0.0, 15)
#
```

```
>      CALL PSYMB(0.88, (ORIG + 0.25), -0.15, 18HLOW PASS        HZ, 0.0,
>     1      18)
>      CALL PSYMB(0.88, ORIG, -0.15, 18HHIGH PASS       HZ, 0.0, 18)
>      CALL PNUMBR(2.14, (ORIG + 0.25), -0.15, FH, 0.0, 'F3.1*')
>      CALL PNUMBR(2.24, ORIG, -0.15, FL, 0.0, 'F2.1*')
>   20 CALL PENUP(4.0, (ORIG + 1.0))
>      DO 30 I = 1, N
>        X = (I - 1) / (RATE*SCALE) + 4.0
>        Y = XX(I) / AMAX + ORIG + 1.0
>   30 CALL PENDN(X, Y)
>      IF (ICALL .EQ. 2) CALL PLTEND
>      RETURN
>      END
>C
>C
>C     ****************************************************************
>      SUBROUTINE OPLOT(V, FREQ, NS, NFRQ, TLIN, STEV, NSF, IBC)
>      DIMENSION V(NS), FREQ(NS), TLIN(20), VV(4100), FF(4100)
>C        **********
>C        A GRAPH IS DRAWN OF THE NORMALISED FOURIER TRANSFORMED OUTPUT
>C        IN THE FREQUENCY DOMAIN.
>C        **********
>      CALL PSYMB(0.8, 7.1, -0.2, TLIN, 0.0, 80)
>      CALL PSYMB(1.0, 6.6, -0.1, 38HDATA SMOOTHED OVER    FREQUENCY POIN
>     1TS, 0.0, 38)
>      CALL PSYMB(1.0, 6.3, -0.1, 29HFREQUENCY RESOLUTION (HZ.) IS, 0.0,
>     1      29)
>      CALL PNUMBR(2.66, 6.6, -0.1, NFRQ, 0.0, 'I2*')
>      CALL PNUMBR(2.9, 6.3, -0.1, FREQ(2), 0.0, 'F8.5*')
>      IF (NSF .LT. 2) GO TO 10
>      CALL PSYMB(7.5, 7.1, -0.2, 16HMEAN OF   EVENTS, 0.0, 16)
>      CALL PNUMBR(8.68, 7.1, -0.2, NSF, 0.0, 'I2*')
>      GO TO 20
>   10 CALL PSYMB(8.0, 7.1, -0.2, 5HEVENT, 0.0, 5)
>      CALL PNUMBR(9.0, 7.1, -0.2, STEV, 0.0, 'C4*')
>   20 BMAX=0.0
>      DO 30 K = 3, NS
>      IF (V(K).GT.BMAX) BMAX=V(K)
>   30 CONTINUE
>      DO 31 K=3,NS
>      FF(K)=FREQ(K)/2.0+0.5
>      IF (IBC.EQ.0) VV(K)=V(K)/72.0+3.0
>      IF (IBC.EQ.2) VV(K)=V(K)*5.0/BMAX+0.5
>        IF (FREQ(K) .GT. 20.0) GO TO 40
>   31 CONTINUE
>   40 M = K - 3
>      CALL PAXIS(0.5, 0.5, 9HFREQUENCY, -9, 10.0, 0.0, 0.0, 2.0, 1.0)
>      IF (IBC.EQ.0) GO TO 61
>      CALL PAXIS (0.5,0.5,18HVELOCITY AMPLITUDE,18,5.0,90.0,0.0,20.0,1.0
>     1)
>      CALL PSYMB (1.0,6.0,-0.1,27HAMPLITUDE SCALING FACTOR IS,0.0,27)
>      CALL PNUMBR (3.2,6.0,-0.1,BMAX,0.0,'F7.1*')
>      GO TO 101
>   61 CALL PAXIS (0.5,0.5,15HPHASE (DEGREES),15,5.0,90.0,-180.0,72.0,.83
>     1333)
>      IF (IBC .EQ. 2) CALL PAXIS(0.5, 0.5, 18HVELOCITY AMPLITUDE, 18,
>     1      5.0, 90.0, YMIN, YF, 1.0)
>      IF (IBC .EQ. 0) CALL PAXIS(0.5, 0.5, 15HPHASE (DEGREES), 15, 4.98,
>     1      90.0, -180.0, 72.0, 0.83)
>  101 CALL PLINE(FF(3),VV(3), M, 1, 0, 0, 1.0)
>      CALL PLTEND
>      RETURN
>      END
>C
>C
>C     ****************************************************************
>      SUBROUTINE PLOTO(V, FREQ, NS, NFRQ, STEV)
>      DIMENSION V(NS), FREQ(NS), VV(8200), FF(8200)
>C        **********
>C        THIS SUBROUTINE PLOTS CRUSTAL TRANSFER RATIOS.
>C        **********
>      CALL PAXIS(1.0, 0.5, 9HFREQUENCY, -9, 10.0, 0.0, 0.0, 2.0, 1.0)
#
```

```
>      CALL PSYMB(1.2, 7.1, -0.2, 22HCRUSTAL TRANSFER RATIO, 0.0, 22)
>      DO 10 N = 1, 5
>        PN = 0.25 * 2 ** (N - 1)
>        PY = 4.0 * ALOG10(2.0) * (N - 3) + 3.5
>   10 CALL PNUMBR(0.3, PY, -0.1, PN, 0.0, 'F4.2*')
>      CALL PENUP(1.0, 0.5)
>      CALL PENDN(1.0, 6.5)
>      CALL PENDN(11.0, 6.5)
>      CALL PENDN(11.0, 0.5)
>      CALL PENUP(11.0, 3.5)
>      CALL PENDN(1.0, 3.5)
>      CALL PSYMB(0.2, 2.7, -0.1, 13HLOG RATIO V/H, 90.0, 13)
>      CALL PSYMB(8.0, 7.1, -0.2, 5HEVENT, 0.0, 5)
>      CALL PNUMBR(9.0, 7.1, -0.2, STEV, 0.0, 'C4*')
>      CALL PSYMB(1.5, 6.7, -0.1, 38HDATA SMOOTHED OVER    FREQUENCY POIN
>     1TS, 0.0, 38)
>      CALL PSYMB(6.0, 6.7, -0.1, 29HFREQUENCY RESOLUTION (HZ.) IS, 0.0,
>     1     29)
>      CALL PNUMBR(3.16, 6.7, -0.1, NFRQ, 0.0, 'I2*')
>      CALL PNUMBR(7.9, 6.7, -0.1, FREQ(2), 0.0, 'F8.5*')
>      BMAX = 0.0
>      DO 20 K = 3, NS
>   20 IF (V(K) .GT. BMAX) BMAX = V(K)
>      DO 30 K = 3, NS
>        FF(K) = FREQ(K) / 2.0 + 1.0
>        IF (V(K) .LT. 0.001) V(K) = 0.001
>        VV(K) = 4.0 * ALOG10(V(K)) + 3.5
>        IF (VV(K) .GT. 6.5) VV(K) = 6.6
>        IF (VV(K) .LT. 0.5) VV(K) = 0.4
>        M = K - 2
>        IF (FREQ(K) .GT. 20.0) GO TO 40
>   30 CONTINUE
>   40 CALL PLINE(FF(3), VV(3), M, 1, 0, 0, 0.0)
>      CALL PLTEND
>      RETURN
>      END
>C
>C
>C     ************************************************************
>      SUBROUTINE OLGPLT(V, FREQ, NS, NFRQ, FLOG, TLOG, RKM, VC, STE, IX)
>      DIMENSION V(NS), FREQ(NS), VV(8200), FF(8200), TLOG(20),
>     1          VVQ(4,8200)
>C        **********
>C        THIS SUBROUTINE PLOTS NORMALISED DISPLACEMENT (IF IX=2) OR
>C        ACCELERATION (IX=3) AMPLITUDE SPECTRA AGAINST FREQUENCY,
>C        ON A LOG-LOG SCALE.
>C        SPECTRA ARE AUTOMATICALLY CORRECTED FOR ATTENUATION AND
>C        PLOTTED FOR EFFECTIVE 'Q' VALUES OF 100, 200 AND 400.
>C        **********
>      CORR = (0.4343*3.1416*RKM) / VC
>      CALL PLGAXS(0.8, 0.7, 9HFREQUENCY, -9, 9.0, 0.0, -1.0, 3.0/9.0)
>      IF (IX .EQ. 3) CALL PLGAXS(0.8, 0.7, 33HNORMALISED ACCELERATION AM
>     1PLITUDE, 33, 9.0, 90.0, -3.0, 3.0/9.0)
>      IF (IX .EQ. 2) CALL PLGAXS(0.8, 0.7, 33HNORMALISED DISPLACEMENT AM
>     1PLITUDE, 33, 9.0, 90.0, -3.0, 3.0/9.0)
>      CALL PSYMB(1.1, 10.5, -0.2, 39HFOURIER TRANSFORM   W.G.RIGDEN    D
>     1GP02, 0.0, 39)
>      CALL PSYMB(1.1, 10.1, -0.2, TLOG, 0.0, 80)
>      CALL PSYMB(1.3, 9.8, -0.1, 38HDATA SMOOTHED OVER    FREQUENCY POIN
>     1TS, 0.0, 38)
>      CALL PSYMB(5.0, 9.8, -0.1, 31HLOGARITHMIC SMOOTHING FACTOR IS,
>     1     0.0, 31)
>      CALL PSYMB(1.3, 9.4, -0.1, 29HFREQUENCY RESOLUTION (HZ.) IS, 0.0,
>     1     29)
>      CALL PSYMB(5.8, 9.4, -0.2, 5HEVENT, 0.0, 5)
>      CALL PNUMBR(2.96, 9.8, -0.1, NFRQ, 0.0, 'I2*')
>      CALL PNUMBR(7.5, 9.8, -0.1, FLOG, 0.0, 'F4.2*')
>      CALL PNUMBR(3.2, 9.4, -0.1, FREQ(2), 0.0, 'F8.5*')
>      CALL PNUMBR(6.8, 9.4, -0.2, STE, 0.0, 'C4*')
>      VMAX = 0.0
>      M = 0
>   10 DO 40 K = 1, NS
#
```

```
>        M = M + 1
>        IF (FREQ(K) .LT. 0.3) M = M - 1
>        IF (FREQ(K) .LT. 0.3) GO TO 40
>        IF (FREQ(K) .GT. 15.0) GO TO 50
>        FF(M) = 3.0 * ALOG10(FREQ(K)) + 3.8
>        IF (V(K) .LE. 0.0) WRITE (6,20) K, V(K), FREQ(K), IX
>  20    FORMAT (1H , 1X, 'WARNING: SUPPRESSED NEGATIVE VALUE OF V IN SUB
>     1ROUTINE OLGPLT'/4X, 'K=', I4, 2X, 'V(K)=', F6.2, 2X, 'FREQ(K)=',
>     2          F6.2, 2X, 'IX=', I1)
>        IF (V(K) .LE. 0.0) V(K) = 0.0001
>C
>C      CORRECT FOR ATTENUATION
>C
>        DO 30 IQ = 2, 4
>          Q = 50.0 * 2 ** IQ
>          VVQ(IQ,M) = ALOG10(V(K)) + CORR * FREQ(K) / Q
>          IF (VVQ(IQ,M) .GT. VMAX) VMAX = VVQ(IQ,M)
>  30    CONTINUE
>  40 CONTINUE
>  50 NS = M - 1
>     DO 70 IQ = 2, 4
>       DO 60 K = 1, NS
>         VV(K) = 3.0 * (VVQ(IQ,K) - VMAX) + 9.7
>         IF (VV(K) .LT. 0.3) VV(K) = 0.3
>  60   CONTINUE
>  70 CALL PLINE(FF(1), VV(1), NS, 1, 0, 0, 0.0)
>C
>C
>      VMAX = RKM * 10.0 ** (VMAX - 3.0)
>      CALL PSYMB(1.3, 9.1, -0.1, 27HAMPLITUDE SCALING FACTOR IS, 0.0,
>     1      27)
>      CALL PNUMBR(3.5, 9.1, -0.1, VMAX, 0.0, 'F9.3*')
>      CALL PLTEND
>      RETURN
>      END
>C
>C
>C      ****************************************************************
>      SUBROUTINE BASE(X, N)
>      DIMENSION X(N)
>      SUMX = 0.0
>      DO 10 I = 1, N
>  10  SUMX = SUMX + X(I)
>      XBAR = SUMX / N
>      DO 20 I = 1, N
>  20  X(I) = X(I) - XBAR
>      WRITE (6,30) XBAR
>  30  FORMAT (2X, 'DATA CORRECTED FOR D.C. BIAS OF ', F7.2)
>      RETURN
>      END
>C
>C
>C      ****************************************************************
>      SUBROUTINE TAPER(X, N, NT, IT)
>      DIMENSION X(N), KIND(3)
>      DATA KIND /'FULL', 'FRNT', 'END'/
>      IKIND = KIND(IT)
>      PHI = 4.0 * ATAN(1.0) / (NT - 1.0)
>      DO 10 I = 1, NT
>        IA = N - I + 1
>        IF (IT .NE. 3) X(I) = 0.5 * X(I) * (1.0 - COS((I - 1)*PHI))
>  10  IF (IT .NE. 2) X(IA) = 0.5 * X(IA) * (1.0 - COS((I - 1)*PHI))
>      WRITE (6,20) IKIND, NT
>  20  FORMAT (2X, A4, ' COSINE TAPERING PERFORMED OVER ', I3, ' DATA SAM
>     1PLES')
>      RETURN
>      END
>C
>C
>C      ****************************************************************
>      SUBROUTINE NEWSMO(V, N, NF)
>      DIMENSION V(N), VA(8200)
#
```

```
>      NF = NF / 2
>      NF = NF * 2 + 1
>      DO 20 I = 1, N
>        VA(I) = 0.0
>        JA = I - (NF - 1) / 2
>        JB = I + (NF - 1) / 2
>        IF (JA .LT. 1) JB = 2 * I - 1
>        IF (JA .LT. 1) JA = 1
>        IF (JB .GT. N) JA = 2 * I - N
>        IF (JB .GT. N) JB = N
>        DO 10 J = JA, JB
>   10   VA(I) = VA(I) + V(J)
>        VA(I) = VA(I) / (JB - JA + 1)
>   20 CONTINUE
>      DO 30 I = 1, N
>   30 V(I) = VA(I)
>      RETURN
>      END
>C
>C
>C     ****************************************************************
>      SUBROUTINE LOGSMO(V, F, N, FL)
>      DIMENSION V(N), F(N), VSUM(8200), FSUM(8200), K(8200)
>C        **********
>C        A VERY SIMPLE MOVING WINDOW ROUTINE TO APPLY ADDITIONAL
>C        SMOOTHING TO THE HIGH FREQUENCY END OF A LOGARITHMIC PLOT
>C        **********
>      DO 20 I = 1, N
>        FMIN = F(I) / FL
>        FMAX = F(I) * FL
>        VSUM(I) = 0.0
>        FSUM(I) = 0.0
>        K(I) = 0
>        DO 10 J = 1, N
>          IF (F(J) .LT. FMIN .OR. F(J) .GT. FMAX) GO TO 10
>          VSUM(I) = VSUM(I) + V(J)
>          FSUM(I) = FSUM(I) + F(J)
>          K(I) = K(I) + 1
>          IF (J .EQ. N) GO TO 30
>   10   CONTINUE
>   20 CONTINUE
>   30 N = I
>      DO 40 L = 1, N
>        V(L) = VSUM(L) / K(L)
>   40 F(L) = FSUM(L) / K(L)
>      RETURN
>      END
>C
>C
>C     ****************************************************************
>      SUBROUTINE COOL(N, XX, SIGNI)
>      DIMENSION W(14), XX(1), NBIT(20), JNT(20)
>C        **********
>C        THIS SUBROUTINE PERFORMS THE FOURIER TRANSFORM
>C        **********
>      INTEGER OFFSET
>      ROOT2 = SQRT(2.0)
>      NX = 2 ** N
>      NX2 = NX + NX
>      NX2LS1 = NX2 - 1
>      NX2LS2 = NX2 - 2
>      NXON8 = NX / 8
>      NXON4 = NXON8 + NXON8
>      NXON2 = NXON4 + NXON4
>      NX3ON4 = NXON2 + NXON4
>      CON1 = (8.*ATAN(1.)) / FLOAT(NX)
>      IF (SIGNI .GT. 0.0) GO TO 20
>C
>      DO 10 K = 1, NX2LS1, 2
>   10 XX(K + 1) = -XX(K + 1)
>C
>   20 DO 30 K = 1, N
#
```

```
>   30 JNT(K) = 2 ** (N - K)
>C
>       LSTART = N - N / 3 * 3 + 1
>       IF (LSTART .EQ. 1) GO TO 70
>       IF (LSTART .EQ. 2) GO TO 50
>       LBLOK2 = NXON2
>       L2BLOK = LBLOK2 - 1
>C
>       DO 40 K0 = 1, L2BLOK, 2
>         K1 = K0 + LBLOK2
>         K2 = K1 + LBLOK2
>         K3 = K2 + LBLOK2
>         A0R = XX(K0) + XX(K2)
>         A0I = XX(K0 + 1) + XX(K2 + 1)
>         A1R = XX(K0) - XX(K2)
>         A1I = XX(K0 + 1) - XX(K2 + 1)
>         A2R = XX(K1) + XX(K3)
>         A2I = XX(K1 + 1) + XX(K3 + 1)
>         A3R = XX(K1) - XX(K3)
>         A3I = XX(K1 + 1) - XX(K3 + 1)
>         XX(K0) = A0R + A2R
>         XX(K0 + 1) = A0I + A2I
>         XX(K1) = A0R - A2R
>         XX(K1 + 1) = A0I - A2I
>         XX(K2) = A1R - A3I
>         XX(K2 + 1) = A1I + A3R
>         XX(K3) = A1R + A3I
>   40 XX(K3 + 1) = A1I - A3R
>C
>       GO TO 70
>   50 LBLOK2 = NX
>       L2BLOK = LBLOK2 - 1
>C
>       DO 60 K0 = 1, L2BLOK, 2
>         K1 = K0 + LBLOK2
>         A1R = XX(K1)
>         A1I = XX(K1 + 1)
>         XX(K1) = XX(K0) - A1R
>         XX(K1 + 1) = XX(K0 + 1) - A1I
>         XX(K0) = XX(K0) + A1R
>   60 XX(K0 + 1) = XX(K0 + 1) + A1I
>C
>   70 DO 180 LAYER = LSTART, N, 3
>         LBLOK2 = NX / 2 ** (LAYER + 1)
>         L2BLOK = LBLOK2 - 1
>         LBLOK1 = L2BLOK - 1
>         LBLOK8 = LBLOK2 * 8
>         LBLAST = NX2 - LBLOK8 + 1
>C
>         DO 80 K = 4, N
>   80    NBIT(K) = 0
>C
>         NW = 0
>         ASSIGN 100 TO ISTNUM
>C
>         DO 170 OFFSET = 1, LBLAST, LBLOK8
>           IF (OFFSET .EQ. 1) GO TO 90
>           ARG = CON1 * FLOAT(NW)
>           W(1) = COS(ARG)
>           W(2) = SIN(ARG)
>           CSSQA = W(1) * W(1)
>           W(3) = CSSQA + CSSQA - 1.0
>           W(4) = W(1) * W(2)
>           W(4) = W(4) + W(4)
>           W(5) = W(3) * W(1) - W(4) * W(2)
>           W(6) = W(4) * W(1) + W(3) * W(2)
>           CSSQ2A = W(3) * W(3)
>           W(7) = CSSQ2A + CSSQ2A - 1.0
>           W(8) = W(4) * W(3)
>           W(8) = W(8) + W(8)
>           W(9) = W(7) * W(1) - W(8) * W(2)
>           W(10) = W(8) * W(1) + W(7) * W(2)
#
```

```
>          CSSQ3A = W(5) * W(5)
>          W(11) = CSSQ3A + CSSQ3A - 1.0
>          W(12) = W(6) * W(5)
>          W(12) = W(12) + W(12)
>          W(13) = W(7) * W(5) - W(8) * W(6)
>          W(14) = W(8) * W(5) + W(7) * W(6)
>   90     LBLOKO = OFFSET + LBLOK1
>C
>          DO 130 K0 = OFFSET, LBLOKO, 2
>            K1 = K0 + LBLOK2
>            K2 = K1 + LBLOK2
>            K3 = K2 + LBLOK2
>            K4 = K3 + LBLOK2
>            K5 = K4 + LBLOK2
>            K6 = K5 + LBLOK2
>            K7 = K6 + LBLOK2
>            XK0WR = XX(K0)
>            XK0WI = XX(K0 + 1)
>            GO TO ISTNUM, (100, 110)
> 100        XK1WR = XX(K1)
>            XK1WI = XX(K1 + 1)
>            XK2WR = XX(K2)
>            XK2WI = XX(K2 + 1)
>            XK3WR = XX(K3)
>            XK3WI = XX(K3 + 1)
>            XK4WR = XX(K4)
>            XK4WI = XX(K4 + 1)
>            XK5WR = XX(K5)
>            XK5WI = XX(K5 + 1)
>            XK6WR = XX(K6)
>            XK6WI = XX(K6 + 1)
>            XK7WR = XX(K7)
>            XK7WI = XX(K7 + 1)
>            GO TO 120
>C
> 110        XK1WR = XX(K1) * W(1) - XX(K1 + 1) * W(2)
>            XK1WI = XX(K1) * W(2) + XX(K1 + 1) * W(1)
>            XK2WR = XX(K2) * W(3) - XX(K2 + 1) * W(4)
>            XK2WI = XX(K2) * W(4) + XX(K2 + 1) * W(3)
>            XK3WR = XX(K3) * W(5) - XX(K3 + 1) * W(6)
>            XK3WI = XX(K3) * W(6) + XX(K3 + 1) * W(5)
>            XK4WR = XX(K4) * W(7) - XX(K4 + 1) * W(8)
>            XK4WI = XX(K4) * W(8) + XX(K4 + 1) * W(7)
>            XK5WR = XX(K5) * W(9) - XX(K5 + 1) * W(10)
>            XK5WI = XX(K5) * W(10) + XX(K5 + 1) * W(9)
>            XK6WR = XX(K6) * W(11) - XX(K6 + 1) * W(12)
>            XK6WI = XX(K6) * W(12) + XX(K6 + 1) * W(11)
>            XK7WR = XX(K7) * W(13) - XX(K7 + 1) * W(14)
>            XK7WI = XX(K7) * W(14) + XX(K7 + 1) * W(13)
> 120        A0R = XK0WR + XK4WR
>            A0I = XK0WI + XK4WI
>            A1R = XK1WR + XK5WR
>            A1I = XK1WI + XK5WI
>            A2R = XK2WR + XK6WR
>            A2I = XK2WI + XK6WI
>            A3R = XK3WR + XK7WR
>            A3I = XK3WI + XK7WI
>            A4R = A0R + A2R
>            A4I = A0I + A2I
>            A5R = A0R - A2R
>            A5I = A0I - A2I
>            A6R = A1R + A3R
>            A6I = A1I + A3I
>            A7R = A3I - A1I
>            A7I = A1R - A3R
>            XX(K0) = A4R + A6R
>            XX(K0 + 1) = A4I + A6I
>            XX(K1) = A4R - A6R
>            XX(K1 + 1) = A4I - A6I
>            XX(K2) = A5R + A7R
>            XX(K2 + 1) = A5I + A7I
>            XX(K3) = A5R - A7R
#
```

```
>            XX(K3 + 1) = A5I - A7I
>            A0R = XK0WR - XK4WR
>            A0I = XK0WI - XK4WI
>            A8R = XK1WR - XK5WR
>            A8I = XK1WI - XK5WI
>            A1R = A8R - A8I
>            A1I = A8R + A8I
>            A2R = XK6WI - XK2WI
>            A2I = XK2WR - XK6WR
>            A8R = XK3WR - XK7WR
>            A8I = XK3WI - XK7WI
>            A3R = A8R - A8I
>            A3I = A8R + A8I
>            A4R = A0R + A2R
>            A4I = A0I + A2I
>            A5R = A0R - A2R
>            A5I = A0I - A2I
>            A6R = (A1R - A3I) / ROOT2
>            A6I = (A1I + A3R) / ROOT2
>            A7R = (A3R - A1I) / ROOT2
>            A7I = (A3I + A1R) / ROOT2
>            XX(K4) = A4R + A6R
>            XX(K4 + 1) = A4I + A6I
>            XX(K5) = A4R - A6R
>            XX(K5 + 1) = A4I - A6I
>            XX(K6) = A5R + A7R
>            XX(K6 + 1) = A5I + A7I
>            XX(K7) = A5R - A7R
> 130      XX(K7 + 1) = A5I - A7I
>C
>          DO 150 K = 4, N
>            IF (NBIT(K) .NE. 0) GO TO 140
>            NBIT(K) = 1
>            NW = NW + JNT(K)
>            GO TO 160
> 140        NBIT(K) = 0
> 150      NW = NW - JNT(K)
>C
> 160      ASSIGN 110 TO ISTNUM
> 170    CONTINUE
> 180 CONTINUE
>C
>      NW = 0
>C
>      DO 190 K = 1, N
>        JNT(K) = JNT(K) + JNT(K)
> 190 NBIT(K) = 0
> 200 CONTINUE
>C
>      K = 0
>      IF (NW .LE. K) GO TO 210
>      HOLDR = XX(NW + 1)
>      HOLDI = XX(NW + 2)
>      XX(NW + 1) = XX(1)
>      XX(NW + 2) = XX(2)
>      XX(1) = HOLDR
>      XX(2) = HOLDI
>C
> 210 DO 230 M = 1, N
>        IF (NBIT(M) .NE. 0) GO TO 220
>        NBIT(M) = 1
>        NW = NW + JNT(M)
>        GO TO 240
> 220    NBIT(M) = 0
> 230 NW = NW - JNT(M)
>C
> 240 DO 280 K = 2, NX2LS2, 2
>        IF (NW .LE. K) GO TO 250
>        HOLDR = XX(NW + 1)
>        HOLDI = XX(NW + 2)
>        XX(NW + 1) = XX(K + 1)
>        XX(NW + 2) = XX(K + 2)
#
```

```
>        XX(K + 1) = HOLDR
>        XX(K + 2) = HOLDI
>C
> 250    DO 270 M = 1, N
>          IF (NBIT(M) .NE. 0) GO TO 260
>          NBIT(M) = 1
>          NW = NW + JNT(M)
>          GO TO 280
> 260      NBIT(M) = 0
>          NW = NW - JNT(M)
> 270    CONTINUE
> 280  CONTINUE
>C
>      IF (SIGNI .GT. 0.0) GO TO 300
>C
>      DO 290 K = 1, NX2LS1, 2
> 290  XX(K + 1) = -XX(K + 1)
>C
> 300  RETURN
>      END
#
```

REFERENCES

ABDALLAH, A., COURTILLOT, V., KASSER, M., Le DAIN, A.-Y., LÉPINE, J.-C., ROBINEAU, B., RUEGG, J.-C., TAPPONNIER, P., TARANTOLA, A., 1979
Relevance of Afar seismicity and volcanism to the mechanics of accreting plate boundaries, Nature, 282, p.17-23.

ADAMS, R.D., 1977
Survey of practice in determining magnitudes of near earthquakes part 2: Europe, Asia, Africa, Australasia, the Pacific, World Data Center A for Solid Earth Geophysics, Report SE-8, NOAA, Boulder, Colorado.

AKI, K., 1967
Scaling law of seismic spectrum, J. Geophys. Res., 72, p.1217-1231.

AKI, K., 1969
Analysis of the seismic coda of local earthquakes as scattered waves, J. Geophys. Res., 74, p.615-631.

AL-CHALABI, M., 1971
Reliability of the rotation pole in continental fitting, Earth Planet Sci. Lett., 11, p.257-262.

AL-CHALABI, M., 1972
Interpretation of gravity anomalies by non-linear optimisation, Geophys. Prospect., 20, p.1-16.

ALLAN, T.D., 1970
Magnetic and gravity fields over the Red Sea, Phil. Trans. R. Soc. Lond., A267, p.153-180.

ALLAN, T.D., PISANI, M., 1966
Gravity and magnetic measurements in the Red Sea, Geol. Surv. Pap. Can., 66-14, p.62-64.

ALLARD, P., TAZIEFF, H., DAJLEVIC, D., 1979
Observations of seafloor spreading in Afar during the November 1978 fissure eruption, Nature, 279, p.30-33.

ALLEN, R.V., 1978
Automatic earthquake recognition and timing from single traces, Bull. Seism. Soc. Am., 68, p.1521-1532.

AMBUTER, B.P., SOLOMON, S.C., 1974
An event-recording system for monitoring small earthquakes, Bull. Seism. Soc. Am., 64, p.1181-1188.

ARCHAMBEAU, C.B., 1968
General theory of elastodynamic source fields, Rev. Geophys., 3, p.241-288.

ARCHAMBEAU, C.B., FLINN, E.A., 1965
Automated analysis of seismic radiation for source characteristics, Proc. IEEE, 53, p.1876-1884.

ARCHAMBEAU, C.B., FLINN, E.A., LAMBERT, D.G., 1969
Fine structure of the upper mantle, J. Geophys. Res., 73, p.5825-5865.

ARCHULETA, R.J., FRAZIER, G.A., 1978
Three-dimensional numerical simulations of dynamic faulting in a half-space, Bull. Seism. Soc. Am., 68, p.541-572.

ARMOUR, A.R., 1977
A seismic refraction study of the crustal structure of North West Scotland and adjacent continental margin, Ph.D. Thesis, University of Durham.

ARNOLD, L.R.A., 1974
Seimicity of the East African rift system determined from the Kaptagat array, M.Sc. Dissertation, University of Durham.

ARTHAUD, F., CHOUKROUNE, P., 1976
Mis en évidence d'une phase de compression à 3.5 M.A. séparant deux épisodes d'ouverture du rift océanique de Tadjourah (T.F.A.I.), C. R. Acad. Sci. Paris, D283, p.13-16.

ATWATER, T., MacDONALD, K.C., 1977
Are spreading centres perpendicular to their transform faults? Nature, 270, p.715-719.

BÄCKER, H., LANGE, K., RICHTER, H., 1975
Morphology of the Red Sea central graben between Subair Islands and Abul Kizaan, Geol. Jb., D13, p.79-123.

BAILEY, D.K., 1972
Uplift, rifting and magmatism in continental plates, J. Earth Sci. (Leeds), 8, p.225-239.

BAILEY, D.K., MacDONALD, R., 1970
Petrochemical variations among mildly peralkaline (comendite) obsidians from the oceans and continents, Contrib. Mineral. Petrol., 28, p.340-351.

BAKER, B.H., 1970
The structural pattern of the Afro-Arabian rift system in relation to plate tectonics, Phil. Trans. R. Soc. Lond., A267, p.283-291.

BAKER, B.H., MOHR, P.A., WILLIAMS, L.A.J., 1972
Geology of the Eastern Rift System of Africa, Geol. Soc. Am., special paper 136.

BAKER, B.H., WOHLENBERG, J., 1971
Structure and evolution of the Kenya rift valley, Nature, 229, p.538-541.

BAKUN, W.H., LINDH, A.G., 1977
Local magnitudes, seismic moments and coda durations for earthquakes near Oroville, California, Bull. Seism. Soc. Am., 67, p.615-629.

BANNERT, D., BRINCKMANN, J., KÄDING, K.-C., KNETSCH, G., KÜRSTEN, M., MAYRHOFER, H., 1970
Zur Geologie der Danakil-Senke (Nördliches Afar-Gebiet, NE-Äthiopien), Geol. Rdsch., 59, p.409-443.

BARBERI, F., BIZOUARD, J., VARET, J., 1971
Nature of the clinopyroxene and iron enrichment in alkalic and transitional basaltic magmas, Contrib. Mineral. Petrol., 33, p.93-107.

BARBERI, F., BONATTI, E., MARINELLI,G., VARET,J., 1974
Transverse tectonics during the split of a continent: data from the Afar rift, Tectonophysics, 23, p.17-29.

BARBERI, F., BORSI, S., FERRARA, G., MARINELLI, G., SANTACROCE, R., TAZIEFF, H., VARET, J., 1972b
Evolution of the Danakil depression (Afar, Ethiopia) in light of radiometric age determinations, J. Geol., 80, p.720-729.

BARBERI, F., BORSI, S., FERRARA, G., MARINELLI, G., VARET, J., 1970
Relations between tectonics and magmatology in the northern Danakil Depression (Ethiopia), Phil. Trans. R. Soc. Lond., A267, p.293-311.

BARBERI, F., CIVETTA, L., VARET, J., 1980
Sr isotopic composition of Afar volcanics and its implication for mantle evolution, Earth Planet Sci. Lett., 50, p.247-259.

BARBERI, F., FERRARA, G., SANTACROCE, R., TREUIL, M., VARET, J., 1975b
A transitional basalt-pantellerite sequence of fractional crystallisation, the Boina centre (Afar rift, Ethiopia), J. Petrology, 16, p.22-56.

BARBERI, F., FERRARA, G., SANTACROCE, R., VARET, J., 1975a
Structural evolution of the Afar triple junction, in Pilger, A., and Rösler, A., eds., Afar Depression of Ethiopia: Stuttgart, E. Schweizerbart'sche Verlagsbuchhandlung, p.38-54.

BARBERI, F., SANTACROCE, R., VARET, J., 1974
Silicic peralkaline volcanic rocks of the Afar Depression (Ethiopia), Bull. Volcan., 38, p.755-790.

BARBERI, F., TAZIEFF, H., VARET, J., 1972a
Volcanism in the Afar Depression: its tectonic and magmatic significance, Tectonophysics, 15, p.19-29.

BARBERI, F., VARET, J., 1970
The Erta'Ale volcanic range (Afar, Ethiopia), Bull. Volcan., 34, p.848-917.

BARBERI, F., VARET, J., 1975
Recent volcanic units of Afar and their structural significance, in Pilger, A., and Rösler, A., eds., Afar Depression of Ethiopia: Stuttgart, E. Schweizerbart'sche Verlagsbuchhandlung, p.174-178.

BARBERI, F., VARET, J., 1977
Volcanism of Afar: small-scale plate tectonics implications, Bull. geol. Soc. Am., 88, p.1251-1266.

BASHAM, P.W., ELLIS, R.M., 1969
The composition of P codas using magnetic tape seismograms, Bull. Seism. Soc. Am., 59, p.473-486.

BÅTH, M., 1973
Introduction to seismology, Birkhäuser Verlag, Basel and Stuttgart.

BÅTH, M., 1974
Spectral Analysis in Geophysics, Developments in solid earth geophysics, vol. 7, Elsevier Scientific Publishing Co., Amsterdam/Oxford/New York.

BÅTH, M., 1978a
A note on recurrence relations for earthquakes, Tectonophysics, 51, p.T23-T30.

BÅTH, M., 1978b
Some properties of earthquake-frequency distributions, Tectonophysics, 51, p.T63-T69.

BEHLE, A, MAKRIS, J., BAIER, B., DELIBASIS, N., 1975
Salt thickness near Dallol (Ethiopia) from seismic reflection measurements and gravity data, in Pilger, A., and Rösler, A., eds., Afar Depression of Ethiopia: Stuttgart, E. Schweizerbart'sche Verlagsbuchhandlung, p.156-167.

BENIOFF, H., 1951
Earthquakes and rock creep (Part 1: creep characteristics of rocks and the origin of aftershocks), Bull. Seism. Soc. Am., 41, p.31-62.

BERCKHEMER, H., JACOB, K.H., 1968
Investigation of the dynamic process in earthquake foci by analyzing the pulse shape of body waves, Final report, Contract AF61(052)-801, Inst. of Meteorol. and Geophys., Univ. of Frankfurt, Germany.

BERCKHEMER, H., BAIER, B., BARTELSEN, H., BEHLE, A., BURKHARDT, H., GEBRANDE, H., MAKRIS, J., MENZEL, H., MILLER, H., 1975
Deep seismic soundings in the Afar region and on the highlands of Ethiopia, in Pilger, A., and Rösler, A., eds., Afar Depression of Ethiopia: Stuttgart, E. Schweizerbart'sche Verlagsbuchhandlung, p.89-107.

BERKTOLD, G., HAAK, V., ANGENHEISTER, G., 1975
Magnetotelluric measurements in the Afar area, in Pilger, A., and Rösler, A., eds., Afar Depression of Ethiopia: Stuttgart, E. Schweizerbart'sche Verlagsbuchhandlung, p.66-79.

BEYDOUN, Z.R., 1970
Southern Arabia and Somalia: comparative geology, Phil. Trans. R. Soc. Lond., A267, p.267-292.

BEYTH, M., 1978
A comparative study of the sedimentary fills of the Danakil Depression (Ethiopia) and Dead-Sea rift (Israel), Tectonophysics, 46, p.357-367.

BIRTILL, J.W., WHITEWAY, F.E., 1965
The application of phased arrays to the analysis of seismic body waves, Phil. Trans. R. Soc. Lond., A258, p.421-493.

BISZTRICSANY, E., 1958
A new method for the determination of earthquake magnitudes, Geofiz. Kozlemen, 7, p.69-96.

BIZOUARD, H., BARBERI, F., VARET, J., 1976
Minéralogie de séries volcaniques axiales de l'Afar: précisions sur les processus et les conditions de fractionnement des magmas basaltiques dans les zones en accrétion, Bull. Soc. géol. Fr., 18, p.837-840.

BLACK, R., MORTON, W.H., REX, D.C., 1975
Block tilting and volcanism within the Afar in the light of recent K/Ar age data, in Pilger, A., and Rösler, A., eds., Afar Depression of Ethiopia: Stuttgart, E. Schweizerbart'sche Verlagsbuchhandlung, p.296-300.

BLACK, R., MORTON, W., REX, D., SHACKLETON, R., 1972a
Sur la découverte en Afar (Ethiopie) d'un granite hyperalcalin miocène: le massif de Limmo, C. R. Acad. Sci. Paris, D274, p.1453-1456.

BLACK, R., MORTON, W.H., TSEGAYE HAILU, 1974
Early structures around the Afar triple junction, Nature, 248, p.496-497.

BLACK, R., MORTON, W.H., VARET, J., 1972b
New data on Afar tectonics, Nature phys. Sci., 240, p.170-173.

BLOCH, S., HALES, A.L., LANDISMAN, M., 1969
Velocities in the crust and upper mantle of Southern Africa, from multi-mode surface wave dispersion, Bull. Seism. Soc. Am., 59, p.1599-1629.

BOATWRIGHT, J., 1980
A spectral theory for circular seismic sources; simple estimates of source dimension, dynamic stress drop, and radiated seismic energy, Bull. Seism. Soc. Am., 70, p.1-28.

BOLT, B.A., 1960
The revision of earthquake epicentres, focal depths and origin-times using a high-speed computer, Geophys. J. R. Astr. Soc., 3, p.433-440.

BONATTI, E., EMILIANI, C., OSTLUND, G., RYDELL, H., 1971
Final dessication of the Afar rift, Ethiopia, Science, 172, p.468-469.

BONJER, K.-P., FUCHS, K., WOHLENBERG, J., 1970
Crustal structure of the East African rift system from spectral response ratios of long-period waves, Zeitschrift Geophys., 36, p.287-297.

BOTT, M.H.P., 1971
The interior of the Earth, Edward Arnold Ltd., London.

BOUCARUT, M., CLIN, M., 1976
Conceptions nouvelles sur les relations Mer Rouge - Golfe d'Aden, à partir du Territoire des Afars et des Issas, C. R. Acad. Sci. Paris, D282, p.1145-1148.

BRACEWELL, R.N., 1978
The Fourier transform and its applications, McGraw-Hill Book Co. (2nd edition).

BRANDSDÓTTIR, B., EINARSSON, P., 1979
Seismic activity associated with the September 1977 deflation of the Krafla central volano in north-eastern Iceland, J. Volcan. Geoth. Res., 6, p.197-212.

BRIDEN, J.C., GASS, I.G., 1974
Plate movement and continental magmatism, Nature, 248, p.650-653.

BROWN, C., GIRDLER, R.W., 1980
Interpretation of African gravity and its implication for the breakup of the continents, J. Geophys. Res., 85, p.6443-6455.

BRUNE, J.N., 1970
Tectonic stress and the spectra of seismic shear waves from earthquakes, J. Geophys. Res., 75, p.4997-5009.

BRUNE, J.N., 1971
Correction to "Tectonic stress and the spectra of seismic shear waves from earthquakes", J. Geophys. Res., 76, p.5002.

BRUNE, J.N., ARCHULETA, J.A., HARTZELL, S., 1979
Far-field S-wave spectra, corner frequencies, and pulse shapes, J. Geophys. Res., 84, p.2262-2272.

BULAND, R., 1976
The mechanics of locating earthquakes, Bull. Seism. Soc. Am., 66, p.173-187.

BULL. SOC. GÉOL. FR., 1976
Collected papers given at the colloquium on "Creation de la lithosphere oceanique, Bull. Soc. geol. Fr., 18, p.789-947.

BULLEN, K.E., 1965
An introduction to the theory of seismology, Cambridge University Press (3rd edition).

BUREK, P.J., 1970
Palaeomagnetic evidence for an anti-clockwise rotation of the Danakil Alps, Ethiopia, EOS (Trans. Am. Geophys. Un.), 51, p.271.

BUREK, P.J., 1974
Plattentektonische Probleme in der weiteren Umbegung Arabiens sowie der Danakil-Afar-Senke, Geotekt. Forsch., 47, p.1-93.

BUREK, P.J., 1978
Zur Entwicklung von Riftsystemen im Frühstadium (Hebung-Spaltung-Vulkanismus-Spreading) am Beispiel der Afar Senke, Geol. Rdsch., 67, p.576-597.

BYERLY, P., 1955
Nature of faulting as deduced from seismograms, Geol. Soc. Am. special paper 62, p.75-86.

CAGNETTI, V., PASQUALE, V., 1979
The earthquake sequence in Friuli, Italy, 1976, Bull. Seism. Soc. Am., 69, p.1797-1818.

CAPUTO, T., CONSOLE, P., 1980
Statistical distribution of stress drop and faults of seismic regions, Tectonophysics, 67, p.T13-T20.

CHASE, C.G., 1978
Plate kinematics : the Americas, East Africa, and the rest of the world, Earth Planet Sci. Lett., 37, p.355-368.

CHESSEX, R., DELALOYE, M., MÜLLER, J., WEIDMANN, M., 1975
Evolution of the volcanic region of Ali Sabieh (T.F.A.I.) in the light of K-Ar age determinations, in Pilger, A., and Rösler, A., eds., Afar Depression of Ethiopia: Stuttgart, E. Schweizerbart'sche Verlagsbuchhandlung, p.221-227.

CHRISTENSEN, N.I., 1970
Composition and evolution of the oceanic crust, Marine Geol., 8, p.139-154.

CHRISTIANSEN, T.B., SCHAEFER, H.-U., SCHONFELD, M., 1975
Southern Afar and adjacent areas: geology, petrology, geochemistry, in Pilger, A., and Rösler, A., eds., Afar Depression of Ethiopia: Stuttgart, E. Schweizerbart'sche Verlagsbuchhandlung, p.259-277.

CIVETTA, L., de FINO, M., GASPARINI, P., GHIARA, M., La VOLPE, L., LIRER, L., 1975a
Structural meaning of east-central Afar volcanism (Ethiopia, T.F.A.I.), J. Geol., 83, p.363-373.

COCHRAN, J.R., 1981
The Gulf of Aden: structure and evolution of a young ocean basin and a continental margin, J. Geophys. Res., 86, p.263-287.

COOLEY, J.W., TUKEY, J.W., 1965
An algorithm for the machine calulation of complex Fourier series, Math. Comput., 19, p.297-301.

CORBISHLEY, D.J., 1969
Measurements of the derivative of the P-wave travel time curve by means of an array network, Ph.D. Thesis, University of Durham.

COURTILLOT, V.E., 1980
Opening of the Gulf of Aden by progressive tearing, Phys. Earth Plan. Int., 21, p.343-350.

COURTILLOT, V.E., GALDEANO, A., Le MOUEL, J.L., 1980
Propagation of an accreting plate boundary; a discussion of new aeromagnetic data in the Gulf of Tadjourah and southern Afar, Earth Planet Sci. Lett., 47, p.144-160.

COURTILLOT, V.E., TAPPONNIER, P., VARET, J., 1974
Surface features associated with transform faults: a comparison between observed examples and an experimental model, Tectonophysics, 24, p.317-329.

CROSSON, R.S., 1972
Small earthquakes, structure and tectonics of the Puget Sound region, Bull. Seism. Soc. Am., 62, p.1133-1177.

CROSSON, R.S., 1976a
Crustal structure modeling of earthquake data 1. Simultaneous least squares estimation of hypocenter and velocity parameters, J. Geophys. Res., 81, p.3036-3046.

CROSSON, R.S., 1976b
Crustal structure modeling of earthquake data 2. Velocity structure of the Puget Sound region, Washington, J. Geophys. Res., 81, p.3047-3054.

CROSSON, R.S., KOYANAGI, R.Y., 1979
Seismic velocity structure below the island of Hawaii from local earthquake data, J. Geophys. Res., 84, p.2331-2342.

DAHLEN, F.A., 1974
On the ratio of the P-wave to S-wave corner frequencies for shallow earthquake sources, Bull. Seism. Soc. Am., 64, p.1159-1180.

DAKIN, F.M., 1975
A preliminary survey of the distribution and characteristics of earthquake sequences in Ethiopia and T.F.A.I., Bull. geophys. Obs. Addis Ababa, 15, p.51-70.

DAKIN, F.M., GOUIN, P., SEARLE, R.C., 1971
The 1969 earthquakes in Serdo (Ethiopia), Bull. geophys. Obs. Addis Ababa, 13, p.19-56.

DAS, S., AKI, K., 1977
Fault plane with barriers: a versatile earthquake model, J. Geophys. Res., 82, p.5658-5670.

DANIEL, R.G., 1979
An intermediate-period field system using a short-period seismometer, Bull. Seism. Soc. Am., 69, p.1623-1626.

DAVIES, D., TRAMONTINI, C., 1970
Some recent seismic refraction results from the Red Sea, Phil. Trans. R. Soc. Lond., A267, p.181-189.

de FINO, M., La VOLPE, L., LIRER, L., VARET, J.. 1973a
Geology and petrology of Manda-Inakir range and Moussa Alli volcano, central eastern Afar (Ethiopia and T.F.A.I.), Revue Géogr. phys. Géol. dyn., 15, p.373-386.

de FINO, M., La VOLPE, L., LIRER, L., 1973b
Volcanology and petrology of the Assab Range (Ethiopia), Bull. Volcan., 37, p.95-110.

DELIBRIAS, G., MARINELLI, G., STIELTJES, L., 1975
Spreading rate of the Asal Rift: a geological approach, in Pilger, A., and Rösler, A., eds., Afar Depression of Ethiopia: Stuttgart, E. Schweizerbart'sche Verlagsbuchhandlung, p.214-221.

DEMANGE, J., STIELTJES, L., 1975
Géologie de la région sud-ouest du T.F.A.I. (région lac Abhé - lac Asal), Bull. B. R. G. M., sect 4, 2e serie, p.83-119.

DESAI, C.S., ABEL, J.F., 1972
Introduction to the finite element method, Van Nostrand Reinhold Co., New York.

DIXEY, F., 1956
The East African rift system, Bull. colon. Geol. Miner. Resour., Suppl.

DOUGLAS, A., 1967
Joint epicentral determination, Nature, 215, p.47-48.

DOUGLAS, B.M., RYALL, A., 1972
Spectral characteristics and stress drop for ...icroearthquakes near Fairview Peak, Nevada, J. Geophys. Res., 77, p.351-359.

DRAKE, C.L., GIRDLER, R.W., 1964
A geophysical study of the Red Sea, Geophys. J., 8, p.473-495.

EATON, J.P., O'NEILL, M.E., MURDOCK, J.N., 1970
Aftershocks of the 1966 Parkfield-Cholame, California, earthquakes: a detailed study, Bull. Seism. Soc. Am., 60, p.1151-1197.

EINARSSON, P., 1974
Seismic activity recorded in Surtsey during the summer of 1966, Surtsey Res. Progress Rept. 7, p.83-90.

EINARSSON, P., BRANDSDÓTTIR, B., 1980
Seismological evidence for lateral magma intrusion during the July 1980 deflation of the Krafla volcano in NE-Iceland, J. Geophys., 47, p.160-165.

EINARSSON, P., KLEIN, F.W., BJÖRNSSON, S., 1977
The Borgarfjördur earthquakes of 1974 in West Iceland, Bull. Seism. Soc. Am., 67, p.187-208.

ELDER, J.W., 1966
Penetrative convection: its role in vulcanism, Bull. Volcan., 29, p.327-342.

EL-ETR, H.A., ABDALLAH, A.M., ABDEL-RAHMAN, M.A., 1976
Dike distribution in the southern part of the Gulf of Suez region, Egypt, in Pilger, A., and Rösler, A., eds., Afar between continental and oceanic rifting: Stuttgart, E. Schweizerbart'sche Verlagsbuchhandlung, p.144-148.

ELLIS, R.M., BASHAM, P.W., 1968
Crustal characteristics from short-period P waves, Bull. Seism. Soc. Am., 58, p.1681-1700.

ENGDAHL, E.R., GUNST, R.H., 1966
Use of a high-speed computer for the preliminary determination of earthquake hypocenters, Bull. Seism. Soc. Am., 56, p.325-336.

EVERNDEN, J.F., 1953
Direction of approach of Rayleigh waves and related problems (part 1), Bull. Seism. Soc. Am., 43, p.335-374.

EVERNDEN, J.F., 1967
Magnitude determinations at regional and near-regional distances in the United States, Bull. Seism. Soc. Am., 57, p.591-639.

EVERNDEN, J.F., 1969
Precision of epicenters obtained by small numbers of world-wide stations, Bull. Seism. Soc. Am., 59, p.1365-1398.

FAIRHEAD, J.D., 1979
A gravity link between the domally uplifted Cainozoic volcanic centres of North Africa and its similarity to the East African rift system anomaly, Earth Planet Sci. Lett., 42, p.109-113.

FAIRHEAD, J.D., GIRDLER, R.W., 1970
The seismicity of the Red Sea, Gulf of Aden and Afar triangle, Phil. Trans. R. Soc. Lond., A267, p.49-74.

FAIRHEAD, J.D., GIRDLER, R.W., 1971
The seismicity of Africa, Geophys. J. R. Astr. Soc., 24, p.271-301.

FEATHERSTONE, P.S., 1976
A geophysical investigation of the South-East Greenland continental margin, Ph.D. Thesis, University of Durham.

FERNANDEZ, L.M., 1967
Master curves for the response of layered systems to compressional seismic waves, Bull. Seism. Soc. Am., 57, p.515-543.

FERRARA, G., TREUIL, M., 1974
Petrological implications of trace-element and Sr isotope distribution in basalt-pantellerite series, Bull. Volcan., 38, p.548-574.

FISHER, R.A., 1953
Dispersion on a sphere, Phil. Trans. R. Soc. Lond., A217, p.295-305.

FLETCHER, R., 1970
A new approach to variable metric algorithms, Comput. J., 13, p.317-322.

FLETCHER, R., POWELL, M.J.D., 1963
A rapidly convergent descent method for minimization, Comput. J., 6, p.163-168.

FLINN, E.A., 1960
Local earthquake location with an electronic computer, Bull. Seism. Soc. Am., 50, p.467-470.

FLINN, E.A., 1965a
Confidence regions and error determinations for seismic event location, Rev. Geophys., 3, p.157-185.

FLINN, E.A., 1965b
Signal analysis using rectilinearity and direction of particle motion, Proc. IEEE, 53, p.1874-1876.

FLÓVENZ, Ó.G., 1980
Seismic structure of the Icelandic crust above layer 3 and the relation between body wave velocity and the alteration of the basaltic crust, J. Geophys., 47, p.211-220.

FÖRSTER, H., 1976
Continental drift in Iran in relation to the Afar structures, in Pilger, A., and Rösler, A., eds., Afar between continental and oceanic rifting: Stuttgart, E. Schweizerbart'sche Verlagsbuchhandlung, p.182-190.

FORTH, P.A., 1975
The structure of the upper mantle beneath East Africa, Ph.D. Thesis, University of Durham.

FOULGER, G., EINARSSON, P., 1980
Recent earthquakes in the Hengill - Hellisheidi area of SW-Iceland, J. Geophys., 47, p.171-175.

FRANCIS, T.J.G., PORTER, I.T., 1971
A statistical study of Mid-Atlantic ridge earthquakes, Geophys. J. R. Astr. Soc., 24, p.31-50.

FRANCIS, T.J.G., PORTER, I.T., LILWALL, R.C., 1978
Microearthquakes near the eastern end of St. Paul's Fracture Zone, Geophys. J. R. Astr. Soc., 53, p.201-217.

FRAZIER, S.B., 1970
Adjacent structures of Ethiopia: that portion of the Red Sea coast including Dahlak Kebir Island and the Gulf of Zula, Phil. Trans. R. Soc. Lond., A267, p.131-141.

FREEDMAN, H.W., 1966
The "little variable factor": a statistical discussion of the reading of seismograms, Bull. Seism. Soc. Am., 56, p.593-604.

FREEDMAN, H.W., 1968
Seismological measurements and measurement error, Bull. Seism. Soc. Am., 58, p.1261-1271.

FREUND, R., 1970
Plate tectonics of the Red Sea and East Africa, Nature, 228, p.453.

FREUND, R., GARFUNKEL, Z., ZAK, I., GOLDBERG, M., WEISSBROD, T., DERIN, B., 1970
The shear along the Dead Sea rift, Phil. Trans. R. Soc. Lond., A267, p.107-130.

FUCHS, K., MÜLLER, G., 1971
Computation of synthetic seismograms with the reflectivity method and comparison with observations, Geophys. J. R. Astr. Soc., 23, p.417-433.

GARSON, M.S., KRS, M., 1976
Geophysical and geological evidence of the relationship of Red Sea transverse tectonics to ancient fractures, Bull. geol. Soc. Am., 87, p.169-181.

GARZA, T., LOMNITZ, C., de VELASCO, C.R., 1977
An interactive epicenter location procedure for the RESMAC seismic array: I, Bull. Seism. Soc. Am., 67, p.1577-1586.

GARZA, T., LOMNITZ, C., de VELASCO, C.R., 1979
An interactive epicenter location procedure for the RESMAC seismic array: II, Bull. Seism. Soc. Am., 69, p.1215-1236.

GASS, I.G., 1970
The evolution of volcanism in the junction area of the Red Sea, Gulf of Aden and Ethiopian rifts, Phil. Trans. R. Soc. Lond., A267, p.369-381.

GASS, I.G., 1972a
The role of lithothermal systems in magmatic and tectonic processes, J. Earth Sci. (Leeds), 8, p.261-273.

GASS, I.G., 1972b
Proposals concerning the variation of volcanic products and processes within the oceanic environment, Phil. Trans. R. Soc. Lond., A271, p.131-140.

GASS, I.G., 1975
Magmatic and tectonic processes in the development of the Afro-Arabian dome, in Pilger, A., and Rösler, A., eds., Afar Depression of Ethiopia: Stuttgart, E. Schweizerbart'sche Verlagsbuchhandlung, p.10-18.

GASS, I.G., 1977
The age and extent of the Red Sea oceanic crust, Nature, 265, p.722-723.

GASS, I.G., GIBSON, I.L., 1969
Structural evolution of the rift zones in the Middle East, Nature, 221, p.926-930.

GASS, I.G., MALLICK, D.I.J., COX, K.G., 1973
The volcanic islands of the Red Sea, J. geol. Soc. London, 129, p.275-310.

GASSE, F., 1974
Nouvelles observations sur les formations lacustres quaternaires dans la basse vallée de l'Awash et quelques grabens adjacents (Afar, Ethiopie et T.F.A.I.), Revue Géogr. phys. Géol. dyn., 16, p.101-118.

GASSE, F., 1975
Fluctuations of the Afar lake levels during the late Quaternary period, in Pilger, A., and Rösler, A., eds., Afar Depression of Ethiopia: Stuttgart, E. Schweizerbart'sche Verlagsbuchhandlung, p.284-288.

GASSE, F., ROGNON, P., 1973
Le quaternaire des bassins lacustres de l'Afar, Revue Géogr. phys. Géol. dyn., 15, p.405-414.

GEHLEN, K.u., FORKEL, W., SPIES, O., 1975
Petrological interpretation of geophysical data from the Afar depression, Ethiopia, in Pilger, A., and Rösler, A., eds., Afar Depression of Ethiopia: Stuttgart, E. Schweizerbart'sche Verlagsbuchhandlung, p.151-155.

GEOMAP, 1969
Topographic map of Northern Afar, from GEOMAP Geological Surveys, 21 Via Lamarmora, 50121 Firenze, Italy (4 sheets).

GERSTER, G., 1976
Grand design: the earth from above, Paddington Press, New York and London.

GIBB, Sir A. and Partners (consulant engineers), in association with Hunting Services Ltd., 1973
Feasibility study of the Lower Awash valley, for Imperial Ethiopian Government Awash Valley Authority, Progress report for second steering committee (unpublished).

GIBOWICZ, S.J., 1973
Stress drop and aftershocks, Bull. Seism. Soc. Am., 63, p.1433-1446.

GIBSON, I.L., 1972
The chemistry and petrogenesis of a suite of pantellerites from tne Ethiopian rift, J. Petrology, 13, p.31-44.

GIBSON, I.L., 1974
A review of the geology, petrology and geochemistry of the volcano Fantale, Bull. Volcan., 38, p.791-802.

GIBSON, I.L., TAZIEFF, H., 1970
The structure of Afar and the northern part of the Ethiopian rift, Phil. Trans. R. Soc. Lond., A267, p.331-338.

GIRDLER, R.W., 1966
The role of translational and rotational movements in the formation of the Red Sea and Gulf of Aden, Geol. Surv. Pap. Can., 66-14, p.65-77.

GIRDLER, R.W., 1970
An aeromagnetic survey of the junction of the Red Sea, Gulf of Aden and Ethiopian rifts - a preliminary report, Phil. Trans. R. Soc. Lond., A267, p.359-368.

GIRDLER, R.W., BROWN, C., NOY, D.J.M., STYLES, P., 1980
A geophysical survey of the westernmost Gulf of Aden, Phil. Trans. R. Soc. Lond., A298, p.1-43.

GIRDLER, R.W., DARRACOTT, B.W., 1972
African poles of rotation, Comments Earth Sci., Geophys., 2, p.131-138.

GIRDLER, R.W., HALL, S.A., 1972
An aeromagnetic survey of the Afar Triangle of Ethiopia, Tectonophysics, 15, p.53.

GIRDLER, R.W., STYLES, P., 1974
Two stage Red Sea floor spreading, Nature, 247, p.7-11.

GIRDLER, R.W., STYLES, P., 1976
The relevance of magnetic anomalies over the southern Red Sea and Gulf of Aden to Afar, in Pilger, A., and Rösler, A., eds., Afar Depression of Ethiopia: Stuttgart, E. Schweizerbart'sche Verlagsbuchhandlung, p.156-170.

GIRDLER, R.W., STYLES, P., 1978
Seafloor spreading in the western Gulf of Aden, Nature, 271, p.615-617.

GOUIN, P., 1970
Seismic and gravity data from Afar in relation to surrounding areas, Phil. Trans. R. Soc. Lond., A267, p.339-358.

GOUIN, P., 1975
Kara Kore and Serdo epicentres: relocation and tectonic implications, Bull. geophys. Obs. Addis Ababa, 15, p.15-25.

GOUIN, P., 1976
Seismic zoning in Ethiopia, Bull. geophys. Obs. Addis Ababa, 17, p.1-46.

GOUIN, P., 1979
Earthquake history of Ethiopia and the Horn of Africa, IDRC-118e, Ottawa, Canada.*

GRASTY, R., MILLER, J.A., MOHR, P.A., 1963
Preliminary results of potassium-argon age determinations on some Ethiopian Trap Series basalts, Bull. geophys. Obs. Addis Ababa, 6, p.97-102.

GRIFFIN, J.N., 1966
Applications and development of polarization (REMODE) filters, Seismic Data Laboratory Report 141, Teledyne Inc., Alxandria, Va. (AD-630-515).

GROVE, A.T., GOUDIE, A.S., 1971
Late Quaternary lake levels in the rift valley of southern Ethiopia and elsewhere in tropical Africa, Nature, 234, p.403-405.

---

*This book did not become available to me until the text of this thesis was completed. With the exception of Figure 8.3.5, citations refer to an early draft of a section of the manuscript very kindly given me by Father Gouin in 1975.

GUMPER, F., POMEROY, P.W., 1970
Seismic wave velocities and earth structure of the African continent, Bull. Seism. Soc. Am., 60, p.651-668.

GURBUZ, C. 1973
The magnitude determination of local earthquakes in East Africa, M.Sc. Dissertation, University of Durham.

GUTENBERG, B., 1945a
Amplitudes of P, PP and S and magnitudes of shallow earthquakes, Bull. Seism. Soc. Am., 35, p.57-69.

GUTENBERG, B., 1945b
Magnitude determinations for deep-focus earthquakes, Bull. Seism. Soc. Am., 35, p.117-130.

GUTENBERG, B., RICHTER, C.F., 1944
Frequency of earthquakes in California, Bull. Seism. Soc. Am., 34, p.185-188.

GUTENBERG, B., RICHTER, C.F., 1954
Seismicity of the Earth, Princeton Univ. press, Princeton, N.J.

GUTENBERG, B., RICHTER, C.F., 1956
Magnitude and energy of earthquakes, Annls Geophys., 9, p.1-15.

HALES, A.L., SACKS, F.S., 1959
Evidence for an intermediate layer from crustal structure in the Eastern Transvaal, Geophys. J. R. Astr. Soc., 2, p.15-23.

HALL, S., 1970
Total intensity magnetic anomaly chart of the junction of the Red Sea, Gulf of Aden and Ethiopian rifts, University of Newcastle-upon-Tyne, unpublished.

HANKS, T.C., 1977
Earthquake stress drops, ambient tectonic stresses and stresses that drive plate motions, Pure Appl. Geophys., 115, p.441-458.

HANKS, T.C., 1979
b values and $w^{-\gamma}$ seismic source models: implications for tectonic stress variations along active crustal fault zones and estimation of high-frequency ground motion, J. Geophys. Res., 84, p.2235-2242.

HANKS, T.C., THATCHER, W., 1972
A graphical representation of seismic source parameters, J. Geophys. Res., 77, p.4393-4405.

HANKS, T.C., WYSS, M., 1972
The use of body-wave spectra in the determination of seismic-source parameters, Bull. Seism. Soc. Am., 62, p.561-589.

HARRISON, C.G.A., BONATTI, E., STIELTJES, L., 1975
Tectonism of axial valleys in spreading centers: data from the Afar rift, in Pilger, A., and Rösler, A., eds., Afar Depression of Ethiopia: Stuttgart, E. Schweizerbart'sche Verlagsbuchhandlung, p.178-198.

HARTZELL, S.H., FRAZIER, G.A., BRUNE, J.N., 1978
Earthquake modeling in a homogeneous half-space, Bull. Seism. Soc. Am., 68, p.301-316.

HASEGAWA, H.S., 1971
Crustal transfer ratios of short- and long-period body waves recorded at Yellowknife, Bull. Seism. Soc. Am., 61, p.1303-1320.

HASKELL, N.A., 1953
The dispersion of surface waves on multilayered media, Bull. Seism. Soc. Am., 43, p.17-34.

HASKELL, N.A., 1962
Crustal reflection of plane P and SV waves, J. Geophys. Res., 67, p.4751-4767.

HASKELL, N.A., 1964
Total energy and energy spectral density of elastic wave radiation from propagating faults, Bull. Seism. Soc. Am., 54, p.1811-1842.

HASKELL, N.A., 1966
Total energy and energy spectral density of elastic wave radiation from propagating faults. Part 2. A statistical source model, Bull. Seism. Soc. Am., 56, p.125-140.

HELMBERGER, D.V., JOHNSON, L.R., 1977
Source parameters of moderate size earthquakes and the importance of receiver crustal structure in interpreting observations of local earthquakes, Bull. Seism. Soc. Am., 67, p.301-313.

HERMANCE, J.F., 1973
An electrical model for the sub-Icelandic crust, Geotectonics, 38, p.3-13.

HERRIN, E., TAGGART, J., BROWN, C.F.,Jr., 1962
Machine computation of earthquake hypocenters, J. Grad. Res. center, 30, p.79-106.

HERRMANN, R.B., 1975
The use of duration as a measure of seismic moment and magnitude, Bull. Seism. Soc. Am., 65, p.899-913.

HILGER, WATTS, 1964
Instruction manual for the Willmore seismometer MkII, published by Hilger and Watts Ltd., 98, St. Pancras Way, London NW4.

HODGSON, J.H., 1957
Nature of faulting in large earthquakes, Bull. geol. Soc. Am., 68, p.611-644.

HOFMANN, A.W., HART, S.R., 1978
An assessment of local and regional isotopic equilibrium in the mantle, Earth Planet Sci. Lett., 38, p.44-62.

HOLWERDA, J.G., HUTCHINSON, R.W., 1968
Potash-bearing evaporites in the Danakil area, Ethiopia, Econ. Geol., 63, p.124-150.

HUTCHINSON, R.W., ENGELS, G.G., 1970
Tectonic significance of regional geology and evaporite lithofacies in North East Ethiopia, Phil. Trans. R. Soc. Lond., A267, p.313-329.

HUTCHINSON, R.W., ENGELS, G.G., 1972
Tectonic evolution in the southern Red Sea, Bull. geol. Soc. Am., 83, p.2989-3002.

HUTCHINSON, R.W., GASS, I.G., 1971
Mafic and ultramafic xenoliths associated with undersaturated basalt on Kod Ali Island, Southern Red Sea, Contrib. Mineral. Petrol., 31, p.94-101.

HYNDMAN, R.D., 1979
Poisson's ratio in the oceanic crust - a review, Tectonophysics, 59, p.321-333.

IDA, Y., AKI, K., 1972
Seismic source time function of propagating longitudinal-shear cracks, J. Geophys. Res., 77, p.2034-2044.

ISC
Regional Catalogues of Earthquakes (biannual) and Bulletins of the International Seismological Centre (monthly), published by ISC, Berkshire, UK.

JACKSON, D.D., 1972
Interpretation of inaccurate, insufficient and inconsistent data, Geophys. J. R. Astr. Soc., 28, p.97-109.

JACKSON, D.D., 1976
Most squares inversion, J. Geophys. Res., 81, p.1027-1030.

JACKSON, L.P., 1975
The crustal structure of the Alborz mountains, Iran: a preliminary study, M.Sc. Dissertation, University of Durham.

JAMES, D.E., SACKS, I.S., LAZO, E.L., APARICIO, P.G., 1969
On locating local earthquakes using small networks, Bull. Seism. Soc. Am., 59, p.1201-1212.

JAMES, F., 1967
Monte Carlo for nuclear physicists, in Nikolic, M., ed., Methods in subnuclear physics, 4, Part 3, publ. Gordon and Breach.

JAMES, F., ROOS, M., 1974
MINUIT, a system for minimizing a function of n parameters and computing the parameter errors and correlations, CERN Computer Centre Program Library, D506/D516.

JEFFREYS, H., 1948
Theory of Probability, Clarendon Press, Oxford (2nd edition).

JOHNSON, H.P., MERRILL, R.T., 1978
A direct test of the Vine-Matthews hypothesis, Earth Planet Sci. Lett., 40, p.263-269.

JOHNSON, L.R., 1979
Seismic source theory, Rev. Geophys. and Space Phys., 17, p.328-336.

JONES, P.B., 1968
Surface wave dispersion and crustal structure between the Gulf of Aden and Addis Ababa, Bull. geophys. Obs. Addis Ababa, 12, p.19-26.

JONES, P.W., 1976
Age of the lower flood basalts of the Ethiopian plateau, Nature, 261, p.567-569.

JUCH, D., 1975
Geology of the South-Eastern Escarpment of Ethiopia between 39° and 42° longitude East, in Pilger, A., and Rösler, A., eds., Afar Depression of Ethiopia: Stuttgart, E. Schweizerbart'sche Verlagsbuchhandlung, p.310-316.

JUNG, D., KÜRSTEN, M.O.C., TARKIAN, M., 1976
Post-Mesozoic volcanism in Iran and its relation to the subduction of the Afro-Arabian under the Eurasian plate, in Pilger, A., and Rösler, A., eds., Afar between continental and oceanic rifting: Stuttgart, E. Schweizerbart'sche Verlagsbuchhandlung, p.175-181.

KAILA, K.L., NARAIN, H., 1971
A new approach for preparation of quantitative seismicity maps as applied to Alpide Belt - Sunda Arc and adjoining areas, Bull. Seism. Soc. Am., 61, p.1275-1291.

KANASEWICH, E.R., 1975
Time sequence analysis in geophysics, Univ. of Alberta Press, Edmonton, Canada (2nd edition).

KARNIK, V., KONDORSKAYA, N.V., RIZNICHENKO, J.V., SAVARENSKY, E.F., SOLOVYOV, S.L., SHEBALIN, N.V., VANEK, J., ZATOPEK, A., 1962
Standardization of the earthquake magnitude scale, Studia Geophys. Geod., 6, p.41-48.

KAZMIN, V., GARLAND, C.R., 1973
Evidence of Precambrian block-faulting in the western margin of the Afar depression, Ethiopia, Geol. Mag., 110, p.55-57.

KAZMIN, V., SCHIFFERAW, A., BALCHA, T., 1978
The Ethiopian basement: stratigraphy and possible manner of evolution, Geol. Rdsch., 57, p.531-546.

KHAN, M.A., MANSFIELD, J., 1971
Gravity measurements in the Gregory Rift, Nature phys. Sci., 229, p.72-75.

KING, B.C., 1970
Vulcanicity and rift tectonics in East Africa, in Clifford, T.N., Gass, I.G., eds., African magmatism and tectonics: Oliver and Boyd, Edinburgh, p.263-283.

KNOPOFF, L., 1964
Q, Rev. Geophys., 2, p.625-640.

KNOPOFF, L., FREDRICKS, R.W., GANGI, A.F., PORTER, L.D., 1957
Surface amplitudes of reflected body waves, Geophysics, 22, p.842-847.

KNOPOFF, L., GILBERT, F., 1960
First motion from seismic sources, Bull. Seism. Soc. Am., 50, p.117-134.

KNOPOFF, L., MOUTON, J.O., 1975
Can one determine seismic focal parameters from the far-field radiation?, Geophys. J. R. Astr. Soc., 42, p.591-606.

KNOPOFF, L., SCHLUE, J.W., 1972
Rayleigh wave phase velocities for the path Addis Ababa - Nairobi, Tectonophysics, 15, p.157-163.

KNOTT, S.T., BUNCE, E.T., CHASE, R.L., 1966
Red Sea seismic reflection studies, Geol. Surv. Pap. Can., 66-14, p.33-61.

KRONBERG, P., SCHONFELD, M., GUNTHER, R., TSOMBOS, P., 1975
ERTS 1 data on the geology and tectonics of the Afar/Ethiopia and adjacent regions, in Pilger, A., and Rösler, A., eds., Afar Depression of Ethiopia: Stuttgart, E. Schweizerbart'sche Verlagsbuchhandlung, p.19-27.

KUNZ, K., KREUZER, H., MULLER, P., 1975
Potassium-argon age determinations of the Trap basalt of the south-eastern part of the Afar rift, in Pilger, A., and Rösler, A., eds., Afar Depression of Ethiopia: Stuttgart, E. Schweizerbart'sche Verlagsbuchhandlung, p.370-374.

KURITA, T., 1969
Spectral analysis of seismic waves. Part 1. Data windows for the analysis of transient waves, Spec. Contrib. Geophys. Inst., Kyoto Univ., 9, p.97-122.

KÜRSTEN, M.O.C., 1975
Tectonic inventory of the Danakil Depression, in Pilger, A., and Rösler, A., eds., Afar Depression of Ethiopia: Stuttgart, E. Schweizerbart'sche Verlagsbuchhandlung, p.170-74.

LALOU, C., van NGUYEN, H., FAURE, H., MOREIRA, L., 1970
Datation par la méthode uranium-thorium des hauts niveaux de coraux de la dépression de l'Afar (Ethiopie), Revue Géogr. phys. Géol. dyn., 12, p.3-8.

LANGENKAMP, D., COMBS, J., 1974
Microearthquake study of the Elsinore fault zone, Southern California, Bull. Seism. Soc. Am., 64, p.187-203.

LANGGUTH, H.R., POUCHAN, P., 1975
Caracteres physiques et conditions de stabilite du Lac Assal (T.F.A.I.), in Pilger, A., and Rösler, A., eds., Afar Depression of Ethiopia: Stuttgart, E. Schweizerbart'sche Verlagsbuchhandlung, p.250-258.

LARSEN, G., GRÖNVOLD, K., THORARINSSON, S., 1979
Volcanic eruption through a geothermal borehole at Námafjall, Iceland, Nature, 278, p.707-710.

LAUGHTON, A.S., 1966a
The Gulf of Aden, in relation to the Red Sea and the Afar Depression of Ethiopia, Geol. Surv. Pap. Can., 66-14, p.78-97.

LAUGHTON, A.S., 1966b
The Gulf of Aden, Phil. Trans. R. Soc. Lond., A259, p.150-171.

LAUGHTON, A.S., 1970
A new bathymetric chart of the Red Sea, Phil. Trans. R. Soc. Lond., A267, p.21-22.

LAUGHTON, A.S., TRAMONTINI, C., 1969
Structure of the Gulf of Aden, Tectonophysics, 8, p.359-375.

LAUGHTON, A.S., WHITMARSH, R.B., JONES, M.T., 1970
The evolution of the Gulf of Aden, Phil. Trans. R. Soc. Lond., A267, p.227-266.

Le BAS, M.J., 1971
Peralkaline volcanism, crustal swelling and rifting, Nature, 230, p.85-87.

LEBLANC, G., 1967
Truncated crustal transfer functions and fine crustal structure determination, Bull. Seism. Soc. Am., 57, p.719-733.

LEBLANC, G., HOWELL, B.F., 1967
Spectral study of short-period P-waves, Can. J. Earth Sci., 4, p.1049-1063.

LEE, W.H.K., BENNETT, R.E., MEAGHER, K.L., 1972
A method of estimating magnitude of local earthquakes from signal duration, U.S. Geol. Surv., Open File Rept.

LEE, W.H.K., LAHR, J.C., 1975
HYPO71 (revised): a computer program for determining hypocenter, magnitude, and first motion pattern of local earthquakes, U.S. Geol. Surv., Open File Rept. 75-311.

Le PICHON, X., 1968
Sea-floor spreading and continental drift, J. Geophys. Res., 73, p.3661-3697.

Le PICHON, X., FRANCHETEAU, J., 1978
A plate-tectonic analysis of the Red Sea - Gulf of Aden area, Tectonophysics, 46, p.369-406.

Le PICHON, X., HEIRTZLER, J.R., 1968
Magnetic anomalies in the Indian Ocean and sea-floor spreading, J. Geophys. Res., 73, p.2101-2117.

LÉPINE, J.-C., RUEGG, J.-C., 1973
Premiers enseignements de la crise sismique survenue dans la région de Djibouti (T.F.A.I.) en Mars-Avril 1973, C. R. Acad. Sci. Paris, D277, p.33-36.

LÉPINE, J.-C., RUEGG, J.-C., 1976
La sismicité du T.F.A.I., Bull. Soc. géol. Fr., 18, p.841-846.

LÉPINE, J.-C., RUEGG, J.-C., STEINMETZ, L., 1972
Seismic profiles in the Djibouti area, Tectonophysics, 15, p.59-64.

LEWIS, B.T.R., MEYER, R.P., 1968
A seismic investigation of the upper mantle to the west of Lake Superior, Bull. Seism. Soc. Am., 58, p.565-596.

LILWALL, R.C., DOUGLAS, A., 1970
Estimation of P-wave travel times using the joint epicentre method, Geophys. J. R. Astr. Soc., 19, p.165-181.

LINDE, A.T., SACKS, I.S., 1972
Dimensions, energy and stress release for South American deep earthquakes, J. Geophys. Res., 77, p.1439-1451.

LOMNITZ, C., 1977
A fast epicenter location program, Bull. Seism. Soc. Am., 67, p.425-431.

LOMNITZ, C., 1978
Reply [to comments by Smith, E.G.C.], Bull. Seism. Soc. Am., 68, p.847.

LONG, L.T., 1974
Earthquake sequences and b values in the southeast United States, Bull. Seism. Soc. Am., 64, p.267-273.

LONG, R.E., 1974a
Seismicity investigations at dam sites, Eng. Geol., 8, p.199-212.

LONG, R.E., 1974b
A compact portable seismic recorder, Geophys. J. R. Astr. Soc., 37, p.91-98.

LONG, R.E., 1976a
The deep structure of the East African rift and its relation to Afar, in Pilger, A., and Rösler, A., eds., Afar between continental and oceanic rifting: Stuttgart, E. Schweizerbart'sche Verlagsbuchhandlung, p.130-137.

LONG, R.E., 1976b
Lower Awash Feasibility Study: Tendaho dam - seismicity study, Unpublished Report.

LONG, R.E., BACKHOUSE, R.W., 1976
The structure of the western flank of the Gregory Rift. Part II, the mantle, Geophys. J. R. Astr. Soc., 44, p.677-688.

LONG, R.E., BACKHOUSE, R.W., MAGUIRE, P.K.H., SUNDARALINGAM, K., 1972
The structure of East Africa using surface wave dispersion and Durham seismic array data, Tectonophysics, 15, p.165-178.

LONG, R.E., SUNDARALINGAM, K., MAGUIRE, P.K.H., 1973
Crustal structure of the East African rift zone, Tectonophysics, 20, p.269-281.

LOWELL, J.D., GENIK, G.J., 1972
Sea-floor spreading and structural evolution of the southern Red Sea, Bull. Am. Ass. Petrol. Geol., 56, p.247-259.

McCONNELL, R.B., 1970
Evolution of rifting in Africa, Nature, 227, p.699.

McDOUGALL, I., MORTON, W.H., WILLIAMS,M.A.J., 1975
Age and rates of denudation of Trap Series basalts at Blue Nile Gorge, Ethiopia, Nature, 254, p.207-209.

McKENZIE, D.P., DAVIES, D., MOLNAR, P., 1970
Plate tectonics of the Red Sea and East Africa, Nature, 226, p.243-248.

MAASHA, N., MOLNAR, P., 1972
Earthquake fault parameters and tectonics in Africa, J. Geophys. Res., 77, p.5731-5743.

MADARIAGA, R., 1976
Dynamics of an expanding circular fault, Bull. Seism. Soc. Am., 66, p.639-666.

MADARIAGA, R., 1979
On the relation between seismic moment and stress drop in the presence of stress and strength inhomogeneity, J. Geophys. Res., 84, p.2243-2250.

MAGUIRE, P.K.H., 1974
The crustal structure of East Africa through earthquake seismology, Ph.D. Thesis, University of Durham.

MAKRIS, J., 1975
Afar and Iceland - a geophysical comparison, in Pilger, A., and Rösler, A., eds., Afar Depression of Ethiopia: Stuttgart, E. Schweizerbart'sche Verlagsbuchhandlung, p.379-390.

MAKRIS, J., MENZEL, H., ZIMMERMANN, J., 1972
A preliminary interpretation of the gravity field of Afar, North East Ethiopia, Tectonophysics, 15, p.31-39.

MAKRIS, J., MENZEL, H., ZIMMERMAN, J., GOUIN, P., 1975
Gravity field and crustal structure of North Ethiopia, in Pilger, A., and Rösler, A., eds., Afar Depression of Ethiopia: Stuttgart, E. Schweizerbart'sche Verlagsbuchhandlung, p.135-144.

MAKRIS, J., THIELE, P., ZIMMERMANN, J., 1970
Crustal investigation from gravity measurements at the scarp of the Ethiopian plateau, Zeitschrift Geophys., 36, p.299-311.

MAKRIS, J., ZIMMERMANN, J., BACHEM, H.C., RITTER, B., 1973
Gravity survey of South Afar, Ethiopia, Zeitschrift Geophys., 39, p.279-290.

MARINELLI, G., VARET, J., 1973
Structure et evolution du sud du "Horst Danakil" (T.F.A.I. et Ethiopie), C. R. Acad. Sci. Paris, D276, p.1119-1122.

MARRIOTT, D., 1969
Preliminary study of feasibility of establishing a geothermal pilot plant to generate power for T.P.S.C., Unpublished paper for the Central and East African Conference of Electricity Undertakings.

MEGRUE, G.H., NORTON, E., STRANGEWAY, D.W., 1972
Tectonic history of the Ethiopian rift as deduced by K-Ar ages and palaeomagnetic measurements of basaltic dikes, J. Geophys. Res., 77, p.5744-5754.

MEYER, W., PILGER, A., RÖSLER, A., STETS, J., 1975
Tectonic evolution of the northern part of the Main Ethiopian rift in southern Ethiopia, in Pilger, A., and Rösler, A., eds., Afar Depression of Ethiopia: Stuttgart, E. Schweizerbart'sche Verlagsbuchhandlung, p.352-362.

MICENKO, M., 1977
The structure of the upper mantle beneath Turkana, East Africa, M.Sc. Dissertation, University of Durham.

MITCHELL, B.J., 1973
Radiation and attenuation of Rayleigh waves from the Southeastern Missouri earthquake of October 21, 1965, J. Geophys. Res., 78, p.886-899.

MOGI, K., 1963
Some discussions on aftershocks, foreshocks and earthquake swarms - the fracture of a semi-infinite body caused by an inner stress origin and its relation to the earthquake phenomena, Bull. Earthquake Res. Inst., 41, p.615-658.

MOHR, P.A., 1967a
The Ethiopian rift system, Bull. geophys. Obs. Addis Ababa, 11, p.1-65.

MOHR, P.A., 1967b
Major volcano-tectonic lineament in the Ethiopian rift system, Nature, 213, p.664-665.

MOHR, P.A., 1968a
Transcurrent faulting in the Ethiopian rift system, Nature, 218, p.938-940.

MOHR, P.A., 1968b
Annular faulting in the Ethiopian rift system, Bull. geophys. Obs. Addis Ababa, 12, p.1-9.

MOHR, P.A., 1968c
The Cainozoic volcanic succession in Ethiopia, Bull. Volcan., 32, p.5-14.

MOHR, P.A., 1970a
The Afar triple junction and sea-floor spreading, J. Geophys. Res., 75, p.7340-7352.

MOHR, P.A., 1970b
Plate tectonics of the Red Sea and East Africa, Nature, 228, p.547-548.

MOHR, P.A., 1971a
The Ethiopian triple-rift junction in terms of plate tectonics, Bull. geophys. Obs. Addis Ababa, 13, p.1-17.

MOHR, P.A., 1971b
Tectonics of the Dobi Graben region, Central Afar, Ethiopia, Bull. geophys. Obs. Addis Ababa, 13, p.73-89.

MOHR, P.A., 1971c
Ethiopian rift and plateaus: some volcanic petrochemical differences, J. Geophys. Res., 76, p.1967-1984.

MOHR, P.A., 1972a
Surface structure and plate tectonics of Afar, Tectonophysics, 15, p.3-18.

MOHR, P.A., 1972b
Tectonic maps of the Ethiopian rift system, and an apology, Bull. Volcan., 36, p.507-511.

MOHR, P.A., 1974
Mapping of the major structures of the African rift system, Smithson. Astrophys. Obs., Spec. Rep.

MOHR, P.A., 1975
Structural setting and evolution of Afar, in Pilger, A., and Rösler, A., eds., Afar Depression of Ethiopia: Stuttgart, E. Schweizerbart'sche Verlagsbuchhandlung, p.27-37.

MOHR, P.A., 1978
Afar, Ann. Rev. Earth Planet Sci., 6, p.145-172.

MOHR, P.A., ROGERS, A.S., 1966
Gravity traverses in Ethiopia (2nd interim report, with extended discussions on geology), Bull. geophys. Obs. Addis Ababa, 9, p.7-58.

MOHR, P.A., WOOD, C.A., 1976
Volcano spacings and lithospheric attenuation in the Eastern Rift of Africa, Earth Planet Sci. Lett., 33, p.126-144.

MOLNAR, P., FITCH, T.J., ASFAW, L.A., 1970
A microearthquake survey in the Ethiopian Rift, Earthquake Notes, 41, p.37-44.

MOLNAR, P., TUCKER, B.E., BRUNE, J.N., 1973
Corner frequencies of P and S waves and models of earthquake sources, Bull. Seism. Soc. Am., 63, p.2091-2104.

MOLNAR, P., WYSS, M., 1972
Moments, source dimensions and stress drops of shallow-focus earthquakes in the Tonga-Kermadec arc, Phys. Earth Plan. Int., 6, p.263-278.

MONTALBETTI, J.F., KANASEWICH, E.R., 1970
Enhancement of teleseismic body phases with a polarization filter, Geophys. J. R. Astr. Soc., 21, p.119-129.

MOORE, J.M., DAVIDSON, A., 1978
Rift structures in southern Ethiopia, Tectonophysics, 46, p.159-173.

MORBIDELLI, L., NICOLETTI, M., PETRUCCIANI, C., PICCIRILLO, E.M., 1975
Ethiopian South-Eastern Plateau and related escarpment: K/Ar ages of the main volcanic events (Main Ethiopian Rift from 8°10' to 9°00' latitude north), in Pilger, A., and Rösler, A., eds., Afar Depression of Ethiopia: Stuttgart, E. Schweizerbart'sche Verlagsbuchhandlung, p.362-369.

MORGAN, W.J., 1972
Deep mantle convection plumes and plate motions, Bull. Am. Ass. Petrol. Geol., 56, p.203-212.

MORTON, W.H., BLACK, R., 1975
Crustal attenuation in Afar, in Pilger, A., and Rösler, A., eds., Afar Depression of Ethiopia: Stuttgart, E. Schweizerbart'sche Verlagsbuchhandlung, p.55-65.

MUELLER, S., BONJER, K.-P., 1973
Average structure of the crust and upper mantle in East Africa, Tectonophysics, 20, p.283-193.

MUNSTER, J.B., JORDAN, T.H., 1978
Present-day plate motions, J. Geophys. Res., 83, p.5331-5354.

MURPHY, J.R., DAVIS, A.H., WEAVER, N.L., 1971
Amplification of seismic body waves by low-velocity surface layers, Bull. Seism. Soc. Am., 61, p.109-145.

NAVARRO, R., BROCKMAN, S.R., 1970
Seismic activity in September 1969 near the Rulison nuclear test site, Publ. USCGS no. 746-5.

NEEDHAM, H.D., CHOUKROUNE, P., CHEMINÉE, J.L., Le PICHON, X., FRANCHETEAU, J., 1976
The accreting plate boundary: Ardoukôba rift (northeast Africa) and the oceanic rift valley, Earth Planet Sci. Lett., 28, p.439-453.

NELDER, J.A., MEAD, R., 1964
A simplex method for function minimization, Comput. J., 7, p.308-313.

NORDQUIST, J.M., 1962
A special-purpose program for earthquake location with an electronic computer, Bull. Seism. Soc. Am., 52, p.431-438.

NUR, A., 1971
Effects of stress on velocity anisotropy in rocks with cracks, J. Geophys. Res., 76, p.2022-2034.

NUR, A., SCHULTZ, P., 1973
Fluid flow and faulting, 2: a stiffness model for seismicity, in Kovach, R.L., Nur, A., eds., Proc. Conf. Tectonic Problems San Andreas Fault System, Stanford Univ., Stanford, Calif.

NUTTLI, O.W., 1972
Magnitude, intensity and ground motion relations for earthquakes in the Central United States, Proc. Intern. Conf. Microzonation, Seattle, Wash., 1, p.307-318.

OLDENBURG, D.W., BRUNE, J.N., 1972
Ridge transform fault spreading pattern in freezing wax, Science, 178, p.301-304.

OTTONELLO, G., VANNUCCI, R., BEZZI, A., PICCARDO, G.B., 1975
Genetic relationships between ultramafic xenoliths and enclosing alkali basalts in the Assab region (Afar, Ethiopia) based on their trace elements geochemistry, in Pilger, A., and Rösler, A., eds., Afar Depression of Ethiopia: Stuttgart, E. Schweizerbart'sche Verlagsbuchhandlung, p.206-214.

OTTONELLO, G., PICCARDO, G.B., JORON, J.L., TREUIL, M., 1978
Evolution of the upper mantle under the Assab Region (Ethiopia): suggestions from petrology and geochemistry of tectonitic ultramafic xenoliths and host basaltic lavas, Geol. Rdsch., 67, p.547-575.

OXBURGH, E.R., TURCOTTE, D.L., 1974
Membrane tectonics and the East African rift, Earth Planet Sci. Lett., 22, p.133-140.

PAGE, R., 1968
Focal depths of aftershocks, J. Geophys. Res., 73, p.3897-3903.

PÁLMASON, G., 1971
Crustal structure of Iceland from explosion seismology, Soc. Sci. Island., Rit. 40, 188pp.

PÁLMASON, G., SAEMUNDSSON, K., 1974
Iceland in relation to the mid-Atlantic Ridge, Ann. Rev. Earth Planet Sci., 2, p.25-50.

PEARCE, R.G., 1981
Complex P waveforms from a Gulf of Aden earthquake, Geophys. J. R. Astr. Soc., 64, p.187-200.

PEPPIN, W.A., BUFE, C.G., 1980
Induced versus natural earthquakes: search for a seismic discriminant, Bull. Seism. Soc. Am., 70, p.269-281.

PHILLIPS, J.D., 1970
Magnetic anomalies in the Red Sea, Phil. Trans. R. Soc. Lond., A267, p.205-217.

PHILLIPS, J.D., WOODSIDE, J., BOWIN, C.O., 1969
Magnetic and gravity anomalies in the central Red Sea, in Degens, E.T., Ross, D.A., eds., Hot brines and recent heavy metal deposits in the Red Sea, Springer, New York, p.98-113.

PHINNEY, R.A., 1964
Structure of the earth's crust from spectral behavior of long-period body waves, J. Geophys. Res., 69, p.2997-3017.

PILGER, A., RÖSLER, A., 1976
Temporal relationships in the tectonic evolution of the Afar Depression (Ethiopia) and the adjacent Afro-Arabian rift system, in Pilger, A., and Rösler, A., eds., Afar between continental and oceanic rifting: Stuttgart, E. Schweizerbart'sche Verlagsbuchhandlung, p.1-25.

PLAUMANN, S., 1975
Some results of a detailed gravimetric survey of the southern Red Sea, Geol. Jb., D13, p.155-166.

PONTOISE, B., LÉPINE, J.-C., RUEGG, J.-C., 1976
Attenuation des ondes sismiques en T.F.A.I., Bull. Soc. géol. Fr., 18, p.847-849.

PURCELL, P.G., 1976
The Marda Fault zone, Ethiopia, Nature, 261, p.569-571.

RASCHKA, H., MULLER, P., 1975
Contributions to the geochemistry of volcanic rocks, Afar region, Ethiopia, in Pilger, A., and Rösler, A., eds., Afar Depression of Ethiopia: Stuttgart, E. Schweizerbart'sche Verlagsbuchhandlung, p.341-351.

REAL, C.R., TENG, T.L., 1973
Local Richter magnitude and total signal duration in Southern California, Bull. Seism. Soc. Am., 63, p.1809-1827.

REX, D.C., GIBSON, I.L., DAKIN, F., 1971
Age of the Ethiopian flood basalt succession, Nature phys. Sci., 230, p.131-132.

RICHARDSON, E.S., HARRISON, C.G.A., 1976
Opening of the Red Sea with two poles of rotation, Earth Planet Sci. Lett., 30, p.135-142.

RICHTER, C.F., 1935
An instrumental earthquake magnitude scale, Bull. Seism. Soc. Am., 25, p.1-32.

ROBERTS, D.G., 1969
Structural evolution of the rift zones in the Middle East, Nature, 223, p.55-57.

ROBERTS, D.G., 1970
A discussion, Phil. Trans. R. Soc. Lond., A267, p.399-405.

ROBERTS, D.G., WHITMARSH, R.B., 1969
A bathymetric and magnetic survey of the Gulf of Tadjoura, western Gulf of Aden, Earth Planet Sci. Lett., 5, p.253-258.

ROESER, H.A., 1975
A detailed magnetic survey of the southern Red Sea, Geol. Jb., D13, p.131-153.

ROESER, H.A., 1976
Magnetic anomalies of the African Red Sea shelf and their implications for the anomalies of Atlantic continental margins, J. Geophys., 42, p.73-80.

ROGERS, A.M.,Jr., KISSLINGER, C., 1972
The effect of a dipping layer on P-wave transmission, Bull. Seism. Soc. Am., 62, p.301-324.

ROGERS, A.S., 1966
Some comments on the rift in Ethiopia, Geol. Surv. Pap. Can., 66-14, p.98.

ROGERS, J.W.W., GHUMA, M.A., NAGY, R.M., GREENBERG, J.K., FULLAGAR, P.D., 1978
.lutonism in Pan-African belts and the geologic evolution of northeastern Africa, Earth Planet Sci. Lett., 39, p.109-117.

ROGNON, P., 1975
Tectonic deformations in central Afar basins in the Upper Pleistocene and Holocene periods, from the study of lacustrine deposits, in Pilger, A., and Rösler, A., eds., Afar Depression of Ethiopia: Stuttgart, E. Schweizerbart'sche Verlagsbuchhandlung, p.198-200.

ROGNON, P., GASSE, F., 1973
Dépôts lacustres quaternaires de la basse vallée de l'Awash (Afar, Ethiopie); leurs rapports avec la tectonique et la volcanisme sous-aquatique, Revue Geogr. phys. Geol. dyn., 15, p.295-316.

ROONEY, D., HUTTON, V.R.S., 1977
A magnetotelluric and magnetovariational study of the Gregory Rift Valley, Kenya, Geophys. J. R. Astr. Soc., 51, p.91-119.

ROTHMAN, R.L., GREENFIELD, R.J., HARDY, H.R.,Jr., 1974
Errors in hypocenter location due to velocity anisotropy, Bull. Seism. Soc. Am., 64, p.1993-1996.

ROUBET, C., TAZIEFF, H., van NGUYEN, H., DELIBRIAS, G., LALOU, C., FAURE, H., 1969
Age des calcaires coralliens pleistocenes et neotectoniques de l'Afar (mer Rouge, Ethiopie), Ann. Fasc. Sci. Univ. Clermont-Fd., Géol et Min., 19, p.17-18.

RUEGG, J.-C., 1975a
Structure profonde de la croûte et du manteau supérieur du Sud-Est de l'Afar d'après des données sismiques, Annls Géophys., 31, p.329-360.

RUEGG, J.-C., 1975b
Main results about the crustal and upper mantle structure of the Djibouti region (T.F.A.I.), in Pilger, A., and Rösler, A., eds., Afar Depression of Ethiopia: Stuttgart, E. Schweizerbart'sche Verlagsbuchhandlung, p.120-134.

RUEGG, J.-C., LÉPINE, J.-C., TARANTOLA, A., LEVEQUE, J.J., 1981
The Somalian earthquakes of May, 1980, East Africa, Contrib. Institut de Physique du Globe no. 497, submitted for publication.

RYKOUNOV, L.N., SEDOV, V.V., SAVRINA, L.A., BOURMIN, V.J., 1972
Study of microearthquakes in the rift zones of East Africa, Tectonophysics, 15, p.123-130.

SAVAGE, J.C., 1966
Radiation from a realistic model of faulting, Bull. Seism. Soc. Am., 56, p.577-592.

SAVAGE, J.C., 1972
Relation of corner frequency to fault dimensions, J. Geophys. Res., 77, p.3788-3795.

SAVAGE, J.C., 1974
Relation between P- and S-wave corner frequencies in the seismic spectrum, Bull. Seism. Soc. Am., 64, p.1621-1627.

SAVAGE, J.E.G., 1979
A seismic investigation of the lithosphere of the Gregory rift, Ph.D. Thesis, University of Durham.

SAX, R.L., MIMS, C.H., 1965
Rectilinear motion detection (REMODE), Seismic Data Laboratory Report 118, Teledyne Inc., Alexandria, Va. (AD-460-631).

SCHAEFER, H.-U., 1975
Investigations on crustal spreading in southern and central Afar (Ethiopia), in Pilger, A., and Rösler, A., eds., Afar Depression of Ethiopia: Stuttgart, E. Schweizerbart'sche Verlagsbuchhandlung, p.289-296.

SCHILLING, J.-G., 1973
Afar mantle plume: rare earth evidence, Nature phys. Sci., 242, p.2-5.

SCHOLZ, C.H., 1968
The frequency-magnitude relation of microfracturing in rock and its relation to earthquakes, Bull. Seism. Soc. Am., 58, p.399-415.

SCHOLZ, C.H., SYKES, L.R., AGGARWAL, Y.P., 1973
Earthquake prediction: a physical basis, Science, 181, p.803-810.

SCHULT, A., 1975
Palaeomagnetic results from the Ethiopian South-Eastern Plateau and the Danakil Block, in Pilger, A., and Rösler, A., eds., Afar Depression of Ethiopia: Stuttgart, E. Schweizerbart'sche Verlagsbuchhandlung, p.80-85.

SEARLE, R.C., 1970
Lateral extension in the East African rift valleys, Nature, 227, p.267-268.

SEARLE, R.C., 1975
The dispersion of seismic waves across southern Afar, in Pilger, A., and Rösler, A., eds., Afar Depression of Ethiopia: Stuttgart, E. Schweizerbart'sche Verlagsbuchhandlung, p.113-120.

SEARLE, R.C., GOUIN, P., 1971a
An analysis of some local earthquake phases originating near the Afar triple junction, Bull. Seism. Soc. Am., 61, p.1061-1071.

SEARLE, R.C., GOUIN, P., 1971b
Notes on a gravity survey of the Tendaho-Serdo-Asayita region, Central Afar, Ethiopia, Bull. geophys. Obs. Addis Ababa, 13, p.57-71.

SEARLE, R.C., GOUIN, P., 1972
Local earthquake phases observed at Addis Ababa, Ethiopia, Tectonophysics, 15, p.55-57.

SEARLE, R.C., ROSS, D.A., 1975
A geophysical study of the Red Sea axial trough between 20.5° and 22°N, Geophys. J. R. Astr. Soc., 43, p.555-572.

SELF, S., GUNN, B.M., 1976
Petrology, volume and age relations of alkaline volcanics from Terceira, Azores, Contrib. Mineral. Petrol., 54, p.293-313.

SEMENOV, A.M., 1969
Variations in the travel-time of transverse and longitudinal waves before violent earthquakes, Izv. Earth Phys., 4, p.72-77.

SHIMSHONI, M., SMITH, S.W., 1964
Seismic signal enhancement with three-component detectors, Geophysics, 29, p.664-671.

SHORT, N.M., LOWMAN, P.D.,Jr., FREDEN, S.C.,
FINCH, W.A.,Jr., 1976
Mission to Earth: LANDSAT views the world, NASA SP-360, Washington, D.C.

SHUEY, R.T., 1974
Comments on "Interpretation of gravity anomalies by non-linear optimization", Geophys. Prospect., 22, p.181-182.

SIGURDSSON, H., 1967
The Icelandic basalt plateau and the question of sial, in Björnsson, S., ed., Iceland and mid-ocean ridges, Soc. Sci. Islandica, 38, p.32-49.

SOMERVILLE, M.R., PEPPIN, W.A., Van WORMER, J.D., 1980
An earthquake sequence in the Sierra Nevada - Great Basin boundary zone: Diamond Valley, Bull. Seism. Soc. Am., 70, p.1547-1555.

SOWERBUTTS, W.T.C., 1969
Crustal structure of the East African plateau and rift valleys from gravity measurements, Nature, 223, p.143-146.

SPIES, O., 1965
Inclusion-bearing Pliocene peralkaline silicic ignimbrites from south-west of Mt. Ayelu, Southern Afar (Ethiopia), in Pilger, A., and Rösler, A., eds., Afar Depression of Ethiopia: Stuttgart, E. Schweizerbart'sche Verlagsbuchhandlung, p.334-340.

STAUDER, W., 1962
The focal mechanism of earthquakes, Adv. Geophys., 9, p.1-76.

STEIN, S., 1978
A model for the relation between spreading rate and oblique spreading, Earth Planet Sci. Lett., 39, p.313-318.

STEWART, S.W., 1977
Real-time detection and location of local seismic events in Central California, Bull. Seism. Soc. Am., 67, p.433-452.

STIELTJES, L., 1973
Evolution tectonique récente du Rift d'Asal, Revue Géogr. phys. Géol. dyn., 15, p.425-430.

STIELTJES, L., JORON, J.-L., TREUIL, M., VARET, J., 1976
Le rift de l'Asal, segment de dorsale émergé: discussion pétrologique et géochimique, Bull. Soc. géol. Fr., 18, p.851-862.

SUNDARALINGAM, K., 1971
Seismic investigation of the crust and upper mantle of East Africa, Ph.D. Thesis, University of Durham.

SUTEAU, A.M., WHITCOMB, J.H., 1979
A local earthquake coda magnitude and its relation to duration, moment M_o, and local Richter magnitude M_L, Bull. Seism. Soc. Am., 69, p.353-368.

SWARTZ, D.H., ARDEN, D.D., 1960
Geologic history of the Red Sea area, Bull. Am. Ass. Petrol. Geol., 44, p.1621-1637.

SYKES, L.R., 1970
Earthquake swarms and sea-floor spreading, J. Geophys. Res., 75, p.6598-6611.

SYKES, L.R., LANDISMAN, M., 1964
The seismicity of East Africa, the Gulf of Aden and the Arabian and Red Seas, Bull. Seism. Soc. Am., 54, p.1927-1940.

TAIEB, M., 1971
Aperçus sur les formations quaternaires et la néotectonique de la basse vallée de l'Aouache (Afar méridional, Ethiopie), C. R. Soc. Géol. France, 1971, p.63-65.

TAPPONNIER, P., VARET, J., 1974
La zone de Mak'arrasou en Afar: un équivalent émergé des "failles transformantes" oceaniques, C. R. Acad. Sci. Paris, D278, p.209-212.

TARANTOLA, A., RUEGG, J.-C., LÉPINE, J.-C., 1979
Geodetic evidence for rifting in Afar: a brittle-elastic model of the behaviour of the lithosphere, Earth Planet Sci. Lett., 45, p.435-444.

TARANTOLA, A., RUEGG, J.-C., LÉPINE, J.-C., 1980
Geodetic evidence for rifting in Afar, 2. Vertical displacements, Earth Planet Sci. Lett., 48, p.363-370.

TARLING, D.H., 1970
Palaeomagnetism and the origin of the Red Sea and Gulf of Aden, Phil. Trans. R. Soc. Lond., A267, p.219-226.

TAZIEFF, H., 1968
Relations tectoniques entre l'Afar et la mer Rouge, Bull. Soc. géol. Fr., 10, p.468-477.

TAZIEFF, H., 1970
The Afar triangle, Scient. Am., 222(2), p.32-40.

TAZIEFF, H., 1971
Sur la tectonique de l'Afar central, C. R. Acad. Sci. Paris, D272, p.1055-1058.

TAZIEFF, H., 1972
Tectonics of central Afar, J. Earth Sci. (Leeds), 8, p.171-182.

TAZIEFF, H., VARET, J., BARBERI, F., GIGLIA, G., 1972
Tectonic significance of the Afar (or Danakil) depression, Nature, 235, p.144-147.

THATCHER, W., HANKS, T.C., 1973
Source parameters of Southern California earthquakes, J. Geophys. Res., 78, p.8547-8576.

TOCHER, D., 1957
Anisotropy in rocks under simple compression, Trans. Am. geophys. Un., 38, p.89-94.

TORGE, W., 1975
Methods and accuracy considerations for positioning and height determination for extensive geophysical investigations, in Pilger, A., and Rösler, A., eds., Afar Depression of Ethiopia: Stuttgart, E. Schweizerbart'sche Verlagsbuchhandlung, p.145-150.

TRAMONTINI, C., DAVIES, D., 1969
A seismic refraction survey in the Red Sea, Geophys. J., 17, p.225-241.

TREUIL, M., JORON, J.L., 1975
Utilisation des éléments hygromagmatophiles pour la simplification de la modelisation quantitative des processus magmatiques. Exemples de l'Afar et de la dorsale medio-atlantique, Soc. Ital. Miner. Petr. Milano, 31, p.125-174.

TREUIL, M., JORON, J.L., 1976
Étude géochimique des éléments en trace dans le magmatisme de l'Afar. Implications pétrogénétiques et comparison avec le magmatisme de l'Islande et de la dorsale medio-atlantique, in Pilger, A., and Rösler, A., eds., Afar between continental and oceanic rifting: Stuttgart, E. Schweizerbart'sche Verlagsbuchhandlung, p.26-79.

TREUIL, M., VARET, J., 1973
Critères volcanologiques, pétrologiques et géochimiques de la genèse et de la différentiation des magmas basaltiques: exemple de l'Afar, Bull. Soc. géol. Fr., 15, p.5Ø6.

TRIFUNAC, M.D., 1972
Stress estimates for the San Fernando, California, earthquake of February 9, 1971: main event and thirteen aftershocks, Bull. Seism. Soc. Am., 62, p.721-75Ø.

TRYGGVASON, E., 1973
Seismicity, earthquake swarms, and plate boundaries in the Iceland region, Bull. Seism. Soc. Am., 63, p.1327-1348.

TSAI, N.C., 197Ø
A note on the steady-state response of an elastic half-space, Bull. Seism. Soc. Am., 6Ø, p.795-8Ø8.

TSUMURA, K., 1967
Determination of earthquake magnitude from total duration of oscillation, Bull. Earthquake Res. Inst., Tokyo Univ., 15, p.7-18.

TURCOTTE, D.L., OXBURGH, E.R., 1973
Mid-plate tectonics, Nature, 244, p.337-339.

U.N.D.P., 1973
Reports of the geology, geochemistry and hydrology of hot springs of the East African rift system within Ethiopia, U.N. Tech. Rpt. DP/SF/UN/116, New York: United Nations.

UN / ETHIOPIAN GOVT., no date
Preliminary study of feasibility of establishing a geothermal power plant to generate power for T.P.S.C., unpublished.

USGS
Preliminary Determination of Epicentres (monthly listings). United States Department of the Interior Geological Survey, National earthquake information service, Washington.

UTSU, T., 1966
A statistical significance test of the difference in b-value between two earthquake groups, J. Phys. Earth, 14, p.37-40.

VALETTE, J.N., 1975
Geochemical study of Lake Asal and Ghoubet el Kharab (T.F.A.I.), in Pilger, A., and Rösler, A., eds., Afar Depression of Ethiopia: Stuttgart, E. Schweizerbart'sche Verlagsbuchhandlung, p.239-250.

Van NGOC, P., BOYER, D., Le MOUEL, J.-L., COURTILLOT, V., 1981
Identification of a magma chamber in the Ghoubbet-Asal rift (Djibouti) from a magnetotelluric experiment, Earth Planet Sci. Lett., 52, p.372-380.

VARET, J., BARBERI, F., 1976
Trace des frontières de plaques en Afar: discussion à partir de données volcanologiques, Bull. Soc. géol. Fr., 18, p.831-836.

VARGA, R.S., 1962
Matrix interactive analysis, Prentice-Hall, Inc., Englewood Cliffs, N.J.

VILLARI, L., 1974
The Island of Pantellaria, Bull. Volcan., 38, p.680-724.

VINE, F., 1966
Spreading of the ocean floor: new evidence, Science, 154, p.1405-1415.

VOGT, P.R., 1974
Volcano spacing, fractures, and thickness of lithosphere, Earth Planet Sci. Lett., 21, p.235-252.

WEAVER, S.D., 1976-77
The Quaternary caldera volcano Emuruangogolak, Kenya rift, and the petrology of a bimodal ferrobasalt-pantelleritic trachyte association, Bull. Volcan., 40, p.209-230.

WHITE, J.E., 1964
Motion product seismograms, Geophysics, 29, p.288-298.

WHITEMAN, A.J., 1968
Formation of the Red Sea depression, Geol. Mag., 105, p.231-246.

WILLMORE, P.L., HALES, A.L., GANE, P.G., 1952
A seismic investigation of the crustal structure in the Western Transvaal, Bull. Seism. Soc. Am., 42, p.53-80.

WOHLENBERG, J., 1968
Seismizität der ostafrichaniscken Grabenzonen zwichen 4°N und 12°S sowie 23°E und 40°E, Munchen, Inaugural Dissertation, Ludwig-Maximilians Universität.

WYSS, M., 1973
Towards a physical understanding of the earthquake frequency distribution, Geophys. J., 31, p.341-359.

WYSS, M., HANKS, T.C., 1972
The source parameters of the San Fernando earthquake inferred from teleseismic body waves, Bull. Seism. Soc. Am., 62, p.591-602.

ZANETTIN, B., JUSTIN-VISENTIN, E., 1974
The volcanic succession in central Ethiopia. 2 - The volcanics of the western Afar and Ethiopian rift margins, Mem. Ist. Geol. Miner. Univ. Padua, 31, p.1-20.

ZANETTIN, B., JUSTIN-VISENTIN, E., 1975
Tectonical and volcanological evolution of the Western Afar margin, in Pilger, A., and Rösler, A., eds., Afar Depression of Ethiopia: Stuttgart, E. Schweizerbart'sche Verlagsbuchhandlung, p.300-309.